Mise en place des écoulements granulaires volcaniques Apport du couplage terrain / modélisation numérique

Karim Kelfoun

▶ **To cite this version:**

Karim Kelfoun. Mise en place des écoulements granulaires volcaniques Apport du couplage terrain / modélisation numérique. Volcanologie. Université Blaise Pascal (Clermont Ferrand 2), 2012. tel-03621769

HAL Id: tel-03621769
https://uca.hal.science/tel-03621769

Submitted on 28 Mar 2022

HAL is a multi-disciplinary open access archive for the deposit and dissemination of scientific research documents, whether they are published or not. The documents may come from teaching and research institutions in France or abroad, or from public or private research centers.

L'archive ouverte pluridisciplinaire **HAL**, est destinée au dépôt et à la diffusion de documents scientifiques de niveau recherche, publiés ou non, émanant des établissements d'enseignement et de recherche français ou étrangers, des laboratoires publics ou privés.

Université Blaise Pascal, Clermont-Ferrand, Ecole Doctorale des Sciences Fondamentales

n° d'ordre : 352

Mémoire présenté en vue de l'obtention de l'Habilitation à Diriger des Recherches

par

Karim Kelfoun

Maître de Conférences de l'Université Blaise Pascal,
Laboratoire Magmas et Volcans UMR UBP – CNRS – IRD

Mise en place des écoulements granulaires volcaniques Apport du couplage terrain / modélisation numérique

soutenu le 22 juin 2012,

devant le jury composé de :

Pr. Marcus Bursik	– Rapporteur, University of Buffalo (USA).
Pr. Tim Druit	– Responsable tutélaire, Université Blaise Pascal.
Pr. Claude Jaupart	– Examinateur, Institut de Physique du Globe de Paris.
Pr. Anne Mangeney	– Rapporteur, Institut de Physique du Globe de Paris.
Pr. Benjamin van Wyk de Vries	– Rapporteur, Université Blaise Pascal.

Sommaire

Table des matières
Avant-propos et remerciements
Résumé
Summary

Partie I - Synthèse des travaux de recherche

1. Introduction 2
1.1. Problématiques scientifiques 2
1.2. Contenu du mémoire 3
2. Phénoménologie des écoulements étudiés 4
2.1. Les écoulements pyroclastiques 4
2.2. Les écoulements pyroclastiques dilués 5
2.3. Les avalanches de débris 5
2.4. Les tsunamis associés 5
3. Le logiciel de simulation numérique *VolcFlow* 7
3.1. La version 1-fluide 7
3.1.1. Equations constitutives 7
3.1.2. Schéma numérique 8
3.1.3. Fonctionnement de VolcFlow 9
3.2. La version 2-fluides : écoulement dense / tsunami 12
3.3. La version 2-fluides : écoulement dense / déferlante 13
4. Rhéologie et mise en place des avalanches de débris 17
4.1. Modélisation numérique de l'avalanche de débris de Socompa 17
4.2. Affinement de la mise en place par imagerie et études de terrain 19
4.3. Affinement de la mise en place par géochimie isotopique fine 21
4.4. Généralisation des conclusions 25
5. Simulation numérique des avalanches de débris et des tsunamis associés 26
5.1. Tsunami engendré par une déstabilisation du Piton de la Fournaise 26
5.2. Effondrement de Güìmar : validation du modèle à partir de mesures de dépôts de tsunamis 28
5.3. Autres travaux 30
6. Simulation des écoulements pyroclastiques du volcan Tungurahua (Equateur) 31
6.1. L'éruption d'août 2006 du volcan Tungurahua 31
6.2. Autres simulations d'écoulements pyroclastiques denses 34
7. Simulation des écoulements denses et dilués 35
8. Morphologie des dépôts 37
9. *VolcFlow* : un outil d'évaluation des aléas volcaniques par modélisation numérique ? 40
10. Généralisation et limites du comportement plastique 44
11. Tentative d'explication de la rhéologie plastique 47
12. Perspectives 49
13. Bibliographie 52

Partie II – Publications

Liste de toutes mes publications (depuis le post-doctorat)..... 58

Ecoulements pyroclastiques

1. **Kelfoun K.**, P. Samaniego, P. Palacios, D. Barba, 2009, Testing the suitability of frictional.....61
behaviour for pyroclastic flow simulation by comparison with a well-constrained eruption at Tungurahua volcano (Ecuador). *Bull. Volcanol.*, 71(9), 1057-1075, DOI: 10.1007/s00445-009-0286-6.
2. Roche O., J.C. Phillips, **K. Kelfoun**, *sous presse*, Pyroclastic density currents. *Modeling*.....81
Volcanic Processes (Eds. S.A. Faggents, T.K.P. Gregg, R.C.M. Lopes), Cambridge University Press, p. 321 5
3. Dartevelle S., Rose W. I., Stix J., **Kelfoun K.**, Vallance J. W., 2004: Numerical modeling of.....107
geophysical granular flows: 2. Computer simulations of plinian clouds and pyroclastic flows and surges. *Geochem. Geophys. Geosyst., Vol. 5, No. 8*
4. Legros F., **Kelfoun K.**, 2000: Sustained blasts during large volcanic eruptions*, Geology, v.28,*.....143
n°10: 895-898.
5. Legros F., **Kelfoun K.**, 2000: On the ability of pyroclastic flows to scale topographic obstacles.....147
J. Volcanol. Geoth. Res., 98 : 235-241.

Avalanche de débris

6. **Kelfoun K.**, 2011, Suitability of simple rheological laws for the numerical simulation of dense.....155
pyroclastic flows and long−runout volcanic avalanches, *J. Geophys. Res.*, Solid Earth, doi:10.1029/ 2010JB007622.
7. **Kelfoun K.** and T. Davies, 2011, "Comment on "A random kinetic energy model for rock.....169
avalanches: Eight case studies" T. Preuth, P. Bartelt, O. Korup, and B. W. McArdell.", *J. Geophys. Res.*, doi:10.1029/2010JF001916.
8. Pouget S., Davies T., Kennedy B., **Kelfoun K.** and Leyrit H., 2012, Numerical modelling: a.....173
useful tool to simulate collapsing volcanoes, *Geology Today*, 28 (2), 59-63.
9. Davies T., M. McSaveney, **K. Kelfoun**, 2010, Runout of the Soccompa volcanic debris.....179
avalanche, Chile: a mechanical explanation for low basal shear resistance. *Bull. Volcanol.* 72 (8), page 933 : doi 10.1007/s00445-010-0372-9
10. **Kelfoun K.**, T.H. Druitt, B. van Wyk de Vries, M.–N. Guilbaud, 2008, Topographic reflection.....191
of Socompa debris avalanche, Chile, *Bull. Volcanol.* , doi: 10.1007/s00445-008-0201-6
11. **Kelfoun K.** and T.H. Druitt, 2005, Numerical modelling of the emplacement of the 7500 BP.....211
Socompa rock avalanche, Chile. *J. Geophys. Res.*, B12202, doi : 10.1029/2005JB003758, 2005.

Tsunami

12. **Kelfoun K.**, T. Giachetti, P. Labazuy, 2010, Landslide–generated tsunamis at Réunion Island,.....225
J. Geophys. Res., Earth Surface, doi:10.1029/2009JF001381
13. Giachetti T, Paris R, **Kelfoun K**, Ontowirjo B., 2012*,* Tsunami hazard related to a flank.....243
collapse of Anak Krakatau volcano, Sunda Strait, Indonesia. *Special Publications of the Geological Society*, 361, 79-90, doi: 10.1144/SP361.7.
14. Dondin F., Lebrun J.-F., **Kelfoun K.**, Fournier N. and Randrianasolo A., 2012, Sector collapse.....255
at Kick 'em Jenny submarine volcano (Lesser Antilles): numerical simulation and landslide behaviour. *Bull Volcanol*, doi : 10.1007/s00445-011-0554-0.
15. Giachetti T, Paris R, **Kelfoun K**, Pérez-Torrado FJ., 2011*,* Numerical modelling of the tsunami.....269
triggered by the Güìmar debris avalanche, Tenerife (Canary Islands): comparison with field-based data. *Marine Geology*. doi: 10.1016/j.margeo.2011.03.018

Rapport sur l'estimation des menaces volcaniques du Tungurahua par simulation numérique.....283
(en Espagnol)

.

Avant-propos et remerciements

Au début de mon doctorat, pendant ma première mission sur le volcan Merapi, j'avais été impressionné par la dynamique complexe des écoulements pyroclastiques que j'ai cherché à comprendre en analysant leurs dépôts ainsi que leurs effets sur la végétation, les bâtiments et la population. Cependant, les trois ans d'une thèse et les moyens informatiques de l'époque ne rendaient pas réaliste l'écriture d'un code de simulation de ces phénomènes. J'ai débuté les premières simulations d'écoulements pyroclastiques par l'approche multiphasée pendant mon post-doctorat au Laboratoire National de Los Alamos (LANL, USA) et à l'Institut des Sciences de la Terre de Barcelone (ICT). Mon recrutement à l'Université Blaise Pascal m'a permis de développer réellement mes recherches sur les écoulements granulaires volcaniques en étendant le champ d'étude aux avalanches de débris, terrestre et sous-marines, dont la dynamique me semble proche de celle des écoulements pyroclastiques denses. Parallèlement à l'observation et aux mesures de terrain, j'ai ainsi conçu un code numérique d'écoulements dédié à la compréhension des phénomènes naturels.

Les travaux résumés dans ce mémoire ont été accomplis au cours de mon post-doctorat et depuis mon recrutement à l'Université Blaise Pascal. Les publications relatives à mes travaux sur les écoulements volcaniques sont présentées dans la partie II.

Mes recherches ont bénéficié de collaborations fructueuses, et je souhaite témoigner ma gratitude aux personnes avec qui j'ai eu le plaisir de travailler au cours de ces dernières années : mes responsables de post-doctorat, Greg Valentine (LANL) et Joan Marti (ICT-CSIC), mes collègues du Laboratoire Magmas et Volcans et d'autres laboratoires français, dont Tim Druitt, Olivier Roche, Thomas Giachetti, Régis Doucelance, Philippe Labazuy, David Jessop, Anne Mangeney, Pablo Samaniego, Benjamin van Wyk de Vries, Raphael Paris, Nathalie Thomas, François Legros, Claude Robin, Alain Gourgaud - mon directeur de doctorat - et beaucoup d'autres, ainsi que mes collègues d'Amérique du Sud et plus particulièrement ceux de l'IG et de l'IRD, en Equateur.

Résumé

Les écoulements pyroclastiques et les avalanches de débris sont constitués de particules dont les tailles varient de celles des cendres fines à celles de blocs souvent supérieurs au mètre cube. Ces mélanges de particules, qui interagissent probablement avec des gaz volcaniques et atmosphériques, ont un comportement physique particulièrement complexe. Un des défis majeurs est d'expliquer par quels mécanismes ils deviennent si fluides, capables de s'écouler sur de grandes distances (plusieurs kilomètres à dizaines de kilomètres) avec des épaisseurs relativement faibles (quelques décimètres à dizaines de mètres).

Pour cerner le comportement rhéologique global de tels écoulements, l'approche menée dans ce mémoire consiste à sélectionner des évènements naturels suffisamment bien préservés ou observés pour avoir le maximum de contraintes possibles sur les conditions initiales : débit, volume, topographie, direction d'écoulement, etc. Puis, ces écoulements sont reproduits par simulation numérique en testant des modèles simples de comportement (Coulomb, visqueux, Bingham, etc.), le modèle retenu étant celui qui reproduit au mieux les phénomènes naturels (épaisseurs, extensions, distances atteintes, vitesses, etc.)

Toutes les simulations réalisées convergent vers la même conclusion : les écoulements granulaires naturels ne se comportent pas comme des écoulements granulaires en laboratoire. Ils ne suivent pas une loi Coulomb quelle que soit la valeur de l'angle de frottement utilisée. En revanche, un comportement plastique donne souvent des résultats très proches de la réalité. Il permet de reproduire la mise en place de la plupart des avalanches de débris et des écoulements pyroclastiques étudiés. Il reproduit la morphologie à lobes et levées souvent observée sur le terrain. Il explique aussi les structures de l'avalanche de Socompa (Chili) et fournit un cadre dynamique permettant d'aller plus loin dans la compréhension de la formation des avalanches par des études de terrains de détails et des études de géochimie fine.

Si le comportement plastique reproduit si bien les écoulements naturels, c'est que leur physique est très probablement essentiellement contrôlée par une relation entre l'épaisseur des écoulements et leur capacité à s'écouler. En revanche, cette relation est loin d'être comprise. Les conclusions des travaux présentés ici démontrent la nécessité d'affiner et surtout de comprendre ce comportement général. Il faudra développer des modèles numériques des interactions à l'échelle particules/gaz afin d'éviter au maximum les hypothèses sur une rhéologie globale encore trop mal comprise. Pour s'assurer que les nouveaux modèles reproduiront correctement la réalité, un effort important devra être mené pour obtenir les données de terrain les plus quantifiées possibles sur les écoulements naturels.

Summary

Pyroclastic flows and debris avalanches are formed by particles that vary in size from fine ashes to blocks often larger than a cubic meter. These particle mixtures, which probably also interact with atmospheric and volcanic gases, are very complex physically. One of the major challenges is to explain the mechanism by which they become so fluid and are able to flow over large distances (several kilometres to tens of kilometres) at relatively low thickness (some decimetres to tens of meters).

The approach used here to define the overall rheological behaviour of such flows is to select certain natural events, which are well preserved and/or well described, and to obtain the maximum information on their initial conditions: mass rate, volume, topography, flow direction, etc. These flows are then reproduced by numerical simulation using various models of rheological behaviour, such as Coulomb, viscous and Bingham. The best rheological model is the one which most closely reproduces the natural event in terms of thickness, extension, runout, velocity, etc.

All the simulations carried out here point to the same conclusion: natural long-runout flows do not behave in the same way as laboratory-generated granular flows. They do not follow a Coulomb law no matter what value of friction angle is used. However plastic behaviour produces results which are often very close to reality, allowing the emplacement of most of the debris avalanches and pyroclastic flows studied to be reproduced, as well as the lobe and levee morphology often observed in the field. It also explains the structures and morphology of the Socompa avalanches (Chile) and establishes a dynamic framework on which to further our understanding of avalanche genesis gained from field, imagery and geochemical studies.

The reason why plastic behaviour is successful in reproducing natural flows is because its physics is governed by the relationship between flow thickness and flow capacity. However, this relationship is far from being well understood. The conclusions of the work presented here demonstrate the necessity to refine and in particular to improve our understanding of the overall flow behaviour. We need to develop numerical models of particle-gas interactions in order to avoid evoking poorly understood hypotheses. Finally, to ensure that the models are able to reproduce reality to a high degree of accuracy, a concerted effort should be made in the future to obtain field data on natural flows which is as quantified as possible.

Partie 1

Synthèse des travaux de recherche

1. Introduction

1.1. Problématiques scientifiques

Les écoulements pyroclastiques, les avalanches de débris et les lahars sont des écoulements volcaniques appelés « granulaires » car constitués de particules rocheuses. Ces particules interagissent probablement avec des fluides : eau, gaz volcaniques, atmosphère. Ces écoulements granulaires représentent une menace très importante pour les populations de nombreuses zones volcaniques comme, par exemple, en Amérique du Sud et centrale (Colombie, Equateur, etc.), aux Antilles (Montserrat, Guadeloupe, Martinique, etc.) et en Asie du Sud-Est (Indonésie, Philippines, Japon. Ils peuvent affecter durablement les infrastructures et l'activité économique des zones concernées. L'un des objectifs de la volcanologie est donc de déterminer le plus précisément possible les zones qui seront touchées par tel ou tel type d'écoulements afin d'aider à la mise au point de plans d'évacuation et à la construction d'ouvrages de protection.

L'approche généralement utilisée pour l'établissement de cartes d'aléas consiste à étudier l'activité volcanique historique ainsi que les dépôts des écoulements volcaniques passés. On en déduit alors les activités caractéristiques de l'édifice étudié ainsi que les zones qu'elles menacent. Depuis les années 1980 et le développement du calcul numérique, une voie s'est ouverte vers la modélisation numérique des écoulements volcaniques. L'avantage de l'outil numérique réside dans l'espoir d'une meilleure précision des prévisions : connaissant les conditions à la source (volumes, débits, nature des roches/laves, etc.) et les caractéristiques de la zone étudiée (topographie, nature des sols, type de végétation, etc.) il devrait être théoriquement possible de prédire l'extension, l'épaisseur, la vitesse, la température, et les autres caractéristiques du ou des futurs écoulements. Il serait alors possible de prévoir l'importance des dégâts, de déterminer les temps d'évacuation, de construire des infrastructures de protection adaptées : barrage, voies d'évacuation, bâtiments protégés, etc.

Cependant, la physique des écoulements granulaires volcaniques est complexe. Or, sans une caractérisation suffisamment précise de cette physique, les modèles numériques d'écoulements sont inutilisables quelle que soit la qualité des schémas numériques utilisés. Mais comment déterminer cette physique de premier ordre ? L'approche la plus rigoureuse consiste à décrire mathématiquement les lois censées régir ce type d'écoulements, puis à mettre les lois obtenues dans des modèles pour simuler le phénomène macroscopique. Les écoulements naturels étant trop imprévisibles et difficiles d'accès nous manquons souvent d'observations précises et quantifiées, et les lois sont généralement validées à partir d'écoulements simples produits en laboratoire. Actuellement, cette approche est limitée par plusieurs facteurs. Premièrement, parce que la physique des écoulements naturels est particulièrement complexe et aucun modèle mathématique n'est capable de la décrire pour le moment. Même le comportement d'écoulements simples, constitués uniquement de billes de verre aux caractéristiques identiques, est complexe et ne fut mis en équation que très récemment (Pouliquen, 1999 ; Pouliquen et Forterre, 2002). Deuxièmement, la validation se base généralement sur le postulat que les écoulements de laboratoire reproduisent les caractéristiques des écoulements

naturels. Or, il faut être particulièrement prudent avec cette analogie : certaines caractéristiques naturelles semblant impossibles à reproduire en laboratoire, probablement parce que l'échelle des évènements (quelques décimètres cube en laboratoire / plusieurs millions de mètres cube sur le terrain) est un paramètre clé dans la dynamique.

La seconde approche consiste à déterminer empiriquement les lois les mieux adaptées pour la simulation des écoulements granulaires volcaniques, en confrontant les écoulements et les dépôts numériques obtenus grâce à différentes rhéologies à des données de terrain. La ou les meilleures rhéologies sont celles qui reproduisent le mieux le phénomène naturel : vitesses, épaisseurs des dépôts, extensions, morphologies, etc. Pour tester objectivement les résultats obtenus, il faut donc obtenir des données de terrain les plus quantifiées possibles. Parallèlement, il est nécessaire d'interpréter les résultats numériques en s'aidant de l'observation des phénomènes naturels afin de trouver une explication mécanique aux rhéologies empiriques obtenues.

Les deux approches doivent bien sûr être menées en parallèle mais c'est la seconde qui a essentiellement guidé l'ensemble des travaux que je présente dans ce mémoire.

1.2. Contenu du mémoire

Après une définition des phénomènes étudiés, le mémoire présente le code de simulation numérique *VolcFlow* et ses différentes versions. Le mémoire est ensuite structuré autour des phénomènes étudiés : avalanches de débris, tsunamis associés à leur entrée en mer, écoulements pyroclastiques denses et dilués. Les différentes techniques utilisées y sont détaillées : études de terrain, levés Lidar, géochimie, modélisation, etc. La suite est dédiée aux capacités et limites de *VolcFlow* pour l'estimation des menaces volcaniques. La dernière section de la première partie du mémoire discute des meilleures lois de comportement obtenues en comparant données naturelles et résultats numériques ainsi que des interprétations possibles et des implications sur la dynamique des écoulements volcaniques.

La seconde partie du mémoire rassemble les principaux articles scientifiques que j'ai écrits ou coécrits dans des revues internationales. Toutes les références bibliographiques relatives au sujet ne figurent pas dans la première partie du manuscrit. Le lecteur peut se référer à la bibliographie des articles de la seconde partie pour une bibliographie plus exhaustive.

2. Phénoménologie des écoulements étudiés

2.1. Les écoulements pyroclastiques

Les écoulements pyroclastiques sont des courants de densité constitués de blocs, de scories, de cendres et de gaz. Emis par les volcans, suite à des explosions, des effondrements de colonnes éruptives ou des effondrements de dômes de lave (Sparks et Wilson, 1976 ; Mellors et al., 1988 ; Cole et al., 2002), ils dévalent les pentes à des vitesses de plusieurs dizaines de mètres par secondes jusqu'à des distances de plusieurs kilomètres à plusieurs dizaines de kilomètres. Ils sont généralement classés en deux types : les écoulements denses et les écoulements dilués (Sparks et al., 1973 ; Walker et Wilson, 1983 ; Valentine et Fisher, 1986).

Les **écoulements pyroclastiques denses** (Nairn and Self, 1978 ; Hoblitt, 1986 ; Lube et al., 2007) sont constitués de particules allant de la taille des cendres (<< 1 mm) à des blocs de quelques décimètres cube voire mètres cube. Les particules restent très proches les unes des autres pendant l'écoulement : les écoulements ont donc une densité du même ordre de grandeur que celle des particules qui les constituent et leur épaisseur est proche de celle des dépôts. Les écoulements denses présentés dans ce mémoire ont des volumes de quelques millions de mètres cubes. Ils sont issus d'effondrement de colonnes éruptives ou de dômes de lave, sont généralement peu épais (< 1 m) et sont canalisés au fond des vallées. Ils couvrent des zones relativement limitées mais détruisent presque tout ce qu'ils recouvrent.

Figure 1 : éruption du Volcan Merapi (Indonésie) en 1994. L'écoulement dense, canalisé dans les rivières, est recouvert par la déferlante qu'il a créé et n'est pas visible sur l'image. L'écoulement dilué est indiqué par *déferlante*. La partie convective se situe au dessus de la déferlante et s'élève dans l'atmosphère.

2.2. Les écoulements pyroclastiques dilués

Les **écoulements dilués** (ou **déferlantes pyroclastiques** ou « **surges** », Figure 1) sont constitués de particules fines (< 1 mm) maintenues en suspension par des gaz turbulents (Sparks et al., 1978 ; Bursik et Woods, 1996 ; Dade et Huppert, 1996). Les particules interagissent moins que dans les écoulements denses. La densité de ces écoulements est faible (<1-10 kg/m^3) et les dépôts sont minces (souvent de quelques dizaines de centimètres) par rapport à l'épaisseur de l'écoulement (plusieurs dizaines de mètres). Les déferlantes étudiées dans ce mémoire sont engendrées par les écoulements denses et la mise en suspension de particules les plus fines de leur surface. Les déferlantes sont moins destructives pour les bâtiments que les écoulements denses. En revanche, elles sont particulièrement mobiles et s'échappent facilement des vallées, rendant ces phénomènes particulièrement menaçants pour les populations.

2.3. Les avalanches de débris

Les édifices volcaniques sont instables : ils se construisent rapidement à l'échelle géologique et leurs pentes sont à la limite de stabilité naturelle (30°-35°). Ils sont constitués de roches souvent affaiblies par l'altération des gaz volcaniques, subissent les pressions du système magmatique et sont situés dans des zones souvent sismiquement actives. Une avalanche de débris se produit lorsqu'un flanc de l'édifice volcanique cède, se démantèle en un mélange de cendres et de blocs pouvant atteindre plusieurs centaines de mètres cubes (Voigth et al., 1981 ; Siebert, 1984 ; Melosh, 1990) puis s'écoule sur plusieurs kilomètres. Les avalanches de débris sont épaisses de plusieurs dizaines de mètres et leurs vitesses d'écoulement peuvent atteindre les 100 m/s. Depuis l'éruption du Mont St Helens en 1980, la communauté volcanologique a réinterprété les dépôts volcaniques, prenant conscience que les avalanches de débris sont des phénomènes courants, qui peuvent se produire plusieurs fois à l'échelle de l'histoire d'un volcan (Moore et al., 1989; Normark et al., 1993; Holcomb and Searle, 1991; McMurtry et al., 2004).

Les distances atteintes par les avalanches de débris sont 5 à 10 fois plus grandes que leur hauteur de chute. Leurs dépôts sont généralement épais de quelques dizaines de mètres et couvrent des surfaces de plusieurs kilomètres carrés. Ces caractéristiques indiquent une grande « fluidité » de ces phénomènes dont l'origine fait débat. Le terme matrice est utilisé dans la suite du mémoire pour définir la phase constituée de particules fines qui ennoie généralement les blocs plus volumineux et semble jouer un rôle majeur dans la fluidité des écoulements.

2.4. Les tsunamis associés

Des nombreux édifices volcaniques se situent à proximité de la mer ou de lacs. L'entrée dans l'eau des écoulements granulaires peut engendrer des déplacements d'eau d'autant plus puissants que les débits massiques sont importants (e.g. Keating and McGuire, 2000; Ward, 2001; Harbitz et al., 2006).

Les vagues vont alors se propager formant un tsunami. La prise en compte du couplage eau/avalanche est nécessaire pour tester si les rhéologies obtenues pour les écoulements aériens sont similaires à celles obtenues dans l'eau, pour évaluer tous les aspects du risque volcanique et aussi pour tenter de reconstituer les caractéristiques des écoulements à partir des dépôts de tsunamis, témoins des hauteurs de vagues engendrées.

3. Le logiciel de simulation numérique *VolcFlow*

VolcFlow a été écrit dans l'objectif de simuler des écoulements granulaires volcaniques naturels sur topographie réelle. Les calculs sont basés sur le principe de moyennement vertical des équations de bilan de masse et de quantité de mouvement (voir Kelfoun et Druitt, 2005, pour plus de détails).

Son originalité réside dans son schéma numérique qui a été pensé pour pouvoir simuler le maximum de rhéologies possibles. *VolcFlow* peut ainsi simuler des écoulements visqueux, turbulents, plastiques, frictionnels, etc. ainsi que tout autre comportement défini par l'utilisateur dont le frottement est fonction de la vitesse et/ou de l'épaisseur de l'écoulement. *VolcFlow* n'est donc pas limité à un seul type de rhéologie simple et, par conséquent, est bien adapté à la simulation des écoulements naturels dont le comportement rhéologique est complexe et reste difficile à caractériser.

J'ai développé trois versions de *VolcFlow*. La première, celle que je distribue, simule la mise en place d'un seul type d'écoulement de densité constante. Elle permet de simuler les écoulements pyroclastiques denses, les avalanches de débris, les écoulements d'eau, etc. La deuxième version simule deux écoulements de densité constante et leurs interactions. Elle est utilisée pour simuler l'entrée en mer d'écoulements volcaniques et la genèse de tsunamis associés. La troisième version est capable de simuler le comportement de deux écoulements dont la densité peut varier. Elle permet de simuler les écoulements pyroclastiques denses et dilués ainsi que leurs interactions.

Ce code est désormais utilisé par plus de cinquante personnes un peu partout dans le monde, pour des recherches fondamentales ou pour des études plus appliquées (observatoires volcanologiques d'Equateur, de Colombie, évaluation des menaces au Japon, etc.). Un « manuel d´utilisation » existe sous la forme d´un site internet :

http://wwwobs.univ-bpclermont.fr/lmv/pperm/kelfoun_k/VolcFlow/VolcFlow.html

3.1. La version 1-fluide

3.1.1. Equations constitutives

Les équations de *VolcFlow* sont définies dans un système de coordonnées liées à la topographie, les axes x et y étant localement parallèles au sol et h perpendiculaire. La version 1-fluide de *VolcFlow* résout les équations de bilan de masse (1) et de quantité de mouvement (2, 3) moyennée en épaisseur.

$$\frac{\partial h}{dt}+\frac{\partial}{\partial x}\left(hu_x\right)+\frac{\partial}{\partial y}\left(hu_y\right)=0 \qquad [1]$$

$$\frac{\partial}{\partial t}\left(hu_x\right)+\frac{\partial}{\partial x}\left(hu_x^2\right)+\frac{\partial}{\partial y}\left(hu_xu_y\right)=gh\sin\alpha_x-\frac{1}{2}k_{actpass}\frac{\partial}{\partial x}\left(gh^2\cos\alpha\right)+\frac{T_x}{\rho} \qquad [2]$$

$$\frac{\partial}{\partial t}\left(hu_y\right)+\frac{\partial}{\partial x}\left(hu_yu_x\right)+\frac{\partial}{\partial y}\left(hu_y^2\right)=gh\sin\alpha_y-\frac{1}{2}k_{actpass}\frac{\partial}{\partial y}\left(gh^2\cos\alpha\right)+\frac{T_y}{\rho} \qquad [3]$$

où h est l'épaisseur de l'écoulement, $\mathbf{u} = \left(u_x, u_y\right)$ sa vitesse, α la pente topographique, ρ sa densité, **T** la contrainte résistante, k_{actpass} le rapport des contraintes parallèles sur les contraintes normales (earth-pressure coefficient). Les indices indiquent les composantes dans les directions x et y. Les autres paramètres sont définis dans Kelfoun et Druitt (2005).

La rhéologie de l'écoulement est définie en modifiant l'expression de **T** (et éventuellement k_{actpass}).

Pour un matériau frictionnel sec (du sable par exemple), la contrainte résistante s'écrit :

$$T_x = -\rho h\left(g\cos\alpha + \frac{\mathbf{u}^2}{r}\right)\tan\varphi_{bed}\frac{u}{\|\mathbf{u}\|} \qquad [4]$$

où φ_{bed} est l'angle de frottement entre l'écoulement et le sol et r représente la courbure locale de la topographie. Si le matériau possède une friction interne, k_{actpass} est définie par (Iverson et Denlinger, 2001):

$$k_{actpass} = 2\frac{1\pm\left[1-\cos^2\varphi_{\text{int}}\left(1+\tan^2\varphi_{bed}\right)\right]^{1/2}}{\cos^2\varphi_{\text{int}}} - 1 \qquad [5]$$

où φ_{int} est l'angle de frottement interne. Cette expression est valide pour $\varphi_{\text{bed}}<\varphi_{\text{int}}$. Le signe ± est négatif (et k_{actpass} actif) lorsque l'écoulement est localement divergent. Il est positif (et k_{actpass} passif) lorsque l'écoulement converge localement. Si $\varphi_{\text{bed}}\geq\varphi_{\text{int}}$, k_{actpass} est calculé par :

$$k_{actpass} = \frac{1+\sin^2\varphi_{\text{int}}}{1-\sin^2\varphi_{\text{int}}} \qquad [6]$$

Dans le modèle plastique, souvent utilisé dans la suite de ce manuscrit, la contrainte résistante est constante et opposée au déplacement. Elle est simplement définie par :

$$T_x = \text{- constant}\times\frac{u_x}{\|\mathbf{u}\|} \quad \text{ou} \quad \|\mathbf{T}\| = \|Tx + Ty\| = \text{constant} \qquad [7]$$

L'expression des lois simples les plus couramment utilisées en simulation d'écoulement est donnée dans le tableau 1.

3.1.2. Schéma numérique

Les équations sont résolues en utilisant un double schéma numérique Eulérien « upwind » décentré. Le schéma reproduit précisément les chocs, les détentes et les sauts hydrauliques. Il est stable sur topographie plane et complexe ainsi que sur des surfaces numériquement 'humides' et 'sèches' sans ajouter d'épaisseurs artificielles. Le domaine de calcul est divisé en mailles rectangulaires. Les variables scalaires sont définies au centre des mailles, les vecteurs sur les bordures x et y.

Table 1: Expressions mathématiques des lois rhéologiques sous leurs formes moyennées verticalement.

Type de loi	Equation
Coulomb	$\mathbf{T} = \rho h \left(g \cos\alpha + \frac{\mathbf{u}^2}{r} \right) \tan\varphi_{\text{bed}} \frac{\mathbf{u}}{\|\mathbf{u}\|}$
(un angle, deux angles)	$\left(k_{\text{act/pass}} = 1, \qquad k_{\text{act/pass}} = 2 \frac{1 \pm \left[1 - \cos^2\varphi_{\text{int}} \left(1 + \tan^2\varphi_{\text{bed}} \right) \right]^{1/2}}{\cos^2\varphi_{\text{int}}} - 1 \right)$
Viscous	$\mathbf{T} = 3\mu \frac{\mathbf{u}}{h}$
Voellmy (Coulomb + u^2–term)	$\mathbf{T} = \rho h \left(g \cos\alpha + \frac{\mathbf{u}^2}{r} \right) \tan\varphi_{\text{bed}} \frac{\mathbf{u}}{\|\mathbf{u}\|} + \xi\rho \|\mathbf{u}\| \times \mathbf{u}$
Plastic (constant retarding stress)	$\mathbf{T} = T_0 \frac{\mathbf{u}}{\|\mathbf{u}\|}$
Plastic + u^2–term	$\mathbf{T} = T_0 \frac{\mathbf{u}}{\|\mathbf{u}\|} + \xi\rho \|\mathbf{u}\| \times \mathbf{u}$
Bingham (plastic + viscous)	$\mathbf{T} = T_0 \frac{\mathbf{u}}{\|\mathbf{u}\|} + 3\mu \frac{\mathbf{u}}{h}$

ρ : masse volumique ; h : épaisseur; g : accélération de la pesanteur; α : pente; $\mathbf{u}$: vitesse moyenne; r : courbure; φ_{bed} : angle de frottement basal; φ_{int} : angle de frottement interne; $k_{\text{act/pass}}$: coefficient d'anisotropie des pressions; μ : viscosité; T_0 : seuil de plasticité; ξ : coefficient de la loi de Voellmy.

Pour permettre une plus grande souplesse des calculs et l'ajout de fonction supplémentaires par l'utilisateur, la résolution du système des équations 1, 2 et 3 (Figure 2) a été divisée en trois étapes. La première étape consiste à calculer les vitesses aux bordures à partir des contraintes engendrées par les variations de pression interne à l'écoulement, par son poids et par les frottements (sur le sol dans la version monofluide, au sol et en surface pour la partie inférieure du modèle deux-fluides). La seconde étape consiste à calculer les variations d'épaisseur et de quantité de mouvement aux centres des cellules, associées aux transports de masse des vitesses aux bordures. La dernière étape consiste à calculer l'advection de masse aux bordures et d'en déduire les nouvelles vitesses.

3.1.3. Fonctionnement de VolcFlow

L'utilisation basique de *VolcFlow* est particulièrement simple.

Les simulations sont réalisées à partir d'un fichier d'entrée où doivent être définis :

- la topographie ;
- l'épaisseur initiale de la masse qui s'écoule ;
- la rhéologie de l'écoulement ;
- les paramètres de calcul : pas de temps, temps de calcul.

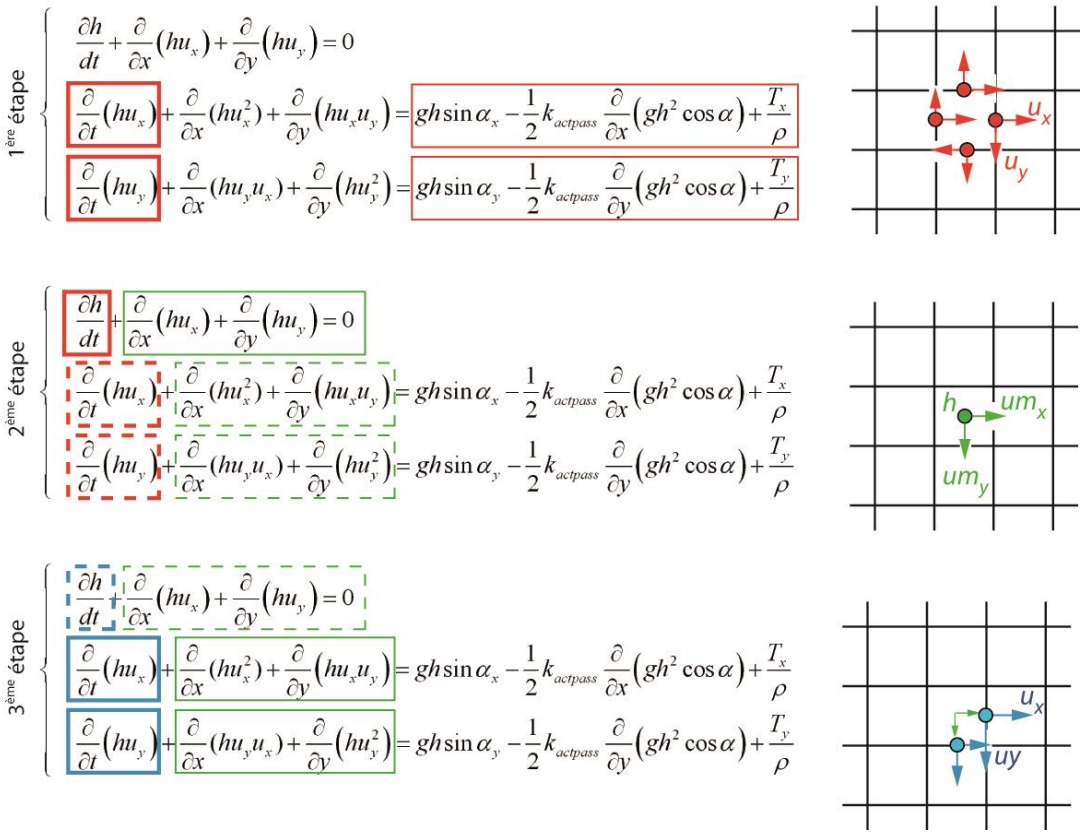

Figure 2 : fonctionnement du schéma numérique de *VolcFlow*. Le schéma numérique est divisé en trois étapes : 1 - calcul des accélérations aux bordures à partir des contraintes, 2 - advection aux centres des mailles, 3 - advection aux bordures. Les traits gras indiquent la partie calculée à chaque étape à partir des autres termes des équations (en traits fins). Les pointillés indiquent les étapes intermédiaires qui nécessitent par exemple un calcul des vitesses au centre avant l'advection aux bordures.

Mais il est aussi possible d'aller plus loin grâce à des fonctions programmables qui peuvent être exécutées à chaque étape de calcul. Ces fonctions étant de petits programmes écrits par l'utilisateur, elles permettent d'atteindre un haut degré de complexité. Les principales fonctions sont listées ci-dessous :

source : sert à modéliser un débit de masse au cours du temps, sur une ou plusieurs cellules, pour simuler la production d'écoulements pyroclastiques, par exemple.

X_Rstress et Y_Rstress : utilisées pour définir des lois de comportements rhéologiques autres que les lois de comportements prédéfinis, la loi $\mu(I)$ par exemple (Pouliquen et Forterre, 2002 ; GdR Midi, 2004).

representation : permet de représenter les résultats. Il peut s'agir d'une instruction simple pour suivre l'évolution du calcul ou d'une représentation plus esthétique (3D, transparence…) pour présenter les résultats.

restart_file : permet de relancer un calcul interrompu. Utile pour des calculs de plusieurs jours. L'instruction peut contenir le nom du fichier de démarrage seulement ou un programme modifiant certains paramètres de ce fichier.

bound_cond : utilisée pour définir les conditions aux limites : épaisseur nulle, masse nulle, relation vitesse/épaisseur pour atténuer les ondes, etc.

sedimentation / **erosion** : utilisées pour définir respectivement la façon dont sédimente l'écoulement et dont il érode le substratum.

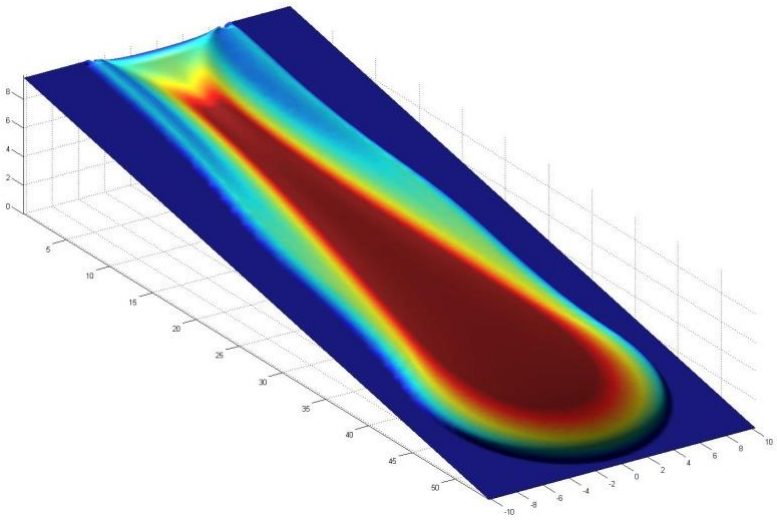

Figure 3 : exemple d'érosion d'un substratum initialement plan par un écoulement

VolcFlow permet aussi de choisir des options de calculs supplémentaires pour simuler un glissement en masse, pour choisir un schéma numérique plus simple, etc. Ecrit sous le logiciel de programmation *Matlab*, il bénéficie de toute la puissance du logiciel pour le pré-traitement (définition de la topographie par exemple) et le post-traitement (calcul de déformations de surface par exemple, Figure 4) des données ainsi que pour la visualisation des résultats.

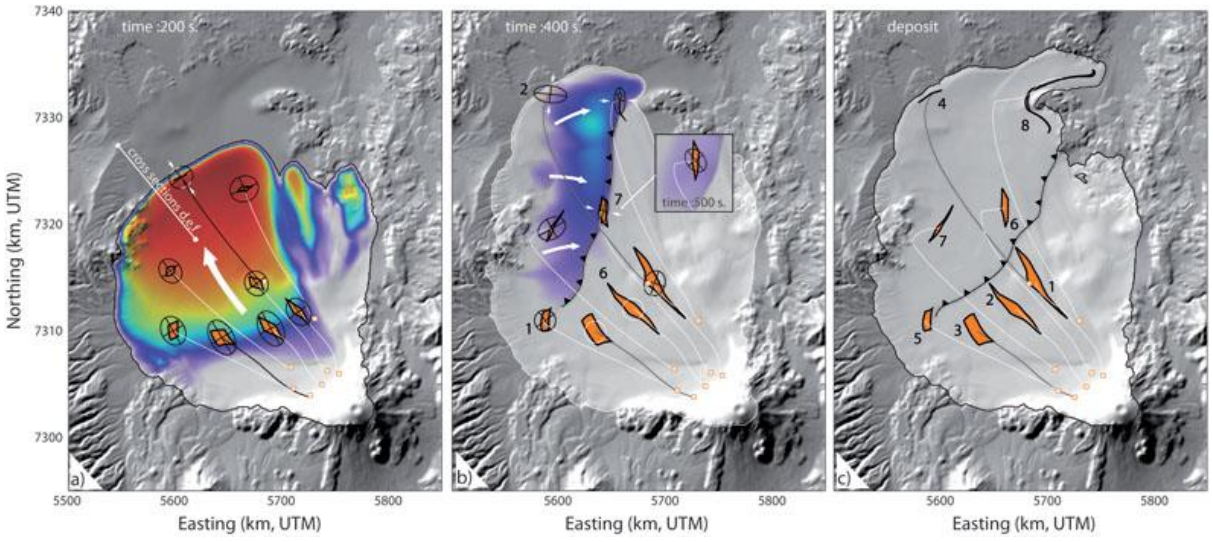

Figure 4 : exemple de post-traitement des données pour lier les structures naturelles aux déplacements simulés (Kelfoun et al., 2008). Les déplacements sont utilisés pour calculer les ellipses de déformation ainsi que l'extension de zones de surface initialement carrées.

3.2. La version 2-fluides : écoulement dense / tsunami

Les volcans croissent fréquemment à proximité de mers ou d'océans (Hawaii, Réunion, Montserrat et les autres volcans des Antilles, Japon, Indonésie, etc.). Les écoulements qu'ils émettent peuvent engendrer des tsunamis en entrant dans l'eau. Inversement, les dépôts de tsunamis peuvent nous renseigner sur la façon dont l'effondrement s'est produit. Afin de simuler ces interactions, j'ai donc développé une version de *VolcFlow* pour coupler l'écoulement volcanique à celui de l'eau.

Les deux écoulements sont simulés par deux systèmes d'équations similaires de bilan de masse et de quantité de mouvement (équations 1-3) ainsi que par des équations supplémentaires d'interactions entre les deux fluides. L'eau est soumise au cisaillement de l'avalanche, à sa pression dynamique ainsi qu'à la déformation du fond de l'océan qu'elle provoque. L'avalanche est freinée par les contraintes exercées par l'eau et sa masse volumique relative varie entre l'air et l'eau.

Cependant, si le couplage entre les deux fluides est trop simple, un soulèvement au niveau du fond, s'exprimera par un soulèvement identique à la surface de l'eau quelle que soit l'épaisseur d'eau. Pour résoudre ce problème, il a fallu utiliser un vrai calcul 3D d'interactions écoulement granulaire / eau puis trouver des expressions analytiques plus simples permettant d'accélérer les calculs (Figure 5).

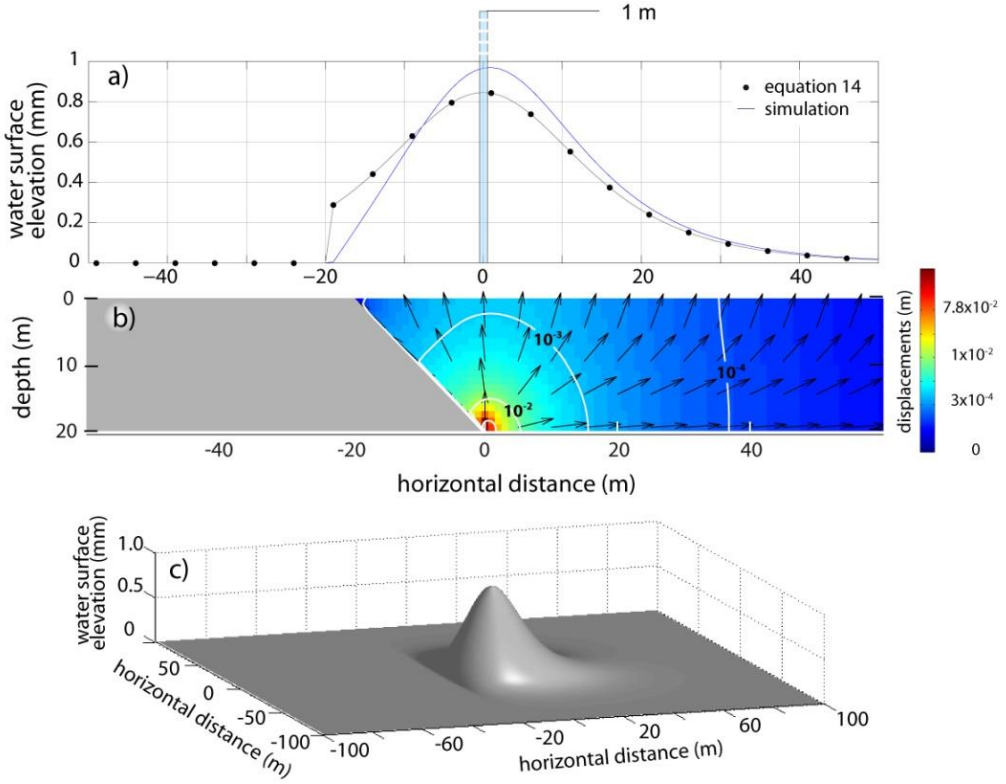

Figure 5 : a) déformation de la surface de l'eau associée à un déplacement vertical de 1 m au niveau du fond. Le graphique indique les résultats obtenus avec un couplage direct (barre bleu clair, 1 m de haut), un vrai calcul 3D (courbe bleue) et l'équation analytique simplifiée (points). b) déplacements de l'eau obtenus grâce à un vrai calcul 3D. c) Simulation 3D de la déformation de la surface induite par un déplacement au niveau de fond. Figure issue de Kelfoun et al. (2010).

Le lecteur peut se référer à l'article de Kelfoun et al. (2010) pour plus de détails sur les équations et la façon de les résoudre.

3.3. La version 2-fluides : écoulement dense / déferlante

Une nouvelle version de *VolcFlow* permet de créer des déferlantes pyroclastiques (écoulements dilués) à partir des écoulements denses et inversement, des écoulements denses à partir d'écoulements dilués. Dans cette version, l'écoulement dilué est alimenté en particules par l'écoulement dense. Il perd de la masse par sédimentation qui, en fonction de l'épaisseur déposée et de la rhéologie choisie pour la partie dense forme soit un écoulement dense, soit un dépôt. L'écoulement dense est simulé par un jeu d'équations similaires à la version 1-fluide excepté l'ajout de termes d'échanges avec l'écoulement dilué. Ce modèle n'étant pas encore publié, il est décrit avec plus de détails que les modèles précédents. Les équations constitutives de la partie dense sont les suivantes :

$$\frac{\partial h_{\mathrm{d}}}{\partial t}+\frac{\partial}{\partial x}\left(h_{\mathrm{d}}u_x\right)+\frac{\partial}{\partial y}\left(h_{\mathrm{d}}u_y\right)=\frac{\phi_{\mathrm{s}}-\phi_{\mathrm{m}}}{\rho_{\mathrm{d}}} \quad [8]$$

$$\frac{\partial}{\partial t}\left(h_{\mathrm{d}}u_x\right)+\frac{\partial}{\partial x}\left(h_{\mathrm{d}}u_x^2\right)+\frac{\partial}{\partial y}\left(h_{\mathrm{d}}u_xu_y\right) = gh_{\mathrm{d}}\sin\alpha_x-\frac{1}{2}k_{act/pass}\frac{\partial}{\partial x}\left(gh_{\mathrm{d}}^2\cos\alpha_x\right)+\frac{\mathbf{T}_x}{\rho_d}+\frac{\phi_{\mathrm{s}}}{\rho_{\mathrm{d}}}\times v_x-\frac{\phi_m}{\rho_{\mathrm{d}}}\times u_x \quad [9]$$

$$\frac{\partial}{\partial t}\left(h_{\mathrm{d}}u_y\right)+\frac{\partial}{\partial x}\left(h_{\mathrm{d}}u_xu_y\right)+\frac{\partial}{\partial y}\left(h_{\mathrm{d}}u_y^2\right) = gh_{\mathrm{d}}\sin\alpha_y-\frac{1}{2}k_{act/pass}\frac{\partial}{\partial y}\left(gh_{\mathrm{d}}^2\cos\alpha_y\right)+\frac{\mathbf{T}_y}{\rho_d}+\frac{\phi_{\mathrm{s}}}{\rho_{\mathrm{d}}}\times v_y-\frac{\phi_m}{\rho_{\mathrm{d}}}\times u_y \quad [10]$$

Le système pour résoudre le comportement de l'écoulement dilué est un peu plus complexe car les variations de densité de ce dernier doivent être prises en compte.

$$\frac{\partial h_{\mathrm{s}}}{\partial t}+\frac{\partial}{\partial x}\left(h_{\mathrm{s}}v_x\right)+\frac{\partial}{\partial y}\left(h_{\mathrm{s}}v_y\right)=\frac{\phi_{\mathrm{m}}-\phi_s}{\rho_{\mathrm{m}}} \quad [11]$$

$$\frac{\partial \rho_{\mathrm{s}}h_{\mathrm{s}}}{\partial t}+\frac{\partial}{\partial x}\left(\rho_{\mathrm{s}}h_{\mathrm{s}}v_x\right)+\frac{\partial}{\partial y}\left(\rho_{\mathrm{s}}h_{\mathrm{s}}v_y\right)=\phi_{\mathrm{m}}-\phi_{\mathrm{s}} \quad [12]$$

$$\frac{\partial}{\partial t}\left(\rho_{\mathrm{s}}h_{\mathrm{s}}v_x\right)+\frac{\partial}{\partial x}\left(\rho_{\mathrm{s}}h_{\mathrm{s}}v_x^2\right)+\frac{\partial}{\partial y}\left(\rho_{\mathrm{s}}h_{\mathrm{s}}v_xv_y\right)=\left(\rho_{\mathrm{s}}-\rho_{\mathrm{a}}\right)gh_{\mathrm{s}}\sin\beta_x -\frac{1}{2}\left(\rho_{\mathrm{s}}-\rho_{\mathrm{a}}\right)\frac{\partial}{\partial x}\left(gh_{\mathrm{s}}^2\cos\beta_x\right)+\mathbf{R}_x+\phi_{\mathrm{m}}\times u_x-\phi_{\mathrm{s}}\times v_x \quad [13]$$

$$\frac{\partial}{\partial t}\left(\rho_{\mathrm{s}}h_{\mathrm{s}}v_y\right)+\frac{\partial}{\partial x}\left(\rho_{\mathrm{s}}h_{\mathrm{s}}v_xv_y\right)+\frac{\partial}{\partial y}\left(\rho_{\mathrm{s}}h_{\mathrm{s}}v_y^2\right)=\left(\rho_{\mathrm{s}}-\rho_{\mathrm{a}}\right)gh_{\mathrm{s}}\sin\beta_y -\frac{1}{2}\left(\rho_{\mathrm{s}}-\rho_{\mathrm{a}}\right)\frac{\partial}{\partial y}\left(gh_{\mathrm{s}}^2\cos\beta_y\right)+\mathbf{R}_y+\phi_{\mathrm{m}}\times u_y-\phi_{\mathrm{s}}\times v_y \quad [14]$$

Les indices *s*, *d* et *m* font respectivement référence à l'écoulement dilué (*s* pour surge), à l'écoulement dense (*d*) et au mélange (*m*) de densité intermédiaire qui alimente l'écoulement dilué. Les autres variables utilisées sont définies dans les lignes suivantes.

Les lois d'échanges définissent le transfert de masse et de quantité de mouvement par sédimentation des particules de l'écoulement dilué vers le dense ainsi que par entrainement des particules de l'écoulement dense pour alimenter le dilué.

Formation de l'écoulement dilué par l'écoulement dense

Dans ce modèle, l'écoulement dilué peut être engendré soit à la source, soit par l'écoulement dense. Dans ce dernier cas, les particules fines quittent la surface de l'écoulement dense et sont mises en suspension par cisaillement entre l'écoulement dense et le fluide ambiant (air ou écoulement dilué, Denlinger, 1987), par fluidisation (Wilson et al, 1984), entrainement de l'air au front de l'écoulement (Wilson and Walker, 1982) et/ou par réchauffement de l'atmosphère au contact des roches chaudes.

Le flux de masse par mètre carré ϕ_m (kg / m² / s) des particules et du gaz provenant de l'écoulement dense dépend de la vitesse de l'écoulement (Hobblit 1986; Denlinger 1987; Kelfoun et al., 2000). Mais la relation vitesse / flux est encore très mal connue. Selon Denlinger (1987), le flux de masse est une fonction linéaire de la vitesse de cisaillement entre la surface de l'écoulement dense et le fluide ambiant (air ou écoulement dilué):

$$\phi_{\mathrm{m}} = a_1 \times \|\mathbf{u} - \mathbf{v}\| \qquad [15]$$

où **u** est la vitesse de l'écoulement dense ou du dépôt ($\|\mathbf{u}\| = 0$ dans ce cas), **v** est la vitesse de l'écoulement dilué ou de l'atmosphère ($\|\mathbf{v}\| = 0$ dans ce cas) et a_1 (kg / m^3) est un paramètre reliant le flux de masse à la différence de vitesse. Selon cette équation, l'écoulement dilué est donc capable de ré-entrainer de la masse préalablement déposée si sa vitesse est suffisamment élevée.

Le mélange de gaz et de particules, une fois décompressé à la température de l'écoulement dilué, influe à la fois sur l'épaisseur et la densité de ce dernier. L'épaisseur de l'écoulement dilué varie localement suivant :

$$\frac{dh_s}{dt} = \frac{\phi_m}{\rho_m} \qquad [16]$$

où ρ_{m} représente la masse volumique du mélange.

Le produit de la masse volumique de l'écoulement dilué par son épaisseur, $\rho_s \times h_s$, qui correspond à la masse d'écoulement dilué par mètre carré de surface, varie aussi en fonction de ϕ_m:

$$\frac{d\left(\rho_s h_s\right)}{dt} = \phi_m \qquad [17]$$

L'approche moyennée verticalement impose que le mélange vertical soit instantané.

Simultanément, l'épaisseur de l'écoulement dense diminue en fonction de ϕ_{m} et de ρ_{d}, la masse volumique de l'écoulement dense étant considérée comme constante :

$$\frac{dh_d}{dt} = -\frac{\phi_m}{\rho_d} \quad [18]$$

Sédimentation des particules

La vitesse de sédimentation, w_{sed}, des particules d'une déferlante pyroclastique (écoulement dilué) dépend de leur densité, leur forme et leur taille (e.g. Sparks *et* al., 1997 ; équation 1 de Doyle *et* al., 2010).

La masse perdue par l'écoulement dilué par sédimentation est calculée par :

$$\phi_s = w_{sed} \times \rho_p \times \frac{\rho_s - \rho_g}{\rho_p - \rho_g} \quad [19]$$

La variation de masse de l'écoulement dilué par mètre carré, $\rho_s \times h_s$ lié à la sédimentation est donnée par :

$$\frac{d(\rho_s h_s)}{dt} = -\phi_s = -w_{sed} \times \rho_p \times \frac{\rho_s - \rho_g}{\rho_p - \rho_g} \quad [20]$$

Le modèle de sédimentation utilisé se base sur les équations 2a-2c de Doyle et al. (2010) où la sédimentation n'affecte que la densité de la déferlante et pas son épaisseur.

La masse perdue par la déferlante peut former un dépôt, peut s'ajouter à un écoulement dense déjà formé ou peut former un écoulement dense secondaire (Druitt et al., 2002), en fonction de la localisation, la masse déposée, la topographie et la rhéologie choisie. La masse perdue par la déferlante égale la masse gagnée par la partie dense (écoulement ou dépôt) et s'exprime par:

$$\frac{d(\rho_d h_d)}{dt} = -\frac{d(\rho_s h_s)}{dt} = \phi_s = w_{sed} \times \rho_p \times \frac{\rho_s - \rho_g}{\rho_p - \rho_g} \quad [21]$$

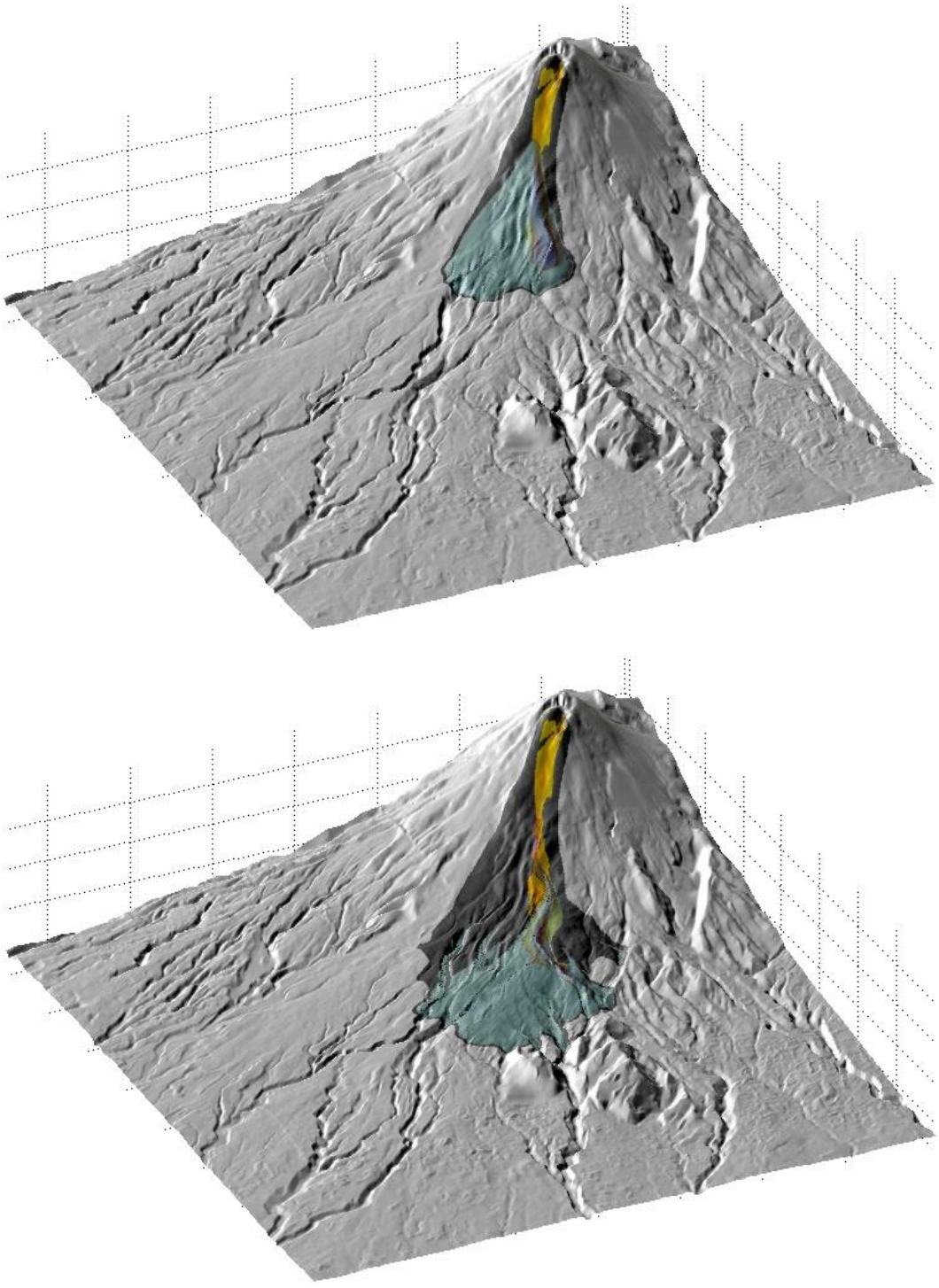

Figure 6 : Simulation des écoulements denses et dilués du volcan Merapi (Indonésie). L'épaisseur de l'écoulement apparaît en jaune/rouge/violet, la déferlante en bleu, le dépôt de déferlante en noir (Kelfoun, 2011).

4. Rhéologie et mise en place des avalanches de débris

Pour caractériser le comportement des avalanches de débris et expliquer leur mise en place, il est nécessaire d'étudier des cas naturels dont les dépôts ont conservé leur morphologie, leur extension et leur épaisseur originelles et dont la distribution des lithologies de surface soit encore visible. Il faut aussi suffisamment d'informations de terrain pour reconstituer le plus précisément possible la topographie initiale ainsi que celle de la surface de glissement. De tels exemples sont assez rares. L'avalanche de Socompa, au Chili, exceptionnellement bien préservé par le climat hyper aride de l'Atacama, est donc une cible idéale.

4.1. Modélisation numérique de l'avalanche de débris de Socompa

L'avalanche du volcan Socompa s'est formée par la déstabilisation de 36 km^3 du flanc Nord du volcan. Le dépôt de l'avalanche de débris s'étend sur 500 km^2 et s'est étalé jusqu'à 40 kilomètres avec une épaisseur de quelques dizaines de mètres. La morphologie est particulièrement bien préservée ainsi que la distribution des lithologies de surface. Les structures principales de l'avalanche sont : les levées Nord (L, Figure 7) bordant une zone présentant des structures en extension très prononcées (CZ). La zone sud (P), au relief moindre, montre une lithologie en bandes orientées SE-NO. Ces deux zones sont séparées par l'escarpement médian (ME), orienté NE-SO, aux structures plutôt compressives et complexes.

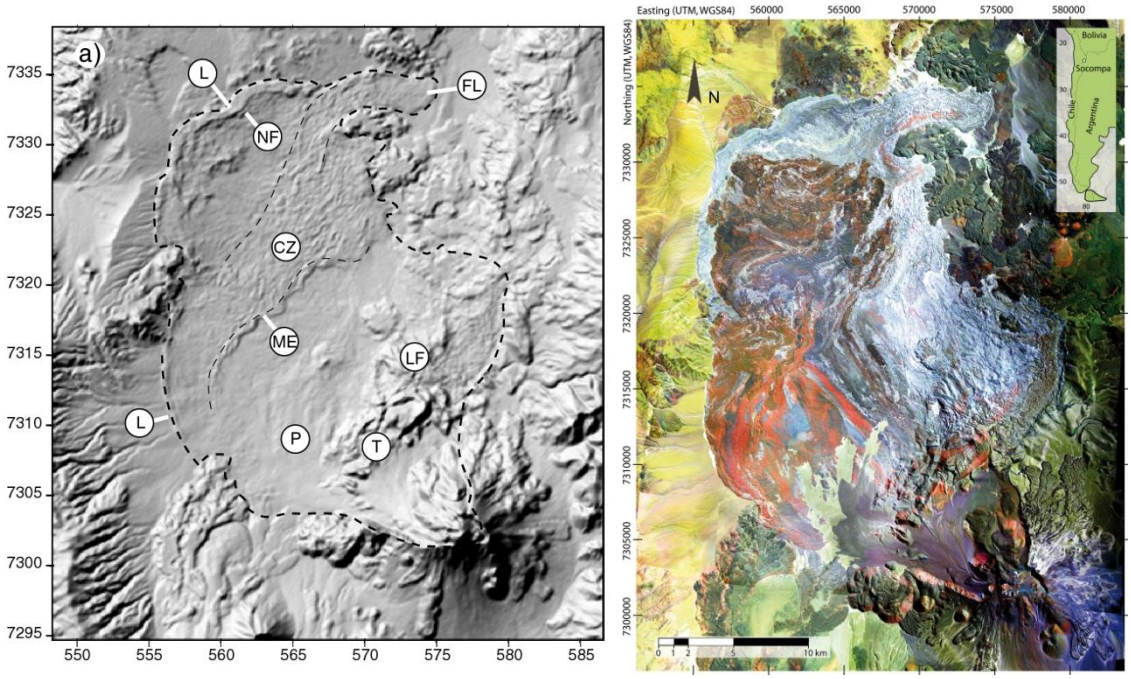

Figure 7 : morphologie de l'avalanche de Socompa et distribution lithologique de surface.

Les études précédentes (Francis et al., 1985 ; Wadge et al., 1995 ; Van wyk de Vries et al., 2001) permettent de reconstituer la forme initiale de l'édifice. Les forages de recherche en eau contraignent localement l'épaisseur du dépôt. Les données de terrain sont suffisantes pour reproduire la topographie pré-avalanche ainsi que celle de la surface de glissement, et réaliser des simulations de mise en place. La procédure consiste à choisir les lois rhéologiques généralement utilisées – visqueuse, Coulomb, plastique, etc. – puis à faire varier les paramètres de ces lois jusqu'à obtenir le dépôt le plus proche de la réalité.

Un des résultats important de l'étude réalisée (Kelfoun et Druitt, 2005) est qu'elle démontre qu'une loi de comportement type Coulomb, souvent utilisée pour simuler les écoulements granulaires, ne permet pas de reproduire les dépôts naturels, ne serait-ce qu'au premier ordre. La loi désormais appelée $\mu(I)$ (Pouliquen, 1999 ; Pouliquen et Forterre, 2002), plus précise pour simuler les écoulements granulaires en laboratoire, ne nous a pas non plus permis de reproduire correctement les dépôts. A cause des nombreux paramètres non contraints de cette loi, nous ne pouvons pas exclure de ne pas avoir exploré l'ensemble des combinaisons. Mais l'augmentation des frottements en fonction de la vitesse de la loi $\mu(I)$ paraît fonctionner à l'inverse de ce qui se passe pour l'avalanche de Socompa. Les lois de Voellmy parfois utilisées pour modéliser ces phénomènes (Tableau 1) ne peuvent pas non plus reproduire les dépôts. Des comportements visqueux et turbulents paraissent aussi inadaptés, en particulier parce qu'ils ne forment pas de dépôts. Aucune combinaison en couplant la loi Coulomb avec d'autres lois n'a donné de résultats corrects. Davies et al. (2010) ont déterminé une équation de comportement liée à une énergie qui serait libérée lors de la fragmentation des roches. Cette loi se résume en une combinaison d'une loi plastique et d'une loi Coulomb. Les résultats sont meilleurs qu'avec les lois précédentes mais moins bons qu'en utilisant le seulement le comportement plastique décrit ci-après (Kelfoun et Druitt, 2005).

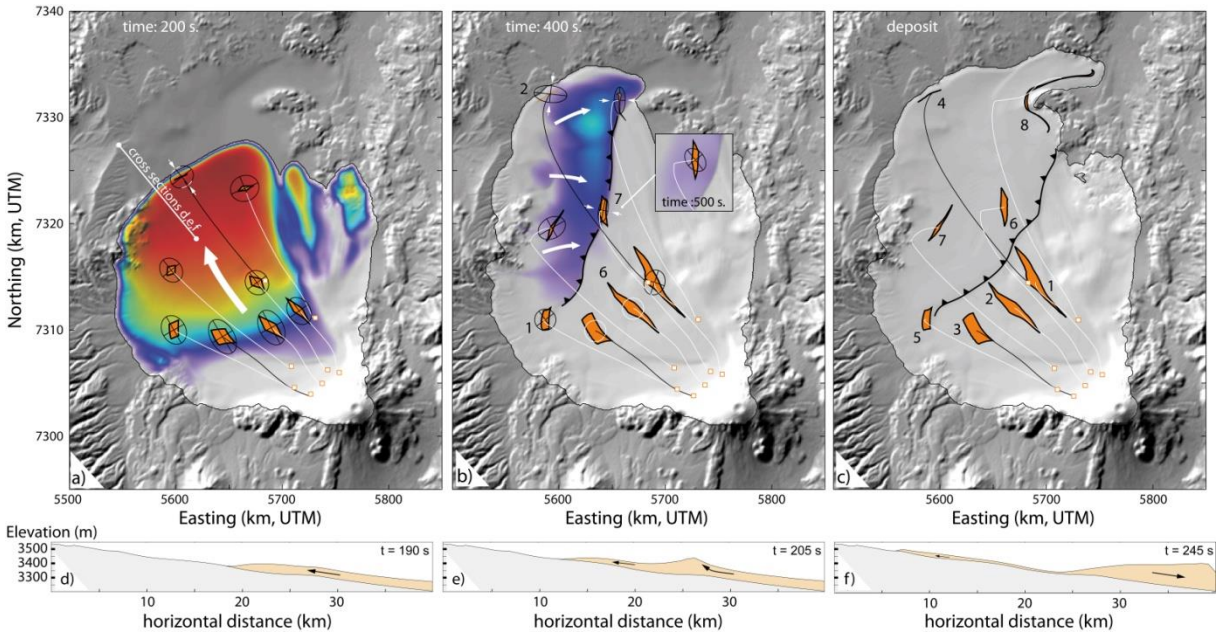

Figure 8 : simulation de la mise en place de l'avalanche de débris de Socompa (Kelfoun et Druitt, 2005)

En effet, un comportement plastique, dont la contrainte résistante constante est fixée à environ 50 kPa, reproduit très bien les dépôts naturels. Cette loi, définie par l'équation 7, permet de former des levées et reproduit l'extension des dépôts et leurs épaisseurs. Surtout le modèle numérique permet, pour la première fois, d'expliquer correctement la mise en place de l'avalanche de Socompa en reproduisant les distributions lithologiques et la formation de toutes les principales structures : levées Nord, escarpement médian, zones de compression et d'extension. Le modèle indique en effet que l'avalanche de Socompa s'est tout d'abord écoulée vers le Nord dans le bassin de Monturaqui. La forme du bassin a empêché l'avalanche de s'étaler davantage, et la masse de l'avalanche s'est accumulée à l'Ouest et au Nord du bassin puis est revenue vers le Socompa en remobilisant les dépôts préalablement mis en place. Le front figé de cette vague de retour d'une quinzaine de kilomètres forme l'escarpement médian. Le modèle reproduit aussi les déplacements de surface qui conduisent à l'ensemble des grandes structures observées : compression des levées Nord, compression au niveau du front de la vague puis extension à l'arrière, zone étirées au Sud.

L'origine du comportement plastique n'est pas claire. Une tentative d'explication est esquissée au chapitre 11.

4.2. Affinement de la mise en place par imagerie et études de terrain

Une fois que le cadre général de la mise en place de l'avalanche de Socompa a été établi grâce au modèle numérique, un retour aux données de terrain permet de confirmer les conclusions numériques et d'aller plus loin dans la compréhension de la dynamique de l'avalanche. L'observation a été menée à la fois sur le terrain et en utilisant l'imagerie, les dimensions de l'avalanche étant trop importantes pour qu'une étude puisse être menée depuis le sol uniquement. Afin d'obtenir des images de haute qualité, ayant une haute résolution mais aussi des couleurs permettant de distinguer les différentes lithologies, il m'a fallu coupler des images aériennes de haute résolution en noir et blanc (Guilbaud, 2002) avec des images satellites (Spot et Landsat). Un exemple d'image haute résolution utilisée et de son interprétation est présenté en Figure 9.

Le couplage imagerie / terrain permet d'interpréter de nombreuses structures ainsi que d'estimer les déplacements de la surface de l'avalanche à partir des distributions lithologiques. Les principales conclusions de cette étude sont les suivantes :

1) ce que nous supposons avoir été au front du glissement initial se retrouve au front de l'avalanche, au niveau des levées Nord. Cette observation déjà notée par Wadge et al. (1995) et van Wyk de Vries et al. (2001) sur le Socompa a été noté sur d'autres avalanches de débris (Shaller, 1991 et références internes; Campbell et al., 1995) et indique que le gradient vertical de vitesses horizontales est faible : l'avalanche se déplace essentiellement en bloc.

2) L'existence et les caractéristiques de cette vague de retour fournissent des informations cruciales sur la mise en place de l'avalanche. La conclusion la plus frappante est l'extrême mobilité de

l'avalanche capable non seulement de s'écouler sur 35 kilomètres sur une pente moyenne inférieure à 3° mais aussi de revenir en arrière sur 15 km sur une pente moyenne de moins de 1°.

3) Le dépôt nous renseigne aussi sur le mode de mise en place. Premièrement, parce que les unités lithologiques changent de direction de part et d'autre de l'escarpement médian tout en restant en continuité ; cette continuité indique que la masse qui revient en arrière ne recouvre pas le dépôt déjà en place mais le remanie. Deuxièmement parce que la mesure du déplacement des roches à partir des distributions lithologiques est compatible avec le modèle numérique qui indique que la vague se déplace plus que la matière : dans la partie nord ouest, là où la vague est revenue sur 15 kilomètres environ, les roches de surface ne se sont déplacées que de 5 km. Ce phénomène s'observe aussi entre l'écume et les vagues en bord de mer. Il ne se produit pas au front de l'écoulement où masse et vague possèdent une vitesse identique. La différence de vitesse indique que la vague qui a formé l'escarpement médian remobilise la majeure partie des dépôts préalablement mis en place. Le « dépôt » reste donc, pendant quelques dizaines de secondes (ce temps ne peut être estimé que par la simulation) dans un état métastable : stable si aucune perturbation ne vient le remobiliser mais facilement remobilisable s'il est perturbé.

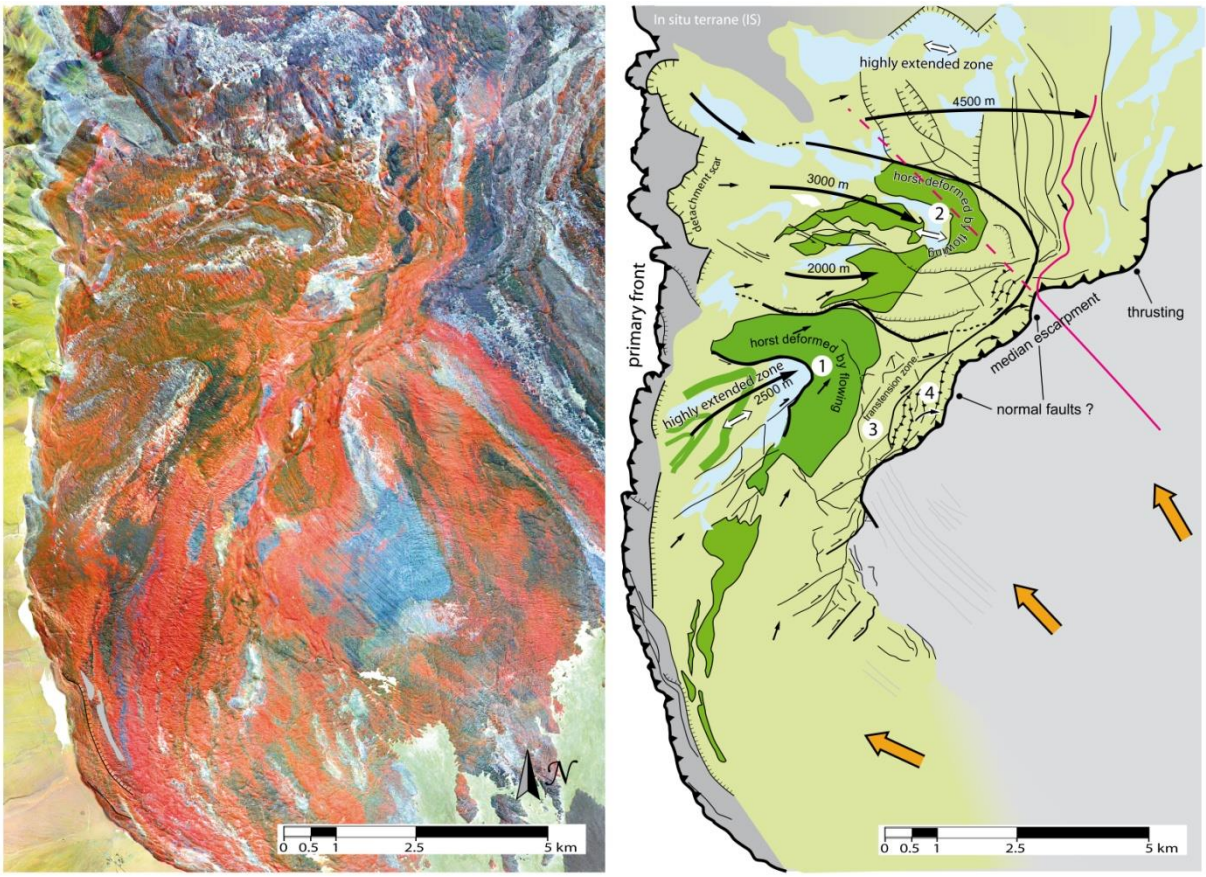

Figure 9 : image haute résolution de la partie sud ouest de l'avalanche de Socompa et interprétation des structures observées.

4) La présence de structures en extension sur l'essentiel de la zone de retour, excepté au niveau du front, indique que l'écoulement se fait essentiellement à l'intérieur de l'avalanche, la surface étant

simplement étirée de façon passive au dessus. Ces observations conduisent à envisager le modèle de mise en place, schématisé sur la Figure 10.

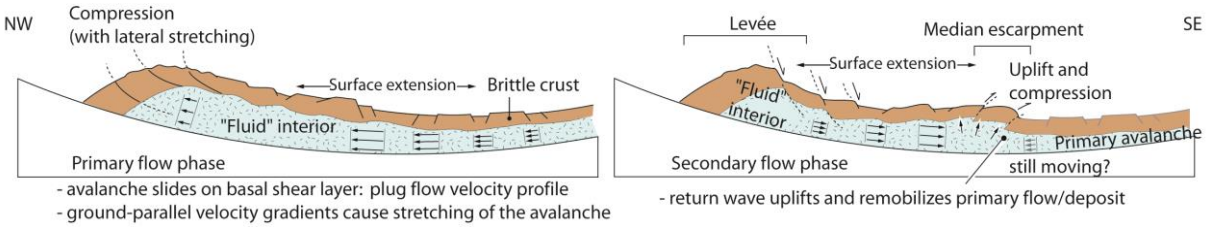

Figure 10 : modèle de mise en place de l'avalanche de Socompa. Les schémas, basés sur des observations de terrain et des modèles numériques expliquent la formation des structures de surface par une vague de retour qui remobilise les dépôts déjà mis en place (Kelfoun et al., 2008).

4.3. Affinement de la mise en place par géochimie isotopique fine

Pour aller plus loin encore dans la compréhension de la mise en place de l'avalanche, nous avons analysé les compositions chimiques des roches et des matrices de Socompa pour tenter de comprendre comment se disloquent les roches. Les compositions en éléments majeurs étant sensiblement les mêmes, il nous a fallu travailler avec les éléments traces et les rapports isotopiques. La géochimie a été menée par Régis Doucelance (LMV) et les résultats font l'objet d'un article très prochainement soumis. 90 échantillons ont été analysés en éléments majeurs, en traces et en isotopes du Sr et Nd (Figure 11 et 12). Les principales conclusions de cette étude sont listées ci-dessous.

1) Les analyses confirment que les couleurs de l'image composite (Figure 11) sont clairement associées à la chimie ou à la minéralogie des roches. Les roches de l'avalanche sont pourtant majoritairement des dacites qu'il est parfois délicat de différencier sur le terrain. Elles démontrent la puissance de l'imagerie satellite dont les faibles variations de couleurs indiquent des variations géochimiques fines.

2) Tous les échantillons de l'avalanche se placent le long d'une courbe de mélange entre deux pôles de compositions chimiques différentes. Les roches de la *Flexura* (LF, Figure 11), supposées constituer le substratum du volcan, se placent aussi le long de cette courbe mais ne forment pas un pôle. Les roches échantillonnées dans l'avalanche se distribuent aussi tout le long de cette courbe, indiquant que le mélange qui affecte les compositions des matrices n'est pas lié à l'avalanche mais à un mélange magmatique à l'origine de la formation de l'édifice du Socompa et des ignimbrites qui forment son soubassement. Cette origine commune à toutes les roches de l'édifice limite l'analyse des mélanges entre les roches pendant la mise en place de l'avalanche.

Figure 11 : localisation des échantillons analysés.

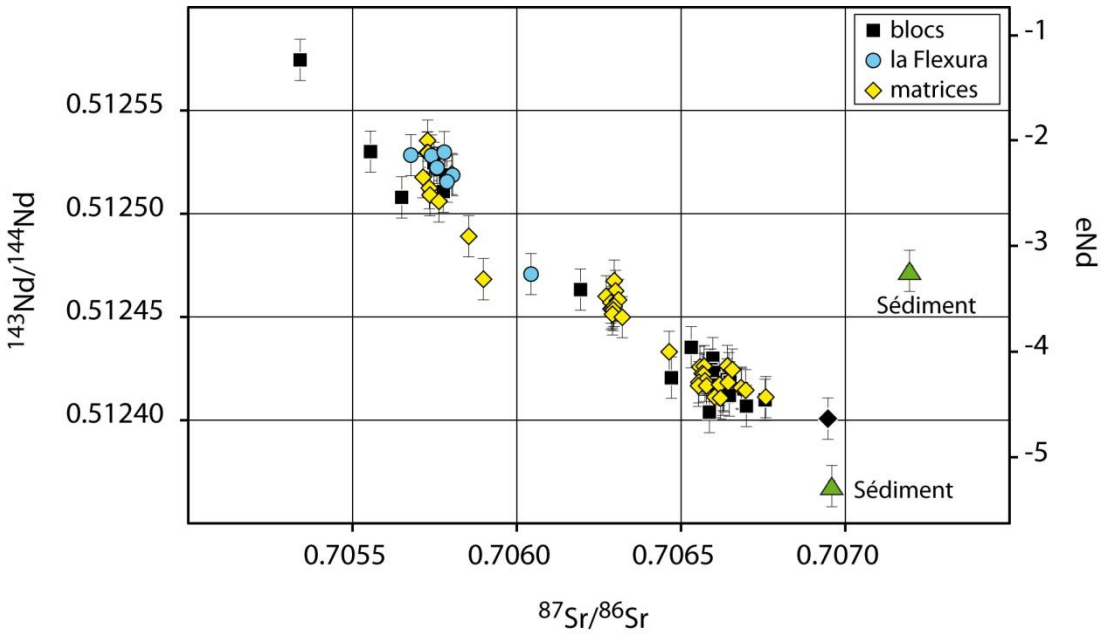

Figure 12 : compositions isotopiques des échantillons analysés.

3) Peu de matrices échantillonnées ont la composition des roches de *La Flexura*. Il est donc probable que l'essentiel de la matrice soit composée des roches broyées de l'édifice plutôt que des roches du substratum, contrairement à ce qui avait été proposé par Wadge et al. (1995) et van Wyk de Vries et al. (2001).

4) Dans la partie Sud (Figure 11), où il n'y a pas eu de retour et où la lithologie se distribue en lignes parallèles, les matrices ont la même composition que les roches avoisinantes. La présence de nombreuses bandes de compositions différentes indiquent que, dans la zone Sud, le mélange latéral joue très peu dans la distribution des lithologies de surface de L'avalanche. Partant du principe qu'il est peu probable que le volcan soit formé de secteurs dont les compositions géochimiques sont homogènes verticalement, les résultats indiquent que la distance de mélange vertical est faible elle aussi pour les matrices situées en surface de l'avalanche. Les relations roches / matrices sont plus compliquées à l'Est et à l'Ouest des bandes où les lithologies des roches elles-mêmes se mélangent.

Analyse en strontium et Néodyme des échantillons

	87Sr/86Sr	Epsilon Nd
(1)	0.706293	-3.60
(2)	0.706296	-3.56
(3)	0.706306	-3.52
(4)	0.706291	-3.64

Composition de la lave sombre au-dessus :

	0.706648	-4.28

Figure 13 : malgré l'ingestion visible de la lave sombre dans la matrice claire (à gauche de ③, les analyses indiquent que la matrice est homogène et ne présente aucun gradient géochimique.

5) Au centre de l'avalanche (①, Figure 11), nous observons que la formation supérieure se détruit en fragments de plus en plus petits qui paraissent être ingérés par la matrice. Pourtant, l'analyse géochimique indique que la matrice est très homogène et ne montre aucun gradient géochimique. Ces résultats signifient qu'à cet endroit, soit il n'y a aucune contamination de la matrice par la formation supérieure, soit le mélange est tellement puissant qu'il efface toute variation géochimique. Au niveau de front de l'escarpement médian (②, Figure 11 et Figure 14), plusieurs matrices sont au contact. Les

matrices sont homogènes et ne montrent aucune contamination entre elles, même à quelques centimètres du contact. En revanche, elles contiennent des fragments rocheux de compositions chimiques très différentes.

Analyse en strontium et Néodyme des échantillons

	87Sr/86Sr	Epsilon Nd
(1)	0.706321	-3.67
(2)	0.706309	-3.51
(3)	0.706554	-4.28
(4)	0.706602	-4.42

Figure 14 : matrices homogènes ne montrant pas de contamination géochimique de part et d'autre du contact (ligne pointillée). Les fragments de lave analysés ont tous une composition différente entre eux et différente des matrices.

6) Dans la partie Nord-Ouest de l'avalanche (③, Figure 11), la géochimie montre clairement que les blocs de roches sont très différents de la matrice sur laquelle ils reposent. A cet endroit l'avalanche est donc constituée de blocs épars ou accumulés sur 1 à 2 mètres, reposant sur une matrice de composition différente mais homogène.

7) Au front de l'avalanche (④, Figure 11) où 12 blocs de roches ont été analysés dans une zone de quelques dizaines de mètres carrés, toutes les compositions sont différentes.

Ces observations, couplées aux résultats d'imagerie et de modélisation, indiquent probablement l'existence de deux phases successives :

1) Une première phase pendant laquelle les matrices sont formées par le broyage de roches différentes dont le mélange est suffisamment efficace pour former des matrices géochimiquement homogènes. L'homogénéisation des matrices semble dépendre de la distance parcourue. Elle épargne la surface de l'avalanche qui s'est peu déplacée (<15 km environ) : au niveau des bandes lithologiques de la partie proximale, les roches sont partiellement broyées mais non mélangées comme l'atteste les compositions identiques roches / matrices. Au contraire, dans les parties plus distales (> 20 km), le mélange est tel qu'il affecte la composition des matrices de surface : les matrices n'ont plus les compositions des roches mais les compositions des roches restent localement homogènes. Au niveau du front, partie de l'avalanche qui a parcouru la plus grande distance (> 40 km), et des interactions complexes entre l'écoulement direct et la vague de retour, le mélange semble avoir été suffisamment fort pour mélanger roches et matrices jusqu'en surface.

2) La seconde phase, probablement liée à une vitesse plus faible de l'avalanche, déplace les différentes unités les unes par rapport aux autres, les mettant en contact sans les mélanger. Les matrices restent suffisamment « fluides » pour que leur contact ne se matérialise pas comme des plans de failles (de petites failles normales on été observée mais leur rejet est faible, de quelques dizaines de centimètres au maximum).

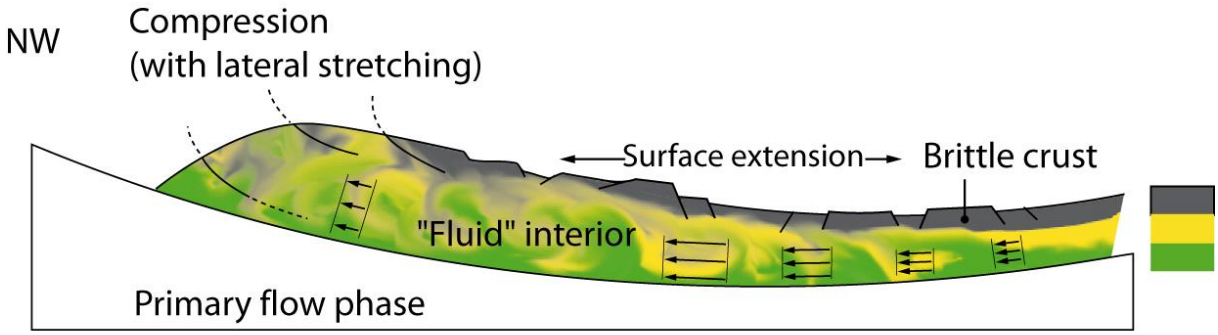

Figure 15 : nouvelle vision de la mise en place de l'avalanche de Socompa en combinant les études précédentes (imagerie, modélisation) aux analyses géochimiques. Le mélange entre les roches semble de plus en plus fort vers le front de l'avalanche jusqu'à atteindre la surface à une distance d'environ 20 km de la cicatrice.

4.4. Généralisation des conclusions

Le travail mené sur l'avalanche de Socompa est trop important pour avoir pu être réalisé sur d'autres édifices avec la même précision. Les conclusions des modélisations d'écoulement ont cependant été confirmées par des études moins poussées sur d'autres avalanches de débris : avalanche secondaire de Socompa, LLullaillaico, Lastaria, Tacna, etc.

L'avalanche secondaire de Socompa (avalanche d'environ 1 km^3 mise en place sur les dépôts de l'avalanche primaire) montre dans sa partie centrale des distributions lithologiques concentriques proches des structures observées au NO de l'avalanche principale (zone sans retour) puis une perte de ces structures en approchant des fronts, bien plus riches en matrices.

L'avalanche de Llullaillaico montre elle aussi des structures similaires. Elle présente par ailleurs une « vague de retour » même si elle est moins marquée qu'à Socompa à cause de la topographie.

Les simulations menées sur les avalanches de Llullaillaico, Lastarria, Chimborazo, Mt St Helens, et sur l'avalanche secondaire de Socompa indiquent que le comportement plastique reproduit toujours mieux les dépôts que les autres types de comportements rhéologiques généralement utilisés. Ce qui ne signifie pas qu'il permet de reproduire exactement tous les dépôts. Une discussion sur les limites de la rhéologie plastique est développée au chapitre 10.

5. Simulation numérique des avalanches de débris et des tsunamis associés

5.1. Tsunami engendré par une déstabilisation du Piton de la Fournaise

Les tsunamis ont été beaucoup étudiés et ont connu un regain d'intérêt après le tsunami du 26 décembre 2004 en Indonésie, qui mit en lumière la vulnérabilité des côtes de l'Océan Indien et démontra les dégâts gigantesques que ce type de cataclysmes peut engendrer. [e.g., Synolakis et al., 2008, et références internes]. Le déclanchement d'un tsunami peut résulter d'un tremblement de terre ou de l'entrée soudaine en mer d'une masse rocheuse [e.g. Ward, 2001; Harbitz et al., 2006; Fritz et al., 2008; Waythomas et al., 2009]. Le volcan de la Réunion est l'un des plus volumineux du monde, comparable en volume et en accumulation verticale de produit (environ 7 km à partir du fond océanique) au volcan Kilauea (Hawaii).

Certaines études de la bathymétrie autour de l'île suggèrent la présence d'au moins 50 dépôts d'avalanches de débris formés depuis 2 millions d'années (c'est-à-dire un tous les 40 000 ans en moyenne) et dont les volumes sont compris entre 1 et 1000 km^3 (Labazuy, 1996; Oehler et al., 2004, 2007). Le dernier évènement pourrait s'être produit il y a 4200 ans (Bachelery and Mairine, 1990).

Le Piton de la Fournaise est découpé par une structure en forme de fer à cheval interprétée comme ayant été formée par un glissement de l'édifice vers l'Est (Lénat and Labazuy,1990; Labazuy, 1996; Merle and Lénat, 2003), et peut être associée avec une subsidence (Michon, 2007). Les mesures récentes réalisées par interférométrie radar indiquent que la structure la plus récente, le Grand Brûlé, glisse vers l'Est (J.-L Froger et al., manuscrit en préparation, 2012). Bien entendu, glissement ne signifie pas forcément déstabilisation et formation de tsunami. Mais c'est une possibilité qu'il faut envisager, d'autant plus qu'à l'échelle géologique ce type de déstabilisation semble courant (Moore et al., 1989; Normark et al., 1993; Holcomb and Searle, 1991; McMurtry et al., 2004).

La majeure partie de la population de l'île de la Réunion vit à proximité du rivage. Les villes principales, les infrastructures, les industries et l'aéroport sont situés à basse altitude à proximité de l'océan. Personne ne pouvant prédire les caractéristiques des vagues engendrées par une éventuelle déstabilisation, la première publication de la version « deux fluides » de *VolcFlow* s'intéresse à cette problématique. L'objectif de l'étude est à la fois de présenter la théorie du modèle « deux fluides » (voir chapitre 3.2) et de prévoir l'amplitude des vagues créées.

Les effets de deux types de déstabilisation ont été testés : effondrement de l'ensemble de la zone du grand brûlé (10 km^3) en une seule fois ou en effondrements multiples. Les simulations indiquent qu'un effondrement du Piton de la Fournaise engendrerait des vagues pouvant atteindre plus de 100 mètres au niveau de l'impact. Ces vagues affecteraient en quelques dizaines de secondes les côtes Sud-Est. L'amplitude diminuerait rapidement vers le Nord-Ouest. Les côtes les plus touchées sont celles dont

l'orientation est perpendiculaire à la progression du tsunami. St Denis, capitale de l'île, serait atteinte en moins d'un quart d'heure par des vagues de 30 mètres environ. La côte SW de l'île Maurice, qui fait directement face à la propagation du tsunami, serait plus affectée que les côtes Nord-Ouest de la Réunion pourtant plus proches. Contrairement à l'impact d'un tsunami d'origine tectonique, celui d'un tel effondrement serait presque négligeable sur les côtes éloignées (Madagascar, Australie, Inde…). Les effets proximaux d'un tsunami lié à une déstabilisation sont dévastateurs mais s'atténuent rapidement.

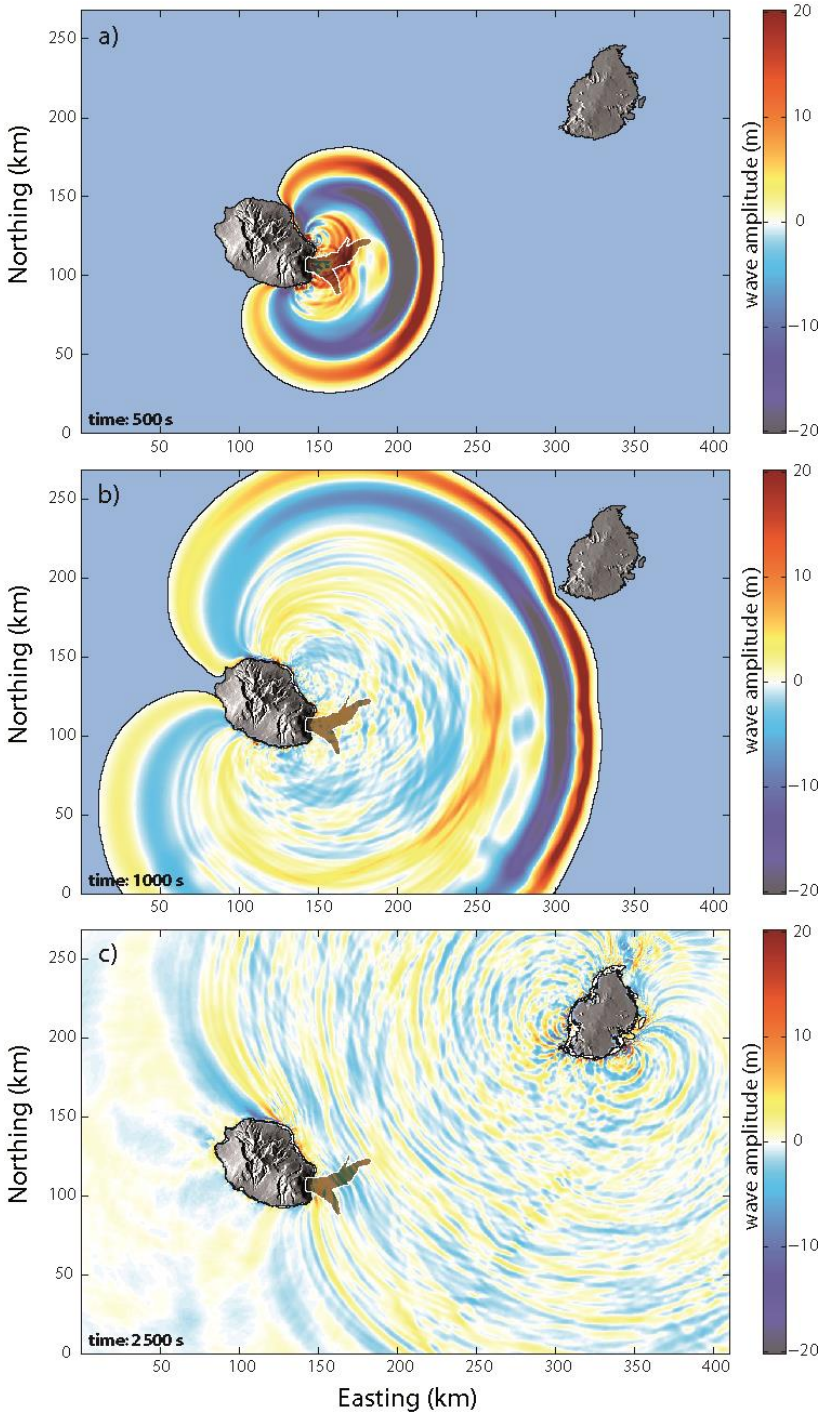

Figure 16 : exemple de vagues engendrées par l'effondrement du Grand Brûlé (Kelfoun et al., 2010)

Table 2 : hauteurs de vagues maximales simulées pour un effondrement de la zone du Grand Brûlé. Les valeurs entre parenthèses indiquent l'amplitude de la première vague si celle-ci n'est pas la plus importante. Les scénarios sont décrits dans Kelfoun et al., 2010.

Scenario	SW of Mauritius	NE of Mauritius	St Denis	Le Port	St Pierre	Ocean−W	Ocean−E
1	85 (38)	5	31 (11)	5.5 (5)	42 (14)	2.7	30
2	75 (60)	7.5 (7)	28 (15)	9 (7)	36 (18)	3.8	46
3	76	12	31	5.5	40	2.8	35
4	70 (65)	9 (6)	30 (10)	6 (5)	56 (12)	2.7	49
5	88 (30)	3.5	36 (10)	4 (3)	14	1.7	19
6	62 (37)	11 (5)	27 (13)	7 (5.5)	39 (15)	2.7	30
7	128	18 (14)	34 (23)	16	41 (29)	11	113
8	30 (18)	5 (2)	19 (4.5)	5.5 (1.6)	37 (4)	1.5 (1.0)	25 (15)

Le modèle indique aussi que des déstabilisations de volumes bien moindres du plateau côtier pourraient engendrer localement des vagues de quelques dizaines de centimètres d'amplitude capables d'affecter les infrastructures portuaires. Les dépôts de faibles volumes étant difficilement détectables, il est certain que nous sous-estimons leur nombre. Les résultats montrent l'importance du développement d'un système de détection des glissements pour alerter le plus rapidement possible les populations et estimer les volumes susceptibles de glisser et par conséquent l'amplitude du tsunami engendré.

L'étude du comportement rhéologique des avalanches sous marines est délicate, en particulier parce que leur observation est plus difficile qu'à terre. Notons cependant que c'est le comportement plastique, comme pour les avalanches à terre, qui reproduit le mieux les dépôts. La valeur du seuil de plasticité est cependant de 20 kPa environ, contre 50 kPa à terre. La comparaison de ces deux valeurs est difficile, les avalanches sous-marines étant soumises à des frottements supplémentaires dus à la présence d'eau. Néanmoins, le rapport seuil de plasticité à terre / seuil de plasticité dans l'eau correspond à peu près au rapport masse volumique de l'avalanche (2000 kg m^{-3}) / masse volumique relative de l'avalanche dans l'eau (1000 kg m^{-3}). La valeur du seuil de plasticité pourrait donc être implicitement reliée à la masse volumique relative de l'avalanche de débris : dans l'eau, les contraintes engendrées par le poids de l'avalanche seraient deux fois moindres, ce qui induirait une résistance basale deux fois plus faible.

5.2. Effondrement de Güìmar : validation du modèle à partir de mesures de dépôts de tsunamis

La difficulté de l'étude de La Réunion est que nous retrouvons très peu de traces de tsunamis passés qui permettraient de valider le modèle. Nous avons trouvé des conglomérats marins et un bloc corallien de plusieurs mètres cubes sur les côtes de l'île Maurice à 11 mètre d'altitude. L'âge de 4425 ± 35 BP (datation C-14 sur une branche de corail, Raphaël Paris, LMV) correspondrait au dernier effondrement du Piton de la Fournaise. Mais les dépôts sont trop rares pour estimer les amplitudes atteintes autour de l'île. C'est pourquoi nous nous sommes intéressés à l'effondrement de Güìmar aux Canaries.

Les îles Canaries se situent dans l'océan Atlantique près de la marge continentale nord-ouest de l'Afrique. L'île de Gran Canaria, située au centre de l'archipel, est approximativement circulaire, avec un diamètre d'environ 40 km et une altitude maximum de 1949 m. Paris et al. (2004) et Pérez-Torrado et al. (2006) ont interprété les conglomérats découverts entre 41 m et 188 m d'altitude sur les bords de la vallée Agaete comme des dépôts de tsunamis. Ils proposèrent que l'effondrement du flanc de Güìmar, sur la côte orientale de Tenerife en face de Gran Canaria (~0.83 Ma; Ancochea et al., 1990; Carracedo et al., 2010), était l'origine la plus probable de ces dépôts. L'effondrement de Güìmar, avec ses dépôts bien connus, était donc une occasion rare de pouvoir valider le modèle numérique.

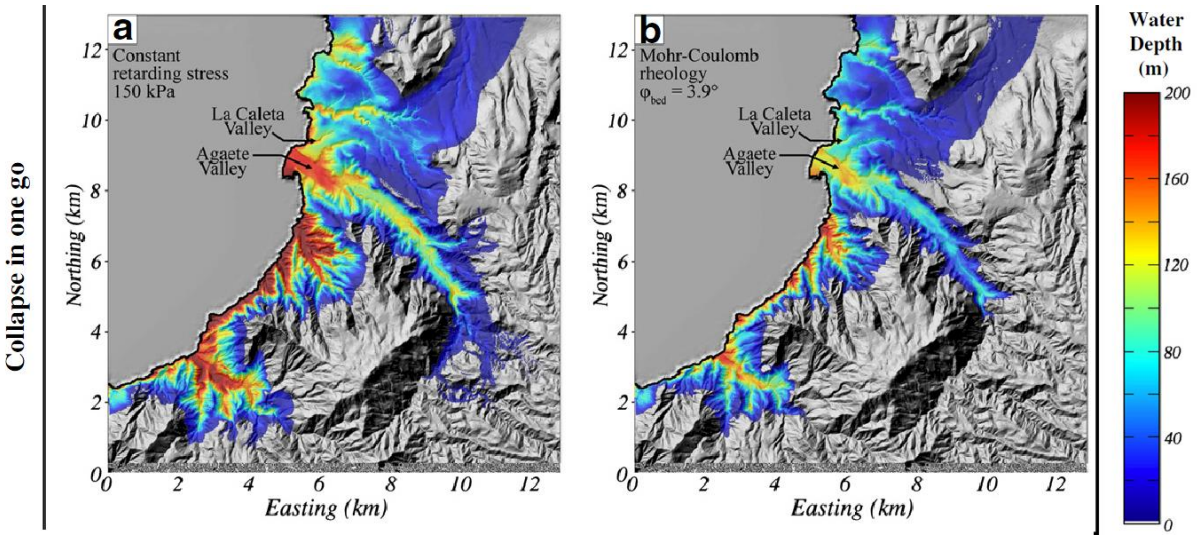

Figure 17 : Simulation des hauteurs de vagues créées par un effondrement immédiat de Güìmar (44 km3). Les résultats indiquent que l'effondrement est très probablement responsable des dépôts de tsunamis rencontrés dans la vallée d'Agaete (Giachetti et al., 2011).

Nous avons montré (Giachetti et al., 2011) que *VolcFlow* était capable de simuler l'effondrement de Güìmar (44 km^3) et de reproduire l'extension (approximative, car les limites du dépôt ne sont pas bien définies partout) des dépôts sous marins de l'avalanche ainsi que des hauteurs de vagues correspondant aux dépôts de tsunami retrouvés dans la vallée d'Agaete. Des vagues de plus de 100 m sont bien capables d'affecter des côtes situées à plusieurs dizaines de kilomètres de la déstabilisation. Les vagues simulées et leur évolution au cours du temps sont par ailleurs compatibles avec les directions d'écoulement mesurées dans les dépôts de tsunami de la vallée d'Agaete (Pérez-Torrado et al. 2006).

L'étude, comme celle menée sur la Réunion, montre également que le scénario d'effondrement joue un rôle essentiel sur la hauteur des vagues engendrées. Un même volume s'effondrant instantanément (quelques minutes), ou en plusieurs phases espacées de quelques minutes chacune, engendrera respectivement des vagues supérieures à 100 mètres ou de l'ordre de quelques mètres. Les vitesses de propagation du tsunami en seront bien entendu affectées.

Les simulations indiquent aussi que l'influence de la rhéologie choisie pour simuler l'avalanche joue sur la distribution et la morphologie des dépôts, mais influence très peu les caractéristiques des vagues

produites. C'est le débit de roches qui influence essentiellement l'amplitude du tsunami. Tous les modèles rhéologiques donnent des débits initiaux assez proches. Les résultats indiquent en revanche qu'il est nécessaire d'utiliser de bons modèles de déstabilisation pour simuler correctement la transition entre le glissement (où la masse reste cohérente) et l'avalanche de débris (où tout est disloqué) si l'on veut estimer précisément les débits rocheux entrant en mer.

Les avalanches de débris sont rares et difficile à observer. Les caractéristiques des tsunamis étant particulièrement sensibles à la façon dont s'effondre les volcans, le couplage dépôts de tsunami / simulation numérique pourrait être une solution pour reconstituer la dynamique des grands glissements de flanc.

5.3. Autres travaux

Nous avons aussi utilisé la version tsunami de *VolcFlow* pour reproduire le glissement du Kick'em Jenny, volcans sous marin des Petites Antilles (Dondin et al., 2012). Une fois de plus la rhéologie plastique semble être mieux adaptée que les autres mais la valeur de T_0, estimée à 150 kPa, est environ trois fois plus importante que pour les autres simulations. Il m'est néanmoins difficile de tirer des conclusions de cette valeur : limite réelle du comportement plastique ou faible précision des données ? En effet, les données bathymétriques de la zone sont difficiles à interpréter et les incertitudes sont probablement grandes quant à la reconstruction de la topographie pré-avalanche.

Nous avons aussi utilisé le modèle pour prévoir l'effet d'un éventuel effondrement de l'Anak Krakatau sur les rives du détroit de la Sonde (Giachetti et al, 2012). L'Anak Krakatau pousse sur le rebord d'une caldeira, configuration qui pourrait mener à sa déstabilisation. Un effondrement de l'édifice entrainerait des vagues de 15 à 30 m sur les côtes de l'archipel de Krakatau (situé à environ 5 km du volcan). Les amplitudes diminueraient pour être inférieures à 2 m sur les côtes du détroit de la Sonde.

VolcFlow a été utilisé dans le cadre de deux thèses :

- Thomas Boulesteix, « Age, récurrence et mécanismes de déstabilisation des flancs des volcans océaniques d'après l'exemple de Tenerife (iles Canaries) », 30 sept. 2011, Orsay, Essonne

- Frédéric Dondin, « Simulations numériques et impact tsunamogène d'une déstabilisation de flanc au volcan sous-marin Kick'em Jenny, Petites Antilles », 13 déc. 2010, Univ. des Antilles et de la Guyane.

6. Simulation des écoulements pyroclastiques du volcan Tungurahua (Equateur)

Les écoulements pyroclastiques, plus fréquents que les avalanches de débris, menacent des milliers d'habitants en Amérique du Sud, Indonésie, Japon, etc. Les simuler correctement est donc essentiel pour évaluer les menaces et mettre au point les scénarios de protection et/ou d'évacuation. Cependant, malgré des progrès importants (par exemple : Burgisser and Bergantz 2002; Neri et al. 2003; Dartevelle 2004), leur rhéologie comme celle des avalanches de débris est trop complexe pour être aujourd'hui comprise et décrite par des lois mathématiques robustes. C'est pourquoi, actuellement, la meilleure approche que nous ayons pour estimer leur rhéologie est de simuler les écoulements avec différentes lois et comparer les résultats aux données naturelles pour déterminer la loi la mieux adaptée.

6.1. L'éruption d'août 2006 du volcan Tungurahua

Le volcan Tungurahua, en Equateur, est entré en éruption en juillet puis en août 2006. Des écoulements pyroclastiques se sont mis en place sur tout son flanc ouest. Pour confronter objectivement les résultats numériques au phénomène naturel, il est essentiel de choisir des éruptions dont il est possible de reconstituer la chronologie. Cette éruption a donc été choisie car elle a été très bien suivie par nos collègues équatoriens de l'Institut Géophysique de Quito (IG-EPN). En plus de leurs observations visuelles, ils ont recueilli les témoignages d'habitants ainsi que des vidéos. Ils ont filmé l'éruption à l'aide d'une caméra thermique et, surtout, mesuré l'activité sismique pendant l'éruption. L'activité sismique est très importante car, en enregistrant les vibrations engendrées par les écoulements, elle témoigne de leur mise en place et fournit des indications sur leurs vitesses. Durant mon affectation à l'IRD, qui a débuté peu de temps après l'éruption, j'ai aussi pu étudier la morphologie des dépôts frais ainsi que la structure interne des dépôts qui apparaissaient au fur et à mesure de leur érosion (Figure 18).

Les données recueillies sur le terrain ont été utilisées pour cartographier précisément les dépôts et mesurer localement leurs épaisseurs. Les données de l'IG-EPN ont servi à déterminer les conditions à la source : les écoulements pyroclastiques ont débuté par des explosions sporadiques donnant des écoulements assez courts. L'éruption s'est terminée par une phase paroxysmale de 40 minutes qui a émis l'essentiel des écoulements. Aucune explosion n'est visible dans les vidéos avant la genèse des écoulements de la phase paroxysmale. Il semble que les écoulements se soient formés par l'accumulation de cendres, de scories et de lithiques issus d'une fontaine de lave. Les produits déposés sur des pentes raides se seraient alors déstabilisés en formant des écoulements.

Les simulations ne concernent ici que les écoulements pyroclastiques denses. Elles mettent en évidence qu'un frottement de type Coulomb ne permet pas de reproduire correctement les dépôts. Pour atteindre les distances naturelles (~6 km) avec un écoulement de type Coulomb, l'angle de frottement basal doit être de 15° environ. Les écoulements obtenus accélèrent sur les pentes les plus

fortes (>15° dans ce cas) pour atteindre des vitesses irréalistes d'environ 150 m/s. Les écoulements simulés affectent aussi bien les chenaux que les interfluves tandis que les écoulements naturels sont très canalisés. Enfin, les écoulements s'accumulent au niveau de leur front sous formes de tas très épais (> 100 m pour une seule unité) avec une pente de 15° environ. Les problèmes ne sont pas liés aux conditions particulières de l'éruption (volume, débit, etc.) mais sont liés essentiellement à la pente du volcan passant de 30° au sommet à 5° à quelques kilomètres. Cette morphologie étant très commune sur les volcans, la conclusion de la non applicabilité du modèle Coulomb simple à la simulation des écoulements pyroclastiques denses semble généralisable. Les autres lois simples (Table 1) ont été utilisées mais elles n'ont pas donné non plus de résultats concluants.

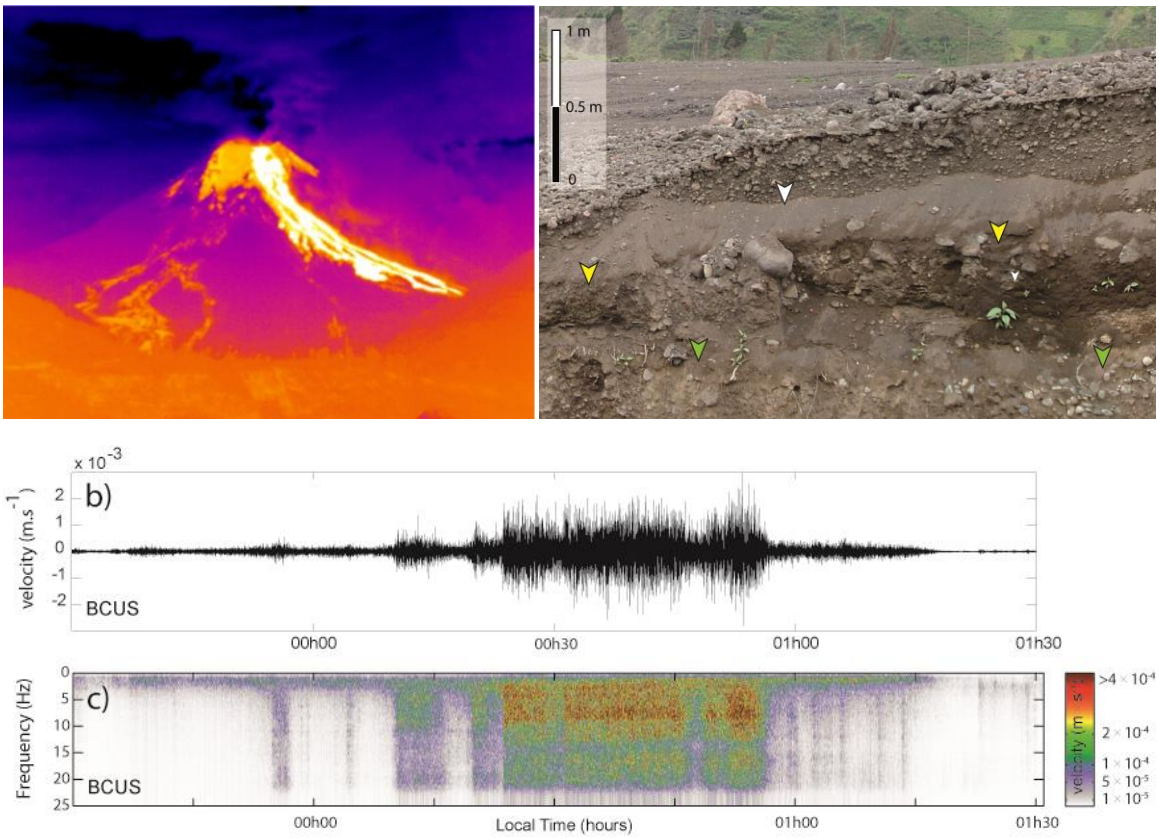

Figure 18 : Parmi les données utilisées pour tester la qualité des résultats numériques, il y a les images thermiques de l'IG-EPN (haut à gauche), les études des dépôts (morphologie et coupes, en haut à droite) ainsi que les enregistrements sismiques de l'IG-EPN (en bas).

En revanche, comme pour les avalanches de débris, le comportement plastique donne les meilleurs résultats : les écoulements simulés sont canalisés au fond des vallées, leur vitesse est compatible avec les observations et toutes les vallées affectées par l'éruption de 2006 sont affectées de la même façon par le modèle. La mise en place de l'écoulement se fait par bouffées successives malgré l'alimentation constante à la source : la masse s'accumule au niveau du cratère jusqu'à ce que sont poids déclenche son écoulement. Elle décélère en dessous d'une certaines épaisseur puis finit par s'arrêter. La masse continue de s'accumuler au niveau du cratère jusqu'à une nouvelle mise en mouvement. Les résultats

indiquent que le seuil de plasticité T_0 doit être de quelques milliers de pascals (1-5 kPa), ce qui est plus d'un ordre de grandeur en dessous des valeurs trouvées pour les avalanches de débris.

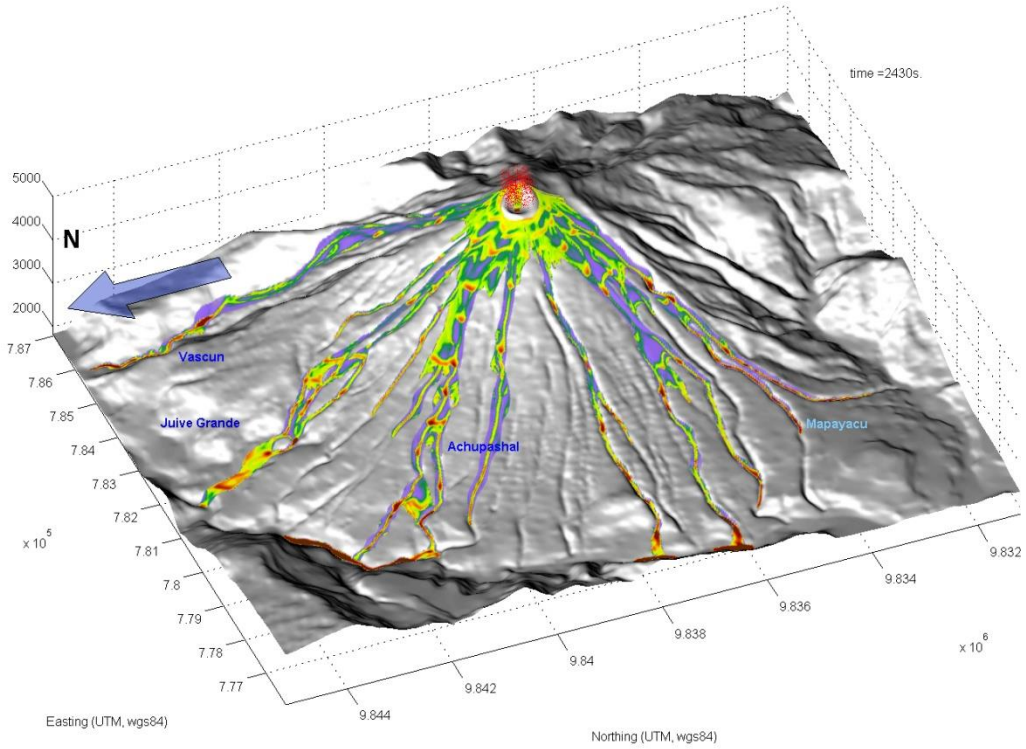

Figure 19 : Simulation de l'éruption de 2006 du Tungurahua (Equateur).
Les dépôts simulés sont très proches des dépôts naturels (voir Kelfoun et al., 2009)

Il est nécessaire de signaler que même si les résultats sont très bons, le comportement plastique ne reproduit pas exactement la réalité. Les accumulations de dépôts en arrivant dans la rivière principale au pied du volcan ne sont pas reproduites (mais il est possible que l'effet de l'eau induise un changement de comportement rhéologique). Il existe aussi un problème de volume : avec le volume total des dépôts, le modèle ne reproduit que l'épaisseur d'une seule unité. Ceci est dû à la relativement mauvaise qualité de la topographie utilisée qui, en élargissant artificiellement les vallées et en adoucissant leurs parois, permet un étalement latéral trop important des écoulements. Or, la capacité d'écoulement d'un modèle plastique est liée à son épaisseur : un écoulement plastique qui s'étale trop latéralement, atteint donc une distance plus faible que s'il ne s'était pas étalé. En conséquence, il lui faut un volume plus important pour atteindre les distances atteintes par les écoulements réels. Néanmoins, ce fait ne remet pas en cause la valeur de T_0 obtenue si nous considérons que les couches plus récentes se mettent en place sur les couches plus anciennes sans les remanier.

6.2. Autres simulations d'écoulements pyroclastiques denses

Des simulations ont aussi été réalisées sur les volcans de la Soufrière Hills de Montserrat, le Merapi en Indonésie, le Lascar au Chili, l'Atacazo et le Reventador en Equateur, le Misti au Pérou, etc. La qualité des observations naturelles n'étant pas suffisante pour sérieusement définir les conditions à la source des écoulements, ces travaux n'ont pas fait l'objet de publications. Il est cependant possible d'affirmer que les conclusions concernant le Tungurahua valent aussi pour les autres édifices. Les valeurs du seuil de plasticité sont proches, les plus faibles ayant été obtenues sur les écoulements de ponces du volcan Lascar (~1 kPa).

Le moins bon résultat a été obtenu sur les écoulements du Merapi de 1994. Il est possible que le problème provienne de la qualité de la topographie utilisée. Or les écoulements du Merapi sont très influencés par la topographie sommitale : une erreur de direction dans les premières centaines de mètres des écoulements induit une mauvaise distribution des dépôts. Il est aussi possible que le comportement plastique ne soit pas compatible avec les comportements des écoulements pyroclastiques formés par des débits trop importants. Dans le cas du Merapi, les effondrements de dômes provoquent des débits importants, d'où une épaisseur importante des écoulements. L'accélération des écoulements à comportement plastique dépendant de l'épaisseur (puisque les forces motrices en dépendent et que la résistance est constante), la vitesse des écoulements simulée est très forte. Pour obtenir une distribution correcte des dépôts, il est nécessaire de limiter la vitesse d'écoulement en ajoutant au frottement plastique un frottement dépendant de la vitesse. Les données de terrain ne permettent malheureusement pas de savoir si ce comportement à une signification physique (turbulence, collisions, par exemple) ou s'il s'agit d'un artefact permettant de compenser une mauvaise prise en compte de la physique de ces écoulements ou de la topographie sommitale. Charbonnier et Gertisser (2012) ont utilisé *VolcFlow* et montrent qu'il est possible de reproduire beaucoup de caractéristiques de l'éruption du Merapi en 2006 avec un comportement plastique associé à une contrainte dépendant de la vitesse au carré. Ils montrent aussi que pour obtenir des résultats corrects avec un comportement Coulomb (en utilisant le code Titan2D), il est nécessaire de faire varier l'angle de frottement en fonction de la pente. Cette variation qui n'a aucune réalité de terrain démontre une fois de plus les failles du comportement Coulomb pour la simulation des écoulements pyroclastiques.

7. Simulation des écoulements denses et dilués

Les écoulements pyroclastiques sont généralement constitués de deux phases : une phase dense canalisée au fond des vallées et une phase diluée souvent plus mobile. Les écoulements denses peuvent engendrer des écoulements dilués et inversement, les écoulements dilués peuvent former des écoulements denses (Fisher, 1979 ; Druitt and Sparks, 1982 ; Druitt et al., 2002).

L'approche la plus adaptée pour ce type de modélisation est très probablement l'approche multiphasée, capable en théorie de simuler aussi bien les écoulements denses que les écoulements dilués voire les phases intermédiaires et les nuages co-ignimbritiques. Dans cette approche, chaque composant est considéré comme une phase : gaz volcanique, atmosphère, particules d'un diamètre donné. Les codes sont généralement basés sur un schéma eulérien : chaque phase représente une proportion d'une zone de l'espace représentée par une maille fixe. Les codes fonctionnent en 2D vertical ou 3D, mais les besoins de calculs de tels codes limitent encore l'approche 3D. J'explique avec plus de détails dans Roche et al. (sous presse, p.81), les caractéristiques des différentes approches numériques dont celles de l'approche multiphasée utilisée ici et celles de l'approche moyennée verticalement que j'ai choisie pour VolcFlow.

En 2000, au laboratoire National de Los Alamos, puis en 2001-2002 à Clermont-Ferrand, j'ai travaillé sur l'adaptation volcanologique de codes multiphasés déjà existants : CFDlib (LANL) et MFix (U.S. Department of Energy laboratories). En collaboration avec Sébastien Dartevelle, nous avons modifié le code MFix pour introduire des lois de comportement plus réalistes à plus forte densité de particules. En effet, les codes précédents prenaient très mal en compte le changement de comportement rhéologique en passant d'un écoulement dilué à un écoulement dense. Le nouveau code, GMfix, prend en compte cette transition entre un écoulement dilué où le gaz joue un rôle essentiel dans la dynamique, un écoulement où les collisions deviennent plus importantes, puis un écoulement où la concentration en particules est telle que les frictions deviennent dominantes.

Les simulations réalisées paraissent très proches de la réalité. Elles reproduisent la formation d'une colonne éruptive dont les parties les plus denses forment un écoulement pyroclastique, les parties les moins denses formant un panache plinien.

Les simulations de colonnes pliniennes sont en accord avec la théorie classique des panaches ainsi qu'avec les éruptions historiques. A des débits massiques élevés (>10^7 kg/s), la colonne plinienne montre des pulsations périodiques liées à la propagation verticale d'ondes acoustiques à l'intérieur du panache. La température de la partie la plus haute du panache tombe à -18° par rapport à la température environnante, ce qui semble compatible avec les éruptions de El Chichon et du Mt. St.Helens (Holasek and Self, 1995 ; Woods and Self, 1992). Les simulations reproduisent aussi la transformation de la partie basale d'un écoulement pyroclastique dilué en écoulement dense. L'écoulement dense peut alors dépasser l'écoulement dilué initial et engendrer son propre écoulement dilué.

Mais ces simulations présentent les mêmes problèmes que les simulations d'écoulements denses : ces modèles résolvent une physique incorporée dans le code et ne la devinent pas. Par conséquent, tant que la physique n'est pas correctement comprise, ces modèles sont aussi incapables de reproduire les phénomènes naturels que les autres approches. Les calculs étant lourds et le nombre de paramètres et de lois trop importants (plusieurs dizaines), une approche par essai/erreur ne peut pas être menée pour obtenir les meilleurs paramètres capables de reproduire un phénomène naturel.

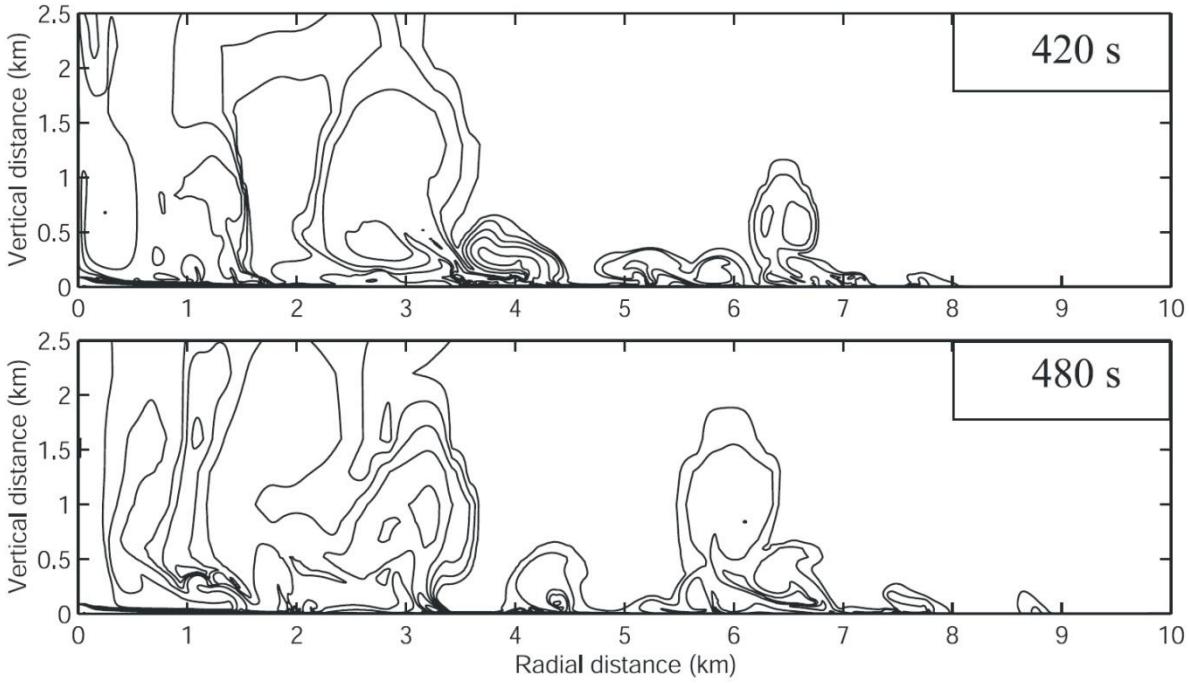

Figure 20 : Simulation de la propagation d'un courant de densité pyroclastique issu d'un effondrement de colonne éruptive (Dartevelle et al. 2004)

C'est pourquoi je cherche désormais à développer une autre approche qui néglige les phases de transition. Dans cette approche, développée au chapitre 3.3, seuls deux écoulements sont pris en comptes : un écoulement dense et un écoulement dilué ; la densité de l'écoulement dilué varie en fonction des apports de particules et de la sédimentation. Cette approche est beaucoup plus simple mais permet de calibrer plus facilement les paramètres (5 environ) par essai/erreur en comparant les résultats numériques au terrain. Les premiers résultats sont encourageants car ils reproduisent les zones détruites par l'éruption de 1994 du Merapi, l'intensité des dégâts ainsi que les directions d'écoulements dilués accessibles par les directions des troncs qu'ils avaient soufflés.

8. Morphologie des dépôts

Les chapitres précédents démontrent que le comportement plastique est la loi de première ordre la mieux adaptée pour reproduire les extensions, les épaisseurs et les vitesses des écoulements pyroclastiques et des avalanches de débris. Mais il reproduit aussi la morphologie globale des dépôts naturels. Ces dépôts présentent très souvent des levées latérales ainsi que des fronts bombés.

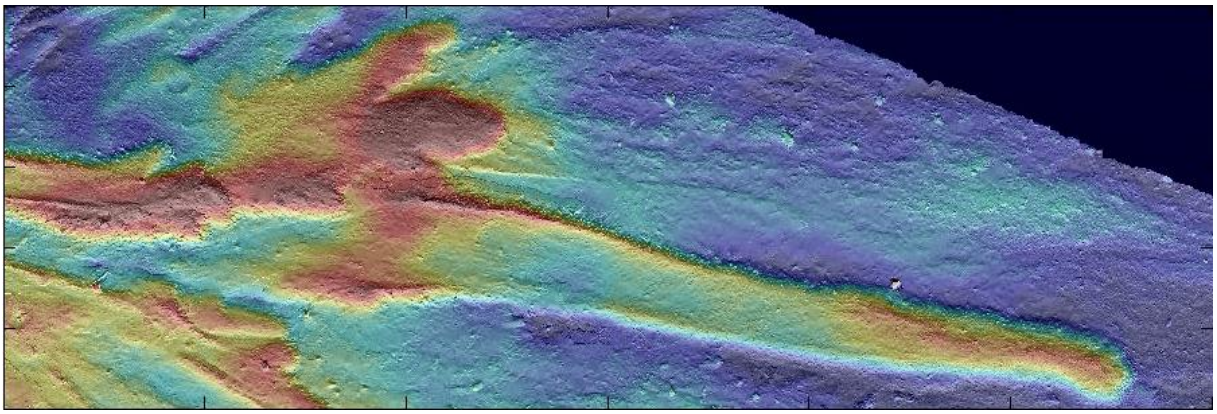

Figure 21 : Morphologie naturelle mesurée par technologie Lidar (Jessop et al., accepté avec modifications).

Pour tester la morphologie obtenue avec le comportement plastique, j'ai travaillé sur des topographies simplifiées ; celles-ci sont obtenues en ajustant des lois mathématiques très simples aux topographies naturelles. L'objectif est d'obtenir une topographie la plus simple possible, réaliste à grande échelle mais sans fluctuations à plus petite échelle susceptibles de créer des perturbations morphologiques. La Figure 22 montre comment est obtenue la topographie, donnée par l'expression mathématique suivante :

$$z = 2000 \times e^{-x_h/3000} - 200 \qquad [22]$$

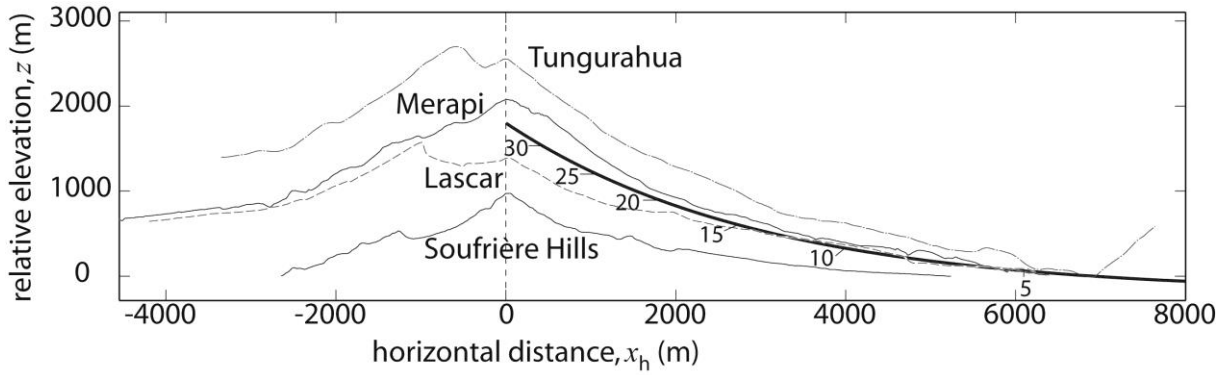

Figure 22 : loi exponentielle obtenue à partir des topographies de quatre volcans ayant récemment produit des écoulements pyroclastiques (Kelfoun, 2011).

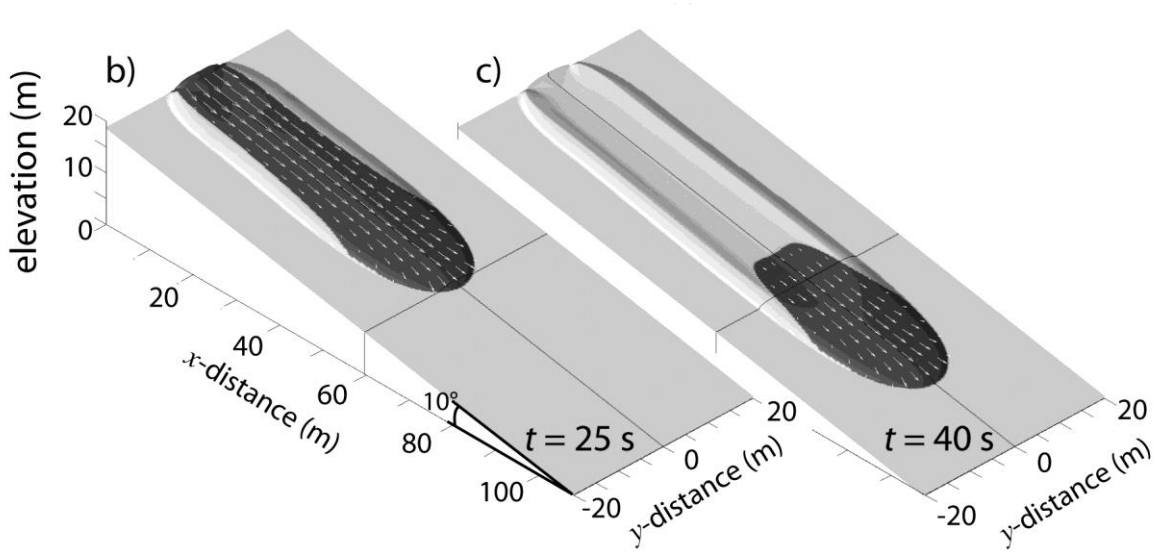

Figure 23 : le comportement plastique permet de reproduire la morphologie naturelle à lobes et levées (Kelfoun, 2011).

Les résultats indiquent que le comportement plastique est capable de créer des lobes et des levées proches de ceux des dépôts naturels (Figure 23). Cette morphologie particulière se forme au front de l'écoulement. Elle s'explique par la direction des déplacements et des contraintes motrices. La forme arrondie du front force la masse latérale à se déplacer perpendiculairement à la direction principale d'écoulement. La contrainte du poids, orientée vers la pente, celle induite par le gradient de pression et l'inertie, toutes deux ayant une composante perpendiculaire à la direction d'écoulement, ne sont pas dirigées dans la même direction. Sur les bords de l'écoulement, le front s'étale, s'amincit et décélère quand les forces motrices sont inférieures au seuil de plasticité T_0 puis s'arrête à une certaine épaisseur. Ce processus crée des bordures statiques qui canalisent le reste de l'écoulement. Une fois la masse canalisée par les bordures, les forces motrices, liées à l'inertie, au poids et au gradient de pression sont toutes orientées dans la même direction. L'écoulement ralentit lorsque ces forces sont inférieures à T_0, et s'écoule donc à plus fine épaisseur que sur les bords. Ce mécanisme forme la morphologie caractéristique à lobes et levées. Les épaisseurs du centre de l'écoulement et des levées sont directement liées à la valeur de T_0 choisie. Un article récent de Johnson et al. (2012) étudie le comportement de grains saturés en eau. Les résultats expérimentaux qu'ils obtiennent sont très proches des déplacements et des morphologies obtenues numériquement avec le comportement plastique (Kelfoun, 2011).

Les comportements Coulomb à angle de frottement constant (Figure 24), Voellmy, visqueux et turbulents sont incapables de former ce type de dépôts quelles que soient les topographies ou les conditions sources utilisées. De toutes les lois testées, seul un comportement Coulomb dont l'angle de frottement varie en fonction de l'épaisseur de l'écoulement permet de reproduire des levées (Mangeney et al., 2007). La ressemblance entre ce comportement et le comportement plastique est discutée au chapitre 11.

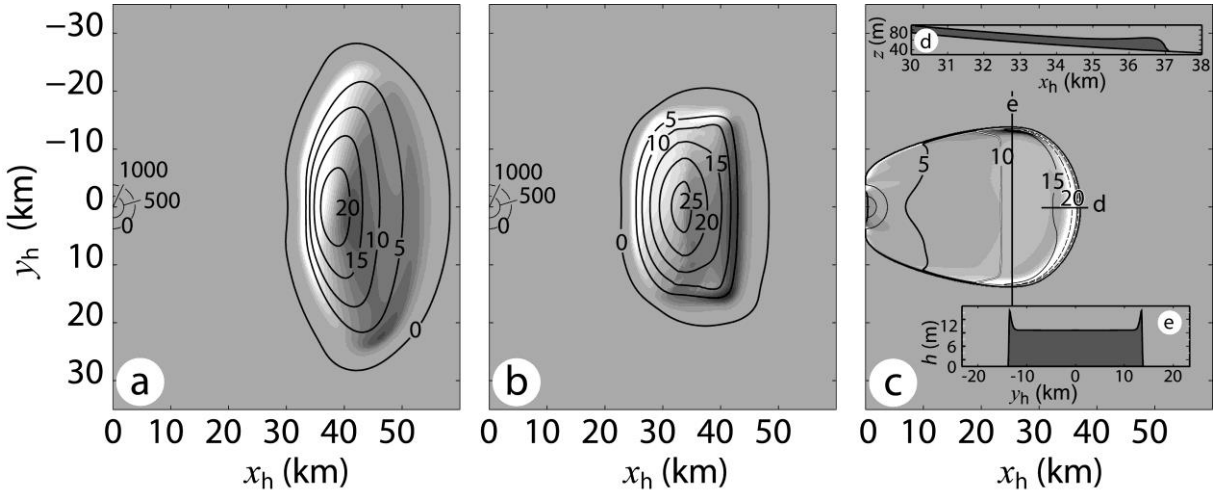

Figure 24 : simulation d'une avalanche de débris sur topographie simplifiée (Kelfoun, 2011). (a) rhéologie Coulomb avec seulement un angle basal, φ_{bed}=2° (b) rhéologie Coulomb avec deux angles de friction, φ_{bed}=2° et φ_{int}=30°, (c) comportement plastique T = 30 kPa. Les dépôts de type Coulomb forment des accumulations coniques tandis que le comportement plastique forme un dépôt à lobes et levées.

9. *VolcFlow* : un outil d'évaluation des aléas volcaniques par modélisation numérique ?

L'aspect le plus concret des recherches concernant les écoulements volcaniques est l'amélioration des cartes de menaces. Mais peut-on actuellement utiliser les modèles numériques pour évaluer les menaces ? Leurs prévisions sont-elles justes, partielles ou erronées ? Peut-on se satisfaire d'un modèle imparfait si les incertitudes liées aux lacunes de connaissances sur la rhéologie des écoulements sont moins importantes que celles liées à notre méconnaissance des conditions à la source ? Dans l'état actuel, la modélisation apporte-t-elle un plus à l'évaluation des menaces ?

Dans le cadre d'un projet de notre partenaire en Equateur, l'Institut Géophysique de l'Ecole Polytechnique nationale (IG-EPN), et du Secrétariat National de Gestion des Risques (SNGR) équatorien, soutenus par la Banque Interaméricaine de Développement (BID), j'ai été contacté pour aider à l'établissement d'une nouvelle carte de menace du volcan Tungurahua par modélisation numérique. Le volcan menace la ville touristique de Baños et les villages voisins (25 000 habitants) ainsi qu'un axe routier principal reliant la Sierra à l'Amazonie. Suite à des discussions que nous avions eues pendant mon détachement à l'IRD, l'IG avait acquis une topographie à haute résolution (5 m) du volcan Tungurahua. La topographie joue énormément sur la dynamique et les zones touchées par les écoulements pyroclastiques. Obtenir une telle précision est un point crucial pour la suite de cette étude.

La première étape consistait à tester la qualité de l'approche en comparant les résultats du modèle d'écoulement aux écoulements réels de l'éruption du Tungurahua en 2006. Il s'agissait non seulement de tester les capacités de *VolcFlow* mais aussi la qualité de la topographie. Les conditions à la source (débits, volumes, etc.) ont été déterminées par les travaux de Kelfoun et al., 2009, (chapitre 6.1). Les résultats démontrent que le modèle reproduit très fidèlement les épaisseurs, les extensions et les distances atteintes par les dépôts de 2006 avec une topographie actualisée et de haute résolution. Dans quelques secteurs en revanche, la qualité de la topographie ne permet pas d'obtenir les vallées correctes (les laves de 2006 par exemple sont sur une zone entièrement interpolée sur la topographie de l'IG). Les résultats numériques sont donc faussés.

Les simulations de déferlantes pyroclastiques ont été effectuées en même temps que celles des écoulements dilués à la demande des collègues équatoriens en utilisant la version deux fluides de *VolcFlow*. Ces modèles n'ayant pas encore été calibrés de façon rigoureuse, les résultats sont à prendre avec prudence. Les lois d'interaction ont été modifiées de façon à ce que la déferlante n'agisse pas sur l'écoulement basal de telle sorte que si la calibration de l'écoulement dilué n'est pas correcte elle ne fausse pas les calculs des écoulements denses.

Plusieurs types de simulations ont été réalisés. Les premiers sont des simulations d'éruptions dont les paramètres sont déterminés en fonction de scénarios éruptifs précis définis par les collègues de l'IG-EPN et de l'IRD. Les résultats indiquent que des écoulements denses de volumes modérés ne peuvent pas affecter le centre de la ville de Baños. En revanche, des variations très faibles par rapport

à 2006 (altitude de la colonne éruptive, volume ou débit) peuvent affecter les abords des rivières Vazcum et Ulba, en périphérie de la ville, où vivent quelques centaines d'habitants et peuvent bloquer simultanément les deux sorties principales de Baños, empêchant toute évacuation. Les habitants devraient alors se réfugier sur les parties élevées de Runtun (en haut à gauche sur l'image de droite de la Figure 25). Les simulations indiquent aussi que la ville de Baños, dans sa totalité, pourrait être détruite par des déferlantes pyroclastiques (mais le modèle dilué n'a pas encore été suffisamment testé pour affirmer que ces conclusions sont correctes).

Les simulations indiquent aussi que les temps de parcours des écoulements entre le cratère et les zones habitées peuvent être très courts, inférieurs à 5 minutes.

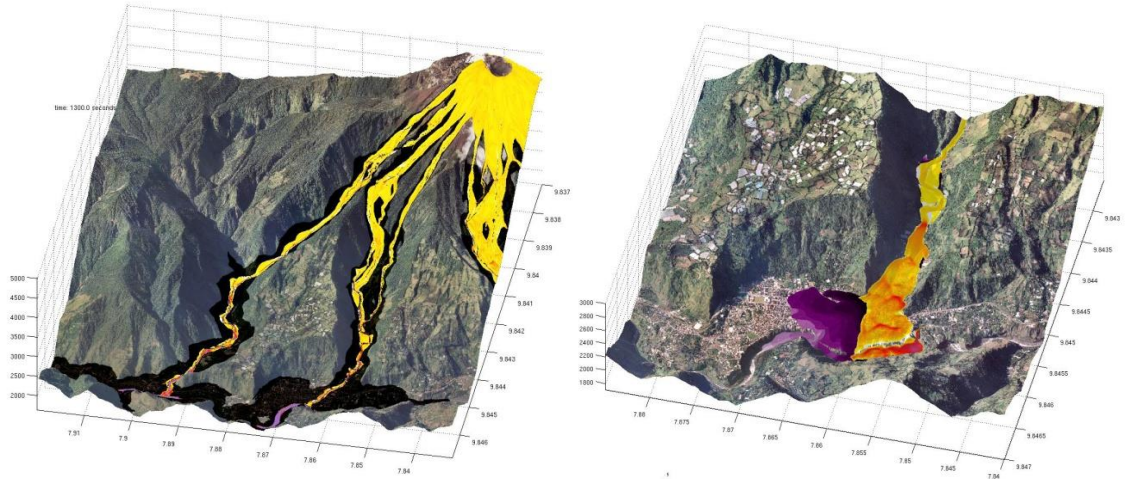

Figure 25 : a) simulation d'une éruption de 300 s et d'un volume de 25 millions de mètres cube. En jaune/rouge/violet : dépôts d'écoulements denses. En noir, dépôts de déferlantes. b) Effet de l'accumulation des dépôts successifs en cas d'éruption durant plusieurs jours. Les dépôts accumulés sont représentés en violet, l'épaisseur du dernier dépôt en jaune/rouge.

L'inconvénient du type d'approche réalisé ci-dessus est qu'il part du principe que nous pouvons déterminer exactement les caractéristiques de la future éruption. Or, il nous est impossible de prévoir le volume, le débit et le mode de genèse des futurs écoulements pyroclastiques. Pour pallier à ces inconvénients, une approche probabiliste a été utilisée. Environ 50 simulations sont réalisées pour chaque cas en variant les paramètres éruptifs et rhéologiques autour de la valeur moyenne définie par le scénario (Figure 26). Les paramètres variables sont le volume émis, le temps de formation, la vitesse initiale d'éjection, la zone de genèse des écoulements, le débit, le taux de formation et de dépôt des déferlantes. Ces cartes indiquent ainsi clairement les zones qui ne seront jamais touchées par un scénario de tel type, celles qui le seront toujours et celles qui ont de forts risques de l'être même si la probabilité ne peut pas être clairement définie.

Des simulations ont aussi été réalisées pour étudier ce qui se passerait en cas d'éruption prolongée. Les modèles indiquent que si la probabilité est très faible pour que des écoulements denses de quelques millions de mètres cubes affectent le centre de la ville de Baños, il en est tout autre si l'éruption dure. En effet, les dépôts accumulés à l'embouchure du rio Vazcum boucheront

progressivement la vallée. Une fois la vallée remplie, les écoulements denses suivant déborderont pour détruire la quasi-totalité des zones habitées (**Figure 25** b).

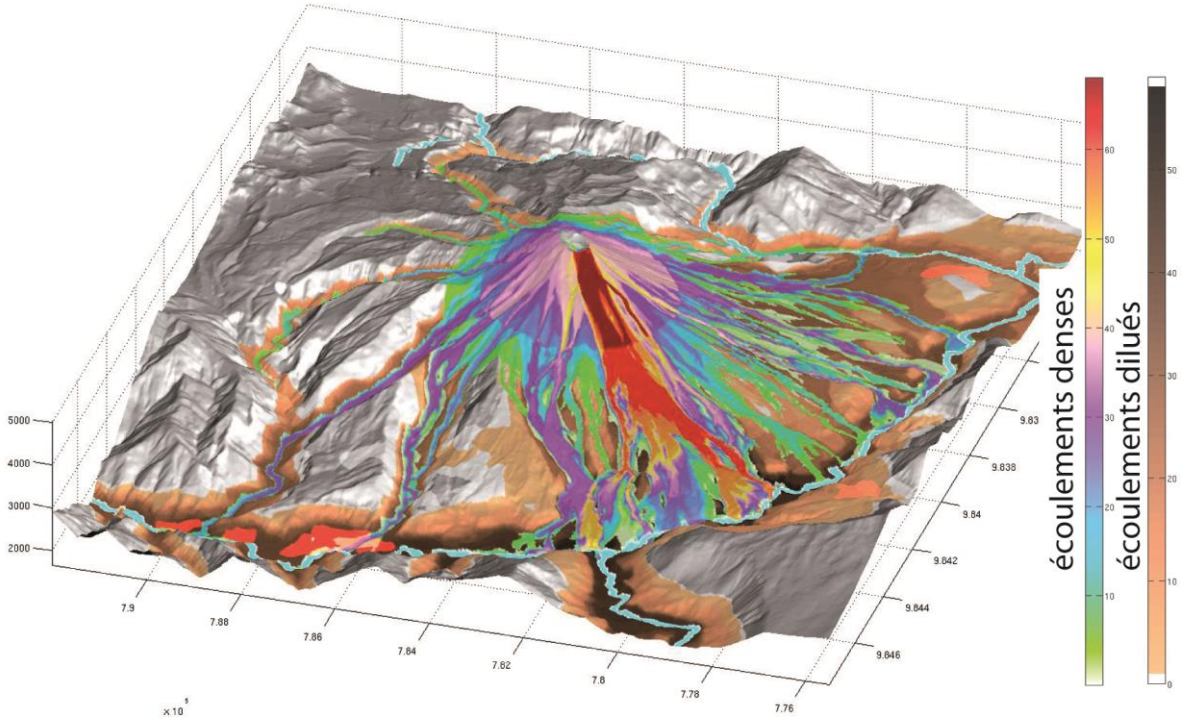

Figure 26 : carte probabiliste pour un volume émis de 10 à 50 millions de m^3. Les couleurs représentent le nombre de fois qu'une zone a été touchée par les simulations. La zone d'Ashupashal, en rouge, est la plus menacée. Les écoulements denses peuvent traverser Baños mais n'atteignent pas le centre ville. Les zones touchées par les déferlantes sont en marron.

En conclusion, et malgré les fortes réserves que j'émettais avant cette étude, je pense que l'outil numérique est particulièrement utile pour l'évaluation des menaces. Les résultats reproduisent correctement les dépôts passés (du Tungurahua mais aussi de l'Atacazo et du Pichincha) et indiquent les zones critiques qui peuvent être affectées par les écoulements pyroclastiques en cas de variations des conditions sources. Les simulations s'adaptent particulièrement bien aux changements topographiques. Bien entendu, la rhéologie des modèles est pour le moment approximative et les phénomènes de ségrégation, d'érosion/entrainement ne sont pas explicitement pris en compte. Il faut donc interpréter les résultats avec prudence, analyser le comportement global des écoulements et ne pas se fier exactement aux limites données par les modèles mais plutôt aux vallées atteintes. Pour des édifices qui n'auraient pas fait l'objet d'études géologiques, l'apport des simulations me paraît encore plus évident. Un autre avantage très important de la simulation numérique est la possibilité de réaliser des animations d'éruptions. Il est ainsi plus facile de faire comprendre à la population comme aux décideurs ce que sont les écoulements pyroclastiques et comment ils se propagent. Une meilleure sensibilisation des risques encourus permet une meilleure gestion de l'évacuation des populations en cas de crise éruptive.

VolcFlow a aussi été utilisé par les collègues de l'IG pour améliorer la carte de menaces du volcan Reventador. J'ai reçu des demandes de plusieurs autres pays d'Amérique du Sud (Chili, Colombie, Pérou, Costa Rica, Mexique, etc.) concernant l'utilisation de *VolcFlow* pour établir des cartes de menace ou reproduire la mise en place d'évènements passés.

10. Généralisation et limites du comportement plastique

Les avalanches de débris et les écoulements pyroclastiques étant constitués de blocs et de cendres, les frottements interparticulaires pourraient conférer à l'écoulement un comportement type Coulomb. Cette hypothèse est confirmée par le comportement très proche entre les écoulements simulés avec la loi Coulomb et les avalanches rocheuses ou les écoulements granulaires en laboratoire (e.g. Gray et al., 2003; Savage and Hutter, 1991; Iverson et al., 2004). C'est probablement la raison pour laquelle ce modèle est souvent utilisé pour les simulations des avalanches de débris et des écoulements pyroclastiques (par exemple : McEwen and Malin,1989; Wadge et al., 1998; Evan et al., 2001; Crosta et al., 2004; Sheridan et al, 2005; Patra et al., 2005; Procter, 2010).

L'angle de frottement mesuré dans les dépôts des écoulements pyroclastiques et des avalanches de débris est d'environ 30°. Si cette valeur est utilisée, les dépôts simulés forment de simples accumulations au pied de la zone de détachement ou au bord du cratère. Pour atteindre des distances réalistes, il faut des angles de frottement bien plus bas : 1° à 5° pour les avalanches de débris, 10° à 15° pour les écoulements pyroclastiques (McEwen and Malin, 1989; Wadge et al., 1998; Evan et al., 2001; Crosta et al., 2004; Sheridan et al, 2005; Patra et al., 2005; Kelfoun and Druitt, 2005; Kelfoun et al, 2009; Procter et al., 2010). Le mécanisme de réduction de friction n'est pas clair et plusieurs explications ont été avancées : pression fluide, fluidisation acoustique, fluidisation mécanique, auto-fluidisation, fragmentation dynamique, etc. (e.g. Davies, 1982; Voight et al., 1983; Campbell et al., 1995; Davies and McSaveney, 1999; Iverson and Denlinger, 2001; Legros, 2002; Collins and Melosh, 2003).

Puisque nous ne comprenons pas quel mécanisme agit sur la dynamique des écoulements pyroclastiques et des avalanches de débris pour leur conférer une si grande mobilité, il n'est pas absurde d'imaginer que le comportement global de ce type d'écoulements puisse suivre un autre comportement que le comportement Coulomb (dont l'angle de frottement ne varie pas en temps et espace). Ceci est d'autant plus sensé que des études récentes ont démontré que même des billes de verre en laboratoire ne suivent pas exactement une loi de Coulomb (Pouliquen and Forterre, 2002). Plusieurs autres lois ont été invoquées pour la simulation des écoulements naturels, leurs auteurs reconnaissant implicitement que cette rhéologie n'est pas idéale quelle que soit la valeur de l'angle de frottement choisie. Heinrich et al. (2001) et Mangeney et al. (2007), par exemple, utilisent un angle de frottement qui varie en fonction de la vitesse et de l'épaisseur des écoulements, basé sur les résultats de Pouliquen (1999). Les avalanches de débris sont parfois considérées comme visqueuses (Sousa and Voight, 1995). Une autre loi souvent utilisée est le comportement Bingham (Table 1). Il a été évoqué pour expliquer les morphologies typiques des dépôts naturels (front bombés, levées) puis utilisé dans les simulations numériques (e.g. Wilson and Head, 1981; Voight et al., 1983; Rossano et al., 1996; Takarada et al., 1999; Palladino and Valentine, 1995).

La rhéologie plastique, rhéologie Bingham sans viscosité, a été proposée par Dade et Huppert (1998) pour expliquer les relations extensions / épaisseurs de dizaines de dépôts d'avalanches de débris. Les simulations présentées ci-dessus confirment leurs conclusions tout comme les simulations

de la plupart des autres cas testés, cas non publiés car les données de terrain disponibles ne permettaient pas d'apporter davantage que les cas précédemment décrits : les avalanches de débris de Llullaillaico (Argentine), du Lastarria (Argentine), du Lengai (Tanzanie), du Chimborazo (Equateur) et l'avalanche de débris secondaire du Socompa (Chili), les écoulements pyroclastiques de la Soufrière Hill (Montserrat), du Lascar (Chili), du Merapi (Indonésie), de l'Atacazo (Equateur), du Guagua Pichincha (Equateur) et du Reventador (Equateur). Le comportement plastique semble aussi adapté à la simulation d'autres types d'écoulements : les avalanches rocheuses non volcaniques comme celles de Huascaran et de Tacna, au Pérou, ou certains glissements martiens.

En revanche, et même en prenant en compte les incertitudes de terrain, il est possible d'affirmer que les comportements Coulomb, Voellmy, visqueux et turbulents ne sont capables de reproduire correctement les caractéristiques de premier ordre d'aucun écoulement et d'aucun dépôt naturel précédemment cité. L'effondrement rocheux de Pandemonium Creek, aux Etats-Unis, peut être très précisément reproduit mais seulement en ajoutant une contrainte turbulente au comportement plastique, contrainte probablement liée à la grande richesse en eau de cette avalanche. Malgré des problèmes de changement de concentration solide et de séparation entre l'eau et les particules non pris en compte par *VolcFlow*, les lahars du Cotopaxi et du Tungurahua (Equateur) peuvent être simulés correctement avec une loi similaire (du moins au premier ordre, les données disponibles n'étant pas très précises).

Certaines simulations indiquent cependant que le comportement plastique seul ne reproduit pas toujours précisément les phénomènes naturels. Pour l'avalanche de débris du Mt St Helens, par exemple, aucun des modèles testés ne parvient à reproduire la mise en place. La raison vient du comportement complexe des avalanches, qui peut être grossièrement subdivisé en 3 phases. Une phase initiale où les roches initialement cohérentes se disloquent pour former l'avalanche, une phase d'écoulement, une phase d'arrêt où le dépôt reprend un comportement Coulomb. Le comportement plastique rend compte de la phase d'écoulement et indirectement du dépôt mais ne peut pas simuler les avalanches où le glissement initial joue un rôle prépondérant sur la mise en place. Quel que soit le modèle rhéologique utilisé, les simulations s'écoulent tout autour du Mont St Helens alors que l'avalanche réelle s'est dirigée vers le Nord uniquement. En forçant le modèle à glisser initialement en masse, avec des lois totalement empiriques, il est possible d'obtenir des dépôts très proches de la réalité. L'avalanche secondaire de Socompa ne peut être simulée correctement qu'avec une loi similaire : comportement plastique plus glissement en masse. Si l'on utilise le comportement plastique sans le glissement en masse il est possible de simuler précisément l'extension de l'avalanche secondaire mais seulement avec un volume 3 fois inférieur au volume réel. L'épaisseur des dépôts simulés est donc 3 fois plus faible qu'en réalité. Un volume plus faible induit une épaisseur initiale plus faible et permet donc d'obtenir une vitesse initiale moins importante, ce qui reproduit plus ou moins et de façon indirecte l'effet de la dislocation initiale. En regardant dans le détail les dépôts de l'avalanche principale de Socompa, nous constatons qu'un glissement en masse s'est probablement produit sur les 5 premiers kilomètres et nous observons une imprécision des simulations plastiques à proximité du volcan. Mais pour cette avalanche, comme pour la plupart des autres avalanches testées,

la morphologie initiale du glissement fait que la non prise en compte de la dislocation initiale dans les simulations a très peu d'influence sur le résultat final.

Un autre problème apparaît pour la modélisation des écoulements pyroclastiques de 1994 au Merapi lorsque des volumes élevés de matériau (>200 000 m^3) s'effondrent en peu de temps (quelques secondes ou dizaines de secondes). Les écoulements simulés avec un comportement plastique sont trop rapides et s'échappent trop facilement des vallées par rapport à la réalité. Dans ce cas, un frottement dépendant de la vitesse de l'écoulement doit être introduit pour obtenir des résultats corrects, les meilleurs résultats étant obtenus pour une dépendance de la vitesse au carré. Il est difficile de savoir si ce frottement a une réalité physique ou n'est qu'artificiel. La dépendance du carré de la vitesse pourrait s'expliquer par un comportement turbulent ou collisionnel. Ces comportements ne paraissent pas aberrants pour des écoulements de particules dont le comportement est si fluide. La vitesse des autres écoulements pyroclastiques testés, ceux du Tungurahua par exemple, étant plus faible à cause du débit plus faible, la présence ou l'absence de ce frein supplémentaire modifie très peu les résultats. Mais d'autres explications peuvent être envisagées pour l'éruption de 1994 du Merapi. La résolution de la topographie numérique utilisée ne permet peut être pas de reproduire la forme exacte des vallées. L'écoulement numérique « voit » des vallées aux parois plus lisses et peut plus facilement s'en échapper. Le rôle de l'érosion du cône sommital par les écoulements pyroclastiques est probablement très important en 1994 comme l'attestent les photographies prises après l'éruption (Voight et al., 2000). *VolcFlow* peut simuler l'érosion comme la sédimentation mais il lui faut des lois de comportement et celles-ci sont actuellement très mal connues. L'érosion pourrait jouer un rôle en ralentissant les écoulements, même si les premières simulations réalisées récemment par Julien Bernard (doctorant LMV) indiquent que cet effet semble faible (généralement même, l'érosion épaissit l'écoulement et l'accélère).

11. Tentative d'explication de la rhéologie plastique

Plusieurs raisons pourraient expliquer pourquoi les écoulements pyroclastiques et les avalanches de débris se comporteraient de façon plastique. Des matériaux cohésifs sans angle de frottement ont un comportement plastique. Mais cette explication ne me semble pas valable pour les écoulements naturels puisqu'il faut expliquer d'où vient une telle « cohésion dynamique » des écoulements alors que les dépôts sont très peu cohésifs.

Il est plus probable que le comportement ne soit plastique qu'au premier ordre et bien plus complexe en réalité. Si le comportement plastique reproduit si bien les dépôts naturels, c'est essentiellement parce qu'il forme des écoulements capables de s'écouler à forte épaisseur et de rester statique à épaisseur plus faible. Il forme aussi des dépôts dont l'épaisseur statique diminue progressivement avec l'inclinaison de la pente. Or ce comportement ne peut pas être reproduit par les autres modèles rhéologiques simples et en particulier par le comportement Coulomb dont la capacité à s'écouler est quasiment indépendant de l'épaisseur. Seul le modèle Coulomb à angle de frottement variable en fonction de l'épaisseur reproduit ce comportement et seul ce modèle parvient aussi à créer des levées (Mangeney et al., 2007). La relation entre l'épaisseur de l'écoulement et sa capacité à s'écouler ressort nettement de l'étude des dépôts de l'avalanche de Socompa. Cette relation explique aussi pourquoi les avalanches de débris et les écoulements pyroclastiques ont une épaisseur qui varie peu le long de leur parcours.

L'origine de la relation épaisseur / capacité d'écoulement n'est cependant pas très claire. Elle pourrait être liée à la diffusion de pression fluide plus rapide dans les écoulements fins que dans les écoulements épais (e.g. Geldart, 1986; Roche et al., 2004; Druitt et al., 2007 et les références qu'ils contiennent). Les écoulements fins perdant plus rapidement les gaz qu'ils contiennent s'arrêteraient avant les écoulements épais. La présence de blocs dans les écoulements pourrait aussi jouer dans ce sens : à fortes épaisseurs, les blocs pourraient peu interagir avec le substratum tandis qu'à épaisseur plus faible, ils toucheraient le sol. Ce comportement pourrait aussi s'expliquer par une augmentation de la résistance mécanique de la base à la surface de ce type d'écoulements. Dans les écoulements épais, l'intérieur au comportement fluide permettrait un écoulement même sur de très faibles pentes. En diminuant d'épaisseur, la surface plus résistante interagirait avec le sol freinant l'écoulement. Cette vision serait tout à fait compatible avec les conclusions tirées des observations de terrain et d'image satellite de Socompa qui conduisent à un modèle d'avalanche fluide entourée d'une « croûte granulaire » au comportement fragile. Ce concept est proche du modèle de « plug flow » proposé pour les coulées de boues, les avalanches de débris et les écoulements pyroclastiques à partir d'études de terrain (e.g. Sparks, 1976; Branney and Kokelaar, 2002 et les références qu'ils contiennent). La ressemblance morphologique entre les dépôts granulaires et les coulées de laves va dans le sens de cette idée de « croûte ». Il est difficile d'expliquer pourquoi la résistance mécanique augmenterait vers la surface. L'origine pourrait être liée à une fluidisation mécanique par cisaillement à la base, à un effet de « fluidisation » par les fluides plus facilement piégés à l'intérieur de l'écoulement qu'en surface, ou encore à la granulométrie inverse qui s'acquiert souvent dans les mélanges granulaires, les grosses

particules laissant plus facilement s'échapper les fluides que les particules fines. Les dépôts pyroclastiques du Tungurahua en 2006 présentent très clairement cette granulométrie inverse. Mais dans certains dépôts, comme ceux du Merapi pourtant bien simulés par un comportement plastique, la variation granulométrique est moins claire. Pour l'avalanche principale de Socompa, l'augmentation de la granulométrie vers la surface est claire mais la « croûte » au comportement plus résistant est plus épaisse que la zone de blocs de surface. L'étude de l'avalanche secondaire de Socompa, mise en place sur les dépôts de la précédente, mène à des conclusions similaires, la « croûte » représentant la moitié de l'épaisseur de l'avalanche.

Figure 27 : coupe dans un dépôt d'écoulement pyroclastique du Tungurahua (éruption d'août 2006). L'unité supérieure, non remaniée, montre un granoclassement particulièrement net.

12. Perspectives

La compréhension de la physique des écoulements granulaires volcaniques est complexe et plusieurs approches doivent être menées de front : expériences de laboratoire, mesures de terrain, simulations numériques. Les approches sont complémentaires et, à terme, leurs conclusions doivent converger. Pour l'instant, certains liens existent mais il reste certaines contradictions apparentes entre ce que montrent le terrain, les expériences et les modèles. Par exemple, le comportement plastique ne reproduit ni la dynamique ni les dépôts des écoulements, fluidisés ou non, obtenus en laboratoire. Une confrontation avec les expériences d'Olivier Roche (LMV) indiquent qu'il faut envisager 3 stades d'écoulements aux rhéologies différentes pour s'approcher des résultats obtenus. En laboratoire, un dépôt se forme à la base de l'écoulement, la dernière partie à s'écouler se trouvant en surface. Le dépôt des avalanches de Socompa (primaire et secondaire) semble plutôt indiquer une structure inverse, la partie la plus résistante se trouvant en surface. Ces comportements sont-ils incompatibles ? Les expériences ne voient-elles que les stades ultimes du dépôt dont nous ne parvenons pas à retrouver de traces sur le terrain ?

Le développement de codes type *VolcFlow,* simplifiés mais capables de simuler en moins de quelques heures les phénomènes naturels à l'échelle d'un volcan, est nécessaire pour la caractérisation de la rhéologie globale et pour améliorer les cartes de menaces. A court terme, je compte développer, tester les limites et améliorer le modèle double-fluide pour simuler les deux phases (écoulements denses, déferlantes) de la plupart des écoulements pyroclastiques.

Mais ce type de code ne nous explique pas l'origine du comportement macroscopique obtenu. En particulier, il est nécessaire de comprendre ce qui confère aux écoulements naturels, au premier ordre du moins, un caractère plastique. Tous les codes numériques utilisés, à ma connaissance, se basent sur des hypothèses très fortes par rapport au comportement physique. Les modèles cherchent à résoudre le comportement d'un écoulement soumis à telle ou telle type de physique mais ne la devine jamais. Si la physique est simple, cette approche est valide. Mais de telles hypothèses peuvent s'avérer dangereuses lorsqu'on s'intéresse à des écoulements complexes dont la physique n'est pas claire. C'est pourquoi, en collaboration avec des collègues du Labex Clervolc, de géologie et de mathématiques, je souhaite développer des simulations à l'échelle des grains. Les particules seront discrètes et se déplaceront dans un gaz qui s'écoulera autour d'elles. La taille des mailles sera plus petite que les particules. Il faut bien entendu utiliser des lois de comportement : interactions entre les particules, comportement des gaz, etc. mais cette physique est mieux connue. L'objectif sera d'étudier le comportement macroscopique d'un mélange de gaz et de plusieurs milliers de grains soumis, par exemple, à des vibrations. Ces simulations seront bien trop complexes pour être utilisées à l'échelle d'un volcan mais elles fourniront des lois probablement plus subtiles que le comportement plastique, lois qu'il sera possible d'utiliser dans des modèles type *VolcFlow* pour leur vérification à partir de données de terrain.

Le dernier aspect est de pouvoir juger objectivement de la qualité des modélisations réalisées. Les modèles sont de plus en plus complexes et les schémas numériques de plus en plus précis. Mais à

mesure que progresseront les modèles, nous serons confrontés à un problème de validation. Le risque est de voir se développer plusieurs modèles différents, qui donneront des résultats différents mais dont il sera impossible de déterminer l'adéquation avec le phénomène modélisé.

Une validation à partir d'expériences de laboratoire - qui ont l'avantage d'être bien contraintes - est nécessaire mais insuffisante. Pour faire évoluer les modèles d'écoulements pyroclastiques il est fondamental de recueillir les données les plus précises possibles des phénomènes naturels. C'est dans cette optique que nous avons obtenu des données morphologiques de haute résolution sur le dépôt de l'avalanche secondaire de Socompa et des coulées de ponce du Lascar. La topographie de l'avalanche a été calculée à partir d'images satellites Ikonos (projet PNTS, Ph. Labazuy) dont la résolution submétrique est adaptée à l'échelle du dépôt étudié (2 km de large, 6 km de long). L'avalanche secondaire de Socompa est particulièrement intéressante car elle interagit avec une topographie complexe grâce à laquelle nous pouvons tester rigoureusement les modèles numériques. Pour les coulées de ponces du Lascar, trop peu épaisses par rapport à leur extension, nous avons utilisé un Lidar sol grâce à une collaboration initiée par Philippe Labazuy (LMV) avec une équipe de topographes d'EDF (Figure 21). La technologie Lidar permet une reconstruction très précise de la morphologie des dépôts (résolution centimétrique), critère fondamental puisqu'elle est très fortement contrainte par la rhéologie complexe des phénomènes naturels. Il est essentiel de continuer ce type d'approche et de mettre au point une base de données des caractéristiques des dépôts naturels.

Mais les caractéristiques des dépôts ne suffisent pas et il nous faut aussi recueillir des données sur la mise en place des écoulements. La topographie pré-éruptive, les conditions à la source, et les vitesses doivent absolument être mesurés pour calibrer sérieusement les futurs modèles numériques. Dans les prochaines années, je souhaite développer des systèmes capables d'acquérir ces paramètres. Je me focaliserai sur les écoulements pyroclastiques car ils sont plus fréquents que les avalanches de débris. Je compte essentiellement cibler les écoulements pyroclastiques issus d'effondrements de dômes car leur volume peut être plus facilement estimé que pour ceux qui sont issus d'effondrements de colonnes. A moyen terme, le système sera basé sur la stéréophotogrammétrie sol. Le dispositif sera constitué de plusieurs couples de caméras installés autour de la source ou focalisés sur la zone sommitale.

Hors période de crise, l'accent sera mis sur le calcul régulier et à haute résolution de la zone sommitale des édifices qui se modifie au gré des éruptions et dont l'influence est primordiale sur le trajet des écoulements. Il sera aussi possible de calculer régulièrement l'évolution des dômes sommitaux et d'évaluer, après l'éruption, le volume de matériaux effondrés. Les modèles numériques indiquent que le volume effondré et la façon dont se produit l'effondrement jouent un rôle essentiel sur la mise en place. Il faut donc caractériser l'effondrement le plus précisément possible.

Les systèmes seront pilotables à distance pour s'adapter au type d'observations voulues. En période de crise, la fréquence des images sera augmentée. Le dispositif permettra de filmer les écoulements pyroclastiques et de caractériser leur mise en place en s'aidant des autres données recueillies : sismique, déformations, imagerie thermique, etc.

Obtenir de telles données doit passer par une observation systématiques de volcans cibles et donc par des collaborations étroites avec les observatoires volcanologiques. Le volcan Merapi, en Indonésie, est une cible idéale pour ce type de travaux. Le système aura le double objectif de recherche et d'alerte en détectant des croissances anormales des dômes sommitaux.

Le dispositif qui sera développé sera bientôt testé sur d'autres types d'édifices et d'activités. Par exemple, une campagne multidisciplinaire est prévue au Stromboli en septembre prochain (2012). Le système de reconstitution 4D sera utilisé pour reconstituer les trajets dans l'espace des bombes volcaniques et en déduire les conditions de pression au moment de l'explosion. La mise au point de tels systèmes est ambitieuse et s'avérera probablement complexe mais il me semble qu'il s'agit d'une étape incontournable pour parvenir à la compréhension de la physique des écoulements volcaniques et à une meilleure gestion des menaces qu'ils représentent.

13. Bibliographie

(Une bibliographie plus complète est fournie dans les articles de la seconde partie)

Ancochea, E., J.M. Fuster, E. Ibarolla, A. Cendrero, J. Coello, F. Hernan, J.M. Cantagrel, C. Jamond (1990). Volcanic evolution of the island of Tenerife (Canary Islands) in light of new K–Ar data. *J. Volcanol. Geotherm. Res.*, 44, 231–249.

Bachelery, P., P. Mairine (1990). Evolution volcano−structurale du Piton de la Fournaise depuis 0.53 M.a., in *Le volcanisme de la Réunion, monographie*, edited by J.−F. Lénat, pp. 213−242, Clermont−Ferrand.

Branney, M. J., P. Kokelaar (2002). Pyroclastic density currents and the sedimentation of ignimbrites. *Geological Society London Memoir,* 27, 143 pp.

Burgisser, A., G.W. Bergantz (2002). Reconciling pyroclastic flow and surge: the multiphase physics of density currents. *Earth. Planet. Sci. Let.,* 202:405–418.

Bursik, M.I., Woods, A.W. (1996). The dynamics and thermodynamics of large ash flows. *Bull. Volcanol.,* 58, 175–193.

Campbell, C. S., P. W. Cleary, M. Hopkins (1995). Large-scale landslide simulations: Global deformation, velocities, and basal friction. *J. Geophys. Res.*, 100, 8267– 8283.

Carracedo, J.C., H. Guillou, S. Nomade, E. Rodriguez-Badiola, F.J. Pérez-Torrado, A. Rodriguez-Gonzalez, R. Paris, V.R. Troll, S. Wiesmaier, A. Delcamp, J.L. Fernandez-Turiel (2010). Evolution of ocean island rifts: the Northeast rift zone of Tenerife, Canary Islands. *Geological Society of America Bulletin*, 30119, 30142. doi:10.1130/ B30119.1.

Charbonnier, S.J., R. Gertisser (2012). Evaluation of geophysical mass flow models using the 2006 block-and-ash flows of Merapi Volcano, Java, Indonesia : Towards a short-term hazard assessment. *J. Volcanol. Geotherm. Res., in press.*

Cole, P.D., E.S Calder, R.S.J. Sparks, A.B. Clarke, T.H. Druitt, S.R. Young, R.A. Herd, C.L. Harford, G.E. Norton (2002). Deposits from dome-collapse and fountain collapse pyroclastic flows at Soufrière Hills Volcano, Montserrat. In: Druitt, T.H., Kokelaar, B.P. (Eds.), The Eruption of Soufriere Hills Volcano, Montserrat, from 1995 to 1999, 21. *Geol. Soc. Mem. Geol. Soc. of London*, London, pp. 231–262.

Collins, G. S., H. J. Melosh (2003). Acoustic fluidization and the extraordinary mobility of sturzstroms. *J. Geophys. Res., 108(B10)*, 2473, doi:10.1029/2003JB002465.

Crosta, G. B., H. Chen, C. F. Lee (2004). Replay of the 1987 Val Pola Landslide*,* Italian Alps. *Geomorphology*, *60 (1−2)*, 127−146.

Dade, W.B., H.E. Huppert (1996). Emplacement of the Taupo ignimbrite by a dilute turbulent flow. *Nature* 381, 509–512.

Dade, W. B., H. E. Huppert (1998). Long−runout rockfalls. *Geology, 26*, 803–806.

Dartevelle, S., W.I. Rose, J. Stix, K. Kelfoun, J.W. Vallance (2004). Numerical modeling of geophysical granular flows: 2. Computer simulations of Plinian clouds and pyroclastic flows and surges. *G-cubed*, 5 (8), Q08004. doi:10.1029/2003GC000637.

Davies, T. R. (1982). Spreading of rock avalanche debris by mechanical fluidization. *Rock Mech., 15*, 9 –24.

Davies, T. R., M. J. McSaveney (1999). Runout of dry granular avalanches. *Can. Geotech. J., 3*, 313– 320.

Denlinger, R.P. (1987). A model for generation of ash clouds by pyroclastic flows, with application to the 1980 eruptions at Mount St. Helens, washington. *J. Geophys. Res.*, 92 (B10), 10,284–10,298.

Dondin, F., J.-F. Lebrun, K. Kelfoun, N. Fournier, A. Randrianasolo (2012). Sector collapse at Kick 'em Jenny submarine volcano (Lesser Antilles): numerical simulation and landslide behaviour. *Bull Volcanol*, DOI 10.1007/s00445-011-0554-0.

Doyle, E.E., A.J. Hogg, H.M. Mader, R.S.J. Sparks (2010). A two-layer model for the evolution and propagation of dense and dilute regions of pyroclastic currents. *J. Volcanol. Geotherm. Res*., 190 (2010) 365–378.

Druitt, T.H., R.S.J. Sparks (1982). A proximal ignimbrite breccia facies on Santorini, Greece. *J. Volcanol. Geotherm. Res.*, 13, 147–171.

Druitt, T.H., E.S. Calder, P.D. Cole, R.P. Hoblitt, S.C. Loughlin, G.E. Norton, L.J. Ritchie, R.S.J. Sparks, B. Voight (2002). Small-volume, highly mobile pyroclastic flows formed by rapid sedimentation from pyroclastic surges at Soufrière Hills Volcano, Montserrat: an important volcanic hazard. In: Druitt, T.H., Kokelaar, B.P. (Eds.), The Eruption of Soufriere Hills Volcano, Montserrat, from 1995 to 1999, 21. *Geol. Soc. Mem. Geol. Soc. of London*, London, pp. 263–279

Druitt, T. H., G. Avard, G. Bruni, P. Lettieri, F. Maez (2007). Gas retention in fine–grained pyroclastic flow materials at high temperatures. *Bull. Volcanol., 69*, 881–901, doi: 10.1007/s00445-007-0116-7.

Evans, S. G., O. Hungr, J.J. Clague (2001). Dynamics of the 1984 rock avalanche and associated distal debris flow on Mount Cayley, British Columbia, Canada; implications for landslide hazard assessment on dissected volcanoes. *Engineering Geology, 61*, 29–51.

Fisher, R.V., 1979. Models for pyroclastic surges and pyroclastic flows. J. Volcanol. Geotherm. Res. 6, 305–318.

Francis, P. W., M. Gardeweg, C. F. Ramirez, and D. A. Rothery (1985), Catastrophic debris avalanche deposit of Socompa volcano, northern Chile. Geology, 13, 600–603.

Fritz, H. M., N. Kalligeris, J. C. Borrero, P. Broncano, and E. Ortega (2008), The 15 August 2007 Peru tsunami runup observations and modeling. *Geophys. Res. Lett.*, 35, L10604, doi:10.1029/2008GL033494.

GDR Midi (2004) On dense granular flows. *E. Phys. J.*, E 14 367-371, article collectif.

Geldart, D. (1986). Gas fluidization technology, Wiley and Sons Ltd.

Giachetti, T., R. Paris, K. Kelfoun, F.J. Pérez-Torrado (2011). Numerical modelling of the tsunami triggered by the Güìmar debris avalanche, Tenerife (Canary Islands): comparison with field-based data. *Marine Geology*, doi: 10.1016/j.margeo.2011.03.018.

Giachetti, T., R. Paris, K. Kelfoun, B. Ontowirjo (2012*).* Tsunami hazard related to a flank collapse of Anak Krakatau volcano, Sunda Strait, Indonesia. *Geological Society, London, Special Publications*, 361, 79-90, doi: 10.1144/SP361.7.

Gray, J.M.N.T., Y.−C. Tai, S. Noelle (2003). Shock waves, dead zones and particle−free regions in rapid granular free−surface flows. *J. Fluid Mech., 91*, 161– 181.

Guilbaud, M.-N. (2005). Dynamique de mise en place de l'avalanche de Socompa, Chili. *Mémoire de DEA, Univ. Blaise Pascal*, 52 pp.

Harbitz, C.B., F. Løvholt, G. Pedersen, D.G. Masson (2006). Mechanisms of tsunami generation by submarine landslides: a short review. *Norw. J. Geol.*, 86, 255–264.

Heinrich, P., G. Boudon, J.−C. Komorowski, R. S. J. Sparks, R. Herd, B. Voight (2001). Numerical simulation of the December 1997 debris avalanche in Montserrat, Lesser Antilles, *Geophysical Research Letters, 28*, 2529–2532.

Hoblitt, R.P. (1986). Observations of eruptions, July 22 and August 7, 1980, at Mount St. Helens, Washington. *U.S.G.S. Prof. Pap.*, 1335, 1–43.

Holasek, R. E., S. Self (1995). GOES weather satellite observations and measurements of the May 18, 1980, Mount St. Helens eruption, *J. Geophys. Res.*, 100, 8469–8487.

Holcomb, R. T., R. C. Searle (1991). Large landslides from oceanic volcanoes, *Mar. Geotech., 10*, 19–32.

Iverson, R. M., R. P. Denlinger (2001). Flow of variably fluidized granular masses across three–dimensional terrain 1. Coulomb mixture theory. *J. Geophys. Res., 106*, 537–552.

Iverson, R.M., M. Logan, R.P. Denlinger (2004). Granular avalanches across irregular three–dimensional terrain: 2. experimental tests. *J. Geophys. Res.*, 109: F01015. doi 10.1029/2003JF000084.

Jessop D., K. Kelfoun, P. Labazuy, A. Mangeney and O. Roche, accepté avec modifications, LiDAR derived morphology of the 1993 Lascar pyroclastic flow deposits, and implication for flow dynamics and rheology, *J. Volcanol. Geotherm. Res.*

Johnson C.J., B.P. Kokelaar, R.M. Iverson, M. Logan, R.G. LaHusen, J.M.N.T. Gray (2012). Grain-size segregation and levee formation in geophysical mass flows. *J. Geophys. Res.*, 117, doi : 10.1029/2011JF002185

Keating, B.H., W.J. McGuire (2000). Island edifice failures and associated tsunami hazards. In: Keating, B.H., Waythomas, C.F., Dawson, A.G. (Eds.), Landslides and Tsunamis. Birkhäuser Verlag, Basel, pp. 899-955.

Kelfoun, K., F. Legros, A. Gourgaud (2000). Statistical study of damaged trees related to the pyroclastic flows of November 22, 1994 at Merapi volcano (central Java, Indonesia): relation between ash-cloud surge and block-and-ash flow. *J. Volcanol. Geoth. Res.*, 100 : 379-393.

Kelfoun, K., T.H. Druitt (2005). Numerical modelling of the emplacement of the 7500 BP Socompa rock avalanche, Chile. *J. Geophys. Res.*, B12202, doi : 10.1029/2005JB003758, 2005.

Kelfoun, K., T. H. Druitt, B. van Wyk de Vries, M.−N. Guilbaud (2008). Topographic reflection of Socompa debris avalanche, Chile, *Bull. Volcanol*., doi: 10.1007/s00445–008–0201–6.

Kelfoun K., P. Samaniego, P. Palacios, D. Barba (2009). Testing the suitability of frictional behaviour for pyroclastic flow simulation by comparison with a well-constrained eruption at Tungurahua volcano (Ecuador). *Bull. Volcanol.*, 71(9), 1057-1075, DOI: 10.1007/s00445-009-0286-6.

Kelfoun K., T. Giachetti, P. Labazuy (2010). Landslide–generated tsunamis at Réunion Island, *J. Geophys. Res., Earth Surface*, doi:10.1029/2009JF001381.

Kelfoun, K. (2011). Suitability of simple rheological laws for the numerical simulation of dense pyroclastic flows and long-runout volcanic avalanches, *J. Geophys. Res.*, 116, B08209, doi:10.1029/2010JB007622.

Labazuy, P. (1996). Recurrent landslides events on the submarine flank of Piton de la Fournaise volcano (Reunion Island)*, Geol. Soc. London, 110*, 293–305.

Legros, F. (2002). The mobility of long−runout landslides, *Eng. Geol., 63(3– 4)*, 301– 331.

Lénat, J.−F., P. Labazuy (1990). Morphologies et structures sous−marines de la Réunion, in *Le volcanisme de la Réunion, monographie*, edited by J.−F. Lénat, pp. 43−74, Clermont−Ferrand.

Lube, G., S. Cronin, T. Platz, A. Freundt, J.N. Procter, C. Henderson, M.F. Sheridan (2007). Flow and deposition of pyroclastic granular flows: a type example from the 1975 Nguaruhoe eruption, New Zealand. *J. Volcanol. Geotherm. Res.*, 161 (4), 362–363.

Mangeney, A., F. Bouchut, N. Thomas, J.P. Vilotte, M.O. Bristeau (2007). Numerical modeling of self−channeling granular flows and of their levee−channel deposits. *J. Geophys. Res.*, v. 112, F02017.

McEwen, A. S., M.C. Malin (1989). Dynamics of Mount St. Helens' 1980 pyroclastic flows, rockslide−avalanche, lahars, and blast. *J. Volcanol. Geotherm. Res., 37*, 205–231.

Moore, J.G., D.A. Clague, R.T. Holcomb, P.W. Lipman, W.R. Normark, M.E. Torresan (1989). Prodigious submarine landslides on the Hawaiian Ridge, *J. Geophys. Res.*, *94*, 17465–17484.

McMurtry, G.M., P. Watts, G.J. Fryer, J.R. Smith, F. Imamura (2004). Giant landslides, mega−tsunamis, and paleo−sea level in the Hawaiian Islands, *Mar. Geol., 203*, 219–233, doi:10.1016/S0025−3227(03)00306−2.

Mellors, R.A., R.B. Waitt, D.A. Swanson, (1988). Generation of pyroclastic flows and surges by hot-rock avalanches from the dome of Mount St. Helens volcano, *USA. Bull. Volcanol.*, 50, 14–25.

Melosh, H. J. (1990). Giant rock avalanches. *Nature*, 348, 483– 484.

Merle, O., J.–F. Lénat (2003). Hybrid collapse mechanism at Piton de la Fournaise volcano, Réunion Island, Indian Ocean, *J. Geophys. Res., 108*(B3), 2166, doi:10.1029/2002JB002014.

Michon, L., F. Saint−Ange (2008). Morphology of Piton de la Fournaise basaltic shield volcano (La Réunion Island): Characterization and implication in the volcano evolution, *J. Geophys. Res.*, *113*, B03203, doi:10.1029/2005JB004118.

Moore, J. G., D.A. Clague, R.T. Holcomb, P.W. Lipman, W.R. Normark, M.E. Torresan (1989). Prodigious submarine landslides on the Hawaiian Ridge, *J. Geophys. Res.*, *94*, 17465–17484.

Nairn, I.A., S. Self (1978). Explosive eruptions and pyroclastic avalanches from Ngauruhoe in February 1975. *J. Volcanol. Geotherm. Res.*, 3, 39–60.

Neri, A., T.E. Esposti Ongaro, G. Macedonio, D. Gidaspow (2003). Multiparticle simulation of collapsing volcanic columns and pyroclastic flow. *J. Geophys. Res.*, 108 (B4), 2202–2224.

Normark, W.R., J.G. Moore, M.E. Torresan (1993). Giant volcano−related landslides and the development of the Hawaiian Islands. in *US Geol. Surv. Bull. 2002*, edited by W. C. Schwab, H. J. Lee, and D.C. Twichell, 184–196.

Oehler, J.–F., P. Labazuy, J.–F. Lénat (2004). Recurrence of major flank landslides during the last 2−Ma−history of Réunion Island, *Bull. Volcanol.*, *66*, 585–598.

Oehler, J.–F., J. –F. Lénat, P. Labazuy (2007). Growth and collapse of the Réunion Island volcanoes, *Bull. Volcanol.*, *70*(6), 717–742, DOI 10.1007/s00445−007−0163−0.

Palladino, D.M., G.A. Valentine (1995). Coarse−tail vertical and lateral grading in pyroclastic flow deposits of the Latera Volcanic Complex (Vulsini, Central Italy): origin and implications for flow dynamics. *J. Volcanol. Geothermal Res. 69 (1995) 343−364.*

Paris, R., F.J. Pérez-Torrado, M.C. Cabrera, P. Wassmer, J.L. Schneider, J.C. Carracedo, (2004). Tsunami-induced conglomerates and debris-flow deposits on the western coast of Gran Canaria (Canary Islands). *Acta Vulcanologica*, 16 (1–2), 133–136.

Patra, A.K., A.C. Bauer, C.C. Nichita, E.B. Pitman, M.F. Sheridan, M. Bursik, B. Rupp, A. Webber, A.J. Stinton, L.M. Namikawa, C.S. Renschler (2005). Parallel adaptive numerical simulation of dry avalanches over natural terrain. *J. Volcanol. Geothermal Res.*, *139 (1)*, 1–22.

Pérez-Torrado, F.J., R. Paris, , M.C. Cabrera, J.-L. Schneider, P. Wassmer, J.-C. Carracedo, A. Rodrìguez-Santana, F. Santana (2006). Tsunami deposits related to flank collapse in oceanic volcanoes: the Agaete Valley evidence, Gran Canaria, Canary Islands. *Marine Geology*, 227, 135–149.

Pouliquen, O. (1999. Scaling laws in granular flows down rough inclined planes: *Physics of Fluids*, *11*, 542–548.

Pouliquen, O., Y. Forterre (2002). Friction law for dense granular flows: Application to the motion of a mass down a rough inclined plane. *J. Fluid Mech., 453*, 133– 151.

Procter, J.N., S.J. Cronin, T. Platz, A. Patra, K. Dalbey, M.F. Sheridan, V. Neall (2010). Mapping block−and−ash flow hazards based on Titan 2D simulations: a case study from Mt. Taranaki, NZ, *Nat Hazards*, *53*, 483–501, DOI 10.1007/s11069−009−9440−x.

Roche, O., M.A. Gilbertson, J.C. Phillips, R.S.J. Sparks (2004). Experimental study of gas−fluidized granular flows with implications for pyroclastic flow emplacement. *J. Geophys. Res.*, *109*, B10201, doi:10.1029/2003JB002916.

Rossano, S., G. Mastrolorenzo, G. De Natale (1996). Computer simulations of pyroclastic flows on Somma–Vesuvius volcano. *J. Volcanol. Geotherm. Res*., *82*, 113–137.

Savage, S.B., K. Hutter K. (1991). The dynamics of avalanches of granular materials from initiation to runout. Part I: Analysis, *Acta Mechanica, 86*, 201–223.

Shaller, P. J. (1991). Analysis and implications of large Martian and terrestrial landslides. *Ph.D. thesis*, Calif. Inst. of Technol., Pasadena, 586 pp.

Sheridan, M.F., A.J. Stinton, A. Patra, E.B. Pitman, A. Bauer, C.C. Nichita (2005). Evaluating Titan2D mass−flow model using the 1963 Little Tahoma Peak avalanches, Mount Rainier, Washington, *J. Volcanol. Geothermal Res.*, *139*, 89–102.

Siebert, L. (1984). Large volcanic debris avalanches: Characteristics of source areas, deposits, and associated eruptions. *J. Volcanol. Geotherm. Res.*, 22, 163–197, doi:10.1016/0377-0273(84)90002-7.

Sousa, J., B. Voight (1995). Multiple−pulsed debris avalanche emplacement at Mount St. Helens in 1980: Evidence from numerical continuum flow simulations. *J. Volcanol. Geotherm. Res., 66 (1−4)*, 227−250.

Sparks, R.S.J., S. Self, G.P.L. Walker (1973). Products of ignimbrite eruptions. *Geology*, 1 (3), 115–118.

Sparks, R.S.J. (1976). Grain size variations in ignimbrites and implications for the transport of pyroclastic flows. *Sedimentology, 23*, 147–188.

Sparks, R.S.J., L. Wilson (1976). A model for the formation of ignimbrite by gravitational column collapse. *J. Geol. Soc. Lond.*, 132, 441–451.

Sparks, R.S.J., L. Wilson, G. Hulme (1978). Theoretical modeling of the generation, movement and emplacement of pyroclastic flows by column collapse. *J. Geophys. Res.*, 83 (B4), 1727–1739.

Sparks, R., M. Bursik, S. Carey, J. Gilbert, L. Glaze, H. Sigurdsson, A. Woods (1997). Volcanic Plumes. Wiley, New Jersey.

Synolakis, C.E., E.N. Bernard, V.V. Titov, U. Kanoglu, and F.I. Gonzalez (2008). Validation and verification of tsunami numerical models, *Pure Appl. Geophys.*, *165*, 2197–2228, doi:10.1007/s00024−004−0427−y.

Takarada, S., T. Ui, Y. Yamamoto (1999). Depositional features and transportation mechanism of valley−filling Iwasegawa and Kaida debris avalanches, Japan, *Bull. Volcanol., 60,* 508–522, 10.1007/s004450050248.

Valentine, G.A., R. Fisher (1986). Origin of layer 1 deposits in ignimbrites. *Geology*, 14 (2), 146–148.

Van Wyk de Vries, B., S. Self, P. W. Francis, L. Keszthelyi (2001). A gravitational spreading origin for the Socompa debris avalanche, *J. Volcanol. Geotherm. Res.*, 105, 225–247.

Voight, B., H. Glicken, R. J. Janda, P. M. Douglas (1981). Catastrophic rockslide avalanche of May 18, in The 1980 Eruptions of Mount St. Helens, Washington. Edited by *P. W. Lipman and D. R. Mullineaux, U.S. Geol. Surv. Prof. Pap.*, 1250, 347–378.

Voight, B., R. Janda, H. Glicken, P.M. Douglas (1983). Nature and mechanics of the Mount St. Helens rockslide−avalanche of 18 May 1980, *Geotechnique, 33,* 243– 273.

Wadge, G., P.W. Francis, C.F. Ramirez (1995). The Socompa collapse and avalanche event, *J. Volcanol. Geotherm. Res.*, 66, 309– 336.

Voight B., R. Sukhyar, A.D. Wirakusamah (2000). Introduction to the special issue on Merapi Volcano. *J. Volcanol. Geotherm. Res.*, 100, 1-8.

Wadge, G., P. Jackson, S.M. Bower, A.W. Woods, E. Calder (1998). Computer simulations of pyroclastic flows from dome collapse. *Geophys. Res. Lett., 25 (19),* 3677–3680.

Walker, G.P.L., C.J.N. Wilson (1983). Lateral variations in the Taupo ignimbrite. *J. Volcanol. Geotherm. Res.*, 18, 117–133.

Ward, S.N. (2001). Landslide tsunami. *J. of Geophys. Res.*, 106, 11,201–11,215.

Waythomas, C.F., P. Watts, F. Shi, J.T. Kirby (2009). Pacific Basin tsunami hazards associated with mass flows in the Aleutian arc of Alaska. *Quat. Sci. Rev., 28 (11−12)*, 1006–1019. doi: 10.1016/j.quascirev.2009.02.019.

Wilson, L., J.W. Head (1981). Morphology and rheology of pyroclastic flows and their deposits, and guidelines for future observations, in Lipman P.W., and Mullineaux D.R., eds. *The 1980 eruptions of Mount St. Helens, Washington. 1250*, 513–524.

Woods, A.W., S. Self (1992). Thermal disequilibrium at the top of volcanic clouds and its effect on estimates of the column height, *Nature*, 355, 628–630.

Partie 2

Publications

Publications depuis le post-doctorat

Les publications présentées dans ce mémoire sont indiquées par un astérisque (*)

1* Giachetti T., Paris R., **Kelfoun K.**, Ontowirjo B., 2012, Tsunami hazard related to a flank collapse of Anak Krakatau volcano, Sunda Strait, Indonesia. *Geol. Soc., London,* 361, 79-90, doi: 10.1144/SP361.7.

2* Dondin F., Lebrun J.-F., **Kelfoun K.**, Fournier N. and Randrianasolo A., 2012, Sector collapse at Kick 'em Jenny submarine volcano (Lesser Antilles): numerical simulation and landslide behaviour. *Bull. Volcanol.*, doi :10.1007/s00445-011-0554-0.

3* Pouget S., Davies T., Kennedy B., **Kelfoun K.** and Leyrit H., 2012, Numerical modelling: a useful tool to simulate collapsing volcanoes, *Geology Today*, 28 (2), 59-63.

4* **Kelfoun K.**, 2011, Suitability of simple rheological laws for the numerical simulation of dense pyroclastic flows and long−runout volcanic avalanches, *J. Geophys. Res.*, Solid Earth, doi:10.1029/ 2010JB007622.

5* Giachetti T., Paris R., **Kelfoun K.**, Pérez-Torrado F.J., 2011, Numerical modelling of the tsunami triggered by the Güìmar debris avalanche, Tenerife (Canary Islands): comparison with field-based data. *Marine Geology*. doi: 10.1016/j.margeo.2011.03.018.

6 Giachetti T., Burgisser A., Arbaret L., Druitt T.H., **Kelfoun K.**, 2011, Textural analysis of products from the 1997 Vulcanian explosions of Soufrière Hills Volcano (Montserrat) using X-ray computed microtomography. *Bull. Volcanol*. doi:10.1007/s00445-011-0472-1.

7* **Kelfoun K.** and Davies T., 2011, "Comment on "A random kinetic energy model for rock avalanches: Eight case studies" T. Preuth, P. Bartelt, O. Korup, and B. W. McArdell.", *J. Geophys. Res.*, doi:10.1029/2010JF001916.

8* **Kelfoun K.**, Giachetti T. and Labazuy P., 2010, Landslide–generated tsunamis at Réunion Island, *J. Geophys. Res.*, Earth Surface, doi:10.1029/2009JF001381.

9* Davies T., McSaveney M. and **Kelfoun K.**, 2010, Runout of the Soccompa volcanic debris avalanche, Chile: a mechanical explanation for low basal shear resistance. *Bull. Volcanol*. 72 (8), page 933 : doi 10.1007/s00445-010-0372-9.

10* **Kelfoun K.**, Samaniego P., Palacios P., Barba D., 2009, Testing the suitability of frictional behaviour for pyroclastic flow simulation by comparison with a well-constrained eruption at Tungurahua volcano (Ecuador). *Bull. Volcanol*., 71(9), 1057-1075, DOI: 10.1007/s00445-009-0286-6.

11 **Kelfoun K.**, 2008, Rheological behaviour of volcanic granular flows, *International Congress on Environmental Modelling and Software, Integrating Sciences and Information Technology for Environmental Assessment and Decision Making*, July 7-10, 2008 - Barcelona, Catalonia, session paper, 6 pages, 2 reviewers.

12* **Kelfoun K.**, Druitt T.H., van Wyk de Vries B., Guilbaud M.–N., 2008, Topographic reflection of Socompa debris avalanche, Chile, *Bull. Volcanol*. , doi: 10.1007/s00445-008-0201-6

13 Carter A., Wyk de Vries B., **Kelfoun K.**, Bachèlery P., Briole P., 2007, Pits, rifts and slumps: the summit structure of Piton de la Fournaise, *Bull. Volcanol.*, 69 (7), doi: 10.007/s00445-006-0103-4

14* **Kelfoun K.** and Druitt T.H., 2005, Numerical modelling of the emplacement of the 7500 BP Socompa rock avalanche, Chile. *J. Geophys. Res.*, B12202, doi : 10.1029/2005JB003758, 2005.

15 Formenti Y., Druitt T.H., **Kelfoun K.**, 2004: Characterisation of the 1997 Vulcanian explosions of Soufrière Hills Volcano, Montserrat, by video analysis, *Bull. Volcanol., pp. 587 - 605*

16* Dartevelle S., Rose W.I., Stix J., **Kelfoun K.**, Vallance J.W., 2004, Numerical modeling of geophysical granular flows: 2. Computer simulations of plinian clouds and pyroclastic flows and surges. *Geochem. Geophys. Geosyst., Vol. 5, No. 8*

17 Donnadieu F., **Kelfoun K.**, van Wyk de Vries B., Cecchi E. and Merle O., 2003, Digital photogrammetry as a tool in analogue modelling: applications to volcano instability. *J. Volcanol. Geoth. Res., 123 : 161-180.*

18 Legros F., **Kelfoun K.**, Marti J., 2000, The influence of conduit geometry on the dynamics of caldera-forming eruptions. *Earth Planet. Sci. Lett.*, 179, 53-61.

19* Legros F., **Kelfoun K.**, 2000, Sustained blasts during large volcanic eruptions, *Geology*, 28(10), 895-898.

20* Legros F., **Kelfoun K.**, 2000, On the ability of pyroclastic flows to scale topographic obstacles. *J. Volcanol. Geoth. Res.*, 98 : 235-241.

21 Jessop D., **Kelfoun K.**, Labazuy P., Mangeney A. and Roche O., accepté avec modifications, LiDAR derived morphology of the 1993 Lascar pyroclastic flow deposits, and implication for flow dynamics and rheology, *J. Volcanol. Geotherm. Res.*

22* Roche O., J.C. Phillips, **K. Kelfoun.**, *sous presse*, Pyroclastic density currents. Modeling Volcanic Processes (Eds. S.A. Faggents, T.K.P. Gregg, R.C.M. Lopes), Cambridge University Press, p. 321 5

Table des matières des travaux présentés

Ecoulements pyroclastiques

1. **Kelfoun K.**, P. Samaniego, P. Palacios, D. Barba, 2009, Testing the suitability of frictional behaviour for pyroclastic flow simulation by comparison with a well-constrained eruption at Tungurahua volcano (Ecuador). *Bull. Volcanol.*, 71(9), 1057-1075, DOI: 10.1007/s00445-009-0286-6. 61
2. Roche O., J.C. Phillips, **K. Kelfoun**, *sous presse*, Pyroclastic density currents. *Modeling Volcanic Processes (Eds. S.A. Faggents, T.K.P. Gregg, R.C.M. Lopes), Cambridge University Press*,. p. 321 5 81
3. Dartevelle S., Rose W. I., Stix J., **Kelfoun K.**, Vallance J. W., 2004: Numerical modeling of geophysical granular flows: 2. Computer simulations of plinian clouds and pyroclastic flows and surges. *Geochem. Geophys. Geosyst., Vol. 5, No. 8* 107
4. Legros F., **Kelfoun K.**, 2000: Sustained blasts during large volcanic eruptions*, Geology, v.28, n°10: 895-898.* 143
5. Legros F., **Kelfoun K.**, 2000: On the ability of pyroclastic flows to scale topographic obstacles. *J. Volcanol. Geoth. Res.*, 98 : 235-241. 147

Avalanche de débris

6. **Kelfoun K.**, 2011, Suitability of simple rheological laws for the numerical simulation of dense pyroclastic flows and long−runout volcanic avalanches, *J. Geophys. Res.*, Solid Earth, doi:10.1029/ 2010JB007622. 155
7. **Kelfoun K.** and T. Davies, 2011, "Comment on "A random kinetic energy model for rock avalanches: Eight case studies" T. Preuth, P. Bartelt, O. Korup, and B. W. McArdell." *J. Geophys. Res.*, doi:10.1029/2010JF001916. 169
8. Pouget S., Davies T., Kennedy B., **Kelfoun K.** and Leyrit H., 2012, Numerical modelling: a useful tool to simulate collapsing volcanoes, *Geology Today*, 28 (2), 59-63. 173
9. Davies T., M. McSaveney, **K. Kelfoun**, 2010, Runout of the Soccompa volcanic debris avalanche, Chile: a mechanical explanation for low basal shear resistance. *Bull. Volcanol*. 72 (8), page 933 : doi 10.1007/s00445-010-0372-9 179
10. **Kelfoun K.**, T.H. Druitt, B. van Wyk de Vries, M.–N. Guilbaud, 2008, Topographic reflection of Socompa debris avalanche, Chile, *Bull. Volcanol*., doi: 10.1007/s00445-008-0201-6, ... 191
11. **Kelfoun K.** and T.H. Druitt, 2005, Numerical modelling of the emplacement of the 7500 BP Socompa rock avalanche, Chile. *J. Geophys. Res.*, B12202, doi : 10.1029/2005JB003758, 2005. 211

Tsunami

12. **Kelfoun K.**, T. Giachetti, P. Labazuy, 2010, Landslide–generated tsunamis at Réunion Island, *J. Geophys. Res.*, Earth Surface, doi:10.1029/2009JF001381 225
13. Giachetti T, Paris R, **Kelfoun K**, Ontowirjo B., 2012*,* Tsunami hazard related to a flank collapse of Anak Krakatau volcano, Sunda Strait, Indonesia. Special Publications of the Geological Society, 361, 79-90, doi: 10.1144/SP361.7. 243
14. Dondin F., Lebrun J.-F., **Kelfoun K.**, Fournier N. and Randrianasolo A., 2012, Sector collapse at Kick 'em Jenny submarine volcano (Lesser Antilles): numerical simulation and landslide behaviour. *Bull. Volcanol.*, DOI 10.1007/s00445-011-0554-0. 255
15. Giachetti T, Paris R, **Kelfoun K**, Pérez-Torrado FJ., 2011*,* Numerical modelling of the tsunami triggered by the Güìmar debris avalanche, Tenerife (Canary Islands): comparison with field-based data. *Marine Geology*. doi: 10.1016/j.margeo.2011.03.018 269

Rapport sur l'estimation des menaces volcaniques du Tungurahua par simulation numérique (en Espagnol) 283

.

Bull Volcanol
DOI 10.1007/s00445-009-0286-6

RESEARCH ARTICLE

Testing the suitability of frictional behaviour for pyroclastic flow simulation by comparison with a well-constrained eruption at Tungurahua volcano (Ecuador)

Karim Kelfoun · Pablo Samaniego · Pablo Palacios · Diego Barba

Received: 8 April 2008 / Accepted: 24 April 2009
© Springer-Verlag 2009

Abstract We use a well-monitored eruption of Tungurahua volcano to test the validity of the frictional behaviour, also called Mohr–Coulomb, which is generally used in geophysical flow modelling. We show that the frictional law is not appropriate for the simulation of pyroclastic flows at Tungurahua. With this law, the longitudinal shape of the simulated flows is a thin wedge of material progressively passing, over several hundreds of metres, from an unrealistic thickness at the front (<<1 mm) to some tens of centimetres. Simulated deposits form piles which accumulate at the foot of the volcano and are more similar to sand piles than natural pyroclastic deposits. Finally, flows simulated with a frictional rheology are not channelised by the drainage system, but affect all the flanks of the volcano. In addition, their velocity can exceed 150 m s^{-1}, allowing pyroclastic flows to cross interfluves at bends in the valley, affecting areas that would not have been affected in reality and leaving clear downstream areas that would be covered in reality. Instead, a simple empirical law, a constant retarding stress (i.e. a yield strength), involving only one free parameter, appears to be much better adapted for modelling pyroclastic flows. A similar conclusion was drawn for the Socompa debris avalanche simulation (Kelfoun and Druitt, J Geophys Res 110:B12202, 2005).

Keywords Pyroclastic flows · Numerical simulation · Rheology · Tungurahua

Editorial responsibility: J.C. Phillips

Electronic supplementary material The online version of this article (doi:10.1007/s00445-009-0286-6) contains supplementary material, which is available to authorized users.

K. Kelfoun
IRD—Instituto Geofisico, Escuela Politecnica Nacional Casilla, 1701-2759 Quito, Ecuador

K. Kelfoun (✉)
Laboratoire Magmas et Volcans, Université Blaise Pascal, CNRS, IRD–OPGC,
5 rue Kessler,
63038 Clermont-Ferrand, France
e-mail: k.kelfoun@opgc.univ-bpclermont.fr
URL: http://wwwobs.univ-bpclermont.fr/lmv/pperm/kelfoun_k

P. Samaniego · P. Palacios · D. Barba
Instituto Geofisico, Escuela Politecnica Nacional Casilla, 1701-2759 Quito, Ecuador

Introduction

Numerical simulations of pyroclastic flows are increasingly being used for hazard assessment on volcanoes and will be essential for future hazard mitigation. A potential problem of such an approach, however, is that the rheological behaviour of such flows is very complex. Several approaches have improved our understanding of these kind of flows by trying to describe, physically, the complexities of pyroclastic density currents (e.g. Burgisser and Bergantz 2002; Neri et al. 2003; Dartevelle 2004). At present, however, this complexity is too high to be fully described. Dense pyroclastic flows, the subject of this paper, are formed by blocks and ash that vibrate, collide, rub together, break and interact by electrostatic forces during transport. Complex interactions also exist between particles and magmatic and atmospheric gases. As we do not understand all the complexities of these interactions at a microscopic level, we cannot simulate them accurately and we have to use simplified rheological laws that fit the general behaviour. Initially, however, we should ensure that they reproduce the first order features of the natural phenomenon.

Published online: 16 May 2009

Existing models of dense pyroclastic flows generally start with the assumption that frictional behaviour is dominant in their rheology and that it plays the major role in deposit formation. This behaviour seems logical because it is exhibited by pyroclastic flow deposits or, more commonly, by sand at rest. This behaviour is inferred from the energy line and energy cone models initially used for rock avalanches (Heim 1882; Hsü 1975), then subsequently for pyroclastic flows (Sheridan 1979). It also approximates well the behaviour of sand flows in the laboratory (e.g. Savage and Hutter 1989; Gray et al. 2003; Pouliquen and Forterre 2002). Patra et al. (2005, 2006) simulate the pyroclastic flows of Colima volcano with the code Titan2D, using a frictional model with two friction angles. Other authors consider the retarding stress as a combination of a frictional stress plus a viscous and/or a turbulent stress: McEwen and Malin (1989) use a kinetic approach to simulate pyroclastic flows on Mt St. Helens; Wadge et al. (1998) and Saucedo et al. (2005) use the same approach to simulate dense flows on Soufrière Hill and Colima volcano, respectively.

The simplest form of the frictional model, also known as Mohr–Coulomb model, states that the resistive shear stress τ_r is a function of both the normal stress σ and the friction angle: $\tau_r=\sigma\tan\varphi$. The frictional stress is thus rate independent. A block with a frictional behaviour which is subjected to both a normal (σ) and a shear stress (τ_d) stays at rest whilst $\tau_d\leq\sigma\tan\varphi$. When the shear stress exceeds the threshold ($\tau_d>\sigma\tan\varphi$), the block accelerates. A block at rest on a slope α is submitted to a driving stress $\tau_d=\rho gh\sin\alpha$ and a retarding stress $\tau_r=\sigma\tan\varphi=\rho gh\cos\alpha\tan\varphi$, where ρ, h and g are respectively the density of the block, its thickness and gravity. It thus begins to slide when the driving stress exceeds the retarding stress $\tau_d>\tau_r$, i.e. when the slope exceeds the friction angle, $\alpha>\varphi$. Note that for the following, this threshold is independent of the thickness of the block. A frictional granular medium at rest exhibits a more complex behaviour than a block due to the additional stress of the pressure gradient. The angle of repose of a sand pile, for example, whose behaviour is frictional, corresponds to its angle of friction. A frictional flow exhibits a much more complex behaviour: It will begin to flow when its surface angle (from the horizontal) exceeds the angle of friction. However, once in movement, its surface angle can be lower or higher than the static value according to slope variations and to inertia.

The following key questions must be addressed before using this behaviour for hazard assessment: Is it realistic to consider pyroclastic flows as mainly frictional and is this behaviour compatible with field observations of their geometry, their relatively low velocity (generally <40 m s^{-1}) and their high mobility?

Tungurahua volcano (Ecuador) erupted in July and August 2006 and pyroclastic flows swept along the west flank of the volcano. The eruption was observed, described and monitored by the staff of the *Instituto Geofisico* of the *Escuela Politécnica Nacional* (IG-EPN), Quito. Based on their data, it is possible to reconstruct the conditions of pyroclastic flow formation, transport and emplacement. Eruptions of Tungurahua are a very interesting case to test the validity of the rheological models used for pyroclastic flow simulations and to answer the fundamental question of the adequacy of the frictional model.

The 2006 eruptions of Tungurahua volcano

General description of Tungurahua

Tungurahua volcano (5,023 m asl, 1°28′ S, 78°27′ W) is a steep-sided andesitic stratovolcano, located in central Ecuador, ranking as one of the most active volcanoes of the Northern Andes. During historical times, Tungurahua experienced important (VEI≥3) pyroclastic flow-forming eruptions in AD 1640–1641, 1773, 1886 and 1916–1918 (Hall et al. 1999; Le Pennec et al. 2008). The current eruptive episode began in 1999 and is still ongoing today (January 2009). Periods of low-to-moderate explosive activity occurred in November–December 1999, August 2001, September 2002 and October–November 2003. These periods were characterised by Strombolian activity, canon-like explosions and light-to-moderate regional ash fallouts. Periods of quiescence have also been observed, the most notable being from February to December 2005.

At the beginning of April 2006, IG-EPN scientists detected some deep long period seismic events (5–15 km depth) that preceded a change in the degassing pattern of the volcano (beginning of May), which was followed by an important deformation in the upper part of the cone (end of May). From the beginning of July, seismic activity increased dramatically and culminated with the 14th July (VEI 2) and 16–17th August 2006 (VEI 3) eruptions (Samaniego et al. 2007; Mothes et al. 2007; Hall et al. 2007). For the first time since the beginning of this eruptive cycle, Tungurahua volcano produced pyroclastic flows which swept over the western half of the cone, as well as giving rise to eruption columns greater than 16 km in height.

The voluminous deposits of the 16th–17th August eruption covered the July 14th deposits and the August eruption was studied in more detail and better monitored. We have thus chosen this eruption to test pyroclastic flow modelling.

Chronology of the 16–17th August eruption

Eruptive activity increased from the morning of August 16th. At 1430 hours (local time = GMT-5), eruptive activity was characterised by a vigorous and continuous ash and

vapour emission, reaching 2–3 km above the crater. The first small pyroclastic flow occurred around 1700 hours and descended down the NW flank, in the Cusua and Chontapamba gullies (Fig. 1). During the next few hours, the eruptive activity increased progressively. It was characterised by an almost continuous lava fountain reaching up to 300 m high, associated with a 3–4-km-high eruption column. Before 2100 hours, other small-volume pyroclastic flows occurred in the Cusua, Juive Grande and Vazcún valleys (Fig. 1). Other sporadic, but probably longer, pyroclastic flows were generated at 2114, 2126, 2143 and 2208 hours, related to explosions and/or an increase of the lava fountaining. Between 2200 and 0000 hours, other pyroclastic flows descended the Cusua–Bilbao area on the northwestern flank and the Juive Grande and Vazcun valleys on the northern flank.

The paroxysmal phase began at about 0015 hours and lasted around 40 min. Eruptive activity was characterised by a powerful lava fountain up to 1,000 m above the crater, a >16-km-high eruption column, and the quasi contemporaneous generation of the most voluminous pyroclastic flows, which descended via several quebradas on the N, NW, W and SW flanks (Vazcun, Juive Grande, Mandur, La Hacienda, Cusua, Achupashal, La Pirámide, Bilbao, Pingullo, Motilones, Chontapamba, de Romero, Ingapirca, Rea, Confesionario, Choglontus and Mapayacu). During this paroxysmal phase, the generation of pyroclastic flows was quasicontinuous as reported by inhabitants of the SW flank of the cone who remained in the Choglontus area (Fig. 1). The flows reached lengths of up to 8.5 km after a descent of 2,600–3,000 m from the summit crater. The pyroclastic flows of the Rea, Romero and Chontapamba formed deltas in the Rio Chambo valley, which was dammed for several hours after the eruption. The Mapayacu pyroclastic flows also dammed the Puela River.

No pyroclastic flow was witnessed on the eastern flank of the cone and no deposits were observed in this region during our helicopter survey. After the paroxysmal phase, both the

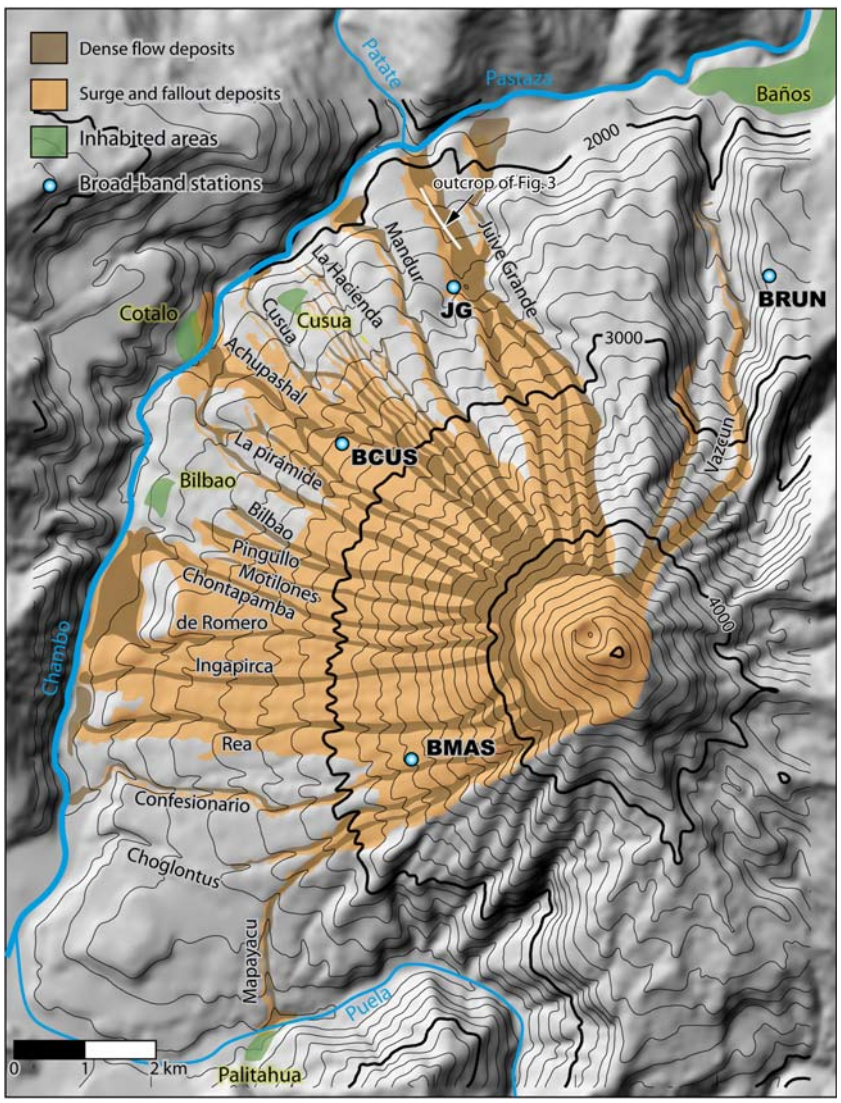

Fig. 1 Map of deposits of the August 2006 eruption of Tungurahua. Dense flow deposits are restricted to the drainage channels and are absent on the eastern flank as on steepest slopes of the summit cone. Seismic stations are *Brun* Runtun, *JG* Juive Grande, *Bcus* Cusua, *Bmas* Mason

seismic and the volcanic activity rapidly decreased and no further pyroclastic flows were emitted. On the afternoon of August 17th, IG-EPN thermal images of the NW flank confirmed the effusion of a voluminous blocky lava flow which was emitted some hours after the paroxysmal phase and which stopped at an elevation of 2,700 m asl (Fig. 2).

Description of deposits

Lithic-rich pyroclastic flow deposits are composed of juvenile, non- or poorly vesiculated blocks, associated cauliflower bombs and scoriae and accidental blocks. Their ratios of dense/vesiculate and juvenile/accidental components vary according to the unit and the valley studied. In Mapayacu, for example, accidentals represent more than 50% of the block facies. The more recent unit in Achupashal contains a high concentration of scoriae and bread crust bombs reaching more than 50 cm in diameter.

At least three distinct flow units were observed after the eruption, at the surface of the deposits, in the lower part (about 2,100 m asl) of the Juive Grande area (Hall et al. 2007), as well as in the Vazcún valley and most gullies on the western flank. Today (January 2009), incipient erosion of these deposits allows us to observe the different units and the internal structure of these pyroclastic flows (Fig. 3a, b). A maximum number of six distinct units can be observed in cross section, although the total number of units is probably even greater, since not all the units occur in each observed section. Each unit, which presents a well-defined front (Fig. 3c), is approximately 1 m thick on slopes <5°, becoming thinner on steeper slopes. It is difficult to quantify the relationship between thickness and slope because the thickness is also governed by changes in valley width. Thus, if the cross section of the deposit is located above the drainage channel, the true deposit thickness is exposed, whereas at the valley margins, the real thickness is underestimated. What is clear, however, from field observations as well as from the thermal image taken after the eruption (Fig. 2) is that few (or no) deposits can form on slopes greater than 25–30° and, which is important for validation of the model, that deposits are present where the slope is less than 25° (beneath 3,800 m asl), their thickness increasing as the slope decreases.

The total volume of the eruptive products, including ashes, has been estimated at more than $20\times10^6 m^3$. The overall volume of dense pyroclastic flow deposits is in the order of $5–10\times10^6 m^3$ (Hall et al. 2007). Due to the shape of the crater, whose NW border has a lower altitude, the deposits are more voluminous in the northwestern area (Achupashal, Cusua) than in the north and southwest drainage areas.

Ash cloud surges accompanied dense flows. Above 3,000 m asl, surges were able to leave the valleys, blowing down trees and creating several decimetre-thick ash deposits up to a distance of a hundred metres from the valley drainages. Below this height, trees were generally only knocked over on the convex sides of the valleys and only up to a distance of a few metres. Along the north and west/southwest drainage areas, there was very little damage to trees on the concave sides of the valleys even at the contact of dense flow deposits. Surge deposits were mainly observed in the northwest part (i.e. the central part) of the damaged area, facing the lowest point of the crater. Metre-thick surge deposits were observed all around the Achupashal valley (Fig. 1), forming ashy dunes with a typical anti-dune morphology. However, even here, trees were only swept down up to several tens of metres from the drainage channels covered by dense flows.

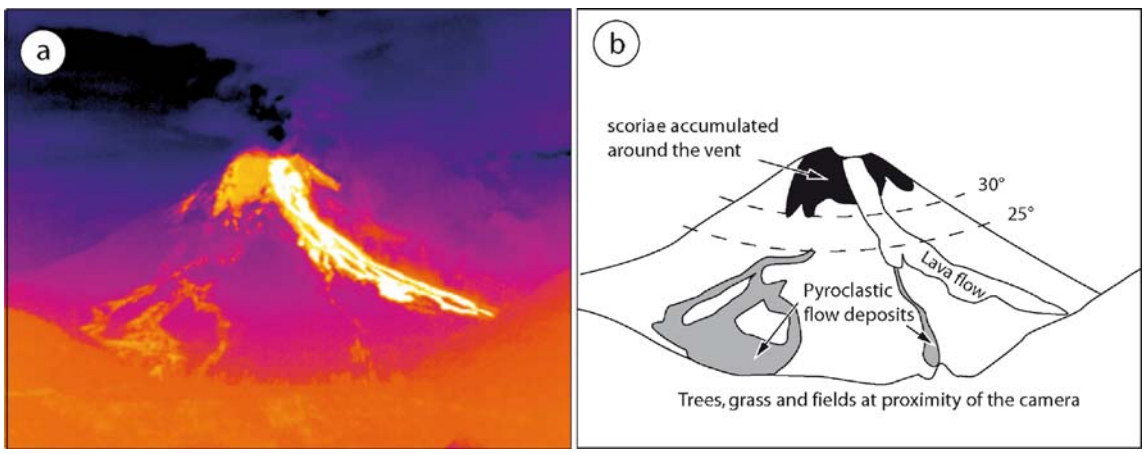

Fig. 2 **a** Thermal infrared image of August pyroclastic flows of Tungurahua and **b** sketch of the image. Note pyroclastic flow deposits on the lower slopes (between 0° and 25–30°, indicated on the *figure*) and scorias accumulated around the crater. The *white area* corresponds to a lava flow that followed pyroclastic flow emplacement. Courtesy of Santiago Arellano, IG-EPN

Fig. 3 **a** Erosion of pyroclastic deposits along Juive Grande (location on Fig. 1, *white line*). The 2008 units lies over older pyroclastic and lahar deposits. **b** Close up of pyroclastic units (*white frame* on **a**). The base of the 2008 flows is well marked by vegetation and objects (plastics, fence wires etc.). Three units, delimited by the *coloured arrows*, can be observed on the image. This kind of outcrop enables the number of units, their thickness and their variation of thickness according to the slope to be estimated. **c** A frontal lobe of the August pyroclastic deposits in Juive Grande

Seismic data

Broad band seismometers were installed around Tungurahua following a cooperative project between IG-EPN and Japan International Cooperation Agency (Kumagai et al. 2007) to monitor volcanic activity and forecast eruptions. Seismometers sample 50 data per second and are able to record frequencies from 1 to 25 Hz. During the crisis, they also recorded signals generated by vulcanian explosions and pyroclastic flows and are a powerful tool to confirm and quantify the emplacement of these flows. To exemplify this, we will focus on seismic signals recorded between 2100 and 2300 hours at Cusua station (located on the NW flank at 4.5 km from the crater, Bcus; Fig. 1). In this record, we observe several high-amplitude short duration (about 30 s) signals (at 2114, 2143 and 2208 hours, local time), which were followed by long coda signals with smaller amplitude (Fig. 4).

The high-amplitude signals were interpreted as explosive events, given that they were detected at nearly the same time by all the seismic stations according to their position relative to the crater. They are characterised by a frequency ranging across the whole spectrum (1 to 25 Hz), with a dominant frequency of 2–3 Hz (Fig. 4b).

The following and longer signals increased in amplitude for 150 s before diminishing. The amplitude increase is associated with an increase in the distribution of detected frequencies from <10 to 20 Hz (Fig. 4). Four observations show that these signals were generated by pyroclastic flows. Firstly, this signal cannot be correlated between the different stations although the recorded amplitudes are strong. The phenomenon that generated it must thus be local. Secondly, the Runtun seismic station, located at the margin of the area affected by the flows (about 600 m from the channel bottom), measured only a very weak increase in amplitude during the paroxysmal phase (Fig. 5). Since this station was able to record explosions at the crater, like the other stations, the lack of increased signal here confirms that the high frequency source recorded by the other stations in the affected area was local. Thirdly, the transmission systems of the stations located in the affected area were destroyed during the paroxysm. The time of destruction in Cusua (2126 hours) corresponds exactly to the arrival of pyroclastic flows. Another station (Juive Grande, not shown) recorded a very strong signal of this type (the strongest it recorded) just before it was destroyed at 0025 hours. Transmission at Mason, a little bit further from the valley, was interrupted at 0049 hours by ash deposits from pyroclastic flows which covered solar panels and antennae. Finally, visual observations confirm that these signals were associated with pyroclastic flow emplacement.

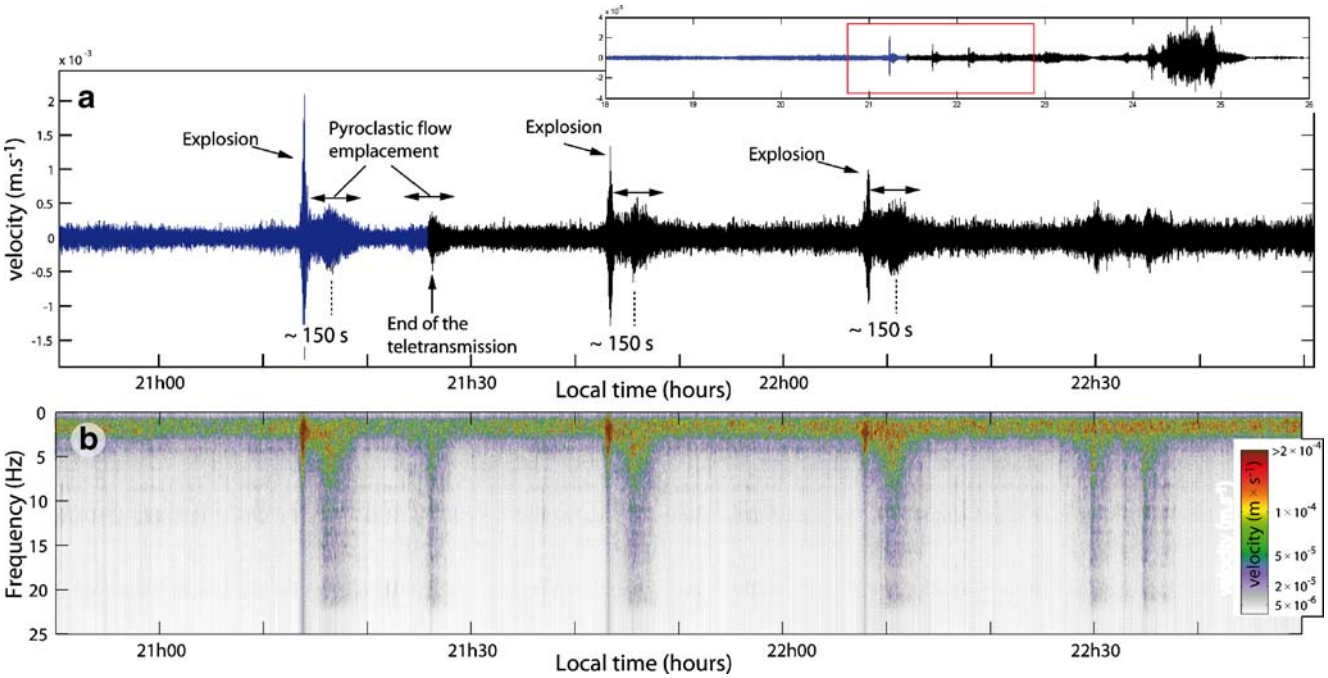

Fig. 4 Amplitude (**a**) and frequency (**b**) of seismic signals (*z*-component) recorded by the Cusua station (~4,500 m NW of the crater) between 2100 and 2300 hours. Initial pyroclastic flows were generated sporadically, either by explosions or not. The station was damaged by a pyroclastic flow at 2126 hours (*dark blue* signal transmitted to the observatory, *black* local record, transmission being cut by PF). Time delay between explosion and flow arrival is about 150 s, giving a pyroclastic flow velocity of about 30 m s^{-1}

We thus conclude that the signals described above are due to pyroclastic flows passing close by the seismic stations. As almost no signal has been recorded at Runtun, 600 m from the flow path, we hypothesise that the pyroclastic flows were only clearly detected where they passed by less than 200 m from the stations.

The same types of signals were recorded during the paroxysmal phase, with higher amplitude (Fig. 5). Seismic records thus confirm the visual observation that pyroclastic flows were generated continuously (but with pulses) over 40 min of the paroxysmal phase.

Velocity of pyroclastic flows and emplacement

IG-EPN scientists-in-charge at the observatory during the July 14th eruptions (P. Ramón and D. Barba) described the first pyroclastic flows as having a "low" velocity. Videos of July 14 and 15th pyroclastic flows allow us to estimate a velocity in the range of 20–30 m s^{-1}. Eyewitnesses of Achupashal flows on August 16th also spoke about "slow" flows but it is impossible to quantify flow velocity from these observations. Unfortunately, no clear video record exists for the August 16th pyroclastic flows since the paroxysmal phase occurred at night, and the volcano was almost completely covered by clouds.

However, seismic records allow us to estimate the velocity of the pyroclastic flows. At Cusua seismic station (~4.5 km from the crater), about 150 s separate the explosions from the maximal amplitude of the seismic signal generated by pyroclastic flows. This gives a mean velocity of about 30 m s^{-1}. This value is typical for this kind of pyroclastic flow (25–40 m s^{-1}, e.g. Hobblit (1986) at Mt St. Helens, USA; Yamamoto et al. (1993) at Unzen, Japan; Cole et al. (1998) at Soufrière Hills, Montserrat; Kelfoun et al. (2000) at Merapi, Indonesia). Geological observations also indicate that dense flows were generally constrained to the valleys and show limited runup around the curves, compatible with such a "low" velocity.

Source conditions and feeding rate

During the paroxysmal eruptive phase, continuous lava fountained up to 1,000 m high, and together with lava spilling out of the crater, it fed a continual stream of fragmented lava onto the cone's upper steep flanks. We believe that pyroclastic flows were formed by the gravitational mobilisation of all the bombs, scoriae and ash poured out around the crater by the fountain activity. The presence of a large apron of hot pyroclastic material after the eruption (Fig. 2) is compatible with this hypothesis. Where observations were possible, no explosion or fountain collapse was found to be the origin of the pyroclastic flows of the paroxysmal phase. Whatever the exact mechanism for the origin of the pyroclastic flow formation, visual observation indicates that they were formed under conditions of zero, or small, initial velocities.

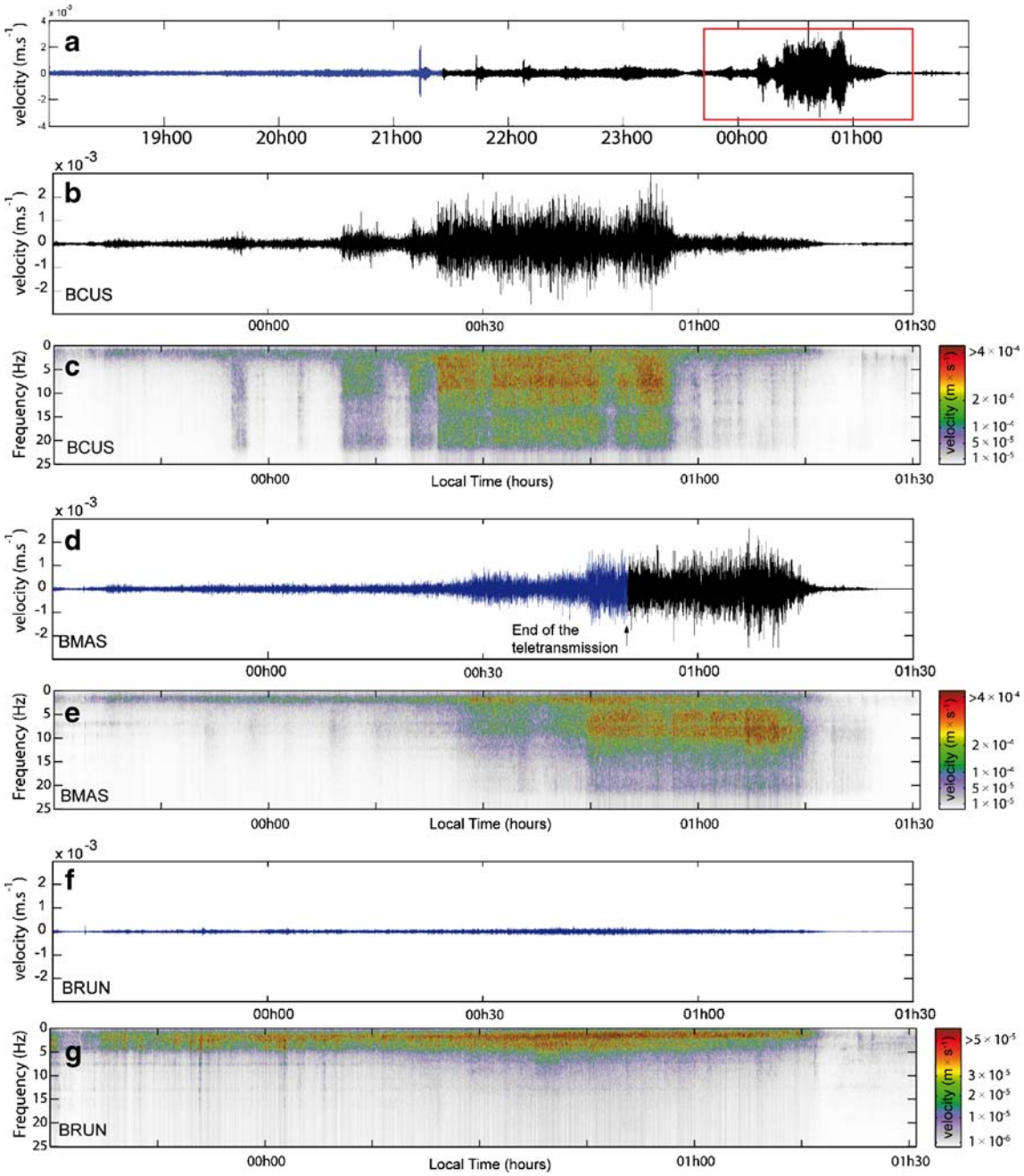

Fig. 5 Seismic records of three stations (*z*-component—Cusua, Mason and Runtun, Fig. 1) between 2330 and 0130 hours (local time), during the paroxysmal phase of the August 2006 eruption. Runtun, 600 m from the pyroclastic flow path, recorded a small amplitude signal. High-amplitude signals recorded by Cusua and Mason are not correlated: They are interpreted as being generated by different pulses of pyroclastic flows. *Dark blue* signal transmitted to the observatory, *black* local record, transmission being cut by pyroclastic flows

The main volume of pyroclastic flows was formed during a continuous phase that lasted about 40 min. The total volume of dense flows being $5–10\times10^6 m^3$, we assume the same volume for the paroxysmal phase given the small volume ($<10^6 m^3$) of sporadic pyroclastic flows previously emplaced. This gives a mean eruption rate of ~2,000–4,000 $m^3\ s^{-1}$.

The Cusua seismic station (~4.5 km, NW of the crater; Fig. 1) first recorded the pyroclastic flows of the continuous paroxysmal phase about 15 min before the nearer Mason station (3.5 km, S–W of the crater). This is related to the shape of the crater, which is lower to the northwest (~4,800 m asl) and indicates that pyroclastic flows were generated at increasing altitude during the first 15 min of

the paroxysmal phase, when the number of rivers affected increased. Flows were able to form on the north and south rim (~4,900 m asl) at about 0030 hours. At about 0055 hours, the eruption waned, pyroclastic flows shortened and were not able to reach the station of Cusua (4.5 km). However, between 0055 and 0120 hours, the station recorded flows that probably stopped some hundreds of metres from it (low amplitude of the signal, but still clearly detectable). Proximal pyroclastic flows continued to be detected with high amplitude at Mason, closer to the crater (3.5 km), 20 min (up to 0115 hours) after Cusua. Distant flows were detected at Mason and Cusua for a further few minutes, then the eruption stopped abruptly (end of pyroclastic flow, lava fountain and tremors). No pyroclastic flow was able to form on the eastern side of the cone, showing that the eruption was unable to form pyroclastic flows at heights greater than the east rim elevation (5,000 m asl).

It is hard to know exactly how the magma rate evolved over 40 min of paroxysmal activity. One hypothesis is that the magma rate increased with time, leading to an increase in the column height that generated pyroclastic flows. Another hypothesis is that the rate was approximately constant over the eruption period, but that a critical quantity of material needed to accumulate around the crater to trigger initiation of the pyroclastic flows. The lower points, covered by a larger quantity of fragmented lava, would have reached this critical threshold more rapidly. Pyroclastic flows shortened towards the end of the eruption, probably due to a decrease in magma rate.

Simulation of pyroclastic flows

Numerical model

Simulations are done with the code *VolcFlow* developed at the *Laboratoire Magmas et Volcans*. It is based on the depth-average approximation. Using a topography-linked coordinate system, with x and y parallel to the local ground surface and h vertical, the general depth-averaged equations of mass (Eq. 1) and momentum (Eqs. 2 and 3) conservation are:

$$\frac{\partial h}{dt}+\frac{\partial}{\partial x}(hu)+\frac{\partial}{\partial y}(hv)=0 \tag{1}$$

$$\frac{\partial}{\partial t}(hu)+\frac{\partial}{\partial x}(hu^2)+\frac{\partial}{\partial y}(huv) = gh\,\sin\alpha_x-\frac{1}{2}k_{\text{actpass}}\frac{\partial}{\partial x}\left(gh^2\cos\alpha\right)+\frac{T_x}{\rho} \tag{2}$$

$$\frac{\partial}{\partial t}(hv)+\frac{\partial}{\partial x}(hvu)+\frac{\partial}{\partial y}\left(hv^2\right) = gh\,\sin\alpha_y-\frac{1}{2}k_{\text{actpass}}\frac{\partial}{\partial y}\left(gh^2\cos\alpha\right)+\frac{T_y}{\rho} \tag{3}$$

where h is flow thickness, $\mathbf{u}=(u, v)$ is flow velocity, α is ground slope, $\mathbf{T}$ takes into account all the retarding stresses that slow down the flow (e.g. viscous, frictional and turbulent stresses), ρ is the bulk density of the pyroclastic flow (assumed to be 1,500 kg m^{-3}) and g is gravity (9.78 m s^{-2}). Subscripts denote components in the x and y directions (Table 1).

The parameter k_{actpass} is the earth pressure coefficient, the ratio of ground-parallel to ground-normal stress (see Savage and Hutter 1991). Its value is a function of the basal (between the avalanche and the ground surface) and the internal friction angle, φ_{bed} and φ_{int}, respectively, and is defined by Iverson and Denlinger (2001) by:

$$k_{\text{actpass}}=2\frac{1\pm\left[1-\cos^2\varphi_{\text{int}}\left(1+\tan^2\varphi_{\text{bed}}\right)\right]^{1/2}}{\cos^2\varphi_{\text{int}}}-1 \tag{4}$$

This expression is only valid if $\varphi_{\text{bed}}\leq\varphi_{\text{int}}$. The sign $\pm$ is negative (and k_{actpass} active) where the flow is locally divergent and is positive (and k_{actpass} passive) where the flow is locally convergent. An isotropic stress is defined by $\varphi_{\text{int}}=0$ and $k_{\text{actpass}}=1$.

The terms on the right-hand side of the equations for momentum conservation indicate, from left to right, the stresses due to the weight, the pressure gradient and the retarding stress which depends on the rheological model chosen. The model allows for simulations of various rheologies, including frictional (with one or two friction angles), Bingham, viscous and Voellmy. More complex rheological laws can also be defined by the user.

For a dry frictional material, the retarding stress $\mathbf{T}$ is of the form:

$$T_x=-\rho h\left(g\cos\alpha+\frac{\mathbf{u}^2}{r}\right)\tan\varphi_{\text{bed}}\frac{u}{\|\mathbf{u}\|} \tag{5}$$

The term $\frac{\mathbf{u}^2}{r}$ takes into account the "overweight" due to the centrifugal acceleration on the topographic curvature (Savage and Hutter 1991). The term $-\frac{u}{\|\mathbf{u}\|}$ allows the x-component of the retarding stress in the direction opposed to the displacement to be calculated.

The equations were solved using a shock-capturing numerical method based on an upwind Eulerian scheme (Kelfoun and Druitt 2005). The scheme can handle shocks, rarefaction waves and granular jumps and is stable even on complex topography. Details and tests of the scheme are presented in more detail in Kelfoun and Druitt (2005). Additional details on the code, other results and downloadable files are shown on http://wwobs.univ-bpclermont.fr/lmv/pperm/kelfoun_k/VolcFlow/VolcFlow.html

Table 1 Main variables used

Symbol	Variable	Value	Unit
g	Gravity	9.78	m s^{-2}
h	Flow thickness	–[a]	m
$k_{actpass}$	Earth pressure coefficient	–[a]	Dimensionless
S_i	Surface of the mesh I	–[a]	m^2
t	Time	–[a]	s
t_{erupt}	Duration of the flow genesis	2,400	s
V	Volume of pyroclastic flows	5×10^6–10^7	m^3
x, y	Space variables	–[a]	m
z_{gen}	Max elevation of flow genesis	5,000	m
$z_{rim,i}$	Elevation of the crater rim Upstream of the mesh i	–[a]	m
$\mathbf{T}=(T_x, T_y)$	Retarding stress of the flow	–[a]	Pa
$\mathbf{u}=(u, v)$	Flow velocity	–[a]	m s^{-1}
$\boldsymbol{\alpha}=(\alpha_x, \alpha_y)$	Ground slope	–[a]	degrees
φ_{bed}	Basal friction angle	0, 15 or 18	degrees
φ_{int}	Internal friction angle	0 or 30	degrees
ρ	Flow density	1,500	kg m^{-3}

[a] Varies during the calculation, in time or in space

Boundary conditions

Topography

The digital elevation model (DEM) was calculated by M. Souris (IRD) digitising then interpolating topographic maps (scale 1/50,000, elevation spacing 40 m) from the Military Geographic Institute of Ecuador. The DEM has a resolution of 10 m. Small topographic drainage features were smoothed locally by the interpolation process, and we have corrected them from field topographic measurements, for example, in the Mapayacu River drainage.

Source conditions

Several source conditions were investigated (increase of the rate with time, constant rate, final decrease etc.), fixing a feeding duration of 40 min (2,400 s) and a total volume of between 5×10^6 and $10^7 m^3$ according to field observations. We assumed that the pyroclastic flows formed close to the crater, and we fixed their source as being at the cells located just outside the crater rim, at a distance of 350 m from its centre (location x=783,940, y=9,837,550). The maximal elevation at which pyroclastic flows are generated was assumed to be z_{gen}=5,000 m, because no pyroclastic flows overflowed the eastern rim, at 5,000 m asl.

The results presented here were obtained with a volume of $10^7 m^3$ and with the simplest scenario, where the rate is constant with time. Further on we discuss other cases. Field observations indicate that a greater volume of pyroclastic flows formed at the low points of the rim than at higher points. We assume that the mass rate at the feeding cells, expressed by the variation of the thickness dh with time t, is a linear function of the difference between the maximal elevation, z_{gen}=5,000 m, where pyroclastic flows were generated and $z_{rim,i}$, the elevation of the crater rim taken radially between the mesh i and the centre of the crater.

$$\begin{cases} \frac{dh_i}{dt} = a\frac{\left(z_{gen}-z_{rim,i}\right)}{S_i} & \text{if } t \le 2,400 \text{ s} \\ \frac{dh}{dt} = 0 & \text{if} t > 2,400 \text{ s} \end{cases} \quad (6)$$

where S_i is the surface of the ith mesh, taking account of the DEM resolution and the local slope. The constant parameter a is calculated from the number of feeding cells, their elevation and the total duration of the eruption t_{erupt} to fit the total volume chosen. Using the 10×10-m-mesh DEM, there are 269 cells encircling the crater. If a volume $V=10^7 m^3$ is chosen, a is defined by

$$a = \frac{V}{t_{erupt}\sum_{i=1}^{269} z_{gen} - z_{rim,i}} \approx 0.121 m^2 s^{-1} \quad (7)$$

The new mass dh is assumed to be poured without velocity, the velocity of the cells at the feeding point being calculated by the conservation of momentum: $u_a = (u_b h_b + 0 \times dh)/(h_b + dh)$, where u_a and u_b are respectively the velocity after and before the new mass is added from the fountain. The parameter h_b is the thickness of pyroclastic material before the new mass is added.

Results

Frictional behaviour

With a basal friction angle alone (internal isotropic stress), the frictional model that best reproduces the extension of the August 2006 eruptions of Tungurahua assumes that $\varphi_{bed}=15°$. At the onset of the eruption, the mass poured on the crater rim immediately begins to flow and rapidly covers all the SW, W and NW flanks with a very thin layer of <<1 mm (Fig. 6a). Not only the main drainage channels are affected but also the interfluves. The mass accelerates along the steep (>30°) slope of the upper part of the cone, reaching a velocity of more than 150 m s^{-1}. The mean velocity of the front, which starts at 0 at the crater rim, is about 80 m s^{-1}, when the pyroclastic flows reach the seismic stations (red points on Fig. 6). The thickness of the pyroclastic flows on the interfluves does not significantly increase with time, but it does increase in the valleys into which the mass drains (Fig. 6b, c). The mass begins to decelerate and accumulate where the slope is less than the friction angle. After the source stops, at t=2,400 s, all the mass deposited on the flank rapidly drains down and accumulates at the foot of the volcano on slopes slightly lower than the friction angle (Fig. 6c, f). There it forms "sand piles" with a surface angle of about 15° (Fig. 7).

Figure 8 illustrates the morphology in cross section of the deposits obtained with the frictional model. The topography of the zoomed area has been artificially smoothed to avoid small-scale perturbations, thus demonstrating the typical morphology of a flow with a frictional behaviour. A very thin wedge of material runs rapidly on slopes steeper than 15° (the basal friction angle chosen). Where the slope of the flow surface is less than 15° (x~370 m, not visible on the figure), the flow begins to slow down and rapidly stops. The mass then

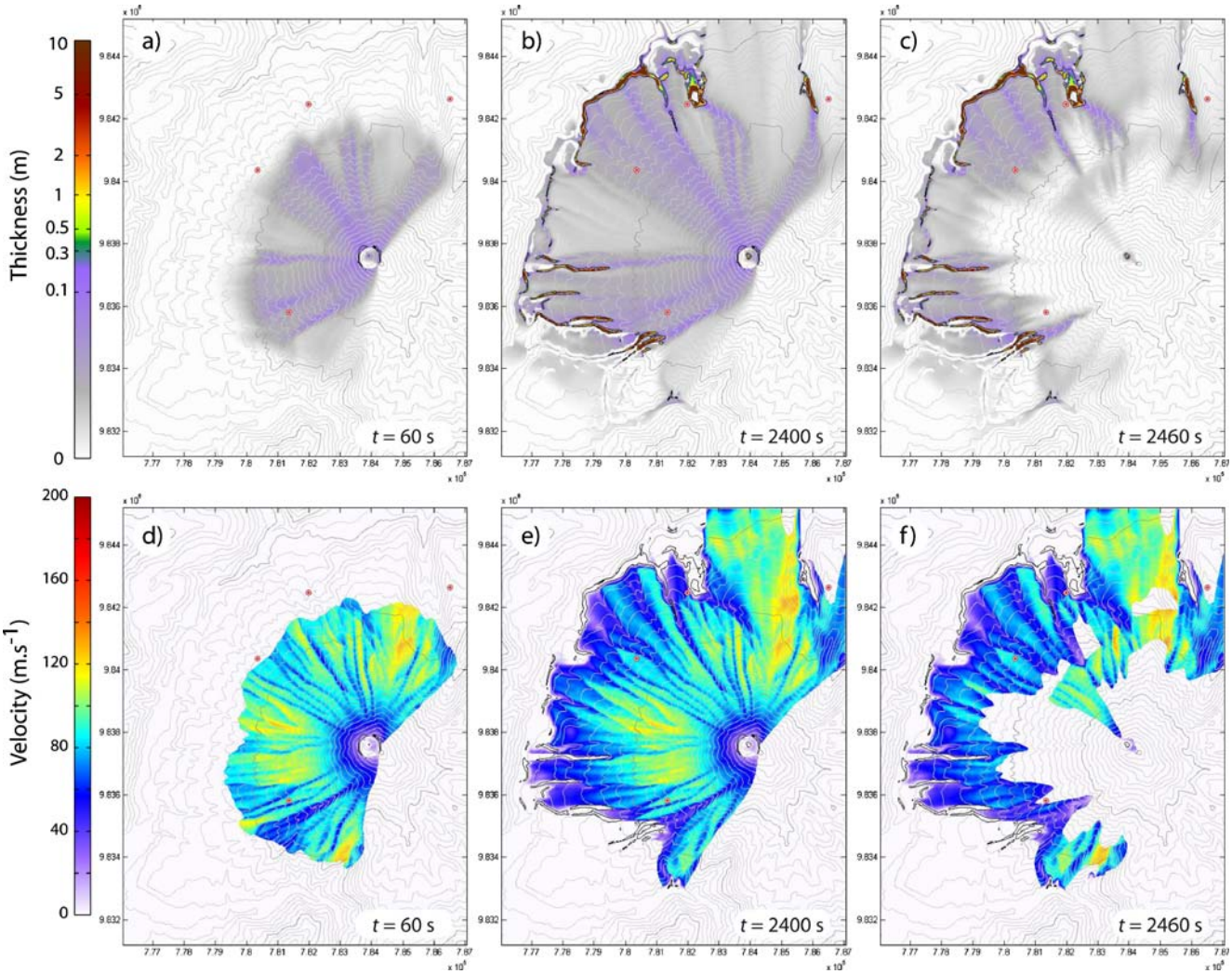

Fig. 6 Thickness (**a**–**c**) and velocity (**d**–**f**) of pyroclastic flows at Tungurahua simulated using the frictional model ($\phi_{bed}=15°$) at t=60 (**a**, **d**), 2,400 (**b**, **e**) and 2,460 s (**c**, **f**). The *colour scale* of the thickness (**a**–**c**) is logarithmic. *Black contours* indicate 0.1 m deposits (no thinner pyroclastic flow deposits were observed in the field). For clarity, velocity is only drawn where the mass is thicker than $1e^{-6}$ m

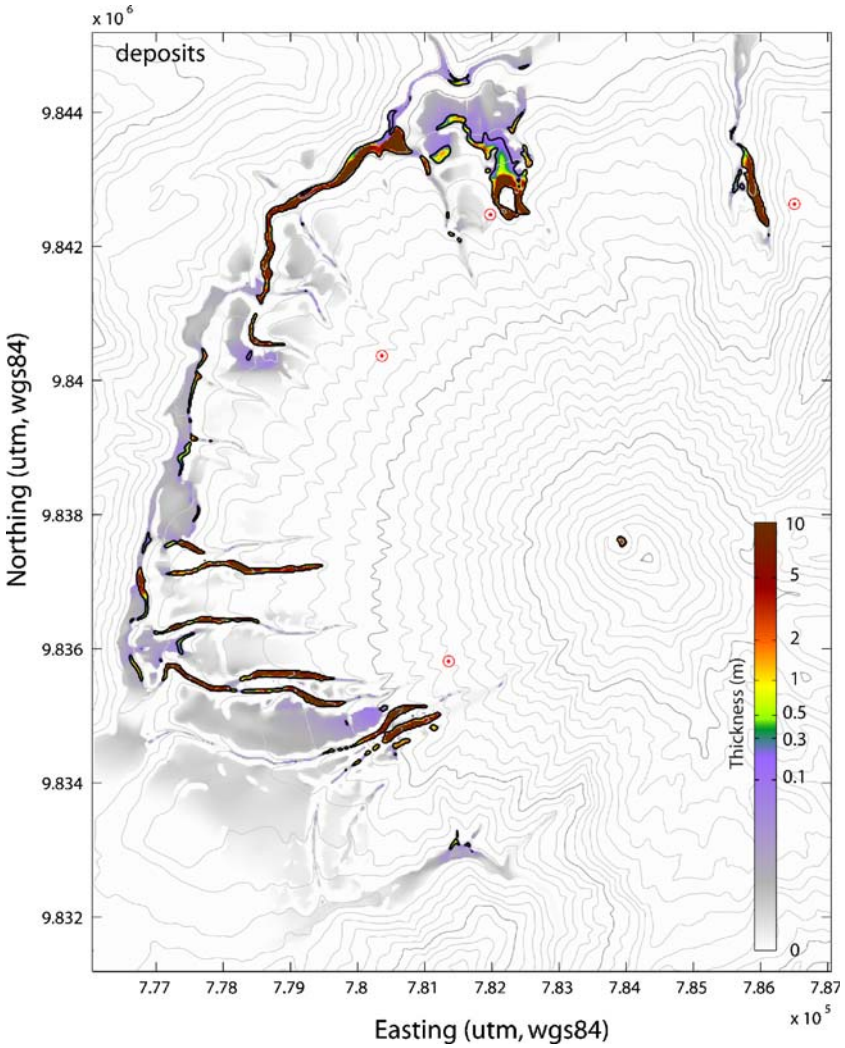

Fig. 7 Thickness of pyroclastic flow deposits of Tungurahua simulated using the frictional model (ϕ_{bed}=15°). The mass accumulates on slopes slightly lower than the friction angle (15°) to form sand pile-like deposits

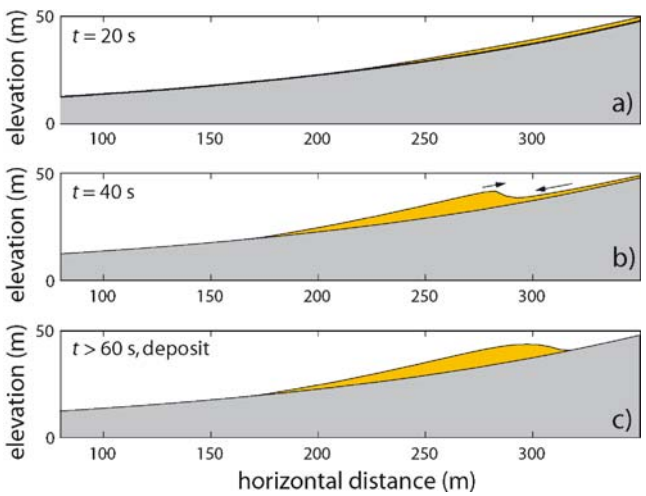

Fig. 8 Typical emplacement of flow and deposit using the frictional model. The mass accumulates on slopes slightly lower than the friction angle (15°) to form sand pile-like deposits. Time is counted from the instant the flow enters the frame (x=350)

accumulates upstream forming a pile with slopes of about 15° (less on the downstream side due to inertia). This behaviour explains the accumulation and the shape of simulated pyroclastic material at the downstream margin of the affected area.

The same behaviour arises using any combination of both internal and basal friction angle (Fig. 9a). The internal angle modifies the effect of the pressure gradient (changing the value of $k_{actpass}$, Eqs. 2, 3 and 4) and thus slightly decreases velocity and runout. However, this effect is small because the flows are very thin compared to the variations of the volcano topography and the stress of the pressure gradient if thus negligible compared to the stress of the weight. This is why results obtained with only one friction angle (φ_{bed}=15°, φ_{int}=0°) are very similar to results obtained with two friction angles (φ_{bed}=15°, ϕ_{int}=30°). A high value of the internal angle is also difficult to reconcile with the apparently high internal fluidity of natural pyroclastic flows.

Changing the velocity of the source does not change the behaviour described above. Figure 9b shows the results

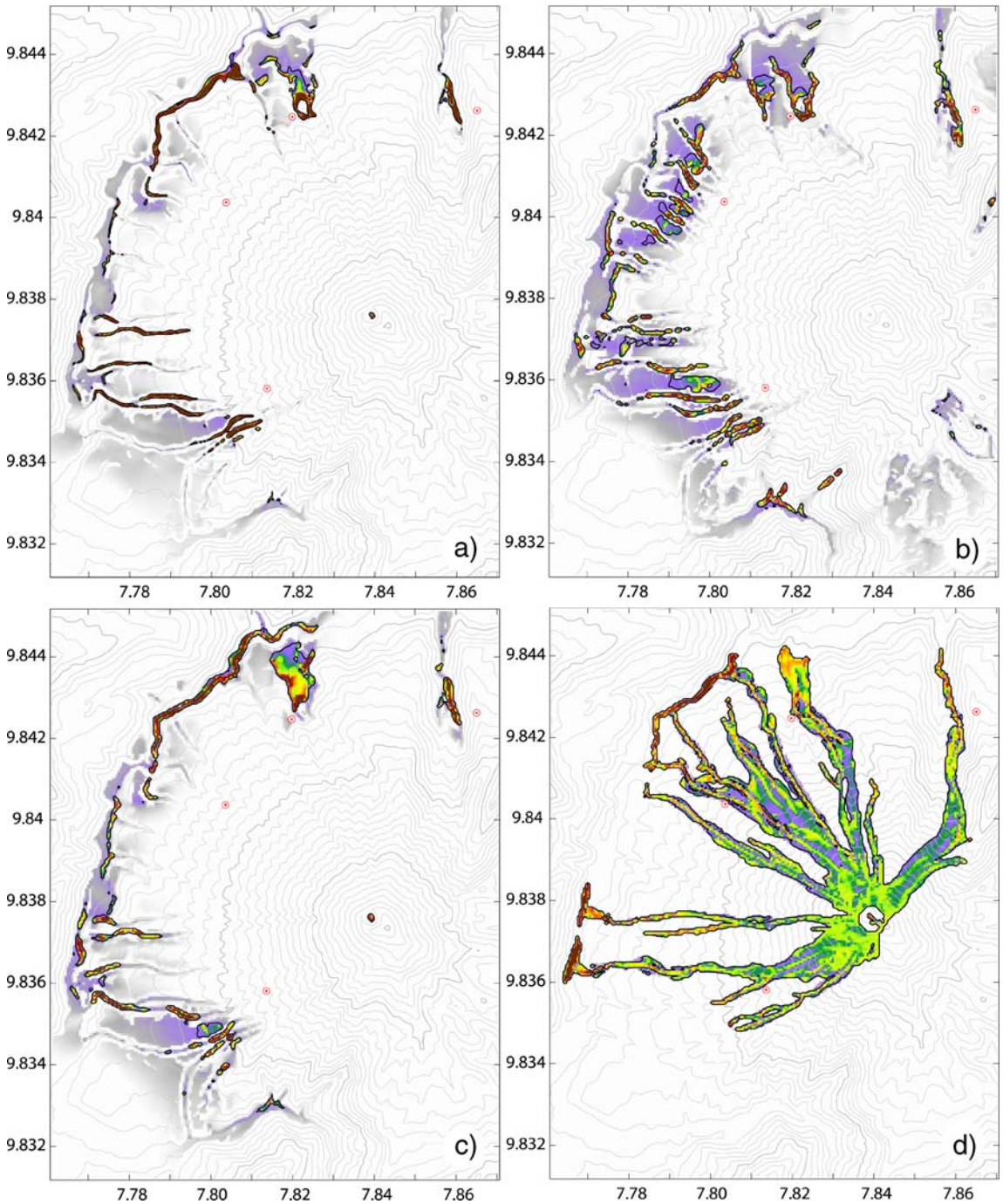

Fig. 9 **a** Simulation of pyroclastic flows with a two friction-angle frictional rheology (φ_{bed}=15° and φ_{int}=30°; same DEM resolution as Figs. 6, 7, 10 and 11). **b–d** Simulations on a lower-resolution topography (50 m). **b** Frictional rheology with one friction angle (φ_{bed}=18°) and a very high (and unrealistic) velocity of 100 m s^{-1} over 2,400 s at the source. **c** Frictional rheology with one friction angle (φ_{bed}=15°; conditions are similar as Fig. 7). **d** Constant retarding stress rheology (**T**=5 kPa; conditions are similar as Fig. 11)

obtained if a very high initial velocity is imposed on the flow (100 m s^{-1} at the source over 2,400 s, which is much higher than what could be inferred from observation). The basal friction angle must be increased (to 18°) to slow down the flow enough to reach the same runout as previously, but the flows still accumulate at the downstream margin to form deposit piles.

Constant retarding stress

As discussed below, the behaviour simulated using the frictional model is very different to that observed in the field. The same difference in behaviour was detected by Kelfoun and Druitt (2005) for their simulation of the Socompa debris avalanche: The frictional model was unable

to reproduce, even to the first order, the emplacement of the avalanche. It formed "dunes" or "hummock"-like piles on the gentler slopes. They showed that a constant retarding stress (Dade and Huppert 1998), also called yield strength, is very much more appropriate than frictional behaviour and enabled all the main features of the avalanche deposit to be reproduced. We have thus tried to simulate the pyroclastic flows at Tungurahua using this simple rheological law.

This empirical law simply states that the retarding stress is constant, independent of the velocity, the thickness or any other parameter of the flow:

$$T_x = \text{Constant} \times -\frac{u_x}{\|u\|} \text{ or } T = \left\|\vec{T}x + \vec{T}y\right\| = \text{Constant} \quad (8)$$

Figure 10 illustrates the emplacement of constant stress pyroclastic flows using the same source conditions as for Figs. 6 and 7. The best fit results are obtained with a constant retarding stress of 5 kPa.

The first difference with the frictional model is that the mass accumulates around the rim before reaching a critical thickness of about 0.5 m, at which point flow is initiated. Simulated flows present a thickness close to the thickness of natural pyroclastic flows (0.5–2 m thick) and are restricted to the valleys (Fig. 10a–c).

Figure 10d–f shows that emplacement of numerical flows is carried out by pulses (see arrows on Fig. 10e, clearest on additional movie material) even if the source rate is constant: The mass accumulates until it reaches a critical thickness (about 0.5 m) which allows flow to take place. The mass then reaccumulates until the critical thickness is reached and a new pulse forms. Numerical pulses are thicker and faster than the neighbouring material and generally run at less than 30 m s^{-1}.

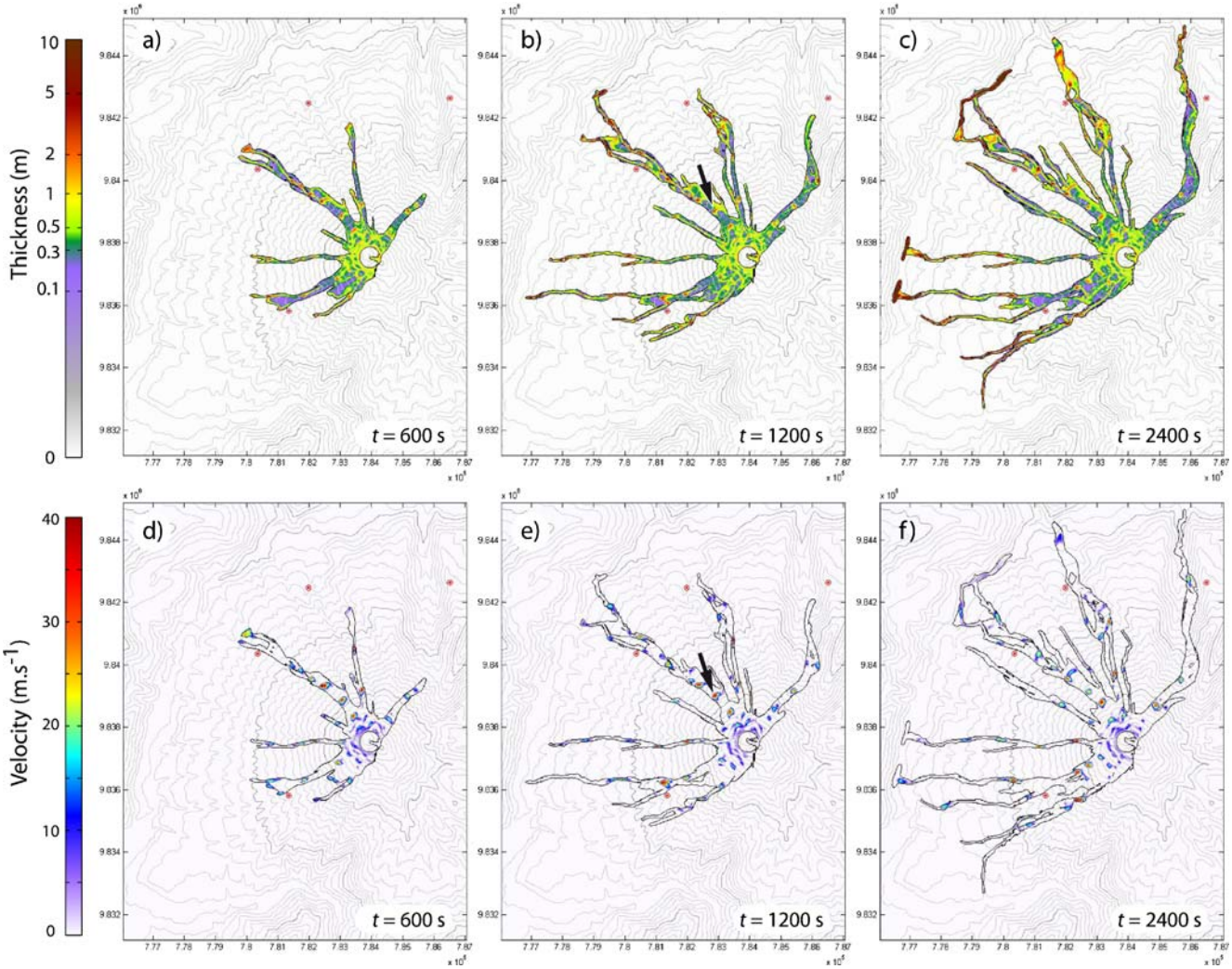

Fig. 10 Thickness (**a**–**c**) and velocity (**d**–**f**) of pyroclastic flows at Tungurahua simulated using the constant stress model (5 kPa) at t=600 (**a**, **d**), 1,200 (**b**, **e**) and 2,400 s (**c**, **f**). The *colour scale* of the thickness (**a**–**c**) is logarithmic. *Black contours* indicate 0.1 m deposits (no thinner pyroclastic flows were observed on the field). *Arrows* locate a pulse characteristic of the emplacement of constant-stress flows

The fronts of the flows are well defined during emplacement. The simulated deposits also show a well-defined front and a progressive decrease of the thickness on steeper slopes (Fig. 11). Figure 12 illustrates the typical form of a flow formed by a constant retarding stress using the same topography as Fig. 8.

Discussion

Frictional model

To a first approximation, the area of deposit generated by the frictional model covers that of natural pyroclastic flow deposits. However, a critical analysis of the results demonstrates that the frictional model is unable to reproduce accurately the behaviour of the dense pyroclastic flows of Tungurahua. The geometry of the deposits obtained from numerical modelling does not resemble that of the natural deposits. Simulated flows are present in the valleys as well as on the interfluves, whereas the latter one remained uncovered by the natural dense flows. We stress that the frictional model only simulates dense flows and that it is unable to reproduce ash-cloud or ash-cloud surge physics. The local resemblance between simulated deposits and natural ash deposits cannot be considered as a validation of the model. Simulated deposits appear as piles accumulated at the foot of the volcano or on gentle valley slopes, rather than as a continuously distributed layer with a small increase in thickness downstream. The very thin wedge of the simulated front (<<1 mm) is also quite unlike those observed in the field.

The simulated velocity of pyroclastic flows (more than 150 m s^{-1}) appears to be incompatible with field observations at Tungurahua, as well as for other volcanoes in the world for dense flows of this volume and thickness (e.g. Hobblit 1986; Yamamoto et al. 1993; Cole et al. 1998; Kelfoun et al. 2000). This is explained by the fact that a frictional body accelerates on slopes steeper than its frictional angle: a drop of about 2,000 m in the case of

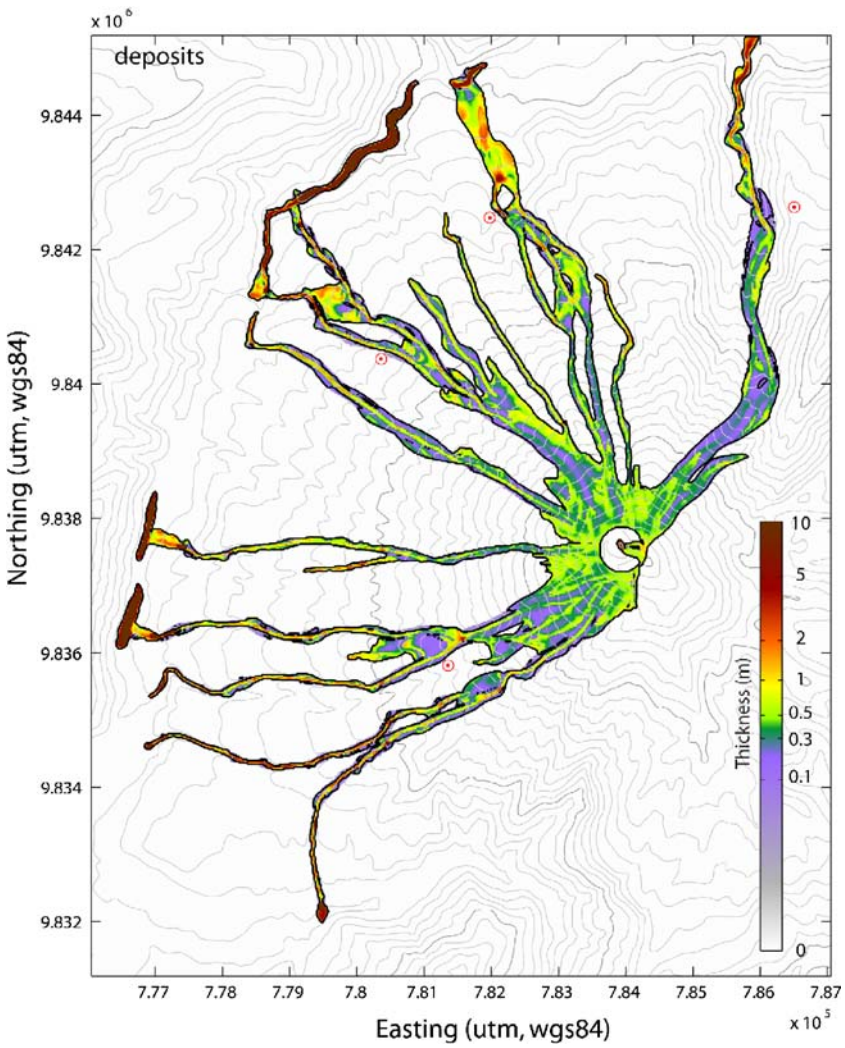

Fig. 11 Thickness of pyroclastic flow deposits at Tungurahua simulated using the constant retarding stress model (5 kPa). The thickness and geographic distribution of deposits resemble the field observations

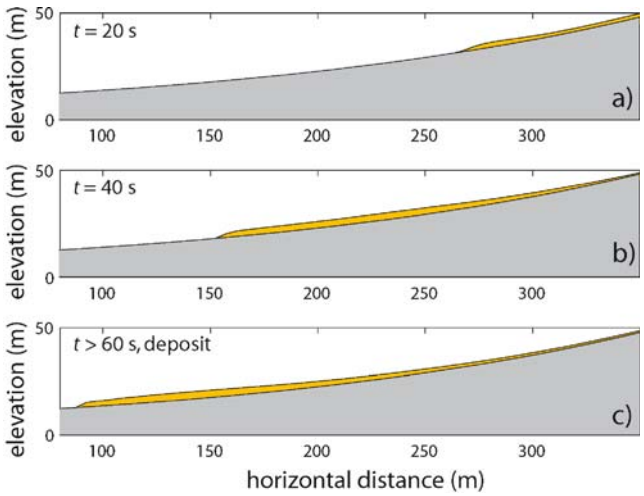

Fig. 12 Typical emplacement of flow and deposit with the constant-stress model. The front is well defined and the thickness progressively decreases upstream. Time is counted from the instant the flow enters the frame (x=350)

Tungurahua, with an acceleration over a distance of about 4,500 m horizontally. Quasiconstant velocity can be reached with a frictional behaviour (e.g. Pouliquen and Forterre 2002) but only with a slope close to the friction angle of the material and not on volcanoes whose slopes typically change from >30° near the crater to less than 5° where the pyroclastic flows stop. With such a high velocity, pyroclastic flows cannot be confined to the valleys and rapidly overflow the interfluves. It is physically meaningless to maintain a frictional regime at such a high velocity and with such a small thickness, but this is implicit in using a simple frictional rheology for pyroclastic flow simulation.

We should emphasise that the incompatibility between numerical results and field data is not due to a problem in the numerical code: Put a grain of frictional material (sand for example) on the surface of a curved slope covered by the same material and the grain will immediately slide down the slope and will stop just beyond where the slope becomes less than the friction angle of the material. Several grains together will all still stop at approximately the same place. Pour the sand over some tens of seconds and the sand will flow and accumulate to form a sand pile. Our frictional results reproduce exactly this frictional behaviour. The "sand pile" shape of flows and deposits can also be observed in the simulations of granular flows in the laboratory (e.g. Pudasaini and Hutter 2006, and reference therein) and in pyroclastic flows using frictional behaviour (e.g. Patra et al. 2005). This last study, however, mainly focuses on the numerical scheme and does not aim to prove whether or not the frictional model is suitable for pyroclastic flows. The numerical results which they obtained were not subsequently compared to the thickness, distribution and morphology of natural deposits.

It should also be noted that all the characteristics described here which show that frictional behaviour differs from natural pyroclastic flows are largely independent of the total volume, feeding conditions, topography and friction angle (see Fig. 9). The same behaviour occurs when the rate, the volume or the way the mass is injected are changed. This conclusion can also be demonstrated with sand in the laboratory: Pouring sand twice as much down a curved slope does not fundamentally change the fact that the flow will accelerate on a slope steeper than the friction angle or that deposits will not be present on these slopes and that the sand will accumulate downstream in a pile. The frictional model is largely independent of the thickness of the flow (the effect of the pressure gradient only) and this is why initial conditions (e.g. volume and rate variations) have little influence on the simulated flows. With a friction angle less than or greater than 15°, the same behaviour occurs, but the distances reached by simulated flows are respectively greater and smaller than in reality. Results of the frictional rheology are also poorly influenced by the resolution of the topography. Figure 9c was carried out with a low-resolution topography (50 m) and simulated deposits are very similar to those presented on Fig. 7. Small differences arise mainly downstream of the narrowest drainage channels, which could not be reproduced accurately enough with a low resolution.

If the source conditions are changed to simulate an increase of the level at which pyroclastic flows were generated with time, the results are slightly improved: The first simulated flows occurred on the NW flank and flows progressively affected the northern and the southwestern flanks, as was the case in reality. However, this does not change the conclusions about the shape of the flows and the deposits, nor the overly high velocity.

The entrainment of accidental clasts does not change our conclusions either. The entrainment would play an important role in the momentum balance of the flows (e.g. in Mapayacu valley) and could shorten the distance they will reach. The best-fit value (of the friction angle and of the constant retarding stress) must then be lowered to reach the natural runout, but the shape of deposits remain similar: Even with a low velocity, a 15° frictional flow is unable to deposit on slopes steeper than 15° (moreover, this value would be lowered due to the mass entrained, in order to compensate for the loss of momentum).

Finally, it should be noted that all the problems raised here are not dependant on conditions particular to Tungurahua, but rather on slope variations which are common to most volcanoes: a slope decreasing from about 30° to few degrees over a distance of several kilometres. Therefore, we think that the discrepancies between the deposits simulated with the frictional model and natural deposits of pyroclastic flows apply to more than just the individual case of Tungurahua.

An important point to underline is that our results do not contradict the results obtained by previous authors who reproduced granular flows with the frictional model (e.g. Iverson et al. 2004; Denlinger and Iverson 2004; Pudasaini and Hutter 2006, and references therein). The good fit they obtained is based on flume or laboratory experiments with sand, eventually adding water. In this case, they have demonstrated that the frictional behaviour plays an important role in the dynamics. What our results show is that the behaviour of natural pyroclastic flows differs from the behaviour of granular flows at a smaller scale. This may be due to the high temperature, the high polydispersity, the presence of very fine particles, the duration of the emplacement or the high volumes involved.

Our results thus underline the problem of using the frictional model for hazard assessment. One could argue that the actual shape of deposits is not important for hazard assessment and that a good map of "inundation" can be obtained with a simple model that does not reproduce the morphology of the phenomenon. However, our results show that the frictional model cannot create a correct inundation map, either. With the frictional model, all the interfluves are affected by numerical dense flows whereas in natural flows, dense flows are restricted to valleys (interfluves may be affected by surges but the frictional model is not able to simulate them). The simulated mass also accumulates in thick piles (up to 50 m) and cannot spread. The model thus underestimates the hazard over a flat area. Finally, the frictional model achieves velocities five times higher than in reality. It is these unrealistically high velocities which enabled simulated flows to cross ridges that they would not be able to cross in reality. The portion of the flow which crosses the ridge is no longer available to follow the drainage and to affect downstream areas. Thus, where valleys deviate from a straight plan view, the frictional model can greatly underestimate downstream areas affected. This occurred on the south flank of Tungurahua, where the simulated flows accelerated on the steep slopes of the terminal cone. The unrealistically high velocity allowed the flows to escape from the Mapayacu River valley and cross the 100-m-high barriers that bound it. The flows then formed deposits to the south (purple to red deposits to the south in Fig. 7); in reality, these areas are unaffected. The mass lost due to this overly high velocity was no longer present in the Mapayacu River. Hazards are thus underestimated at the mouth of the river and in the neighbouring area of the Palitahua village (Fig. 1).

Constant retarding stress model

Our results indicate that a constant stress rheology reproduces to first order the main characteristics of observed pyroclastic flows. The deposits simulated with this rheology are restricted to valleys, and affected areas in the model are similar to those areas affected in reality. The shapes of flow fronts and deposits are closer to reality than for the frictional model and velocity of the pulses is about 30 m s^{-1}, as has been observed.

Some other characteristics of our constant retarding stress simulations appear compatible with field observation. The simulated flow is composed of pulses, each flow having a velocity close to observed velocities. The pulse emplacement of simulated flows appears compatible with pulses observed during emplacement and with lobes and units observed in the field deposits (Fig. 3c). However, we cannot confirm that the frequency of generation or the distance run by each pulse is realistic. The velocity of the simulated front is slow, the flows passing close to the seismic stations about 500 s after the formation of the column, giving a mean velocity of the front of the flows of less than 10 m s^{-1} (the flows being composed of successive pulses with a velocity of 30–40 m s^{-1}). This differs from the 150 s measured for the flows formed by explosions. However, we lack data about the time delay between the initiation of the fountain and the first arrival of pyroclastic flows at the seismic stations, our quantification only concerning explosive events. If, in reality, the mass had to accumulate before flowing, our simulation appears correct. Note that a time of about 150 s can be obtained with the model if a mass of more than $5\times10^4 m^3$ is poured out immediately upstream of a valley, showing that the constant retarding stress model is compatible with the velocity of explosion-generated pyroclastic flows.

The main difficulty in using the constant retarding stress model is its strong dependence on source conditions (volume, rate) and on the topography. This is mainly because the flow capacity of the model is directly related to the thickness of the flows, a thicker flow being very mobile, a thin flow being able to stop on slopes (the flow capacity depends on the difference between the driving force which increases with thickness and the retarding stress that remains constant). If the resolution of the DEM is too low, the shape of the valley is not estimated correctly. In our model, the valleys in the DEM are larger and smoother than in reality. Deposits spread much further laterally, some reaching up to 50 m in width in the model, whereas they are less than 10 m wide in the field. Because the surface of deposition is wider than in reality, not enough mass is available to reach the natural runout if we use the value of the constant retarding stress that would have been obtained on a perfect topography. To reach the natural runout, the value of the constant retarding stress must be reduced, thus reducing the simulated thickness of deposit. This is why, using the volume estimated for the whole deposit, the simulated thickness approximately corresponds to the thickness of one unit (0.5–2 m) but not to the total thickness of

deposits (~5–10 m). This value of 5 kPa is, however, interesting because it gives an estimation of the rheological behaviour of each pyroclastic flow pulse at Tungurahua.

The sensitivity of the constant retarding stress to the resolution of the topography is illustrated in Fig. 9d, where the resolution of the DEM has been reduced at 50 m. It is particularly clear in the southern drainage channels where the valleys are narrow: The poor resolution chosen for Fig. 9 (50 m) forms wider and smoother valleys. The simulated flows spread out too much and start laying down deposits on higher slopes, leaving too little mass available to achieve the runout of the natural flows. With this resolution, the runout distance could only be reached by lowering the value of the constant retarding stress (thus thinning deposits). The low quality of the topography upstream of the small rivers (Bilbao/Chontapamba for example) also explains why the pyroclastic flows in these areas have not been simulated accurately.

The quality of the simulations is clearly dependant on the accuracy and the resolution of the digital topography used. However, whatever the quality of the topography, the characteristics of the constant retarding stress simulations (thickness variations, velocity, shape of the front, geographic distribution of deposits) are much closer to natural phenomena than simulations carried out with the frictional behaviour (Fig. 9).

A similar conclusion has been drawn by Kelfoun and Druitt (2005) for the simulation of the avalanche of Socompa: The main features of the Socompa avalanche (morphology, thickness and lithology distribution) can be reproduced successfully by a constant retarding stress rheology, whilst they are impossible to reproduce with the frictional rheology. The value obtained for the pyroclastic flows of Tungurahua, 5 kPa, is, however, ten times smaller than the value of about 50 kPa of Kelfoun and Druitt (2005). At present, we cannot physically explain this difference. It does seem though that the value of the constant retarding stress is directly related to the thickness of deposits. The higher the value of the constant retarding stress, the thicker the deposits formed. Debris avalanche deposits that are thicker than pyroclastic flow units should thus be simulated with a higher value of the constant retarding stress.

Other rheological laws

Other rheological laws have been used to simulate pyroclastic flows or other geophysical flows. Here, we briefly describe how appropriate they are for Tungurahua pyroclastic flows.

Some authors have used more complex frictional laws. Pouliquen and Forterre (2002) have shown that, even in the laboratory, the rheology of sand is more complex than simple friction. Their results show that the friction angle depends on the velocity and the thickness of the flow. Heinrich et al. (2001) used a partial form of the law of Pouliquen and Forterre (2002) to simulate a debris avalanche at Montserrat. At Tungurahua, the partial form of the law fails to reproduce the deposits mainly because it neglects the strong increase in the friction angle when the speed of the flow decreases: Where the flow slows down, the friction angle decreases and all the mass drains onto the lowest slopes and accumulates in piles. Flow velocities and deposits are, however, closer to natural phenomenon than with the simple friction law. The complete form of the law appears to be better suited, but we were unable to find a combination of the six free parameters that fitted the natural deposits more closely than we reproduced with the constant stress condition. Note that the complete form of the law could produce a behaviour close to the constant retarding stress as the friction coefficient φ decreases when the thickness h increases. It could then be possible for the frictional retarding stress to remain approximately constant whilst the friction angle varies (see "Introduction" section).

A viscous material allows a velocity compatible with field observations to be reached and flows are constrained to the valleys. However, such material cannot form deposits, as all the mass escapes from the investigated area since a viscous flow cannot stop on slopes.

The law combining frictional behaviour with a velocity-dependent retarding stress (e.g. McEwen and Malin 1989; Wadge et al. 1998) allows the velocity of the flows to be limited and appears to be better adapted than a simple frictional law. However, to reach the runout distance, the friction angle has to be lower than 15°. The mass then drains down steeper slopes and forms pile deposits at the foot of the volcano. The Voellmy law, also combining a frictional stress with a velocity squared dependent stress (e.g. Evans et al. 2001), gives the same kind of behaviour and deposits.

Bingham flow, a constant retarding stress plus a viscous stress, gives a good fit with reality if the viscosity is low (<1,000 Pa s). The lack of accuracy of source and topographic conditions does not allow us to state whether this model, proposed by other authors for pyroclastic flows (e.g. Sparks 1976; Freundt and Schmincke 1985), is better or not, or to give a value of the most appropriate viscosity. For the same reason, we cannot exclude that results would be better if a small turbulent stress or collisional stress were added to the constant retarding stress.

We stress that only simple rheological laws have been studied. More complex laws involving, for example, degassing or sedimentation can present behaviour that appears to approximate flow behaviour and natural deposits. Different laws exist which each contain several free parameters, and we were not able to find a combination of parameters that fitted the observations better than with the constant retarding stress condition. These laws are, more-

over, outside the scope of this paper, which aims instead to analyse simple rheological models that can be used for hazard assessment.

Conclusions

A comparison between simulations and well-constrained field data shows that the frictional model cannot simulate pyroclastic flow emplacement and deposits at Tungurahua volcano. We also believe that this conclusion is not restricted to this field case alone because the inadequacy is mainly related to a slope variation which is common to many volcanoes. Friction between the particles that compose pyroclastic flows probably exhibits a Mohr–Coulomb behaviour but it seems that other phenomena act on the dynamics to give a much more complex behaviour to the flow.

The constant retarding model appears to simulate pyroclastic flows much better than the frictional model. The main weak point of the constant stress model is that it is empirical and does not have a physical basis. It should thus be used carefully. We think, however, that the greater suitability of the constant retarding stress proves that the ratio of driving/retarding stress cannot be considered as constant—as for the frictional model—but decreases as the thickness increases. Above a certain thickness, the flow is able to move. Below this thickness, the retarding stress dominates the driving stress and the flow slows down. This produces flow deposits with a more or less constant thickness as seen in the field.

The physics of pyroclastic flows is complex and further research is needed to understand it fully and to obtain a robust physical model. Our results are useful in that they should place constraints on any future, more complex model which would need to explain why a constant stress model is much better adapted than a frictional model for simulating pyroclastic flows. In the meantime, the frictional model appears to be too simple to be used for pyroclastic flow simulations and we believe that it cannot be used for hazard assessment. Constant retarding stress possibly represents an acceptable alternative.

Acknowledgements Those studies have been funded by the French *Institut de Recherche pour le Développement* (IRD). We thanks the *Japan International Cooperation Agency* (JICA) and Dr Hiroyuki Kumagai for the use of seismic data. The paper was improved by Fran van Wyk de Vries and by the useful comments of A. Neri, M. Bursik, an anonymous reviewer and the editor. The authors deeply thank the staff of the Tungurahua Volcano Observatory (IG-EPN), especially those in charge during the July 14th and August 16th eruptions.

References

Burgisser A, Bergantz GW (2002) Reconciling pyroclastic flow and surge: the multiphase physics of density currents. Earth Planet Sci Let 202:405–418

Cole PD, Calder ES, Druitt TH, Hoblitt R, Robertson R, Sparks RSJ, Young SR (1998) Pyroclastic flows generated by gravitational instability of the 1996–97 lava dome of Soufriere Hills Volcano, Montserrat. Geophys Res Let 25(18):3425–3428

Dade WB, Huppert HE (1998) Long-runout rockfalls. Geology 26:803–806

Dartevelle S (2004) Numerical modeling of geophysical granular flows: 1. A comprehensive approach to granular rheologies and geophysical multiphase flows. Geochem Geophys Geosys 5(8): Q08003. doi:10,1029/2003GC000636

Denlinger RP, Iverson RM (2004) Granular avalanches across irregular three-dimensional terrain: 1. Theory and computation. J Geophys Res 109:F01014. doi:10.1029/2003JF000085

Evans SG, Hungr O, Clague JJ (2001) Dynamics of the 1984 rock avalanche and associated distal debris flow on Mount Cayley, British Columbia, Canada; implications for landslide hazard assessment on dissected volcanoes. Eng Geol 61:29–51

Freundt A, Schmincke HU (1985) Lithic-enriched segregation bodies in pyroclastic flow deposits of Laacher See volcano (East Eifel, Germany). J Volcanol Geotherm Res 25:193–224

Gray JMNT, Tai YC, Noelle S (2003) Shock waves, dead zones and particle-free regions in rapid granular free-surface flows. J Fluid Mech 91:161–181

Hall ML, Robin C, Beate B, Mothes P, Monzier M (1999) Tungurahua Volcano, Ecuador: structure, eruptive history and hazards. J Volcanol Geothermal Res 91(1):1–21

Hall ML, Mothes PA, Ramon P, Arellano S, Barba D, Palacios P (2007) Dense pyroclastic flows of the 16–17 August 2006 Eruption of Tungurahua Volcano, Ecuador. AGU Joint Assembly, Acapulco, Mexico

Heim A (1882) Der Bergsturz von Elm. Z Dtsch Geol Ges 34:74–115 (in German)

Heinrich P, Boudon G, Komorowski JC, Sparks RSJ, Herd R, Voight B (2001) Numerical simulation of the December 1997 debris avalanche in Montserrat, Lesser Antilles. Geophys Res Lett 28:2529–2532

Hobblit RP (1986) Observations of the eruptions of July 22 and August 7, 1980, at Mount St. Helens, Washington. USGS Prof Paper, 1335

Hsü J (1975) Catastrophic debris streams (sturzstroms) generated by rockfalls. Geol Soc Amer Bull 86:129–140

Iverson RM, Denlinger RP (2001) Flow of variably fluidized granular masses across three-dimensional terrain 1. Coulomb mixture theory. J Geophys Res 106:537–552

Iverson RM, Logan M, Denlinger RP (2004) Granular avalanches across irregular three-dimensional terrain: 2. Experimental tests. J Geophys Res 109:F01015. doi:10.1029/2003JF000084

Kelfoun K, Druitt TH (2005) Numerical modeling of the emplacement of Socompa rock avalanche. Chile. J Geophys Res 110:B12202. doi:10.1029/2005JB 003758

Kelfoun K, Legros F, Gourgaud A (2000) Statistical study of damaged trees related to the pyroclastic flows of November 22, 1994 at Merapi volcano (central Java, Indonesia): relation between ash-cloud surge and block-and-ash flow. J Volcanol Geothermal Res 100:379–393

Kumagai H, Yepes H, Vaca M, Caceres V, Nagai T, Yokoe K, Imai T, Miyakawa K, Yamashina T, Arrais S, Vasconez F, Pinajota E, Cisneros C, Ramos C, Paredes M, Gomezjurado L, Garcia-Aristizabal A, Molina I, Ramon P, Segovia M, Palacios P, Troncoso L, Alvarado A, Aguilar J, Pozo J, Enriquez W, Mothes P, Hall M, Inoue I, Nakano M, Inoue H (2007) Enhancing volcano-monitoring capabilities in Ecuador. Eos Trans AGU 88 (23):245

Le Pennec JL, Jaya D, Samaniego P, Ramón P, Moreno Yánez S, Egred J, van der Plicht J (2008) The AD 1300–1700 eruptive periods at Tungurahua volcano, Ecuador, revealed by historical

narratives, stratigraphy and radiocarbon dating. J Volcanol Geotherm Res 176:70–81

McEwen AS, Malin MC (1989) Dynamics of Mount St. Helens' 1980 pyroclastic flows, rockslide-avalanche, lahars, and blast. J Volcanol Geotherm Res 37:205–231

Mothes PA and staff IG-EPN (2007) Tungurahua Volcano's 1999–2007 eruptive process, monitoring results and risk mitigation. AGU, Joint Assembly, Acapulco, Mexico

Neri A, Ongaro TO, Macedonio G, Gidaspow D (2003) Multiphase simulation of collapsing volcanic columns and pyroclastic flow. J Geophys Res 108(B4):2202. doi:10.1029/2001JB000508

Patra AK, Bauer AC, Nichita CC, Pitman EB, Sheridan MF, Bursik M, Rupp B, Webber A, Stinton AJ, Namikawa LM, Renschler CS (2005) Parallel adaptive numerical simulation of dry avalanches over natural terrain. J Volcanol Geotherm Res 139(1):1–22

Patra AK, Nichita CC, Bauer AC, Pitman EB, Bursik M, Sheridan MF (2006) Parallel adaptive discontinuous Galerkin approximation of the debris flow equations. Comput Geos 32:912–926

Pouliquen O, Forterre Y (2002) Friction law for dense granular flows: application to the motion of a mass down a rough inclined plane. J Fluid Mech 453:133–151

Pudasaini SP, Hutter K (2006) Avalanche dynamics: dynamics of rapid flows of dense granular avalanches. Springer, Berlin

Samaniego P, Yepes H, Arellano S, Palacios P, Mothes P, Le Pennec JL, Troncoso L, IG-EPN staff (2007) Monitoring a waxing and waning volcanic activity: the July 14th and August 16th 2006 eruptions of Tungurahua volcano (Ecuador). Cities on Volcanoes 5, Shimabara, Japan

Saucedo R, Macias JL, Sheridan MF, Bursik MI, Komorowski JC (2005) Modeling of pyroclastic flows of Colima Volcano, Mexico: implications for hazard assessment. J Volcanol Geotherm Res 139:103–115

Savage SB, Hutter K (1989) The motion of a finite mass of granular material down a rough incline. J Fluid Mech 199:177–215

Savage SB, Hutter K (1991) The dynamics of avalanches of granular materials from initiation to runout. Part I: analysis. Acta Mech 86:201–223

Sheridan MF (1979) Emplacement of pyroclastic flows: a review. Sp Paper Geol Soc Amer 180:125–136

Sparks RSJ (1976) Grain size variations in ignimbrites and implications for the transport of pyroclastic flows. Sedimentology 23:147–188

Wadge G, Jackson P, Bower SM, Woods AW, Calder E (1998) Computer simulations of pyroclastic flows from dome collapse. Geophys Res Lett 25(19):3677–3680

Yamamoto T, Takarada S, Suto S (1993) Pyroclastic flows from the 1991 eruption of Unzen volcano, Japan. Bull Volcanol 55:166–175

Pyroclastic density currents

O. Roche[1], J.C. Phillips[2], K. Kelfoun[1]

[1] Laboratoire Magmas et Volcans, Observatoire de Physique du Globe, UMR Université Blaise Pascal-CNRS-IRD, Clermont-Ferrand, France.
[2] Centre for Environmental and Geophysical Flows, Department of Earth Sciences, University of Bristol, UK.

Submitted to *Modeling Volcanic Processes (The Physics and Mathematics of Volcanism)*, edited by S.A. Fagents, T.K.P. Gregg, and R.M.C. Lopes. Cambridge University Press.

List of Symbols

a_t, a	(transitional) column aspect ratio
a_0, a_1, a_2	numerical constants
c	particle concentration (M L^{-3})
c_0	initial particle concentration (M L^{-3})
c_1, c_2, c_3, c_4	empirical constants
C	constant stress (M L^{-1} T^{-2})
d	particle diameter (L)
F	force (M L^{1} T^{-2})
Fr_0, Fr	(initial) Froude number
g	acceleration of gravity (L T^{-2})
g', g'', g'_p	reduced gravity (L T^{-2})
h_c , h_f	current, flow height (L)
h_i	initial column height (L)
H	ambient medium height (L)
I	inertial number
k	permeability (L^2)
L	current length (L)
L_r	run-out current length (L)
m	mass (M)
P	pressure (M L^{-1} T^{-2})
P_n	normal stress (M L^{-1} T^{-2})
Q	finite 2D volume release (L^2)
Q_0	2D volume of current head (L^2)
Sa	Savage number
t	time (T)
t_c	gravity current duration (T)
t_{fall}	column free fall timescale (T)
u_s	particle settling velocity (L T^{-1})
U	local velocity (L T^{-1})
U_{de}	deaeration rate (L T^{-1})
U_c , U_f	front current, flow velocity (L T^{-1})
U_g	superficial gas velocity (L T^{-1})
U_{mf}	minimum fluidisation velocity (L T^{-1})
U_{mb}	minimum bubbling velocity (L T^{-1})
V_0	initial 2D current volume (L^2)
x	position from source (L)
x_f	flow run-out (L)
x_i	initial column length or radius (L)

α	entrainment constant
β	empirical constant
ΔP	pressure gradient (M L^{-1} T^{-2})
ε	bed porosity
ε_{mf}	bed porosity at U_{mf}
ϕ	friction angle (degree)
ϕ_r	angle of repose (degree)
γ	shear rate (T^{-1})
φ	current head/tail ratio
η	viscosity (M L^{-1} T^{-1})
η_g	gas dynamic viscosity (M L^{-1} T^{-1})
μ	interparticle friction coefficient
$\mu_{(I)}$	macroscopic friction coefficient
μ_1, μ_2	constant friction coefficients
ν_s	particle volume fraction
$\nu_{s,max}$	maximum particle volume fraction
ρ	local density (M L^{-3})
ρ_c	current density (M L^{-3})
ρ_p	particle density (M L^{-3})
ρ_f	interstitial fluid density (M L^{-3})
ρ_g	gas density (M L^{-3})
ρ_{ref}	reference density (M L^{-3})
ρ_0	ambient density (M L^{-3})
τ	shear stress (M L^{-1} T^{-2})
ξ	Voellmy coefficient

1. Characteristics of Pyroclastic Density Currents

Pyroclastic density currents (PDC) are common features of explosive volcanic eruptions. They are generated from the gravitational collapse of lava domes or eruptive columns, or by lateral explosions in case of hydromagmatic activity or sudden decompression of a magma body (Fig. 1). PDC are gravity-driven, gas-particle mixtures within which the interstitial fluid may control the flow dynamics. The pyroclasts result from magma fragmentation and their granulometry commonly ranges from micron-sized ashes to centimetre-sized lapilli and blocks. PDC have typical volumes of 10^6-10^8 m^3, and are highly mobile as they commonly travel on gentle slopes over distances of several kilometres, at speeds of up to approximately 50 m s^{-1}.

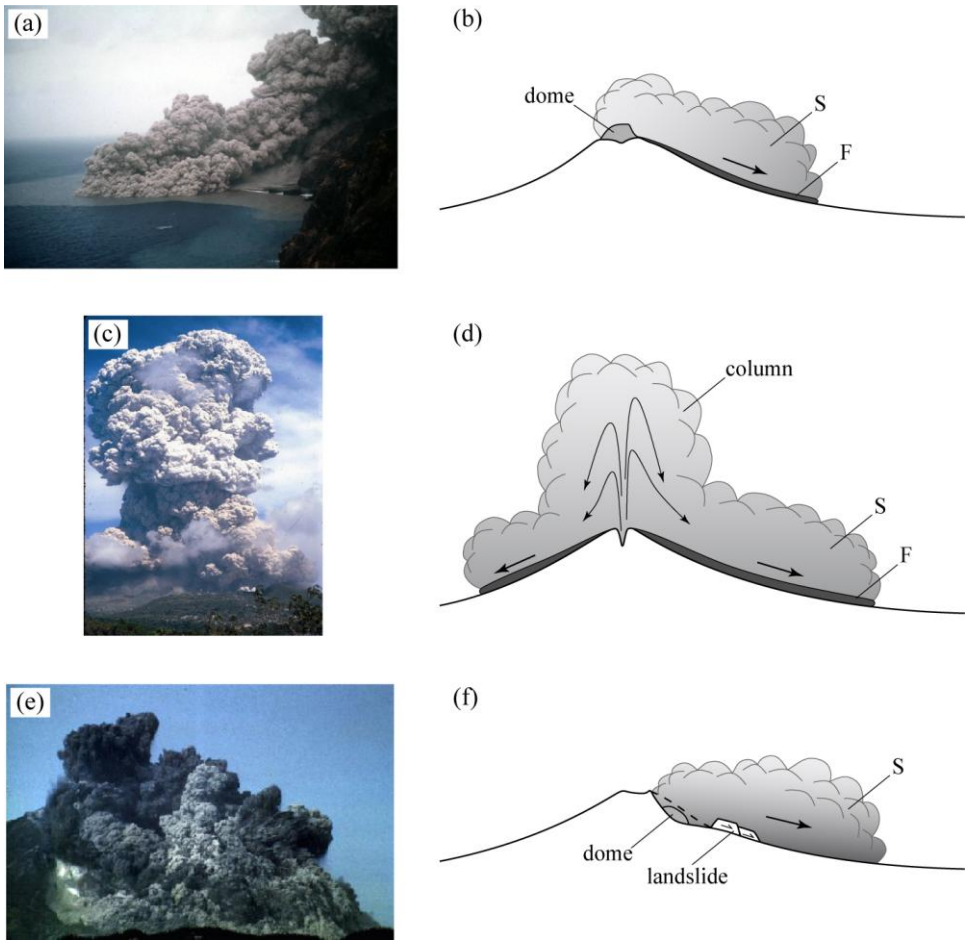

Figure 1. Photographs and schematic diagrams of PDC, generated by various mechanisms. The parts of the flow that are termed *dilute surge* and *dense flow* are labelled *S* and *F*, respectively. (a) Lava dome collapse, Montserrat, 1997 (courtesy of R.S.J. Sparks), and (b) schematic diagram of gravitational or explosive lava dome collapse; (c) Collapse of a Vulcanian eruption column, Montserrat, 1997 (courtesy of A.B. Clarke), and (d) schematic diagram of gravitational collapse of discrete or continuous eruptive column; (e) Lateral explosion, Mt. St. Helens, 18th May 1980 (courtesy of U.S.G.S), and (f) schematic diagram of lateral explosion caused by decompression of a cryptodome following landslide.

As direct observations of PDC are very difficult and rare, their properties are inferred mainly from field analyses of their deposits, and extensive reviews are presented by Cas and Wright (1987), Druitt (1998) and Branney and Kokelaar (2002). PDC can contain a range of particle concentrations, the end-member currents being termed *dilute surges* and *dense flows*, and a single eruption may produce PDC which can range as a continuum between these end-members (Druitt 1992). Most dilute surges are thought to be turbulent suspensions with low solid concentration that increases downwards

through the flow depth, with negligible particle interactions except at their base. they are weakly topographically controlled as they are tens to hundreds of metres thick (Fisher 1966, Wohletz and Sheridan 1979). On the other hand, dense flows (*e.g,*. pumice-and-ash, block-and-ash, and scoria flows) with particle concentrations close to that of their deposits are a few meters thick, topographically-controlled and pond into depressions, and are often associated with an overriding ash-cloud surge that may generate secondary flows as it sediments (Druitt et al. 2002). Two conceptual models for PDC deposition mechanisms represent likely end-members of a range of processes: *en masse* deposition in which the current freezes through its entire height (Sparks 1976, Wilson 1986) and *progressive aggradation* in which the deposit builds up by accumulation of material (Branney and Kokelaar 1992).

In the context of volcanic hazard assessment and mitigation, predictive theoretical models require improved understanding of the complex physics of PDC, and experimental laboratory investigations can help to gain fundamental insights. In this chapter, we first describe the basic physics of buoyancy-driven motion of particle suspensions, and introduce simplified equations of motion for these flows. We then highlight important insights that have been obtained from laboratory experiments on the gravitational collapse of dense fluid suspensions, initially-fluidised particles, and granular columns, emphasizing the distinct effect on the frictional resistance to motion of these different initial states. We then describe numerical methods for solving the equations of motion relevant to emplacement following gravitational collapse, with particular focus on how to combine these dynamical models with complex natural topography for volcanic hazard prediction. Finally we identify current and future research questions.

2. Fundamental Physics of Gravity Currents

2.1 Generalities

Pyroclastic density currents are an example of a predominantly-horizontal, buoyancy-driven flow, more generally known as a *gravity current*. Gravity currents result whenever fluid of one density flows horizontally into a fluid of a different density, and are frequent occurrences in the natural world. Dust storm and sea breeze fronts, thunderstorm and estuarine outflows, deep ocean turbidity flows and PDC are just a few examples (Simpson 1997). In these cases, the contrast in density between the two fluids can arise from compositional or thermal differences between the fluids, or the presence of suspended particles of a different density. The dynamics of gravity currents also depend strongly on whether the fluid that forms the current arises from release of a finite volume or occurs continuously from a sustained source. An important paradigm for gravity current initiation is the gravitational collapse of a column of dense fluid or particles (Figs. 1c, 1d, and 2), and recent experimental studies have lead to the recognition that the dynamics of the collapse of a column of particles in air shares many common features with the fluid case (Lube et al. 2004, Roche et al. 2004, Balmforth and Kerswell 2005, Lajeunesse et al. 2005, Roche et al. 2005, Huppert 2006).

The dynamics of gravity currents is now generally well understood for a wide range of conditions and have been summarised in reviews by Simpson (1982) and Huppert (2006), and in the definitive textbook by Simpson (1997). In this section, we introduce the fundamental dynamics of gravity currents, focussing in particular on the underlying physics and dynamical aspects that are relevant to pyroclastic density currents. We will start by considering the motion that develops between two fluids, which have a small and constant density contrast between them, using energy balances to develop scaling relationships and simple theoretical models for gravity current motion. These approaches will be extended to include the case relevant for pyroclastic density currents where the density contrast varies during the motion of the current, as a consequence of the sedimentation of suspended particles. We will also consider situations where the density contrast between the two fluids is large, including granular flows, where the role of the fluid phase is generally neglected.

Figure 2 shows a series of images of the collapse of a dense fluid and a particle column in a long thin tank. The motion following this collapse can generally be divided into three distinct regimes (Huppert and Simpson 1980, Simpson 1997, Huppert 2006). Initially, the flow dynamics are controlled by the release conditions and geometry. In the second regime, the flow dynamics are

primarily controlled by the balance of inertia and buoyancy forces, and in the final regime, the balance between buoyancy and resistance forces controls the stopping of the flow. In the case of fluid gravity currents with very high viscosity, such as lava flows, the second regime is not observed. Mass conservation in the collapsing flow requires that the depth of the flow decreases as its length increases (Fig. 2). In the case of fluid gravity currents, the stresses that resist motion arise from interactions at boundaries and from the increasing influence of viscous stresses as the current depth decreases. In the case of granular flow, the stresses that resist motion arise as a consequence of interactions between individual particles and the boundaries. PDC motion is characterised by large inertial forces and PDC typically propagate in a regime where inertia and buoyancy forces are in balance (see section 1). In many cases, the motion of PDC is approximately two-dimensional due to propagation on slopes (where the spreading of the current occurs predominantly in the downslope direction) or confining topography such as valleys (see section 1). We thus start to explore the dynamics of PDC by considering two-dimensional, inertially-dominated gravity currents.

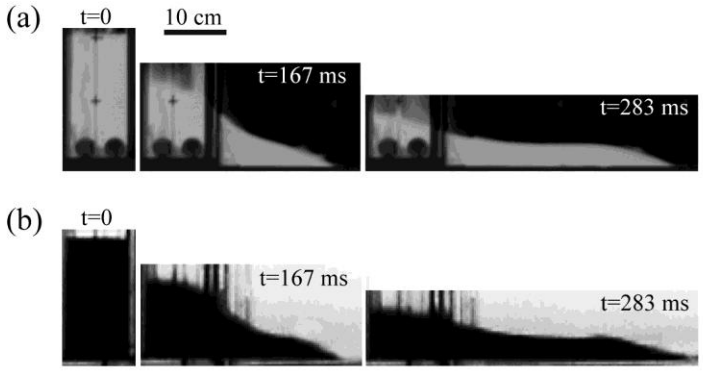

Figure 2. Photographs from laboratory experiments conducted in a horizontal narrow channel showing the collapse in ambient air of (a) an initially fluidised granular column and (b) a water column. Modified from Roche et al. (2005b and submitted).

2.2 Conservation of Momentum

The driving force for gravity current motion is the buoyancy force that acts as a consequence of the density contrast between the current and the surrounding fluid. An appropriate way to express the density difference is as the *reduced gravity*, *g'*, defined as

$$g' = g\frac{\rho_c - \rho_0}{\rho_{ref}} \quad , \qquad (1)$$

where g is the acceleration due to gravity, ρ_c is the bulk density of the current, ρ_0 is the (uniform) density of the surrounding fluid, and ρ_{ref} is a reference density. In the case where density of the current and the density of the surroundings, are not very different in magnitude, the density of the surroundings is the appropriate reference density (*e.g.*, Huppert and Simpson 1980) and we have

$$g' = g\frac{\rho_c - \rho_0}{\rho_0} \quad . \qquad (2)$$

The first theoretical study of gravity current motion by von Kármán (1940) and subsequent re-analysis by Benjamin (1968) consider the motion of a dense gravity current propagating under conditions in which inertia dominates, as shown in Fig. 2 and schematically in Fig. 3a. A current of dense fluid of density ρ_c is shown flowing along a horizontal boundary and displacing a fluid of lower density ρ_0. Due to the extra weight of the dense fluid, a larger hydrostatic pressure exists inside the current as compared to the fluid ahead, and this pressure difference provides the driving force for current motion. Applying conservation of energy at the current front leads to a relationship for the velocity of the front

of a current, U_c, followed by a layer of fluid of depth, h_c, of the form (von Kármán 1940, Benjamin 1968)

$$\frac{U_c}{(g'h_c)^{1/2}} = Fr\,, \qquad (3)$$

where Fr is the Froude number, the ratio of inertial to buoyancy forces. For a current flowing into deep surroundings (h_c<<H), the Froude number is a constant with a theoretical value of $\sqrt{2}$ (von Kármán 1940, Benjamin 1968) for the case of no energy dissipation between the fluid layers, compared with values of approximately 1.2 to 1.4 measured experimentally (Hoult 1972, Huppert and Simpson 1980). In Eq. 3, all resistances to flow propagation such as resistance to flow at the lower boundary, dissipation within the current and dissipation against the surrounding fluid are parameterized in the value of the Froude number. Recent numerical studies have investigated the form of these resistances, and if the flow is depth-averaged so all resistance is considered to operate at the lower boundary, an inertial form is found to best describe experimental data (Hogg and Pritchard 2004). Dimensional considerations also lead inevitably to Eq. 3, as U_c, g' and h_c are the only variables in this problem, so the ratio $U_c/(g'h_c)^{1/2}$ has to be constant when the flow is controlled by a balance between inertia and buoyancy, as pointed out by Huppert (2006). In the case where the depth of the current is comparable to the depth of the surrounding fluid, the Froude number becomes a function of the ratio h_c/H, found from experiments to have the form

$$Fr = \frac{1}{2}\left(\frac{h_c}{H}\right)^{1/3} \text{ for } 0.075 \le \frac{h_c}{H} < 1\,, \qquad (4)$$

(Simpson and Britter 1979, Huppert and Simpson 1980). Equation 3 is a simplified form of conservation of momentum and has been widely used in studies of inertially-controlled gravity currents and suggests that the motion of these gravity currents is controlled at the front. An important consequence is that the dynamics of inertial gravity currents is independent of the slope of the underlying topography up to angles of about 30° (Turner 1979), typical of the conditions for PDC. It is important to note, however, that Eq. 3 is insufficient to specify the current dynamics as it is a single relationship between an unknown velocity and an unknown depth (Huppert and Simpson 1980, Huppert 2006).

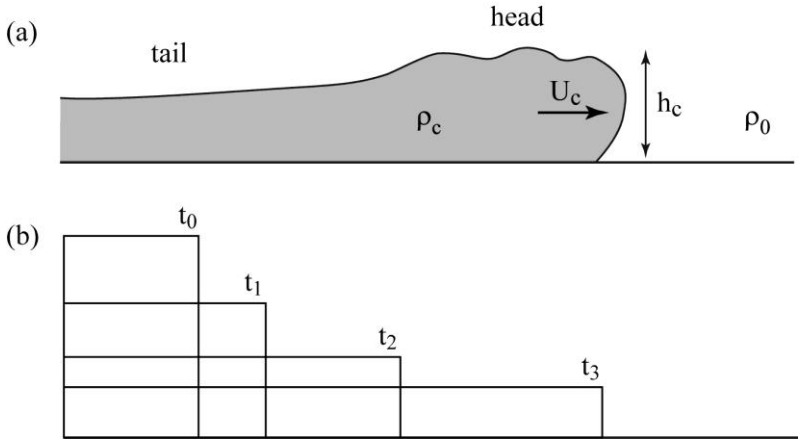

Figure 3. (a) schematic diagram of an inertial gravity current defining densities (ρ_c~ρ_0) and depths, with horizontal arrow for front direction and velocity U_c, and (b) schematic diagram of mass conservation in a box model at times t_0 to t_3.

2.3 Conservation of Mass

A second relationship between gravity current depth and velocity can be derived from a consideration of mass conservation for the current fluid. For a two-dimensional current, the shape of the spreading current can be approximated as a series of equal area (volume in two dimensions) rectangles, as first proposed by Huppert and Simpson (1980). This approach is illustrated schematically in Fig. 3b and is a simplification to the detailed collapse dynamics illustrated in Fig. 2. We can write the relationship for mass conservation for the current fluid as

$$h_c L \approx Q_0 t_c^{\lambda}, \qquad (5)$$

where L is the length of the current, t_c is the duration of fluid release, so $\lambda = 0$ corresponds to the case of a release of finite volume Q_0, and $\lambda = 1$ corresponds to the case of a constant volume flux release. Equations 3-5 can be combined to form a simplified *box model* for gravity current motion, so-called because of the approximation of mass conservation as equal area rectangles (Huppert and Simpson 1980). Since $U_c = dL/dt$, we can eliminate the current depth h_c between Eqs. 3 and 5 and integrate to find

$$L = \left(\frac{7}{12}\right)^{6/7} \left(\frac{6}{6+\lambda}\right)^{6/7} (g'^3 Q_0 H^2)^{1/7} t^{\frac{\lambda+6}{7}}, \qquad (6)$$

in the region of initial collapse (where the current depth can be comparable to that of the surroundings), and

$$L = \left(\frac{3}{2}\right)^{2/3} \left(\frac{2}{\lambda+2}\right)^{2/3} Fr^{2/3} (g' Q_0)^{1/3} t^{\frac{\lambda+2}{3}} \qquad (7)$$

for subsequent motion where inertia and buoyancy are in balance. For the special case of motion in deep surrounding fluid following a finite volume release, the propagation of a gravity current with constant density can be written,

$$L \approx 1.47 (g' Q_0)^{1/3} t^{2/3}. \qquad (8)$$

2.4 Gravity Currents with Particles

In many natural situations, including PDC, the density difference between gravity currents and the surrounding fluid depends on the concentration of suspended dense particles within the current. In this case, the bulk density of the current fluid will vary in time if particles are sedimented at the current base. The framework of box models (or more sophisticated formulations of the conservation equations) can be extended *in the case of relatively low particle concentrations* to consider the case of varying current density by addition of a particle settling law (*e.g.*, Bonnecaze et al. 1993, Dade and Huppert 1995, Harris et al. 2002). The most common approach is to assume that the turbulent velocity scale within the current is sufficiently high to maintain a uniform concentration particle suspension. However, at the base of the flow, where the current fluid interacts with the underlying static boundary, the velocities in the current decrease below that of the settling speed of the particles, and sedimentation can occur. This leads to a particle settling law, sometimes known as *Hazen's Law*, and experimentally verified by Martin and Nokes (1988), of the form

$$c = c_0 \exp\left(-\frac{u_s t}{h_c}\right), \qquad (9)$$

where c is the volume concentration of particles suspended in the current with initial value c_0, and u_s is the settling velocity of the particles. To complete the model, one further relationship is required to describe the change in current density with particle concentration, and in the case where the excess density in the current only arises from the presence of the particles (the density of the current fluid is equal to the density of the surrounding fluid), we can write

$$g' = \frac{g(\rho_p - \rho_0)c}{\rho_0} = g'_p\, c\,, \qquad (10)$$

where ρ_p is the particle density. The solution for the system of equations (3), (5), (9) and (10) for a finite volume release can be written as

$$L^{\frac{5}{2}} = \frac{5Fr(g'_p\, c_0 Q_0^3)^{\frac{1}{2}}}{u_s}\left(1 - \left(\frac{c}{c_0}\right)^{\frac{1}{2}}\right) \qquad (11)$$

(Bonnecaze et al. 1993). If the excess density only arises from the presence of dense particles, the flow comes to a stop when $c = 0$, so the *runout length*, L_r can be found as

$$L_r = \left(\frac{5Fr(g'_p\, c_0 Q_0^3)^{\frac{1}{2}}}{u_s}\right)^{\frac{2}{5}}. \qquad (12)$$

The particle settling speed, u_s, will vary with particle size, so equations of the form of (11) and (12) are applicable to flows containing a single particle size, whose settling velocity can be found from standard settling laws such as Stokes' Law (*e.g.*, Dade and Huppert 1995). Extensions to polydispersed particle suspensions have been recently proposed by Harris et al. (2002).

An axisymmetric formulation of the box model for a particle-driven gravity current (Eqs. 3, 5, 9 and 10) has been applied to investigate the emplacement of the 1800 B.P. Taupo ignimbrite (Dade and Huppert 1996). The distribution of particle sizes in the ignimbrite is described in the model using a probability density function for particle settling speed, and the model is fitted to the proximal deposit thickness in order to set the value of the input volume flux. Based on this initial calibration, the model shows good agreement with measurements of the deposit thickness, concentration of different particle sizes in the deposit, and concentration of particles of given size fractions from the source to a distance of nearly 80 km where the ignimbrite deposit reaches the coast. The flow conditions corresponding to these model predictions were a total volumetric flux of 40 $km^3\ s^{-1}$ for approximately 15 minutes, and the flow had a depth of about 1 km, a temperature of 450 ^oC and a typical speed of 200 $m\ s^{-1}$ (Dade and Huppert 1996). The good agreement of the model predictions with field observations (Wilson 1985) lead Dade and Huppert (1996) to suggest that large-volume ignimbrites could be emplaced by relatively dilute gravity currents, and models with similar formulation were used to investigate the interaction of PDC with topography (*e.g.*, Woods et al. 1998). There is now a developing consensus that PDC comprise a dense basal layer moving as a granular flow with an overlying dilute particle suspension (*e.g.*, Druitt et al., 2002, Huppert 2006), and more complex two-layer models are emerging (Ishimine 2006, Doyle et al. 2008).

With recent advances in computing power, numerical solutions of the complete governing equations can be used as the basis for models for gravity-driven flows, as described in section 5. It is worth noting here that the two-dimensional equations for momentum and mass conservation presented in this section (Eqs. 3 and 5) can be obtained directly from the vector forms of the conservation equations for mass and momentum presented in section 5 (Eqs. 33 and 34) when the flow internal stresses and boundary resistance are empirically approximated as a Froude number and the current is

sufficiently shallow so that the pressure within the flow can be assumed to be hydrostatic. One advantage of using simplified formulations to describe the dynamics of gravity currents is that these can be tested using laboratory experiments, as described in the next section.

3. Experimental Studies of Fluid Gravity Currents

3.1 Lock-Exchange Experiments

Much of the basic physics of inertial gravity current motion described in the previous section has been verified using laboratory experiments (see reviews by Simpson 1982 and Huppert 2006). The most widely-used configuration is a lock-exchange experiment, in which the more dense fluid is released into an adjacent lower density fluid (often of the same depth) by removal of a rigid gate placed between them. The more dense fluid collapses to the base of the tank, and propagates as a gravity current along a rigid boundary (Fig. 2). Typically the volume of the tank on one side of the gate (the *lock*) is smaller than the other side, so this configuration can be used to investigate the spreading of a gravity current into a larger ambient fluid. Two-dimensional flows have been investigated in channels (Simpson 1982, Huppert and Simpson 1980) whereas axisymmetric flows have been investigated in circular tanks (Huppert 2006).

Early lock-exchange experiments in channels (summarised in Simpson 1982) investigated the morphology of inertial gravity currents when the density of the current is close to that of the ambient, particularly at the flow front. The characteristic morphology is shown in Fig. 3a, with a well-defined flow front (often referred to as the *head*) of greater depth than the following gravity current fluid (the *tail*), and turbulent billows which result from fluid instability due to counterflowing motion of the dense and light fluid (Kelvin-Helmholtz instability). By studying the motion of a dense inertial gravity current in a counterflowing lighter fluid using a recirculating water channel, Simpson and Britter (1979) measured the speed of the main body of the flow, and found it to be about 15% greater than the flow at the gravity current front, which suggests that current fluid must be exchanged between these parts of the flow during motion. The propagation of a gravity current initiated in a lock-exchange experiment shows distinctive flow regimes, characterized by different time dependence of the flow velocity (*cf.*, Eqs. 6-8). The initial collapse of dense fluid, or *slumping phase* was investigated by Huppert and Simpson (1980) who found that the Froude number at the flow front was proportional to the fractional depth of the dense fluid in the channel, as summarized by Eq. 4 above. The velocity of the flow in the slumping phase was observed to be constant, and this has been interpreted as resulting from the counterflow of light fluid into the lock region at the channel top required by mass conservation as the slumping dense fluid propagates along the channel base (Huppert and Simpson 1980). The transition from the constant velocity regime to the regime where inertia and buoyancy forces are assumed to be in balance takes place when the reflection of the initial counterflow reaches the flow front (Rottman and Simpson 1983), typically at a distance of about 10 times the horizontal length of the lock region. Recent experiments have considered the initial condition where the total depths of fluid on each side of the lock gate are equal, but where the depth of the dense fluid layer in the lock is some fraction of the depth of the lock, and is overlain by the same fluid as in the main body of the tank (Gladstone et al. 2004). In this case, the stratification of buoyancy in the lock leads to streamwise stratification of the resulting flow, and the stratified currents are observed to propagate initially faster, then more slowly, than their unstratified counterparts. In the inertia-buoyancy regime, the gravity current propagation takes the form of Eq. 8 for a fixed volume release Q_0, and motion in the surrounding fluid plays a negligible role. Finally, as the gravity current energy is dissipated by displacing the surrounding fluid and by frictional interaction with the underlying surface, viscous dissipation becomes important and the current enters a flow regime where viscous and buoyancy forces are in balance (Huppert and Simpson 1980).

3.2 Particle-Laden Gravity Currents

Particle-driven gravity currents have also been widely studied using lock-exchange experiments. Bonnecaze et al. (1993) compared the predictions from a box model of the form developed above with experimental measurements of the areal density of the deposit from a sedimenting particle current containing approximately monodispersed spherical particles. They found good agreement for the observed current dynamics and the distribution of deposit areal density with distance from the lock. This model has also been used to investigate the dynamics and deposition patterns of laboratory gravity currents in which the interstitial fluid is less dense than the fluid into which the current is propagating (Sparks et al. 1993). The dynamics and sedimentation from particle-driven currents becomes much more complex when the current contains a range of particle sizes. Gladstone et al. (1998) conducted lock-exchange experiments using bidispersed and polydispersed particle mixtures and found in particular that the effects of mixing different proportions of fine and coarse particles is strongly non-linear. Adding a small amount of fine particles to a current containing coarse particles has a much larger influence on flow velocity and sedimentation patterns than adding a small amount of coarse particles to a current containing fine particles. Measurements of deposit areal density are not well reproduced by box models for bidispersed and polydispersed particle distributions (Dade and Huppert 1995, Bonnecaze et al. 1996). Particle concentration also influences gravity current dynamics and deposition (Choux and Druitt 2002). Lock-exchange gravity currents containing bidisperse mixtures of dense and light particles with sizes chosen so as to be in hydrodynamic equivalence produce deposits that show normal grading of the dense particles, but the light particle deposition depends strongly on the total particle concentration. The light particles are deposited in hydrodynamic equivalence in dilute flows, but are segregated efficiently in concentrated suspensions (up to 23% by volume, Choux and Druitt 2002). The dynamics of gravity currents composed of high concentration suspensions (up to 40% volume) show an abrupt transition in deposition pattern with distance from their source (Hallworth and Huppert, 1998), which is very different from the deposition profile of a lower concentration current (*e.g.*, Bonnecaze et al. 1993). Above a critical concentration of particles, the gravity currents stop abruptly and deposit the bulk of their sediment load as a relatively thick layer of constant thickness, and a much thinner layer of sediment is deposited from the residual low concentration cloud.

3.3 Mixing Processes

Experiments have also been used to investigate more complex phenomenology of gravity current flow in order to develop simplified formulations to include in theoretical models. An important process relevant to PDC not yet considered is the mixing of inertial gravity currents with the surrounding fluid. The motion of turbulent billows along the upper surface of an inertial gravity current which contains a low or zero concentration of particles (Fig. 3a) leads to incorporation of the surrounding fluid into the gravity current, or *entrainment*. Quantifying this process is important for PDC as dilution of a dense current by lighter ambient fluid reduces the density contrast and hence the flow velocity and run-out. Entrainment of fluid into a turbulent flow is difficult to calculate directly, because the flow structure is three-dimensional and time-dependent, but can be measured in experiments. Hallworth et al. (1993, 1996) conducted experiments in which an alkaline inertial fluid gravity current was released into a two-dimensional channel containing an acidic ambient fluid, with the neutralization visualized using universal indicator in the current. Different initial concentrations of alkali in the current result in neutralization at different distances from the source, so the proportion of current and entrained fluid can be determined with distance from the source. Entrainment is observed to take place primarily into the head of the gravity current, and predominantly in the inertia-buoyancy regime. If the proportion of entrained fluid is defined as the ratio of the volume of entrained fluid to the total volume of the current (*i.e.*, dimensionless), then dimensional considerations suggest that the proportion of entrained fluid depends only on the initial volume of the current and distance from the source, and is independent of the reduced gravity because it is the only quantity with dimensions of time (Hallworth et al. 1993). This result is confirmed in systematic experiments, and leads to a simplified description of entrainment by considering conservation of mass of the fluid in the gravity current head,

$$\frac{dQ}{dx} = \alpha Q^{1/2} - \varphi Q^{1/2}, \qquad (13)$$

with

$$Q(0) = V_0, \qquad (14)$$

where Q is the volume of the current head (area in a two-dimensional current) and V_0 is the initial volume of the current, x is the distance from the current source, α is an *entrainment constant* that describes the amount of entrainment into the current head, and φ is a constant representative of the ratio of the height of the tail to the height of the head (Hallworth et al. 1993). The dependence on $Q^{1/2}$ indicates that the spatial rate of change of volume is proportional to the height of the head. The solution to this equation is

$$\frac{Q}{V_0} = \left(1 - \frac{1}{2}\frac{(\varphi - \varepsilon)x}{V_0^{1/2}}\right)^2, \qquad (15)$$

with the best fit to experimental data suggesting values α=0.078 and φ=0.147 (±3%). Application of this simplified result to the collapse of large volumes of particle-laden fluid that form deep ocean turbidity currents (Hallworth et al. 1993) suggests that dilution of the flow can be significant (particle concentrations reducing from 40% vol. to about 8% vol. within the first quarter of the total run-out distance), and that entrainment provides an efficient mechanism for reducing the particle concentration and buoyancy of PDC. Furthermore, efficient mixing of fluid within the front of inertial gravity currents (Hallworth et al. 1993), and between the front and the following fluid (Simpson and Britter 1979) suggests that dilution will be an important effect throughout the depth and length of PDC.

4. Dynamics of Granular Flows

4.1. Fundamental Physics of Granular Flows

This section describes key differences between the dynamics and rheology of dense granular currents propagating in air, hereafter called *granular flows,* and fluid gravity currents. Granular flows most resemble the dense end-member of PDC, and are characterized by a particle volume fraction ν_s close to $\nu_{s,max}$ at loose packing, so that g''~g. We will focus on end-member regimes of granular flow: *dry granular* and *gas-particle* flows, with negligible and dominant role of the interstitial fluid phase, respectively.

Extensive reviews reveal the phenomenology and complexity of flowing granular matter (Jaeger et al. 1996, Goldhirsch 2003, GDR MiDi 2004, Campbell 2006, Forterre and Pouliquen 2008). In *dry* media, energy dissipation is caused mainly by particle interactions, and flow dynamics depend on the Savage number (*Sa*), which represents the ratio of inertial shear stresses resulting from particle collisions to quasi-static gravitational stresses associated with friction (Savage 1984). If the solid friction angle (ϕ), overburden load, and hydrostatic buoyancy are taken into account, a modified form of the original Savage's (1984) equation is

$$Sa = \frac{\rho_p \gamma^2 d^2}{(\rho_p - \rho_f) g h_f \tan\phi} \qquad (16)$$

(Iverson 1997), where ρ_p and ρ_f are the particles and interstitial fluid density, respectively, γ is the shear rate, d is the particle diameter, and h_f the height of the flow. Inter-particle collisions dominate at $\nu_s << \nu_{s,max}$ and/or high shear rate (Sa>0.1), whereas frictional stresses govern the current dynamics at

$\nu_s \sim \nu_{s,max}$ and/or low shear rate (Sa<0.1) (Savage and Hutter 1989). The frictional, dense flow regime is achieved on rough substrates with inclination close to the angle of repose of the material ($\sim\phi_r$), and steady motion results from balance between driving gravitational and resisting frictional forces. The granular mass is commonly treated as a Coulomb material with constant, rate-independent interparticle friction coefficient (μ) and angle (ϕ), so that

$$\mu = \tan\phi = \frac{\tau}{P_n}, \qquad (17)$$

where τ and P_n are the shear and normal stress respectively. However, under steady flow conditions, the macroscopic friction coefficient depends on a dimensionless parameter called the inertial number, which is the square root of the savage number,

$$I = \frac{\gamma d}{\sqrt{P_n / \rho_p}}, \qquad (18)$$

so that

$$\mu_{(I)} = \mu_1 + \frac{\mu_2 - \mu_1}{I_0 / I + 1}, \qquad (19)$$

where typical values for glass beads are μ_1=tan21°, μ_2=tan33°, and I_0=0.3 (Forterre and Pouliquen 2008).

Segregation according to particle size and density is a fundamental process in polydisperse lows containing particles of different sizes as it may change their dynamics. Kinematic (dynamic) sieving is common and occurs when smaller particles fall into gaps beneath them and percolate downwards as force imbalances squeeze the large particles upwards, leading to reverse grading (Makse et al. 1997). In contrast, normal segregation may occur if large and dense particles can displace particles beneath them and move downwards under gravity, and this acts in opposition to dynamic sieving (Thomas 2000).

Gas-particle flows have been less comprehensively studied than their *dry* counterparts. Interactions between the two phases are likely to reduce particle interactions and to modify momentum transfer. For instance, granular flows that are continuously fluidised down inclines can propagate at slope angles below ϕ_r, and possibly on slopes close to horizontal, because of extreme friction reduction (Ishida et al. 1980, Eames and Gilbertson 2000).

4.2 Experiments on Dry Granular Media

4.2.1 Particle Interactions in Steady Flow

Particle interactions in *dry*, coarse grained PDC can be investigated in shear-cell experiments (Cagnoli and Manga 2004, 2005). For a typical configuration, in which beds of pumice fragments are confined between two vertical and coaxial cyclinders that rest on a rough horizontal rotating disk, energy dissipation occurs within a basal collisional layer at Sa up to ~0.4 (see also Cagnoli and Manga 2003 for the collisional regime). The upper layer acts as a rigid raft but moves relative to the cylinders at a constant velocity, which is independent of the imposed shear rate, and this is interpreted as a frictional Coulomb behaviour. In this layer, reverse segregation of coarse light clasts and normal segregation of coarse dense clasts occurs because of expansion of the matrix and the difference in inertia between the coarse and fine components when these are pushed upwards by collisions originated at the basal layer.

Levées are common features of deposits of coarse-grained PDC and are reproduced in experiments investigating steady finger-shaped flows down rough inclines (Figs. 4a-b, Félix and Thomas 2004). Levées form at the lateral static borders at the rear of the flow front, and result from

emptying of the central channel once source flux has decreased to zero and the flow is no longer steady. Static borders form because downslope gravitational forces are lower than frictional resistance at the flow margins because friction is depth-dependent (Eq. 18, 19), which shows that polydispersity is not necessary for levée formation (Mangeney et al. 2007). The flow dynamics can be inferred from the deposit morphology according to Pouliquen's (1999) method, so that

$$\frac{U_f}{\sqrt{g h_{levée}}} = \beta \frac{h_{levée}}{h_{channel}}, \qquad (20)$$

where U_f is the flow front velocity and β is an empirical constant equal to 0.5 (Félix and Thomas 2004). Although values of substratum inclination and deposit heights cannot be extrapolated directly to natural cases, these studies provide important insights into the dynamics of coarse grained PDC.

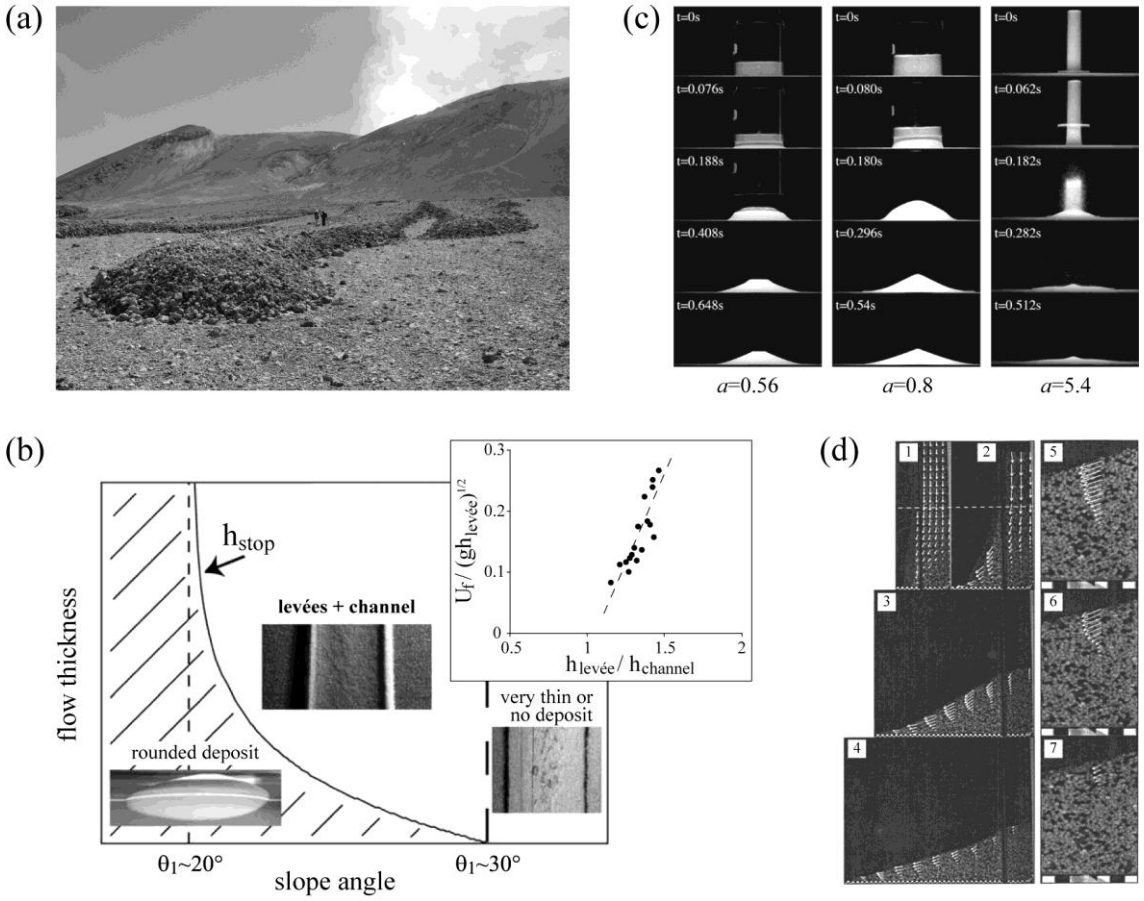

Figure 4. (a) Pumice flow deposits with levées-channel morphology, Lascar volcano, Chile. Persons for scale (photo by O. Roche). (b) Deposit types reported on a h_{stop} diagram (*i.e.*, Pouliquen 1999) in steady-state experiments. Insert: correlation between normalized flow velocity and thicknesses (*cf.*, Eq. 20, with β~0.5); in Félix and Thomas (2004), modified. (c) 3D granular flows generated from the release of a cylindrical reservoir of aspect ratio *a* as a function of time; in Lajeunesse et al. (2004). (d), (1-4) Evolution of the velocity profile with time at *a*=7, and (5-7) detailed view for the same experiment at a distance of one third the flow run-out; in Lube et al. (2005).

4.2.2 Flow Kinematics and Run-out in Unsteady Flow

Recent experimental studies have investigated the unsteady flows that result from the collapse of an initially-static column of granular material, by analogy to lock-exchange gravity currents (Section 3, and Figs. 4c-d). The kinematics and run-out distance of monodisperse flows on a horizontal surface are controlled by the initial aspect ratio of the granular column

$$a = \frac{h_i}{x_i}, \qquad (21)$$

where h_i is the initial height and x_i is the initial length (in two-dimensions) or radius (in three-dimensions) of the column (Lajeunesse et al. 2004 and 2005, Lube et al. 2004 and 2005, Balmforth and Kerswell 2005). Flank avalanches or spreading of the column generate a (truncated) conical deposit at $a<a_t$, where a_t is a critical aspect ratio ~1.7-3, whereas outward propagation of the base of the pile at $a>a_t$ triggers collapse of the upper portion with almost no deformation and this creates a low angle conical deposit. Particles initially at the surface of the pile stay at superficial levels or are incorporated into a thin basal layer when overrun by the front (Lube et al. 2004). This layer is delimited by a dynamical interface that separates deposited and flowing particles, and that propagates towards the upper free surface during emplacement (Lube et al. 2007). The velocity profile within the flowing layer consists of an upper low shear plug-like zone, a middle linear gradient region, and a lower exponentially-decreasing region, resembling that in steady flows down inclines (Savage and Hutter 1989), and contrasting with that in shear-cell experiments (Cagnoli and Manga 2004).

Kinematics are controlled by the timescale of free fall of the column (Lajeunesse et al. 2005),

$$t_{fall} \approx \left(\frac{h_i}{g}\right)^{1/2}. \qquad (22)$$

Flows propagate in three stages, during ~3-3.5t_{fall} in Lajeunesse et al. (2005) experiments. Their front accelerate after release and then propagate at nearly constant velocity provided $a>a_t$, and these two regimes are similar to those observed in fluid gravity currents (see section 2). The flows finally enter a short stopping phase as they quickly decelerate until motion ceases. There is clear power law dependence of the flow run-out (x_f) on a, as

$$(x_f - x_i)/x_i \sim c_1 a \quad (a<a_t), \qquad (23)$$

$$(x_f - x_i)/x_i \sim c_2 a^{2/3} \quad (a>a_t), \qquad (24)$$

in 2D experiments, and as

$$(x_f - x_i)/x_i \sim c_3 a \quad (a<a_t), \qquad (25)$$

$$(x_f - x_i)/x_i \sim c_4 a^{1/2} \quad (a>a_t). \qquad (26)$$

in 3D cases, where $c_{1\text{-}4}$ are constants. Lube et al. (2004) concluded that the analysis is independent of any basal and internal friction parameter and questioned the role of Coulomb friction for most the emplacement, until flows enter the stopping phase. In contrast, Balmforth and Kerswell (2005) showed that the flow run-out (*i.e.*, $c_{1\text{-}4}$) depends on the size and shape of the particles, which control the interparticle friction. It is interesting to note that an erodible substratum has no influence on the flow kinematics and run-out (Lajeunesse et al. 2004), and that a dynamical deposition interface (*c.f.*, *progressive aggradation*) and a sudden motion stop (*c.f.*, *en masse* deposition) are compatible. In nature, the polydispersivity of PDC may complicate the processes described above because granular collapse experiments using two particle sizes show that there is also a strong dependence of flow run-out on the proportion of fine and coarse particles in the flow (Phillips et al. 2006, Roche et al. 2006).

4.3 Gas-particle Flows

4.3.1 Characteristics of Gas-fluidised Pyroclastic Materials

Fluidisation can occur when a gas (or a liquid) ascends vertically through a granular bed (see Rhodes 1998 for review). The fluid exerts a drag force on the particles that increases with the superficial gas velocity (U_g) defined as the mean flow rate divided by the bed cross sectional area, and the weight of the bed can be increasingly supported. The pressure drop across the bed increases with U_g as described by the Ergun equation for a steady flow,

$$\frac{\Delta P}{h_i} = \frac{150(1-\varepsilon^2)\eta_g U_g}{\varepsilon^3 d^2} + \frac{1.75(1-\varepsilon)\rho_g {U_g}^2}{\varepsilon^3 d} \quad , \qquad (27)$$

where $\Delta P/h_i$ is the pressure drop across the bed of height h_i, ε the bed porosity, η_g the gas dynamic viscosity, ρ_g the gas density, and d the surface-volume particle diameter. In the right-hand part of Eq. 27, the first and second terms are the laminar and turbulent components respectively. *Fluidisation* (*s.s.*) occurs when the weight is counterbalanced, so that inter-particle friction is negligible, and fluidisation of fines-rich dense PDC may explain their high mobility. The weight of the particle bed is exactly balanced by the drag force at the minimum fluidisation velocity (U_{mf}) when

$$\frac{\Delta P}{h_i} = (1-\varepsilon_{mf})(\rho_p - \rho_g)\mathrm{g}\,, \qquad (28)$$

where ε_{mf} is the bed porosity at incipient fluidisation, ρ_p the particles density, and g is the gravitational constant. In most cases, U_{mf} can readily be found by equating Eq. 28 with the laminar term of the Ergun equation, so that

$$U_{mf} = \frac{k}{\eta_g}\frac{\Delta P}{h_i}\,, \qquad (29)$$

where

$$k = \frac{{\varepsilon_{mf}}^3 d^2}{150(1-\varepsilon_{mf})^2}\,, \qquad (30)$$

is the bed permeability. Homogeneous fluidisation is achieved in fine particles with grain size of a few tens to hundreds of microns, described as *group A* under the classification of Geldart (1973), and whose beds expand linearly at gas velocities above U_{mf} until gas bubbles form at the minimum bubbling velocity ($U_{mb}>U_{mf}$). On the other hand, fluidisation is heterogeneous in very fine/light powders of *group C* as interparticle cohesion promotes gas flow channelling and poor bed support, and in beds of coarse/dense *group B* or *group D* particles as gas bubbles form readily at U_{mf}. Once the gas supply is turned off, the top of homogeneously expanded beds of *group A* particles collapse at a constant velocity called the *deaeration rate* (U_{de}), and a sedimentation interface that migrates upwards separates basal sedimented particles and settling ones above.

Experimental studies of gas-fluidisation of static beds of pyroclastic materials provide insights into fluidisation processes of PDC. Wilson's (1980, 1984) seminal studies revealed that gas flow channelling readily occurs at room temperature due to cohesion (*i.e.*, *group C*) in fines-rich, poorly-sorted beds of ignimbrite. Later studies showed that high fines content, high temperature, and shear favour homogeneous fluidisation with efficient support (Gravina at al. 2004, Bareschino et al. 2007, Druitt et al. 2004 and 2007). High fines content strongly decreases U_{mf} and U_{de}, whereas temperature above ~200°C and shear inhibit gas flow channelling as the former eliminates moisture-derived

interparticle cohesion and the latter breaks cohesive bonds and particle clusters. When these factors act together, gas-fluidised pyroclastic materials exhibit *group A* behaviour with U_{mf} as low as ~1 mm s^{-1}, and they deaerate slowly due to large bed expansion (up to 60-70% above loose packing) and low U_{de}~0.5-1 cm s^{-1} (Druitt et al. 2004 and 2007). Fluidisation of PDC will depend on the strength and longevity of gas sources but also on the gas retention capacity once supply has become ineffective (Druitt et al. 2007). Retention capacity will depend on the timescales of deaeration and pore pressure diffusion, which raises scaling issues as they will respectively dominate at small, laboratory and large, natural scale.

4.3.2 The Dynamics of Gas-particle Flows

Fluidisation by air entrainment at the front of hot PDC was proposed by McTaggart (1960) as flow run-out in experiments increases with temperature, possibly because of envelopment of cold air by hot particles and subsequent violent expansion. In flows of *group A* particles generated in a rotating drum, air entrainment is promoted by periodic and continuous projection of clusters of particles ahead of the front (Bareschino et al. 2008). This may cause motion-induced, self-fluidisation (*i.e.*, Salatino 2005) and thus explain the weakly inclined free upper surface of the flows (Fig. 5a). This mechanism occurs because the deaeration timescale is much larger than the periodicity of avalanches. Continuously fluidised flows down inclines consist of a lower, concentrated layer (ν_s~0.40-0.45) and an upper, thinner and more dilute layer (Takahashi and Tsujimoto 2000). In contrast to *dry* flows, they have a nonlinear streamwise velocity profile whose gradient increases upwards and the curvature also increases with the mass flow rate (*i.e.*, slope angle).

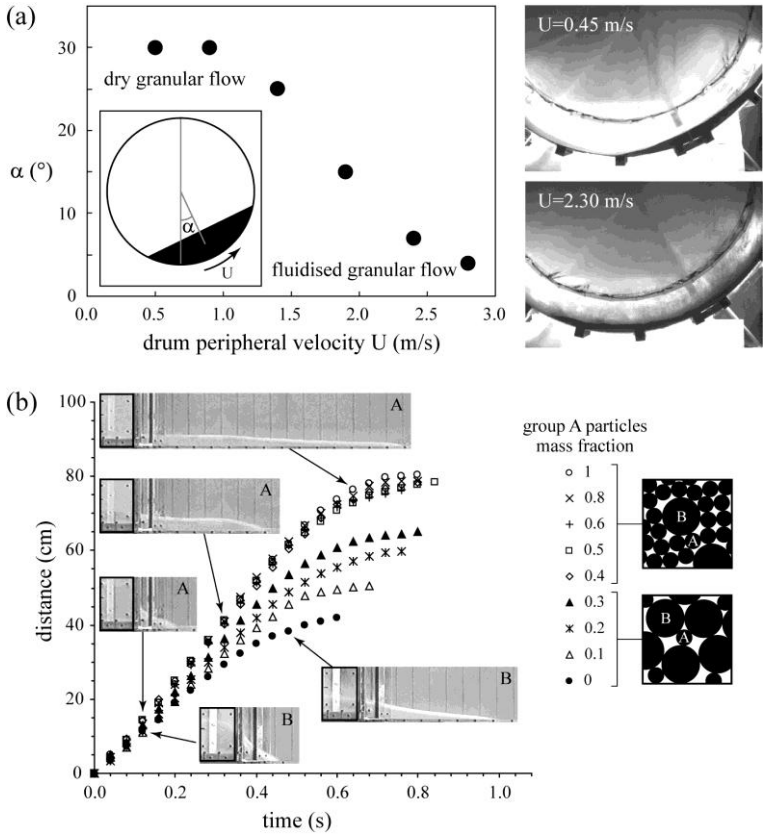

Figure 5. (a) Mean central angle as a function of the peripheral velocity of the rotating drum (radius=0.9 m) and corresponding flow regimes; in Bareschino et al. (2008), modified. (b) Kinematics of flows of mixtures of *group A* (45-90 μm) and *group B* (250-425 μm) particles generated from the release of a granular bed initially fluidised at U_{mf} in the reservoir (black rectangle, 10x15 cm); in Roche et al. (2005a), modified.

Lock-exchange (also called *dam-break* at high *g'*) experiments on highly concentrated air-particle flows ($v_s \sim v_{s,max}$) suggest that PDC may behave as inertial fluid density currents as shown in Figs. 2 and 5b (Roche et al. 2002, 2004, 2005a). When particles are fluidised in a reservoir, and then released into a horizontal channel which does not contain a source of fluidising gas, the flow behaviour depends on the timescale of defluidisation, which in controlled by the pore pressure diffusion timescale and by the degree of air-particle interactions. Flows of coarse particles (*groups B-D*) are defluidised very rapidly and have a morphology similar to *dry* cases (*i.e.*, section 4.2.2) although run-out is enhanced. In contrast, flows of fine particles (*group A*) propagate at almost constant velocity (U_f) and height (h_f) after initial acceleration (*i.e.*, slumping phase), and with Froude number values

$$Fr = \frac{U_f}{(gh_f)^{1/2}}, \qquad (31)$$

are consistent with observations for inertial fluid gravity currents with large reduced gravities as $Fr \sim 2\sqrt{2}$ (Gröbelbauer et al. 1993). As the fluid-like inertial regime is observed in absence of deaeration for initially non-expanded beds at U_{mf}, it is likely to result from slow initial pore pressure diffusion and/or pore pressure generated during motion because of strong air-particle interactions that damp particle-particle interactions, and efficient interstitial air support inhibits a rapid return to a frictional regime although particle concentration is near maximum. Further experiments have confirmed the fluid-like nature of these concentrated flows, as their morphology and front velocity are the same as that of inertial water flows at high *Re* (>>1000) as shown in Fig. 2 (Roche et al. 2005b and submitted). The initial Froude number

$$Fr_0 = \frac{U_f}{(gh_0)^{1/2}}, \qquad (32)$$

of these flows is independent on the aspect ratio of the initial column and has a constant value of $\sim\sqrt{2}$, as commonly reported in *dam-break* water flow experiments (Leal et al. 2006). This suggests that the resistance for these highly concentrated granular flows is similar to that of inertial water flows. This is observed as long as the level of the material in the emptying reservoir is above that of the resulting flow, thus generating a driving pressure gradient, then, the flow returns to a frictional regime until motion ceases. Polydisperse mixtures also propagate in a fluid-like inertial regime, provided *group A* particles form a continuous network (*i.e.*, matrix) embedding coarser components that are transported passively, and very few segregation takes place (Fig. 5b). As the matrix of PDC exhibit *group A* behaviour when fluidised (Druitt et al. 2007), fines-rich (*i.e.*, matrix-supported) pyroclastic flows are likely to propagate as inertial fluid gravity currents for most of their emplacement. Fluidised PDC may be highly expanded, and experimental investigation of pyroclastic material at high temperature shows that the deaeration rate of sheared flows is the same as that determined in static beds at same initial expansion (Girolami et al. 2008). This observation contradicts results obtained in shear cell experiments (Bareschino et al. 2007).

5. Numerical modeling of PDC

5.1. Principles

PDC are transported with a certain velocity and thermal energy that may change with time. The basic concept of numerical simulation is to solve conservation equations of mass (sometimes density or thickness), momentum and energy (sometimes enthalpy). We present below a simple formulation of the conservation equation of density (ρ) and volumetric momentum (ρU) of a compressible flow,

$$\underbrace{\frac{\partial}{\partial t}}_{1}\rho + \underbrace{\vec{\nabla}.(\rho\vec{U})}_{2} = 0 \qquad (33)$$

$$\underbrace{\frac{\partial}{\partial t}}_{3}\rho\vec{U} + \underbrace{\vec{\nabla}.(\rho\vec{U}\vec{U})}_{4} = \underbrace{-\vec{\nabla}P}_{5} + \underbrace{\vec{\nabla}\tau}_{6} + \underbrace{\rho\vec{g}}_{7}. \qquad (34)$$

Equation 33 means that, at a given position, the density only varies with time *t*, (1) according to the flux of the density that (2) enters or leaves this point, *i.e.*, the product of the spatial gradient of density (its variation in space) and the velocity at which it passes through the position. Mass displaces but is conserved. Changing the right-hand-side of Eq. 33 from zero allows mass to be added to the system for example by input of mass from a vent to PDC, and mass to be removed for example by particle sedimentation during flow. The momentum Eq. 34 describes the conservation of momentum per unit volume, ρU, and is a little more complex because momentum is generated and dissipated by stresses. The velocity changes with time (3) according to the flux of momentum (4), but also due to the stresses that act on the flow at a given position. In this example, the stress is induced by pressure (5), mechanical shear stresses (6) and gravity (7). These stress change according to the physics chosen for the simulated flow. To close this system of equations, we need to complete it with initial conditions (*e.g.*, distribution of the density at the start of the simulation), boundary conditions (*e.g.*, flux input, topography) and constitutive equations (*e.g.*, equations relating stress and velocity, or equations of state relating density and temperature) that describe the physical behaviour of the flow. Each model formulation is a simplified description of the natural phenomena, and a wide range of numerical models exists, from the simplest that only deal with a small part of these equations to most complex that attempt to solve systems of several tens of equations.

Conservation equations are complex, containing partial derivatives, and, except for some idealized flows, solutions can only be obtained by numerical treatment. An exact solution is generally impossible to calculate and the standard methodology is to discretise equations in space (and often in time) and obtain approximated solution at the node of the discretised space (*i.e.*, Toro 2001). Different methods (finite differences, finite volumes, finite elements, cellular automata) and algorithms exist and these produce a range of accuracy (Fig. 6). Their accuracy can be assessed by their ability to resolve shocks, which are discontinuous variations of properties (*e.g.*, density) that can occur at the front of flows and also within them (*e.g.*, sudden changes of pressure at the front of explosions, and of thickness at the front of dense flows). First order resolution methods smooth the solutions of differential equations, meaning that shocks cannot be calculated correctly and are gentler than in reality. Consequently, gradients of variables at the position of the shock are incorrect, generating strong perturbations in the velocity field. This induces large errors in velocity, thickness and run-out of simulated PDC. Another indication of the quality of algorithms is their numerical stability. Some algorithms generate very strong unphysical oscillations that disturb the overall behaviour. Another aspect of the numerical simulation of PDC is that, whatever the quality of the model, there is always a compromise between accuracy and rapidity of calculations. The finer the mesh size, the more accurate the solution (as is very clear for shock restitution) but also the larger the computational time required to solve the problem.

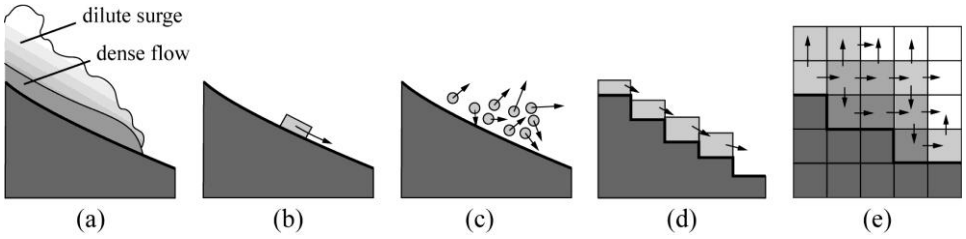

Figure 6. (a) schematization of a natural PDC composed of a dense basal flow and an associated dilute ash-cloud surge. Four types of numerical approaches are schematized: (b) kinetic, (c) discrete element, (d) depth-average, (e) multiphase models.

5.2 Kinetic model

The earliest numerical simulations of PDC were made using the kinetic approach, which only simulates trajectories for the flow front, and considers the flow as a rigid block or a material point (Fig. 6b). The movement is calculated using the fundamental equation of dynamics that can be thought of as a drastic simplification of the equation of momentum conservation

$$\frac{d\vec{U}}{dt} = \frac{\sum \vec{F}}{m}, \qquad (35)$$

were $\Sigma \vec{F}$ represents the sum of forces that act on the block of mass *m*. The block is driven by gravity following the topography, and by a resistive law. The resistive law is generally approximated using a basal friction term (with a constant value), a viscous stress term (which is a function of velocity) and a turbulent or a collisional term (which is a function of the square of the velocity), so the resistive stress has the form (a_0+a_1U+a_2U^2). This approach was developed for PDC by Sheridan and Malin (1983), Beget and Limke (1988), McEwen and Malin (1989), Rossano et al. (2004), and Saucedo et al. (2005). Wadge et al. (1998) also used this approach to simulate the path of dense pyroclastic flows at Montserrat. They improved the model by adding the approach of Bursik and Woods (1996) to calculate the areas that could be affected by a low density surge generated from the dense flow.

Kinetic models significantly oversimplify the physical problem. The simulated flow cannot spread, and its depth, and any depth-dependent mechanical behaviour cannot be determined. This approach may be used to estimate dense flow trajectories but, as it cannot take into account density variations, sedimentation and air ingestion, it is too simplistic for dilute flow simulations. However, this approach can generate results very rapidly. As it is generally very difficult to estimate volumes, rates and initial velocity during a volcanic crisis, the accuracy of such a basic model is generally greater than the knowledge of what will occur. It can thus be a useful tool for rapid evaluation of pyroclastic flow hazards.

5.3 Discrete element model

In this approach, Newton's equations of motion are solved for every particle in the flow, and the motion of each constituent grain is simulated (Fig. 6c). Behaviour laws based on particle elasticity and deformation allow calculation of the dynamics of grain interaction. To our knowledge, the only direct application of this technique to PDC has been made by Mitani et al. (2004). They reproduced both normal and reverse grading in a granular medium (only particles, no interstitial fluid) in movement on a slope and suggested that fluidising gases are not required for the formation of coarse tail grading. This method cannot be used to simulate natural PDC on real topography due to the huge number of particles that are required to obtain meaningful statistics. However, it is being increasingly used in other fields of Science and recent developments combining the discrete element method with a continuum method (such as the multiphase approach described below) appear promising for the study of gas-particle interaction and their effects on PDC rheology at the particle scale.

5.4 Depth-average method

As the emplacement of PDC on natural topography cannot be calculated at the particle level, another solution consists of discretising the space in meshes and averaging the physical properties of particles on each mesh. In the depth-average method, based on this principle, meshes have the form of *columns* (Fig. 6d). All the physical properties are vertically averaged and 3D equations vertically integrated. The depth-average approximation requires that the flow length is much greater than its depth, so that vertical displacements are negligible. All the mass of a column is considered to move either with the same velocity or with a fixed vertical velocity profile depending on the rheology chosen.

The depth-average method has been used to simulate granular flows in laboratory (Savage and Hutter 1989, Pouliquen and Forterre 2002, Gray et al. 2003) and dense geophysical flows like mud

flows, landslides or debris avalanches (*e.g.*, Heinrich et al. 2001, Pitman et al. 2003, Kelfoun and Druitt 2005, Sheridan et al. 2005, Lucas and Mangeney 2007). Titan2D (Patra et al. 2005 and 2006, Sheridan et al. 2005), is probably the most sophisticated application of this method to dense pyroclastic flow simulation. It allows parallelization, and is able to remesh the computational domain to be more accurate in the regions of strong gradients. Kelfoun et al. (submitted) also used a depth-average approach to reproduce the 2006 Tungurahua eruption. Avolio et al. (2006) and Crisci et al. (2005) simulated PDC at Pinatubo and Montserrat respectively. Itoh et al. (2000) reproduced dense and dilute flows of Merapi although they homogenize in a single mixture both dense block-and-ash flow and surges that are clearly separated in the field (Kelfoun et al. 2000).

The integration and resolution of depth-average methods is mainly done for flows whose density is constant in time and space. It is then adapted to the simulation of dense pyroclastic flows but is less adapted for dilute currents that present strong vertical displacements at the end of their path and strong spatial variations of density. The main problem of the present models appears to be the rheology used. The complex and poorly understood physical behaviour should be approximated by first order laws. The most common approximation uses a frictional behaviour (*e.g.*, Patra et al. 2005). Assuming that particle collisions are important in such granular flows, Itoh et al. (2000) used a collisional stress. Kelfoun et al. (2007) showed that a frictional behaviour is not adapted for pyroclastic flow simulation and proposed that retarding stress is rather constant. The same kind of problems occurs in the simulation of other geophysical flows and a large set of rheological behaviour has been used: frictional ($\rho_f g h_f \tan\phi$), constant (C), viscous ($\eta\, \partial U/\partial h_f$), Bingham ($C+\eta\, \partial U/\partial h_f$), or Voellmy ($\rho_f g h_f \tan\phi+\rho_f g U^2/\xi$). The enormous advantage of the depth-average approach is the speed of calculation, because the third dimension is averaged. It is thus of very significant importance for real-time hazard assessment.

5.5 Multiphase approach

To take account of both the temporal and spatial variations of the physical properties, necessary to simulate dilute PDC, the calculation domain should be divided in meshes horizontally and vertically (Fig. 6e). As a first approximation, it is possible to consider pyroclastic flows as a single *dusty gas* where particles and gas form a homogeneous phase: particles and gas move at the same velocity and are in thermal equilibrium (Cordoba 2005, Ishimine 2005). Saito et al. (2001) used a finite difference method to solve the conservation equations in 3D on a real topography, but the model simulates a shock-wave rather than a pyroclastic surge. To go further, gas and particle dynamics need to be distinguished. Particles are considered as a continuous phase, their properties being averaged on each mesh in the same manner as gases. All the phases present (different size classes of particles, gases of various compositions) share the same meshes and interact together. The first application of this approach was made by Wohletz et al. (1984). The models then became more complex as computational power of computer increased (*e.g.*, Valentine 1987, Valentine and Wohletz 1989a and 1989b, Wolhetz and Valentine 1990, Valentine et al. 1991 and 1992, Dartevelle 2004, Dartevelle et al. 2004). Dobran et al. (1993) and Neri and Dobran (1994) introduced one solid phase and two gas phases, air and vapor water. Giordano and Dobran (1994) used a realistic topography. These codes were able to take into account several particle sizes to allows a global estimation of spatial particle segregation, that is, two classes of particles for Neri and Macedonio (1996) and six classes for Neri et al. (2003). The power of computers has limited those studies to a 2D (or an axisymmetric) approach and it is only very recently that first 3D results (or 4D if time is considered) were obtained (Esposti Ongaro et al. 2005, Neri et al. 2007) as shown in Fig. 7. As for the depth-average method, the multiphase approach suffers from our weak knowledge on the physics of dense flows, as some codes are unable to form a deposit for instance. However, results from multiphase models identify complex flow behaviour such as decoupling between a dense basal avalanche and the overriding dilute surge, than cannot be resolved using other approaches, so detailed hazard assessment requires future development of the multiphase approach.

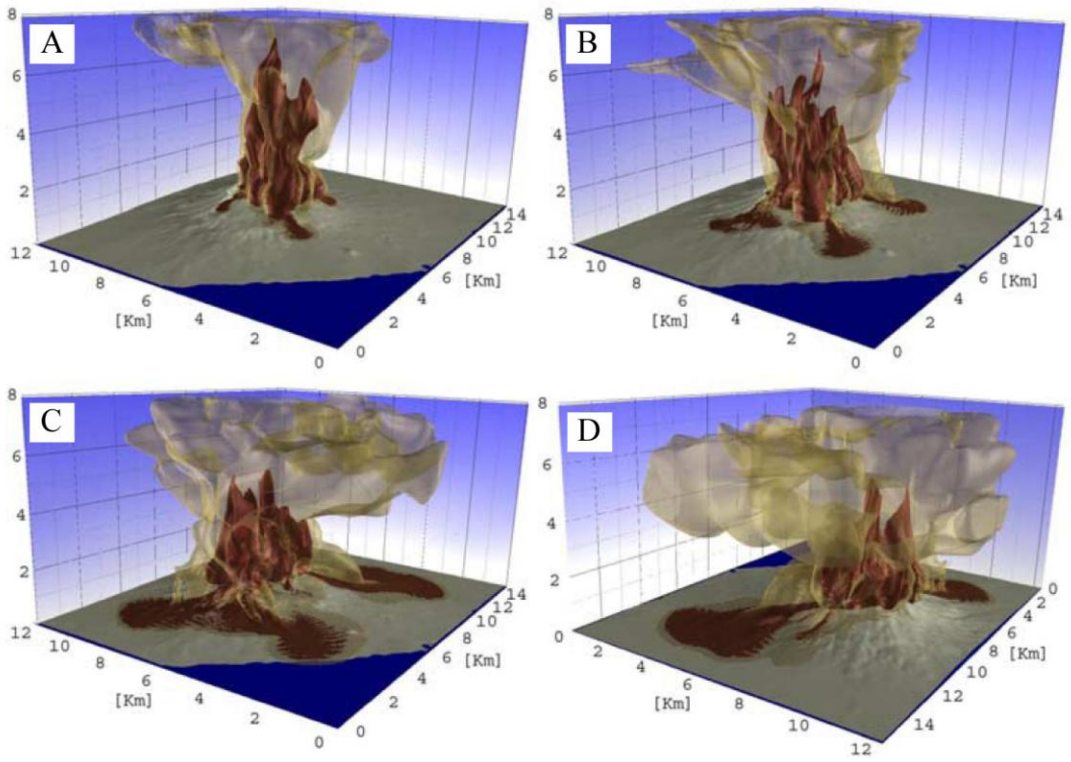

Figure 7. 3D multiphase simulation of PDC as a function of time (A to &D). After Neri et al. (2007), modified. Note that PDC are strongly influenced by the topography even if the column is much higher.

6. Perspectives

Pyroclastic density currents are highly complex flows, and understanding the key controls on their dynamics and sedimentation remains a major challenge. The dynamics and particle transport are strongly time-dependent, vary over a wide range of scales, and the flow may undergo significant interactions with the underlying topography. In order to make progress, idealized flows which share some of the observed features of PDC have been used. An emerging methodology is the use of unsteady granular collapse experiments, which builds on the established fundamental dynamics of fluid collapses and gravity current motion. Outstanding research questions that can be investigated in this way include investigation of the mechanisms of PDC emplacement, the role of particle interactions in controlling flow dynamics and resistance to motion, and measurement of internal velocity profiles. Scaling of these experiments remains an important issue, as, for example, the ratio of the pore pressure diffusion time scale to the flow duration is larger in nature than in experiments.

Recent significant increases in computational power have permitted the development of fully multiphase codes that do not require depth-averaging, and these now offer the possibility of detailed investigation of mechanisms of particle interaction and resistance to flow motion. A major challenge is to address the mismatch in sophistication between experiments and numerical models in order to develop appropriate methodologies for model testing. One possibility is to explore the use of more complex experimental geometries which are closer to variation in natural topography over which PDC propagate. Ultimately more sophisticated field measurements of the properties and dynamics of PDC are required for testing numerical simulations.

7. Exercises

Exercise 1

Consider a dilute PDC (surge) of density ρ_c and height h_c propagating on a sub-horizontal surface at a front velocity U_c in less dense atmosphere of density ρ_0 and height H (considered as semi-infinite).
1/ Calculate the Froude number at the front of the surge.
2/ Field observations reveal that U_c=40 m s^{-1} and h_c=8 m. Calculate the density of the surge (ρ_0=1.2 kg m^{-3}).
3/ Discuss the limitation of the analysis.

Answer:
1/ At the front of the surge, consider points A and B outside and inside the PDC respectively. In A, the pressure is the sum of the dynamic pressure and of the static pressure of the atmosphere, so that

$$P_A = \tfrac{1}{2}\rho_0 {U_c}^2 + \rho_0 g H \,. \qquad \text{(E1)}$$

In B, the pressure is the sum of the static pressure of the surge and of the overlying atmosphere, so that

$$P_B = \rho_c g h_c + \rho_0 g (H - h_c) \,. \qquad \text{(E2)}$$

Assuming P_A=P_B, then

$$\frac{U_c}{\left[g h_c (\rho_c - \rho_0)/\rho_0\right]^{1/2}} = \frac{U_c}{(g' h_c)^{1/2}} \,, \qquad \text{(E3)}$$

which is also the Froude number at the front and Fr=$\sqrt{2}$.
2/ Assuming Fr=$\sqrt{2}$, then

$$\rho_c = \frac{U_c \rho_0}{2 g h_c} + \rho_0 \,, \qquad \text{(E4)}$$

and ρ_c~1.5 kg m^{-3}.
3/ The analysis is valid if $g' \leq g$, so that $(\rho_c - \rho_0)/\rho_0 \leq 1$, and $\rho_c \leq 2\rho_0$.

Exercise 2

Laboratory experiments on subaerial granular flows are carried out to investigate concentrated, coarse grained pyroclastic flows. The particles used are glass beads of grain size d=2 mm and density ρ_p=2500 kg m^{-3}, and the material has an angle of internal friction ϕ=30° and a solid fraction of 0.6. Flows are generated on an inclined rough substrate and have a typical thickness h_f~1 cm. Calculate the range of velocities U_f at which the flows will be in a frictional or in a collisional regime.

Answer:
Considering the Savage number (Eq. 16) and assuming that the shear rate $\gamma = U_f/h_f$, then

$$U_f = \left(\frac{Sa(\rho_p - \rho_0) g {h_f}^3 \tan\phi}{\rho_p d^2} \right)^{1/2} \,. \qquad \text{(E5)}$$

With Sa=0.1, then U_f=0.38 m s^{-1} and the flows will be in frictional (collisional) regime below (above) that velocity.

Exercise 3

An axisymmetric constant-volume gravity current spreads radially from its source such that the position of the flow front r increases with time t, from an initial condition $r = 0$ at $t = 0$. The statement of mass conservation for this current is $Q=\pi r^2 h_c$, and the front condition when inertia and buoyancy forces are in balance is $U_c=Fr(g'h_c)^{1/2}$, where Q is the volume and h_c is the thickness of the current, U_c is the velocity of the current front, Fr is the Froude number, and g' is the reduced gravity. Using these formulae, show that the position of the front r varies as $t^{1/2}$ in the inertia-buoyancy regime. How does the position of the front depend on the volume of the current?

Answer:
From mass conservation $h_c=Q/\pi r^2$, and substituting into the front condition, we find

$$U_c = \frac{dr}{dt} = Fr\left(\frac{g'Q}{\pi r^2}\right)^{1/2}. \qquad \text{(E6)}$$

Re-arranging this equation to separate all terms in r and integrating this equation subject to the boundary condition $r = 0$ at $t = 0$ gives

$$r = \left(\frac{2Fr}{\pi^{1/2}}\right)^{1/2} (g'Q)^{1/4} t^{1/2}. \qquad \text{(E7)}$$

The position of the front depends on $Q^{1/4}$.

References

Avolio, M.V., Crisci, G.M., di Gregorio, S., Rongo, R., Spataro, W. and d´Ambrosio, D. (2006). Pyroclastic flows modelling using cellular automata, Computer and Geosciences 32, 897-911.

Balmforth, N.J. and Kerswell, R.R. (2005). Granular collapse in two dimensions. Journal of Fluid Mechanics, 538, 399-428.

Bareschino, P., Gravina, T., Lirer, L., Marzocchella, A., Petrosino, P. and Salatino, P. (2007). Fluidization and de-aeration of pyroclastic mixtures: the influence of fines content, polydispersity and shear flow. Journal of Volcanology and Geothermal Research 164, 284-292.

Bareschino, P., Marzocchella, A., Salatino, P., Lirer, L. and Petrosino P. (2008). Self-fluidization of subaerial rapid granular flows. Powder Technology 182, 323-333.

Beget, J.E. and Limke, A.J. (1988). Two-dimensional kinematic and rheological modeling of the 1912 pyroclastic flow, Katmai, Alaska. Bulletin of Volcanology 56, 148-160.

Benjamin, T.B. (1968). Gravity currents and related phenomena. Journal of Fluid Mechanics 31, 209-248.

Bonnecaze, R.T., Huppert, H.E. and Lister, J.R. (1993). Particle-driven gravity currents. Journal of Fluid Mechanics 250, 339-369.

Branney, M.J. and Kokelaar, P. (1992). A reappraisal of ignimbrite emplacement: progressive aggradation and changes from particulate to non-particulate flow during emplacement of high-grade ignimbrite: Bulletin of Volcanology 54, 504-520.

Branney, M.J. and Kokelaar, P. (2002). Pyroclastic density currents and the sedimentation of ignimbrites. Memoir of the Geological Society of London, 152 p.

Bursik, M.I. and Woods, A.W. (1996). The dynamics and thermodynamics of large ash flows. Bulletin of Volcanology 58, 175-193.

Cagnoli, B. and Manga, M. (2003). Pumice-pumice collisions and the effect of the impact angle. Geophysical Research Letters 30, 1636.

Cagnoli, B. and Manga, M. (2004). Granular mass flows and Coulomb's friction in shear cell experiments: implications for geophysical flows. Journal of Geophysical Research 109, F04005.

Cagnoli, B. and Manga, M. (2005). Vertical segregation in granular mass flows: a shear cell study. Geophysical Research Letters 32, L10402.

Campbell, C.S. (2006). Granular material flows - an overview. Powder Technology 162, 208-229.

Cas, R.A.F., and Wright, J.V. (1987). Volcanic successions, modern and ancient. Chapman and Hall, London. 528 p.

Choux, C.M. and Druitt, T.H. (2002). Analogue study of particle segregation in pyroclastic density currents, with implications for the emplacement mechanisms of large ignimbrites. Sedimentology 49, 907-928.

Cordoba G. (2005). A numerical model for the dynamics of pyroclastic flows at Galeras Volcano, Colombia. Journal of Volcanology and Geothermal Research 139: 59–71.

Crisci, G.M., Di Gregorio, S., Rongo, R. and Spataro, W. (2005). PYR: a Cellular Automata model for pyroclastic flows and application to the 1991 Mt. Pinatubo eruption. Future Generation Computer Systems 21, 1019-1032.

Dade, W.B. and Huppert, H.E. (1995). A box model for non-entraining, suspension-driven gravity surges on horizontal surfaces. Sedimentology 42, 453-471.

Dade, W.B. and Huppert, H.E. (1996). Emplacement of the Taupo ignimbrite by a dilute turbulent flow. Nature 381, 509-512.

Dartevelle, S. (2004). Numerical modeling of geophysical granular flows: 1. A comprehensive approach to granular rheologies and geophysical multiphase flows, Geochemistry Geophysics Geosystems 5, Q08003, doi:10.1029/2003GC000636.

Dartevelle, S., Rose, W. I., Stix, J., Kelfoun, K. and Vallance, J. W. (2004). Numerical modeling of geophysical granular flows: 2. Computer simulations of plinian clouds and pyroclastic flows and surges, Geochemistry Geophysics Geosystems 5, Q08004, doi:10.1029/2003GC000637.

Dobran, F., Neri, A. and Macedonio, G. (1993). Numerical simulation of collapsing volcanic columns. Journal of Geophysical Research 94, 1867-1887.

Doyle, E.E., Hogg, A.J., Mader, H.M. and Sparks, R.S.J. (2008). Modeling dense pyroclastic basal flows from collapsing columns. Geophysical Research Letterts 35, L04305.

Druitt, T.H. (1992). Emplacement of the 18 May 1980 lateral blast deposit ENE of mount St. Helens, Washington: Bulletin of Volcanology 54, 554-572.

Druitt, T.H. (1998). Pyroclastic density currents. In: Gilbert, J.S., and Sparks, R.S.J. (eds), The physics of explosive volcanic eruptions. Geological Society London Special Publications 145, pp.145-182.

Druitt, T. H., E. S. Calder, P. D. Cole, R. P. Hoblitt, S. C. Loughlin, G. E. Norton, L. J. Ritchie, R. S. J. Sparks, and B. Voight (2002), Small volume, highly mobile pyroclastic flows formed by rapid sedimentation from pyroclastic surges at Soufrière Hills Volcano, Montserrat: An important volcanic hazard. In Druitt, T.H. and Kokelaar, B.P (eds.), The Eruption of Soufrière Hills Volcano Montserrat, From 1995 to 1999. Memoir of the Geological Society of London 21, pp. 263-279.

Druitt, T.H., Avard, G., Bruni, G., Lettieri, P. and Maez, F. (2007). Gas retention in fine-grained pyroclastic flow materials at high temperatures. Bulletin of Volcanology 69, 881-901.

Druitt, T.H., Bruni, G., Lettieri, P. and Yates, J.G. (2004). The fluidization behaviour of ignimbrite at high temperature and with mechanical agitation. Geophysical Research Letters 31, L02604.

Eames, I. and Gilbertson, M.A. (2000)., Aerated granular flow over a horizontal rigid surface. Journal of Fluid Mechanics 424, 169-195.

Esposti Ongaro, T., Clarke, A., Neri, A., Voight, B. and Widiwijayanti, C. (2005). A new high-performance 3D multiphase flow code to simulate volcanic blasts and pyroclastic density currents: example from the Boxing Day event, Montserrat. EOS transaction, AGU 86, 52, Fall Meeting 2005, abstract #V31D-0645.

Félix, G. and Thomas, N. (2004). Relation between dry granular flow regimes and morphology of deposits: formation of levées in pyroclastic deposits. Earth and Planetary Science Letters 221, 197-213.

Fisher R.V. (1966). Mechanism of deposition from pyroclastic flow. American Journal of Science 264, 350-363.

Forterre, Y. and Pouliquen, O. (2008). Flows of dense granular media. Annual Review of Fluid Mechanics 40, 1-24.

GDR MiDi (2004). On dense granular flows. The European Physical Journal E 14, 341-365.

Geldart, D. (1973). Types of gas fluidization. Powder Technology 7, 285-292.

Giordano, G. and Dobran, F. (1994). Computer simulations of the Tuscalano Artemisio's second pyroclastic flow unit (Alban Hills, Latium, Italy). Journal of Volcanology and Geothermal Research 61, 69–94.

Girolami, L., Druitt, T.H., Roche, O. and Khrabrykh, Z. (2008). Propagation and hindered settling of laboratory ash flows. Journal of Geophysical Research 113, B02202.

Gladstone, C., Phillips, J.C. and Sparks, R.S.J. (1998). Experiments on bidisperse, constant-volume gravity currents: propagation and sediment deposition. Sedimentology 45, 833-843.

Gladstone, C., Ritchie, L.J., Sparks, R.S.J. and Woods, A.W. (2004). An experimental investigation of density-stratified inertial gravity currents. Sedimentology 51, 767-789.

Goldhirsch, I. (2003). Rapid granular flows. Annual Review of Fluid Mechanics 35, 267-293.

Gravina, T., Lirer, L., Marzocchella, A., Petrosino, P. and Salatino, P. (2004). Fluidization and attrition of pyroclastic granular solids. Journal of Volcanology and Geothermal Research 138, 27-42.

Gröbelbauer, H.P., Fannelop, T.K. and Britter, R.E. (1993). The propagation of intrusion fronts of high density ratios. Journal of Fluid Mechanics 250, 669-687.

Gray, J.M.N.T., Tai, Y.-C. and Noelle, S. (2003). Shock waves, dead zones and particle-free regions in rapid granular free-surface flows, Journal of Fluid Mechanics 91, 161-181.

Hallworth, M A. and Huppert, H.E. (1998). Abrupt transitions in high-concentration, particle-driven gravity currents. Physics of Fluids 10, 1083-1087.

Hallworth, M.A., Phillips, J., Huppert, H.E. and Sparks, R.S.J. (1993). Entrainment in turbulent gravity currents. Nature 362, 829-831.

Hallworth, M.A., Phillips, J., Huppert, H.E. and Sparks, R.S.J. (1996). Entrainment into two-dimensional and axisymmetric turbulent gravity currents. Journal of Fluid Mechanics 308, 289-312.

Harris, T.C., Hogg, A.J. and Huppert, H.E. (2002). Polydisperse particle-driven gravity currents. Journal of Fluid Mechanics 472, 333-372.

Heinrich, P., Boudon, G., Komorowski, J.C., Sparks, R.S.J., Herd, R. and Voight, B. (2001). Numerical simulation of the December 1997 debris avalanche in Montserrat, Lesser Antilles, Geophysical Research Letters 28, 2529-2532.

Hogg, A.J., and Pritchard, D. (2004). The effects of hydraulic resistance on dam-break and other shallow inertial flows. Journal of Fluid Mechanics 501, 179-212.

Hoult, D.P. (1972). Oil spreading on sea. Annual Review of Fluid Mechanics 4, 341-368.

Huppert, H.E. (2006). Gravity currents: a personal perspective. Journal of Fluid Mechanics 554, 299-322.

Huppert, H.E. and Simpson, J.E. (1980). The slumping of gravity currents. Journal of Fluid Mechanics 99, 785-799.

Ishida, M., Hatano, H. and Shirai, T. (1980). The flow of solid particles in an aerated inclined channel. Powder Technology 27, 7-12.

Ishimine, Y. (2005). Numerical study of pyroclastic surges. Journal of Volcanology and Geothermal Research 139, 33-57.

Itoh, H., Takahama, J., Takahashi, M. and Miyamoto, K. (2000). Hazard estimation of the possible pyroclastic flow disasters using numerical simulation related to the 1994 activity at Merapi volcano. Journal of Volcanology and Geothermal Research 100 (1–4), 503-516.

Iverson, R.M. (1997). The physics of debris flows. Reviews of geophysics 35, 245-296.

Iverson, R.M. and LaHusen, R.G. (1989. Dynamic pore-pressure fluctuations in rapidly shearing granular materials. Science 246, 796-799.

Jaeger, H.M., Nagel, S.R., and Behringer, R.P. (1996). Granular solids, liquids, and gases. Reviews of Modern physics 68, 1259-1273.

Kelfoun, K., Legros, F. and Gourgaud, A. (2000). Statistical study of damaged trees related to the pyroclastic flows of November 22, 1994 at Merapi volcano (central Java, Indonesia): relation between ash-cloud surge and block-and-ash flow. Journal of Volcanology and Geothermal Research 100, 379-393.

Kelfoun, K. and Druitt, T.H. (2005) Numerical modeling of the emplacement of Socompa rock avalanche, Chile. Journal of Geophysical Research 110, B12202, doi:10.1029/2005JB003758.

Kelfoun, K., Palacio, P., Barba and D. and Samaniego, P. Pyroclastic flow simulation and frictional behavior: confrontation with a well constrained eruption at Tungurahua volcano (Ecuador). Submitted to Bulletin of Volcanology.

Lajeunesse, E., Mangeney-Castelnau, A. and Vilotte, J.-P. (2004). Spreading of a granular mass on a horizontal plane. Physics of Fluids 16, 2371-2381.

Lajeunesse, E., Monnier, J.B. and Homsy, G.M. (2005). Granular slumping on a horizontal surface. Physics of Fluids 17, 103302.

Leal, J. G. A. B., Ferreira, R. M. L. and Cardoso, A. H. (2006). Dam-break wave-front celerity. Journal of Hydraulic Engineering 132, 69-76.

Lube, G., Huppert, H.E., Sparks, R.S.J. and Freundt, A. (2005). Collapses of two-dimensional granular columns. Physical Review E 72, 041301.

Lube, G., Huppert, H.E., Sparks, R.S.J. and Freundt, A (2007). Static and flowing regions in granular collapses down channels. Physics of Fluids 19, 043301.

Lube, G., Huppert, H.E., Sparks, R.S.J. and Hallworth, M.A. (2004). Axisymmetric collapses of granular columns. Journal of Fluid Mechanics 508, 175-199.

Lucas, A. and Mangeney, A. (2007). Mobility and topographic effects for large Valles Marineris landslides on Mars, Geophysical Research Letters 34, L10201, doi:10.1029/2007GL029835.

Makse, H.A., Havlin, S., King, P.R. and Stanley, H.E. (1997). Spontaneous stratification in granular mixtures. Nature 386, 379-381.

Mangeney, A., Bouchut, F., Thomas, N., Vilotte, J.P. and Bristeau, M.O. (2007). Numerical modeling of self-channeling granular flows and their levée-channel deposits. Journal of Geophysical Research 112, F02017.

Martin, D. and Nokes, R. (1988). Crystal settling in a vigorously convecting magma chamber. Nature 332, 534-536.

McEwen, A.S. and Malin, M.C. (1989). Dynamics of Mount St. Helens' 1980 pyroclastic flows, rockslide-avalanche, lahars, and blast. Journal of Volcanology and Geothermal Research 37, 205-231.

McTaggart, K.C. (1960). The mobility of nuées ardentes. American Journal of Science 258, 369-382.

Mitani, N.K., Matuttis H.G. and Kadono T. (2004). Density and size. segregation in deposits of pyroclastic flow, Geophysical Research Letters 31, 15, L15606. 10.1029/2004GL020117.

Neri, A. and Dobran, F. (1994). Influence of eruption parameters on the thermofluid dynamics of collapsing volcanic columns, Journal of Geophysical Research 99, 11833-11857.

Neri, A. and Macedonio, G. (1996). Numerical simulation of collapsing volcanic columns with particles of two sizes, Journal of Geophysical Research 101, 8153-8174.

Neri, A., Esposti Ongaro, T., Macedonio, G. and Gidaspow, D. (2003). Multiparticle simulation of collapsing volcanic columns and pyroclastic flows. Journal of Geophysical Research 108, 2202, doi:10.1029/2001JB000508.

Neri, A., Esposti Ongaro, T., Menconi, G., De'Michieli Vitturi, M., Cavazzoni, C., Erbacci, G. and Baxter, P. J. (2007). 4D simulation of explosive eruption dynamics at Vesuvius, Geophysical Research Letters 34, L04309, doi:10.1029/2006GL028597

Patra, A.K., Bauer, A.C., Nichita, C.C., Pitman, E.B., Sheridan, M.F., Bursik, M., Rupp, B., Webber, A., Stinton, A.J., Namikawa, L.M. and Renschler, C.S. (2005). Parallel adaptive numerical simulation of dry avalanches over natural terrain. Journal of Volcanology and Geothermal Research 139 (1), 1-22.

Patra, A.K., Nichita, C.C., Bauer, A.C., Pitman, E.B., Bursik, M. and Sheridan, M.F. (2006). Parallel Adaptive Discontinuous Galerkin Approximation of the Debris Flow Equations. Computers and Geosciences 32: 912-926.

Phillips, J.C., Hogg, A.J., Kerswell, R.R. and Thomas, N.H. (2006). Enhanced mobility of granular mixtures of fine and coarse particles. Earth and Planetary Science Letters 246, 466-480.

Pitman, E.B., Patra, A., Bauer, A., Sheridan, M. and Bursik, M. (2003). Computing debris flows and landslides. Physics of Fluids 15 (12), 3638-3646.

Pouliquen, O. (1999). Scaling laws in granular flows down rough inclined planes. Physics of Fluids 11, 542-548.

Pouliquen, O. and Forterre, Y. (2002). Friction law for dense granular flows: application to the motion of a mass down a rough inclined plane, Journal of Fluid Mechanics 453, 133-151.

Rhodes, M.J. (1998). Introduction to Particle Technology. Chichester, John Wiley and Sons, 315 p.

Roche, O., Gilbertson, M., Phillips, J.C. and Sparks, R.S.J. (2002). Experiments on deaerating granular flows and implications for pyroclastic flow mobility. Geophysical Research Letters 29 (16), 40.

Roche, O., Gilbertson, M.A., Phillips, J.C. and Sparks, R.S.J. (2004). Experimental study of gas-fluidized granular flows with implications for pyroclastic flow emplacement. Journal of Geophysical Research 109, B10201.

Roche, O., Gilbertson, M.A., Phillips, J.C. and Sparks, R.S.J. (2005a). Inviscid behaviour of fines-rich pyroclastic flows inferred from experiments on gas-particle mixtures. Earth and Planetary Science Letters 240, 401-414.

Roche, O., Gilbertson, M.A., Phillips, J.C. and Sparks, R.S.J. ((2006). The influence of particle size on the flow of initially fluidized powders. Powder Technology 166, 167-174.

Roche, O., Montserrat, S., Niño, Y. and Tamburrino, A. (2005b). Propagation and final deposition of granular flow: dam-break experiments with water and gas-fluidized grains. Proceedings 4th River Coastal and Estuarine Morphodynamics, pp. 7. University of Illinois, Urbana Champaign, USA.

Roche, O., Montserrat, S., Niño, Y. and Tamburrino, A. Experimental observations of water-like behaviour of initially fluidized , unsteady dense granular flows and their relevance for the propagation of pyroclastic flows. Submitted to Journal of Geophysical Research.

Rossano, S., Mastrolorenzo, G. and De Natale, G. (2004). Numerical simulation of pyroclastic density currents on Campi Flegrei topography: a tool for statistical hazard estimation. Journal of Volcanology and Geothermal Research 132, 1-14.

Rottman, J. W. and Simpson, J. E. (1983). Gravity currents produced by instantaneous releases of a heavy fluid in a rectangular channel. Journal of Fluid Mechanics 135, 95-110.

Saito, T., Eguchi, T., Takayama, K. and Taniguchi, H. (2001). Hazard predictions for volcanic explosion. Journal of Volcanology and Geothermal Research 106, 39-51.

Salatino, P. (2005). Assessment of motion-induced fluidization of dense pyroclastic gravity currents. Annals of Geophysics 48, 843-852.

Saucedo, R., Macias, J.L., Sheridan, M.F., Bursik, M.I. and Komorowski, J.C. (2005). Modeling of pyroclastic flows of Colima Volcano, Mexico: implications for hazard assessment. Journal of Volcanology and Geothermal Research 139, 103-115.

Savage, S.B. (1984). The mechanics of rapid granular flows. Advances in Applied Mechanics 24, 289-366.

Savage, S.B. and Hutter, K. (1989). The motion of a finite mass of granular material down a rough incline. Journal of Fluid Mechanics 199, 177-215.

Sheridan, M.F. and Malin, M.C. (1983). Application of computer-assisted mapping to volcanic hazard evaluation of surge eruption: Vulcano, Lipari, and Vesuvius. Journal of Volcanology and Geothermal Research 17, 187-202.

Sheridan, M.F., Stinton, A.J., Patra, A., Pitman, E.B., Bauer, A. and Nichita, C.C. (2005). Evaluating Titan2D mass-flow model using the 1963 Little Tahoma Peak avalanches, Mount Rainier, Washington. Journal of Volcanology and Geothermal Research 139, 89-102.

Simpson, J.E. (1997). Gravity Currents in the Environment and the Laboratory. Cambridge University Press.

Simpson, J.E. and Britter, R.E. (1980). A laboratory model of an atmospheric mesofront. Quarterly Journal of the Royal Meteorological Society 106, 485-500.

Simpson, J.E. (1982). Gravity Currents in the laboratory, atmosphere and ocean. Annual Review of Fluid Mechanics 14, 213-234.

Sparks, R.S.J. (1976). Grain size variations in ignimbrites and implications for the transport of pyroclastic flows: Sedimentology 23, 147-188.

Sparks, R.S.J., Bonnecaze, R.T., Huppert, H.E., Lister, J.R., Hallworth, M.A., Mader, H.M. and Phillips, J.C. (1993). Sediment-laden gravity currents with reversing buoyancy. Earth and Planetary Science Letters 114, 243-257.

Takahashi, T. and Tsujimoto, H. (2000). A mechanical model for Merapi-type pyroclastic flow. Journal of Volcanology and Geothermal Research 98, 91-115.

Thomas, N. (2000). Reverse and intermediate segregation of large beads in dry granular media. Physical Review E 62, 961-974.

Toro, E.F. (2001). Shock-capturing methods for free-surface shallow flows. John Wiley and Sons, Ltd., New York, 309 pp.

Turner, J.S. (1979). Buoyancy Effects in Fluids. Cambridge University Press.

Valentine, G.A. (1987). Stratified flow in pyroclastic surges. Bulletin of Volcanology 49, 616–630.

Valentine, G.A. and Wohletz, K. H. (1989a). Numerical models of plinian eruption columns and pyroclastic flows. Journal of Geophysical Research. 94, 1867-1887.

Valentine, G.A. and Wohletz, K.H. (1989b). Environmental hazards of pyroclastic flows determined by numerical models. Geology 17: 641-644.

Valentine, G.A., Wohletz, K.H. and Kieffer, S.W. (1991). Sources of unsteady column dynamics in pyroclastic flow eruptions. Journal of Geophysical Research 96, 21887-21892.

Valentine, G.A., Wohletz, K.H. and Kieffer, S.W. (1992). Effects of topography on facies and compositional zonations in caldera-related ignimbrites. Geological Society of America Bulletin 104, 154-165.

von Kármán, T. (1940). The engineer grapples with nonlinear problems. Bulletin of the American Mathematical Society 46, 615-683.

Wadge, G., Jackson, P., Bower, S. M., Woods, A.W. and Calder, E. (1998). Computer simulations of pyroclastic flows from dome collapse, Geophysical Research Letters 25, 3677-3680, doi: 98GL00710.

Wilson, C.J.N. (1980). The role of fluidization in the emplacement of pyroclastic flows: an experimental approach. Journal of Volcanology and Geothermal Research 8, 231-249.

Wilson, C.J.N. (1984). The role of fluidization in the emplacement of pyroclastic flows, 2: experimental results and their interpretation. Journal of Volcanology and Geothermal Research 20, 55-84.

Wilson, C.J.N. (1985). The Taupo eruption New Zealand, 2. The Taupo ignimbrite. Philosophical Transactions of the Royal Society of London A 314, 229-310.

Wilson, C.J.N. (1986). Pyroclastic flows and ignimbrites. Sci. Prog. Oxf. 70, 171-207.

Wohletz, K.H., McGetchin, T.R., Sandford, M.T. and Jones, E.M. (1984). Hydrodynamic aspects of caldera-forming eruptions: Numerical models. Journal of Geophysical Research 89, 8269-8285.

Wohletz, K. and Sheridan, M. (1979). A model of pyroclastic surge. Geological Society of America Special Paper 180, 177-194.

Wohletz, K.H. and Valentine, G.A. (1990). Computer simulations of explosive volcanic eruptions. In: Magma Transport and Storage (MP Ryan, Ed.), Wiley, London, Chapter 8, 113-135.

Woods, A.W., Bursik, M.I. and Kurbatov, A.V. (1998). The interaction of ash flows with ridges. Bulletin of Volcanology 60, 38-51.

Geochemistry Geophysics Geosystems G3
AN ELECTRONIC JOURNAL OF THE EARTH SCIENCES
Published by AGU and the Geochemical Society

Article
Volume 5, Number 8
18 August 2004
Q08004, doi:10.1029/2003GC000637
ISSN: 1525-2027

Numerical modeling of geophysical granular flows: 2. Computer simulations of plinian clouds and pyroclastic flows and surges

Sébastien Dartevelle
Department of Geological and Mining Engineering, Michigan Technological University, 630 Dow Building, 1400 Townsend Drive, Houghton, Michigan 49931, USA

Now at Los Alamos National Laboratory, Geophysics EES-11, MS D443, Los Alamos, New Mexico 87545, USA (sdart@lanl.gov)

William I. Rose
Michigan Technological University, Department of Geological and Mining Engineering, 630 Dow Building, 1400 Townsend Drive, Houghton, Michigan 49931, USA

John Stix
Earth and Planetary Sciences, McGill University, 3450 University Street, Montreal, Quebec, Canada H3A 2A7

Karim Kelfoun
Laboratoire des Magmas et Volcans, OPGC, Blaise-Pascal Université, 5, rue Kessler, 63038 Clermont-Ferrand, France

James W. Vallance
Cascade Volcano Observatory, 1300 SE Cardinal Court, Building 10, Suite 100, Vancouver, Washington 98683, USA

[1] Geophysical granular flows display complex nonlinear, nonuniform, and unsteady rheologies, depending on the volumetric grain concentration within the flow: kinetic, kinetic-collisional, and frictional. To account for the whole spectrum of granular rheologies (and hence concentrations), we have used and further developed for geophysical-atmospheric applications a multiphase computer model initially developed by U.S. Department of Energy laboratories: (Geophysical) Multiphase Flow with Interphase Exchange. As demonstrated in this manuscript, (G)MFIX can successfully simulate a large span of pyroclastic phenomena and related processes: plinian clouds, pyroclastic flows and surges, flow transformations, and depositional processes. Plinian cloud simulations agree well with the classical plume theory and historical eruptions in the upper altitude of the cloud (H_T) versus mass flux diagram. At high mass flux ($>10^7$ kg/s), plinian clouds pulsate periodically with time because of the vertical propagations of acoustic-gravity waves within the clouds. The lowest undercooled temperature anomalies measured within the upper part of the column can be as low as −18 K, which agrees well with El Chichón and Mt. St. Helens eruptions. Vertical and horizontal speed profiles within the plinian cloud compare well with those inferred from simple plume models and from umbrella experiments. Pyroclastic flow and surge simulations show that both end-members are closely tight together; e.g., an initially diluted flow may generate a denser basal underflow, which will eventually outrun the expanded head of the flow. We further illustrate evidence of vertical and lateral flow transformation processes between diluted and concentrated flows, particularly laterally from a turbulent ''maintained over time fluidized zone'' near source. Our comprehensive granular rheological model and our simulations demonstrate that the main depositional process is mainly a progressive vertical aggradation.

Components: 15,254 words, 18 figures, 5 tables, 6 videos.

Keywords: plinian cloud; granular gravity currents; pyroclastic flows; granular rheologies; depositional process; turbulence.

Copyright 2004 by the American Geophysical Union

Index Terms: 3210 Mathematical Geophysics: Modeling; 3220 Mathematical Geophysics: Nonlinear dynamics; 8414 Volcanology: Eruption mechanisms.

Received 17 September 2003; **Revised** 26 April 2004; **Accepted** 21 June 2004; **Published** 18 August 2004.

Dartevelle, S., W. I. Rose, J. Stix, K. Kelfoun, and J. W. Vallance (2004), Numerical modeling of geophysical granular flows: 2. Computer simulations of plinian clouds and pyroclastic flows and surges, *Geochem. Geophys. Geosyst.*, *5*, Q08004, doi:10.1029/2003GC000637.

1. Introduction

[2] In the companion paper, *Dartevelle* [2004] has shown that it is possible to mathematically formulate granular viscous dissipation effects due to the turbulent kinetic motions of grains (i.e., free flights), inelastic collisions between grains of same size, and frictional contacts between grains at high concentrations. Two granular rheological models are used: a rate-of-strain-dependent for the kinetic and kinetic-collisional behavior (i.e., fluidized granular flows) and a rate-of-strain-independent for high concentration frictional-plastic granular flows. Both models are unified through a unique stress tensor for the granular phase [*Dartevelle*, 2004]. As demonstrated herewith, multiphase flow models within the Implicit MultiField formalism [e.g., *Harlow and Amsden*, 1975; *Ishii*, 1975; *Rivard and Torrey*, 1977] and with the granular model from *Dartevelle* [2004] can successfully simulate a large spectrum of pyroclastic phenomena (e.g., plinian and coignimbrite clouds and pyroclastic surges, flows, and deposits), flow transformation processes, and depositional processes.

[3] We focus on multiphase aspects not yet modeled previously and currently subject to debates in volcanology, which are abridged as follows:

[4] 1. Are numerical multiphase models able to simulate a complete and stable plinian cloud (i.e., column and umbrella) over a long period of time into the atmosphere [e.g., *Sparks et al.*, 1997] (see section 3)? This task is difficult as it requires powerful computers able to work in parallel with ad hoc parallelized codes. The ability to properly simulate plinian clouds with multiphase flow codes also depends on the global resolution (i.e., grid size) and the exact turbulence formulation.

[5] 2. Are pyroclastic flows expanded or concentrated? In other words, how do pyroclastic flows move [e.g., *Cas and Wright*, 1988; *Druitt*, 1998; *Freundt and Bursik*, 1998; *Calder et al.*, 2000] (see section 4)? This question has never been answered by previous theoretical models as they only consider one end-member of the concentration spectrum at the time (dilute or concentrated), hence imposing a priori the concentration to be expected in the flow.

[6] 3. What is the main depositional process of pyroclastic flows (i.e., en masse or progressive aggradation) [e.g., *Cas and Wright*, 1988; *Druitt*, 1998; *Freundt and Bursik*, 1998] (see section 4.2.2)? Classically, if pyroclastic flows move as high concentration plug flows, then they deposit their material by en masse freezing and the transport and deposit are essentially the same. Alternatively, if the flow is diluted and fluidized, then, as the particles rain down to form a basal flow, it progressively freezes from bottom to top. In this latter case, the whole flow is stratified, subject to sharp concentration gradients, and the deposit is diachronous.

[7] 4. Is there a continuum between pyroclastic flows and surges [e.g., *Cas and Wright*, 1988] (see section 4.2.1 and section 4.2.3)? And how does flow transformation occur?

[8] These questions will be answered in the discussion sections (section 3.2 for plinian clouds and section 4.2 for pyroclastic flows), where our numerical results will be further discussed in terms of field and remote-sensing observations.

[9] This manuscript is organized as follow. First, we present the numerical methodology, viz., the computer codes (G)MFIX (section 2.1) and the initial and boundary conditions for all our simulations (section 2.2). Second, we discuss the plinian cloud simulations, emphasizing on the validation aspect and compare with various remote-sensing data (section 3). Third, we discuss the pyroclastic flow and surge simulations in the light of the granular rheological model and previous field observations (section 4). Computer-generated movies of all the simulations can be watched. All the symbols, constants, physical parameters, and equations in this manuscript have been thoroughly defined in the companion paper [*Dartevelle*,

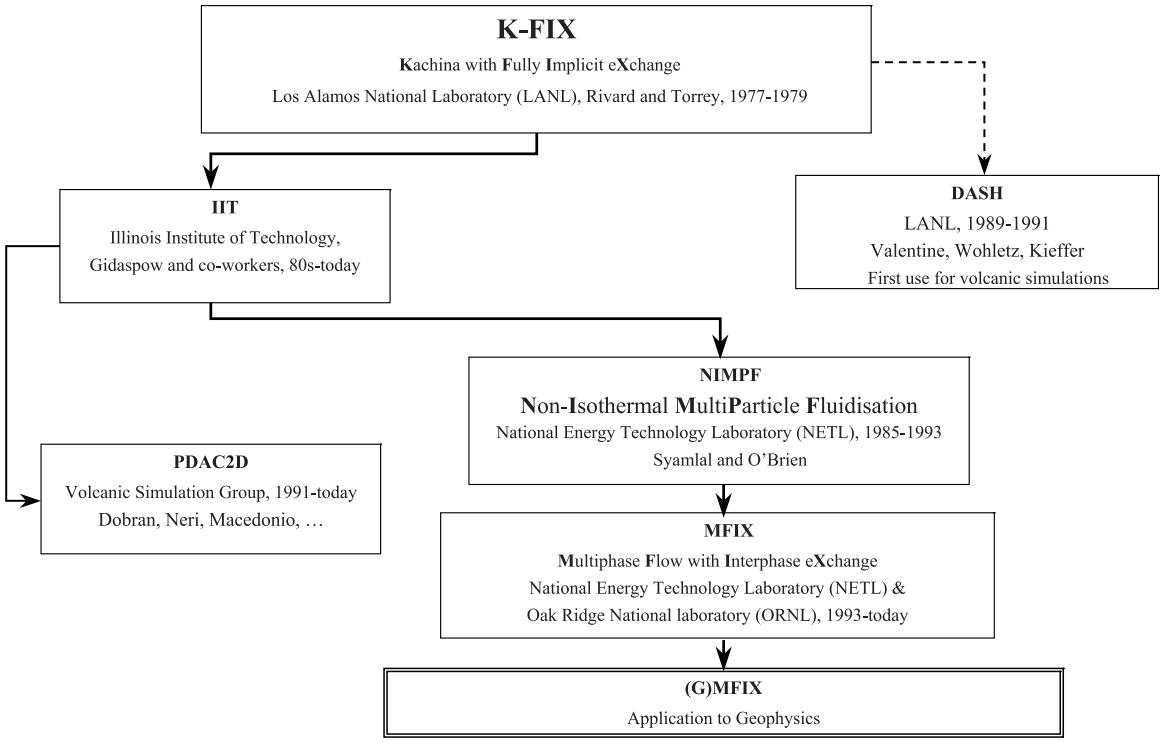

Figure 1. History of the "FIX" family computer codes used in chemical engineering, nuclear reactor dynamic, and geophysics-volcanology. For K-FIX codes, see *Rivard and Torrey* [1977, 1978, 1979] and its use in volcanology (DASH code) [e.g., see *Valentine and Wohletz*, 1989; *Valentine et al.*, 1991]; for the PDAC2D code and its earlier versions in volcanology, see, e.g., *Dobran et al.* [1993], *Neri and Macedonio* [1996], *Neri et al.* [2002], and *Todesco et al.* [2002]; for IIT and related codes, see, e.g., *Gidaspow* [1986]; for NIMPF and MFIX codes, see, e.g., *Syamlal et al.* [1993], *Syamlal* [1994, 1998], *D'Azevedo et al.* [2001], *Pannala et al.* [2003], and *Dartevelle* [2003]. The exact relationship between DASH and K-FIX is simplified as some intermediary codes may be involved (K. Wohletz, Los Alamos National Laboratory, personal communication, 2003).

2004, Appendices A and B] and will not be repeated herewith.

2. Numerical Methodology

2.1. Numerical Technique

[10] MFIX (Multiphase Flow with Interphase Exchange) is a FORTRAN 90 general purpose computer code developed at the National Energy Technology Laboratory and Oak Ridge National Laboratory for describing the hydrodynamics, heat transfer and chemical reactions in fluid-solid systems [*Syamlal et al.*, 1993; *Syamlal*, 1994, 1998]. Initially, MFIX has been adapted from the Los Alamos National Laboratory's K-FIX codes (Kachina with Fully Implicit Exchange) used to model the interaction of water and steam in a nuclear reactor [*Rivard and Torrey*, 1977, 1978, 1979]. We have adapted MFIX into a Geophysical version, (G)MFIX, in keeping all the capabilities of MFIX and adding new ones for typical geophysical-atmospheric applications (work associated with volumetric variations of the gas phase, universal atmospheric profiles, the static *Smagorinsky* [1963, 1993] Large Eddy Simulation turbulence model, the *Zehner and Schlunder* [1970] model, the Sub-Grid turbulent Heat flux; for further details, see also *Dartevelle* [2003, 2004]).

[11] The historical relationship between MFIX, (G)MFIX, K-FIX, PDAC2D, DASH and other multiphase codes is shown on Figure 1. The "FIX" family codes have been used many times in volcanology in the past with success [e.g., *Valentine and Wohletz*, 1989; *Valentine et al.*, 1991; *Dobran et al.*, 1993; *Neri and Macedonio*, 1996; *Neri et al.*, 2002, 2003; *Todesco et al.*, 2002]. The IMF formalism adopted by the "FIX" family codes permits all degrees of coupling between the fields from very loose coupling as occurs in separated flows to very high coupling as occurs in true dispersed flows [*Harlow and Amsden*, 1975; *Ishii*, 1975; *Rivard and Torrey*, 1977; *Lakehal*, 2002]. Scalar quantities (e.g., mass, temperature, granular tem-

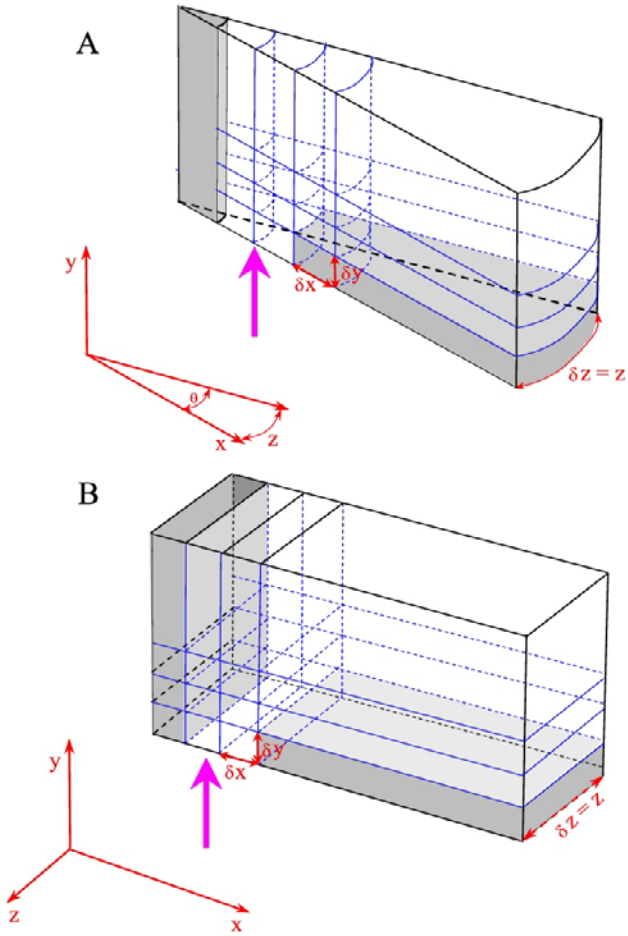

Figure 2. (a) Axisymmetric (Cylindrical) geometry for plinian cloud simulations (PL group). (b) Cartesian geometry for pyroclastic surge and flow simulations (PSF group). For both groups the vent is next to the free-slip left-side vertical wall. See Table 1a for the dimension of the computational domain. δx, δy, and δz represent the elemental length of a computational cell in the X, Y, and Z directions, respectively. As shown in these figures, all simulations are in two dimensions, which means there is no discretization along the Z direction (i.e., Z length = δz).

perature) are computed at the cell center, whereas velocity components are computed on a staggered grid coinciding with the cell boundaries [*Patankar*, 1980].

[12] The discretization of the hydrodynamic equations uses a finite volume method, which divides the physical domain into discrete three-dimensional (3-D) control volumes (i.e., cells) and then formally integrates the governing equations over them. This integration step ensures global conservation of mass, momentum, and energy independence of the grid size [*Patankar*, 1980]. (G)MFIX uses an implicit backward Euler method of time discretization and includes various first-order (e.g., FOU) and second-order (e.g., Superbee, Smart, Minmod) accurate schemes for discretizing the convection terms [*Syamlal*, 1998]. We have favored FOU (First-Order Upwinding) for its stability, better convergence, and because we have not seen any significant differences in our geophysical simulations with the second-order schemes (such as Superbee). A detailed account of the numerical techniques can be found in Appendix B.

[13] MFIX has been extensively validated over the past years [e.g., *Boyle et al.*, 1998]. Grid-independence has been established in Fluid Cracking Catalytic risers [e.g., *Guenther and Syamlal*, 2001] and for plinian clouds simulation (see Appendix A). For pyroclastic flow simulations, the grid resolution on the ground is critical [e.g., *Dobran et al.*, 1993; *Neri et al.*, 2003] because an excessively coarse grid may simply prevent from particle settling and building a deposit. Hence careful grid size independence analysis must be achieved as shown in Appendix A.

Table 1a. Geometry, Initial and Boundary Conditions, and Various Physical Properties Used for All the Simulations[a]

Eruption	Plinian PL Group			Pyroclastic Flows and Surges PSF Group		
	PL_1	PL_2	PL_3	PF_1	PF_2	PF_3 (Inviscid)
Geometry	Cylindrical	Cylindrical	Cylindrical	Cartesian	Cartesian	Cartesian
Radial/horizontal length X, km	20	40	60	18	18	18
Radial/horizontal resolution ΔX, m	30 to 1000	50 to 1000	80 to 1000	10 to 800	10 to 800	10 to 800
Number of grid points in the X direction	145	168	150	950	950	950
Vertical length Y, km	18	25	36	10	10	10
Vertical resolution ΔY, m	30	50	80	2.5 to 1000	2.5 to 1000	2.5 to 1000
Number of grid points in the Y direction	601	501	401	95	95	95
Vent diameter/length r, m	120	400	800	100	100	100
Mixture vertical speed V_y, m/s	110	110	160	50	25	50
Volumetric solid concentration ε_s, vol.%	0.1	0.1	0.1	3.0	3.0	3.0
Grain diameter d, μm	50	50	50	250	250	250
Grain microscopic density ρ_s, kg/m^3	1500	1500	1500	2500	2500	2500
Mixture temperature at the vent T_m, K	900	900	900	900	900	900
Gas pressure at the vent P_g, Pa	10^5	10^5	10^5	10^5	10^5	10^5
Mass fraction of water vapor at the vent	1.0	1.0	1.0	1.0	1.0	1.0
Calculated mixture density ρ_m, kg/m^3	1.74	1.74	1.74	45.2	45.2	45.2
Calculated mass flux, kg/s	3.15×10^6	2.41×10^7	1.39×10^8	2.26×10^7	1.13×10^7	2.26×10^7

[a] See also Figure 2. In Cylindrical geometry the mass flux at the vent is calculated by $\pi.r^2.V_y.\rho_m$, where V_y is defined by equation (1) and ρ_m is defined by equation (2). In Cartesian geometry the mass flux is calculated by $r^2.V_y.\rho_m$, where r^2 is the surface area made by the dimension of a fissure-like vent along the X and Z directions (i.e., 100 m in both directions). The third dimension (Z direction) is made of only one cell; hence there is no discretization of the differential equations along Z. The length in the Z direction is 100 m in Cartesian geometry and is equal to arctg(1)·X in Cylindrical geometry, where X is the length of the domain along the X direction.

[14] All numerical data at each grid point of the physical domain were postprocessed by MATLAB® with interpolation functions to generate graphical results (snapshots and animation movies). Data sampling at specific locations within the data file were exported to spreadsheets to generate all the graphs shown in the next sections.

2.2. Initial and Boundary Conditions

[15] Plinian cloud simulations (PL group) were carried out in 2-D Cylindrical geometry, where the axis of symmetry is a vertical free-slip reflector (left sidewall, Figure 2a). The pyroclastic surge (PS) and flow (PF) simulations (PSF group) were done in a 2-D Cartesian geometry where the left-side vertical wall is a free slip wall (Figure 2b). We have favored the Cartesian geometry because, in all of our simulations, PF and PS are small events which cannot be reconciled with an axisymmetric geometry: they tend not to spread all around the volcano but they are rather channeled and they flow down drainages [*Druitt*, 1998]; that is, they flow in a specific direction. This is also the case in more important eruptions (e.g., Mt. St. Helens) and in analog experiments [*Woods and Caulfield*, 1992; *Sparks et al.*, 1997]. For all simulations, the ground is a no-slip wall, the vertical right-side and horizontal top boundaries are transient free outflow/inflow boundaries, i.e., each scalar (P, T, ρ_g, ε, etc.) within the boundary is equal to the value of the corresponding variable within the next adjacent domain cell. Therefore these boundaries are, at any time and at any altitude, in equilibrium with the atmosphere within the flow domain. Different top boundaries have also been tested, e.g., outflow/inflow at constant pressure and temperature and free-slip wall (closed top boundary). The influence of all these boundary conditions on the global flow dynamic is very minor, which is consistent with other numerical models and previous modeling [*Neri et al.*, 2003; K. Wohletz, personal communication, 2004; unpublished data].

[16] Table 1a details the geometrical, boundary, and initial conditions for all simulations. At the vent, all simulations are carried out with (1) a constant discharge gas pressure balanced with the local atmospheric pressure, (2) thermodynamic equilibrium between gas and pyroclasts, (3) only water vapor in the erupting mixture, (4) constant mass flux at the vent throughout the whole simulation time (i.e., 1 hour for the PL group and 8 min for the PSF group), (5) within the same atmospheric environment assumed to be a dry, quiet and temperate standard atmosphere (Table 1b), and (6), for the PSF group, a nil granular temperature as an initial condition (the end result is insensitive of the

Table 1b. Identical Atmospheric Conditions for All Simulations[a]

Atmospheric Property	Value
Pressure at vent level	10^5 Pa
Temperature at vent level	298 K
Calculated gas density at vent level	1.169 kg/m^3
Vapor mixing ratio at vent level	0 (dry atmosphere)
Tropospheric temperature gradient (0–11 km)	−7 K/km (temperate atmosphere)
Lower stratospheric temperature gradient (19–32 km)	+1.8 K/km
Upper stratospheric temperature gradient (32–47 km)	+2.8 K/km
Tropopause	11–19 km

[a] A temperate, dry, idle standard atmosphere.

initial value chosen for the granular temperature). ''Vent diameter or vent length'' must be understood as the diameter/length measured exactly where the mixture is not bounded anymore by a vertical wall. For instance, in PL_3 simulation (Table 1a), the large diameter of 800 m can be interpreted as the one of a large crater as seen in the 1990 Lascar eruption (which had a 1200 m diameter) [*Sparks et al.*, 1997].

[17] From Table 1a, the only difference between the simulation of a given group is the initial mass flux at the vent. Within the PL group, there is about a factor of ten between each plinian simulation, while within the PSF group, there is a factor two between PF_1 and PF_2 simulation. In order to compare the benefits of a comprehensive granular rheological model, we have performed a third simulation (PF_3) in which the granular phase is assumed to be inviscid and compared with an identical simulation (PF_1, same initial/boundary conditions) which has a full kinetic-collisional-plastic formulation.

[18] These grid size configurations were mostly prescribed by our available computer resources. For the PL group, the overall size of the computational domain has been chosen to ensure that the whole plinian flow would remain inside the domain in order to capture the entire plinian activity (column, umbrella, shape, temperature anomalies) and to capture, with the best possible resolution possible, the column, its edges, and the transition between the jet, the buoyant column and the umbrella. The grid size is uniform along the vertical direction and slowly increases radially away from the axis of symmetry. For the PSF simulations, the grid size is thoroughly nonuniform over the whole computational domain with the highest horizontal resolution on the left-side (10 m over a horizontal distance of 9 km) and the highest vertical resolution at the ground (2.5 m over a height of 100 m). This resolution configuration has been chosen to enable us to capture flow transformations, sedimentation, depositional processes and to capture the exact relationship between PF and PS. Grid size analysis and grid size effects is further detailed in Appendix A.

[19] We do not claim to comprehensively simulate ''real'' plinian clouds or pyroclastic flows and surges with this limited set of initial and boundary conditions and with the limitation of our mathematical model [*Dartevelle*, 2004]. Instead, we humbly aim (at this stage) to reproduce some of the known or expected physics of those volcanic events. Specifically, in this manuscript, we would like to demonstrate the importance of granular rheologies to capture some well-known features of PF and PS (e.g., formation of the deposit, outrun of the dilute part of flow by a more concentrated PF, lateral and vertical flow transformation processes) and demonstrate that multiphase flow models can simulate some of the well-known features of plinian clouds (column and umbrella).

[20] We have carried out all our simulations with only one particle size because we wanted to keep the complexity of the model as ''low'' as possible in order to capture only the fundamental physics of our rheological model (more grain sizes would have implied supplementary assumptions and constitutive equations). Of course, natural granular flows are multisized which may have important effects upon flow dynamics [e.g., *Neri and Macedonio*, 1996; *Neri et al.*, 2003]. Yet such supplementary complexity would have obscured (at this stage) the underlying physics behind granular rheologies. In the long run, supplementary particle sizes may be introduced in our model. In the same vein, the boundary condition at the ground is a flat surface because 2-D topography would not have added anything relevant to our current modeling objectives.

[21] In the following, we define the mean mixture value of a given variable (Ψ) such as speed (U_x or V_y) or temperature (T_m) and the mean mixture

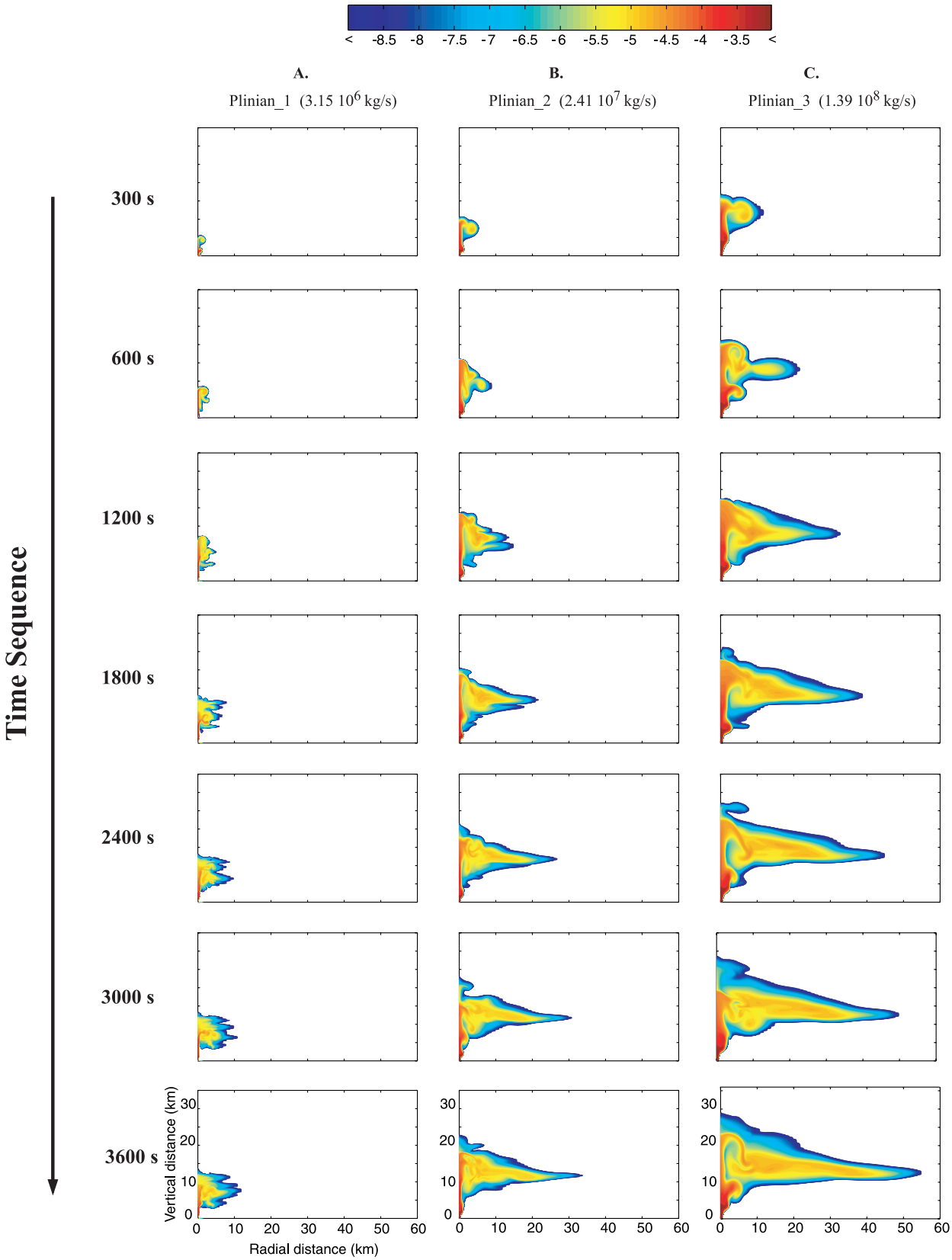
< -8.5 -8 -7.5 -7 -6.5 -6 -5.5 -5 -4.5 -4 -3.5 <
A.
Plinian_1 (3.15 10^6 kg/s)
B.
Plinian_2 (2.41 10^7 kg/s)
C.
Plinian_3 (1.39 10^8 kg/s)
Time Sequence
300 s
600 s
1200 s
1800 s
2400 s
3000 s
3600 s
Vertical distance (km)
0
10
20
30
0 10 20 30 40 50 60
Radial distance (km)

Figure 3

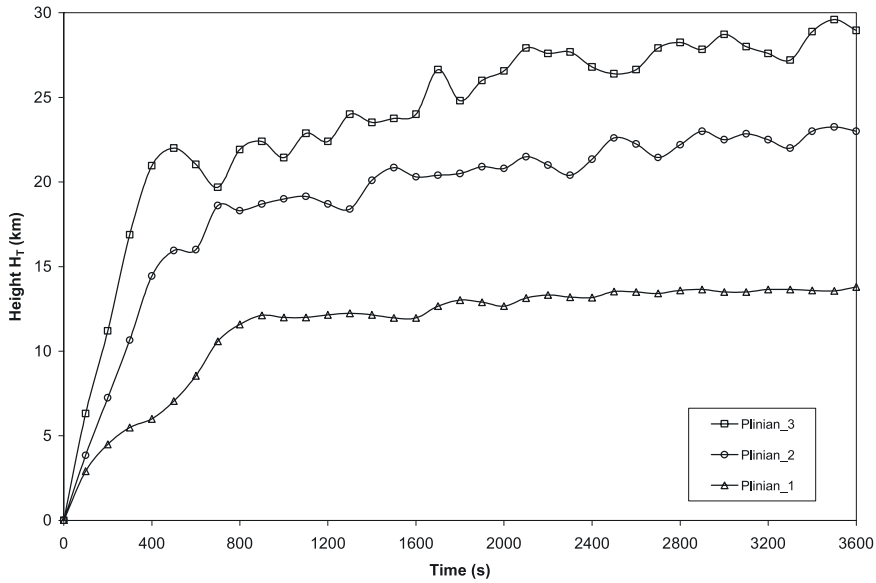

Figure 4. Variation of the top altitude of the column (H_T) with time (between 0 and 3600 s) for the three plinian column simulations. Note the fluctuating and pulsating behavior of PL_2 and PL_3 clouds with time.

density (ρ_m) as [*Valentine and Wohletz*, 1989; *Dobran et al.*, 1993]:

$$\Psi = \frac{\varepsilon_s \rho_s \psi_s + \varepsilon_g \rho_g \psi_g}{\rho_m}, \quad (1)$$

$$\rho_m = \varepsilon_s \rho_s + \varepsilon_g \rho_g, \quad (2)$$

where ψ_s and ψ_g are the corresponding variable of a given phase (all other symbols are defined in the Appendix A of *Dartevelle* [2004]).

3. Plinian Cloud Modeling

[22] Figure 3 represents various snapshots of the logarithm of the volumetric grain concentration, $\log_{10}(\varepsilon_s)$ (from 10^{-2} to 10^{-9}), taken at different times (from 300 s to 3600 s) for three plinian simulations. Figure 4 represents the altitude of the top (H_T) of the plinian column versus time. The following description is also based on the computer-generated movies of three plinian simulation (Movie 1 to Movie 3 for simulation PL_1 to PL_3, respectively).

3.1. General Descriptions

[23] First, simulation PL_1 ("small" eruption, $\sim 10^6$ kg/s). The jet part is quickly decelerated to an altitude of about 1 km from which a rising buoyant convective plume develops. At 200 s, the plume has reached an altitude of 4.5 km (Figure 4). At that time, a partial collapse of the system occurs at the transition between the jet and lower part of the plume, forming small pyroclastic flows (Movie 1). This partial collapse drastically reduces the growth of the column (Figure 4). Once the system is relieved from this excess of materials (400 s), the plume regains enough buoyancy to move upward to higher altitudes. At 2400 s, the whole plinian system stabilizes over time and gently spreads radially with no noticeable change of H_T. Within an hour, H_T is about 13.5 km and the maximal radial distance is about 12 km. The umbrella is clearly sheared as the mixture mean radial speed (U_x)

Figure 3. Time sequence over 1 hour of three plinian clouds. The color code represents the logarithm of the volumetric solid concentration ($\log_{10}\varepsilon_s$): the redder, the more concentrated; the bluer, the more diluted (the blue atmosphere has initially no grains). (a) Simulation PL_1 (3.15×10^6 kg/s). (b) Simulation PL_2 (2.41×10^7 kg/s). (c) Simulation PL_3 (1.39×10^8 kg/s). It is worth noting the heterogeneity in grain volumetric concentration throughout the whole plinian flow (column and umbrella) and the very low grain concentration veil at the top of the plinian column and surrounding its umbrella.

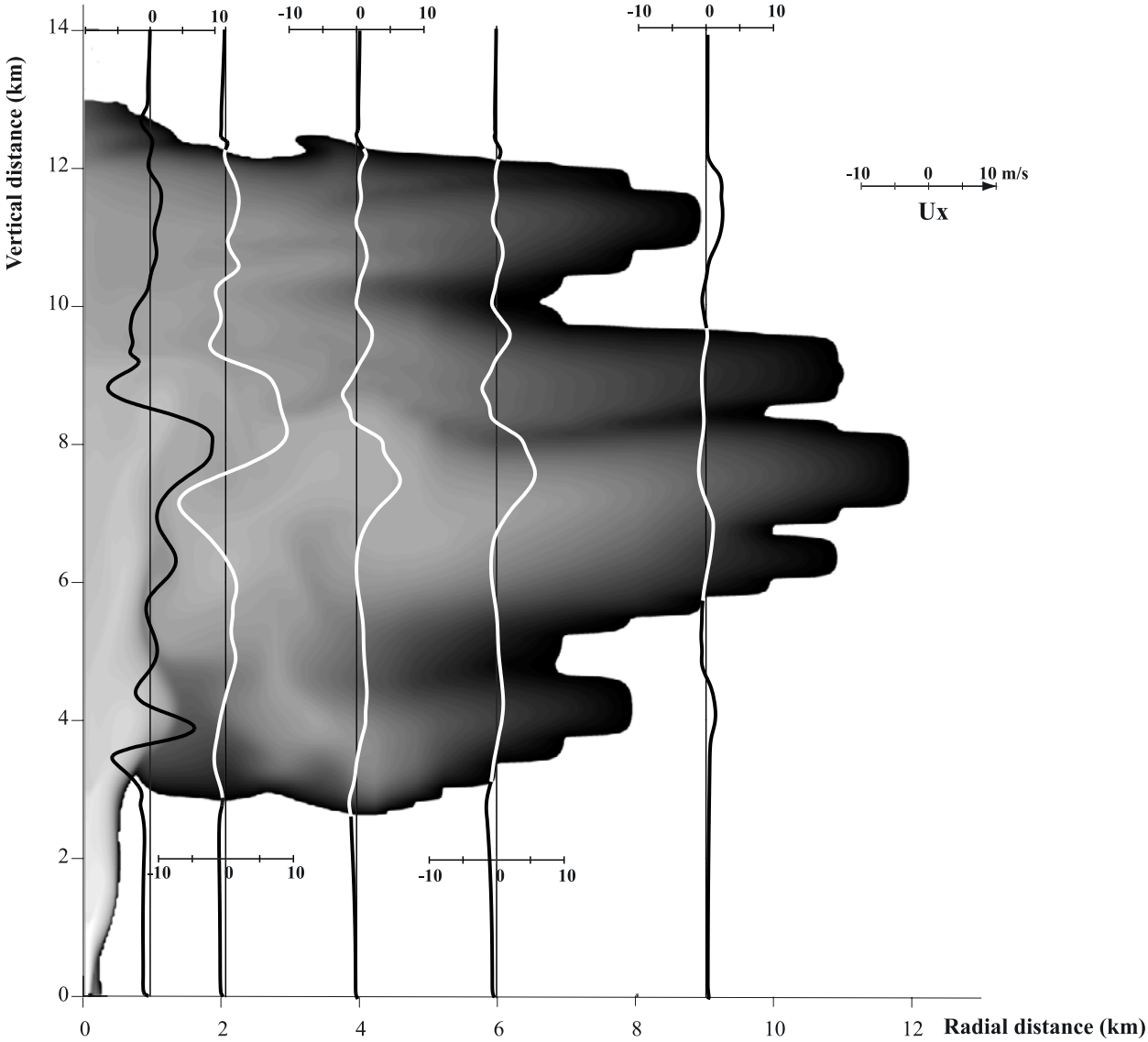

Figure 5. Radial speed profiles (U_x in m/s) along the vertical direction (between 0 and 14 km) at different radial positions within the plinian cloud for simulation PL_1. The gray background color of the cloud represents the intensity of volumetric solid concentration gradient in any direction (the steeper the gradient, the darker). Note backward radial draughts shearing the umbrella, which explains its finger-like morphology.

shows very complex backward and forward profiles (Figure 5). For instance, after one hour, at a radial distance of 6 km, backward currents are well-developed at an altitude of 6, 9, and 10 km, which explains this fingering shape. Also, note the systematic backward current at the bottom of the umbrella.

[24] From Movie 1, turbulence and eddy developments are the most active between a radial distance of 1 and 2 km, i.e., within the transitional zone between the column and the umbrella. This explains the complex radial speed profiles at a distance of 1 km in Figure 5 where an important entrainment of air in the column between an altitude of 2 and 3.8 km and reentrainment of pyroclastic materials to the column at higher altitudes occurs (e.g., at altitudes of 4.4, 5.5 km, and between 8.5 and 10 km). These radial speed profiles, backward currents within the umbrella, and multilayered umbrellas are in a qualitative agreement with the experimental observations of *Holasek et al.* [1996]. However, in PL_1 simulation, it can be seen from Figure 3 and Movie 1 that multiumbrellas are formed very early as the column rises in the atmosphere. In addition, their

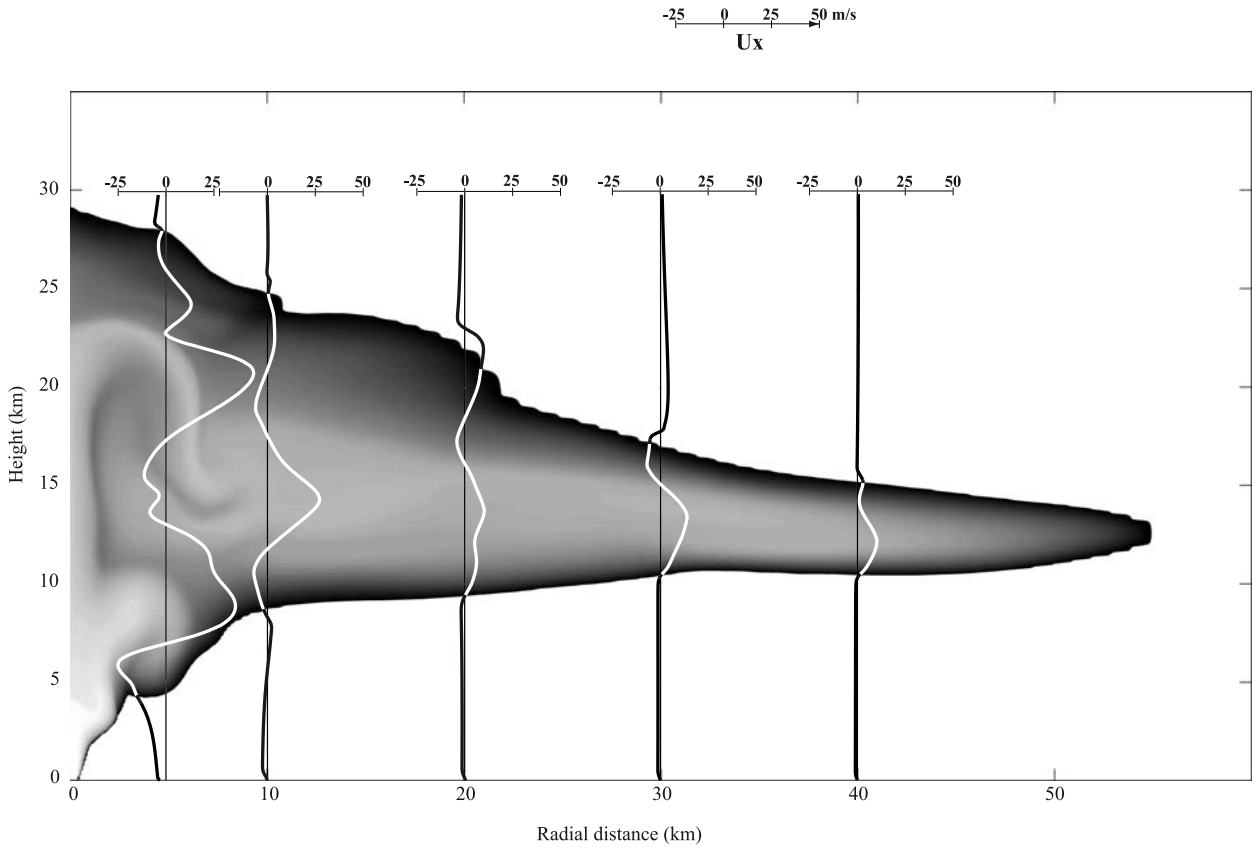

Figure 6. Radial speed profiles (U_x in m/s) along the vertical direction (between 0 and 30 km) at different radial positions within the plinian cloud for simulation PL_3. Same gray background color as in Figure 5.

development is strongly dependent on the exact state of turbulence and eddies within the clouds. Hence the multilayered umbrellas are caused by the nonlinear dynamics within the clouds and cannot solely be attributed to a secondary sedimentation of particles along the edges of the column from another, higher up, preexisting umbrella as suggested by *Holasek et al.* [1996].

[25] Second, the simulation PL_3 which has a mass flux ~100 times higher than PL_1 (i.e., $\sim 10^8$ kg/s). Because the jet suffers strong deceleration while ''pushing'' against the atmosphere, it converts nearly all its initial kinetic energy into heat. Hence the top of the jet is characterized by much higher pressure than the ambient (e.g., after 3600 s, it has an excess of 15 hPa at 2.4 km) [*Valentine and Wohletz*, 1989]. Above the top overpressurized jet, the plume drastically expands and accelerates outward (altitude 4 km in Figure 3c). It therefore reduces its density and becomes positively buoyant (e.g., note the ''bulgy'' shape of the column above the jet between 4 and 6 km in Figure 3c). At 300 s, the plume has reached an altitude of ~17 km (see Figure 4) and starts to spread laterally to form an umbrella. However, the plume is still moving upward to an altitude of 22 km owing to its inertia. In Figure 3c (600 s), the top of the column is therefore 5 km higher (i.e., 21 km) than the umbrella which lies between 12 and 16 km. Afterward, the column is gently growing to higher altitudes with the formation of secondary diluted clouds topping the column itself (see Figure 3c at 2400 s and Movie 3). After one hour, the plinian column has reached a maximum altitude of about 29 km and a radial distance of about 52 km.

[26] Figure 6 represents radial speed profiles along the vertical direction measured at different positions after one hour. Again, the umbrella is clearly sheared. It has a well-developed positive radial speed of 26 m/s at 10 km decreasing to less than 10 m/s at 40 km away from source. U_x tends to be maximum in the central part of the umbrella and to be negative at the top and bottom where friction with the atmosphere is maximum. Because of the active turbulent area between the column and umbrella (e.g., at a radial position of 5 km), U_x shows complex back and forth speed profiles with an important entrainment of fresh air at the bottom

of the column, specially where it expands the most (between 4 and 7 km of altitude).

[27] Figure 7 shows V_y profiles taken after one hour at different heights within PL_3 cloud. At an altitude of 1 km within the jet, V_y has a classical Gaussian shape profile where V_y is maximum at the center of the column and exponentially decreases toward the edges. At 4 km, at about the transition between the jet-plume, V_y tends to be minimal at the center of the column and maximal at the edges where entrainment is the most active. This is consistent with negative U_x profile at the bottom just next to the column as in Figure 6. At 6 km, V_y is positive along the whole radial direction (from center to edges) owing to the cloud expansion and the active entrainment of fresh air. At higher altitude vertical speed profiles tend again to Gaussian profiles, although disturbed by turbulence, reentrainment, and the formation of vertical convective supercells between the plume and the umbrella.

[28] As noted by *Dobran et al.* [1993] and as seen in Figure 8, it is difficult to determine exactly the transition between the strongly thrusting jet and the buoyant plume itself. Figure 8 shows the variation along the vertical direction inside the plinian column PL_3, at time 3600 s, of the averaged mixture temperature (Figure 8a), the pressure anomaly relative the ambient (Figure 8b), the averaged mixture vertical speed (Figure 8c), and the density differences relative to the ambient (Figure 8d) of the macroscopic gas phase density ($\Delta\rho_g$, dashed curve) and the macroscopic solid phase density ($\Delta\rho_s$, plain curve) of the column. Just above the vent (80 m), the jet is overpressured relative to the ambient (+59 hPa, not seen on Figure 8b) which is also shown by a slight decrease in V_y owing to the conversion of kinetic energy into pressure. Higher up, the jet tends to reequilibrate with the ambient showing a sharp decrease in ΔP_g (down to +0.96 hP) and a slight increase in V_y. The thrusting decelerating jet into the atmosphere causes a second pressure maximum (+15 hPa) at a height of 2.4 km suggesting a classical flaring characteristics or diamond-like structure of overpressured jets [*Valentine and Wohletz*, 1989]. At 3.9 km, ΔP_g decreases to a negative value (decompression) down to −12 hPa, hence the column expands, which drastically reduces the density of the system in making the solid phase positively buoyant relative to the ambient (Figure 8d). The expansion of the system also reduces the temperature by nearly 200 K (Figure 8a), hence causing a slight decrease in buoyancy of the gas phase (Figure 8d). Owing to the inertia of the jet, at a height of 3.9 km, V_y is minimum at the center of the column while at its edges, V_y is ∼+73 m/s. The radially fast expanding system and the sharp increase of buoyancy cause the system to reaccelerate upward and outward from slightly less than 0 m/s to 80 m/s at 6.4 km causing a third maximum in ΔP_g at ∼9.8 km. Clearly, between the top of the thrusting jet and the fully buoyant plume, there is a transitional zone which extends between the second maximum in pressure (altitude 2.4 km) and the altitude of full positive buoyancy (i.e., 3.9 km).

[29] The intermediate plinian simulation (PL_2) presents very similar features as PL_3 (see Movie 2 and Figure 3b). The transition between the jet and the plume is at about 2 km with a well developed "swelling" at the top of the jet owing to the expansion of the plume. Both PL_2 and PL_3 simulations clearly show a pulsating behavior with time (see Movie 2, Movie 3, and Figure 4).

3.2. Discussion

3.2.1. Top Altitude Versus Mass Flux

[30] Plinian column upper heights (H_T) have been often related to the mass flux at the vent because this flux represents the amount of energy released and available to the plinian column. Figure 9 represents H_T of the plinian column versus the inferred mass flux at the vent for different historical eruptions and our plinian simulations (PL_1, PL_2, and PL_3) where H_T is measured at 3600 s. Also shown on Figure 9, the best fit curve between the past eruptions [*Wilson et al.*, 1978; *Settle*, 1978; *Sparks et al.*, 1997] and two curves from *Morton et al.*'s [1956] theory for two temperatures at the vent [from *Wilson et al.*, 1978]. Knowing the uncertainties for historical eruptions to infer the exact H_T and, most importantly, the mass flux at the vent, the top altitude predicted by our model is in excellent agreement with past eruptions and quite surprisingly with *Morton et al.* [1956] theory which was initially developed for plume within the troposphere only [*Sparks*, 1986]. From Figure 9, we may conclude that (G)MFIX model can accurately be compared with classical plume theory [e.g., *Morton et al.*, 1956; *Wilson et al.*, 1978; *Sparks*, 1986] and most importantly real observations.

3.2.2. Temperature Anomalies

[31] Temperature anomalies at the top of the column are important features to capture as they can

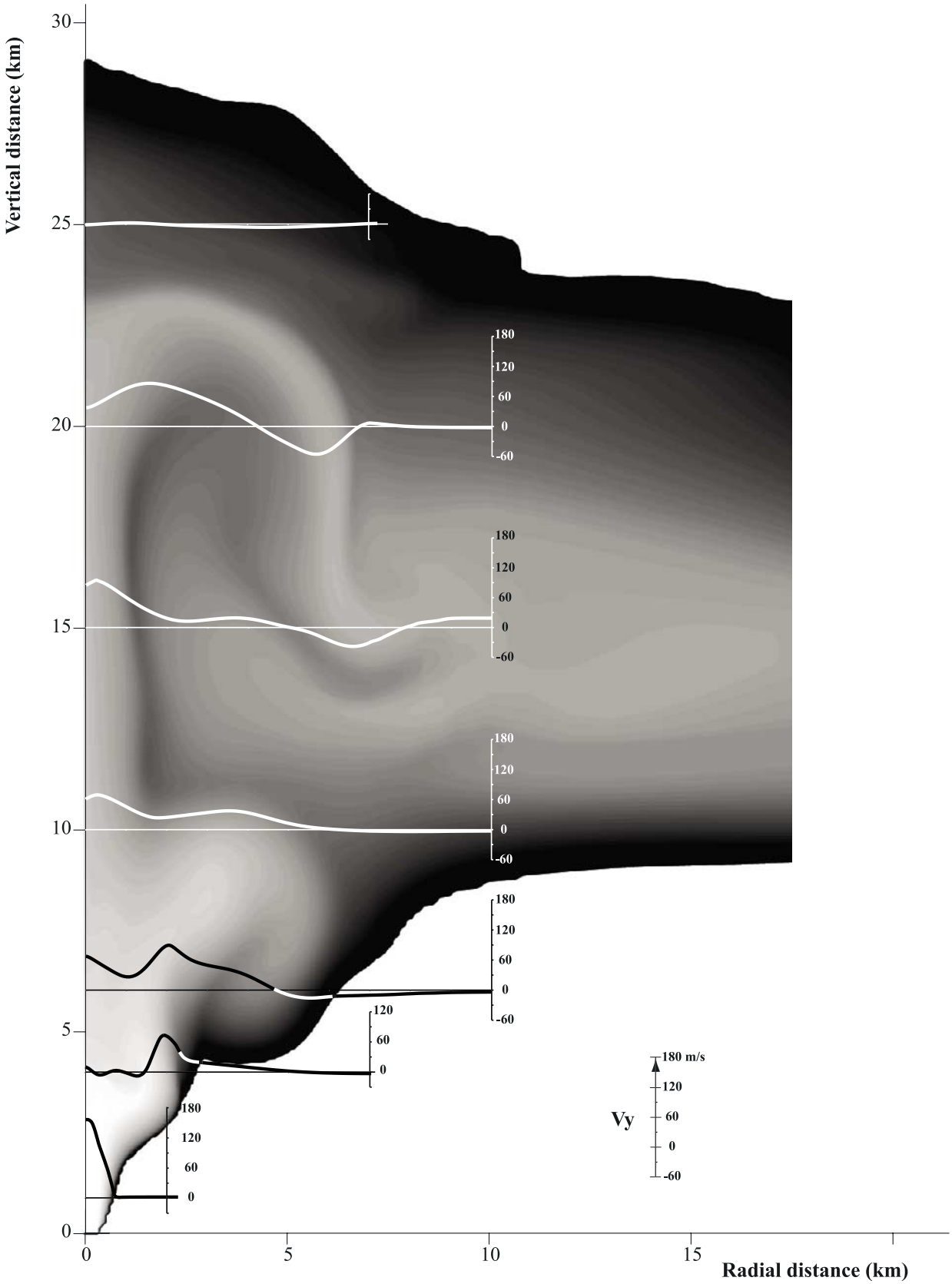

Figure 7. Vertical speed profiles (V_y in m/s) along the radial direction (between 0 and 10 km) at different altitudes within the plinian cloud for simulation PL_3. Same gray background color as in Figure 5.

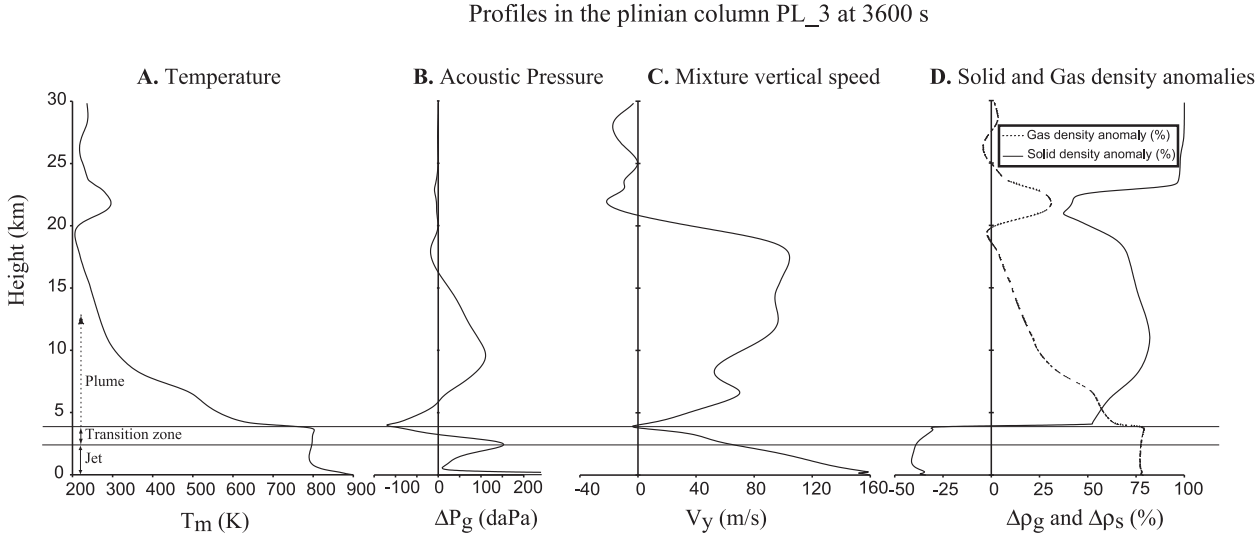

Figure 8. Vertical profiles within the plinian column PL_3 taken at 3600 s. (a) Averaged mixture temperature (T_m in K) calculated by equation (1). (b) Acoustic pressure: difference between the gas pressure inside the column and the undisturbed atmospheric pressure ($\Delta P_g = P_g - P_{atm}$ in daPa, where 100 daPa = 1000 and Pa = 10 hPa). (c) Averaged mixture vertical speed (V_y in m/s). (d) Density anomalies: difference between the atmospheric density and the gas macroscopic density within the column ($\Delta\rho_g = 1 - \varepsilon_g\rho_g/\rho_{atm}$) or the solid macroscopic density ($\Delta\rho_s = 1 - \varepsilon_s\rho_s/\rho_{atm}$) within the plinian column (in %). Note at 3.9 km, where the system is expanding the most, the sharp decrease of temperature (by nearly 200 K), hence the slight decrease of buoyancy of the gas phase but the dramatic increase of buoyancy of the solid phase (dilution).

be inferred by satellite remote sensors. This would provide a supplementary way to compare with real data. Figure 10 and Movie 4 show the temperature anomalies relative to the ambient (ΔT) versus time for the simulation PL_3. In Figure 10, we match H_T variation with ΔT measured at the "tip of the top" of the plinian column. During the early stages, the column rises into the atmosphere where the ambient pressure decreases, hence the column expands which causes a sharp decrease of temperature at the top of the column: at 500 s and a height of 22 km, the top of the column is undercooled relative to the ambient by 11 K. As the column drops (to 19.6 km at 700 s), the column contracts and adiabatically warms up (+19 K). Since the column PL_3 has a natural tendency to pulsate, H_T changes with time, so does ΔT (Figure 10). From Movie 4, these temperature anomalies can be seen throughout the whole cloud. In particular, vertical convective supercells are developed between the column and the umbrella where the downdraughts and updraughts are warmer and colder, respectively, than the ambient.

[32] *Holasek and Self* [1995] have measured temperature anomalies between −6 K and −15 K in Mt. St. Helens plume and, for El Chichón, *Woods and Self* [1992] have inferred temperature anomalies as low as −20 K. Those data match very well with the −11 K measured at the "tip of top" of our simulated plinian column (PL_2 and PL_3), but also with the temperature anomalies deeper inside the PL_3 column which are as low as −18 K (not shown on Figure 10). Simulation PL_2 shows the same trend of ΔT variations at the top of the column but within a smaller temperature span (−9 K and +15 K). Simulation PL_1 only shows small temperature anomalies as it rises in the atmosphere (−10 K) and after 500 s, the top of the cloud has the same temperature as the ambient.

3.2.3. Nonuniform Clouds and Remote Sensors

[33] A close inspection of the umbrellas in Figure 3, Movie 1, Movie 2, and Movie 3 suggests that plinian clouds are very heterogeneous in terms of the volumetric solid concentrations both in time and space (vertical and lateral variations), even far away from the column. This is an important result for remote-sensing techniques which assume the cloud is somehow homogenous within the pixel where measurement is carried out. For instance, the retrieval of sizes and particle burden within volcanic clouds with the AVHRR band 4 and 5 [*Wen and Rose*, 1994] relies on a perfectly homogenous single layer umbrella, which is not the case in Figure 3a (multilayered umbrellas) or Figure 3b

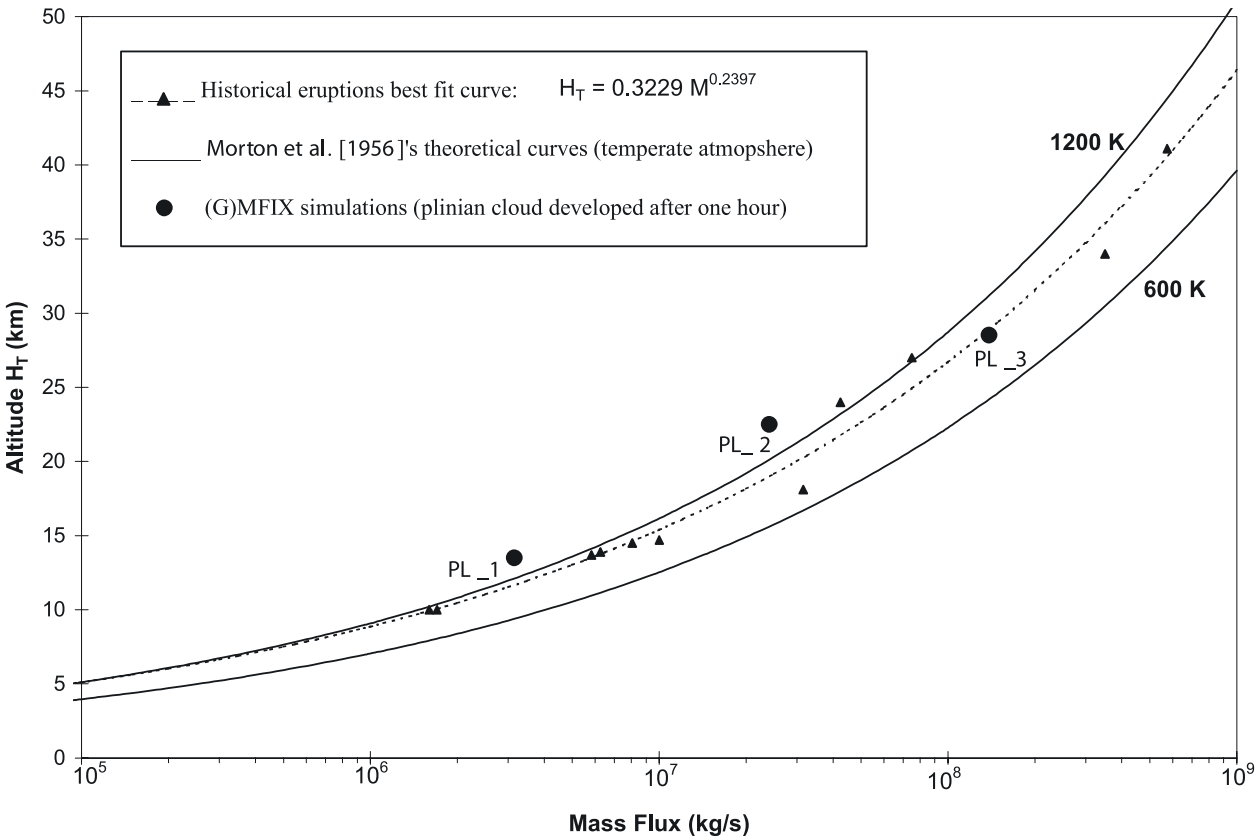

Figure 9. Top altitude of the plinian cloud (H_T in km) versus mass flux at the volcanic vent (kg/s). Triangles are for historical eruptions from which H_T and the mass flux have been inferred from field studies and remote-sensing observations (i.e., not inferred by some previous modeling) (data from *Wilson et al.* [1978], *Settle* [1978], and *Sparks et al.* [1997]); the dashed curve is the best regression fit between these historical eruption data; the plain curves are from the *Morton et al.* [1956] theory calculated for two initial magma temperatures at the vent (600 K and 1200 K); and the circles are for (G)MFIX's three plinian simulations. Knowing all the uncertainties of historical eruptions for determining the mass flux at the vent and H_T, we may conclude that there is an excellent agreement between (G)MFIX's simulations and past historical eruptions.

and Figure 3c, which show complex concentration profiles within the first 10 to 20 km from the source. Another widely used remote-sensing technique like cloud temperature retrieval relies on a fully opaque and homogenous cloud where it is the densest [*Sparks et al.*, 1997]. However, it is well-known [*Sparks et al.*, 1997] that plumes present at their tops low ash concentrations regions, which is fully confirmed by our numerical models (Figure 3 for all three plinian simulations). Consequently, the factual temperature measured by remote sensors is at an undetermined depth within the plume where it becomes fully opaque and is not necessarily measured at the "tip of the top" of the plume (as shown in Figure 10). Hopefully, in a near future, multiphase flow modeling will provide further useful hints about the nonuniformity of plinian clouds which may eventually help for the development of better and more accurate retrieval remote-sensing algorithms.

3.2.4. Unsteady Clouds

[34] Strong plinian columns tend to be highly unsteady and pulsate with time [*Rose et al.*, 1995; *Zurn and Widmer*, 1996; *Tahira et al.*, 1996; *Johnson*, 2003]. This unsteady behavior is also well known by field volcanologists who have observed that many plinian fall deposits exhibit variation in particle size as a function of the stratigraphic height. Usually, reverse grading is more common and is interpreted as due to an increasing eruption intensity with time [*Cas and Wright*, 1988; *Sparks et al.*, 1997]. That is exactly what is shown for PL_3 in Figure 4 and Figure 10, where, at 700 s, the altitude is 19.8 km and within

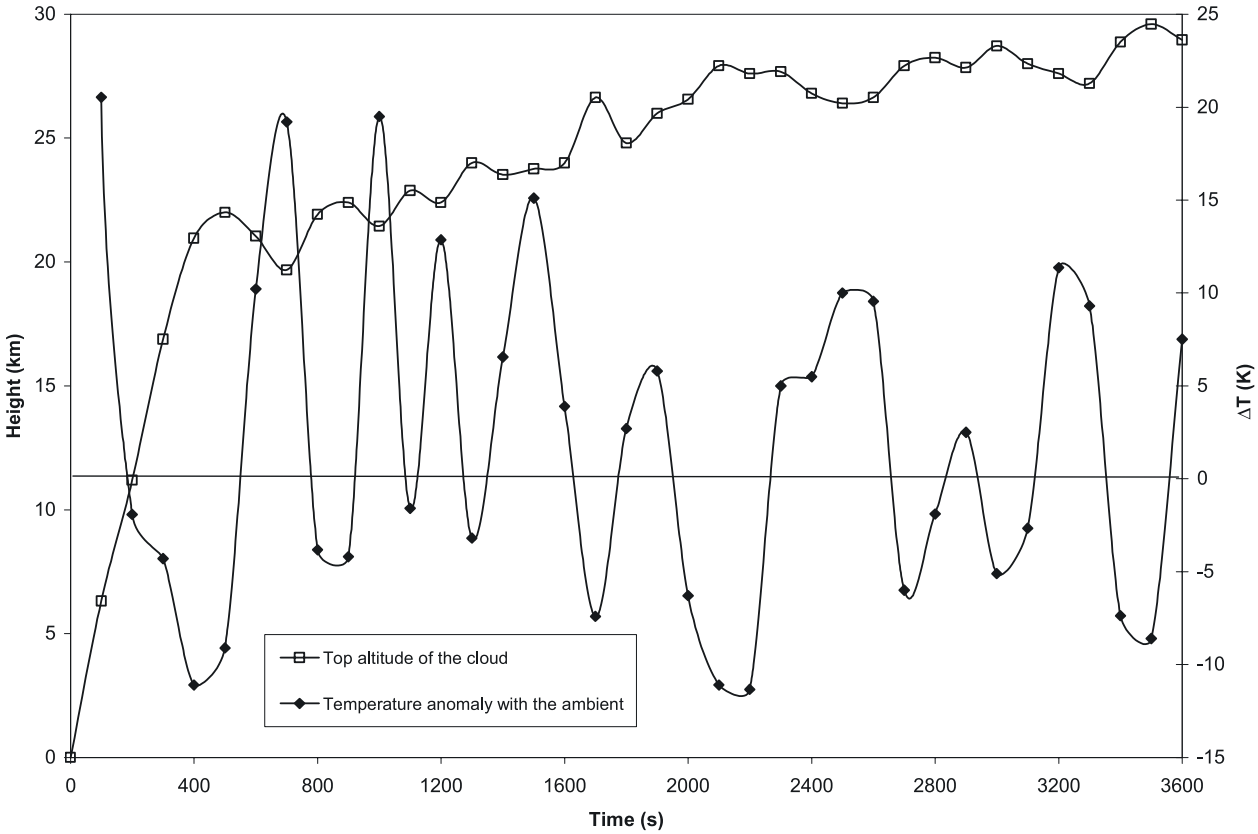

Figure 10. Top height of the PL_3 cloud (H_T, left vertical axis) and temperature anomalies at the top of the cloud relative to the ambient ($\Delta T = T_m - T_{atm}$, right vertical axis) versus time (between 0 and 3600 s). The horizontal line represents $\Delta T = 0$ K.

the next 2900 s the altitude increases to about 29 km. It is even possible that PL_3 cloud has not yet reached its maximum altitude after one hour of simulation.

[35] Another interesting feature of plinian simulations PL_2 and PL_3 are the small vertical bursts and pulsations of the column of about ±1 to 3 km and with a periodicity of about 5 min (Figure 4, Figure 10, and Movie 2 to Movie 4). *Rose et al.* [1995], using real-time radar observations, showed that the altitude of Crater Peak September 12, 1992 eruption column fluctuated within ±2 km, which is consistent with our simulations. Such vertical gravity-acoustic waves as seen in Movie 2 and Movie 3 are also well-confirmed by measurement of acoustic and worldwide Rayleigh waves generated by powerful eruptions [e.g., *Zurn and Widmer*, 1996; *Tahira et al.*, 1996; *Johnson*, 2003]. Typically, in the cases of strong eruptions such as Mt. St. Helens [*Mikumo and Bolt*, 1985] and Mt. Pinatubo [*Tahira et al.*, 1996; *Zurn and Widmer*, 1996], more than 10 hPa of pressure anomalies with a periodicity of a few minutes have been measured. The magnitude of those measured pressure anomalies are also confirmed by our simulations as seen in Figure 8b. Those vertical acoustic-gravity waves are recognized as a positive feedback, self-organized, and self-excited natural oscillator [*Zurn and Widmer*, 1996]. For instance, the rising and expansion of the plume within the atmosphere excites a large spectrum of acoustic and gravity waves (i.e., plume forcing of the atmosphere). On the other hand, the plume experiences harmonically varying buoyancy forces which makes the plume fluctuate in height (i.e., atmosphere forcing of the plume). This latter forcing is caused by harmonic pressure fluctuation within the plume and by the difference between compressibility of the atmosphere and the plume [*Zurn and Widmer*, 1996]. In addition, such an effect may be enhanced by the unsteadiness and nonuniform compressibility of the plume. These harmonic variations of the plume will again trigger new acoustic and gravity waves (positive feedback).

[36] Our simulations suggest that these periodic fluctuations as well as the global progressive increase in altitude of the column should not be ipso facto interpreted as variations at the vent level (e.g., widening of the vent, V_y or mass flux

variations) but should rather be seen as an inner, nonlinear, and chaotic feature of strong plinian clouds. In all our simulations, the vent conditions were maintained constant over the whole simulation time. Clearly, from Movie 3, it can be seen that the trigger mechanism of the gravity-acoustic waves is the pressure anomalies between the jet and the plume and not any oscillating phenomena inside the volcano. Our results are in complete agreement with the observation of *Zurn and Widmer* [1996] for the 1991 climactic eruption of Mt. Pinatubo.

[37] This is a new aspect of the physics of the plinian cloud dynamics, which has never been modeled before. It also confirms the significance of pressure anomalies for the control of the dynamic of the plinian cloud and therefore confirms the importance of including such phenomenon in an ad hoc mathematical model [*Valentine and Wohletz*, 1989].

4. Pyroclastic Flow and Surge Modeling

[38] In Figure 4 of the companion paper, *Dartevelle* [2004] has shown that the granular rheological behavior and the coupling with the gas phase turbulence are deeply dependent on the volumetric grain concentrations (ε_s). It is possible to recognize different regimes which overlap each other. First, the purely kinetic regime for very dilute suspension ($\varepsilon_s < \sim 10^{-3}$ vol.%) where collisions do not occur, the granular temperature tends to be maximized, and so does the granular shear viscosity. Second, the transitional kinetic-collisional regime, $10^{-3} < \varepsilon_s < 1$ vol.%, collisions progressively become more and more important so that the granular temperature is decreased, and so is the shear viscosity. Third, the predominantly collisional regime, $1 < \varepsilon_s < 50$ vol.%, collisions are predominant so that the granular temperature is decreased to negligible values (because of inelastic collisions), and the granular shear viscosity has reached a minimum. Fourth, the frictional regime, $\varepsilon_s > 50$ vol.%, the plastic behavior becomes more and more predominant, hence shear frictional viscosity asymptotically goes to infinity, so does the strength of the granular material, and at ~64 wt.% (the maximum possible volumetric concentration for a randomly packed structures), the granular ''flow'' freezes (i.e., granular deposit). Hence, in this view, friction only acts as a physical process between the collisional flowing regime and a static deposit.

[39] Following *Sparks et al.* [1997], the pyroclastic surges belong in the kinetic and kinetic-collisional regime (i.e., $\varepsilon_s \ll 1$ vol.%), where the random chaotic kinetic motion of grains is the dominant mechanism of momentum and energy transfer between sheared layers. Pyroclastic flows belong to the predominantly collisional and plastic-frictional regime ($1 < \varepsilon_s < 60$ vol.%). Hence pyroclastic flows cover a quite appreciable range of volumetric grain concentrations and can be still seen as partially fluidized flows in their low concentration range.

[40] In the interpretation of our numerical results (PF_1, PF_2, and PF_3), we will only focus on four themes: (1) relative dynamic behavior between PS and PF and flow transformation, (2) formation of a deposit, (3) dynamics close to the source, and (4) the relevance of a nonlinear rheological model for granular flows (viscous or inviscid). Figure 11 and Figure 12 show the development of PF/PS over 8 min for simulations PF_1 and PF_2, respectively. Each curve represents a solid volumetric iso-concentration contour line between 10^{-9} and 10^{-1}. Movie 5 and Movie 6 show the development of the PF_1 and PF_2 simulations, respectively. Figure 13 (PF_1) and Figure 14 (PF_2) show the height variation of granular volumetric concentration, average mixture horizontal speed, granular temperature, and granular shear viscosity taken at different positions and different times.

4.1. General Descriptions

4.1.1. Simulation PF_1 (Figures 11a–11b, Movie 5, and Figure 13a)

[41] After 30 s, the flow has reached a distance of 1.4 km with a well-developed head of 400 m high and with ε_s ranging from 9×10^{-5} vol.% at the base to $\sim 10^{-2}$ vol.% higher up (Figure 13a). The horizontal speed of the head is 9 m/s at the base and 34 m/s at a height of 20 m. The head has a well-developed overhang (nose) acting as a funnel for air (preferential entrainment). Consequently, the bottom of the head is much more diluted and slower than higher up. According to our classification scheme, this head has all the properties of a surge (predominately kinetic and mildly collisional). At 80 s, the head is 3.7 km away from source and has so much entrained fresh air that its concentration has decreased by a factor 10^3 (e.g., $\varepsilon_s \sim 10^{-5}$ vol.%). Such drop in concentration has drastically decreased the horizontal momentum (e.g., $U_x \sim 13$ m/s). At 100 s, the front of the flow is at a distance of 4.3 km with a basal collisional

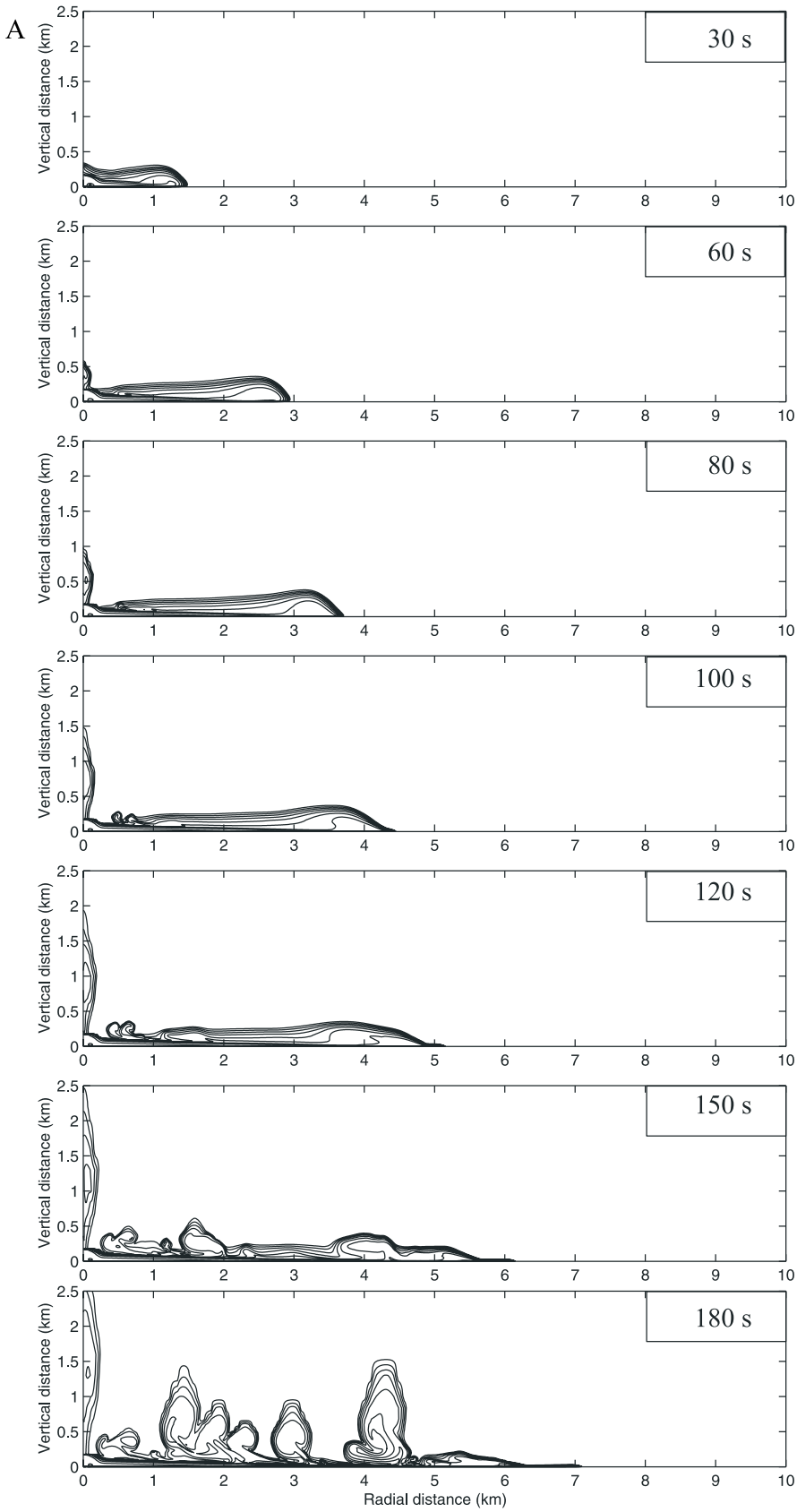

Figure 11
123

pyroclastic flow outrunning what remains of the dissipated head (see Figure 13a and Figures 11a–11b at 80s, 100s, 120s). The basal pyroclastic flow has a concentration of ~30 vol.% and travels at a maximum horizontal speed of ~45 m/s. Because this basal undercurrent lies in the purely collisional regime its granular temperature and granular shear-viscosity are very low ($\ll 10^{-4}$ m^2/s^2 and $\sim 10^{-3}$ Pa·s, respectively; see Figure 13a) [*Dartevelle*, 2004]. The other striking feature is that within a height of 5 m the volumetric concentration decreases from 30 to 0.1 vol.%, suggesting a sharp concentration gradient between the basal PF and the overlying PS. In other words, there is no progressive transition between the basal dense PF (purely collisional regime) and the overlying diluted PS (kinetic regime). We will explain below how and where this basal concentrated flow is formed (section 4.2.1). At 180 s, the basal PF has outrun the rest of the flow and has traveled 7.2 km. Closer to source, phoenix clouds start to form because the flow system is losing its horizontal momentum which leads to sedimentation on the ground and dilutes the upper part of the flow which becomes positively buoyant [*Dobran et al.*, 1993]. At 240 s, the flow front is detached from the rest of the flow system, and being not fed anymore, it progressively becomes more and more dilute until it comes to rest at about 300 s and 8.8 km. Note the inward draughts at the base of the rising phoenix cloud (between 3.5 and 6 km) which produces a necking effect within the rising coignimbrite cloud [*Dobran et al.*, 1993] as seen for instance during coignimbrite ash cloud development in the 1991 Mt. Pinatubo eruption [*Woods and Wohletz*, 1991; *Sparks et al.*, 1997]. At 480 s, the system forms a granular deposit ($\varepsilon_s \sim 60$ vol.%) between 3.6 and 5.4 km with a thickness as high as 12.5 m and a second minor deposit between 6.6 and 7 km with a thickness of about 7.5 m.

4.1.2. Simulation PF_2 (Figure 12, Movie 6, and Figure 14a)

[42] After 10 s, the head of the flow is well formed but more dilute, smaller, and slower than in PF_1: 80 m high, with concentration 2×10^{-5} vol.% at the base, and 10^{-3} vol.% at the nose level, traveling with horizontal speeds of 5 m/s at the base and 12 m/s at the nose level. This head will eventually be outrun by a denser basal pyroclastic flow but much quicker than PF_1: at 40 s, this basal underflow has a concentration of 15 vol.% with a maximum horizontal speed of 39 m/s, and granular shear viscosity of 2×10^{-3} Pa·s. The shear viscosity has decreased relative to the head because collisions dissipate the granular temperature; from ~1 m^2/s^2 at 30 s (PS) down to $\sim 10^{-3}$ m^2/s^2 at 40 s (PF). This undercurrent will eventually travel to 8 km (300 s), then be detached from the main system and as it is progressively diluted, it will be halted by inward winds at 9 km. In the meantime, the system starts to develop a phoenix cloud at 1.5 km from the source (much closer than PF_1 owing to the lower initial momentum). Secondary minor phoenix clouds are developed at a distance of about 4.8 km at 210 s and at 6 km at 480 s. Note that those phoenix clouds are much less vigorous than in PF_1 and tend to bend inward and even slide backward, pushed by draughts (Movie 6). At 480 s, the system forms a granular deposit ($\varepsilon_s >$ 60 vol.%) between 3.5 and 4.7 km with thickness of up to 10 m.

[43] The simulation PF_2 produces the same kind of results as PF_1 but much earlier in the time sequence (deposit, basal PF outrunning the head of the flow, etc.), more concentrated, a slower (head, PF) with a deposit having a smaller extent. Owing to the lower horizontal momentum of the PF_2 basal undercurrent, it is detached from the flow system at a later time (300 versus 240 s).

4.2. Discussion

4.2.1. Proximal Deflation Zone and Flow Transformations (Lateral and Vertical)

[44] A denser (predominantly collisional PF) basal underflow systematically outran downstream the initially more diluted suspension current (purely kinetic PS). This is well documented in various eruptions, e.g., in Montserrat, Katmai, Mount Pinatubo, Lascar [*Druitt*, 1998; *Calder et al.*, 2000]. We speculate that the initial highly diluted

Figure 11. Time sequence over 8 min of simulation PF_1 (1.78×10^7 kg/s). (a) Time between 30 and 180 s. (b) Time between 210 and 480 s. The curves represent the logarithm of the volumetric solid concentration ($\log_{10}\varepsilon_s$) between −1 and −9 (the atmosphere has initially no grain). Size of the domain: 10 km (radial) × 2.5 km (height). The computational domain is initially much bigger, but beyond 10 km and 2.5 km the grid resolution is so poor that it has no practical interest to be shown. The poor grid resolution to higher altitudes explains why the coignimbrite (phoenix) clouds have such a vertical elongated shape.

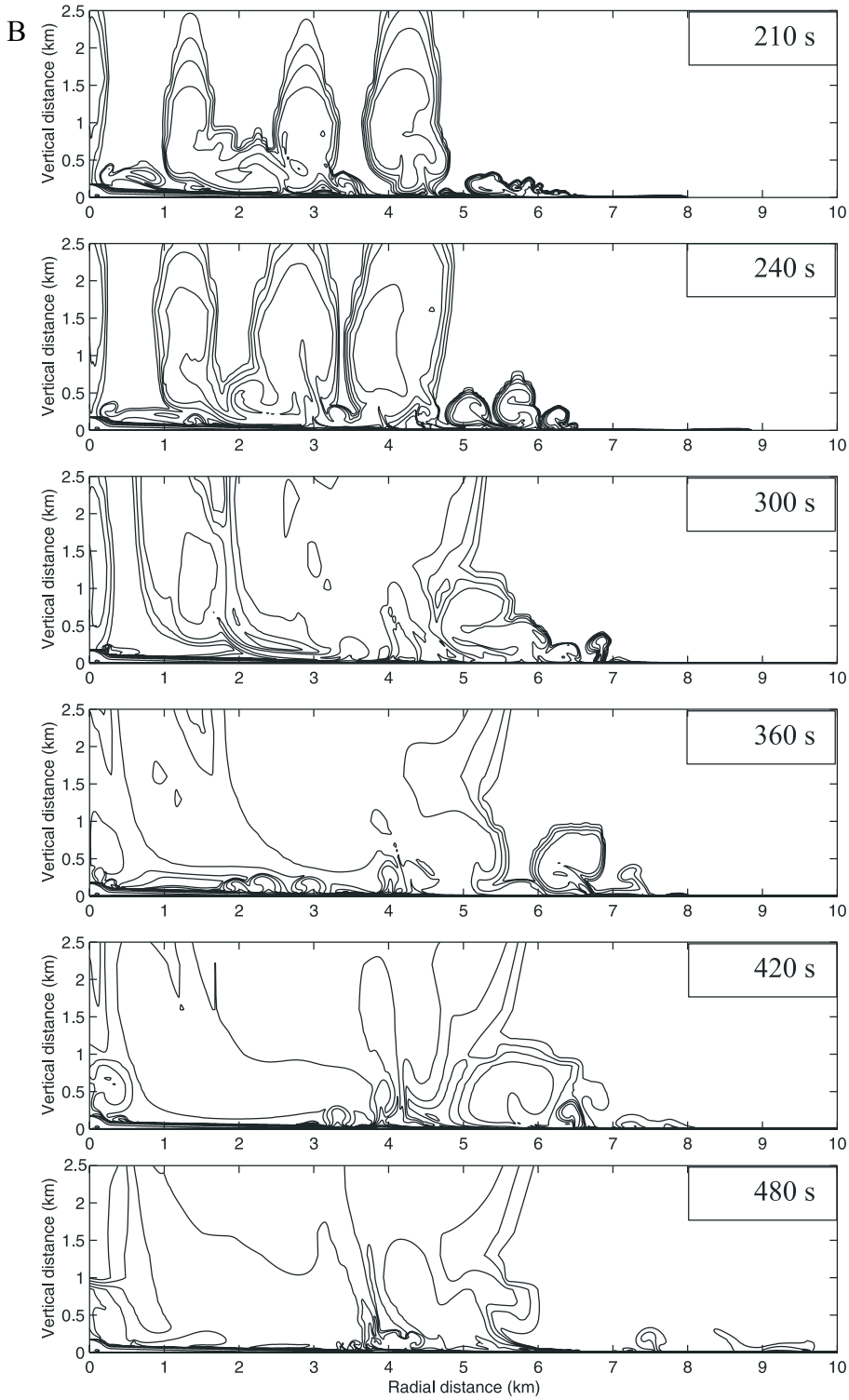

Figure 11. (continued)

head may deposit a thin layer, often named "ground layer," "ground surges," or "layer 1," found at the bottom of pyroclastic flow deposits (hence deposited first; see discussion by *Cas and Wright* [1988]). In our simulations, this ground-layer deposit cannot be modeled owing to the lack of vertical resolution. In the context of our simulations, the question is therefore where is this collisional undercurrent formed? *Sparks and Walker* [1977], *Sparks et al.* [1978], and *Walker*

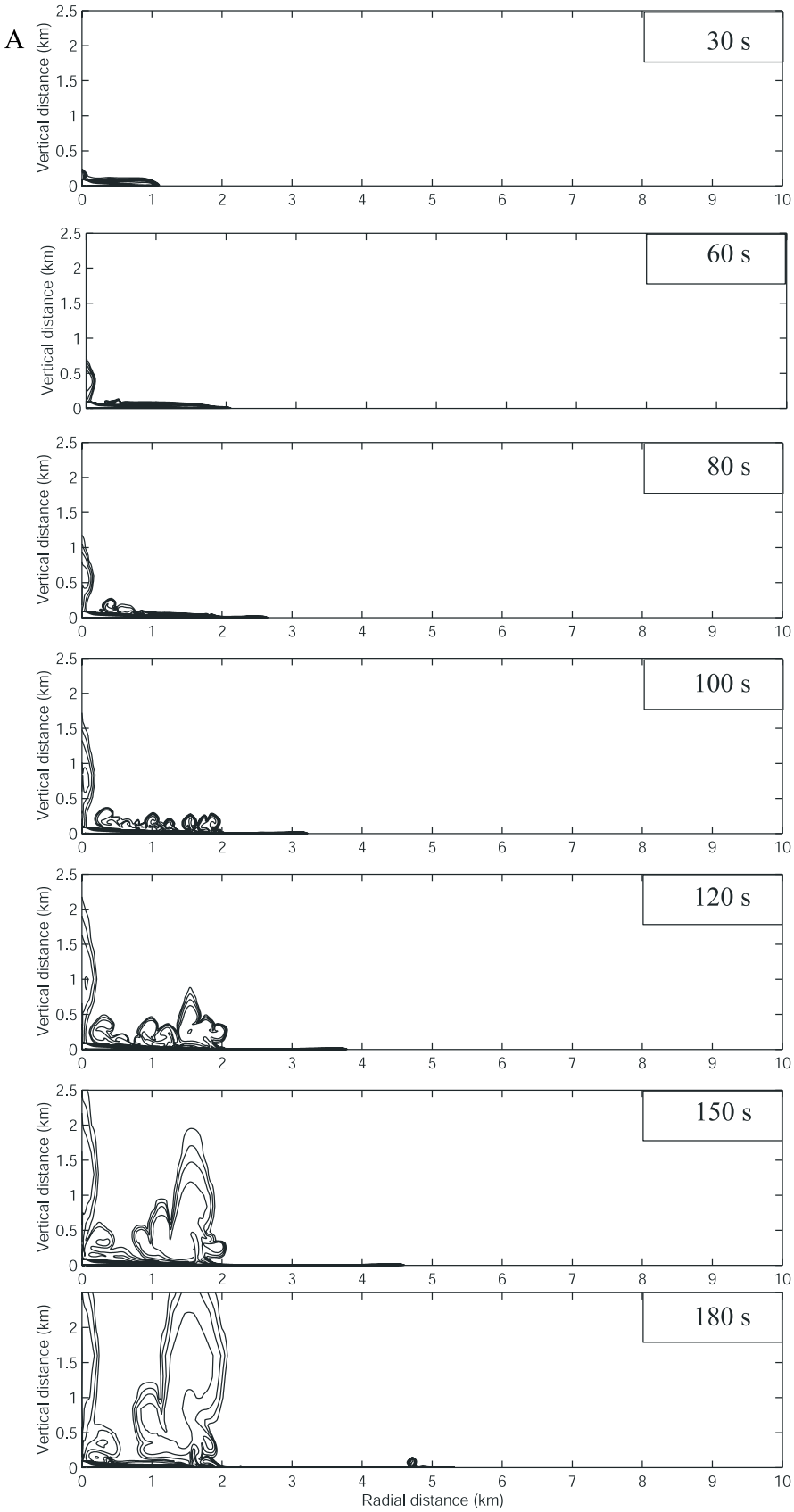

Figure 12

126

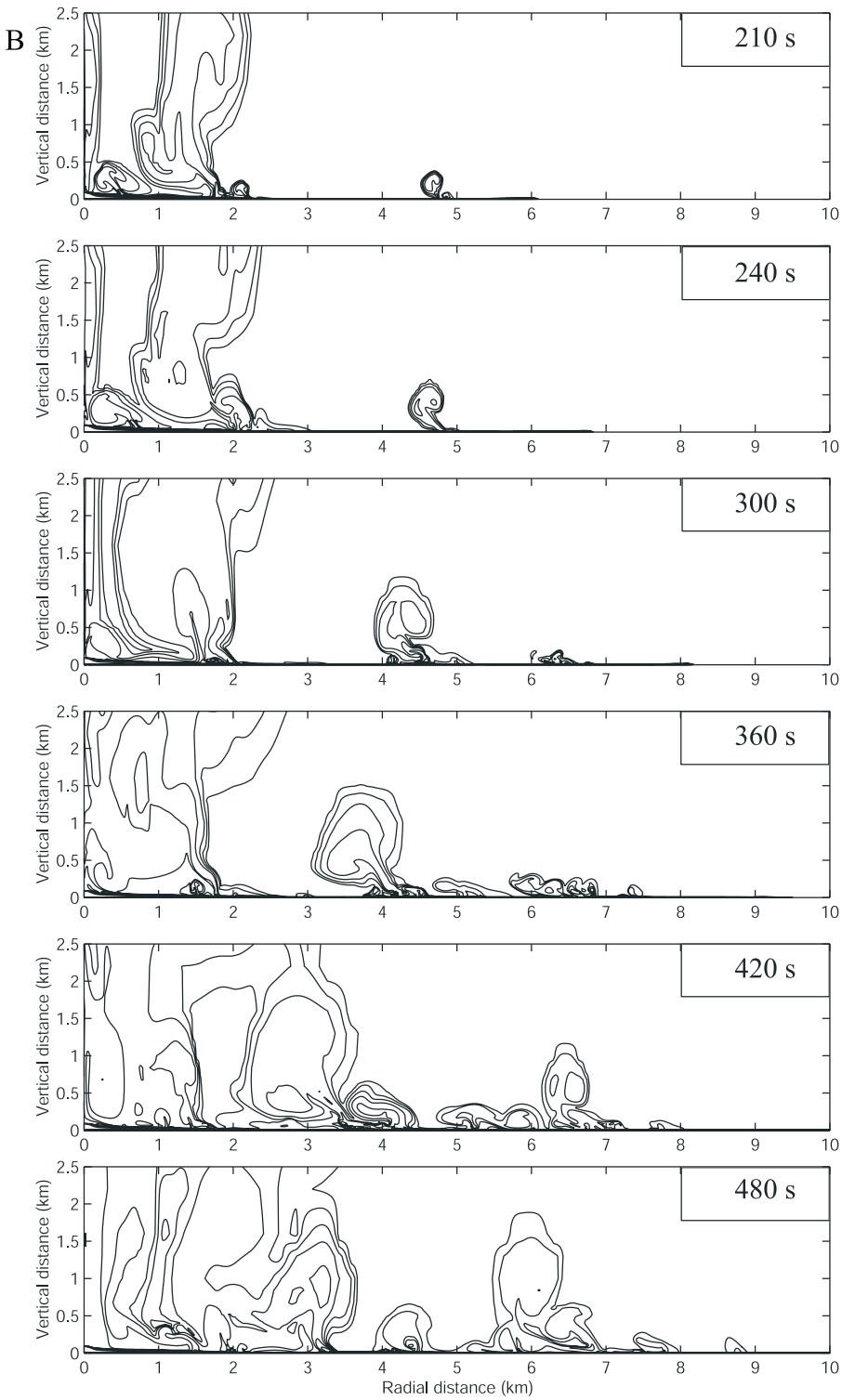

Figure 12. (continued)

Figure 12. Time sequence over 8 min of simulation PF_2 (8.89 × 10^6 kg/s). (a) Time between 30 and 180 s. (b) Time between 210 and 480 s. Same volumetric concentration curves, domain size, and comments as in Figure 11.

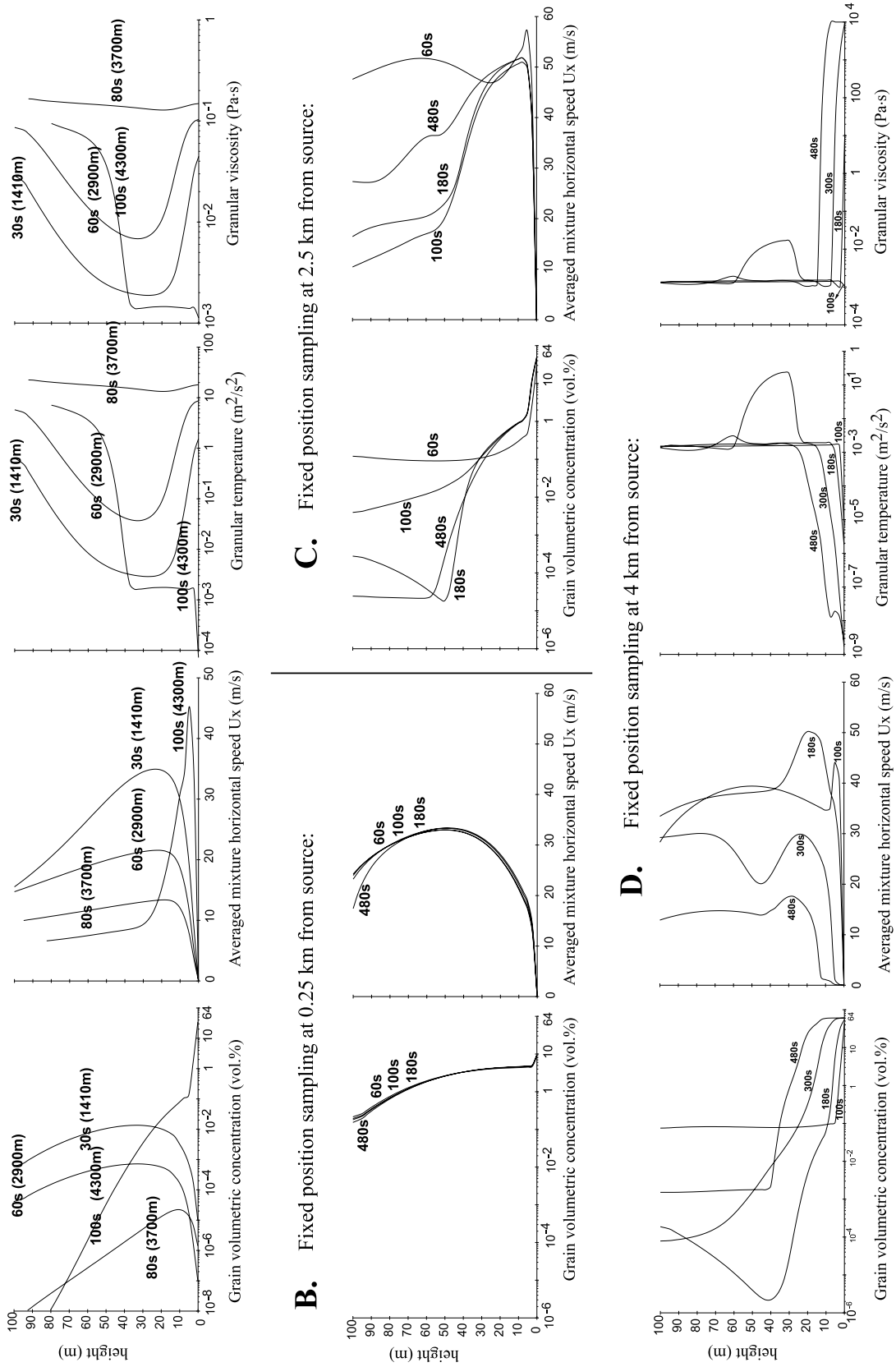
A.
Variable position and time sampling within the head of the flow:
60s (2900m)
100s (4300m)
30s (1410m)
80s (3700m)
Grain volumetric concentration (vol.%)
Averaged mixture horizontal speed Ux (m/s)
Granular temperature (m2/s2)
Granular viscosity (Pa·s)
B.
Fixed position sampling at 0.25 km from source:
C.
Fixed position sampling at 2.5 km from source:
D.
Fixed position sampling at 4 km from source:
480s
300s
180s
100s
60s
height (m)

Figure 13

[1985] have suggested the existence of a "deflation zone" near the vent where denser pyroclastic flows are selectively segregating from a highly turbulent, diluted, expanded low-concentration flow (see also the discussion by *Valentine and Wohletz* [1989]). Figure 13b (simulation PF_1) and Figure 14b (simulation PF_2) show ε_s and U_x within the flow sampled at different times 250 m from source, while Figure 13c and Figure 14c show the same variable sampling within the same time frame but 2.5 km from source. For both simulations, at 250 m from source, the concentrations ($\sim$0.1 to $\sim$12 vol.%) and U_x ($\sim$13 to $\sim$33 m/s) do not change significantly with time suggesting a self-maintained fluidized zone next to the vent. At 2.5 km, the situation is different as the concentration at the bottom of the flow increases with time (e.g., for PF_1 at 2.5 km: 32 vol.% at 60 s to $\sim$50 vol.% at 480 s) and U_x values are much higher than at 250 m from source (i.e., for PF_1: between 40 to 58 m/s and for PF_2: 28 to 36 m/s). Hence, from this observation, we may conclude that the denser basal PF has been partially segregated from an upstream source.

[45] The second important feature is the relationship between the overlying PS and the basal PF. For instance, in Figure 13c, there is a sharp decrease of ε_s along the vertical direction within 5 m (at 480 s, from 50 vol.% at the base to less 0.1 vol.% at a height of 30 m) which shows the presence in this simulation of an active dilute suspension flow (a kinetic-collisional pyroclastic surge moving as fast as 50 m/s) over a basal underflow (predominantly collisional, slightly frictional moving at 40 m/s). This indicates that overlying dilute suspensions may also have an important role in the grain "feeding" of the basal PF. Yet, in simulation PF_2 (Figure 14c, Movie 6), there is no obvious overlying surge further downstream than 2 km, which would suggest, in this case, that the denser basal PF is solely laterally segregated from the proximal "deflation zone."

[46] The term "deflation" zone deserves to be clarified in this context. As previously noted by *Valentine and Wohletz* [1989], the concentrations in the "deflation" zone can be much higher than further downstream. For instance, simulation PF_1 (Figures 13b and 13c), at 480 s, 40 m high, $\varepsilon_s \sim 5$ vol.% which is a predominantly a collisional regime (i.e., a maintained fluidized PF) and, at 2.5 km downstream, $\varepsilon_s \sim 10^{-2}$ vol.%, which is a kinetic-collisional regime (i.e., a dilute PS). Simulation PF_2 shows even sharper trends: at 480 s, 5 m high, at 250 m away from source, $\varepsilon_s \sim 3$ vol.% (Figure 14b) and, at 2.5 km from source, $\varepsilon_s \sim 10^{-3}$ vol.% (Figure 14c). Hence the deflation zone is not necessarily where the particle-laden flow is the most dilute. Nevertheless, it is certainly where basal concentrated pyroclastic flows start to laterally segregate. It also indicates that higher up in the flow, there is a lateral transformation from a fluidized, collisional PF (near source) to a much more diluted and kinetic PS further downstream. We would rather suggest renaming "deflation zone" to "maintained fluidized zone" as the former term would be synonym of "dilute" in the volcanological context.

4.2.2. Progressive Aggradation Versus en Masse Deposition

[47] For many decades volcanologists have debated whether pyroclastic flows and other geophysical granular gravity currents are deposited en masse (i.e., the flow suddenly and as a whole "freezes") or by progressive vertical aggradation (i.e., by a sustained sedimentation from a more diluted overlying current) [e.g., *Branney and Kokelaar*, 1992; *Druitt*, 1998; *Calder et al.*, 2000]. In the former case, the thickness of the flow unit and the parent flow are essentially the same, while in the latter, it implies a continuous sediment feeding from a more dilute current above the deposit. Any stratification within the aggradational deposit would reflect changes in flow steadiness, in the materials supplied at the source, or sedimentation time-break [*Branney and Kokelaar*, 1992; *Druitt*, 1998]. Since our model specifically links together granular shear viscosity, yield strength of the granular flow, and its concentration through the plastic potential and critical state theories [*Dartevelle*, 2004], our simulations may shed light on the exact nature of the depositional process.

Figure 13. Various time and space sampling along a height of 100 m within the flow PF_1. (a) Sampling at different positions and times within the head of the flow; from left to right: volumetric grain concentration (ε_s in vol.%), mean mixture horizontal speed (U_x in m/s), granular temperature (Θ in m^2/s^2), and granular shear viscosity (in Pa·s). (b) Sampling of ε_s and U_x at a fixed position 250 m from source at different time (60, 100, 180, 480 s). (c) Same sampling as in Figure 13b but at 2.5 km from source. (d) Sampling of ε_s, U_x, Θ, and granular shear viscosity at a fixed position 5 km from source for different times (100, 180, 300, 480 s).

A. Variable position and time sampling within the head of the flow:
B. Fixed position sampling at 0.25 km from source:
C. Fixed position sampling at 2.5 km from source:
D. Fixed position sampling at 3.7 km from source:
height (m)
Grain volumetric concentration (vol.%)
Averaged mixture horizontal speed Ux (m/s)
Granular temperature (m2/s2)
Granular viscosity (Pa·s)
40s (1300m)
10s (350m)
170s (5000m)
60 s
100 s
180 s
200 s
300 s
480 s

Figure 14

[48] Figure 13d (PF_1) and Figure 14d (PF_2) show at a fixed position (4 and 3.7 km, respectively) the volumetric grain concentration, averaged mixture horizontal speed, granular temperature, and granular shear viscosity of the flow sampled at different times. PF_1 has, at 100 s, a basal concentration of 44 vol.% and is flowing with a horizontal speed of ~40 m/s. This collisional pyroclastic flow has low granular temperature ($\sim 10^{-5}$ m^2/s^2) and low granular viscosity ($\sim 10^{-3}$ Pa·s). At 180 s, the flow shows plastic-frictional behavior ($\varepsilon_s \sim 55$ vol.%) with U_x at the base reduced to 26 m/s, and granular shear viscosity increased by a factor of ten thousand (~10 Pa·s). At 300 s, the basal part of the flow has reached a concentration of ~60 vol.% over a height of 7.5 meters and, at 480 s, over a height of 12.5 meters. At those concentrations, at the base of the flow, $U_x \sim 0$ m/s, the granular temperature is negligible and shear granular viscosity is $\sim 10^4$ Pa·s (the maximum allowed in our model). Simulation PF_2 shows the same trends, however slower and more progressive, at a distance of 3.7 km: at the base, at 200 s, $\varepsilon_s \sim 51$ vol.%; at 360 s, $\varepsilon_s \sim 58$ vol.% (not shown on Figure 14d), and at 480 s, $\varepsilon_s \sim 60$ vol.% over a height of 7.5 m (which is quasi-idle: $U_x \sim 0$ m/s).

[49] From these figures, with time, the overall deposit is progressively building upward, which supports a progressive aggradation mechanism as the main depositional process. At any given location, the deposit as a whole is diachronous [*Druitt*, 1998]. The base is formed from sediments deposited much earlier from either above or from upstream locations. While, progressively upward in the deposit sequence, sediments are deposited from later and upstream parts of the flow. This is demonstrated by the progressive reduction of U_x with time and at any given height within the flow and, also, by the reduction of U_x from bottom to top (e.g., Figure 13d).

[50] It should be also mentioned that PF_1 and PF_2 have an important differences in the nature of the overlying surges: these are dilute and quasi nonexistent or PF_2 (Figure 14d), while active, fast, and moving further downstream for PF_1 (Figure 13d). Hence vertical aggradation and formation of a subsequent deposit are the result of two processes for PF_1: (1) sedimentation from the overlying surge and (2) supply of fresh granular materials by frictional flow coming from upstream. For PF_2, the major source of sediments is mainly from what is brought by frictional flow coming from upstream locations. In all the cases, these plastic-frictional flows are initially generated from the "maintained fluidized zone," near source, following this lateral flow transformation:

Collisional fluidized PF (near source) → kinetic PS → collisional PF → frictional PF → deposit.

[51] This implies that at any given height within the deposit sequence, an elementary flow unit stops when its yield strength becomes infinite, hence when its concentration is close to $^{max}\varepsilon_s \sim$ 64 vol.%. Therefore our mathematical model fundamentally generates a deposit by en masse freezing of an elementary flow unit when concentrations reaches ~64 vol.%. Each flow unit is built with fresh sediment brought either from upstream sources (lateral accumulation by plastic-frictional flows) or, if any, from overlying surges (vertical accumulation by sedimentation). Our model implies that en masse freezing is not at all antagonistic with vertical aggradation; the former acts on an elementary flow unit, the latter acts over the whole deposit sequence as seen on Figure 13d and Figure 14d. Our model and numerical results are consistent with field observations [e.g., *Calder et al.*, 2000] and naturally reconciles opposing views of depositional processes.

4.2.3. Pyroclastic Flow and Surge Relationships

[52] A close inspection of Figure 13 and Figure 14 demonstrates that both pyroclastic flows and surges have an intertwined history. As initial conditions, the flow was diluted at the source (see Table 1a) and eventually segregates into a denser basal pyroclastic flow and into a more dilute suspension above it. By sedimentation and by continuous feeding from upstream the bottom of the flow will eventually come to rest. In the previous section, we

Figure 14. Various time and space sampling along a height of 100 m within the flow PF_2. (a) Sampling at different positions and times within the head of the flow; from left to right: volumetric grain concentration (ε_s in vol.%), mean mixture horizontal speed (U_x in m/s), granular temperature (Θ in m^2/s^2), and granular shear viscosity (in Pa·s). (b) Sampling of ε_s and U_x at a fixed position 250 m from source at different time (60, 100, 180, 480 s). (c) Same sampling as in Figure 14b but at 2.5 km from source for time 100, 180, and 480 s. (d) Sampling of ε_s, U_x, Θ, and granular shear viscosity at a fixed position 3.7 km from source for different times (200, 300, 480 s).

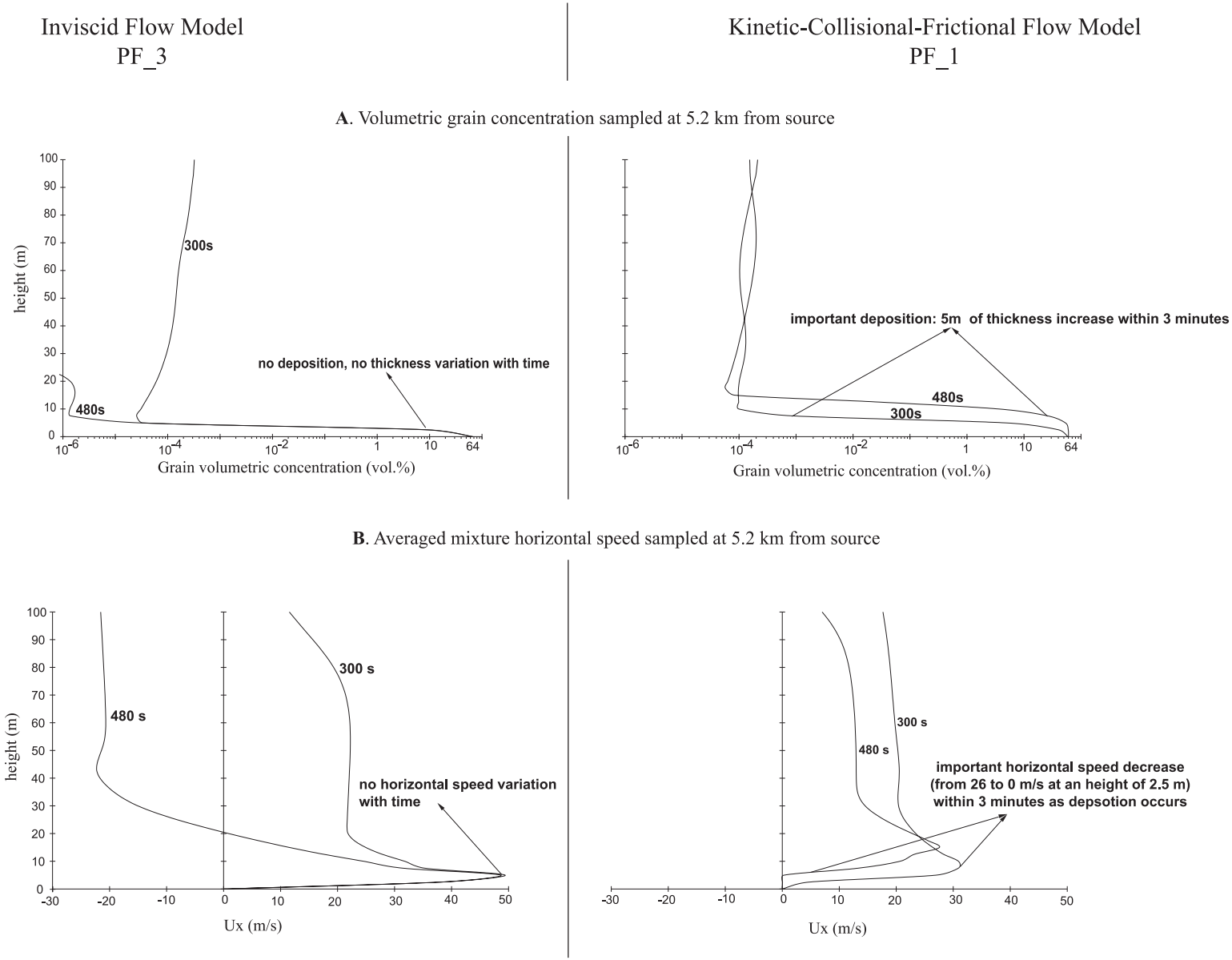
Inviscid Flow Model
PF_3
Kinetic-Collisional-Frictional Flow Model
PF_1
A. Volumetric grain concentration sampled at 5.2 km from source
height (m)
300s
480s
no deposition, no thickness variation with time
Grain volumetric concentration (vol.%)
important deposition: 5m of thickness increase within 3 minutes
480s
300s
Grain volumetric concentration (vol.%)
B. Averaged mixture horizontal speed sampled at 5.2 km from source
height (m)
300 s
480 s
no horizontal speed variation with time
Ux (m/s)
300 s
480 s
important horizontal speed decrease (from 26 to 0 m/s at an height of 2.5 m) within 3 minutes as depsotion occurs
Ux (m/s)

Figure 15

have seen a lateral flow transformation occurs from PF close to source into PS further downstream. In addition, by sedimentation, the overriding PS current looses its momentum and becomes sufficiently dilute to loft and form phoenix clouds as seen in Figure 11 (e.g., 180 s) and Figure 12 (e.g., 100 s). These coignimbrite clouds may afterward feed the system with new fallouts as they are pushed back and forth by inward and outward draughts.

[53] From Figure 13 and Figure 14, any properties of the flow (concentration, velocities, so forth) sharply change with time (unsteadiness) and space (nonuniformity, both vertically and horizontally) [*Freundt and Bursik*, 1998]. Globally, it is difficult to see the whole pyroclastic phenomenon with only one of the end-members (i.e., either dilute or concentrated), which justifies a multiphase model approach, able to model the whole spectrum of volumetric grain concentrations provided that a comprehensive rheological model is implemented in the code (see section 4.2.4).

4.2.4. Viscous Versus Inviscid Flow

[54] As mentioned in the companion paper [*Dartevelle*, 2004], a vast array of granular viscosities have been measured in chemical engineering, fluid dynamics, and volcanology. For instance, after the 1980 eruptions of Mt. St. Helens, *Wilson and Head* [1981] measured, in the newly deposited pyroclastic flows, viscosities in the range $O(10)$ to $O(10^4)$ Pa·s from which they rightly suggested that concentrated pyroclastic flows may behave plastically. It is worth noting that in our simulations when the pyroclastic flows reaches a volumetric grain concentration of 60 vol.%, our calculated granular shear viscosities are in the same range as those measured by *Wilson and Head* [1981] (e.g., see Figure 13, Figure 14, and also Figure 4 of *Dartevelle* [2004]). However, to date, most current models of pyroclastic flows and surges assume either empirical low-viscosity linear rheologies (e.g., Newtonian, Bingham) or no viscosity at all.

[55] To compare our model with an inviscid model, we have computed simulation PF_1 assuming that there is no kinetic-collisional-plastic behavior and setting the granular shear and bulk viscosities and the granular plastic pressure to zero. However, it is still necessary to use the normal component of the solid stress to prevent the particles from reaching impossible high values [e.g., *Bouillard et al.*, 1991; *Gidaspow*, 1994; *Neri and Macedonio*, 1996; *Todesco et al.*, 2002]. Since we have now turned off the plastic formulation of ${}^{f}P$ [*Dartevelle*, 2004, equation (T5.19)], we will use the same empirical formulation as in PDAC2D codes to roughly estimate the solid pressure [e.g., *Neri and Macedonio*, 1996; *Todesco et al.*, 2002]:

$$\nabla P_s \approx G(\varepsilon_s)\,\nabla\varepsilon_s = 10^{-3.33+8.76\varepsilon_s}\,\nabla\varepsilon_s, \qquad (3)$$

where the "compressibility modulus," $G(\varepsilon_s)$ in Pa, is an empirical best fit (among many others) of chemical engineering fluidization data [*Bouillard et al.*, 1991]. $G(\varepsilon_s)$ is sometimes named "elastic modulus" and the whole expression given by equation (3) is named "Coulombic component" [e.g., *Neri and Macedonio*, 1996; *Todesco et al.*, 2002], which is a misleading terminology because $G(\varepsilon_s)$ is only empirical and not related to any elastoplastic theoretical model. With this in mind, it is easy to implement ∇P_s given by equation (3) into the momentum equations of the solid phase [*Dartevelle*, 2004, equation (T1.6)].

[56] Figure 15 shows the solid volumetric concentration and averaged mixture horizontal speed versus the height at a location of 5.2 km from source for time 300 and 480 s. The full rheological model (right side of Figure 15) shows a vertical aggradation (~64 vol.% over a height of 5 m) and a sharp decrease of U_x to nil value (i.e., deposit). The inviscid model (left side of Figure 15) shows no deposition and no vertical aggradation at all. Even though ε_s is as high as 66 vol.% on the ground with the inviscid model, the horizontal speed is still as high as 40 m/s, which is physically questionable for such a high concentration. Note also the very different velocity and concentration profiles higher up in the dilute part of the flow. The inviscid model makes the dilute part of the flow strongly sensitive to inward draughts, i.e., surges and coignimbrite flows cannot move on their own as they cannot offer any rate-of-strain "resistance" imposed by draughts, hence they "fly" along the

Figure 15. Comparison of numerical results from a fully inviscid model (left side) and a full rheological granular model (right side) involving kinetic-collisional and plastic formulations as in *Dartevelle* [2004]. Sampling at a fixed distance of 5.2 km from source at two different times (300 and 480 s). (a) Volumetric grain concentration versus height in the flow. (b) Averaged mixture horizontal speed versus height. The inviscid model is unable to build up a deposit (no vertical aggradation) and to stop; i.e., the horizontal speed is higher than 40 m/s for concentrations as high as 66 vol.%.

main draught directions. The runout distance of the flow is only imposed by the severity of the counter-drafts.

5. Conclusions

[57] Within the assumptions of our physical models (e.g., 2-D simulation, one grain size, no water phase change, no coupling between turbulence in the gas and dispersed solid phase, see *Dartevelle* [2004]), we have performed plinian cloud, pyroclastic surge and flow simulations in order to validate and compare our numerical results with remote-sensing data, historical eruptions, classical plume theories and field observations and, also, to shed new light on some of the most debated issues in volcanology about the nature and dynamic of pyroclastic flows.

[58] Our plinian column simulations correlate well with *Morton et al.* [1956] plume theory and historical eruptions in the top altitude of the cloud (H_T) versus mass flux diagram. The high mass flux eruption columns ($>10^7$ kg/s) are highly nonlinear, chaotic and subject to quasiperiodic vertical acoustic-gravity waves generated at the transition jet-plume area. H_T fluctuates with time over 1 hour; hence temperature anomalies at "the tip of the top" of the cloud range between −11 K and +20 K. These results compare well with Mt. Pinatubo, El Chichón and Mt. St. Helens eruptions. The largest plinian simulation shows the development of important convective supercell in phase with the vertical propagation of acoustic-gravity waves. The plinian simulations show complex, unsteady, and heterogeneous velocity and solid volumetric concentration profiles within the clouds (in the column and in the umbrella). To our the best of our knowledge, to date, (G)MFIX is the first multiphase model able to simulate complete stable plinian clouds.

[59] The pyroclastic flow and surge simulations display nonlinear and highly viscous behaviors. Our simulations show complex lateral flow transformation processes (pyroclastic surges↔pyroclas-pyroclastic flows). The head of the flow is diluted and has all the properties of a pyroclastic surge, which is eventually outrun by a collisional, denser basal undercurrent pyroclastic flow. Our simulations suggest that the depositional process is mostly gradual with materials supplied either by downstream currents or/and by sedimentation from overlying surges. However, it is shown that gradual deposition is not incompatible with en masse deposition. The subsequent deposit is diachronous from base to top. Deposition does not occur uniformly everywhere, e.g., our simulations show the presence of "maintained fluidized zone" near source.

[60] In the long run, our multiphase simulations suggest that the Large Eddy Simulation (LES) should be the ideal mathematical and physical framework to further develop multiphase turbulence models in accounting for the coupling between phasic turbulence effects and for mass transfers between phases (e.g., Sub-Grid Mass flux for water phase change).

Appendix A: Grid Size Analysis for Geophysical Flows

[61] Although previous studies have shown that MFIX codes produce results independent on the grid size [*Guenther and Syamlal*, 2001], this must be also demonstrate for geophysical applications (plinian cloud and pyroclastic flow and surge simulations). This is important to establish owing the relative poor resolution of all our simulations and the simplifications in our model [*Dartevelle*, 2004]. Of course, a highly coarse grid size may produce unrealistic physics, may prevent from obtaining a solution (no convergence), and/or may prevent from forming a granular deposit at the ground level in the pyroclastic flow simulations. In addition, the values of any seemingly realistic solutions can only be valued if grid size independence is somehow demonstrated within the typical range of grid size used in this project.

[62] Table A1 presents two identical plinian simulations achieved with different grid sizes: a grid size of 50 m over the whole height and over a radial distance of 6.2 km and a grid size of 100 m over the whole height and over a radial distance of 7 km. Figure A1 shows the results over one hour for both simulations. Clearly no significant differences can be seen even if as expected more details in the eddy structures and the umbrella shape (multilayered, thickness) appeared between both simulations. However, both radial distance and top altitude are essentially the same. Since the plinian column simulations have been achieved with a grid size much smaller than 100 m (i.e., 30 m for PL_1, 50 m for PL_2, 80 m for PL_3), we may conclude that the numerical results produced in this manuscript are grid size independent.

[63] Table A2 presents four identical simulations of pyroclastic flows and surges achieved with differ-

Table A1. Grid Size Analysis for Plinian Cloud Simulations: Initial and Boundary Conditions

Eruption	Grid 50 m	Grid 100 m
Geometry	Cylindrical	Cylindrical
Vertical length Y, km	30	30
Vertical resolution ΔY, m	50	100
Number of grid point in the Y direction	601	301
Radial length X, km	30	30
Radial resolution from 0 to 6.2 km ΔX, m	50	100
Radial resolution from 6.2 to 7.0 km ΔX, m	100	100
Radial resolution from 7.0 to 7.4 km ΔX, m	200	200
Radial resolution from 7.4 to 8.2 km ΔX, m	400	400
Radial resolution from 8.2 to 9.0 km ΔX, m	800	800
Radial resolution from 9.0 to 30.0 km ΔX, m	1000	1000
Number of grid point in the X direction	158	96
Vent diameter, m	200	200
Mixture vertical speed V_y, m/s	80	80
Volumetric solid concentration ε_s, vol.%	0.1	0.1
Grain diameter d, μm	50	50
Grain microscopic density ρ_s, kg/m^3	1500	1500
Mixture temperature at the vent T_m, K	900	900
Gas pressure at the vent P_g, Pa	10^5	10^5
Mass fraction of water vapor at the vent	1.0	1.0
Calculated mixture density ρ_m, kg/m^3	1.74	1.74
Calculated mass flux, kg/s	1.75×10^7	1.75×10^7

ent grid size at the ground. One run has a very high vertical resolution at the ground level (1.25 m), the others have a coarser vertical resolution by a factor two: 2.5, 5.0, 10 meters. The results of these four simulations are shown in Figure A2 at two different times (40 and 100 s) and in Figure A3, where we compare the solid volumetric concentration (ε_s) and the averaged horizontal speed (Ux) at 40 s and 100 s. In Figure A2, there is no difference on the global scale: all produce at the same distance from source the same coignimbrite ash cloud. However, the coarser the grid size at the ground level, the more delayed the formation of the deposit (for the 10 m grid size run, it has not yet happened) as seen on Figure A3. There is no significant difference for the 1.25, 2.5 and 5.0 m in the formation of a concentrated deposit at the bottom. The only difference is that the deposit is developed very early in the time sequence with the high resolution grid, 1.25 m (therefore being well-frozen after 100 s), while just barely formed after 100 s with the 5.0 m grid (and not yet quite frozen). The grid resolution of 10 m seems not to be adequate because deposition only occurs over on height of 12 m, which cannot be capture with a grid size of similar scale. In all the cases, it can be seen that there is a sharp deceleration between 40 s and 100 s due to the grain deposition and the plastic rheological model of *Dartevelle* [2004]. In conclusion, Figures A2 and A3 suggest that the choice we have made for a 2.5 m grid size at the ground for simulation PF_1 and PF_2 is fully adequate to capture the main features of sedimentation processes. A higher resolution at the ground would only be possible with much more powerful computer capabilities. These results are fully consistent with *Dobran et al.* [1993] and *Neri et al.* [2003].

Appendix B: Overview of the Numerical Schemes Used in MFIX and (G)MFIX

[64] In a typical multiphase system, the momentum and energy equations (and also mass if phase transition occurs) are highly coupled through exchange terms. Those exchange terms strongly couple the components of velocity, temperature (and possibly mass) in a given phase to the corresponding variable in the other phase. This property is called the "interequation coupling." In addition, the discretized equations are nonlinear because the coefficients of the discretized equation depend on the values of the variable to be found. (G)MFIX uses a semi-implicit numerical scheme which must specifically deal with the interequation coupling and the nonlinearity of the discretized equations. To linearize the equations, the iterative method of Newton could be used [*Press et al.*, 1986] but it is more economical and practical, particularly for the momentum equations, to use the Patankar and Spalding's SIMPLE algorithm (Semi-implicit for Pressure Linked Equations) [*Patankar*, 1980; *Spalding*, 1981, 1983; *Patankar et al.*, 1998; *O'Rourke et al.*, 1998; *Syamlal*, 1998;

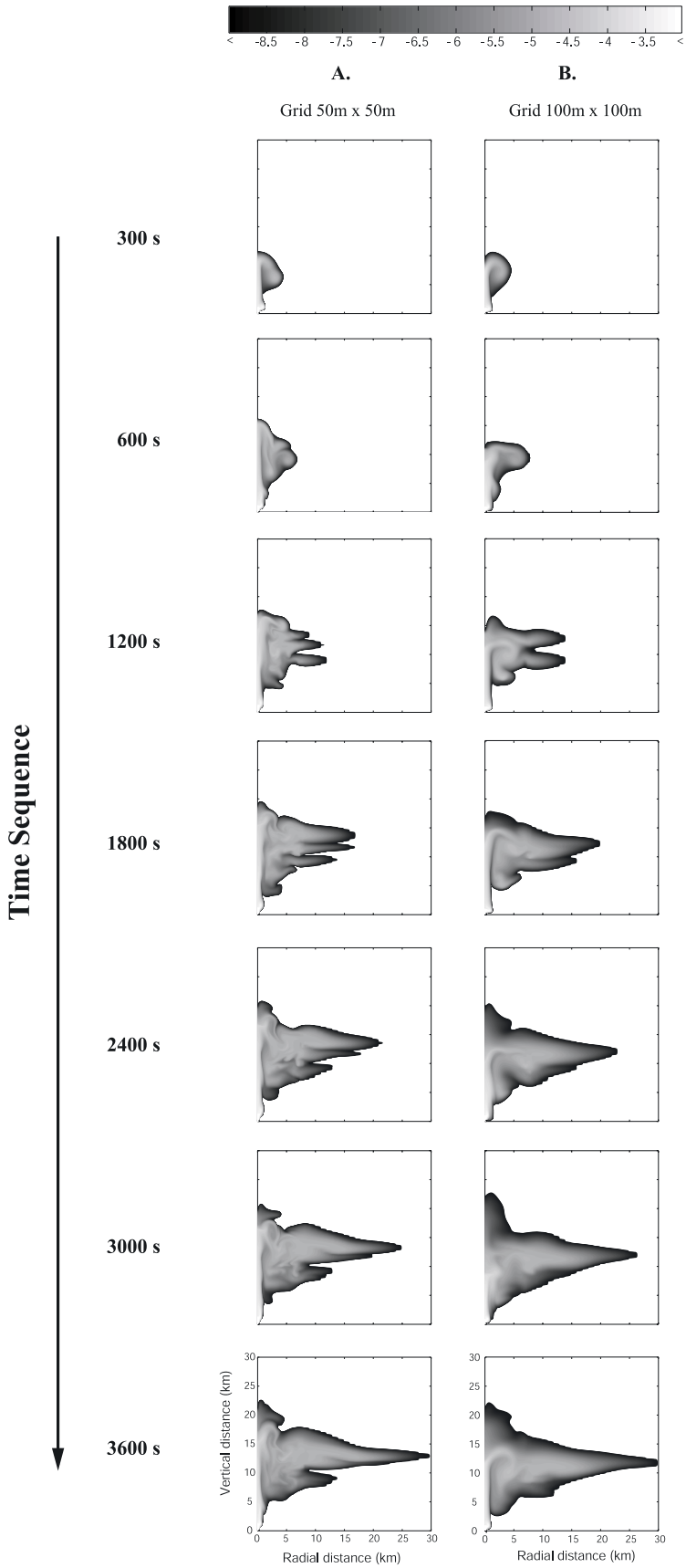

Figure A1

136

Table A2. Grid Size Analysis for Pyroclastic Flow Simulations: Initial and Boundary Conditions

Eruption	Grid 1.25 m	Grid 2.5 m	Grid 5.0 m	Grid 10 m
Geometry	Cartesian	Cartesian	Cartesian	Cartesian
Vertical length Y, km	10	10	10	10
Vertical resolution from 0 to 50 m ΔY, m	1.25	2.5	5.0	10.0
Vertical resolution from 50 to 100 m ΔY, m	2.5	2.5	5.0	10.0
Vertical resolution from 100 to 150 m ΔY, m	5.0	5.0	5.0	10.0
Vertical resolution from 150 to 400 m ΔY, m	10.0	10.0	10.0	10.0
Vertical resolution from 400 to 1000 m ΔY, m	20,40,80,160	20,40,80,160	20,40,80,160	20,40,80,160
Vertical resolution from 1 km to 10 km ΔY, m	300,600,1000	300,600,1000	300,600,1000	300,600,1000
Number of grid point in the Y direction	115	95	75	60
Radial length X, km	16	16	16	16
Radial resolution from 0 to 5 km ΔX, m	500	500	500	500
Radial resolution from 5 to 8 km ΔX, m	20,40,80,160	20,40,80,160	20,40,80,160	20,40,80,160
Radial resolution from 5 to 8 km ΔX, m	400,800,4800	400,800,4800	400,800,4800	400,800,4800
Number of grid point in the X direction	550	550	550	550
Vent diameter, m	50	50	50	50
Mixture vertical speed V_y, m/s	50	50	50	50
Volumetric solid concentration ε_s, vol.%	5.0	5.0	5.0	5.0
Grain diameter d, μm	250	250	250	250
Grain microscopic density ρ_s, kg/m^3	2500	2500	2500	2500
Mixture temperature at the vent T_m, K	900	900	900	900
Gas pressure at the vent P_g, Pa	10^5	10^5	10^5	10^5
Mass fraction of water vapor at the vent	1.0	1.0	1.0	1.0
Calculated mixture density ρ_m, kg/m^3	296	296	296	296
Calculated mass flux, kg/s	1.48×10^8	1.48×10^8	1.48×10^8	1.48×10^8

Pannala et al., 2003]. In the SIMPLE algorithm (Table B1), a system of coupled implicit equations is solved by associating with each equation an independent solution variable and solving implicitly for the value of the associated solution variable that satisfies the equation, while keeping the other solution variables fixed. For instance, pressure appears in all the momentum equations of all the phases (gas pressure in the gas momentum equations and solid pressure in the solid momentum equations), therefore making the velocity components dependent on the pressure value and vice versa (hence making the momentum equations nonlinear). Therefore, in the gas momentum equations, the pressure is chosen as independent variable and special treatment is used for solving the gas pressure (i.e., the pressure correction equation of *Patankar* [1980]; see also *Spalding* [1983], *Patankar et al.* [1998], and *Syamlal* [1998]). In the solid momentum equation, the solid volume fraction is chosen as an independent variable (i.e., the solid volume fraction correction equation) [*Syamlal*, 1998]. To help convergence during the SIMPLE iteration process, an underrelaxation technique is used to slow down the changes in the coefficient from iteration to iteration with an underrelaxation factor, ω, less than unity [*Patankar et al.*, 1998] (see Table B1). The interequation coupling must be dealt with some degree of implicitness to ensure fast convergence in anticipating the effects of a change in the local property of one phase on the properties of the other phase at the same location and simultaneously [*Spalding*, 1981]. This is accomplished with the Partial Elimination Algorithm (PEA) of *Spalding* [1981] [see also *Syamlal*, 1998]. With PEA, in a given phase, all the coefficients of the discretized equations involving the exchange terms (e.g., momentum exchange, K, and heat transfer, Q, between phases; [see *Dartevelle* [2004, equation (T1.5) to equation (T1.8)]) and the value of the corresponding variable from the other phase (e.g., velocities and temperature) are treated as source terms evaluated from the previous time step iteration [*Syamlal*, 1998]. Once both linea-

Figure A1. Time sequence over one hour of two plinian clouds. (a) The vertical grid size is 50 m and the radial grid size is 50 m over a distance of 6.2 km. (b) Same plinian cloud simulation but within a coarser grid size 100 m vertical and 100 m radial (over a distance of 7 km). Although many more details are captured with a high-resolution grid, the behavior and shape of the plinian clouds are essentially identical.

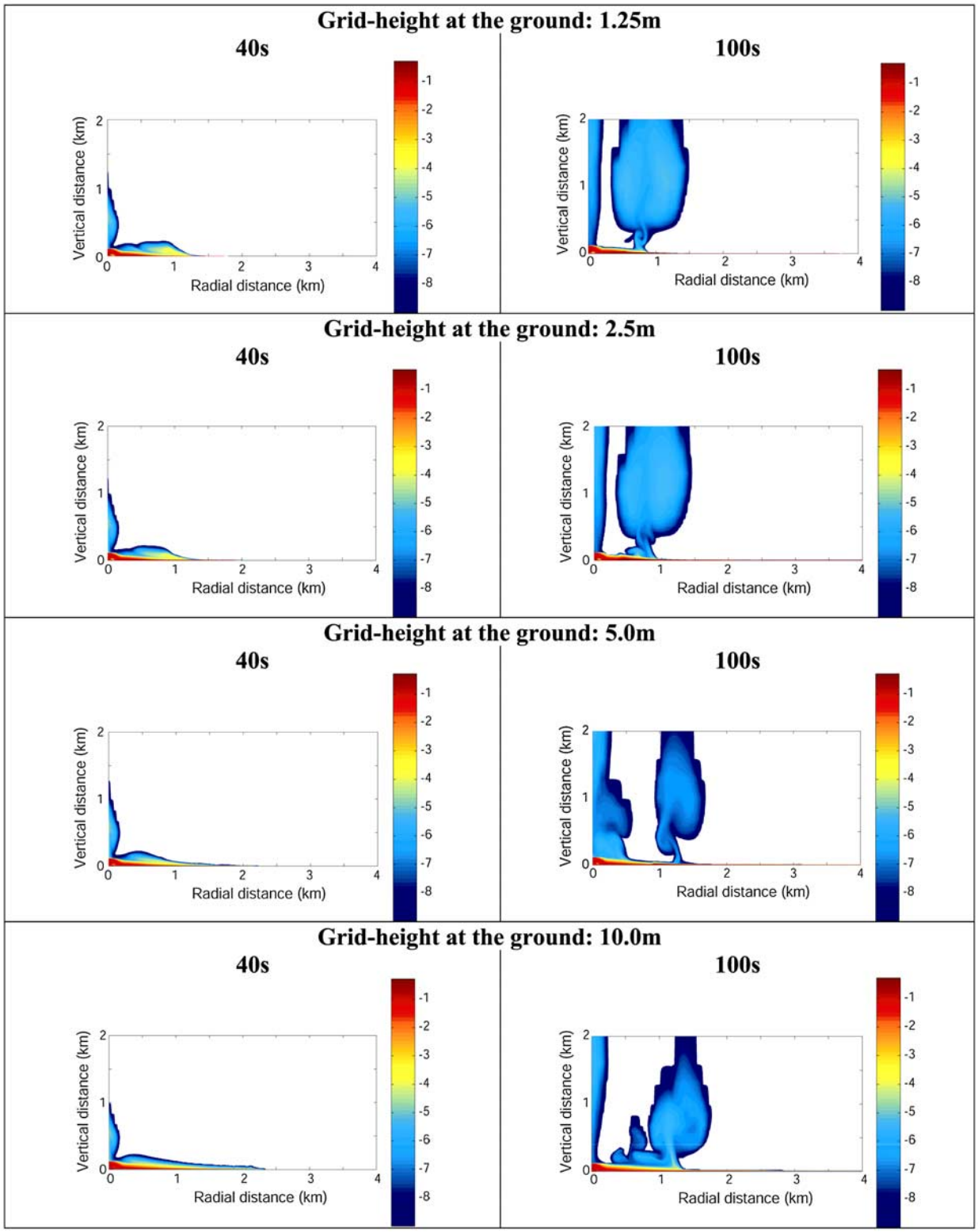

Figure A2. Snapshots taken at 40 s and 100 s of the same pyroclastic flow simulation but with different vertical grid size at the ground level: 1.25 m, 2.5 m, 5 m, and 10 m over a height of 50 m. It is worth noting that after 100 s in all cases, a phoenix cloud loft at a distance of 0.8 km and 1.2 km. With a coarser grid height both the formation of a deposit and of a phoenix cloud are somehow delayed in both time and space. A grid as coarse as 10 m does not seem appropriate to fully capture the sedimentation process within this time span.

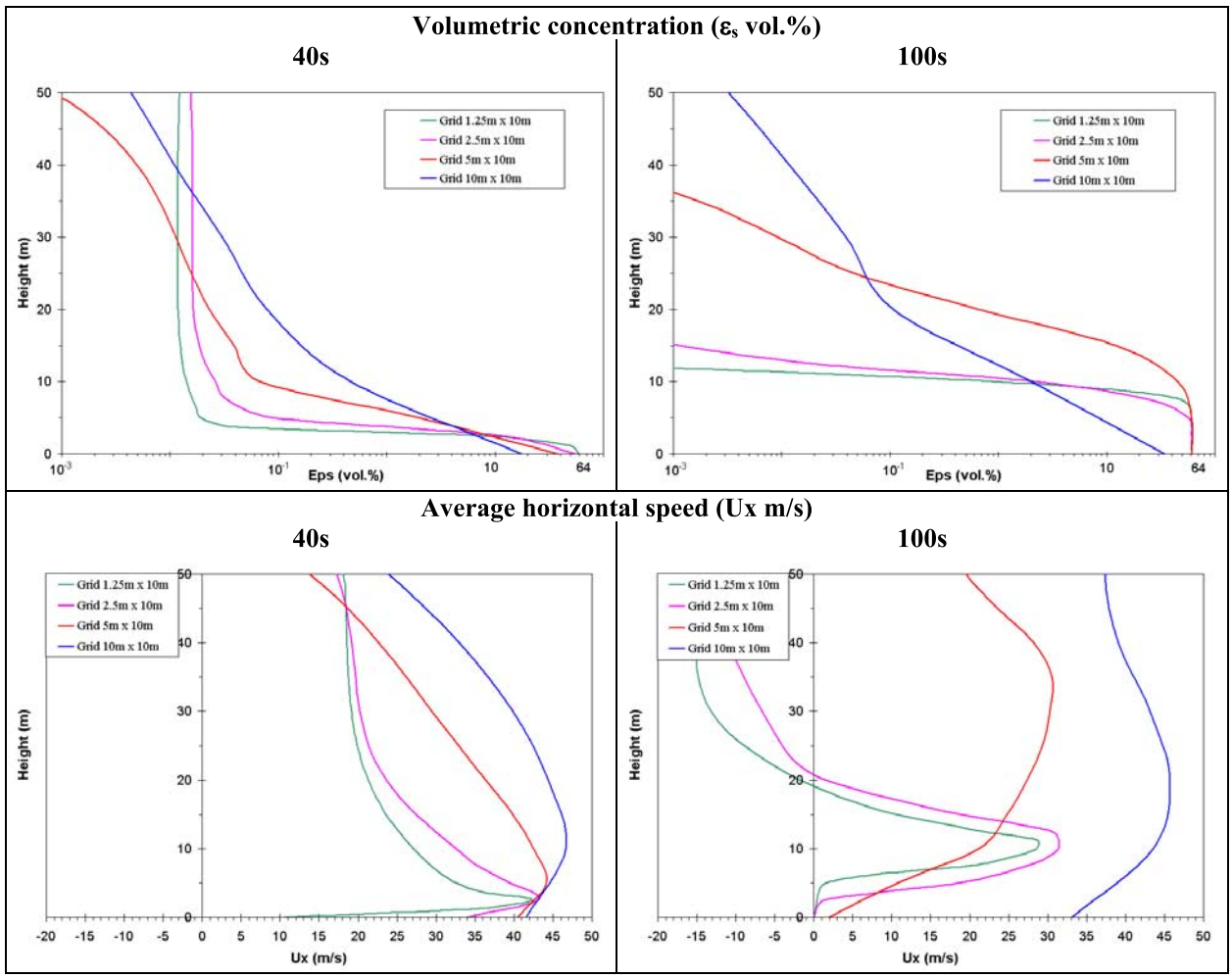

Figure A3. Grain volumetric concentration (ε_s in vol.%) and horizontal mixture speed (U_x in m/s) over a height of 100 m. After 100 s, a deposit is building up for all the grid heights except 10 m. This is also shown in the horizontal speed figures, where $U_x \sim 0$ m/s for the 1.25 m and 5 m grid and $\sim$2 m/s for the 5 m grid. The flow has barely decelerated within the 10 m grid. These figures suggest that the coarser the grid, the more delayed the sedimentation process. The typical grid size used in this manuscript (2.5 m) is largely sufficient to capture the sedimentation and depositional process and, more importantly, this 2.5 m grid size display results grid size independent.

rization and interequation are dealt, within the SIMPLE algorithm, (G)MFIX can solve the discretized equation using a classical linear solver iterative method (a point iteration, also called relaxation), such as the generalized minimal residual method (GMRES) [*Saad and Schultz*, 1986], and a more stable variant of the biorthogonal-conjugate gradient method (BI-CGSTAB of *van der Vorst* [1992]). See Table B1 for the specific linear solver/variable combination used in our simulations.

[65] (G)MFIX uses an automatic time step adjustment to reduce the total run time in achieving the best ratio of "time step"/"number of iteration needed for convergence" and this at any given simulation time [*Syamlal*, 1998]. For instance, the semi-implicit algorithm imposes a very small time step for very dense gas-solid flow simulations or whenever sharp gradient develops within the flow field. On the other hand for quasi-steady diluted flows, a small time step would make the run unnecessarily long. MFIX monitors the total number of iterations needed for convergence for several previous time steps. If there is a favorable reduction in the number of iterations per second of simulation, then a small upward time step adjustment is performed. Or, for instance, if the simulation fails to converge for a given time step, then the time step is decreased till convergence is obtained [*Syamlal*, 1998]. Convergence of iterations in the linear equation solvers is judged from the residuals of various equations

Table B1. "SIMPLE" Algorithm for Multiphase Granular Flows in MFIX and (G)MFIX Codes[a]

Step	Procedure
1	Start of a new time step iteration. Calculate physical properties and exchange coefficients.
2	Calculate guessed velocity fields of both solid and gas phase ($^{\circ}\mathbf{u}_s$ and $^{\circ}\mathbf{u}_g$) on the basis of the available current pressure fields ($^{\circ}P_s$ and $^{\circ}P_g$) and volumetric concentrations ($^{\circ}\varepsilon_s$ and $^{\circ}\varepsilon_g$). Use BI-CGSTAB and PEA.
3	Calculate the gas pressure correction with BI-CGSTAB: $\ddot{}P_g$.
4	Update the gas pressure field with underrelaxation technique: $P_g = {}^{\circ}P_g + \varpi_g \ddot{}P_g$, where the underrelaxation factor for the gas phase: $0 < \varpi_g < 1$.
5	Calculate gas velocity correction fields ($\ddot{}\mathbf{u}_g$) from $\ddot{}P_g$ and update velocity fields: $\mathbf{u}_g = {}^{\circ}\mathbf{u}_g + \ddot{}\mathbf{u}_g$.
6	Calculate tentative estimates of solid velocity field knowing the updated $\mathbf{u}_g$ and P_g values: ${}^{1}\mathbf{u}_s$.
7	Calculate the solid volumetric concentration correction with BI-CGSTAB: $\ddot{}\varepsilon_s$.
8	Calculate solid velocity correction fields ($\ddot{}\mathbf{u}_s$) and update velocity fields: $\mathbf{u}_s = {}^{1}\mathbf{u}_s + \ddot{}\mathbf{u}_s$.
9	Update the solid volumetric concentration: $\varepsilon_s = {}^{\circ}\varepsilon_s + \varpi_s \ddot{}\varepsilon_s$, where the underrelaxation factor for the solid phase: • if $\ddot{}\varepsilon_s > 0$ (i.e., solid volumetric faction is increasing) and $\varepsilon_s > {}^{f}\varepsilon_s$ (i.e., where the contact between particle is frictional), then $0 < \varpi_s < 1$. • otherwise, $\varpi_s = 1$.
10	Update the gas volumetric concentration: $\varepsilon_g = 1 - \varepsilon_s$.
11	Update the solid pressure field P_s from ε_s.
12	Calculate solid and gas temperatures with BI-CGSTAB and PEA.
13	Calculate the granular temperature (if needed) with BI-CGSTAB.
14	Check for convergence judged from the normalized residuals of the linear equation solvers used in steps 2, 3, 7, 12, and 13: • If reached, start the next time step (step 1) and automatically adjust the time step. • If not reached, restart the iteration process (step 2) with the new corrected velocity fields, pressure fields, and concentration values.

[a] Multiphase SIMPLE algorithm in relation with Partial Elimination Algorithm and linear solver techniques used in the (G)MFIX codes. For the calculation techniques of pressure correction equation, solid volumetric correction equation, velocity field correction equations, underrelaxation factors, and Partial Elimination Algorithm (PEA) see *Patankar* [1980], *Spalding* [1983], *Syamlal* [1998], and *Patankar et al.* [1998]. For the linear equation solver techniques, such as the biorthogonal-conjugate gradient stable method (BI-CGSTAB), see *van der Vorst* [1992]. All symbols are defined in Appendix A of the companion paper [*Dartevelle*, 2004]. The physical properties and exchange coefficient are given in Tables 3 and 4 and Table 2, respectively, of *Dartevelle* [2004]. Typically, between 5 and 20 iterations are needed before declaring convergence. Note that at convergence the gas pressure ($\ddot{}P_g$) and solid volume fraction ($\ddot{}\varepsilon_s$) corrections must go to zero [*Syamlal*, 1998].

over the whole computational domain. Convergence is declared whenever each residual of each discretized equation within the same iteration tends to zero. If the residuals are not reduced, a supplementary iteration will be performed. If convergence is not obtained within a specified number of iterations (30 in our simulations), or if the system is divergent, then "nonconvergence" is declared and the time step is decreased.

[66] (G)MFIX uses portable OPEN-MP (for shared memory multiprocessors) and MPI (for distributed memory parallel computers) in a unified source code. The MFIX codes has been ported to a Beowulf Linux cluster, SGI SMP, Compaq SC cluster, IBM SP, and Windows2000/XP workstation (2 to 4 CPUs in SMP) and can be used on Hybrid-computer SMP-DMP on a Linux cluster [*Pannala et al.*, 2003].

[67] All the "Fix-family" codes (e.g., K-FIX, MFIX, (G)MFIX) are property of the U.S. government through the Department of Energy (DOE). The MFIX codes can be freely accessed at http://www.mfix.org. In the same vein, a similar code, CFDlib, may also be used for multiphase flow dynamic at http://www.lanl.gov/orgs/t/t3/codes/cfdlib.shtml.

Acknowledgments

[68] This research was partially funded by the "National Science Foundation" (NSF Grant EAR 0106875) and by the "Natural Sciences and Engineering Research Council of Canada." SD thanks T. Druit for financially supporting his stay in Clermont-Ferrand, France. A. Neri, an anonymous reviewer, and P. van Keken are warmly acknowledged for their thorough reviews of this paper.

References

Bouillard, J. X., D. Gidaspow, and R. W. Lyczkowski (1991), Hydrodynamics of fluidization: Fast-bubble simulation in a two-dimensional fluidized bed, *Powder Technol.*, *66*, 107–118.

Boyle, E. J., W. N. Sams, and S. M. Cho (1998), MFIX validation studies: December 1994 to January 1995, *DOE/FETC-97/1042 (DE97002161)*, *CRADA PC94–026*, U.S. Dep. of Energy, Washington, D. C.

Branney, M. J., and P. A. Kokelaar (1992), A reappraisal of ignimbrite emplacement: Progressive aggradation and changes from particulate to non-particulate flow during emplacement of high-grade ignimbrite, *Bull. Volcanol.*, *54*, 504–520.

Calder, E. S., R. S. J. Sparks, and M. C. Gardeweg (2000), Erosion, transport and segregation of pumice and lithic clasts in pyroclastic flows inferred from ignimbrite at Lascar Volcano, Chile, *J. Volcanol. Geotherm. Res.*, *104*, 201–235.

Cas, R. A. F., and J. V. Wright (1988), *Volcanic Successions: Modern and Ancient*, 528 pp., Chapman and Hall, New York.

Dartevelle, S. (2003), Numerical and granulometric approaches to geophysical granular flows, Ph.D. dissertation thesis, Dep. of Geol. and Min. Eng., Mich. Technol. Univ., Houghton.

Dartevelle, S. (2004), Numerical modeling of geophysical granular flows: 1. A comprehensive approach to granular rheologies and geophysical multiphase flows, *Geochem. Geophys. Geosyst.*, *5*, doi:10.1029/2003GC000636, in press.

D'Azevedo, E., P. Sreekanth, M. Syamlal, A. Gel, M. Prinkley, and T. O'Brien (2001), Parallelization of MFIX: A multiphase CFD code for modeling fluidized beds, paper presented at Tenth SIAM Conference on Parallel Processing for Scientific Computing, Soc. for Ind. and Appl. Math., Portsmouth, Va.

Dobran, F., A. Neri, and G. Macedonio (1993), Numerical simulations of collapsing volcanic columns, *J. Geophys. Res.*, *98*, 4231–4259.

Druitt, T. H. (1998), Pyroclastic density currents, in *The Physics of Explosive Volcanic Eruptions*, edited by J. S. Sparks and R. S. J. Sparks, *Geol. Soc. Spec. Publ.*, *145*, 145–182.

Freundt, A., and M. Bursik (1998), Pyroclastic flow transport mechanisms, in *From Magma to Tephra: Modeling Physical Processes of Explosive Volcanic Eruptions*, edited by A. Frendt and M. Rosi, pp. 173–243, Elsevier Sci., New York.

Gidaspow, D. (1986), Hydrodynamics of fluidization and heat transfer: Supercomputer modeling, *Appl. Mech. Rev.*, *39*, 1–23.

Gidaspow, D. (1994), *Multiphase Flow and Fluidization: Continuum and Kinetic Theory Descriptions*, 467 pp., Academic, San Diego, Calif.

Guenther, C., and M. Syamlal (2001), The effect of numerical diffusion on isolated bubbles in a gas-solid fluidized bed, *Powder Technol.*, *116*, 142–154.

Harlow, F. H., and A. Amsden (1975), Numerical calculation of multiphase fluid flow, *J. Comput. Phys.*, *17*, 19–52.

Holasek, R. E., and S. Self (1995), GOES weather satellite observations and measurements of the May 18, 1980, Mount St. Helens eruption, *J. Geophys. Res.*, *100*, 8469–8487.

Holasek, R. E., A. W. Woods, and S. Self (1996), Experiments on gas-ash separation processes in volcanic umbrella plumes, *J. Volcanol. Geotherm. Res.*, *70*, 169–181.

Ishii, M. (1975), *Thermo-fluid Dynamic Theory of Two-Phase Flow*, 248 pp., Eyrolles, Paris.

Johnson, J. B. (2003), Generation and propagation of infrasonic airwaves from volcanic explosions, *J. Volcanol Geotherm. Res.*, *121*, 1–14.

Lakehal, D. (2002), On the modeling of multiphase turbulent flows for environmental and hydrodynamic applications, *Int. J. Multiphase Flow*, *28*, 823–863.

Mikumo, T., and B. A. Bolt (1985), Excitation mechanism of atmospheric pressure waves from the 1980 Mount St. Helens eruption, *Geophys. J. R. Astron. Soc.*, *81*, 445–461.

Morton, B. R., G. F. R. S. Taylor, and J. S. Turner (1956), Turbulent gravitational convection from maintained and instantaneous sources, *Proc. R. Soc. London, Ser. A*, *234*, 1–23.

Neri, A., and G. Macedonio (1996), Numerical simulation of collapsing volcanic columns with particles of two sizes, *J. Geophys. Res.*, *101*, 8153–8174.

Neri, A., A. D. Muro, and M. Rosi (2002), Mass partition during collapsing and transitional columns by using numerical simulations, *J. Volcanol Geotherm. Res.*, *115*, 1–18.

Neri, A., T. Esposti Ongaro, G. Macedonio, and D. Gidaspow (2003), Multiparticle simulation of collapsing volcanic columns and pyroclastic flow, *J. Geophys. Res.*, *108*(B4), 2202, doi:10.1029/2001JB000508.

O'Rourke, P. J., D. C. Haworth, and R. Ranganathan (1998), Three-dimensional computational fluid dynamic, *LA–13427–MS*, Los Alamos Natl. Lab., Los Alamos, N. M.

Pannala, S., E. D'Azevedo, M. Syamlal, and T. O'Brien (2003), Hybrid (OpenMP and MPI) parallelization of MFIX: A multiphase CFD code for modeling fluidized beds, paper presented at ACM SAC 2003, Assoc. for Comput. Mach., Melbourne, Fla.

Patankar, S. (1980), *Numerical Heat Transfer and Fluid Flow*, 197 pp., Taylor and Francis, Philadelphia, Pa.

Patankar, S., K. C. Karki, and K. M. Kelkar (1998), Finite volume method, in *The Handbook of Fluid Dynamics*, edited by R. W. Johnson, pp. 27-1–27-6, CRC Press, Boca Raton, Fla.

Press, W. H., B. P. Flannery, S. A. Teukolsky, and W. T. Vetterling (1986), *Numerical Recipes: The Art of Scientific Computing*, 818 pp., Cambridge Univ. Press, New York.

Rivard, W. C., and M. D. Torrey (1977), K-FIX: A computer program for transient, two-dimensional, two-fluid flow, *LA-NUREG-6623*, Los Alamos Natl. Lab., Los Alamos, N. M.

Rivard, W. C., and M. D. Torrey (1978), PERM: Corrections to the K-FIX code, *LA-NUREG-6623 Suppl.*, Los Alamos Natl. Lab., Los Alamos, N. M.

Rivard, W. C., and M. D. Torrey (1979), THREED: An extension of the K-FIX code for three-dimensional calculations, *LA-NUREG-6623 Suppl. II*, Los Alamos Natl. Lab., Los Alamos, N. M.

Rose, W. I., A. B. Kostinski, and L. Kelley (1995), Real-time C-band radar observations of 1992 eruption clouds from Crater Peak, Mount Spurr Volcano, Alaska, in *The 1992 Eruption of Crater Peak Vent, Mount Spurr Volcano, Alaska*, edited by T. E. C. Keith, *U.S. Geol. Surv. Bull.*, *2139*, 19–26.

Saad, Y., and M. H. Schultz (1986), GMRES: A generalized minimal residual algorithm for solving nonsymmetric linear systems, *SIAM J. Sci. Stat. Comput.*, *7*, 856–869.

Settle, M. (1978), Volcanic eruptions clouds and the thermal power output of explosive eruptions, *J. Volcanol. Geotherm. Res.*, *3*, 309–324.

Smagorinsky, J. (1963), General circulation experiments with the primitive equations: I. The basic experiment, *Mon. Weather Rev.*, *91*, 99–164.

Smagorinsky, J. (1993), Some historical remarks of the use of nonlinear viscosities, in *Large Eddy Simulation of Complex Engineering and Geophysical Flows*, edited by B. Galperin and S. A. Orszag, pp. 3–36, Cambridge Univ. Press, New York.

Spalding, D. B. (1981), Numerical computation of multiphase fluid flow and heat transfer, in *Numerical Computation of Multi-phase Flows*, *Lecture Series 1981–2*, edited by J. M. Buchlin and D. B. Spalding, von Karmán Inst. for Fluid Dyn., Rhode-Saint-Genèse, Belgium.

Spalding, D. B. (1983), Developments in the IPSA procedure for numerical computation of multiphase-flow phenomena with interphase slip, unequal, temperature, etc., in *Numerical Properties and Methodologies in Heat Transfer*, edited by T. M. Shih, pp. 421–436, Taylor and Francis, Philadelphia, Pa.

Sparks, R. S. J. (1986), The dimension and dynamics of volcanic eruption columns, *Bull. Volcanol.*, *48*, 3–15.

Sparks, R. S. J., and G. P. L. Walker (1977), The significance of vitric-enriched air-fall ashes associated with crystal-enriched ignimbrites, *J. Volcanol. Geotherm. Res.*, *2*, 329–341.

Sparks, R. S. J., L. Wilson, and G. Hulmes (1978), Theoretical modeling of the generation, movement and emplacement of pyroclastic flows by column collapse, *J. Geophys. Res.*, *83*, 1727–1739.

Sparks, R. S. J., M. I. Bursik, S. N. Carey, J. S. Gilbert, L. S. Glaze, H. Sigurdson, and A. W. Woods (1997), *Volcanic Plumes*, 574 pp., John Wiley, Hoboken, N. J.

Syamlal, M. (1994), MFIX documentation: User's manual, *DOE/METC-95/1013*, *DE9500,031*, 87 pp., U.S. Dep. of Energy, Washington, D. C.

Syamlal, M. (1998), MFIX documentation: Numerical technique, 80 pp., *DOE/MC/31346-5824*, *DE98002029*, U.S. Dep. of Energy, Washington, D. C.

Syamlal, M., W. Rogers, and T. J. O'Brien (1993), MFIX documentation: Theory guide, 49 pp., *DOE/METC-94/1004*, *DE9400,097*, U.S. Dep. of Energy, Washington, D. C.

Tahira, M., M. Nomura, Y. Sawada, and K. Kamo (1996), Infrasonic and acoustic-gravity waves generated by the Mount Pinatubo eruption of June 15, 1991, in *Fire and Mud: Eruptions and Lahars of Mount Pinatubo, Philippines*, edited by C. G. Newhall and R. S. Punonybanan, pp. 601–613, Univ. of Washington Press, Seattle.

Todesco, M., A. Neri, T. Esposti Ongaro, P. Papale, G. Macedonio, R. Santacroce, and A. Longo (2002), Pyroclastic flow hazard assessment at Vesuvius (Italy) by using numerical modeling. I. Large-scale dynamics, *Bull. Volcanol.*, *64*, 155–177.

Valentine, G. A., and K. H. Wohletz (1989), Numerical models of plinian eruption columns and pyroclastic flows, *J. Geophys. Res.*, *94*, 1867–1887.

Valentine, G. A., K. H. Wohletz, and S. Kieffer (1991), Sources of unsteady column dynamics in pyroclastic flow eruptions, *J. Geophys. Res.*, *96*, 21,887–21,892.

Van der Vorst, H. A. (1992), BI-CGSTAB: A fast and smoothly converging variant of BI-CG for the solution of nonsymmetric linear systems, *SIAM J. Sci. Stat. Comput.*, *13*, 631–644.

Walker, G. P. L. (1985), Origin of coarse lithic breccias near ignimbrite source vents, *J. Volcanol. Geotherm. Res.*, *25*, 157–171.

Wen, S., and W. I. Rose (1994), Retrieval of sizes and total masses of particles in volcanic clouds using AVHRR band 4 and 5, *J. Geophys. Res.*, *99*, 5421–5431.

Wilson, L., and J. W. Head (1981), Morphology and rheology of pyroclastic flows and their deposits, and guidelines for future observations, in *The 1980 Eruption of Mount St. Helens, Washington*, edited by P. W. Lipman and D. R. Mullineaux, *U.S. Geol. Surv. Prof. Pap.*, *1250*, 513–524.

Wilson, L., R. S. J. Sparks, T. C. Huang, and N. D. Watkins (1978), The control of volcanic column heights by eruption energetic and dynamics, *J. Geophys. Res.*, *83*, 1829–1836.

Woods, A. W., and C.-C. P. Caulfield (1992), A laboratory study of explosive volcanic eruptions, *J. Geophys. Res.*, *97*, 6699–6712.

Woods, A. W., and K. Wohletz (1991), Dimensions and dynamics of co-ignimbrite eruptions columns, *Nature*, *350*, 225–227.

Woods, A. W., and S. Self (1992), Thermal disequilibrium at the top of volcanic clouds and its effect on estimates of the column height, *Nature*, *355*, 628–630.

Zehner, P., and E. U. Schlunder (1970), Warmeleiftahigkeit von Schuttungen bei maβigen Temperaturen, *Chem. Ing. Tech.*, *42*, 933–941.

Zurn, W., and R. Widmer (1996), Worldwide observation of bichromatic long-period Rayleigh waves excited during the June 15, 1991, eruption of Mount Pinatubo, *Fire and Mud: Eruptions and Lahars of Mount Pinatubo, Philippines*, edited by C. G. Newhall and R. S. Punonybanan, pp. 615–624, Univ. of Washington Press, Seattle.

Sustained blasts during large volcanic eruptions

F. Legros*
Instituto Jaume Almera, Consejo Superior de Investigaciones Científicas, Lluís Solé i Sabarís s/n, 08028 Barcelona, Spain
K. Kelfoun
Département des Sciences de la Terre, 5 rue Kessler, 63038 Clermont-Ferrand, France

ABSTRACT

We carried out numerical simulations to investigate magma ascent in wide conduits during large explosive eruptions. Wide conduits allow high discharge rates, low frictional pressure losses, and shallow levels of explosive fragmentation of the magma within the conduit. In contrast with the commonly modeled lower rate eruptions during which magma fragments inside the conduit at depth and feeds a vertical eruptive jet, we find that for sufficiently high discharge rates (>10^{10} kg·s^{-1}) the fragmentation level may rise up to the surface. Gas-rich, unfragmented magma reaches the surface at high pressure and feeds a sustained volcanic blast. Geologic evidence for very high discharge rate eruptions, wide conduits, and shock waves in large pyroclastic flows supports the occurrence of this type of explosive eruption.

Keywords: magma ascent, conduit flow, volcanic blast, fragmentation.

INTRODUCTION

During volcanic eruptions, magma stored in a chamber at depth rises to the surface through a conduit. Decompression of magma as it rises causes an increasing fraction of its gas to exsolve and expand. The discharge rate and the eruptive style, effusive or explosive, depend on magma properties, conduit geometry, chamber pressure and depth, and country-rock permeability (Wilson et al., 1980; Jaupart and Allègre, 1991; Dobran, 1992; Woods and Koyaguchi, 1994; Woods, 1995; Papale, 1998). At low discharge rates, a large amount of gas escapes from the magma through the pervious conduit walls and eruptions tend to be effusive. A gas-poor, unfragmented magma reaches the vent at atmospheric pressure and feeds a lava flow or dome (Jaupart and Allègre, 1991; Woods and Koyaguchi, 1994). For higher discharge rates, eruptions tend to be explosive. Magma is fragmented in the conduit, and a mixture of gas and magma particles is erupted from the vent at high velocity as a vertical jet (Wilson et al., 1980; Dobran, 1992; Woods, 1995; Papale, 1998). Here we examine what happens at still higher discharge rates, typical of some caldera-forming eruptions, and show that magma may not fragment in the conduit. Instead, a different type of eruption occurs, in which the gas-rich magma reaches the surface unfragmented. This process does not give rise to an effusive eruption, however, because the gas-rich magma reaches the vent at high pressure and must therefore fragment at the surface and feed a sustained volcanic blast (Fig. 1).

*E-mail: flegros@ija.csic.es.

Conduit flow models have so far been applied to eruptions with discharge rates lower than 10^9 kg·s^{-1}, typical of eruptions that produce sustained Plinian columns and pyroclastic flows. However, there is increasing evidence that some large ignimbrites were deposited by pyroclastic flows with discharge rates to 10^{11} kg·s^{-1} or more (Dade and Huppert, 1996; Bursik and Woods, 1996; Freundt, 1999). For given magmatic conditions (magma viscosity and water content, chamber depth and pressure), a higher discharge rate implies a wider conduit, hence a lower pressure drop due to a lower friction in the conduit, and a shallower fragmentation level. In the following, we show that, for discharge rates sufficiently high, the fragmentation level may rise up to the surface.

CONDUIT FLOW MODEL

In order to estimate the conditions for which magma fragments at the surface, we use a steady, homogeneous, isothermal conduit-flow model, first developed by Wilson et al. (1980) and subsequently modified and refined by several authors (Jaupart and Allègre, 1991; Dobran, 1992; Woods, 1995; Papale, 1998). For a complete description of the model, the reader is referred to these papers. The steady-state assumption is justified as long as the eruption is much longer than the transit time of magma in the conduit. The isothermal and homogeneous assumptions do not significantly affect the conduit-flow model below the fragmentation level (Dobran, 1992; Papale, 1998) and so are adequate for this study. The model also assumes equilibrium degassing. Disequilibrium degassing has not yet been incor-

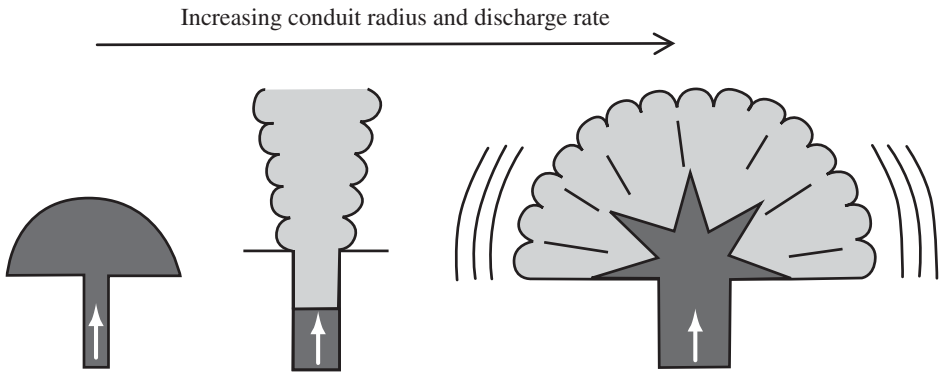

Figure 1. Schematic representation of magma ascent and eruption for increasing discharge rate.

porated into any existing conduit flow model. The effect would be to delay fragmentation, which would occur at shallower levels than in equilibrium degassing models, as discussed in a later section.

We simulate magma ascent for various initial conditions, reported in Table 1. We solve the equations for mass and momentum conservation along the conduit, parameterize the friction term and exsolution of volatiles with decompression, and impose a choking velocity at the vent (following Wilson et al., 1980). We allow the magma viscosity to increase with gas exsolution (following Woods, 1995; Jaupart and Allègre, 1991). Input data include initial viscosity (before exsolution), temperature and water content of the magma, depth and pressure of the chamber, and geometry and size of the conduit. Note that in this model, temperature determines only the exit velocity and has a minor influence on discharge rate and fragmentation depth. Viscosity is assumed to be temperature independent, a simplification allowed by the fact that the system is considered isothermal. We assume cylindrical conduits and vary the radius so as to obtain discharge rates between 10^7 and 10^{12} kg·s^{-1}. Fragmentation is assumed to occur either at a fixed gas-volume fraction of 0.77 (Wilson et al., 1980; Woods, 1995) or by brittle failure induced by the high elongational strain rates that affect the magma when it accelerates (Dingwell, 1996; Mader et al., 1996; Papale, 1999). For the latter criterion, we use a value of the elastic modulus of 25 GPa (following Papale, 1999). The two criteria predict fragmentation at nearly the same level because the strong accelerations responsible for strong elongational strain rates always occur for strong gradients of the gas-volume fraction between 0.6 and 0.85 (Papale, 1999).

TABLE 1. RESULTS OF MAGMA-ASCENT SIMULATIONS

Input data					Results	
H (m)	η_0 (Pa · s)	H_2O (wt%)	$P_0 - P_l$ (MPa)	R (m)	Z_f (m)	Q (kg · s^{-1})
4000	5 x 10^4	0.03	0	50	-519	2.1 x 10^8
4000	5 x 10^4	0.03	0	100	-78	1.3 x 10^{10}
4000	5 x 10^4	0.03	0	200	0	1.1 x 10^{11}
4000	5 x 10^4	0.04	0	100	-588	1.2 x 10^{10}
4000	5 x 10^4	0.04	0	200	-69	7 x 10^{10}
4000	5 x 10^4	0.04	0	500	0	9.1 x 10^{11}
4000	5 x 10^4	0.05	0	200	-644	6.5 x 10^{10}
4000	5 x 10^4	0.05	0	500	0	7.1 x 10^{11}
4000	5 x 10^4	0.06	0	500	-489	5.8 x 10^{11}
4000	5 x 10^4	0.06	0	1000	-6	3.3 x 10^{12}
7000	5 x 10^4	0.04	0	50	-1089	2.3 x 10^{09}
7000	5 x 10^4	0.04	0	100	-368	1.5 x 10^{10}
7000	5 x 10^4	0.04	0	200	0	1.2 x 10^{11}
2000	5 x 10^4	0.04	0	200	-361	5.5 x 10^{10}
2000	5 x 10^4	0.04	0	500	-2	5.8 x 10^{11}
2000	5 x 10^4	0.04	0	1000	0	3.1 x 10^{12}
4000	5 x 10^3	0.04	0	50	-235	3.9 x 10^{09}
4000	5 x 10^3	0.04	0	100	0	2.7 x 10^{10}
4000	5 x 10^5	0.04	0	200	-1155	4.7 x 10^{10}
4000	5 x 10^5	0.04	0	1000	-53	2.9 x 10^{12}
4000	5 x 10^4	0.04	20	100	-155	2.1 x 10^{10}
4000	5 x 10^4	0.04	20	200	0	1.7 x 10^{11}
4000	5 x 10^4	0.04	-20	700	-53	9.7 x 10^{11}
4000	5 x 10^4	0.04	-20	1000	-4	2.3 x 10^{12}

Note: Variables are as follows: H = chamber depth, η_0 = magma viscosity before exsolution, H_2O = initial water content, $P_0 - P_l$ = pressure in the chamber minus lithostatic pressure, R = conduit radius, Z_f = depth of fragmentation, Q = discharge rate. Densities of liquid magma and country rocks are 2300 and 2700 kg · m^{-3}, respectively, and magma temperature is 1100 K. This table presents only selected runs from the whole set of simulations performed to obtain the curves in Figures 2 and 3.

RESULTS

Magma can reach the surface unfragmented when the discharge rate is such that the exit pressure is still too high to allow fragmentation. Results in Table 1 show that depending on the input values for initial magma viscosity, water content, chamber depth, and pressure, the discharge rate above which magma fragments at the surface varies between 10^9 and 10^{11} kg·s^{-1}, implying that sustained blasts are likely to occur in some great eruptions. Figure 2 shows how the depth of fragmentation varies as a function of the discharge rate for various initial viscosities, water contents, chamber depths, and chamber pressures. The discharge rate above which magma fragments at the surface increases with increasing magma viscosity because this enhances the pressure drop due to friction. The discharge rate above which magma fragments at the surface also increases with increasing water content because this provokes fragmentation at higher pressure. An overpressure in the chamber increases the pressure at any level in the conduit and so allows the magma to reach the surface unfragmented at lower discharge rates. Chamber depth is seen to have only a minor effect on the level of fragmentation. Figure 3 shows the gas-volume fraction as a function of the depth below surface for various discharge rates and initial conditions as indicated in the caption. Whereas for discharge rates of 10^8 and 10^9 kg·s^{-1}, the model shows that fragmentation occurs at depth in the conduit, for discharge rates of 10^{10} kg·s^{-1} and more, magma does not fragment before it reaches the surface.

DISEQUILIBRIUM DEGASSING

The conduit-flow model we use assumes that pressure in the gas phase is always at equilibrium with pressure in the liquid magma. However, because in real magmas there is some delay in bubble nucleation and growth, pressure in the gas phase may be higher and gas-volume fraction lower than in the equilibrium model (Proussevitch and Sahagian, 1998; Navon and Lyakhovsky, 1998). For high magma-ascent velocities, this delay may become so important compared to the time of ascent, and the overpressure in the gas phase may become so high, that magma could reach the surface unfragmented (Proussevitch and Sahagian, 1998), although the pressure in the liquid would be lower than the threshold pressure for fragmentation in an equilibrium model. This process would allow unfragmented magma to reach the surface in eruptions with smaller discharge rates than those shown in Figure 2. However, for the effect of disequilibrium to be important, high magma-ascent velocities are required (Proussevitch and Sahagian, 1998), so disequilibrium could play a significant role at high discharge rates only. Bubble growth is more delayed in more viscous magmas, but these magmas also have lower ascent velocities, making the overall effect of viscosity difficult to evaluate a priori.

FRAGMENTATION PROCESS

An additional possible cause of fragmentation delay comes from the fragmentation process itself. Fragmentation of various materials upon sudden decompression has been experimentally observed to occur at a distinct front propagating into the material as a fragmentation wave, rather than disrupting it instantaneously (Phillips et al., 1995; Sugioka and Bursik, 1995; Alidibirov and Dingwell, 1996). The restriction of fragmentation to a narrow front zone has been explained by the recompression of the unfragmented material due to the acceleration of the fragmented material at the front (Sugioka and Bursik, 1995). It is unknown whether hydrated magmas would fragment in this way during sustained eruptions but, if such is the case, one can imagine two possibilities: (1) fragmentation-wave velocity is higher than magma-ascent velocity and, from the beginning of the eruption, the fragmentation front propagates downward until it reaches its equilibrium level, as in the experiments by Mader et al. (1997); (2) magma-ascent velocity is higher than fragmentation-wave velocity, and magma can reach the surface unfragmented. The latter possibility is less likely to occur in ex-

periments where expansion of gas is the only driving process of the eruption, but more likely in nature, where magma can acquire a high ascent velocity just because of its density difference with the country rocks.

For very high discharge rates, the pressure drop and the consequent magma expansion in the conduit are relatively low, and the flow is mainly driven by the density contrast between the bubbly magma and country rocks. There is no strong acceleration within the conduit. Instead, the high velocity is acquired where magma enters the conduit. Note that acceleration at the conduit entrance is unlikely to trigger brittle fragmentation of the magma in most cases. In order to cross the glass transition, a magma with an initial viscosity as high as 10^6 Pa·s should be affected by a strain rate in excess of 100 s^{-1} (Papale, 1999), which corresponds to an increase in velocity of 100 $m \cdot s^{-1}$ over a distance of <1 m. Continuity requires that the distance of greatest acceleration at the conduit entrance be of the same order of magnitude as the conduit diameter, which, for the discharge rates with which we are concerned, implies distances of acceleration in excess of 100 m and strain rates lower than 1 s^{-1}. Strain-induced fragmentation of the magma at the base of the conduit, as proposed by Mader et al. (1997) on the basis of their experiments, would only be possible for shallow magma chambers in which magma is already highly vesiculated and viscous.

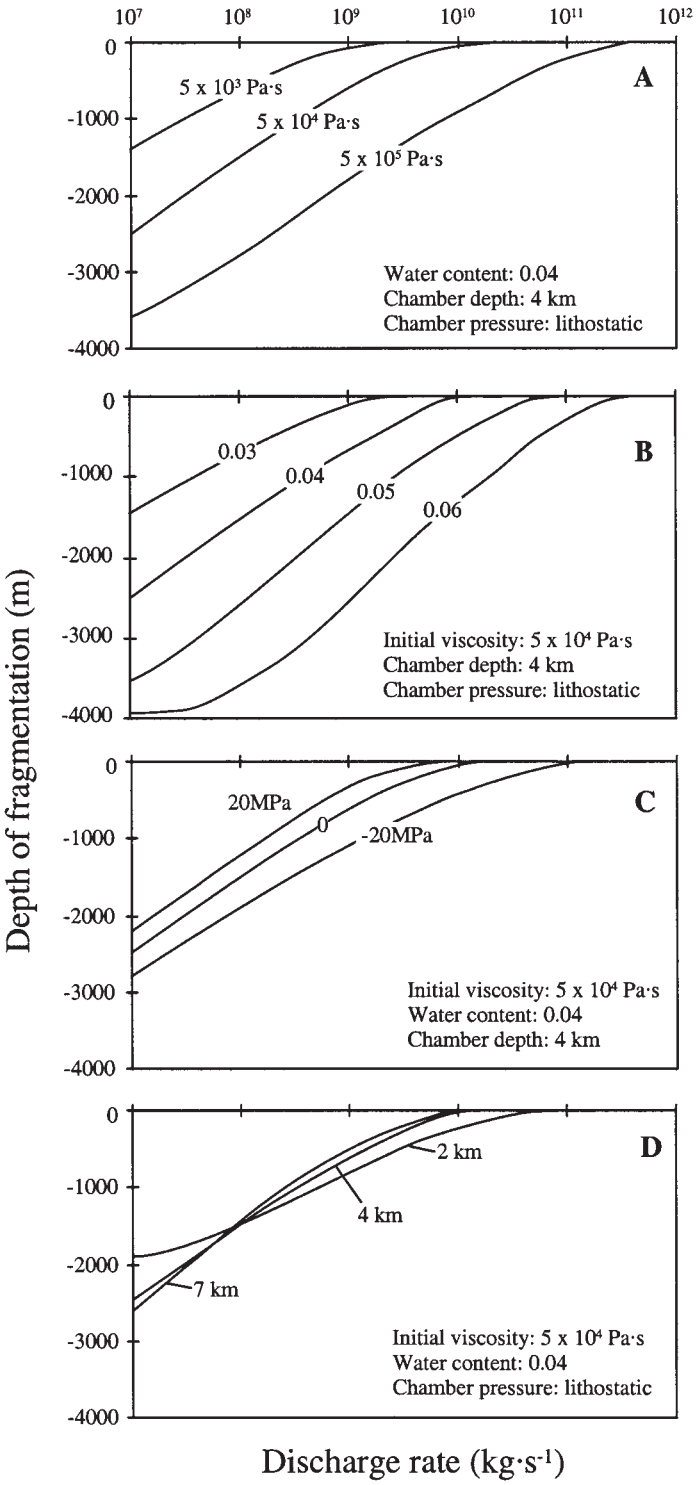

Figure 2. Depth of fragmentation vs. discharge rate for various initial conditions. Each graph shows effect of varying one parameter: (A) initial viscosity, (B) water content, (C) difference between chamber pressure and lithostatic, and (D) chamber depth. Densities of liquid magma and country rocks are 2300 and 2700 $kg \cdot m^{-3}$, respectively, and magma temperature is 1100 K.

DISCUSSION

The high discharge rates associated with caldera collapses are not necessarily associated with very wide cylindrical conduits. In some cases they may be due to the opening of long ring fissures, as proposed for the Bishop Tuff (Hildreth and Mahood, 1986) and the Crater Lake ignimbrite (Druitt and Bacon, 1986). For a given discharge rate, a fissure geometry favors a higher friction against the walls and a higher pressure drop in the conduit, and thus favors fragmentation at depth. However, for many calderas, the role of ring fissures as major conduits for magma has been seriously questioned (Walker, 1984). This is the case for the Taupo 1.8 ka (Walker, 1984) and the Aira 22 ka calderas (Aramaki, 1984), which have both produced eruptions with estimated discharge rates of 10^{11} $kg \cdot s^{-1}$ (Dade and Huppert, 1996; Bursik and Woods, 1996). For likely input variables at Taupo (initial viscosity 10^{4-5} Pa·s, water content 4.3%, chamber depth 4 km; Dunbar et al., 1989), the conduit radius required for such a discharge rate is 500–600 m. This radius gives a conduit volume of 3–4 km^3, comparable to the ~2.1 km^3 of lithic fragments in the ignimbrite (Wilson, 1985). Conduits as wide as 1 km that fed pyroclastic eruptions have been described beneath ancient eroded volcanic centers (Reedman et al., 1987; Kano et al., 1997). Enlargement of the central conduit could be prepared by hydrothermal weakening of the rocks and triggered by an underpressure

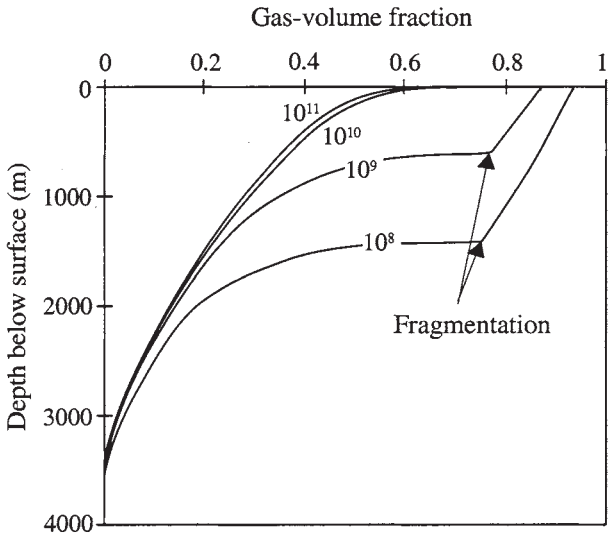

Figure 3. Variation of gas volume fraction with depth in conduit for discharge rates between 10^8 and 10^{11} $kg \cdot s^{-1}$. In these calculations, magma has water content of 0.04 and viscosity of 5×10^4 Pa·s before exsolution, chamber depth is 4 km, chamber pressure is lithostatic, densities of liquid magma and country rocks are 2300 and 2700 $kg \cdot m^{-3}$, respectively, and magma temperature is 1100 K.

greater in the conduit than in the chamber (Macedonio et al., 1994). A more detailed discussion of the effects of conduit geometry on caldera-forming eruptions has been presented elsewhere (Legros et al., 2000).

Fragmentation of magma at the surface is consistent with sedimentological features of some large ignimbrites such as large wave-like bedforms, interpreted as the result of shock waves (Self and Wright, 1983; Valentine et al., 1989). Rapidly expanding, high-velocity gas-particle mixtures are highly heterogeneous in density and velocity and may explain the proximal characteristics of large ignimbrites (Anilkumar et al., 1993). Heterogeneity is likely due to high acceleration rather than high velocity, suggesting that proximal characteristics of large ignimbrites may record a decompression zone. The often-quoted similarity between the Taupo 1.8 ka ignimbrite and the deposit of the Mount St. Helens blast (e.g., Walker and McBroome, 1983) also suggests a similar origin.

Textural characteristics of pumice from sustained blasts of hydrated magma should be similar to those produced by fragmentation in the conduit. In particular, tube pumice could be formed, because this texture results from elongational strain during magma acceleration rather than from shear strain due to friction against the conduit walls (Martí et al., 1999). The ascent to the surface of unfragmented magma at pressure higher than lithostatic also has implications for the mechanisms of conduit erosion, because they depend mainly on the characteristics of the flow (turbulent vs. laminar, bubbly magma vs. gaseous suspension) and on the pressure contrast between conduit and country rocks (Varekamp, 1993; Macedonio et al., 1994). The possible occurrence of sustained blasts during large eruptions also has implications for large pyroclastic flow modeling, which currently often considers gravity as the only driving force (Dade and Huppert, 1996; Bursik and Woods, 1996; Freundt, 1999), as well as for hazard assessment.

ACKNOWLEDGMENTS

Legros is supported by a contract from the European Union (ERBFMBICT-983445). The paper has benefited from the review by D. Sahagian and an anonymous reader.

REFERENCES CITED

Alidibirov, M., and Dingwell, D.B., 1996, Magma fragmentation by rapid decompression: Nature, v. 380, p. 146–148.

Anilkumar, A.V., Sparks R.S.J., and Sturtevant, B., 1993, Geological implications and applications of high-velocity two-phase flow experiments: Journal of Volcanology and Geothermal Research, v. 56, p. 145–160.

Aramaki, S., 1984, Formation of the Aira caldera, southern Kyushu, ~22,000 years ago: Journal of Geophysical Research, v. 89, p. 8485–8501.

Bursik, M.I., and Woods, A.W., 1996, The dynamics and thermodynamics of large ash flows: Bulletin of Volcanology, v. 58, p. 175–193.

Dade, W.B., and Huppert, H.E., 1996, Emplacement of the Taupo ignimbrite by a dilute turbulent flow: Nature, v. 381, p. 509–512.

Dingwell, D.B., 1996, Volcanic dilemma: Flow or blow?: Science, v. 273, p. 1054–1055.

Dobran, F., 1992, Nonequilibrium flow in volcanic conduits and application to the eruptions of Mount St. Helens, 1980, and Vesuvius in AD 79: Journal of Volcanology and Geothermal Research, v. 49, p. 285–311.

Druitt, T.H., and Bacon, C.R., 1986, Lithic breccia and ignimbrite erupted during the collapse of Crater Lake caldera, Oregon: Journal of Volcanology and Geothermal Research, v. 29, p. 1–32.

Dunbar, N., Hervig, R.L., and Kyle, P.R., 1989, Determination of pre-eruptive H_2O, F and Cl contents of silicic magmas using melt inclusions: Examples from Taupo volcanic centre: Bulletin of Volcanology, v. 51, p. 177–184.

Freundt, A., 1999, Formation of high-grade ignimbrites: Part II. A pyroclastic suspension current model with implications also for low-grade ignimbrites: Bulletin of Volcanology, v. 60, p. 545–567.

Hildreth, W., and Mahood, G.A., 1986, Ring-fracture eruption of the Bishop Tuff: Geological Society of America Bulletin, v. 97, p. 396–403.

Jaupart, C., and Allègre, C.J., 1991, Gas content, eruption rate and instabilities of eruption regime in silicic volcanoes: Earth and Planetary Science Letters, v. 102, p. 413–429.

Kano, K., Matsuura, H., and Yamauchi, S., 1997, Miocene rhyolitic welded tuff infilling a funnel-shaped eruption conduit, Shiotani, southeast of Matsue, SW Japan: Bulletin of Volcanology, v. 59, p. 125–135.

Legros, F., Kelfoun, K., and Martí, J., 2000, The influence of conduit geometry on the dynamics of caldera-forming eruptions: Earth and Planetary Science Letters, v. 179, p. 53–61.

Macedonio, G., Dobran, F., and Neri, A., 1994, Erosion processes in volcanic conduits and an application to the AD 79 eruption of Vesuvius: Earth and Planetary Science Letters, v. 121, p. 137–152.

Mader, H.M., Philips, J.C., Sparks, R.S.J., and Sturtevant, B., 1996, Dynamics of explosive degassing of magma: Observations of fragmenting two-phase flows: Journal of Geophysical Research, v. 101, p. 5547–5560.

Mader, H.M., Brodsky, E.E., Howard, D., and Sturtevant, B., 1997, Laboratory simulations of sustained volcanic eruptions: Nature, v. 388, p. 462–464.

Martí, J., Soriano, C., and Dingwell, D.B., 1999, Tube pumices as strain markers of the ductile-brittle transition during magma fragmentation: Nature, v. 402, p. 650–653.

Navon, O., and Lyakhovsky, V., 1998, Vesiculation processes in silicic magmas, *in* Gilbert, J., and Sparks, R.S.J., eds., The physics of explosive volcanic eruptions: Geological Society [London] Special Publication 145, p. 27–50.

Papale, P., 1998, Volcanic conduit dynamics, *in* Freundt, A., and Rosi, M., eds., From magma to tephra: Modeling physical processes of explosive volcanic eruptions: Amsterdam, Elsevier, p. 55–89.

Papale, P., 1999, Strain-induced magma fragmentation in explosive eruptions: Nature, v. 397, p. 425–428.

Phillips, J.C., Lane, S.J., Lejeune, A.M., and Hilton, M., 1995, The gum rosin-acetone system as an analogue to the degassing behaviour of hydrated magmas: Bulletin of Volcanology, v. 57, p. 263–268.

Proussevitch, A.A., and Sahagian, D.L., 1998, Dynamics and energetics of bubble growth in magmas: Analytical formulation and numerical modeling: Journal of Geophysical Research, v. 103, p. 18,223–18,251.

Reedman, A.J., Park, K.H., Merriman, R.J., and Kim, S.E., 1987, Welded tuff infilling a volcanic vent at Weolseong, Republic of Korea: Bulletin of Volcanology, v. 49, p. 541–546.

Self, S., and Wright, J.V., 1983, Large wave forms from the Fish Canyon Tuff, Colorado: Geology, v. 11, p. 443–446.

Sugioka, I., and Bursik, M., 1995, Explosive fragmentation of erupting magma: Nature, v. 373, p. 689–692.

Valentine, G.A., Buesch, D.C., and Fisher, R.V., 1989, Basal layered deposits of the Peach Springs Tuff, north-western Arizona, USA: Bulletin of Volcanology, v. 51, p. 395–414.

Varekamp, J.C., 1993, Some remarks on volcanic vent evolution during Plinian eruptions: Journal of Volcanology and Geothermal Research, v. 54, p. 309–318.

Walker, G.P.L., 1984, Downsag calderas, ring faults, caldera sizes, and incremental caldera growth: Journal of Geophysical Research, v. 89, p. 8407–8416.

Walker, G.P.L., and McBroome, L.A., 1983, Mount St. Helens 1980 and Mount Pelée 1902: Flow or surge?: Geology, v. 11, p. 571–574.

Wilson, C.J.N, 1985, The Taupo eruption, New Zealand: II. The Taupo ignimbrite: Royal Society of London Philosophical Transactions, ser. A, v. 314, p. 229–310.

Wilson, L., Sparks, R.S.J., and Walker, G.P.L., 1980, Explosive volcanic eruptions: IV. The control of magma properties and conduit geometry on eruption column behaviour: Royal Astronomical Society Geophysical Journal, v. 63, p. 117–148.

Woods, A.W., 1995, The dynamics of explosive volcanic eruptions: Reviews of Geophysics, v. 33, p. 395–430.

Woods, A.W., and Koyaguchi, T., 1994, Transitions between explosive and effusive eruption of silicic magmas: Nature, v. 370, p. 641–644.

Manuscript received February 2, 2000
Revised manuscript received July 10, 2000
Manuscript accepted July 17, 2000

ELSEVIER

Journal of Volcanology and Geothermal Research 98 (2000) 235–241

Journal of volcanology and geothermal research

www.elsevier.nl/locate/jvolgeores

On the ability of pyroclastic flows to scale topographic obstacles

F. Legros[a,*], K. Kelfoun[b]

[a]*Instituto Jaume Almera, Consejo Superior de Investigaciones Científicas, Lluís Solé i Sabarís s/n, 08028 Barcelona, Spain*
[b]*Département des Sciences de la Terre, Université Blaise Pascal, 5 rue Kessler, 63038 Clermont-Ferrand, France*

Received 1 June 1999; accepted 8 November 1999

Abstract

We present a simple analysis of momentum dissipation in a pyroclastic flow with high initial velocity and show that the deceleration is inversely proportional to the volumetric flow rate. Consequently, for a given mass flow rate, dense flows slow down more rapidly than dilute flows. The analysis ignores density stratification and flow unsteadiness, and assumes that deceleration is due to turbulent dissipation alone, but the results have implications for a wide range of flow regimes. We apply our analysis to the distribution of the 1800-year-old deposits of the Taupo pyroclastic flow, the velocity of which is constrained by the height of topographic obstacles that it scaled. The volumetric flow rate required to maintain velocities high enough to overtop the rugged topography is consistent with a dilute flow, but strongly argues against the dense flow hypothesis. The same conclusion applies to other pyroclastic flow deposits distributed over rugged terrain. © 2000 Elsevier Science B.V. All rights reserved.

Keywords: pyroclastic flow; topographic obstacles; ignimbrite

1. Introduction

The recognition of widespread ignimbrites, extending several tens of kilometres radially away from the source vent, and mantling topographic relief over 1000 m high (Wilson, 1985; Fisher et al., 1993; Baer et al., 1997), has major volcanic hazard implications and represents a challenging puzzle for volcanologists. A pumice-rich pyroclastic flow may be generated when a volcanic eruption column collapses (Sparks et al., 1978), or when a magma chamber is suddenly unroofed (Self and Wright, 1983; Valentine et al., 1989; Druitt, 1992). In both cases, the initial pyroclastic flow is likely to be dilute. In a dilute current, particles have low volume concentration ($<1\%$) and are maintained in suspension by turbulence. Even if turbulence keeps particles suspended, there is always a net downward settling of particles, which may produce a dense flow at the base of the dilute current. The dense flow may have a solids concentration of up to several tens of volume percent (Sparks, 1976). The behaviour of particles within the dense flow is controlled by a combination of particle buoyancy, viscous drag by the matrix, and grain-to-grain interactions. During transport, the dense flow may become decoupled from the dilute current and follow an independent path (Valentine, 1987; Branney and Kokelaar, 1992; Druitt, 1992; Valentine and Fisher, 1993).

Within this widely accepted view, there has been persistent debate between two end-member models, here called the dense flow and the dilute flow models (e.g. Sparks, 1976; Sparks et al., 1978; Wilson, 1985;

* Corresponding author. Fax: +34-93-4110012.
E-mail address: flegros@ija.csic.es (F. Legros).

0377-0273/00/$ - see front matter © 2000 Elsevier Science B.V. All rights reserved.
PII: S0377-0273(99)00184-5

Valentine, 1987; Druitt, 1992; Fisher et al., 1993; Dade and Huppert, 1996; Baer et al., 1997). The dense flow model assumes that a dense flow forms rapidly by "deflation" of the dilute current and then travels independently to greater distances. The region of transition is called the deflation zone and is restricted to the near-vent area (Sparks et al., 1978; Wilson, 1985). The dense flow is thought to overtop topographic obstacles due to its high velocity, acquired from the collapsing volcanic column and on the volcano slopes (Sparks et al., 1978). Dissipative losses of kinetic energy may be reduced by an upward flux of gas and air through the flow which partly fluidizes it (Sparks, 1976).

The dilute flow model assumes that the dilute part of the flow is responsible for sediment transport to the distal limit of the deposit while the dense, basal part of the flow, if any, is responsible only for local drainage into topographic lows (Valentine, 1987; Druitt, 1992; Fisher et al., 1993; Baer et al., 1997). There is no deflation zone as the density of the current decreases with distance (Bursik and Woods, 1996). The overall distribution of the deposit is controlled by the dilute current while sedimentary features at the outcrop scale are determined by conditions in the denser basal depositional layer (Branney and Kokelaar, 1992). The dilute current is able to scale topographic obstacles both because of its great depth and its high velocity.

The choice between these two models is more than an academic question. Knowledge of the state in which a pyroclastic flow travels is essential for modelling its transport. The impact of a flow on man-made structures would be much greater for a high-velocity, dense pyroclastic flow, than for a fast, dilute flow and its associated denser but slower basal depositional system (Valentine, 1998). If a pyroclastic flow is essentially driven by its dense basal part, natural or man-made dams may offer some protection, but attempts to block or divert a flow driven by its dilute portion may be useless.

Two recent papers have applied a model of sedimentation from a dilute current to ignimbrite-forming pyroclastic flows (Bursik and Woods, 1996; Dade and Huppert, 1996). Neither deals with possible transport by the dense basal part of the flow and thus both envisage the end-member case where the deposit distribution is controlled only by the dilute current. With this assumption, both studies are successful in predicting the large-scale geometry of deposits as widespread as the largest known ignimbrites, for eruptions with high discharge rates (10^{10}–10^{11} kg s^{-1}), even if they are not able to predict all the sedimentary structures (Wilson, 1997). This result hints that a dilute flow model, with high discharge rate, may be appropriate for pyroclastic flows that form large ignimbrites. However, it does not rule out the possibility that real ignimbrite-forming eruptions have lower discharge rates and small deflation zones, beyond which the transporting flows are predominantly dense. The aim of this study is to test this possibility based on a physical analysis of momentum dissipation in pyroclastic flows and the observation that some leave deposits atop topographically high relief.

2. Physical analysis

We analyse the 1800-year-old Taupo ignimbrite because it has a wide, radial distribution (~80 km) over rugged terrain and is probably the best-documented of its kind (Wilson, 1985). Models of sedimentation from dilute currents have shown that an eruption with discharge rate 10^{11} kg s^{-1}, and a grainsize distribution similar to that of the Taupo ignimbrite, would produce a deposit with the same grainsize and thickness distribution (Bursik and Woods, 1996; Dade and Huppert, 1996). The models of sedimentation from dilute currents are robust. They are based on well-understood settling laws, combined with simple gravity current physics. They have been tested in the laboratory (e.g. Bonnecaze et al., 1993) and are applied with success to sedimentation from Plinian clouds (Bursik et al., 1992; Sparks et al., 1992). Explaining the distribution of the Taupo ignimbrite by sedimentation from a dilute current requires only the assumptions that the flow was initially dilute, reasonable for a pyroclastic flow generated by column collapse or blast, and that the discharge rate was indeed in the order of 10^{11} kg s^{-1}. If the discharge rate was less, the dilute flow would have reached a shorter distance, and the rest of the deposit could only have been emplaced by dense transporting flows. For example, a discharge rate in the order of 10^{9} kg s^{-1} would have allowed the dilute flow to reach a distance

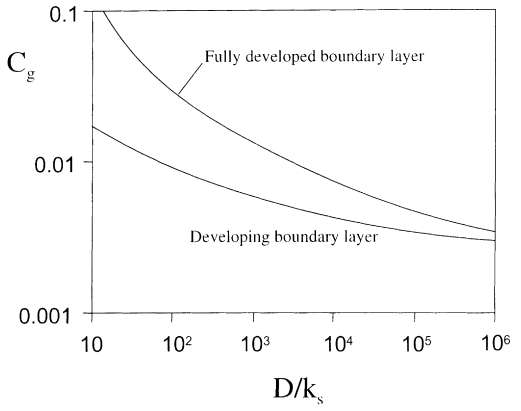

Fig. 1. Value of the drag coefficient (C_g) as a function of the thickness of the flow (D) divided by the size of the roughness element (k_s). Curves are calculated from Sparks et al. (1978) for a developing boundary layer and a fully developed boundary layer.

of about 10 km from the vent (Bursik and Woods, 1996). This is about the distance at which the flow would have "deflated" in the model of Wilson (1985). From 10 km to the distal limit, the ignimbrite would have been emplaced by a transporting dense flow. A discharge rate higher than 10^{11} kg s^{-1} would have maintained the dilute flow farther than the actual distal limit of the deposit.

We will therefore test whether a dense flow might also explain the general distribution of the Taupo ignimbrite with the limitation that the discharge rate be less than 10^{11} kg s^{-1}. Because there is no physical model for the transport and deposition of material by dense pyroclastic flows, a simple test is applied, based on the momentum equation and the observation that the Taupo pyroclastic flow was able to scale several tall obstacles.

At 60 km from the inferred vent, remnants of the ignimbrite are found on Ruapehu volcano up to an elevation 1500 m higher than the surrounding plain and vent (Wilson, 1985). The minimum velocity (U) necessary to reach this height (H) can be found by converting all the kinetic energy into potential energy, $U = \sqrt{2gH}$, which for $H = 1500$ m gives a minimum velocity $\sim$170 m s^{-1} (Wilson, 1985). This velocity calculation is valid as long as the flow depth is small compared to the obstacle height, which is the case for the dense flow considered here, as shown a posteriori. Woods et al. (1998) showed that for deep (dilute) flows, the gravitational potential energy in the flow is non-negligible in driving it over a ridge. Because the flow at Taupo travelled radially away from the vent, as shown by the deposit (Wilson, 1985), the mass flow rate at a certain distance R can be expressed by $M = 2\pi RUD\rho$, where D is the flow depth, U its velocity and ρ its density. The mass flow rate at R is related to the initial mass discharge rate (M_0) by $M = M_0 P_{(R)}$, where $P_{(R)}$ is the mass proportion of the deposit which lies beyond the distance R. About 20% of the mass of the Taupo ignimbrite lies beyond 60 km from the vent (Wilson, 1985).

For an initial discharge rate of 10^{11} kg s^{-1}, and with the constraint that $U > 170$ m s^{-1}, the maximum depth of the flow (D) at 60 km may be calculated as a function of its density. Considering a dense flow of density 500 kg m^{-3} (Wilson, 1985), corresponding to 30–50% solids volume concentration and about half the density of the ignimbrite, yields a flow depth of less than 0.6 m at $R = 60$ km. This small depth justifies a posteriori the validity of the velocity calculation. Note that this depth is a maximum limit if we want to explain the emplacement of the ignimbrite by a flow of this density because the discharge rate used (10^{11} kg s^{-1}) is that for which a dilute current is able to explain the deposit.

The small depth calculated for this hypothetical dense pyroclastic flow at Taupo casts doubts on its ability to maintain a high velocity far from the vent. This is shown by a simple analysis of momentum dissipation with distance. We use an analysis that has already been applied to the deceleration of pyroclastic flows (Sparks et al., 1978), and which assumes that the movement is resisted dominantly by turbulence in the body of the flow. This assumption is discussed further below. For simplicity, we do not envisage density stratification (Valentine, 1987). Assuming steady conditions and a flow much denser than air with no lateral density gradient yields:

$$U\,\mathrm{d}U/\mathrm{d}R + U^2(\mathrm{d}M/M)/\mathrm{d}R$$

$$= g(\sin\alpha - (\mathrm{d}D/\mathrm{d}R)\cos\alpha) - C_g U^2/2D, \qquad (1)$$

where α is the slope angle and C_g is the drag coefficient with a typical value around 0.01 (Sparks et al., 1978). Eq. (1) is not a complete flow model, but is just a form of the momentum equation. The second term on the left-hand side is the contribution to the momentum loss by sedimentation rather than by deceleration.

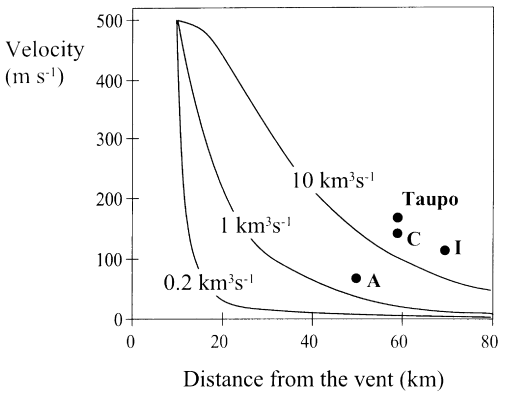

Fig. 2. Theoretical velocity (from Eq. (1)) for the Taupo pyroclastic flow spreading over 360° on a horizontal floor with an initial velocity of 500 m s^{-1} at 10 km and with different flow rates. The velocity decreases with distance from the vent due to turbulent dissipation. In these calculations $C_g = 0.01$, and the flow density is not relevant. The rate of mass loss $(dM/M)/dR$ is measured from the thickness of the Taupo ignimbrite and so the curves are specific to that pyroclastic flow. However, neglecting sedimentation (Eq. (1) without the second term on the left-hand side) does not greatly affect the curves, which are approximately valid for any pyroclastic flow. Solid circles: velocities necessary to explain the topographical obstacles passed by various pyroclastic flows ($U = \sqrt{2gH}$): I = Ito (Baer et al., 1997), C = Campanian (Fisher et al., 1993), A = Aniakchak (Miller and Smith, 1977).

This assumes that particles leave the current with zero momentum. A similar hypothesis is used by Van Gassen and Cruden (1989) in a dynamical model for debris avalanches, in which the progressive loss of mass by the flow allows it to maintain a high velocity despite momentum loss due to friction. Bursik and Woods (1996), in their dilute pyroclastic flow model, use a different approach as they assume that momentum is lost with the settling particles. It is unclear which is the more correct approach and we choose that of Van Gassen and Cruden (1989), which favours lower deceleration of the flow. The value of $(dM/M)/dR$ varies with R and is found from the thickness distribution of the veneer facies of the ignimbrite (Wilson, 1985).

We use a constant value of the drag coefficient, $C_g = 0.01$. Fig. 1 shows the value of C_g as a function of the ratio between the thickness of the flow and k_s, the size of the roughness element (cf. Sparks et al., 1978; Valentine, 1987). It is likely that the size of the roughness element that the flow "sees" depends on the flow scale. For flows about 1 km thick, topographical elements from a few metres to hundreds of metres are likely to control turbulence, while for flows about 1 m thick the relevant roughness elements must be centimetric to decimetric. Therefore the ratio D/k_s should not vary greatly and the practical approach that considers a constant value for C_g seems reasonable. Even for a thick flow (~100 m) and a small k_s (~1 cm), C_g would not fall below 0.004. Note that a fast, dense flow is unlikely to maintain a thickness of 100 m far from the vent, as shown by the above mass conservation arguments.

It is interesting to note that in Eq. (1), which remains valid as long as the flow density is much higher than the density of ambient air, deceleration does not depend on the flow density. The deceleration is inversely proportional to the flow depth, hence, for a given velocity and distance from vent, to the volumetric flow rate. Therefore, for a given mass flow rate, a dense flow is expected to decelerate more rapidly than a dilute one as it would have a lower volumetric flow rate.

From Eq. (1), the velocity of the Taupo pyroclastic flow as a function of the distance from the vent has been calculated numerically for various flow rates, a very high initial velocity (500 m s^{-1}), and a very large fountain radius $R_0 = 10$ km. At Taupo, between the vent and Ruapehu, the topography is subhorizontal ($\alpha \sim 0°$). Fig. 2 shows that a flow rate higher than 10 km^3 s^{-1} is necessary to explain the height climbed at Ruapehu, a result consistent with the dilute flow model of Dade and Huppert (1996). For a dense flow with density 500 kg m^{-3}, this would require a mass discharge rate in excess of 5×10^{12} kg s^{-1} and an eruption duration of less than 6 s for the whole ignimbrite (3×10^{13} kg), which is unrealistically short. Moreover, this discharge rate is more than 50 times greater than that required for a dilute flow to achieve 80 km runout (10^{11} kg s^{-1}, Bursik and Woods, 1996; Dade and Huppert, 1996). A flow with such a high discharge rate would likely transport particles in dilute suspension over several hundred kilometres (Bursik and Woods, 1996; Dade and Huppert, 1996). The lower curve of Fig. 2 is for a volumetric flow rate of 2×10^8 m^3 s^{-1}, which, for a flow of density 500 kg m^{-3}, corresponds to a mass flow rate of 10^{11} kg s^{-1}. It may be seen that this flow would dissipate its initial velocity within a few kilometres of vent, which remains true even for a C_g

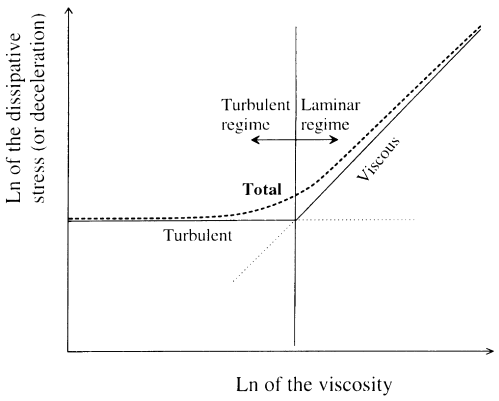

Fig. 3. Schematic relation between dissipative stresses (or deceleration caused by them) and viscosity, for flows of fixed discharge rate. Turbulent stress is not affected by viscosity while viscous stress varies linearly with it. Laminar regime occurs when viscous stress dominates turbulent stress, corresponding to an increase in total dissipative stress.

as low as 0.001. These results present a serious problem for the application of the dense flow model to the Taupo ignimbrite.

Fig. 2 also shows the velocities necessary to explain the topographic obstacles passed by three other pyroclastic flows. Strictly, the curves of Fig. 2 are valid only for the Taupo pyroclastic flow, as the term (dM/M)/dR in Eq. (1) is taken from the distribution of the deposit. This is a consequence of the way we take into account sedimentation in the momentum dissipation analysis. However, if we consider that momentum is lost with the settling particles (cf. Bursik and Woods, 1996), we may drop the term containing (dM/M)/dR from the left-hand side of Eq. (1). The curves thus obtained are actually very close to those of Fig. 2 and are valid for any pyroclastic flow. They show that emplacement of the Aniakchak, Campanian and Ito ignimbrites by dense pyroclastic flows requires extremely high discharge rates ($>10^{12-13}$ kg s^{-1}) while discharge rates of 10^{10-11} kg s^{-1} suffice with a dilute flow model.

3. Discussion

The analysis used here is similar to that used by Sparks et al. (1978). However, these authors reached a different conclusion, that dense pyroclastic flows are able to maintain high velocities far from the vent. The present Eq. (1) differs from their Eq. (3) in that one term is added on the left-hand side, U^2(dM/M)/dR, and one on the right-hand side, $-g$(dD/dR) cos α. The term containing dD/dR is always very small and always tends to reduce the deceleration since we did not consider the possible entrainment of air. The term involving dM/M is the part of the momentum loss accommodated by mass loss rather than velocity loss. Thus, both terms tend to lower the deceleration and should help to maintain higher velocities. In Sparks et al. (1978, Fig. 6), the flow rate is not explicitly expressed. The volumetric flow rate one may calculate from the vent radius and exit velocity is the flow rate at vent. This is different (and much less) than the flow rate after entrainment and heating of air in the fountain, used in the calculation of the curves. In fact, the upper curve of Sparks et al. (1978, Fig. 6) corresponds to a flow rate of about 6 km^3 s^{-1}, which for a dense flow ($\sim$500 kg m^{-3}), implies a mass flow rate of 3×10^{12} kg s^{-1}. As stated by Sparks et al. (1978), the curves are for dilute pyroclastic flows and "thinner, denser flows would experience greater frictional drag and so would exhibit greater deceleration". The importance of this statement, however, has not been fully appreciated and, following Sparks et al. (1978), it has been widely assumed that dense pyroclastic flows could maintain high velocities far from vent. Inspection of our Eq. (1), or Sparks et al. (1978, Eqs. (2) and (3)), reveals that deceleration is inversely proportional to the thickness or volume flow rate. Hence for a given mass flow rate, a dense pyroclastic flow with a density of 500 kg m^{-3} would experience a deceleration 100 times greater than a dilute flow of density 5 kg m^{-3}, or the same as a dilute flow with a mass flow rate 100 times less. At constant mass flow rate, a flow that would experience a deceleration of 1 m s^{-2} if dilute, and hence could maintain a high velocity over a long distance, would experience a deceleration of about 100 m s^{-2} when dense. It is therefore unlikely that dense pyroclastic flows can maintain velocities sufficient to pass high obstacles far from the vent, unless extremely high discharge rates can be justified. In that case, however, the dilute flow would be able to transport particles very far before they would settle in the dense basal flow (Bursik and Woods, 1996; Dade and Huppert, 1996).

In Eq. (1), we assume steady conditions for

simplicity. In fact the Taupo pyroclastic flow was a very short-lived current, for which the peak discharge rate may have lasted less than the transport time of a particle from the vent to the distal limit of the deposit. As such, the true velocity of the flow would be less than is calculated here, and its ability to pass obstacles would also be lower.

The assumption made here of turbulent dissipation of kinetic energy seems reasonable given the high flow velocities considered. Even much smaller and slower pyroclastic flows have been successfully modelled as turbulent flows (Levine and Kieffer, 1991). However, what would happen under another flow regime? For example, considering a Newtonian fluid, would a flow at the same velocity but in the laminar regime dissipate less energy? No, because for a given flow rate, the transition from a turbulent to a laminar regime implies an increase in both viscosity and total dissipative stress (Fig. 3). This may seem counter intuitive because it is normal to consider the transition from turbulent to laminar regime due to decreasing flow rates in flows of fixed viscosity. In that case, the transition implies a decrease in the dissipative stress but also a decrease in velocity. Here, we are interested in the possibility of decreasing the dissipative stress in order to *increase* the velocity for a given flow rate. In order to be in the laminar regime, a flow must have a low Reynolds number ($Re = \rho UD/\eta$), where η is the flow viscosity. Given the expression for the mass flow rate ($M = 2\pi R\rho UD$), the Reynolds number can be written $Re = M/2\pi R\eta$. This shows that, for a given mass flow rate, only an increase in viscosity can lower the Reynolds number at a given distance from vent. The dissipative viscous stress ($\approx \eta U/D$) increases linearly with viscosity. By definition, the flow is laminar when viscous stress dominates over turbulent stress, so laminar flows must have higher total dissipative stresses and deceleration than turbulent flows of the same flow rate (Fig. 3).

In flows involving mixtures of fluid and granular material, relations between the various dissipative stresses, including viscous drag, turbulence, intergranular collisions, and Coulomb friction, are commonly examined using dimensionless numbers, analogous to the Reynolds number, that indicate which stresses are dominant and which negligible (e.g. Iverson, 1997). The relation between turbulence and granular stresses is poorly understood and the stresses are probably not strictly additive. Nevertheless, following the reasoning developed above for a Newtonian fluid, it may be assumed that, in an increasingly concentrated suspension, turbulent stresses become negligible only when exceeded by another stress. Therefore, for a given flow rate, a dense pyroclastic flow is either turbulent, and our calculation of the momentum dissipation is valid, or it is in another flow regime in which the dominant dissipative stress must be higher than the calculated turbulent stress. In this latter case, the deceleration is actually more efficient than calculated here, so as to make it even more difficult for a dense flow to preserve a high velocity far from vent.

Some great debris avalanches are known to have climbed topographic obstacles (Voight, 1978), although lower and nearer to source than those climbed by pyroclastic flows. Such debris avalanches are often quoted as examples of unambiguously dense flows that have gained elevation owing to their momentum. However, because they typically involve a great volume of material, released essentially instantaneously, that passes through a limited width, such debris avalanches have very high flow rates per unit width which allow them to maintain great depths and velocities far from the source. In contrast, we have seen that the depth of a radially spreading, dense pyroclastic flow rapidly decreases away from the vent. Consequently the deceleration of such a flow is rapid and the high velocity required to scale large topographic obstacles cannot be maintained far from vent.

4. Conclusions

An analysis has been presented of the momentum dissipation in an unstratified, steady, turbulent pyroclastic flow. Its application to the 186 AD Taupo eruption shows that a dense pyroclastic flow cannot explain the observed presence of ignimbrite atop high topographic obstacles. This suggests that a dilute current was responsible for transporting the volcanic particles up to the distal limit of the deposit, while a dense basal flow was responsible only for local drainage into topographic lows. Several other pyroclastic flows have overtopped high barriers far from the vent (Miller and Smith, 1977; Fisher et al., 1993;

Baer et al., 1997) and the same analysis applied to them leads to the same conclusion (Fig. 2). For the Ito and Campanian ignimbrites, transport by a dilute current has already been proposed on the basis of imbrication of iron-bearing, elongate grains measured by the anisotropy of magnetic susceptibility (Fisher et al., 1993; Baer et al., 1997). The noted difficulty for dense flows to maintain high velocities far from vent suggests that most unconfined ignimbrites are likely to be transported by dilute pyroclastic currents.

Acknowledgements

We thank T. Druitt, W. Hildreth, M. Nathenson, G. Valentine and C. Wilson for comments on an earlier version of the paper, and M. Branney and M. Bursik for detailed reviews. G. Ablay revised the English text. F.L. is supported by a grant from the EC (ERBFMBICT983445).

References

Baer, E.M., Fisher, R.V., Fuller, M., Valentine, G.A., 1997. Turbulent transport and deposition of the Ito pyroclastic flow: determinations using anisotropy of magnetic susceptibility. J. Geophys. Res. 102, 22 565–22 586.

Bonnecaze, R.T., Huppert, H.E., Lister, J.R., 1993. Particle-driven gravity currents. J. Fluid Mech. 250, 339–369.

Branney, M.J., Kokelaar, P.A., 1992. A reappraisal of ignimbrite emplacement: progressive aggradation and changes from particulate to non-particulate flow during emplacement of high-grade ignimbrite. Bull. Volcanol. 54, 504–520.

Bursik, M.I., Woods, A.W., 1996. The dynamics and thermodynamics of large ash flows. Bull. Volcanol. 58, 175–193.

Bursik, M.I., Sparks, R.S.J., Gilbert, J.S., Carey, S.N., 1992. Sedimentation of tephra by volcanic plumes. I. Theory and its comparison with a study of the Fogo A plinian deposit, Sao Miguel (Azores). Bull. Volcanol. 54, 329–344.

Dade, W.B., Huppert, H.E., 1996. Emplacement of the Taupo ignimbrite by a dilute turbulent flow. Nature 381, 509–512.

Druitt, T.H., 1980. Emplacement of the 18 May 1980 lateral blast deposit ENE of Mount St. Helens, Washington. Bull. Volcanol. 54, 554–572.

Fisher, R.V., Orsi, G., Ort, M., Heiken, G., 1993. Mobility of a large-volume pyroclastic flow: emplacement of the Campanian ignimbrite, Italy. J. Volcanol. Geotherm. Res. 56, 205–220.

Iverson, R.M., 1997. The physics of debris flows. Rev. Geophys. 35, 245–296.

Levine, A., Kieffer, S.W., 1980. Hydraulics of the August 7, 1980, pyroclastic flow at Mount St. Helens, Washington. Geology 19, 1121–1124.

Miller, T.P., Smith, R.L., 1977. Spectacular mobility of ash flows around Aniakchak and Fisher calderas, Alaska. Geology 5, 173–176.

Self, S., Wright, J.V., 1983. Large wave forms from the Fish Canyon Tuff, Colorado. Geology 11, 443–446.

Sparks, R.S.J., 1976. Grain size variations in ignimbrites and implications for the transport of pyroclastic flows. Sedimentology 23, 147–188.

Sparks, R.S.J., Wilson, L., Hulme, G., 1978. Theoretical modeling of the generation, movement and emplacement of pyroclastic flows by column collapse. J. Geophys. Res. 56, 145–160.

Sparks, R.S.J., Bursik, M.I., Ablay, G.J., Thomas, R.M.E., Carey, S.N., 1992. Sedimentation of tephra by volcanic plumes. Part 2: controls on thickness and grain-size variations of tephra fall deposits. Bull. Volcanol. 54, 685–695.

Valentine, G.A., 1987. Stratified flow in pyroclastic surges. Bull. Volcanol. 49, 616–630.

Valentine, G.A., 1998. Damage to structures by pyroclastic flows and surges, inferred from nuclear weapons effects. J. Volcanol. Geotherm. Res. 87, 117–140.

Valentine, G.A., Fisher, R.V., 1993. Glowing avalanches: new research on volcanic density currents. Science 259, 1130–1131.

Valentine, G.A., Buesch, D.C., Fisher, R.V., 1989. Basal layered deposits of the Peach Springs Tuff, north-western Arizona, USA. Bull. Volcanol. 51, 395–414.

Van Gassen, W., Cruden, D.M., 1989. Momentum transfer and the friction in the debris of rock landslides. Can. Geotech. J. 26, 623–628.

Voight, B. (Ed.), 1978. Rockslides and Avalanches. 1. Natural Phenomena. Elsevier, Amsterdam, 833 pp.

Wilson, C.J.N., 1985. The Taupo eruption, New Zealand. II. The Taupo ignimbrite. Philos. Trans. R. Soc. London Ser. A 314, 229–310.

Wilson, C.J.N., 1997. Emplacement of the Taupo ignimbrite. Nature 385, 306–307.

Woods, A.W., Bursik, M.I., Kurbatov, A.V., 1998. The interaction of ash flows with ridges. Bull. Volcanol. 60, 38–51.

Suitability of simple rheological laws for the numerical simulation of dense pyroclastic flows and long-runout volcanic avalanches

Karim Kelfoun[1]

Received 9 April 2010; revised 1 May 2011; accepted 1 June 2011; published 23 August 2011.

[1] The rheology of volcanic rock avalanches and dense pyroclastic flows is complex, and it is difficult at present to constrain the physics of their processes. The problem lies in defining the most suitable parameters for simulating the behavior of these natural flows. Existing models are often based on the Coulomb rheology, sometimes with a velocity-dependent stress (e.g., Voellmy), but other laws have also been used. Here I explore the characteristics of flows, and their deposits, obtained on simplified topographies by varying source conditions and rheology. The Coulomb rheology, irrespective of whether there is a velocity-dependent stress, forms cone-shaped deposits that do not resemble those of natural long-runout events. A purely viscous or a purely turbulent flow can achieve realistic velocities and thicknesses but cannot form a deposit on slopes. The plastic rheology, with (e.g., Bingham) or without a velocity-dependent stress, is more suitable for the simulation of dense pyroclastic flows and long-runout volcanic avalanches. With this rheology, numerical flows form by pulses, which are often observed during natural flow emplacement. The flows exhibit realistic velocities and deposits of realistic thicknesses. The plastic rheology is also able to generate the frontal lobes and lateral levées which are commonly observed in the field. With the plastic rheology, levée formation occurs at the flow front due to a divergence of the driving stresses at the edges. Once formed, the levées then channel the remaining flow mass. The results should help future modelers of volcanic flows with their choice of which mechanical law corresponds best to the event they are studying.

Citation: Kelfoun, K. (2011), Suitability of simple rheological laws for the numerical simulation of dense pyroclastic flows and long-runout volcanic avalanches, *J. Geophys. Res.*, *116*, B08209, doi:10.1029/2010JB007622.

1. Introduction

[2] Pyroclastic flows (PF) are fast-moving density currents composed of hot gas and rocks. They generally comprise two parts: a dense part and a dilute part [e.g., *Lacroix*, 1904; *Sparks*, 1976]. The dense part follows existing valleys; its thickness and density are thought to be close to those of the deposit and its dynamics are probably ruled by the interaction of its particles [e.g., *Sparks*, 1976; *Branney and Kokelaar*, 2002]. The dilute part of the flow is known as a pyroclastic surge or ash cloud surge. It is less confined by the topography and its dynamics are mainly governed by the gas it contains [e.g., *Valentine*, 1987]. Only the dense portion of the flow is studied here, and the abbreviation PF is used to refer to this part alone. Long-runout volcanic debris avalanches (LRA) are sudden and rapid movements of rock due to gravity, usually resulting from a collapse of the volcano flank [e.g., *Siebert*, 1984; *Voight et al.*, 1981]. LRA deposits are several tens of meters thick and can extend to a distance of some tens of kilometers from where the collapse occurred [e.g., *Shaller*, 1991; *Hayashi and Self*, 1992].

[3] Even though PF and LRA are triggered by very different processes, they share a number of similarities. They are both characterized by high mobility and an apparently very fluid behavior [e.g., *Sparks et al.*, 1978; *Hayashi and Self*, 1992; *Legros*, 2002]. They are both composed of polydisperse rock fragments, ranging in size from fine ashes to large blocks (in the order of one cubic meter for PF, and more than several tens of cubic meters for LRA). In both cases the deposit thickness is very small relative to the runout, and the deposits are present on a wide range of slopes (0 to ~30°). In addition they often share similar morphological features, such as raised lateral edges (levées) and a rounded front (Figure 1) [e.g., *Sparks et al.*, 1978; *Nairn and Self*, 1978; *Shaller*, 1991].

[4] There is a real need to estimate the first order rheology of these types of flows. In terms of hazard assessment, the rheology determines the thickness, extension and the velocity of simulated flows. A poor estimation of the rheology results in a concomitantly poor estimate of endangered areas, thus rendering numerical simulation useless. For example, a poor

[1]Laboratoire Magmas et Volcans, CNRS, UMR 6524, IRD, Université Blaise Pascal Clermont-Ferrand II, Clermont-Ferrand, France.

Copyright 2011 by the American Geophysical Union.
0148-0227/11/2010JB007622

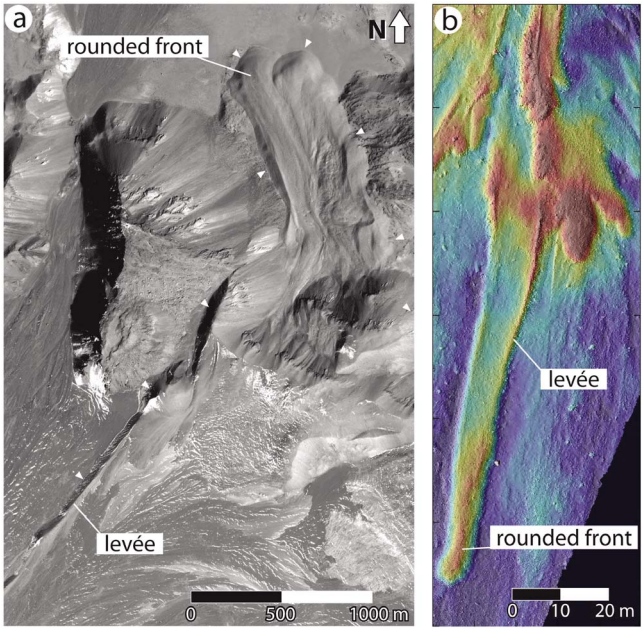

Figure 1. (a) Morphology with levées and rounded front of a debris avalanche (the ~1 km^3 secondary avalanche of Socompa that formed on the toreva topography of the principal avalanche ~26 km^3), Chile, 24°21′S, 68°18′W (courtesy of P. Labazuy, LMV). The white triangles indicate the deposit boundary. The scar is located 4 km to the southeast and is not visible on the image. (b) Pumice flows of Lascar volcano, Chile (23°23′20″S, 67°43′14″W). Morphology calculated by ground lidar (D. E. Jessop et al., submitted manuscript, 2011).

estimation of the velocity on natural topography will hinder the prediction of whether a flow is able to cross a given obstacle. Moreover, a calculated velocity which is too high allows the numerical flows to escape the valleys and to deposit on the interfluves, thus reducing the mass which continues to flow down the river drainage. Hazard assessment at Tungurahua volcano, for example [*Kelfoun et al.*, 2009], illustrates how an overestimation of the velocity induces an underestimation of the hazards in some sectors. From a more fundamental point of view the estimation of a correct first-order rheology of natural events is essential to test the validity of future, more complex models of the physics of such flows: even if, for computational reasons, for example, the future models only focus on small volumes of material, a test of their validity would be to reproduce and/or to explain the first-order rheology obtained by fitting simpler numerical results to field observations.

[5] Since these dense flows are constituted of rocks, grains and ashes, friction between these particles during emplacement could confer a Coulomb behavior to the whole flow. This is confirmed by the good fit between Coulomb simulations and the behavior of small rock avalanches and granular material in flumes and laboratory experiments [e.g., *Gray et al.*, 2003; *Savage and Hutter*, 1991; *Iverson et al.*, 2004]. These results explain why the Coulomb model is often used for the numerical modeling of PF and LRA, sometimes associated with a velocity-dependent term [e.g., *McEwen and Malin*, 1989; *Wadge et al.*, 1998; *Evans et al.*, 2001; *Crosta et al.*, 2004; *Sheridan et al.*, 2005; *Patra et al.*, 2005; *Procter et al.*, 2010].

[6] The angle of friction measured in PF and LRA deposits, as for many other rocks, ashes and sands, is about 30° [e.g., *Yamashita and Miyamoto*, 1993; *Miura and Yagi*, 2003; *Cecconi et al.*, 2010]. This can also be checked in the field by using the repose angle of deposits. However, if this value is used for the friction angle in numerical simulations, then the resulting simulated deposits are simply piles accumulated at the foot of the detachment scar, or close to the crater, and do not resemble either LRA or PF deposits [e.g., *Kelfoun and Druitt*, 2005; *Kelfoun et al.*, 2009]. To reach the natural runout using a simulation, the friction angle has to be lowered: 1° to 5° for LRA, 10° to 15° for pyroclastic flows [*McEwen and Malin*, 1989; *Wadge et al.*, 1998; *Evans et al.*, 2001; *Crosta et al.*, 2004; *Sheridan et al.*, 2005; *Patra et al.*, 2005; *Kelfoun and Druitt*, 2005; *Kelfoun et al.*, 2009; *Procter et al.*, 2010]. The mechanism for the reduction in friction for such complex flows has not been fully explained and various mechanisms have been evoked: fluid pressure, acoustic fluidization, mechanical fluidization, self-lubrication, dynamic fragmentation, etc. [e.g., *Davies*, 1982; *Voight et al.*, 1983; *Campbell et al.*, 1995; *Davies and McSaveney*, 1999; *Iverson and Denlinger*, 2001; *Legros*, 2002; *Collins and Melosh*, 2003].

[7] Since it is not clear which mechanism acts on the dynamics of LRA and PF to increase their runout, it is possible that these flows are subject to an overall mechanical behavior that does not follow a purely Coulomb law, i.e., with a friction angle that remains constant through time and along the whole flow. This is all the more relevant since studies have demonstrated that even glass bead flows in the laboratory do not exactly follow a Coulomb law [*Pouliquen and Forterre*, 2002]. Various rheological laws have been invoked for the simulation of natural granular flows, with the authors implicitly acknowledging that a simple Coulomb behavior is not ideal, whatever the value of friction angle used. *Heinrich et al.* [2001] and *Mangeney et al.* [2007], for example, used a friction angle that varied according to the velocity and thickness of the flows, based on the results of *Pouliquen* [1999]. Debris avalanches have sometimes been considered as viscous [*Sousa and Voight*, 1995]. Another law, commonly found in the literature for both PF and LRA, is the Bingham law (Table 1). It has been evoked to explain the typical morphology of natural deposits (bulbous front, levées), and is used in numerical simulations [e.g., *Wilson and Head*, 1981; *Voight et al.*, 1983; *Rossano et al.*, 1998; *Takarada et al.*, 1999; *Palladino and Valentine*, 1995]. This rheology is often interpreted by the authors as being related to plug flow emplacement [*Sparks*, 1976]. Based on statistical studies of LRA deposits, *Dade and Huppert* [1998] proposed a plastic rheology, i.e., the shear stress is constant whatever the thickness or the velocity of the flow. A plastic rheology can be thought of as a Bingham rheology with no viscosity. *Kelfoun and Druitt* [2005] have shown that the plastic rheology (termed the constant retarding stress) allows the morphology, lithology distribution and extension of the LRA of Socompa to be reproduced successfully. Study of Tungurahua volcano [*Kelfoun et al.*, 2009] has shown that a plastic rheology also appears to be well suited to PF simulations, even if Bingham behavior with a minor viscous response cannot be excluded.

Table 1. Mathematical Expressions of Rheological Laws Used in the Depth Average Form[a]

Name of the Law	Equation
Coulomb	$\mathbf{T} = \rho h\left(g\cos\alpha + \frac{\mathbf{u}^2}{r}\right)\tan\varphi_{\text{bed}}\frac{\mathbf{u}}{\|\mathbf{u}\|}$
One angle	$k_{\text{act/pass}} = 1$
Two angles	$k_{\text{act/pass}} = 2\frac{1 \pm [1-\cos^2\varphi_{\text{int}}(1+\tan^2\varphi_{\text{bed}})]^{1/2}}{\cos^2\varphi_{\text{int}}} - 1$
Viscous	$\mathbf{T} = 3\mu\frac{\mathbf{u}}{h}$
Voellmy (Coulomb + u^2 term)	$\mathbf{T} = \rho h\left(g\cos\alpha + \frac{\mathbf{u}^2}{r}\right)\tan\varphi_{\text{bed}}\frac{\mathbf{u}}{\|\mathbf{u}\|} + \xi\rho\|\mathbf{u}\| \times \mathbf{u}$
Plastic (constant retarding stress)	$\mathbf{T} = T_0\frac{\mathbf{u}}{\|\mathbf{u}\|}$
Plastic + u^2 term	$\mathbf{T} = T_0\frac{\mathbf{u}}{\|\mathbf{u}\|} + \xi\rho\|\mathbf{u}\| \times \mathbf{u}$
Bingham (plastic + viscous)	$\mathbf{T} = T_0\frac{\mathbf{u}}{\|\mathbf{u}\|} + 3\mu\frac{\mathbf{u}}{h}$

[a]Terms are ρ, density; h, thickness; g, gravity; α, slope; u, depth-averaged velocity; r, slope curvature; φ_{bed}, basal friction angle; φ_{int}, internal friction angle; $k_{\text{act/pass}}$, earth pressure coefficient; μ, viscosity; T_0, yield strength; ξ, Voellmy coefficient.

[8] To improve our understanding of PF and LRA rheology, two complementary approaches can be used. The first is to define the physics of natural flows accurately. This approach is, at present, quite impossible to achieve due to the very high complexity of the natural phenomena. The second approach, which I follow here, is to determine first order empirical laws by comparing numerical results with observations and measurements of the natural events and, then, to interpret the laws and the values obtained. In the following sections I present numerical simulations of PF and LRA carried out using the various rheological laws found in the literature. I describe the typical features of each rheology, i.e., the characteristics that are common to all topographies, volumes, source conditions, etc., and explain how the simulated flows are emplaced. Finally the simulated deposits are compared with the characteristics (thickness, area of deposition, morphology) of their natural counterparts.

2. Topographies and Source Conditions Used

[9] Three topographies are used. The first topography is a simple mathematical expression that aims to capture the main characteristics of the slopes surrounding pyroclastic flows. The second topography mimics the slopes around debris avalanches. The third topography is an inclined plane that approximates the slope surrounding the front of pyroclastic flow deposits.

2.1. Pyroclastic Flow

[10] To calculate a mathematical expression that mimics a natural slope, 4 volcanoes that have recently emitted pyroclastic flows have been chosen (Figure 2): Tungurahua (Ecuador), Merapi (Indonesia), Lascar (Chile) and Soufriere Hill (Montserrat). As can be seen on Figure 2, volcanoes that emit pyroclastic flows vary in size, but generally share the common characteristic that the slope is steep close to the crater (30–35°) and decreases progressively downslope.

[11] The slope used for the simulations has been chosen to be a mean value that aims to reproduce these characteristics. The topographic elevation, z, is given by

$$z = 2000 \times e^{-x_h/3000} - 200 \quad (1)$$

where x_h represents the horizontal distance from the crater. The PF simulations for this topography are carried out in 1D. This allows the rheological behavior to be observed under the simplest possible conditions, and is compatible with the common observation that PF are often confined to valleys (note however that the interaction with the valley walls is not taken into account in equations (6), (7), and (8)). The

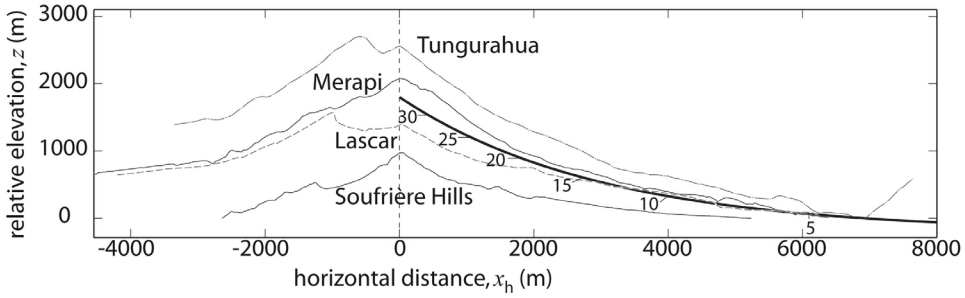

Figure 2. Four topographies of volcanoes that recently emitted pyroclastic flows. The profiles have been shifted both horizontally and vertically to place the crater rim (highest point of the slope) at the same horizontal location ($x_h = 0$) and the lowest point at $z = 0$. The thick black line is the topography used for the simulations (equation (1)). Values indicate the slope of the topography in degrees.

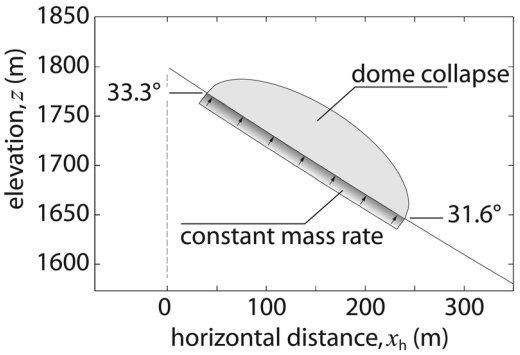

Figure 3. Initial geometry used for pyroclastic flow simulations. The mass of the dome collapse is released instantaneously. For the constant mass rate, the same mass is supplied over 60 s and 600 s.

volume of PF chosen is 10 000 m^3 per linear meter, which is compatible with the volume of deposits observed in the field, 6 to 8 km long and with a mean thickness of about 1 m [e.g., *Wilson and Head*, 1981; *Lube et al.*, 2007; *Kelfoun et al.*, 2009]. Numerical cells are 2 m long horizontally.

[12] Three source conditions are investigated. For all the simulations, the source is a zone ~236.41 m long (200 m horizontally), horizontally defined between $40 < x_h < 240$, and covering a slope between 33.3° and 31.6° (Figure 3). The first case reproduces a dome collapse. The initial thickness, calculated from the source zone normal to the slope, is given by

$$h = a\sqrt{1 - \left(\frac{x_h - 140}{100}\right)^2} \tag{2}$$

where $a \sim 53.76$ gives a volume of 10 000 m^3/m, calculated normal and parallel to the ground. The mass is released without velocity and accelerates by gravity alone. The two other cases simulate a continuous feeding of the same volume (10 000 m^3/m) over 60 s and 600 s, respectively. The same volume is introduced into each cell at each time step (the added thicknesses differ slightly since the surface of the cells changes with the slope). The velocity of each source cell is calculated from momentum conservation, the new mass being introduced without velocity. Following *Kelfoun et al.* [2009] the bulk density is assumed to be 1300 kg/m^3 for pyroclastic flows.

2.2. Long Runout Debris Avalanche

[13] In a similar manner, the profile of the topography for the LRA is obtained by fitting natural topographies of actual volcanic debris avalanches to a simple mathematical expression. The debris avalanches chosen are Shasta (USA), Socompa (Chile), Llullaillaco (Argentina) and Mount St Helens (USA). In the same way as for the pyroclastic flows above, the first topography used is a simple 1D expression (Figure 4a).

[14] The elevation of the sliding surface used for the simulation is defined by

$$z = 1500 \times e^{-x_h/10000} \tag{3}$$

The initial thickness is a 15° wedge defined by

$$h = 1000 - x_h \tan(15^\circ) \tag{4}$$

where h is positive ($x_h < 3732$ m). The volume is a little less than 2×10^6 m^3 per linear meter. The extension of the calculation domain is 60 km and the mesh size is 10 m horizontally.

[15] However, because LRA are often emplaced onto an open topography, a 2D mathematical expression is also used. The domain of calculation is 70 × 70 km^2 with mesh sizes of 100 × 100 m^2. The slope is a function of x_h alone (horizontal along the y axis) and is also given by equation (3). The initial shape of the mass is defined by a half cone with a 15° slope:

$$h = 1000 - d\tan(15^\circ) \tag{5}$$

where $d = \sqrt{x_h^2 + y_h^2}$, the horizontal distance from a point located at the center of the left margin ($x_h = 0$, $y_h = 0$, Figure 4b). Equation (4) equals the profile of equation (5) along the x_h axis at $y_h = 0$. The volume of the LRA is about 7.5 km^3, more than that of Mount St Helens (2.5 km^3 [*Voight et al.*, 1983]) and Llullaillaco (~2 km^3 [*Richards and Villeneuve*, 2001]), but less than that of Socompa (26 km^3 [*Wadge et al.*, 1995]) and Shasta (26 km^3 [*Crandell et al.*, 1984]). The bulk density is assumed to be 2000 kg/m^3 for debris avalanches [*Kelfoun and Druitt*, 2005].

2.3. The Flow Front in Detail

[16] To improve the observation of the morphology of the simulated flows and of the deposits, the third topography is 2D and focuses on the final 100 m of the frontal area of pyroclastic flows. The calculation domain is 110 m × 40 m, with a resolution of 10 cm. The parameters are chosen to approximate the characteristics of the pumice flow deposit of the 1993 eruption at Lascar volcano (Figure 1b). The slope is an inclined plane of 10° along the x_h axis. This planar

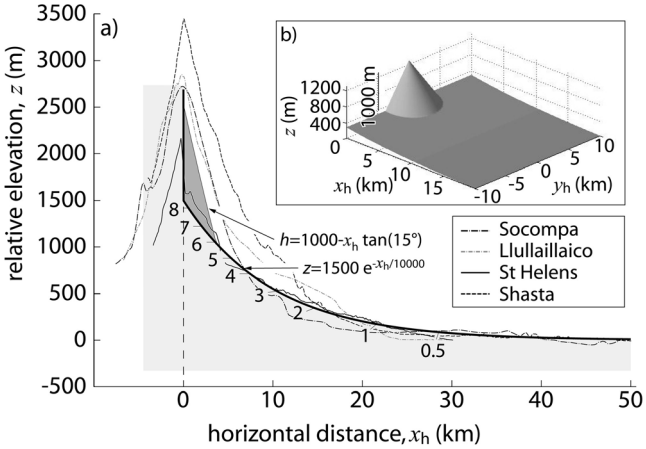

Figure 4. (a) Natural topographic profiles along the maximum extent of four debris avalanche deposits. As for Figure 2, profiles have been shifted. The pale gray area represents the topography used and the darker wedge the initial shape of the mass that will flow. (b) 3D view of the 2D topography used and of the initial shape of the mass.

Table 2. Simulations Performed[a]

	Coulomb 1 Angle: φ_{bed}	Coulomb 2 Angles: φ_{bed} φ_{int}	Voellmy φ_{bed} ξ	Plastic T_0	Plastic + $f(u^2)$ T_0 ξ
PF, 1D, dome	(1) 15°	(4) 15° 30°	(7) 5° 0.1	(10) 20 kPa	(13) 3 kPa 0.1
PF, 1D, 60 s	(2) 15°	(5) 15° 30°	*(8)* 5° 0.1	(11) 20 kPa	(14) 3 kPa 0.1
PF, 1D, 600 s	(3) 15°	(6) 15° 30°	*(9)* 5° 0.1	(12) 20 kPa	(15) 3 kPa 0.1
LRA, 1D	(16) 4°	(17) 4° 30°	*(18)* 4° 0.1	(19) 80 kPa	*(20)* 20 kPa 0.1
LRA, 2D	(21) 2°	(22) 2° 30°	*(23)* 2° 0.1	(24) 30 kPa	*(25)* 10 kPa 0.1
FF, 2D	*(26)* 11°	*(27)* 11° 30°	*(28)* 11° 0.1	(29) 2 kPa	*(30)* 2 kPa 0.1

[a]Numbers in parentheses indicate the case number, the others the rheological parameters used. Cases in italic are not presented on figures. PF, pyroclastic flow; LRA, long-runout avalanche; FF, flow front in detail.

topography has also been chosen to verify that conclusions drawn from the first cases are not due to the exponential law used. At the left side of the domain ($x = 0$), the flow is considered to have a semielliptical shape, 1.5 m high and 10 m wide (surface ~11.78 m^2), with a constant x parallel velocity of 3 m/s over a time frame of 30 s. After 30 s, the source supply ceases. The volume of the deposit is ~1057 m^3 (11.78 m^2 × 3 m/s × 30 s). These boundary conditions are assumed from the morphology of pumice flow deposits and from nondimensional comparison with granular flows in the laboratory (D. E. Jessop et al., Lidar derived morphology of the 1993 Lascar pyroclastic flow deposits, and implication for flow dynamics and rheology, submitted to *Journal of Volcanology and Geothermal Research*, 2011). The bulk density is assumed to be 1300 kg/m^3, as for the other simulations of PF. Rheological parameters are fixed to approximate the runout (~100 m) and the thickness (~1 m) of Figure 1b.

2.4. Model

[17] The numerical model is based on the depth average resolution of mass conservation (6) and momentum balance equations (equations (7) and (8)). For the simulations on a 2D topography, horizontal in the y direction, the conservation equations are as follows:

$$\frac{\partial h}{\partial t} + \frac{\partial}{\partial x}(hu) + \frac{\partial}{\partial y}(hv) = 0 \tag{6}$$

$$\frac{\partial}{\partial t}(hu) + \frac{\partial}{\partial x}\left(hu^2\right) + \frac{\partial}{\partial y}(huv) = gh\sin\alpha - \frac{1}{2}k_{act/pass}\frac{\partial}{\partial x}\left(gh^2\cos\alpha\right) - \frac{T_x}{\rho} \tag{7}$$

$$\frac{\partial}{\partial t}(hv) + \frac{\partial}{\partial x}(huv) + \frac{\partial}{\partial y}\left(hv^2\right) = -\frac{1}{2}k_{act/pass}\frac{\partial}{\partial y}\left(gh^2\right) - \frac{T_y}{\rho} \tag{8}$$

The terms including v and y disappear for simulations on 1D topographies. The flow thickness is h (calculated normal to the ground), t is time, $\mathbf{u} = (u, v)$ is flow velocity along the slope, α is ground slope, ρ is the bulk density of the flow. The gravity is g (9.8 m/s^2), and x and y denote directions along the slope. Details about the equations and VolcFlow, the code that solves them, are presented by *Kelfoun and Druitt* [2005] and *Kelfoun et al.* [2009]. The variable $\mathbf{T} = (T_x, T_y)$ expresses the basal shear stress, which varies according to the rheology chosen. Table 1 gives the mathematical expressions of $\mathbf{T}$ for the different rheologies used.

[18] The Coulomb friction relates the shear stress $\mathbf{T}$ to both the normal stress at the base of the flow and the friction angle φ_{bed} between the flow and the ground (Table 1). Two models are used. In the first model, the internal friction of the flowing material, φ_{int}, implicitly equals the basal friction angle between the flow material and the ground surface, φ_{bed}, and the internal stress is considered to be isotropic ($k_{act/pass} = 1$, equations (7) and (8)). In the second model, φ_{int} differs from φ_{bed} and modifies the effect of the pressure gradient through $k_{act/pass}$, the earth pressure coefficient (equations (7) and (8)). Equations describing how $k_{act/pass}$ is calculated from φ_{bed} and φ_{int} are developed by *Iverson and Denlinger* [2001] and are given in Table 1. For all the other rheological laws used in the following sections, the internal stress in the flow is considered as being isotropic ($k_{act/pass} = 1$).

[19] Viscous rheology relates the basal shear stress to the velocity, the viscosity and the inverse of the thickness of the flow (Table 1): under the same conditions a thin flow will move more slowly than a thick one. The Voellmy law (Table 1) consists of adding to the Coulomb friction a stress which depends on the square of the velocity, incorporating a coefficient, ξ, which is used to represent the effect of turbulence and/or collisions [*Hutter and Nohguchi*, 1990; *Evans et al.*, 2001].

[20] A plastic solid (sometimes called a yield stress fluid) remains at rest while the shear stress applied to it is inferior to the yield stress T_0. Then, once movement begins, the shear stress exerted by the material is constant (i.e., it equals T_0) regardless of its thickness and velocity. If the driving stress drops back below T_0 the material decelerates and stops. A Bingham friction is one in which a viscous term is added to the plastic term (Table 1). In this case, once the yield strength, T_0, is overcome, the velocity of the flow is related to T_0, and to the viscosity, thickness and the shear stresses applied.

3. Results

[21] More than thirty simulations were performed, varying the source conditions, the topographies and the rheology. Their characteristics are listed in Table 2. Simulations incorporating viscous behavior (purely viscous, Coulomb + viscous, Bingham) are only evoked in the text, the velocity, the thickness and the deposit morphology being comparable to what is presented with the addition of a stress related to the square of the velocity (u^2 term, Table 1). For each topography and source condition, the values of the rheological parameters (e.g., basal friction angle or yield strength) are chosen to fit best to the runout of natural phenomena. This estimation,

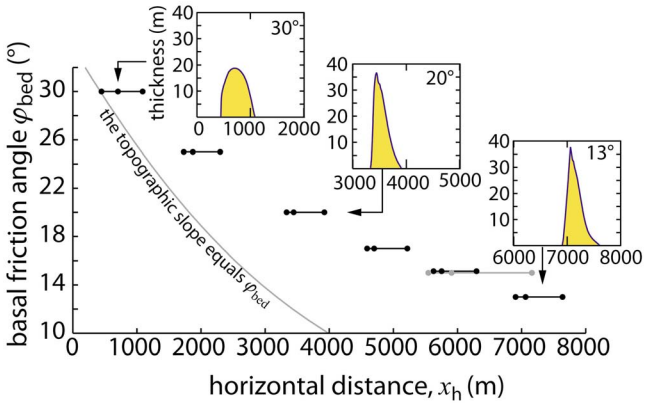

Figure 5. Distances covered by Coulomb flow deposits according to their basal friction angle. Other conditions are similar to case 2 (Table 2). Captions present the deposit geometries for φ_{bed} = 13°, 20° and 30°. The three points represent the location of the tail, the maximal thickness and the head of deposits, from left to right (volume: 10,000 m^3/m) The three gray points are obtained with a volume of 20,000 m^3/m and φ_{bed} = 15°. The gray line locates the area where the topographic slope equals the basal friction angle.

often followed by modelers who attempt to reproduce an existing event, is not based on mechanical estimations.

3.1. The Coulomb Rheology

[22] The Coulomb basal sliding is the law which is most frequently used in the simulation of PF, LRA and granular flows in the laboratory [e.g., *McEwen and Malin*, 1989; *Wadge et al.*, 1998; *Evans et al.*, 2001; *Crosta et al.*, 2004; *Sheridan et al.*, 2005; *Patra et al.*, 2005; *Pudasaini and Domnik*, 2009; *Procter et al.*, 2010]. It is thus necessary to explore its behavior in detail to determine which characteristics of long runout events it is, or is not, able to reproduce.

[23] The first simulations of PF (cases 1–3, Table 2) are carried out with an internal isotropic stress ($k_{act/pass}$ = 1, equations (7) and (8)). A basal friction angle of 15° is necessary to reach distances of ~6 km (Figure 5), commonly reached in reality by pyroclastic flows [e.g., *Ui et al.*, 1999; *Cole et al.*, 1998; *Kelfoun et al.*, 2000; *Kelfoun et al.*, 2009].

[24] For the three source conditions chosen (cases 1–3, Table 2), the behavior is rather similar. The mass leaves the source area and accelerates where the slope of the flow surface (very close to the topographic slope) is steeper than the basal friction angle, i.e., for about 3000 m along the slope (x_h ~ 2734.5 m). Acceleration over such a distance gives the flow a velocity of nearly 100 m/s (Figure 6). Then the velocity diminishes but the high inertia allows the flow to travel about 3300 m more. The mass then accumulates over a limited distance (<1 km long, Figure 5) into a 15 to 40 m thick pile (Figure 7) with an upstream slope equaling the basal friction angle and a gentler downstream slope, due to inertia. For all the simulations done with a Coulomb material, the front stops while the tail is still flowing. The acceleration on slopes steeper than the friction angle, whatever the thickness of the flow and the shape of deposits, is typical of a material exhibiting a Coulomb basal friction [see *Pudasaini and Hutter*, 2006, and references therein]. A similar deposit shape is obtained by *Doyle et al.* [2010, Figure 9] for simulations carried out with Coulomb friction alone.

[25] The differences in behavior between the three simulations are related to the initial shape of the mass that flows. For a dome collapse (case 1), the rounded shape induces a higher initial pressure gradient than for the other simulations and thus a greater acceleration. Moreover, the center of mass is slightly higher initially than for the other cases. Thus this flow reaches the furthest runout.

[26] Simulations were also performed using two different friction angles [*Iverson and Denlinger*, 2001] (cases 4–6). As in the previous simulations, the basal friction angle is fixed at 15°, and in addition an internal friction angle of 30° is applied (the normal value for a pyroclastic deposit [e.g., *Yamashita and Miyamoto*, 1993; *Miura and Yagi*, 2003; *Cecconi et al.*, 2010]). Results obtained are very close to the previous simulation. The internal friction angle acts on $k_{act/pass}$ and thus on the stress induced by the pressure gradient (equations (7) and (8)). The stress induced by the pressure gradient being weak compared to the stress induced by the weight, because the flow is very thin over a large portion of its path, the effect of a high internal friction is consequently weak too. Deposits obtained with an internal friction angle are slightly shorter and more spread out because the internal friction opposes the convergence of material at the accumulation position (Figure 7).

[27] The density value has no influence on the emplacement of a Coulomb flow (see equations (6), (7), and (8) and

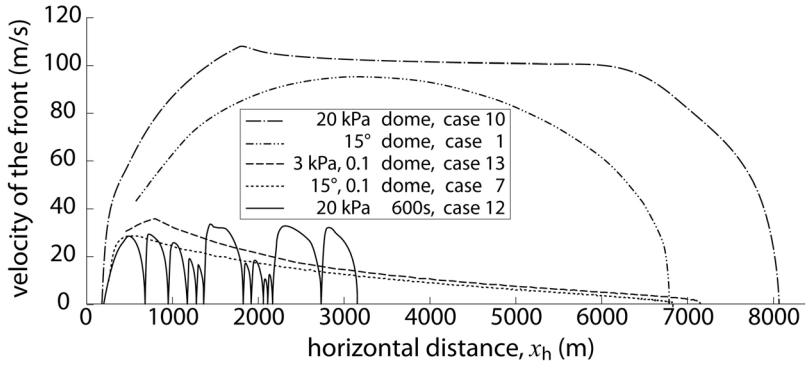

Figure 6. Velocities of the fronts of simulated pyroclastic flows for different rheologies and different source conditions.

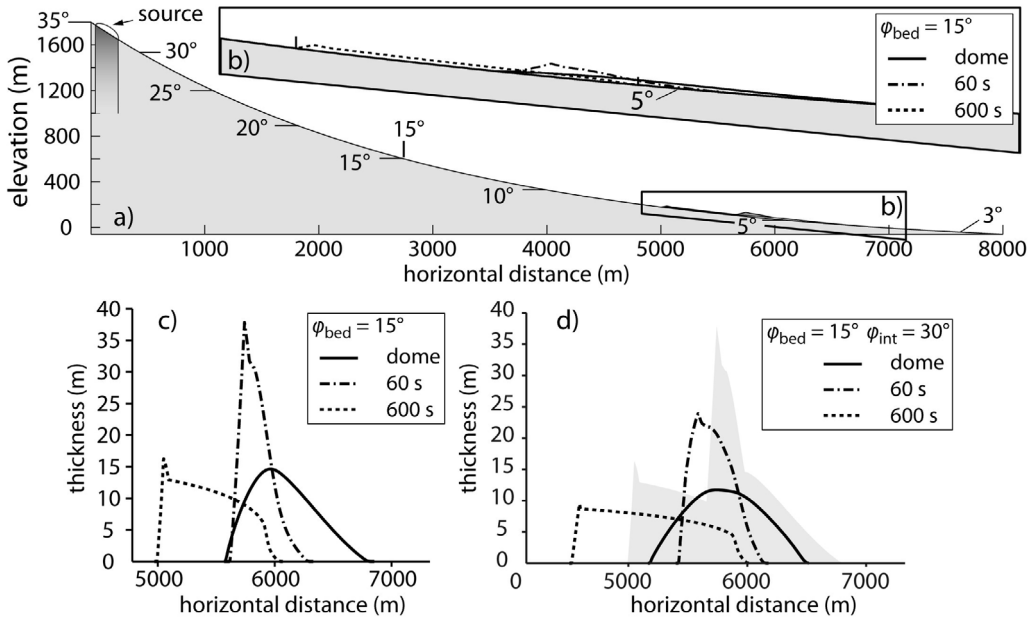

Figure 7. (a) View of the topography defined by equation (1). Coulomb deposits are restricted to a limited area (in the frame). (b) Close-up of frame in Figure 7a. (c) Deposit thicknesses obtained for the three different source conditions for a Coulomb material with φ_{bed} = 15° and $k_{act/pass}$ = 1. (d) Deposit thicknesses obtained for a Coulomb material with φ_{bed} = 15° and φ_{int} = 30°. The gray area shows the location of the curves from Figure 7c.

Table 1) because the term ρ is canceled out. Figure 5 shows that the runout changes according to the basal friction angle but that the deposits share similar characteristics.

[28] The behavior of a Coulomb flow, as shown above, remains similar whatever the source conditions, the dimensions, the volume and the value of the basal friction angle. However, for LRA, the mean slope of the surrounding topography is generally low (Figure 4) and thus a very low basal friction angle (<5°) is required to reach the natural runout. The deposit then covers a large area compared to the area covered by the PF deposits of cases 1 to 6. For case 16 (Table 2 and Figure 8), the deposit covers about 40 km of the slope and the front forms a very thin wedge, passing progressively from 110 m to 0 m over about 30 km. The angle of this frontal wedge (<0.3°) is lower than the basal friction angle (4°) due to strong spreading caused by inertia. For case 17 (Table 2) the internal friction angle is higher than the basal friction angle, thus opposing the flow of the mass, and thereby decreasing its runout. Its effect is stronger than for the PF case because the topographic slope is gentler and the flow is thicker. The deposit for case 17 is thus emplaced closer to the source. The front also forms a thin wedge (Figure 8).

[29] For the simulation of a debris avalanche on a 2D surface (case 21), the mass flows on slopes steeper than the basal friction angle to accumulate as a pile on a limited range of slopes (Figure 9a). The effect of deposit accumulation over a large distance, observed in 1D for the LRA simulation, is less marked in 2D because the mass is free to flow around the mass which is already at rest. When the internal friction angle is higher than the basal friction angle (case 22) there is less lateral spreading of the mass (Figure 9b).

[30] For 2D simulations focused on the flow front, the flow can reach a runout of about 100 m only if the basal friction angle is slightly higher than the slope of the inclined plane. The slope being constant, the Coulomb material can be deposited over the whole domain of calculation. For higher basal friction angle values, the deposits accumulate closer to the source. For values lower than the slope, the flow accelerates continuously and no deposit forms. One particular characteristic of case 26 (Table 2) is that levées can be observed close to the source area: the thickness imposed by the boundary condition (1.5 m) is higher than the surrounding thickness of the flow (<0.4 m), since the flow is spreading rapidly. When the imposed velocity ceases, the mass of the left border accelerates due to the strong thickness gradient. This increased velocity enables the downslope deposit to remobilize the mass close to the source, forming a thinner center compared to the unaffected edges.

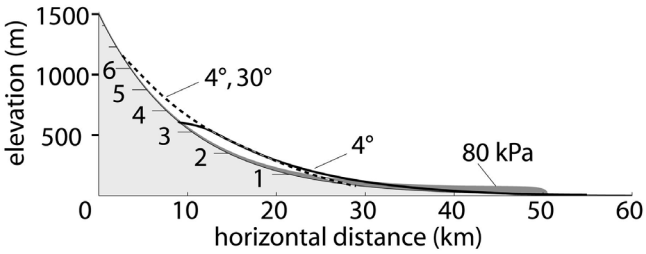

Figure 8. A 1D simulation of debris avalanches with a basal friction angle of 4° (solid line), a basal friction angle of 4° plus an internal friction angle of 30° (dotted line), and a plastic rheology of 80 kPa (shaded).

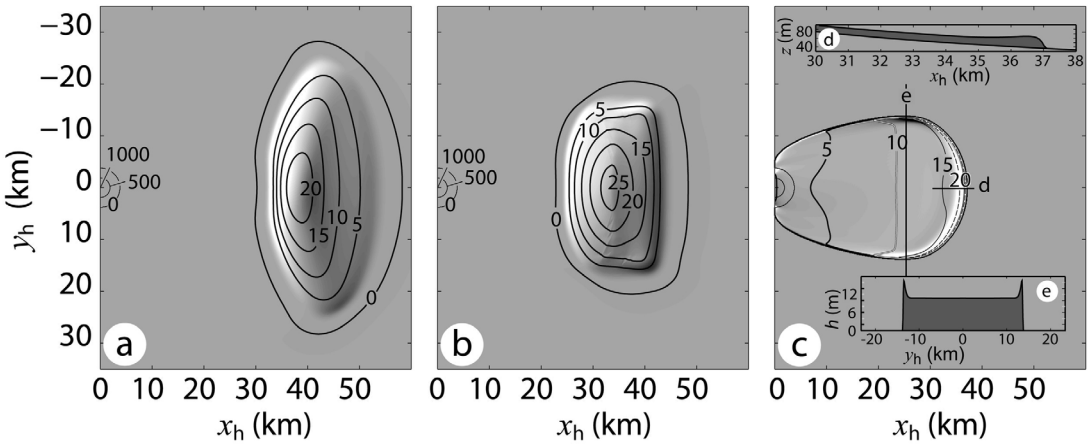

Figure 9. A 2D simulation of a debris avalanche with (a) Coulomb behavior with $\varphi_{bed} = 2°$, (b) Coulomb behavior with $\varphi_{bed} = 2°$ and $\varphi_{int} = 30°$, and (c) plastic rheology of 30 kPa. Profiles D and E are located by the rectilinear black lines. Note the formation of levées and of a well marked front. Contours indicate the deposit thickness in meters.

As will be shown in the following sections, this mechanism of levée formation differs from the mechanism exhibited by the plastic rheology.

3.2. Coulomb Rheology Plus a Velocity-Dependent Law

[31] A velocity-dependent term is often used in the literature [e.g., *McEwen and Malin*, 1989; *Wadge et al.*, 1998; *Evans et al.*, 2001], for example adding a viscous law or using a Voellmy law (Table 1). With an additional velocity-dependent stress, the friction angle must be lowered to reach the same runout as previously described. Figure 10 shows results obtained for PF simulated using a Voellmy law whose parameters are $\varphi_{bed} = 5°$ and $\xi = 0.1$ (case 7). As for the previous models, the Coulomb material begins to flow whatever the thickness. However, its velocity is reduced by the velocity-dependent term. The deposit forms a pile as previously described, but due to the lower inertia of the flow, the mass accumulates closer to the point where the slope equals the friction angle. The higher the coefficient ξ, the closer the center of mass is to this point.

[32] If Coulomb friction is combined with viscous stress, deposits form whose morphology is similar to cases 1 to 6 (purely Coulomb), but only after a very long calculation time (an infinite time is needed for all the mass to stop). This is because the resisting stress of the viscous law is proportional to the inverse of its thickness, i.e., a thin flow displaces very slowly. Note that the use of velocity-dependent laws alone (e.g., a viscous law or a law related to the square of the velocity) does not allow a deposit to form; instead the mass flows out of the calculation domain.

3.3. Plastic Rheology

[33] To reach a realistic runout of PF with the plastic rheology and dome collapse conditions (case 10), the value of the basal shear stress should be about 20 kPa (Figure 11). At the source, a shear stress of 20 kPa is very low compared to the driving stresses induced by the weight and the pressure gradient of the dome, thus the acceleration is high and the flow reaches a very high velocity of more than 100 m/s. The constant stress rheology is very sensitive to source and geometrical conditions chosen. Decreasing the source rate reduces the flow velocity drastically, and thus the runout. A feeding time of 60 s (case 11) forms flows whose maximal velocity is 70 m/s. The flow emplaces in three pulses: at the source the mass accumulates, but remains in place until its thickness is such that the driving stress exceeds the yield stress, T_0. It then accelerates, forming a flow that thins, but in doing so it lowers the driving stress to less than T_0, thus it decelerates and stops. At the source, the mass accumulates again. When the driving stress once more exceeds the yield strength, a new pulse forms and restarts movement in the previous pulse which had come to a standstill. With the conditions in case 12 (a slow mass rate over 600 s), the flow emplaces by 12 pulses with peak velocities of the front of less than 40 m/s (Figure 6). The flow front stops after a runout of less than 3.5 km. The lower the mass rate is, the lower the velocity of the flow, and the greater the number of resultant pulses. If the mass is supplied over a duration of 600 s, a value of ~12 kPa is needed to reach a runout of ~6 km. For the equivalent runout in 2D models T_0 should have a value of only a few kPa, since the mass spreads laterally, thus

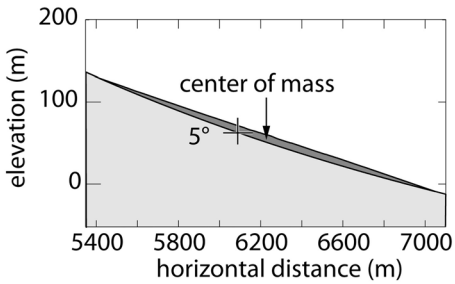

Figure 10. Deposit obtained with a Voellmy law, $\varphi_{bed} = 5°$, $\xi = 0.1$ and a dome collapse (case 7). Due to the low inertia of the material, the center of mass is close to the point where the slope equals the friction angle. Vertical exaggeration = 4.

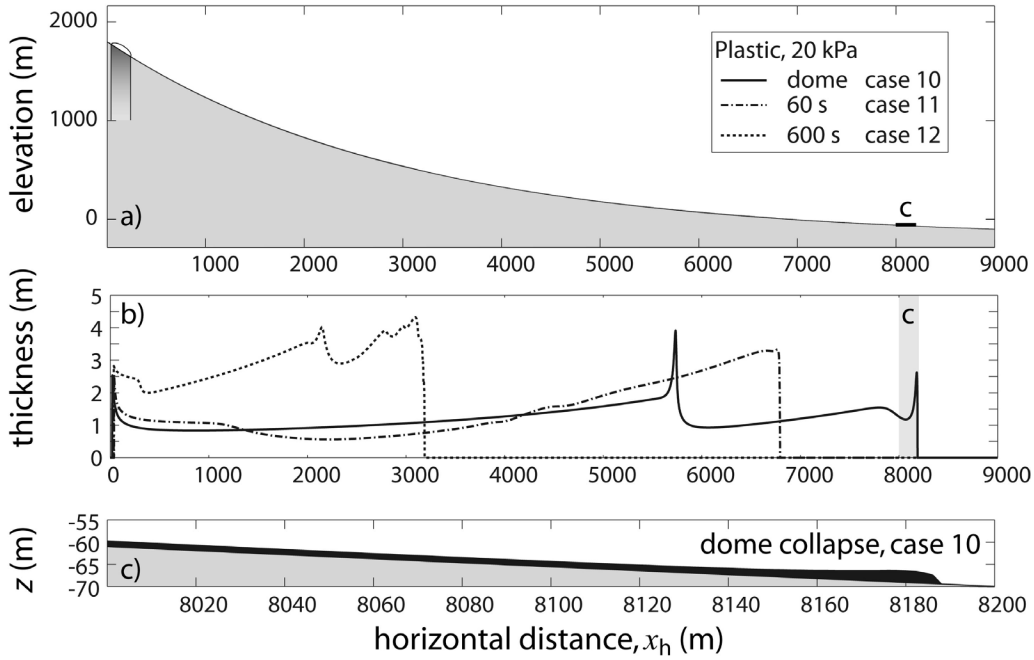

Figure 11. Simulations of PF using a plastic rheology. (a) View of the topography used and of the location of the source. The black rectangle indicates the location of Figure 11c. (b) Thickness of deposits showing a progressive increase in thickness downstream. (c) Enlargements of rectangle from Figure 8a, with the same scale for the x and z axes.

reducing the thickness of the flow and consequently the driving stress.

[34] A common characteristic of the plastic rheology (cases 10, 11, 12, 19, 24, and 29) is that the deposits cover all the areas reached by the flows and that their thickness increases where the slope angle decreases. The front of both the flow and the deposit is rounded (Figures 8, 9, 11, and 12 and Animation S1 of the auxiliary material).[1] In contrast to the Coulomb rheology, the tail of a given pulse stops while the front is still flowing and the front only stops after the source has ceased.

[35] On 2D topography, the formation of levées and a bulbous front is characteristic of this rheology (Figures 9c and 12). It occurs with all volumes, all source conditions and all topographies tested, and whatever the value of T_0: from 2 kPa for the PF in case 29 to some tens of kPa for LRA (Figures 9 and 12). This particular morphology forms at the flow front and is explained by the directions of the displacements and the driving stresses. The rounded shape of the flow front forces the mass to move laterally in this region, toward the horizontal slope of the y axis. The stress induced by the weight (oriented downslope), the stress induced by the pressure gradient and the momentum (both with a marked y parallel component) are not oriented in the same direction. At the sides of the flow front the flow spreads, thins and decelerates when the resulting driving stress is inferior to the yield strength T_0 and stops once a certain thickness is reached. This process forms static edges that channel the upstream mass (Figure 12b). Once the flow is channelized by these lateral static edges (Figure 12c), its momentum, weight and pressure stresses, all oriented downslope, favor flow which is thinner than the lateral edges. This forms the typical levée morphology (Figure 12c). The thicknesses of the deposits and of the levées are directly related to the value of T_0 chosen.

3.4. Plastic Rheology With a Velocity-Dependent Law

[36] Simulations presented in Figure 13 are carried out with a constant shear stress of 3 kPa and a large stress related to the square of the velocity $\xi = 0.1$ (cases 13–15, Table 1). The profiles of these deposits share the same characteristics as a purely plastic flow: a progressive increase of thickness as the slope angle decreases, and a markedly rounded front. The effect of the velocity-dependent term is principally to reduce the velocity and the runout of the flow. For example, the velocity of pyroclastic flows generated by a dome collapse is less than 35 m/s (case 13). With this high value of the coefficient ξ, the shape and location of the deposit is almost independent of the source rate (Figure 13). A high coefficient ξ also tends to mask pulse formations because it smoothes velocity differences by reducing the highest velocities and also because it decreases the overall flow velocity, allowing the pulses to merge together close to the source. The lateral levées, which are related to inertia, also disappear when a high velocity-dependent stress is introduced.

4. Discussion

4.1. Coulomb Rheology

[37] Simulations carried out with the Coulomb basal friction reproduce the emplacement and the shape of sand deposits in the laboratory, sand being a material that is considered to have a Coulomb behavior at this scale [e.g.,

[1] Auxiliary materials are available in the HTML. doi:10.1029/2010JB007622.

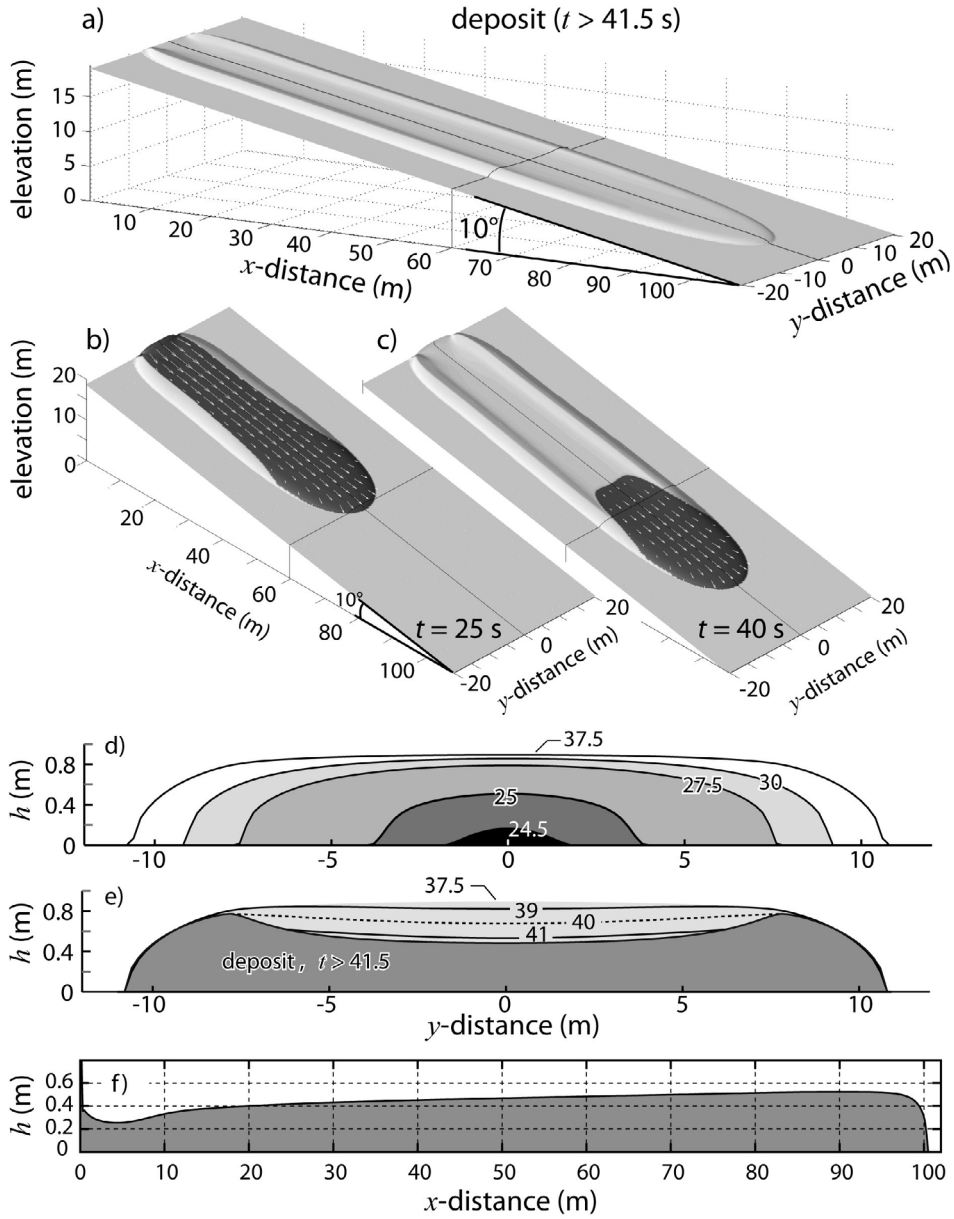

Figure 12. Simulation of a plastic flow for T = 2 kPa and a planar topography (case 29). (a) A 3D view of deposits. Black lines indicate location of Figure 12d. (b–c) The zone of displacement is shown in black. Note the formation of static edges. (d–e) Cross section of the flow at x_h = 60 m and t = 24.5, 25, 27.5, 30, 37.5, 39, 40, 41 s and the deposit. At any location covered by the flow, the thickness and the width rapidly increase with time. When the feeding rate stops, the mass of the central part drains down. The final deposit exhibits well-defined levées and a well-marked frontal lobe which is thicker than the upper parts. (f) Longitudinal section of numerical deposits (at y = 0).

Gray et al., 2003; *Pudasaini and Hutter*, 2006]. They also resemble deposits formed at the foot of cliffs by rockfalls [e.g., *Pirulli and Mangeney*, 2008, Figure 2; *Lipovsky et al.*, 2008, Figure 1].

[38] The results show, however, that the Coulomb model does not reproduce the morphology of PF and LRA deposits. Coulomb deposits only form as piles on a limited range of slopes, while their natural counterparts present sheet–like geometries if not topographically constrained, can be observed on all slopes <30°, with their thickness progressively increasing as the slope decreases, and often exhibit levées and a rounded frontal lobe [e.g., *Nairn and Self*, 1978; *Shaller*, 1991]. The runout distance of a Coulomb body only increases slightly when the volume increases (Figure 5), whereas natural flows are strongly influenced by this [*Hayashi and Self*, 1992]. Finally, the friction angle that fits natural flow runouts is often less than 15° for PF and less than 4° for LRA [e.g., *McEwen and Malin*, 1989; *Heinrich et al.*, 2001; *Sheridan et al.*, 2005; *Kelfoun and Druitt*, 2005; *Kelfoun et al.*, 2009]. With such a low value for

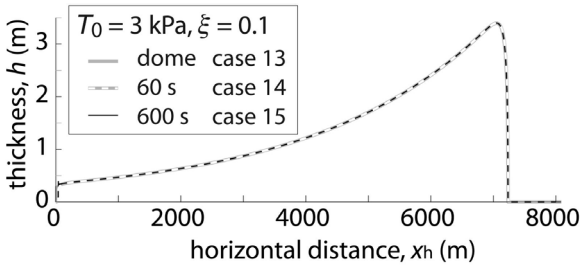

Figure 13. Deposits obtained with a plastic rheology and a term related to the square of the velocity (T_0 = 3 kPa, ξ = 0.1). The three curves obtained by varying the source conditions (case 13–15) are nearly overlapping.

the basal friction angle, the mass that accelerates on slopes steeper than the friction angle may accelerate over several kilometers, particularly for PF emitted at the summit crater. This can induce unrealistic velocities, of around 100 m/s, on intermediate slopes even for small-volume PF ($<10^6$ m^3). If used on a natural topography, the high velocity of simulated flows allows them to escape out of the drainage channels and to affect the interfluves, whereas in the field they are channelized, which makes it questionable to use the Coulomb model for PF simulation and, consequently, for hazard assessment of PF. Adding a velocity-dependent term allows more realistic velocities to be obtained, but still forms deposits with unrealistic morphologies for long-runout events.

4.2. Plastic Rheology

[39] Characteristics of deposits obtained using a plastic rheology resemble the natural long-runout deposits in the following features. First, they form well-defined levées and a rounded, bulbous frontal lobe, as often observed in the field (Figures 1, 9, and 12). Second, the plastic rheology forms sheet-like deposits on all the slopes, with the thickness increasing downslope. Note that the absence of levées on any natural deposit cannot be automatically used to reject the plastic model. According to the results, the levées form only on open topographies. They cannot be observed if the flow is confined, or on gentle slopes where inertia is low.

[40] The pulses produced by the model resemble the pulses which are often observed during real PF emplacement [e.g., *Schwarzkopf et al.*, 2005; *Kelfoun et al.*, 2009], and lead to lobes comparable to those observed on deposits (Figure 1). However, to my knowledge, it is impossible from field observation to determine that pulses are linked to the rheology of the flows or to variations in source conditions.

[41] For the simulation of PF where there is a high rate of mass release onto steep slopes, (case 10, dome collapse), the velocity obtained with the plastic rheology is too high to be compatible with any natural examples of observed velocity. PF reach a velocity of 100 m/s, which is unrealistic for this kind of flow [e.g., *Hoblitt*, 1986; *Yamamoto et al.*, 1993; *Cole et al.*, 1998; *Kelfoun et al.*, 2000; *Jolly et al.*, 2002]. Two explanations can be envisaged. It is possible that a velocity-dependent term really affects the rheology of LRA and PF, for example due to particle collisions or turbulence. An alternative explanation is that this term may be an artifact linked to the incapacity of the existing numerical models to simulate the initial stage of rock dismantling during dome collapse and LRA simulations. Strong frictional forces might be present during the dismantling stage and could have a strong influence in reducing the initial velocity of the flow. The velocity-dependent term is correspondingly high since the velocity is high. It could then artificially reproduce a similar effect because the highest velocities are located close to the source. For the simulation of the pyroclastic flows of Tungurahua, for which the mass rate was relatively low (~0.15 m^3/s for each square meter of the source area) [*Kelfoun et al.*, 2009], and of the debris avalanche of Socompa where the basal slope was gentle (about 13°) [*Kelfoun and Druitt*, 2005], the velocity-dependent term does not exist or is small enough to be undetectable. Quantification of this velocity-related stress is difficult without very accurate measurement of the flow rates, volumes and velocities of natural flows.

[42] The results show that some mechanisms that occur in the dynamics of PF and LRA modify their behavior to the extent that the plastic rheology describes their emplacement and the deposit more accurately than any other simple law. However, the plastic rheology should be considered as no more than a first order description of the rheology of long-runout granular flows. With the simple topographies used, it is not able, for example, to reproduce the small-scale structures that often characterize LRA deposit surfaces, such as hummocks. It neglects the initial stage of LRA where destabilized rocks initially behave as a Coulomb body and probably slide en masse before forming an avalanche (e.g., Mount St Helens avalanche [*Voight et al.*, 1981]). It is also able to form deposits on slopes >35° and neglects the fact that materials revert to a Coulomb behavior after, or at the end of, flow.

[43] Moreover, the plastic rheology is not explained from a mechanical point of view. It stipulates that the shear stress at the base of the flow is independent of the thickness of the flow (in contrast to the Coulomb model, for example). One explanation would be that the material constituting LRA and PF exhibits a cohesive frictionless behavior, the static angle of friction being eliminated during the flow. Other explanations for the constant stress can also be envisaged. For example, assuming that the Coulomb friction is the main stress in the flow, a constant basal friction of the flow $T = \rho g h \tan \varphi_{bed}$ can be obtained if the friction angle φ_{bed} increases as the flow thickness, h, decreases. This increase of the friction angle is present in the law used by *Mangeney et al.* [2007] and also allows them to form levées. Although speculative, several hypotheses can be envisaged to explain this inverse relationship between thickness and friction angle. Among them, the presence of resistant blocks or coherent panels in a fluidized matrix could increase the solid interaction with the ground where flows thin to a value close to that of the thickness of the blocks. It is also well known that interstitial gas (volcanic or atmospheric) acts on particles to reduce their interaction and that, for the same permeability, thin flows lose their gas more rapidly than thicker ones [e.g., *Geldart*, 1986; *Roche et al.*, 2004; *Druitt et al.*, 2007, and references therein]. Thus the friction angle increases more rapidly in thin flows relative to thick ones.

[44] A vertical structure within the flow that would induce an increase in the resisting stress from the base of the flows

Figure 14. Longitudinal section of pyroclastic flow deposits (Tungurahua, August 2006 eruption, courtesy of P. Samaniego). White arrows indicate the base of the last emplaced unit. Note the strong inverse grading.

up toward their surface might also be another explanation for the inverse relationship between thickness and friction. In thick flows, the low-friction interior in contact with the ground would permit flow even on gentle slopes, the more frictional outer part simply being rafted. As the flow thins, the influence of the more resistant part would increase. The morphological resemblance between PF and LRA deposits and lavas (lobes, levées and rounded fronts) appears to support a vertical variation of the rheology in long-runout natural flows. This concept is close to the plug flow model proposed from field observations for mudflows, debris avalanches and pyroclastic flows [e.g., *Sparks*, 1976; *Branney and Kokelaar*, 2002, and references therein]. It is compatible with detailed observations of the Socompa avalanche, which has been interpreted as a fluid-like interior surrounded by a more resistant brittle exterior [*Kelfoun et al.*, 2008]. This upward increase in the friction may be induced by the vertical variations of the flow granulometry. Deposits often present strong inverse grading: the base is composed of a matrix of fine particles, and the mean size of particles increases toward the surface. This has been observed in LRA deposits [e.g., *Shaller*, 1991, and references therein] as well as in PF deposits (Figure 14). Gas, for example, is one mechanism which is more efficient at reducing friction between finer than coarse particles. [e.g., *Geldart*, 1986]. With such a vertical structure, where the flow thins, the influence of the coarser frictional surface would induce an increase of the friction angle at the base of the flow.

5. Conclusion

[45] This article explores the behavior of flows using simple first-order rheologies for the simulation of pyroclastic flows and long runout volcanic avalanches. I carried out more than 30 simulations on simple topographies that are representative of the characteristics of natural relief. The plastic rheology reproduces, to the first order, the main morphological features of natural long-runout granular flow deposits: levées, inverse relationship between thickness of deposits and slope, bulbous front. Future models of PF and LRA will have to reproduce a global behavior close to the plastic behavior in order to be validated and will have to explain why the plastic rheology fits the morphology of PF and LRA deposits better than the Coulomb rheology. While this question remains, as yet, unanswered, the success of the plastic rheology over the Coulomb rheology might indicate that the friction angle at the base of LRA and PF decreases depending on the thickness of the flow and cannot be considered as constant, although it is not clear which process induces this behavior. The results show, however, that for a high mass rate of material (dome collapse for example) this first-order rheology is too simple, perhaps because it does not describe the dismantling stage, or because a real velocity-dependent stress acts on fast flows. To refine this first-order rheology and improve our knowledge of its limitations, accurate field data are needed, and volcanic monitoring needs to focus on the acquisition of pyroclastic flow characteristics during their emplacement, for example volume, flow rate and velocity. In the meantime, the data available are accurate enough to state that the simple Coulomb friction is too far removed from natural deposits to be suitable for the simulation of PF and LRA. Thus, given our current state of knowledge, behavior laws based on a plastic rheology are a better alternative.

[46] **Acknowledgments.** The study has been funded by the French Institut de Recherche pour le Développement (IRD) and by the program ANR Volbiflo (ANR-07-jcjc-0114). The paper was improved by Fran van Wyk de Vries and by the useful and detailed comments of two anonymous reviewers. The numerical code used for the simulations, VolcFlow, is available upon request for academic research.

References

Branney, M. J., and P. Kokelaar (2002), *Pyroclastic Density Currents and the Sedimentation of Ignimbrites*, *Geol. Soc. Mem.*, *27*, 143 pp.

Campbell, C. S., P. W. Cleary, and M. Hopkins (1995), Large-scale landslide simulations: Global deformation, velocities, and basal friction, *J. Geophys. Res.*, *100*, 8267–8283, doi:10.1029/94JB00937.

Cecconi, M., M. Scarapazzi, and G. Viggiani (2010), On the geology and the geotechnical properties of pyroclastic flow deposits of the Colli Albani, *Bull. Eng. Geol. Environ.*, *69*(2), 185–206, doi:10.1007/s10064-009-0250-x.

Cole, P. D., E. S. Calder, T. H. Druitt, R. Hoblitt, R. Robertson, R. S. J. Sparks, and S. R. Young (1998), Pyroclastic flows generated by gravitational instability of the 1996–1997 lava dome of Soufrière Hills Volcano, Montserrat, *Geophys. Res. Lett.*, *25*(18), 3425–3428, doi:10.1029/98GL01510.

Collins, G. S., and H. J. Melosh (2003), Acoustic fluidization and the extraordinary mobility of sturzstroms, *J. Geophys. Res.*, *108*(B10), 2473, doi:10.1029/2003JB002465.

Crandell, D. R., C. D. Miller, H. X. Glicken, R. L. Christiansen, and C. G. Newhall (1984), Catastrophic debris avalanche from ancestral Mount Shasta volcano, *Calif. Geol.*, *12*(3), 143–146.

Crosta, G. B., H. Chen, and C. F. Lee (2004), Replay of the 1987 Val Pola landslide, Italian Alps, *Geomorphology*, *60*(1–2), 127–146, doi:10.1016/j.geomorph.2003.07.015.

Dade, W. B., and H. E. Huppert (1998), Long-runout rockfalls, *Geology*, *26*, 803–806.

Davies, T. R. (1982), Spreading of rock avalanche debris by mechanical fluidization, *Rock Mech.*, *15*, 9–24, doi:10.1007/BF01239474.

Davies, T. R., and M. J. McSaveney (1999), Runout of dry granular avalanches, *Can. Geotech. J.*, *36*, 313–320, doi:10.1139/t98-108.

Doyle, E. E., A. J. Hogg, H. M. Mader, and R. S. J. Sparks (2010), A two-layer model for the evolution and propagation of dense and dilute regions of pyroclastic currents, *J. Volcanol. Geotherm. Res.*, *190*, 365–378, doi:10.1016/j.jvolgeores.2009.12.004.

Druitt, T. H., G. Avard, G. Bruni, P. Lettieri, and F. Maez (2007), Gas retention in fine-grained pyroclastic flow materials at high temperatures, *Bull. Volcanol.*, *69*, 881–901, doi:10.1007/s00445-007-0116-7.

Evans, S. G., O. Hungr, and J. J. Clague (2001), Dynamics of the 1984 rock avalanche and associated distal debris flow on Mount Cayley, British Columbia, Canada; implications for landslide hazard assessment on dissected volcanoes, *Eng. Geol.*, *61*, 29–51, doi:10.1016/S0013-7952(00)00118-6.

Geldart, D. (1986), *Gas Fluidization Technology*, John Wiley, Hoboken, N. J.

Gray, J. M. N. T., Y. C. Tai, and S. Noelle (2003), Shock waves, dead zones and particle-free regions in rapid granular free-surface flows, *J. Fluid Mech.*, *491*, 161–181, doi:10.1017/S0022112003005317.

Hayashi, J. N., and S. Self (1992), A comparison of pyroclastic flow and debris avalanche mobility, *J. Geophys. Res.*, *97*, 9063–9071, doi:10.1029/92JB00173.

Heinrich, P., G. Boudon, J. C. Komorowski, R. S. J. Sparks, R. Herd, and B. Voight (2001), Numerical simulation of the December 1997 debris avalanche in Montserrat, Lesser Antilles, *Geophys. Res. Lett.*, *28*, 2529–2532, doi:10.1029/2001GL012968.

Hoblitt, R. P. (1986), Observations of the eruptions of July 22 and August 7, 1980, at Mount St. Helens, Washington, *U.S. Geol. Surv. Prof. Pap.*, *1335*, 1–44.

Hutter, K., and U. Nohguchi (1990), Similarity solutions for a Voellmy model of snow avalanches with finite mass, *Acta Mech.*, *82*, 99–127, doi:10.1007/BF01173741.

Iverson, R. M., and R. P. Denlinger (2001), Flow of variably fluidized granular masses across three-dimensional terrain: 1. Coulomb mixture theory, *J. Geophys. Res.*, *106*, 537–552, doi:10.1029/2000JB900329.

Iverson, R. M., M. Logan, and R. P. Denlinger (2004), Granular avalanches across irregular three-dimensional terrain: 2. Experimental tests, *J. Geophys. Res.*, *109*, F01015, doi:10.1029/2003JF000084.

Jolly, A. D., G. Thompson, and G. E. Norton (2002), Locating pyroclastic flows on Soufriere Hills volcano, Montserrat, West Indies, using amplitude signals from high dynamic range instruments, *J. Volcanol. Geotherm. Res.*, *118*, 299–317, doi:10.1016/S0377-0273(02)00299-8.

Kelfoun, K., and T. H. Druitt (2005), Numerical modeling of the emplacement of Socompa rock avalanche, Chile, *J. Geophys. Res.*, *110*, B12202, doi:10.1029/2005JB003758.

Kelfoun, K., F. Legros, and A. Gourgaud (2000), Statistical study of damaged trees related to the pyroclastic flows of November 22, 1994 at Merapi volcano (central Java, Indonesia): Relation between ash-cloud surge and block-and-ash flow, *J. Volcanol. Geotherm. Res.*, *100*, 379–393, doi:10.1016/S0377-0273(00)00147-5.

Kelfoun, K., T. H. Druitt, B. van Wyk de Vries, and M. N. Guilbaud (2008), Topographic reflection of Socompa debris avalanche, Chile, *Bull. Volcanol.*, *70*, 1169–1187, doi:10.1007/s00445-008-0201-6.

Kelfoun, K., P. Samaniego, P. Palacios, and D. Barba (2009), Is frictional behaviour suitable for pyroclastic flow simulation: Comparison with a well constrained eruption at Tungurahua volcano (Ecuador), *Bull. Volcanol.*, *71*, 1057–1075, doi:10.1007/s00445-009-0286-6.

Lacroix, A. (1904), *La Montagne Pelée et ses Eruptions* (in French), Masson et Cie, Paris.

Legros, F. (2002), The mobility of long-runout landslides, *Eng. Geol.*, *63*, 301–331.

Lipovsky, P. S., et al. (2008), The July 2007 rock and ice avalanches at Mount Steele, St. Elias Mountains, Yukon, Canada, *Landslides*, *5*, 445–455, doi:10.1007/s10346-008-0133-4.

Lube, G., S. J. Cronin, T. Platz, A. Freundt, J. N. Procter, C. Henderson, and M. F. Sheridan (2007), Flow and deposition of pyroclastic granular flows: A type example from the 1975 Ngauruhoe eruption, New Zealand, *J. Volcanol. Geotherm. Res.*, *161*, 165–186, doi:10.1016/j.jvolgeores.2006.12.003.

Mangeney, A., F. Bouchut, N. Thomas, J. P. Vilotte, and M. O. Bristeau (2007), Numerical modeling of self-channeling granular flows and of their levee-channel deposits, *J. Geophys. Res.*, *112*, F02017, doi:10.1029/2006JF000469.

McEwen, A. S., and M. C. Malin (1989), Dynamics of Mount St. Helens' 1980 pyroclastic flows, rockslide-avalanche, lahars, and blast, *J. Volcanol. Geotherm. Res.*, *37*, 205–231, doi:10.1016/0377-0273(89)90080-2.

Miura, S., and K. Yagi (2003), Mechanical behavior and particle crushing of volcanic coarse-grained soils in Japan, in *Characterisation and Engineering Properties of Natural Soils*, edited by T. S. Tan et al., pp. 1169–1202, A. A. Balkema, Lisse, Netherlands.

Nairn, I. A., and S. Self (1978), Explosive eruptions and pyroclastic avalanches from Ngauruhoe in February, 1975, *J. Volcanol. Geotherm. Res.*, *3*, 39–60, doi:10.1016/0377-0273(78)90003-3.

Palladino, D. M., and G. A. Valentine (1995), Coarse-tail vertical and lateral grading in pyroclastic flow deposits of the Latera Volcanic Complex (Vulsini, central Italy): Origin and implications for flow dynamics, *J. Volcanol. Geotherm. Res.*, *69*, 343–364, doi:10.1016/0377-0273(95)00036-4.

Patra, A. K., et al. (2005), Parallel adaptive numerical simulation of dry avalanches over natural terrain, *J. Volcanol. Geotherm. Res.*, *139*, 1–21, doi:10.1016/j.jvolgeores.2004.06.014.

Pirulli, M., and A. Mangeney (2008), Results of back-analysis of the propagation of rock avalanches as a function of the assumed rheology, *Rock Mech. Rock Eng.*, *41*(1), 59–84, doi:10.1007/s00603-007-0143-x.

Pouliquen, O. (1999), Scaling laws in granular flows down rough inclined planes, *Phys. Fluids*, *11*, 542–548, doi:10.1063/1.869928.

Pouliquen, O., and Y. Forterre (2002), Friction law for dense granular flows: Application to the motion of a mass down a rough inclined plane, *J. Fluid Mech.*, *453*, 133–151, doi:10.1017/S0022112001006796.

Procter, J. N., S. J. Cronin, T. Platz, A. Patra, K. Dalbey, M. F. Sheridan, and V. Neall (2010), Mapping block-and-ash flow hazards based on Titan 2D simulations: A case study from Mt. Taranaki, NZ, *Nat. Hazards*, *53*, 483–501, doi:10.1007/s11069-009-9440-x.

Pudasaini, S. P., and B. Domnik (2009), Energy considerations in accelerating rapid shear granular flows, *Nonlin. Processes Geophys.*, *16*, 399–407, doi:10.5194/npg-16-399-2009.

Pudasaini, S. P., and K. Hutter (2006), *Avalanche Dynamics: Dynamics of Rapid Flows of Dense Granular Avalanches*, 602 pp., Springer, New York.

Richards, J. P., and M. Villeneuve (2001), The Llullaillaco volcano, northwest Argentina: Construction by Pleistocene volcanism and destruction by sector collapse, *J. Volcanol. Geotherm. Res.*, *105*, 77–105, doi:10.1016/S0377-0273(00)00245-6.

Roche, O., M. A. Gilbertson, J. C. Phillips, and R. S. J. Sparks (2004), Experimental study of gas-fluidized granular flows with implications for pyroclastic flow emplacement, *J. Geophys. Res.*, *109*, B10201, doi:10.1029/2003JB002916.

Rossano, S., G. Mastrolorenzo, and G. De Natale (1998), Computer simulations of pyroclastic flows on Somma-Vesuvius volcano, *J. Volcanol. Geotherm. Res.*, *82*, 113–137, doi:10.1016/S0377-0273(97)00060-7.

Savage, S. B., and K. Hutter (1991), The dynamics of avalanches of granular materials from initiation to runout. Part I: Analysis, *Acta Mech.*, *86*, 201–223, doi:10.1007/BF01175958.

Schwarzkopf, L. M., H. U. Schmincke, and S. J. Cronin (2005), A conceptual model for block-and-ash flow basal avalanche transport and deposition, based on deposit architecture of 1998 and 1994 Merapi flows, *J. Volcanol. Geotherm. Res.*, *139*, 117–134, doi:10.1016/j.jvolgeores.2004.06.012.

Shaller, P. J. (1991), Analysis and implications of large Martian and terrestrial landslides, Ph.D. thesis, 583 pp., Calif. Inst. of Technol., Pasadena.

Sheridan, M. F., A. J. Stinton, A. Patra, E. B. Pitman, A. Bauer, and C. C. Nichita (2005), Evaluating Titan 2D mass-flow model using the 1963 Little Tahoma Peak avalanches, Mount Rainier, Washington, *J. Volcanol. Geotherm. Res.*, *139*, 89–102, doi:10.1016/j.jvolgeores.2004.06.011.

Siebert, L. (1984), Large volcanic debris avalanches: Characteristics of source areas, deposits, and associated eruptions, *J. Volcanol. Geotherm. Res.*, *22*, 163–197, doi:10.1016/0377-0273(84)90002-7.

Sousa, J., and B. Voight (1995), Multiple-pulsed debris avalanche emplacement at Mount St. Helens in 1980: Evidence from numerical continuum flow simulations, *J. Volcanol. Geotherm. Res.*, *66*, 227–250, doi:10.1016/0377-0273(94)00067-Q.

Sparks, R. S. J. (1976), Grain size variations in ignimbrites and implications for the transport of pyroclastic flows, *Sedimentology*, *23*, 147–188, doi:10.1111/j.1365-3091.1976.tb00045.x.

Sparks, R. S. J., L. Wilson, and G. Hulme (1978), Theoretical modeling of the generation, movement and emplacement of pyroclastic flows by column collapse, *J. Geophys. Res.*, *83*, 1727–1739, doi:10.1029/JB083iB04p01727.

Takarada, S., T. Ui, and Y. Yamamoto (1999), Depositional features and transportation mechanism of valley-filling Iwasegawa and Kaida debris avalanches, Japan, *Bull. Volcanol.*, *60*, 508–522, doi:10.1007/s004450050248.

Ui, T., N. Matsuwo, M. Sumita, and A. Fujinawa (1999), Generation of block and ash flows during the 1990–1995 eruption of Unzen Volcano, Japan, *J. Volcanol. Geotherm. Res.*, *89*, 123–137, doi:10.1016/S0377-0273(98)00128-0.

Valentine, G. A. (1987), Stratified flow in pyroclastic surges, *Bull. Volcanol.*, *49*, 616–630, doi:10.1007/BF01079967.

Voight, B., H. Glicken, R. J. Janda, and P. M. Douglas (1981), Catastrophic rockslide avalanche of May 18, in *The 1980 Eruptions of Mount St. Helens, Washington*, edited by P. W. Lipman and D. R. Mullineaux, *U.S. Geol. Surv. Prof. Pap.*, *1250*, 347–378.

Voight, B., R. Janda, H. Glicken, and P. M. Douglas (1983), Nature and mechanics of the Mount St. Helens rockslide-avalanche of 18 May 1980, *Geotechnique*, *33*, 243–273, doi:10.1680/geot.1983.33.3.243.

Wadge, G., P. W. Francis, and C. F. Ramirez (1995), The Socompa collapse and avalanche event, *J. Volcanol. Geotherm. Res.*, *66*, 309–336, doi:10.1016/0377-0273(94)00083-S.

Wadge, G., P. Jackson, S. M. Bower, A. W. Woods, and E. Calder (1998), Computer simulations of pyroclastic flows from dome collapse, *Geophys. Res. Lett.*, *25*, 3677–3680, doi:10.1029/98GL00710.

Wilson, L., and J. W. Head (1981), Morphology and rheology of pyroclastic flows and their deposits, and guidelines for future observations, in *The 1980 Eruptions of Mount St. Helens, Washington*, edited by P. W. Lipman and D. R. Mullineaux, *U.S. Geol. Surv. Prof. Pap.*, *1250*, 513–524.

Yamamoto, T., S. Takarada, and S. Suto (1993), Pyroclastic flows from the 1991 eruption of Unzen volcano, Japan, *Bull. Volcanol.*, *55*, 166–175, doi:10.1007/BF00301514.

Yamashita, S., and K. Miyamoto (1993), Model of pyroclastic flow and its numerical simulation, in *Sediment Problems: Strategies for Monitoring, Prediction and Control*, *IAHS Publ.*, *217*, 67–74.

K. Kelfoun, Laboratoire Magmas et Volcans, CNRS, UMR 6524, IRD, R 163, Université Blaise Pascal Clermont-Ferrand II, BP 10448, F-63000 Clermont-Ferrand, France. (K.Kelfoun@opgc.univ-bpclermont.fr)

Comment on "A random kinetic energy model for rock avalanches: Eight case studies" by T. Preuth et al.

Karim Kelfoun[1,2,3] and Tim Davies[4]

Received 2 November 2010; revised 11 January 2011; accepted 21 January 2011; published 3 March 2011.

Citation: Kelfoun, K., and T. Davies (2011), Comment on "A random kinetic energy model for rock avalanches: Eight case studies" by T. Preuth et al., *J. Geophys. Res.*, *116*, F01014, doi:10.1029/2010JF001916.

[1] *Preuth et al.* [2010] present an original mechanism to explain the long runout of landslides and show that this mechanism allows for the simulation of a large number of landslides without case-by-case calibration of the model. However, *Preuth et al.* [2010] present no unequivocal data to demonstrate that their key new mechanism, random kinetic energy (RKE), exists at an intensity sufficient to cause the effects they claim. In that respect their model is, in our opinion, at present in the same category as other mechanisms such as undrained loading, acoustic fluidization, and frictionite (molten rock): they are plausible ideas that lack independent verification. This opinion is based on the following considerations.

[2] 1. The justification presented for the concept is that *Preuth et al.* [2010] have previously found that *assuming* the occurrence of RKE in experimental snow avalanches allows the velocity distributions measured in these avalanches to be explained. In this paper they present no evidence that they have observed or measured RKE in reality. The obvious place to look for RKE (or reports of it), in the context of rock avalanches, is in laboratory studies of the gravity flow of sand, but they report no attempt to do this, nor do they quote existing reports of it. Even this phenomenon, though, takes place under very low confining pressure compared with that beneath several tens of meters of rock avalanche debris, so it would not demonstrate that RKE is significant in rock avalanches. RKE is assumed to be generated by random components of the motion of the grains. This requires that the grains in motion must be capable of achieving appropriate velocities in all three dimensions. This is certainly the case in shallow grain flows, and near the surface of deep ones, where the confining gravitational stress is insufficient to keep grains in continuous contact, and impact and rebound can certainly cause high time-variant velocity components. In the case of grain flows sufficiently deep to represent rock avalanches, however, the confining pressure is such that grains have little space to move and are probably always in continuous contact, sliding past each other under shear. This behavior is known as dense granular flow [*Campbell*, 2002], and in this case the only random KE that can be generated in rigid grains is that due to grains moving laterally as they shear past each other. It is essential to explain how RKE can be sufficiently energetic in these conditions to cause the effects claimed by *Preuth et al.* [2010].

[3] 2. Even if RKE does exist, it is essential to prove that it is able to play a significant role in natural flows. The influence of RKE in the *Preuth et al.* [2010] model is mainly related to the values of two parameters, α and β, which are assumed rather than being measured or calculated. The parameter α controls the genesis of RKE by shearing, while β controls the way the RKE decays, which is assumed to be exponential [*Preuth et al.*, 2010, equation (15)]. The value of β is 0.8 s^{-1} [*Preuth et al.*, 2010, paragraph 45]. This means, for example, that after 1 s, the kinetic energy is still 45% of the initial energy (9% at 3 s, 4% at 4 s). The time scale for particle vibrations to be considered as having stopped, once external inputs have ceased, is thus a few seconds, which does not appear realistic. Stainless steel beads, for example, which exhibit a coefficient of restitution of about 0.9, reach 9% of the initial kinetic energy only 40 ms after the external source has ceased [e.g., *Grasselli et al.*, 2009]. The coefficient of elasticity of rocks being lower, the energy decrease will be faster, more than 100 times faster than that given by *Preuth et al.* [2010, equation (15)]. For debris avalanches composed of a large proportion of very fine material, the mechanism is still more difficult to believe. It is necessary to explain how the vibration energy is not absorbed during the displacement of the blocks in the fine matrix, and how shocks are not damped by the matrix. A rock falling onto the surface of a matrix-rich debris avalanche will not bounce and will only produce a weak sound. By what mechanism could the rate of decay of mechanical energy be low enough at the base of debris avalanches to maintain the kinetic energy of particles for the duration of several seconds? The chosen value of α is 5 [*Preuth et al.*, 2010, paragraph 47] (although this could be a misprint since in paragraph 19 it states that $\alpha \in [0, 1]$). This would mean that the random energy generated by the friction is 5 times higher than energy lost by friction itself, which is not possible. With this choice of the parameters α and β, the friction is thereby strongly, but artificially, reduced, nor does it prove that RKE exists in natural flows.

[1] Laboratoire Magmas et Volcans, Université Blaise Pascal, Clermont Université, Clermont-Ferrand, France.
[2] CNRS, UMR 6524, Clermont-Ferrand, France.
[3] IRD, M 163, Clermont-Ferrand, France.
[4] Department of Geological Sciences, University of Canterbury, Christchurch, New Zealand.

Copyright 2011 by the American Geophysical Union.
0148-0227/11/2010JF001916

[4] For these reasons we remain unconvinced of the significance of RKE in large rock avalanches. *Preuth et al.*'s [2010] RKE process is very similar (in fact it appears identical) to the "acoustic fluidization" mechanism [e.g., *Collins and Melosh*, 2003]; both rely on the shear-induced vibratory motion of grains to cause variations in intergranular direct stresses that allow shearing under unusually low shear stresses. Acoustic fluidization, however, has been shown to be insufficiently energetic to be capable of causing the effects its proponents claim [*Sornette and Sornette*, 2000], and we suspect the same might apply to RKE.

[5] There are a number of assumptions and simplifications in the RKE model. The flow is assumed to follow a Voellmy law, and the RKE only modifies the two coefficients of that law. Although *Preuth et al.* [2010, paragraphs 4 and 6] admit that the Voellmy relation provides little insight into rock avalanche behavior, it is nonetheless used as the basis of their model. The laws describing the increase and the decay of the RKE are also empirical ("[o]ne method to produce random energy is to proportion it linearly with the frictional work rate" [*Preuth et al.*, 2010, paragraph 19]) although all the model results depend on these relationships [*Preuth et al.*, 2010, equation (14)]. Some parameters are derived from snow avalanches, assuming dynamically similar behavior between rock and snow/ice. For some simulations, they are modified according to particular conditions [e.g., *Preuth et al.*, 2010, paragraph 48]. The initial topographies, the failure surfaces and the way the masses initially collapsed are not accurately constrained. The effect of the (assumed) release of energy by initial fragmentation is not taken into account. These issues all make the model questionable. The use of too many unconstrained parameters gives possible but nonunique solutions.

[6] The authors' assumption, that all the fragmentation that occurs in a rock avalanche takes place at the start of the landslide motion, is energetically untenable. For a start, what is the source of the energy to cause the intense fragmentation at the beginning of the motion? Only a small quantity of potential energy has been transformed into useful kinetic energy at this stage. *McSaveney and Davies* [2007] showed that at least 90% of the debris deposit of the 10^7 m^3 1991 Mt. Cook (New Zealand) rock avalanche was composed of particles which were less than 10 microns in diameter; the power (rate of energy release) required to accomplish this generation of fines in a short period at initiation of the landslide would be similar to that of a nuclear bomb. The common presence of shattered undisaggregated clasts in the distal regions of rock avalanches [*Davies et al.*, 1999; *Davies and McSaveney*, 2002; *McSaveney*, 1978, 2002] proves that fragmentation occurs throughout the runout, not just at the start, and the energy analysis of *Preuth et al.* [2010], which does not take this into account, is therefore incomplete.

[7] We are distinctly uncomfortable with the analogy between snow avalanches and rock avalanches used to support the RKE mechanism for the latter. The substantial difference in physical properties (e.g., failure stress, elasticity, coefficient of restitution, fracture toughness, density, melting point) between rock fragments and snow or ice particles requires a formal demonstration that the analogy is quantitatively supported if it is to be credible.

[8] In some of the *Preuth et al.* [2010] simulations, basal friction was reduced to a very low value (e.g., 0.1–0.2 [*Preuth et al.*, 2010, paragraph 48]). This appears to be assuming the required result at the outset; since the whole purpose of the RKE mechanism is to *explain* the low friction needed to cause the observed deposit geometries, this assumption appears to predetermine the required outcome.

[9] Our final comment is that a much more detailed empirical test of the RKE mechanism is required. It is relatively easy to approximately match poorly constrained field data with a numerical model, which is what the authors appear to have accomplished, judging by the data presented. In our opinion a stringent test of the empirical validity of the RKE process would be its ability to accurately model a well-constrained field case in three dimensions. This comment applies in general to all studies based on numerical simulations of geophysical flows. Simulating only the runout of a given example is not enough to conclude that a model is correct. Comparing the runout and the lateral extension of deposits is not a serious test in steep-sided valleys because the flows are constrained by the steep topography: thus, all models can give good results. In steep-sided topography, the comparison of runups all along the path and not only at the front is very important to check if the model can accurately reproduce the velocities of natural flows. To state that a model accurately reproduces a natural case, we have to compare not only the runout and the runups, but also the available field data: the thickness, structures, and surface morphologies of both the natural and the numerical deposits. The resolution of the topography should be accurate enough to reproduce the first order structures. Since the initial dislocation stage of a debris avalanche, when the coherent edifice is transformed into an avalanche, is generally not simulated correctly, it is also important to choose examples whose dislocation stage was rapid enough to have only a small impact on the whole emplacement. Otherwise, without information of how the collapse occurs, some field cases are impossible to simulate. One of the best field examples we know is the Socompa deposit, which is exceptionally well preserved and whose preevent topography and deposit morphology have been described in detail [e.g., *Francis et al.*, 1985; *van Wyk de Vries et al.*, 2001; *Kelfoun et al.*, 2008]. This allows the avalanche history to be reconstructed and an accurate comparison of the runout, the extension, the thickness, and the morphological features obtained by numerical modeling with field data [*Kelfoun and Druitt*, 2005; *Davies et al.*, 2010]. For the validation of future numerical models, there is a real need for this type of unambiguous and quantified field data, which would be available to everybody. In order to genuinely advance the science of the mechanics of large landslides and debris avalanches, the whole community needs to contribute in order to be able to test future numerical models objectively and with sufficient precision.

References

Campbell, C. S. (2002), Granular shear flows at the elastic limit, *J. Fluid Mech.*, *465*, 261–291, doi:10.1017/S002211200200109X.

Collins, G. S., and H. J. Melosh (2003), Acoustic fluidization and the extraordinary mobility of sturzstroms, *J. Geophys. Res.*, *108*(B10), 2473, doi:10.1029/2003JB002465.

Davies, T. R. H., and M. J. McSaveney (2002), Dynamic simulation of the motion of fragmenting rock avalanches, *Can. Geotech. J.*, *39*, 789–798, doi:10.1139/t02-035.

Davies, T. R. H., M. J. McSaveney, and K. A. Hodgson (1999), A fragmentation-spreading model for long-runout rock avalanches, *Can. Geotech. J.*, *36*, 1096–1110, doi:10.1139/cgj-36-6-1096.

Davies, T., M. McSaveney, and K. Kelfoun (2010), Runout of the Socompa volcanic debris avalanche, Chile: A mechanical explanation for low basal shear resistance, *Bull. Volcanol.*, *72*, 933–944, doi:10.1007/s00445-010-0372-9.

Francis, P. W., M. Gardeweg, C. F. Ramirez, and D. A. Rothery (1985), Catastrophic debris avalanche deposit of Socompa volcano, northern Chile, *Geology*, *13*, 600–603, doi:10.1130/0091-7613(1985)13<600:CDADOS>2.0.CO;2.

Grasselli, Y., G. Bossis, and G. Goutallier (2009), Velocity-dependent restitution coefficient and granular cooling in microgravity, *Europhys. Lett.*, *86*, doi:10.1209/0295-5075/86/60007(EPL).

Kelfoun, K., and T. H. Druitt (2005), Numerical modeling of the emplacement of Socompa rock avalanche, Chile, *J. Geophys. Res.*, *110*, B12202, doi:10.1029/2005JB003758.

Kelfoun, K., T. H. Druitt, B. van Wyk de Vries, and M.-N. Guilbaud (2008), Topographic reflection of Socompa debris avalanche, Chile, *Bull. Volcanol.*, *70*, 1169–1187, doi:10.1007/s00445-008-0201-6.

McSaveney, M. J. (1978), Sherman Glacier rock avalanche, Alaska, USA, in *Rockslides and Avalanches*, vol. 1, *Natural Phenomena*, *Dev. Geotech. Eng.*, vol. 14A, edited by B. Voight, pp. 197–258, Elsevier, Amsterdam.

McSaveney, M. J. (2002), Recent rockfalls and rock avalanches in Mount Cook National Park, New Zealand, in *Catastrophic Landslides: Effects, Occurrence, and Mechanisms*, *Rev. Eng. Geol*, vol. 15, edited by S. G. Evans and J. V. DeGraff, pp. 35–70, Geol. Soc. of Am., Boulder, Colo.

McSaveney, M. J., and T. R. Davies (2007), Rockslides and their motion, in *Progress in Landslide Science*, edited by K. Sassa et al., pp. 113–134, Springer, Berlin, doi:10.1007/978-3-540-70965-7_8.

Preuth, T., P. Bartelt, O. Korup, and B. W. McArdell (2010), A random kinetic energy model for rock avalanches: Eight case studies, *J. Geophys. Res.*, *115*, F03036, doi:10.1029/2009JF001640.

Sornette, D., and A. Sornette (2000), Acoustic fluidization for earthquakes?, *Bull. Seismol. Soc. Am.*, *90*(3), 781–785, doi:10.1785/0119990040.

van Wyk de Vries, B., S. Self, P. W. Francis, and L. Keszthelyi (2001), A gravitational spreading origin for the Socompa debris avalanche, *J. Volcanol. Geotherm. Res.*, *105*, 225–247, doi:10.1016/S0377-0273(00)00252-3.

T. Davies, Department of Geological Sciences, University of Canterbury, Private Bag 4800, Christchurch, New Zealand.

K. Kelfoun, Laboratoire Magmas et Volcans, Université Blaise Pascal, Clermont Université, 5 rue Kessler, F- 63038 Clermont-Ferrand, France. (k.kelfoun@opgc.univ-bpclermont.fr)

Feature

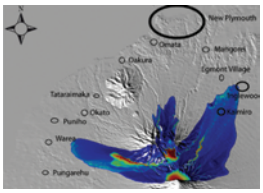

Numerical modelling: a useful tool to simulate collapsing volcanoes

Solène Pouget[1], Tim Davies[2], Ben Kennedy[3], Karim Kelfoun[4] & Hervé Leyrit[5]

[1]Solène Pouget, dept of Geology, University at Buffalo, NY 14260, USA solenepo@buffalo.edu
[2]Tim Davies, Dept of Geological Sciences, University of Canterbury, Private Bag 4800 Christchurch, New Zealand, tim.davies@canterbury.ac.nz
[3]Ben Kennedy, Dept of Geological Sciences, University of Canterbury, Private Bag 4800 Christchurch, New Zealand, ben.kennedy@canterbury.ac.nz
[4]Karim Kelfoun, Laboratoire des Magmas et Volcans, OPGC, Blaise-Pascal Université, 5 rue Kessler, Clermont-Ferrand, 63038 France, k.kelfoun@opgc.univ-bpclermont.fr
[5]Hervé Leyrit, Institut Polytechnique Lasalle Beauvais, Direction de l'Enseignement, rue Pierre Waguet, BP 30313,60026 Beauvais, France, herve.leyrit@lasalle-beauvais.fr

Since the nineteenth century scientists have tried to reproduce natural events in order to study and understand them through the technique of modelling. However, technology has evolved rapidly in the past two decades and now sophisticated numerical models are widely used to reproduce past events or simulate new scenarios. These models are particularly useful to reproduce the large scale and complexity of geological events. To illustrate the use and potential of numerical modelling in geological sciences, we describe a simulation of a large debris avalanche caused by the collapse of the north flank of the Taranaki volcano in New Zealand and the value of this information in the context of disaster planning.

What is a debris avalanche?

A volcanic debris avalanche is a large volume (> 10^6 m^3) of volcanic rocks flowing from a volcano at high velocity. This process was observed and studied for the first time in 1980 during the eruption and catastrophic failure of Mount St Helens, USA. Since then, debris avalanche deposits have been recognized on many volcanoes all around the world, some of them (e.g. Socompa (Chile), Taranaki (New Zealand), Cantal (France)) of enormous size. Even though a number of simulation models and other studies have been carried out, and knowledge has improved quickly, volcanic debris avalanches are not yet fully understood. One of the major challenges for scientists is to be able to predict the volume of a debris avalanche that can occur from a given volcano, and the area that will be affected by it, in order to create hazard maps and to plan for such events.

The Taranaki situation

Taranaki volcano, North Island, New Zealand (Fig. 1) is a tall stratovolcano of such slenderness as to cause concern about its stability during eruptive (and even non-eruptive) episodes. In its vicinity are rich agricultural lands, valuable industries, a city (New Plymouth) and a large population, so the volcanic debris avalanche hazard needs to be assessed and hazard maps constructed.

Debris avalanche hazard of the region

Volcanic activity started in the early Pleistocene (around 2 million years ago) in the sedimentary back-arc basin of the Taranaki region. Since the beginning of the activity, it produced four remnant edifices. These andesitic cones are aligned on a NNW–SSE trend known as the Taranaki Volcanic Lineament (Fig. 2). Activity has progressed southwards along this fracture with time, leading to the creation of the most recent edifice known as Taranaki, less than 0.12 Ma ago. Its last known eruption was in 1750 AD.

Several debris avalanche deposits have been recognized in the ring plain of these volcanoes and at least eight distinct formations have been mapped. These deposits affect a total area of about 3000 km^2 and have individual volumes of at least 0.15 km^3.

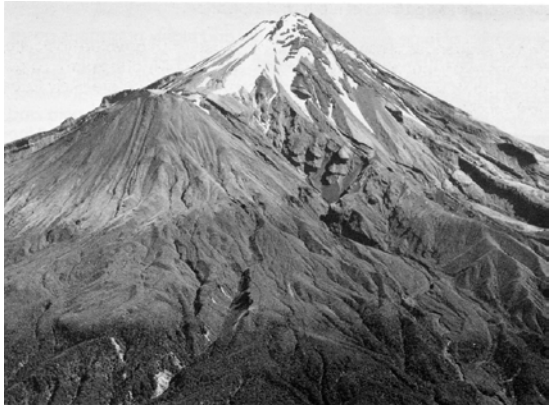

Fig.1. Mt Taranaki looking north, showing Fanthams Peak on the southern flank of the volcano.

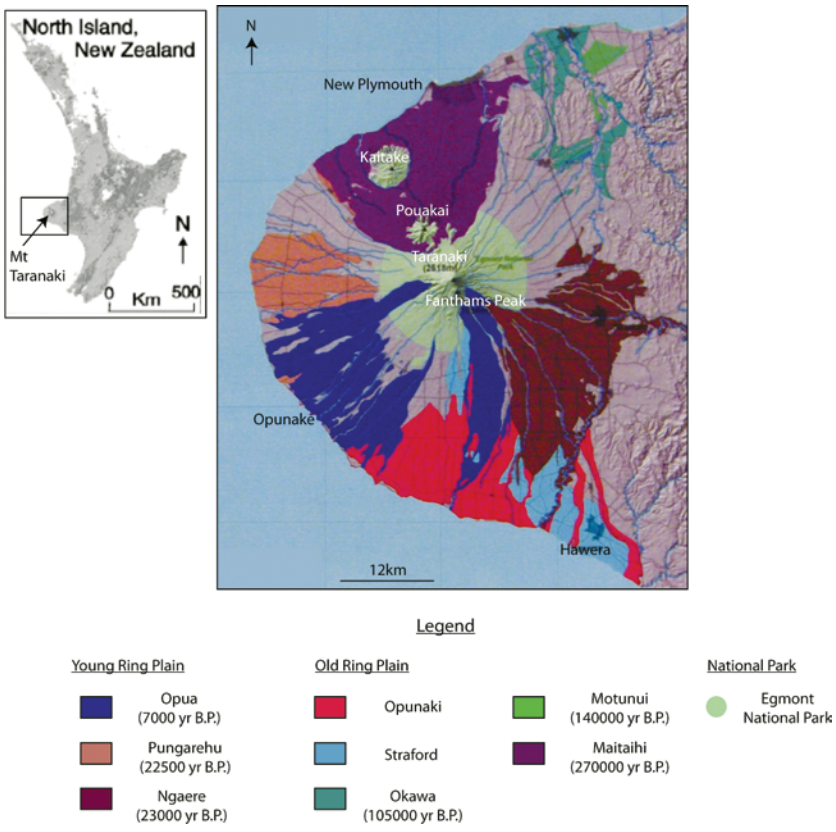

Fig.2. Debris avalanche deposit map.

The topography of the environment has probably affected some of the geometrical characteristics of the avalanche deposits as some of them are bifurcated (Okawa Formation) or channelized (Ngaere Formation). Because the city of New Plymouth lies to the north of Taranaki, we focus on this area where two debris avalanches previously occurred in that part of the lineament: the Maitahi and the Motunui formations. The Maitahi Formation consists of debris-flow and avalanche deposits derived from Pouakai volcano (the pre-Taranaki edifice, now severely degraded) whereas the origin of the Motunui Formation is unclear; it may have originated from a youthful ancestral Taranaki volcano or an actively degrading Pouakai volcano. The Taranaki Volcanic Lineament edifices have repeatedly collapsed over their history, and generated at least eight debris avalanche deposits over its 127 ka history.

Vulnerability of the region

The vulnerability of an area to natural processes results from the combined spatial distributions of natural processes and human activity (demography, economy and real estate). From a demographic point of view, the Taranaki region has 104 000 inhabitants, 66% of whom live in the New Plymouth District north of the volcano. The economy of the region relies on agriculture, manufacturing and tourism; however, the most important contributor to the economy is the oil and gas industry. The region produces all the commercial oil and gas of New Zealand. The area is still under-exploited and the potential for very large oil and gas reserves in deep water further off the Taranaki coast is high (estimated reserves of 55 million barrels of oil remain, together with an estimated 147 million barrels in known non-producing fields). New Plymouth District is the site of two methanol plants. Infrastructure is also rapidly developing with new retailing, industrial and residential areas. Given the population, industry and infrastructure, the New Plymouth District is vulnerable to debris avalanches from Taranaki. It is therefore necessary to estimate the risk from this hazard, and we shall show that appropriate numerical modelling is a crucial contributor to this assessment.

Simulation of a debris avalanche

Volcflow

The numerical code used for these simulations is called *VolcFlow*. It has been developed to simulate volcanic flows (e.g. pyroclastic flows, debris avalanches). This code is based on a depth-average approximation, where equations are solved using a shock-capturing numerical method based on a double upwind Eulerian scheme. The depth-average approximation is computed on a topography-linked coordinate system with x and y as horizontal directions (parallel to the local ground surface) and h perpendicular to the ground. This code can be used for several purposes, such as determining the rheological behaviour of the flow and visualizing the surface deformation or the area affected by the flow. This last use is the most interesting one for this study as geometrical results can be compared with existing hazard maps and thus have a direct bearing on future studies and disaster management planning. VolcFlow has been extensively tested on other volcanic debris avalanches, with impressive results in reproducing and explaining the emplacement of the avalanche of Socompa (Chile), including a reflected wave. Since the rheology of debris avalanches is not completely understood yet, approximations based on other examples are applied to Taranaki, leading to results that need to be interpreted with care.

Simulation of the northern debris avalanche of the Taranaki volcano

The numerical code was used to simulate a debris avalanche on the north flank of the Taranaki volcano. It was run on a digital elevation model (DEM) of the Taranaki region with a contour interval of 50 m. We selected the geometry of the collapse scar to determine the flow volume. Since there are presently no large collapse scars on Taranaki, we used

© Blackwell Publishing Ltd, The Geologists' Association & The Geological Society of London,

Fig.3. The city of New Plymouth and Taranaki volcano (view from Paritutu Rock).

a bowl-shaped scar for simplicity. The dimensions of the collapse scar were modified to obtain four different volumes. These volumes (0.77, 2.19, 3.67 and 4.78 km^3) were chosen to be realistic in the context of the shape of the present volcano and the volumes of debris avalanches deposits. We do not ascribe any particular trigger mechanism to the scar formation; it may be syn-eruptive or non-eruptive. A constant basal resistance of 50 kPa was used to simulate the debris avalanche (this value was previously used for the Socompa simulation). This rheology simulates debris avalanches well but does not represent the early sliding phase of an avalanche; it assumes an immediate collapse of the failing part of the volcano.

The simulations show that a debris avalanche on the north flank of the volcano moves in three main directions: north, east and west (Fig. 4). The smallest volume tends to give a deposit concentrated between the volcano and the Pouakai range and reaches a maximum distance of 12 km in the direction of Inglewood. Increasing volume from 0.77 km^3 to 3.67 km^3 increases the runout—the debris avalanche reaches a maximum distance of 24 km, and the deposit then affects a part of Inglewood. The maximum runout of 25 km is reached for a volume of 4.78 km^3.

Discussion

The simulations were carried out in order to highlight the impact of the topography on the runout path and distance of a debris avalanche. The first observation from the simulations was that even with the largest volume, the city of New Plymouth is not affected because the natural barrier of the Pouakai range detains most of the avalanche and diverts the rest. However, some other towns such as Inglewood are affected by the avalanche, as well as a good proportion of the New Plymouth district. The Pouakai range protects the northern part of the Taranaki region (most of New Plymouth district). In each simulation a small percentage of the avalanche overtopped the central part of the range to travel towards the city. Thus, part of the region described as 'unlikely to be affected by avalanches' on the existing hazards map (Fig. 5) may in fact be affected. This applies particularly to the western part of the New Plymouth District, bordered by the Waiwhakaiho River and the Stony River, since the results show that a small proportion of the debris avalanche enters this area, even for a volume smaller than 1 km^3.

However, several limitations of these simulations must be considered. The debris avalanche deposit depends on the initial shape of the collapse scar and its location on the flank. These simulations were run without any knowledge of actual weaknesses in the summit and the collapse area. This means that the next north-flank debris avalanche collapse scar will not be exactly like those created in these simulations. Secondly, if the collapse scar is slightly more to the

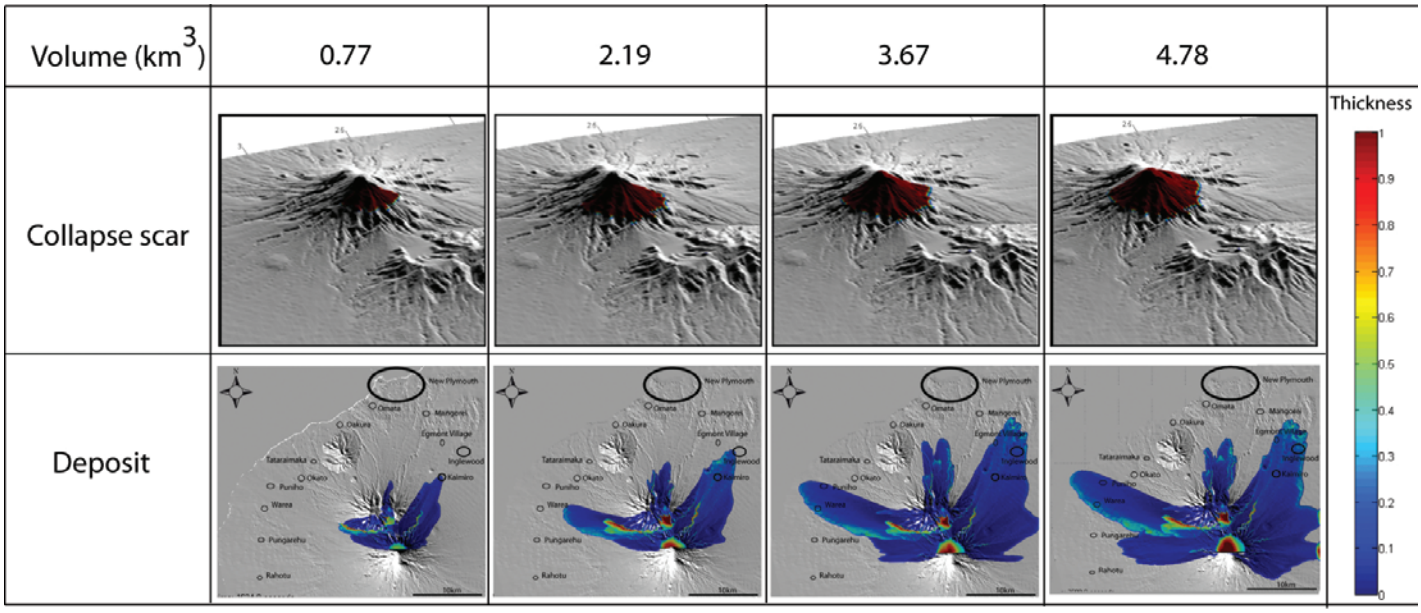

Fig.4. Results of the numerical simulations.

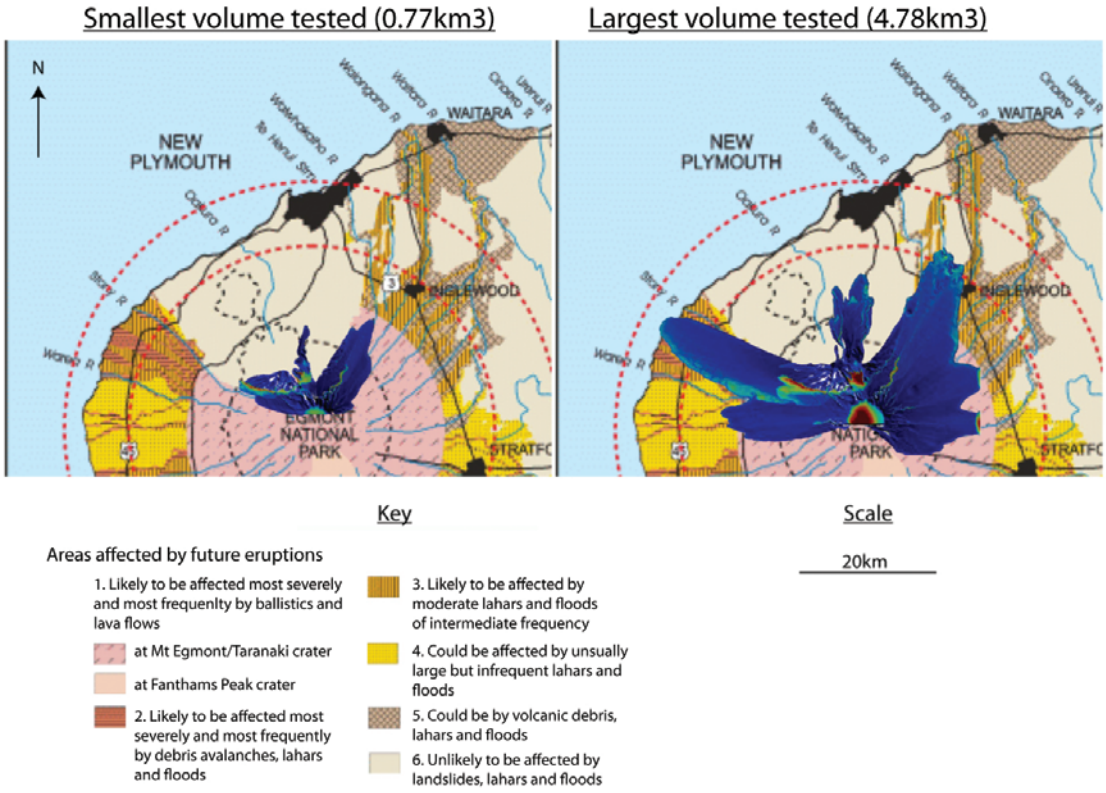

Fig.5. Geological hazard map with the smallest and largest deposits from the simulations.

east or west, the proportion of the avalanche going in one of the three main directions will be different. However, the large size of the scars suggests that there may be relatively little effect of detailed scar geometry on deposit geometry.

The numerical modelling technique clearly highlights the control that topography has upon debris avalanches in the Taranaki region. From a hazard management point of view, these results suggest a reassessment of the existing plans as the western part of the New Plymouth District, also represented by

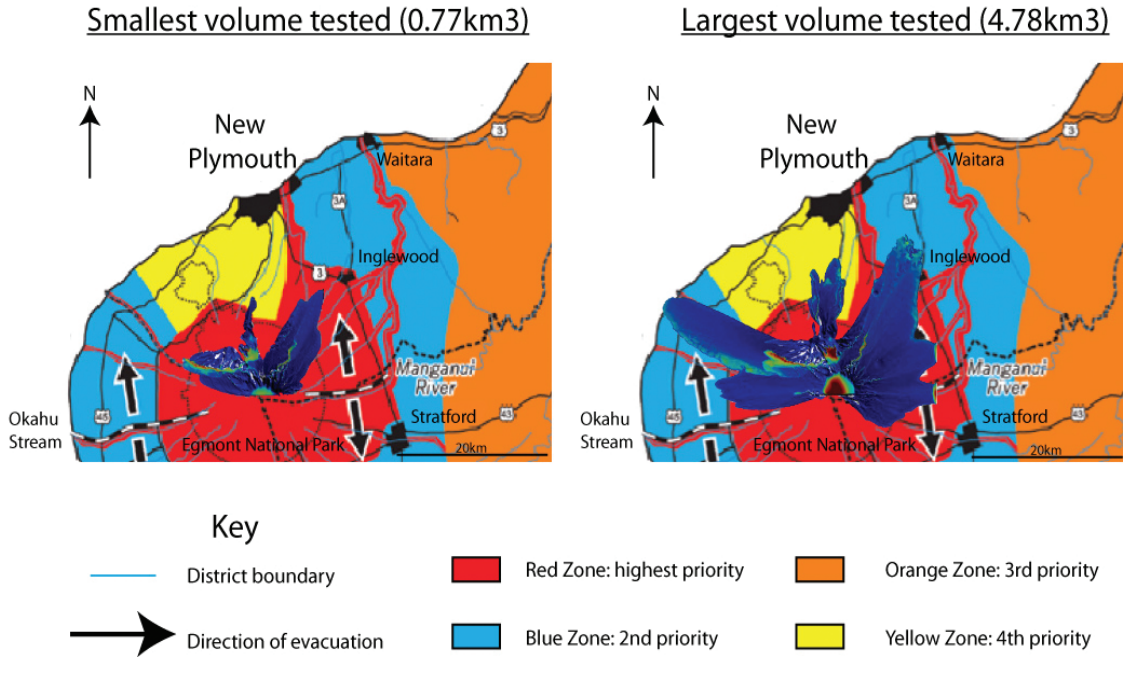

Fig.6. Evacuation map with the smallest and largest deposits from the numerical simulations.

© Blackwell Publishing Ltd, The Geologists' Association & The Geological Society of London, *Geology Today*, Vol. 28, No. 2, March–April 2012

the yellow zone on the evacuation map (Fig. 6), has never been considered to be potentially affected by debris avalanche and is the lowest priority evacuation zone. Clearly more work is required on a precise characterisation of this threat and its quantification. With time, the topography of the Pouaki range will change, which will alter its ability to protect the city. Simulations using DEM should be regularly updated to incorporate any topographical changes that might modify the results.

Conclusion

This simple and rapid simulation model shows that a preliminary model can utilize an existing DEM to identify specific areas at risk from debris avalanches. However, it is reassuring to know that New Plymouth city itself does not appear to be vulnerable to debris avalanches as long as the Pouakai range is there. A powerful application of this technique is to run models during periods of activity at volcanoes susceptible to collapse, in order to refine the evacuation zones because the actual topography of a volcano is needed to accurately predict the path of a debris avalanche, and this may alter during an eruption.

Suggestions for further reading

Davies, T.R.H., McSaveney, M.J. & Kelfoun, K. 2010. Runout of the Socompa volcanic debris avalanche, Chile: a mechanical explanation for low basal shear resistance. *Bulletin of Volcanology*, v.72, doi: 10.1007/s00445-010-0372-9/

Kelfoun, K. & Druitt, T.H. 2005. Numerical modeling of the emplacement of Socompa rock avalanche, Chile. *Journal of Geophysical Research*, v.110, pp.1–13.

Kelfoun K., Druitt T., van Wyk de Vries B., Guilbaud M.-N. 2008. Topographic reflection of the Socompa debris avalanche, Chile. *Bulletin of Volcanology* v.70, pp.1169–1187.

Neall, V.E., Stewart, R.B. & Smith, I.E.M. 1986. History and Petrology of the Taranaki Volcanoes. *In*: Smith, I.E.M. (ed.), *Late Cenozoic Volcanism in New Zealand*, pp. 251–263. Royal Society of New Zealand Bulletin.

Pouget, S. 2010. *Influence of the volume, fall height and environment on volcanic debris avalanche deposit*. Unpublished MSc thesis, Canterbury University, Christchurch, New Zealand.

Procter, J.N., Cronin, S.J. and Zernack, A.V. 2009. Landscape and sedimentary response to catastrophic debris avalanches, western Taranaki, New Zealand. *Sedimentary Geology*, v.220, pp.271–287.

Shea, T. & Van Wyk de Vries, B. 2010. Collapsing volcanoes: the sleeping giants' threat. *Geology Today*, v.26, pp.72–77.

Turnbull, J.M. & Davies, T.R.H. 2006. A mass movement origin for cirques. *Earth Surface Processes and Landforms*, v.31, pp.1129–1148.

Ui, T., Takarada, S. and Yoshimoto, M. 2000. Debris avalanches. *In:* Sigurdsson, H., Houghton, B., McNutt, S.R., Rymer, H. & Stix, J. (eds), *Encyclopedia of Volcanoes*, pp.617–626. Academic Press, London.

Bull Volcanol
DOI 10.1007/s00445-010-0372-9

RESEARCH ARTICLE

Runout of the Socompa volcanic debris avalanche, Chile: a mechanical explanation for low basal shear resistance

Tim Davies · Mauri McSaveney · Karim Kelfoun

Received: 30 April 2009 / Accepted: 18 May 2010
© Springer-Verlag 2010

Abstract We propose a mechanical explanation for the low basal shear resistance (about 50 kPa) previously used to simulate successfully the complex, well-documented deposit morphology and lithological distribution produced by emplacement of the 25 km^3 Socompa volcanic debris avalanche deposit, Chile. Stratigraphic evidence for intense basal comminution indicates the occurrence of dynamic rock fragmentation in the basal region of this large granular mass flow, and we show that such fragmentation generates a basal shear stress, retarding motion of the avalanche, that is a function of the flow thickness and intact rock strength. The topography of the Socompa deposit is realistically simulated using this fragmentation-derived resistance function. Basal fragmentation is also compatible with the evidence from the deposit that reflection of the avalanche from topography caused a secondary wave that interacted with the primary flow.

Keywords Volcanic debris avalanche · Socompa deposit · Runout simulation · Dynamic fragmentation · Retarding stress · Debris avalanche reflection · Deposit morphology

Editorial responsibility: J. Phillips

T. Davies (✉)
Department of Geological Sciences, University of Canterbury,
Private Bag 4800,
Christchurch, New Zealand
e-mail: tim.davies@canterbury.ac.nz

M. McSaveney
GNS Science Ltd,
PO Box 30368, Lower Hutt, New Zealand

K. Kelfoun
Laboratoire Magmas et Volcans, OPGC,
UMR Clermont Université-CNRS-IRD,
5 rue Kessler,
63038 Clermont-Ferrand, France

Nomenclatures

F_f	proportion (by volume) of grains fragmenting simultaneously
k_1, k_2	constants
O[ ]	of the order of
P_C	minimum value needed to cause fragmentation
P_E	spatially-averaged effective intergranular direct stress within the fragmenting layer
P_{fa}	apparent fragmenting pressure
P'_f	spatially-averaged fragmentation pressure in the fragmenting layer; mean longitudinal fragmentation pressure.
P_{OB}	direct stress on the top of the fragmenting layer
P_R	frictional resistance in a fragmenting granular flow
Q	intact static compressive strength
μ	dynamic friction coefficient

Introduction

Collapses from volcanic edifices cause some of the largest subaerial landslides on Earth (e.g. the 45 km^3 18,500-year old Nevado de Colima event, Mexico; Stoops and Sheridan 1992: the 25 km^3 Mt Shasta event, USA, ~300,000 years ago; Crandell et al. 1984: and the similarly-sized Socompa event, Chile, 7500 years ago; van Wyk de Vries et al. 2001; Wadge et al. 1995). The extraordinarily large areas covered by such events have given rise to extensive speculation about the transport mechanics involved, and Takarada et al. (1999) list the suggestions that have been put forward. To date no proposed explanation for the behaviour of volcanic debris avalanches has been widely accepted, though there

Published online: 12 June 2010

appears to be increasing evidence that some mechanism for reducing basal friction is likely to be involved (Kelfoun and Druitt 2005; Kelfoun et al. 2008).

In this work we follow up the implications of the successful simulation of the Socompa deposit reported by Kelfoun and Druitt (2005) and Kelfoun et al. (2008). That simulation used a spatially- and temporally-constant basal retarding stress of about 50 kPa to reproduce with remarkable accuracy the morphology and lithological distribution of the Socompa deposit. We choose this deposit to test our hypothesis of fragmentation-controlled runout because of these successful simulations, and because it has been extensively investigated and its distinctive morphology and lithological distribution well reported; in particular, the pre-existing topography has been reported in the context of groundwater exploration, providing a good basis for runout modelling (Kelfoun and Druitt 2005).

We begin by summarising the general characteristics of volcanic debris avalanches, then provide a brief outline of dynamic rock fragmentation and the stresses it generates, before applying this concept to the reported structure of the Socompa deposit and the dynamics of its emplacement. We show that the rheology used by the Kelfoun and Druitt (2005) simulation corresponds closely to that resulting from the occurrence of intense rock fragmentation near the base of the moving avalanche demonstrated by Van Wyk de Vries et al. (2001) and Le Corvec (2005). Finally we show that the fragmentation mechanism is compatible with the reflection of the primary debris avalanche wave recorded in the Socompa deposit and described by Kelfoun et al. (2008).

Volcanic debris avalanches

A volcanic debris avalanche results from initial detachment of a substantial part of a volcano edifice by deep-seated failure. The detached mass accelerates rapidly from rest and begins to disaggregate through shear under gravity - this part of the sequence is well shown in the spectacular photos of the 1980 Mt St Helens debris avalanche taken by G. Rosenquist (Voight et al. 1981). As it leaves the edifice, the moving mass collapses into a granular flow, advancing across the landscape at velocities up to ~100 ms^{-1}, spreading and thinning as it goes. After many km of travel (the Socompa debris avalanche travelled up to 40 km), the material decelerates to rest, leaving a deposit featuring all or some of:

- highly comminuted debris;
- prominent conical mounds on the surface ('hummocky terrain');
- raised edges;
- lateral and/or longitudinal ridges; and
- an average thickness of the order of 30 m, apparently irrespective of intial volume.

The most striking feature of large-volume volcanic debris avalanches is their surprisingly small average depth relative to areal extent, implying surprising ability to spread laterally and longitudinally. They appear to spread relatively much more than small-scale, water-saturated debris-flows (Iverson et al. 1998); on average, they also seem to extend about twice as far from source as non-volcanic rock avalanches of equivalent volume (Siebert 1984), again implying greater mobility and spreading.

In volcanic debris avalanche deposits with vertical sections visible to the base, two major strata are reported fairly consistently: 'blocky facies' in the upper part of the deposit, and 'matrix facies' in the basal region. These descriptions refer to appearance rather than sedimentological distinctiveness; blocky facies look blocky but matrix facies do not. Also, these strata are often reported to be mixed. Typically a thin matrix facies underlies a thicker blocky or mixed facies (Crandell et al. 1984), though the high-speed translation of the avalanche across uneven terrain often confuses the sequence, as does the incorporation of erodible substrate material into the avalanche in places (as also in rock avalanches: Hewitt 2003; Dufresne and Davies 2009; Dufresne et al. 2009). The origin of this stratification has not been investigated in detail. It is clear, however, that during the travel of the debris avalanche across terrain the basal region experiences high normal and shear stresses, and that these result in intense comminution of the rock debris in that region (Van Wyk de Vries et al. 2001; Le Corvec 2005).

Volcanic edifices comprise porous, hydrothermally altered rock, often with significant void space, so it is common for volcanic debris avalanches to contain substantial volumes of water. The 1980 Mt St Helens event may or may not be widely representative, but Glicken (1996) estimated it to have an initial porosity of 14% and saturation of 92%, while at deposition it had 25% porosity and 45% saturation thanks to a total volume increase of 0.4 km^3 due to comminution and bulking of the debris. During runout it seems reasonable to expect that the water in a volcanic debris avalanche will be found in the lower part of the debris, since this is the position it occupied in the stationary edifice before the motion began and the lack of vertical mixing in debris avalanches is well-known (Van Wyk de Vries et al. 2001). We thus expect that a region at the base of the avalanche will tend to be saturated, while the overlying strata may tend to be unsaturated. Thus the intense comminution reported at the base of debris avalanches, which we suggest constrains the available resistance to avalanche motion, may take place in a granular medium saturated with water. With respect to the

Socompa event, Kelfoun et al. (2008) stated: 'As noted by previous authors (e.g., van Wyk de Vries et al. 2001), most of the avalanche cannot have been saturated with water during flow, since there is no evidence for mudflows formed by post-emplacement decantation. Saturation of a thin basal layer cannot, however, be ruled out.'

While this outline of debris avalanche composition suggests considerable potential for generating complex behaviour during runout, it does not immediately offer an obvious explanation for the extraordinary spreading of large volcanic debris avalanches and the consequent relative thinness of their deposits. Recent studies of the Socompa debris avalanche deposit by Van Wyk de Vries et al. (2001), Le Corvec (2005), Kelfoun and Druitt (2005), and Kelfoun et al. (2008), however, provide useful insights into the processes occurring.

The Socompa debris avalanche deposit (Van Wyk de Vries et al. 2001; Le Corvec 2005)

The Socompa debris avalanche occurred about 7200 years ago. It involved a total volume of about 36 km^3, 11 km^3 of which remain close to the source area as "toreva" blocks. One of the largest subaerial volcanic debris avalanche deposits in the world, it extends a distance of 40 km from the edifice and covers 500 km^2; it is also one of the best-preserved examples due to the extreme aridity of the Atacama desert in which it is situated. Van Wyk de Vries et al. (2001) and Wadge et al. (1995) indicate that the collapse was non-eruptive, and was caused by gravitational spreading over a failing substrate of Salin formation (Fig. 1). This formation comprises gravels, conglomerates and ignimbrites, and prior to the collapse it was inferred to be ~200 m in thickness beneath the edifice.

The Salin Formation-derived part of the debris avalanche deposit overlies undisturbed Salin Formation; the former comprises 80% of the total debris-avalanche deposit volume, and it underlies debris sourced from the volcano edifice (known as "Socompa breccia": Le Corvec 2005). The Salin-formation-derived component of the avalanche deposit has been progressively and pervasively fragmented ("complete fragmentation"; Van Wyk de Vries et al. 2001 p 234; Le Corvec 2005) during emplacement and is known as "Reconstituted Ignimbrite Facies" (RIF). It has well-defined thin internal shear bands. At Socompa the RIF becomes finer with runout distance, being dominated by ash-sized (~10 μ) material in distal locations; by contrast the overlying Socompa breccia does not show runout fining (Le Corvec 2005). Again this indicates substantial and ongoing comminution in the RIF, and little comminution of the overlying Socompa breccia, during runout.

The Socompa simulation (Kelfoun and Druitt 2005)

Kelfoun and Druitt (2005) simulated numerically the well-preserved but complex morphology of the Socompa deposit (Fig. 2b), starting from well-constrained reconstructions of the original edifice and deposition area geometries defined by geological investigations and trialling a variety of friction-based rheologies in a depth-averaged granular-flow model. None of these rheologies was able to reproduce the deposit geometry satisfactorily. A very good match between model and prototype deposit geometries, however, was eventually achieved using a constant basal resistance of about 50 kPa throughout the emplacement, irrespective of the depth and velocity of the moving mass and of the topographic gradient of the surface over which runout took place. This very simple (pure plastic) rheology resulted in good representation (Fig. 2a) of

- the extent of the deposit;
- depth variations in the deposit (i.e. mass distribution);
- lithological variations within the deposit;
- the nature of the deposit edges ("L");
- the well-defined NE-SW trending escarpment across the centre of the deposit ("ME");
- the rough topography to the north of this scarp ("CZ"); and
- the prominent distal lobe ("FL").

The success of the model in reproducing all these characteristics over an area of 500 km^2 is notable,

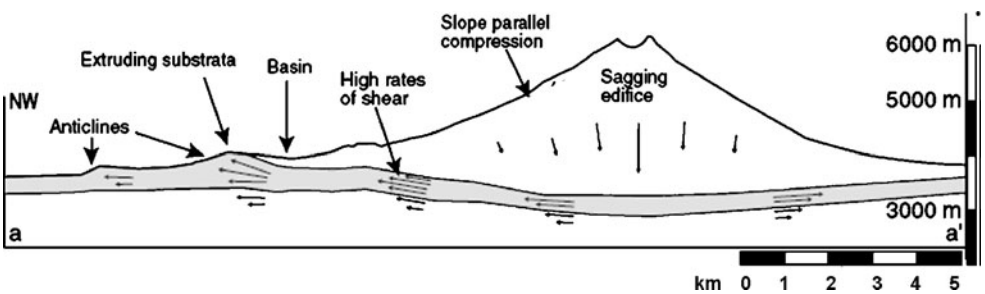

Fig. 1 Location of groundwater-bearing Salin formation (grey) below the pre-failure edifice of Socompa volcano. The rest of the edifice is effectively dry due to the hyper-arid climate. (After Van Wyk de Vries et al. 2001)

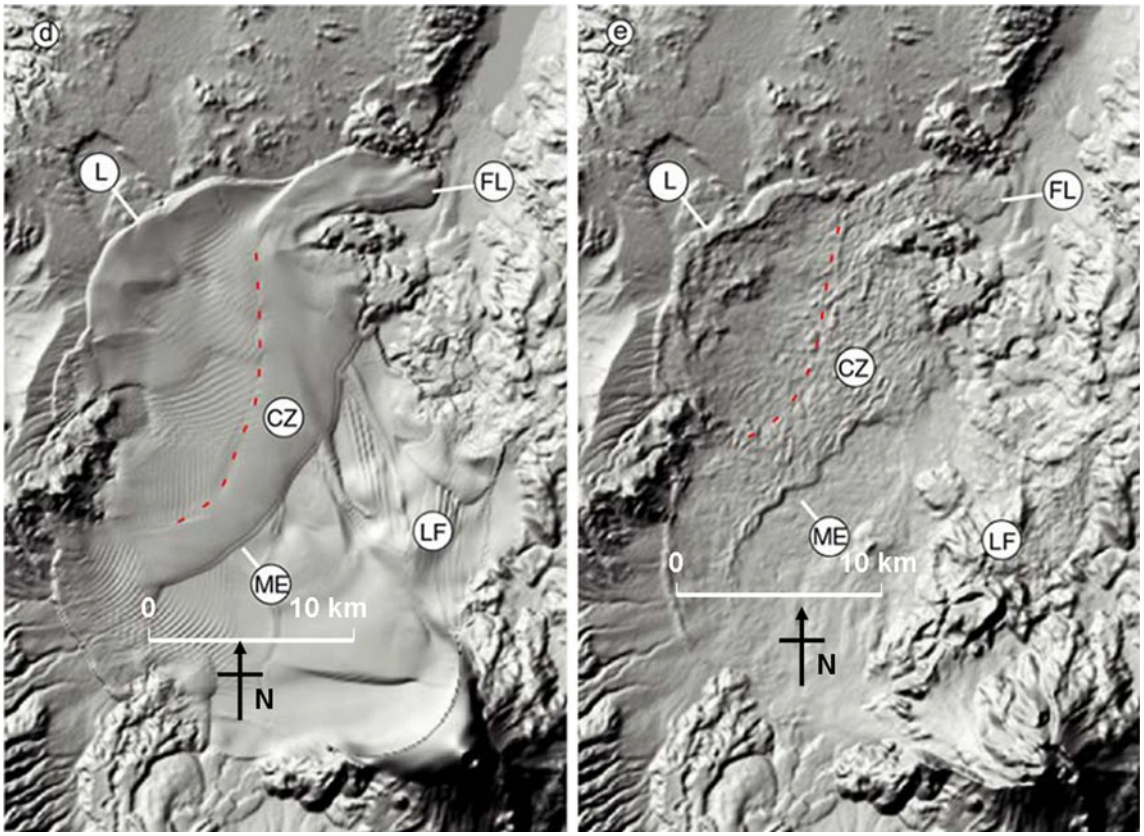

Fig. 2 **a** Shaded relief map of the simulated Socompa deposit. **b** Shaded relief map of the real deposit. Circled letters indicate some corresponding morphological elements of the deposit. (From Kelfoun and Druitt 2005; simulation with retarding stress =52 kPa)

considering the use of a very simple rheology with a single constant parameter (whose value was chosen by trial and error). It is difficult to avoid the conclusion that the primary characteristics of the runout behaviour have been largely captured by the model, in particular the magnitude and (lack of) variation of the basal retarding stress.

Kelfoun and Druitt (2005) pointed out that the suggestion of a basal retarding stress in the range 10–100 kPa had previously been made by Dade and Huppert (1998) on energy grounds. However, that suggestion referred to the spatially-averaged basal resistance over the whole duration of the avalanche motion, rather than the constant local and short-term resistance used in the Socompa simulation. Hence the success of the Socompa model is much more significant in constraining runout dynamics than the Dade and Huppert (1998) analysis.

It therefore appears worthwhile to explore the basis of a low and constant retarding stress during runout. This material rheology is unusual, but has been found to reproduce other volcanic mass-movement deposits successfully (e.g. Kelfoun et al. 2009); it suggests that processes additional to those of normal granular flow are involved. We now demonstrate that the processes of intense comminution in a debris avalanche result in an approximately constant retarding stress of similar value to that used by the successful Kelfoun and Druitt (2005) Socompa simulation.

Dynamic rock fragmentation

"Dynamic rock fragmentation" is the term introduced by Grady and Kipp (1987) to describe the response of intact brittle rock to rapid strain under a confining stress. Briefly, an intact rock particle (that is, one with only "Griffiths" microcracks) in a shearing granular mass becomes distorted by the forces exerted on it by the surrounding rock particles. It deforms elastically, storing elastic strain energy abstracted from the general shearing motion around it, until its local strength is exceeded. It then fails or "fragments", breaking violently on many new, rapidly-propagating fracture surfaces, and a substantial proportion of its stored elastic strain energy is released as kinetic energy of the fragments moving away from the original centre of mass (Bergstrom 1963; McSaveney and Davies 2009) or, in the case of confined granular flow, as pressure on the surroundings. In particular, Bergstrom (1963) demonstrated with laboratory data that in brittle failure of spherical rock grains caused by slow unconfined compression of rock, about half of the maximum

possible stored elastic strain energy was released from breaking grains as kinetic energy. Zeleny and Piret (1962) showed that using Pyrex (a material lacking granular structure, and thus of high strength homogeneity) this proportion increased to about 85%. The stress distribution within a grain at failure is never uniform, so these results show that a large proportion of the total stored energy is released at failure as free (i.e. available) energy. The effect of this energy release on the dynamics of comminuting grain-flow has hitherto been ignored (e.g. Abe and Mair 2005; Mair and Abe 2008), largely because of the misconception that it all transforms directly to "surface energy" associated with the new surface created by breakage (e.g. Cocco et al. 2006; Crosta et al. 2007; Locat et al. 2006), and thus is never available to the system. We have recently examined this concept (McSaveney and Davies 2009), and shown that prior to its eventual dissipation to frictional heat the released energy is manifest as kinetic or pressure energy—as confirmed empirically by the experimental data of Bergstrom (1963) and Zeleny and Piret (1962). It is also well-known that rock-bursts in mines generate high fragment velocities (McGarr 1997), which must derive from elastic strain energy stored in the rock mass; and we note that the seismic energy released in earthquakes also comes from elastic strain energy stored in highly-stressed rock.

The pressure exerted on the surrounding material by these fragments is of the same order of magnitude as the compressive strength of the intact rock at the applied confining stress and strain rate (Bourne et al. 1998; Benz and Ausphaug 1995; Dlott 1999; Reches and Dewers 2005; Davies and McSaveney 2009). The intact static compressive strength (Q) of volcanic rocks is generally in the range 10–100 MPa, and may be twice this under strain rates of the order of those expected at the base of a debris avalanche (~1−10 s^{-1}; Kobayashi 1970), so this is the order of local pressure delivered to the interior of the grain-flow by a fragmenting grain. Note that a non-intact rock particle disaggregating under stress along pre-existing joints stores and releases much less energy, and does not affect the system dynamics significantly.

Dynamic rock fragmentation appears to be a fractal process acting in similar fashion at all scales, because it invariably generates fractal grain-size distributions (McSaveney and Davies 2007; Kuelen et al. 2007); this means that the processes we describe below operate on intact rock at all scales in a debris mass ranging in particle size from boulders to very fine ash; but note that smaller grains are more likely to be intact than larger ones.

Mechanics of rock fragmentation

We have elsewhere described in some detail the processes of rock fragmentation in granular flow (e.g. McSaveney and Davies 2007; Davies and McSaveney 2009). To summarise the processes briefly, frictional resistance is transmitted through shearing grain-flows mainly in diagonally-aligned 'force chains' or 'grain bridges', each comprising O[10] grains (Rice 2006). As a clast in a force-chain is strained towards failure it stores elastic strain energy abstracted from the kinetic energy of the flow. The other grains in the force-chain that are applying the stresses to a clast also deform, storing still more energy. If the stresses in the weakest force-chain grain exceed its strength, that grain fails by fragmentation. Upon failure, most of the strain energy stored in the force-chain converts to outward-directed energy of the fragments of the failed grain; this transforms to pressure on the adjacent grains, so the result of a grain fragmentation is an outward-directed pressure. By equating the total stored elastic strain energy in a clast to the work done on the surroundings by its failure, it is found that the elastic strain energy stored in a single grain in uniaxial compression is capable of causing an isotropic pressure of ≈Q/3 on its surroundings when released by fragmentation (Davies and McSaveney 2009); while the presence of shear forces alters this somewhat (Herget 1988) the order of magnitude remains correct. Taking into account the strain energy also stored in the O[10] force-chain grains that apply the failure stress (Rice 2006), we estimate the effective magnitude of this pressure to be ≈3Q, where Q is the strength of the intact grain (Davies and McSaveney 2009).

The effect of a fragmenting grain in a force-chain on local frictional resistance is illustrated by Fig. 3. The forces transmitted to the shear layer boundary by a typical intact force-chain are a normal force sufficient to offset the confining force, and a shear force equal in magnitude to the normal force multiplied by a friction coefficient (Fig. 3a). The surrounding grains are much less highly stressed, and transmit much less shear resistance. When a grain fragments, the fragmentation force is carried by instantaneously-forming radial force-chains to the shear boundaries (Fig. 3b); the fragmenting grain itself has no shear strength, so the transfer of shear between the shear boundaries by the force-chain becomes zero. The resulting forces on the shear boundaries are the components of the radial force-chain forces; the summed normal components equal the normal force in Fig. 3(a), but the shear components sum to zero because temporary force-chain forces are (at least statistically) isotropic. Hence the result of a grain fragmenting is that the shear resistance reduces to that remaining in the weakly-stressed force chains in the neighbourhood.

Because the normal component of fragmentation force is distributed over a significant area of shear boundary, it reduces the effective stress on the weaker neighbouring force-chains, reducing further their ability to resist shear. Extending this concept to a large area of a shear layer, the shear resistance of all simultaneously-fragmenting force-chains reduces to zero. The residual shear resistance in the

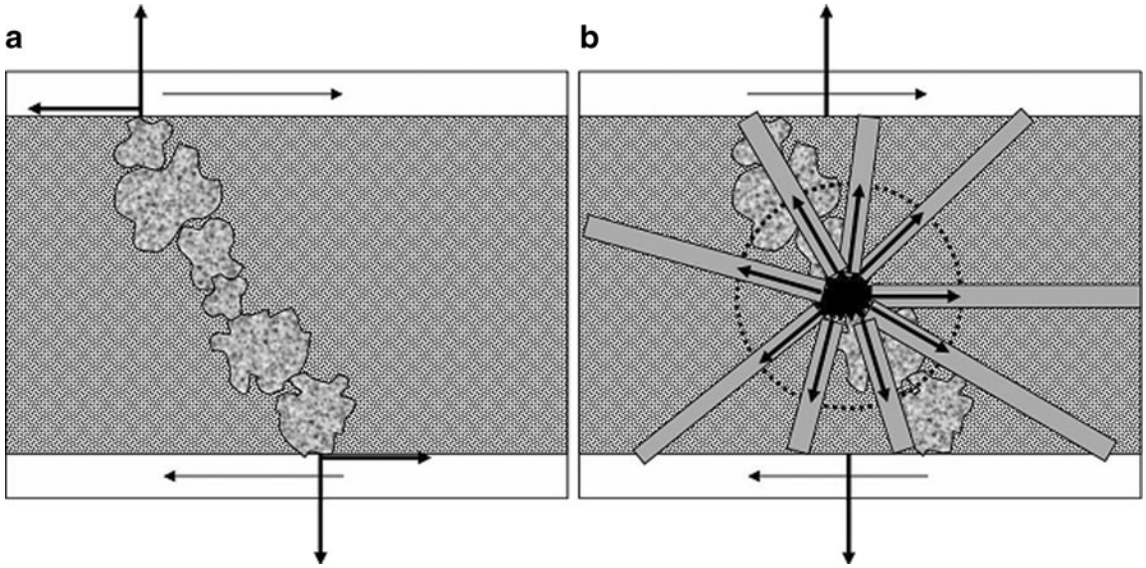

Fig. 3 Forces transmitted across a shear layer by (**a**) a non-fragmenting force-chain and (**b**) a fragmenting force-chain, with instantaneous force-chains (solid grey) transmitting force to the surroundings. Note surrounding weak force-chains are not shown for clarity. Light arrows indicate shear sense; heavy arrows represent forces

surrounding grains during a fragmentation event is then equal to the residual normal stress they experience multiplied by a conventional (Byerlee) friction coefficient.

Preliminary analysis indicates that a variety of reported rapid, high-stress, low-friction situations (rock avalanches, blockslides, fault motion, laboratory rock friction tests) can be quantitatively explained by this mechanism (Davies et al. 2006, 2007; Davies and McSaveney 2009).

In the following section we assess the magnitude of the frictional resistance in a granular shear flow in which fragmentation is occurring. We do this by calculating the residual effective stress within the shear layer while part of the normal stress applied to the layer is resisted by the normal stress components of fragmenting grains; then the shear resistance is the residual effective stress multiplied by a conventional friction coefficient.

Stresses in fragmenting shear (Davies and McSaveney 2009)

The effect of fragmentation on shear resistance depends on the spatial concentration of simultaneously-fragmenting grains; the higher this concentration, the lower the effective direct stress within the grain flow. If the fragmentation concentration becomes sufficiently high, the applied normal stress is completely balanced by the normal fragmentation pressure; the effective stress becomes zero, and fragmentation ceases. Cessation of fragmentation, however, causes the effective stress to revert to the applied normal stress, and as a result fragmentation recommences under the continuing shear motion. We assume that this oscillating situation rapidly adjusts itself so that the fragmentation concentration becomes steady at that which just allows fragmentation to continue under the applied normal load. Thus the fragmentation concentration in the shear layer is not a function of the strain rate.

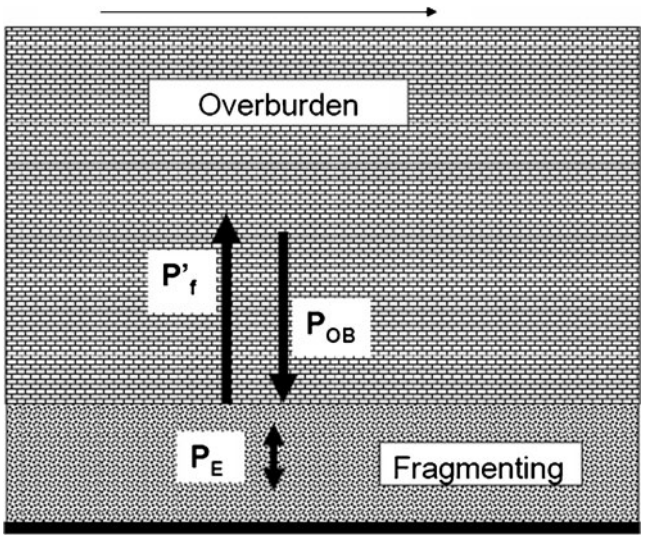

Fig. 4 Forces on a shear layer. P_{OB} is the overburden pressure; P'_f is the fragmentation pressure; P_E is the effective pressure in the fragmenting layer

Figure 4 represents steady-state shear of a granular fragmenting stratum between an overburden stratum and a base: P_{OB} is the normal stress on the top of the fragmenting layer, P'_f is the spatially-averaged fragmentation pressure in the fragmenting layer and P_E is the spatially-averaged effective intergranular direct stress within the fragmenting layer. Applying a vertical stress balance at the top of the fragmenting layer:

$$P_E = P_{OB} - P'_f \quad (1)$$

From above, each fragmenting grain generates an apparent pressure $P_{fa} \approx 3Q$, so

$$P'_f \approx 3Q F_f \quad (2)$$

where F_f is the proportion (by volume) of grains fragmenting simultaneously. We assume (for simplicity, and in the absence of other information) that F_f depends linearly on the amount by which P_E exceeds the minimum value needed to cause fragmentation P_C:

$$F_f = k_2(P_E - P_C)/P_C \quad (3)$$

and k_2 is a constant.

P_C is the smallest value of overburden normal stress that causes grain fragmentation to occur under shear. To estimate the values of P_C and k_2 we use data from the deposit and a simulation of the Falling Mountain rock avalanche, New Zealand (Davies and McSaveney 2002). In this event, fragmentation occupied >80% of the ~50 m flow depth. The rock involved was greywacke (metamorphosed sandstone). The minimum normal stress required to cause fragmentation (P_C) was that at the base of the relatively unfragmented ~10 m-deep surface carapace of the deposit (McSaveney et al. 2000; Dunning 2004); this was ~0.3 MPa, or close to 10^{-3} times the value of Q for this rock (~250 MPa; Stewart 2007). We shall assume that this relationship applies to fragmenting shear flows of all rock types:

$$P_C \sim 10^{-3} Q \quad (4)$$

The precision of this relationship is somewhat better than order-of magnitude; we estimate the coefficient could lie in the range 2×10^{-3} to 5×10^{-4}.

The mean longitudinal fragmentation pressure P'_f required to explain the measured runout distance (about 4.5 km) in the simulation of Davies and McSaveney (2002) was ~2.5 MPa, which required $F_f \sim 0.01$. The mean overburden pressure P_{OB} corresponding to this stress was ~0.7 MPa. This simulation was equivalent to assuming that $P_E = P_{OB}$, with conventional friction throughout; hence in (3) $P_E - P_C = 0.4$ MPa. Applying these empirical data to (3), $0.01 = k_2 \times 0.4 \times 10^6/(0.3 \times 10^6)$ and $k_2 = 7.5\times10^{-3}$. We believe this is an order-of magnitude estimate.

From (1), (2) and (3)

$$P_E \sim P_{OB} - k_2(3Q)(P_E - P_C)/P_C \quad (5)$$

$$\sim P_{OB} - k_2(3 \times 10^3 P_E - 3Q)$$

Hence

$$P_E \sim (P_{OB} + 3k_2 Q)/23.5$$

or, acknowledging the approximations involved,

$$P_E \sim 0.04 P_{OB} + 10^{-3} Q \quad (6)$$

If we apply a friction coefficient $\mu = 0.8$ (a typical value for angular rock; Byerlee 1978), then the frictional resistance in a fragmenting granular flow is given by $P_R = \mu P_E$, or

$$P_R \approx 0.03 P_{OB} + 8 \times 10^{-4} Q \quad (7)$$

Application to the Socompa event

We used Eq. 7 as an input to the Kelfoun and Druitt (2005) runout model of the Socompa debris avalanche. The simulated deposit was of approximately the correct outline (Fig. 5b) but was less accurate in internal detail than the very successful 50 kPa constant resisting stress simulation of Kelfoun and Druitt (2005) (Fig. 5a). However, simply reducing the first coefficient on the right-hand side of Eq. 7 by 50% gave a very good match with the successful simulation (Fig. 5c). This adjustment is well within the margin of error of the derivation of the coefficients in Eq. 7, as noted above; it suggests that the value of k_2 derived from the Falling Mountain simulation is about twice as high as it should be for Socompa, perhaps as a result of different rock strength.

Evidently further back-tuning of Eq. 7 could yield even better results; we note in particular that putting the first coefficient equal to zero and Q equal to 65 MPa yields a truly constant basal stress of 52 kPa, identical to the Kelfoun and Druitt (2005) value. However, we prefer to retain the partial friction dependence indicated by the analysis leading to Eq. 7 as being physically-based rather than arbitrary.

Equation 7 indicates that F_R is a function of debris depth via P_{OB}, so it will not be truly constant because the flow depth of the avalanche varies in both time and space. However P_R is relatively insensitive to depth—it varies

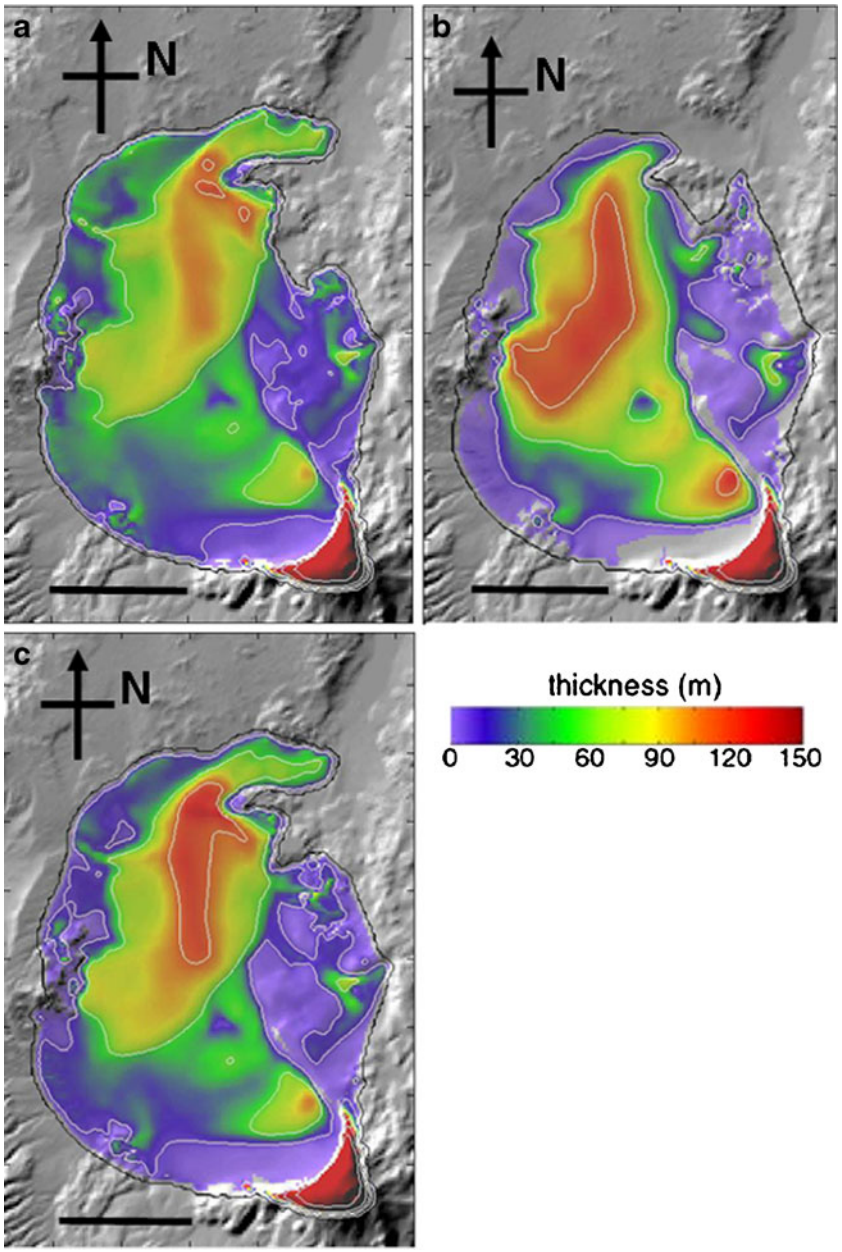

Fig. 5 Simulations of the Socompa debris avalanche deposit. **a** 50 kPa constant basal resistance (Kelfoun and Druitt 2005). **b** Basal resistance as per Eq. 7. **c** Basal resistance as per Eq. 7 with coefficient 0.015 instead of 0.03 Scale bar=10 km

only by a factor of 4 while depth varies by a factor of >100 (Fig. 6a), so the successful assumption of a constant retarding stress by Kelfoun and Druitt (2005) does not rule out the possibility that some variation occurred, as they note. Figure 6b shows that the apparent friction angle varies drastically with avalanche depth, which is quite uncharacteristic of a simple frictional material; we conclude that fragmenting material cannot realistically be modelled as simply frictional. Kelfoun and Druitt (2005), Crosta et al. (2009) and Pirulli (2009) have come to an equivalent conclusion from investigation of a number of debris avalanche simulations; the avalanche behaviour is not frictional. By contrast, relatively constant basal shear resistance appears to satisfactorily explain a variety of volcanic mass flow phenomena (Kelfoun et al. 2009).

Fragmentation in a saturated layer

Davies and McSaveney (2009) have recently discussed the influence of interstitial water on fragmentation in granular shear, concluding that the resulting alteration to shear resistance is probably second-order. This is because while

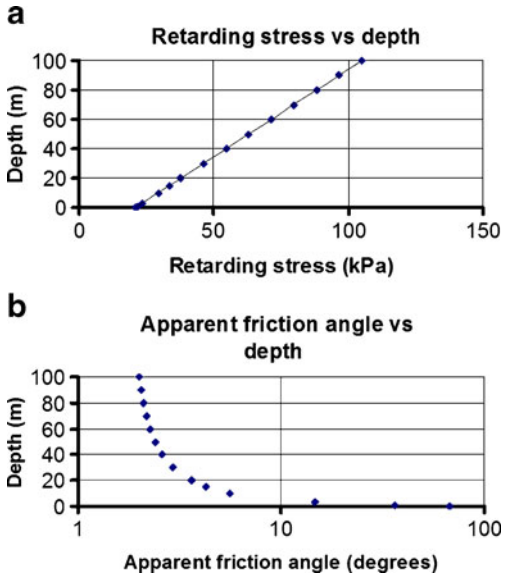

Fig. 6 **a** Retarding stress and (**b**) apparent friction angle as functions of debris depth for Socompa debris avalanche with basal fragmentation

some of the energy released by a fragmenting clast transfers to the pore water instead of to the adjacent grains, the effect of a pulse of positive pore water pressure reduces effective stress in the shearing layer in the same way as a pulse of intergranular pressure. Thus, although the possibility remains that shearing in the Socompa debris avalanche occurred in saturated material (Kelfoun and Druitt 2005), this may not have a first-order effect on Eq. 7, nor on the outcomes presented herein.

Effect of basal fragmentation

An important question remains regarding the effect of basal layer fragmentation in a volcanic debris avalanche: since the material overlying the fragmenting shear layer is not (as in the case of a blockslide) a rigid, intact block, can the solid-transmitted stresses generated by basal layer fragmentation in fact support the weight of the overlying granular material and reduce the effective stresses in the fragmenting layer? While it is less self-evident than in the case of an intact block (e.g. Davies et al. 2006), there are reasons for suggesting that this will indeed be the case.

Comminuting grains within a rapidly-fragmenting layer continuously generate a high dispersive pressure P_F that is not associated with any corresponding shear stress. This dispersive pressure acts throughout the rapidly-fragmenting layer and on both its upper and lower boundaries. Since the shearing grains are tightly packed (under high overburden stress and with a wide fractal size distribution—that is why they fragment), they cannot easily migrate in response to a pressure gradient so the fragmentation-derived pressure in the shear layer is effectively transmitted to the overlying material at the layer boundary. Because fragmentation in the overlying material is much less intense or absent, there is a lower fragmentation pressure above the boundary than below it. The effect on the upper boundary is thus that of a net upward pressure, partly supporting the weight of the overlying material and reducing the effective stress within the rapidly-fragmenting layer. This logic is supported by many dry grain-flow simulations (e.g. Campbell and Brennen 1985; Campbell 1989, 2006), in which dispersive stresses caused by high grain "temperatures" (i.e. vibration intensities) at the boundary of the high-shear layer do not dissipate significantly into the overlying, more densely-packed material.

To maintain fragmentation in granular material of Q = O [100 MPa], an overburden pressure P_C of O[100 kPa] is required (Eq. 4). This corresponds to a depth of O[3 m]. The overburden can thus be very thin, and still be sufficient to maintain fragmentation in the underlying basal facies; this explains the very thin, and correspondingly very extensive, deposits of many volcanic debris avalanches (e.g. Crandell et al. 1984).

Discussion

Reflection of the Socompa debris avalanche

One of the remarkable features of the Socompa deposit is the evidence that the debris avalanche reflected from the western and northern margins of the basin into which it was emplaced, leaving a marginal levee, and "… forming a secondary flow that continued to travel 15 km down a gentle slope at an oblique angle to the primary flow, the front of the return wave being preserved frozen on the surface of the deposit as a prominent escarpment." (Kelfoun et al. 2008; see Fig. 2 herein in which ME denotes the ~35 m high escarpment). The implication is that the reflected flow took place either by incorporating and redirecting the still-moving primary flow, or on top of its recently-halted deposit.

This behaviour provides a further test of the ability of the proposed fragmentation mechanism to explain the Socompa deposit. For the mechanism to function with a reflected flow is potentially difficult, because if the debris halts (even momentarily) during the reflection process, shear and thus fragmentation cease; to restart fragmentation under very low surface slopes against conventional basal friction is likely to be difficult. We note, however, that because the reflection of the Socompa debris avalanche was oblique, at no stage was the debris that took part in the reflected flow stationary; indeed the minimum velocity during the reflection in the simulation of Kelfoun and Druitt (2005) was about 20 ms^{-1}, so basal fragmentation would have been continuous.

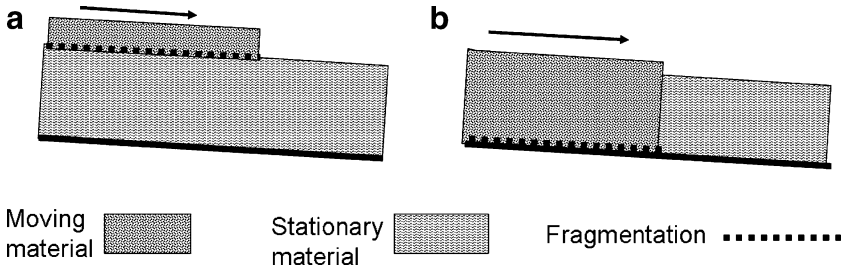

Fig. 7 **a** A moving avalanche overriding low-gradient stationary material is unlikely to be able to remobilise it to full depth and restart basal fragmentation. **b** Full-depth remobilisation can remobilise stationary material at low gradient

It is also clear from the deposit characteristics that, in forming the escarpment across the middle of the deposit, the reflected flow did not override the primary material, but caused it to increase in depth, rather like "...the bores formed by flow reversals in turbidity currents (Edwards 1993)" (Kelfoun et al. 2008). This requires that the reflected flow exerted sufficient shear stress on the base of the stationary primary flow to cause the full depth of the latter to be remobilized, and for fragmentation to begin again at the base of the primary flow. It is unlikely that a low-gradient overriding flow could have this effect on a stationary primary deposit (Fig. 7a); however, only the last stage of the reflected motion at Socompa took place with respect to stationary primary material. The first encounter of the reflected wave was with primary material still moving with basal fragmentation, and the full depth of this material was thus able to be redirected into the reflected wave motion. When the full-depth reflected wave later encountered stationary primary material, it had sufficient momentum to cause full-depth remobilization of this material with basal fragmentation (Fig. 7b). This same process of propagation of increased depth through a recently-halted stationary deposit, remobilising the latter, was reported by Davies et al. (1992) in debris-flows at Jiangjia Ravine, China.

Kelfoun et al. (2008) also note that the much greater depth in the reflected flow evidently caused lower basal friction than elsewhere, allowing flow to continue at low gradients. This corresponds with the pattern of behaviour resulting from the fragmentation model (Fig. 6).

Runout of volcanic and non-volcanic avalanches

It is well documented that volcanic debris avalanches tend to have longer runouts (by a factor of the order of 2–3) than non-volcanic rock avalanches of the same volume (e.g. Siebert 1984). Equation 7 shows that the frictional resistance of fragmenting rock varies with its intact rock strength. The rock involved in non-volcanic rock avalanches is often massive, overconsolidated crustal rock exhumed from depth; it is thus generally stronger than the more recent, normally-consolidated, often hydrothermally altered and therefore substantially weakened material of the volcanic edifices from which debris avalanches originate. Hence the mean value of intact rock strength Q for volcanic debris avalanches is likely to be considerably smaller than that of nonvolcanic rock avalanches, and Eq. 7 predicts that frictional resistance in the fragmenting layer varies linearly with Q; so the runout of volcanic rock avalanches should be generally greater than that of equal-volume nonvolcanic debris avalanches, in accord with experience.

Towards a truly predictive model?

The proposal that fragmentation occurring in a basal layer generates a relatively low retarding stress corresponds to the intense basal fragmentation and modelled emplacement of the Socompa avalanche deposit. Further, Eq. 7 allows the basal resisting stress required by the Kelfoun and Druitt (2005) simulation to be predicted quantitatively from the estimated rock properties. This gives remarkably good results (Fig. 5b), given that no data from the Socompa deposit have been used. The improvement seen in Fig. 5c indicates that accurate prediction of debris avalanche runout is achievable on the basis that basal resistance is determined by fragmentation stresses, if k_2 can be more accurately estimated. Evidently the fit with the DEM could be improved by further adjusting the coefficients in (7), but we have not undertaken this exercise herein because our objective is to demonstrate the potential of the fragmentation-based rationalization for further development. Further experimental work is under way to better constrain the coefficients of Eq. 7 for a range of lithologies; these are at present estimated using data from a rock avalanche deposit of quite different size, lithology and setting.

Some of the proposals herein remain to be formally tested, and as noted, more work is required to obtain more precise estimates of P_C and k_2. However, application of the effects of dynamic rock fragmentation to processes near the base of volcanic debris avalanches is evidently able to reproduce the success of the Socompa simulation model of Kelfoun and Druitt (2005). That success depended on trial-and-error selection of one parameter, the retarding stress,

and the assumption that it is constant; our analysis of the stresses resulting from dynamic rock fragmentation enables the magnitude of the retarding stress to be predicted as a function of rock strength and flow depth. This in principle eliminates the need to use trial and error to match the Socompa deposit characteristics. Our approach thus has the potential for genuinely predictive modeling of debris avalanche runout, without the need for variable "tuning" or back-analysis.

Conclusions

1. The simulation of the Socompa debris avalanche morphology by Kelfoun and Druitt (2005) is sufficiently successful in reproducing the deposit mass distribution, morphology and lithological distribution to justify the assumption that it represents realistically the dominant features of the emplacement dynamics.
2. Dynamic rock fragmentation at the base of a granular flow partly supports the weight of overlying material, reducing the effective stress in the rapidly-fragmenting layer and hence reducing the frictional resistance able to be transferred from the stationary substrate to the overlying material through the rapidly-fragmenting layer.
3. Analysis of dynamic rock fragmentation in granular flows leads to prediction of the basal retarding stress as a function of rock strength and flow depth in large debris avalanches.
4. This prediction (Eq. 7) simulates the runout of the Socompa event extremely well, if the first coefficient is reduced by 50%—an adjustment well within its margin of error.
5. This mechanism is also compatible with the reflection of part of the Socompa debris across the primary flow to form a prominent escarpment in the deposit.
6. Dynamic rock fragmentation appears to offer a potential basis for genuinely predictive modeling of debris avalanche runout, based on rock strength, eliminating the need for data from the same deposit to select appropriate variable values. More work is required to constrain the values of P_C and k_2.

Acknowledgements We gratefully acknowledge constructive reviews by Charles Campbell, Emily Brodsky and Jeremy Phillips.

References

Abe S, Mair K (2005) Grain fracture in 3D numerical simulations of granular shear. Geophys Res Lett 32:doi:10.1029/2004GL022123

Benz W, Ausphaug E (1995) Simulations of brittle solids using smooth particle hydrodynamics. Comput Phys Commun 87:253–265

Bergstrom BH (1963) Energy and size distribution aspects of single particle crushing. In: Fairhurst C (ed) Rock mechanics. Proc 5th Symposium Rock Mech 1962. Pergamon Press, New York, pp 155–172

Bourne N, Millett J, Rosenberg Z, Murray N (1998) On the shock induced failure of brittle solids. J Mech Phys Sol 46:1887–1908

Byerlee J (1978) Friction of rocks. PAGEOPH 116:615–626

Campbell CS (1989) Self-lubrication for long-runout landslides. J Geol 97:653–665

Campbell CS (2006) Granular material flows—an overview. Powder Technol 162:208–229

Campbell CS, Brennen CE (1985) Computer simulation of granular shear flows. J Fluid Mech 151:167–188

Cocco M, Spudich P, Tinti E (2006) On the mechanical work absorbed on faults during earthquake ruptures. *Earthquakes: Radiated Energy and the Physics of Faulting*. Geophysical Monograph Series, 170: AGU doi:10.1029/170GM24

Crandell DR, Glicken HX, Christiansen RL, Newhall CG (1984) Catastrophic debris avalanche from ancestral Mt Shasta volcano, California. Geology 12:143–146

Crosta GB, Frattini P, Fusi N (2007) Fragmentation in the Val Pola rock avalanche, Italian Alps. Geophys Res 112:F01006. doi:10.1029/2005FJ000455

Crosta GB, Imposimato S, Roddeman D (2009) Numerical modelling of entrainment/deposition in rock and debris-avalanches. Eng Geol 109:135–145. doi:10.1016/j.enggeo.2008.10.004

Dade WB, Huppert HE (1998) Long-runout rockfalls. Geology 26:803–806

Davies TRH, McSaveney MJ (2002) Dynamic simulation of the motion of fragmenting rock avalanches. Can Geotech J 39:789–798

Davies TRH, McSaveney MJ (2009) The role of dynamic rock fragmentation in reducing frictional resistance to large landslides. Eng Geol 109:67–79. doi:10.1016/j.enggeo.2008.11.004

Davies TRH, Phillips CJ, Pearce AJ, Zhang, XB (1992) "Debris flow behaviour—an integrated overview". In Debris Flows and Environment in Mountain Regions, DE Walling, TRH Davies and B Hasholt (eds). IAHS Publication No. 209, pp 217–225

Davies TRH, McSaveney MJ, Beetham RD (2006) Rapid block glides—slide-surface fragmentation in New Zealand's Waikaremoana landslide. Q J Eng Geol Hydrogeol 39:115–129

Davies TRH, McSaveney MJ, Deganutti AM (2007) Dynamic rock fragmentation causes low rock-on-rock friction. In: Eberhardt E, Stead D, Morrison T (eds) Rock Mechanics—meeting society's challenges and demands. Taylor and Francis, London, pp 959–966

Dlott DD (1999) Ultrafast spectroscopy of shock waves in molecular materials. Ann Rev Phys Chem 50:251–278

Dufresne AM, Davies TRH (2009) Longitudinal ridges in mass movement deposits. Geomorph 105:171–181. doi:10.1016/j.geomorph.2008.09.009

Dufresne AM, Davies TRH, McSaveney MJ (2009) Influence of runout path material on the emplacement of the Round Top rock avalanche, New Zealand. Earth Surf Proc doi:10.1002/esp.1900

Dunning SA (2004) Rock Avalanches in high mountains. PhD thesis, Luton Univ. UK, 271 p + App

Edwards DA (1993) Turbidity currents: dynamics, deposits and reversals. Lect Notes Earth Sci 44:1–173

Glicken HX (1996) Rockslide-debris avalanche of May 18, 1980, Mt St Helens volcano, Washington. US Geol Surv Open-file Report 96–677, p 90

Grady DE, Kipp ME (1987) Dynamic rock fragmentation. In fracture mechanics of rock. Academic Press, London, UK, pp 429–475

Herget G (1988) Stresses in rock. Balkema, Rotterdam, p 179

Hewitt K (2003) Rock avalanches with complex runout and emplacement, Karakoram Himalaya, Inner Asia. In Evans SG, Martino S (Eds) NATO Advanced Research Workshop: Massive rock slope failure: New Models for hazard assessment. Celano, Italy, June 16–21, 2002

Iverson RM, Schilling SP, Vallance JW (1998) Objective delineation of lahar-inundation hazard areas. Bull Geol Soc Amer 110:972–984

Kelfoun K, Druitt TH (2005) Numerical modelling of the Socompa rock avalanche, Chile. J Geophys Res 110:B12202. doi:10.1029/2005JB003758

Kelfoun K, Druitt T, van Wyk de Vries B, Guilbaud M-N (2008) Topographic reflection of the Socompa debris avalanche, Chile. Bull Volcanol 70:1169–1187. doi:10.1007/s00445-008-0201-6

Kelfoun K, Samaniego P, Palacios P, Barba D (2009) Testing the suitability of frictional behaviour for pyroclastic flow simulation by comparison with a well-constrained eruption at Tungurahua volcano (Ecuador). Bull Volcanol 71:1057–1075. doi:10.1007/s00445-009-0286-6

Kobayashi R (1970) On mechanical behaviours of rocks under various loading rates. Rock Mech Jpn 1:56–58

Kuelen N, Heilbronner R, Stünitz A, Bouiller A-M, Ito H (2007) Grain size distributions of fault rocks: a comparison between experimentally and naturally-formed granitoids. J Struct Geol 29:1282–1300

Le Corvec N (2005) Socompa volcano destabilisation (Chile) and fragmentation of debris avalanches. MSc thesis, Université Blaise Pascal, Clermont-Ferrand, France, p 67

Locat P, Couture R, Leroueil S, Locat J, Jaboyedoff M (2006) Fragmentation energy in rock avalanches. Can Geotech J 43:830–851

Mair K, Abe S (2008) 3D numerical simulations of fault gouge evolution during shear: Grain size reduction and strain localization. Earth Plan Sci Lett 274:72–81

McGarr A (1997) A mechanism for high wall-rock velocities in rockbursts. PAGEOPH 150:381–391

McSaveney MJ, Davies TRH (2007) Rockslides and their motion. In: Sassa K, Fukuoka H, Wang F, Wang G (eds), Progress in landslide science. Springer-Verlag, pp 113–134

McSaveney MJ, Davies TRH (2009) Surface energy is not one of the energy losses in rock comminution. Eng Geol 109:109–113. doi:10.1016/j.enggeo.2008.11.001

McSaveney MJ, Davies TRH, Hodgson KA (2000) A contrast in deposit style and process between large and small rock avalanches. In: Bromhead E, Dixon N, Ibsen M-L (eds) Landslides in Research, Theory and Practice, Proc 8th Int Symp Landslides, Cardiff, Wales. Thomas Telford Publishing, London, pp 1053–1058

Pirulli M (2009) The Thurwieser rock avalanche (Italian Alps): description and dynamic analysis. Eng Geol 109:80–92. doi:10.1016/j.enggeo.2008.10.007

Reches Z, Dewers TA (2005) Gouge formation by dynamic pulverization during earthquake rupture. Earth Plan Sci Lett 235:361–374

Rice JR (2006) Heating and weakening of faults during earthquake slip. J Geophys Res 111:B05311. doi:10.1029/2005JB004006

Siebert L (1984) Large volcanic debris avalanches: characteristics of source areas, deposits and associated eruptions. J Volcanol Geotherm Res 22:163–197

Stewart S (2007) Rock mass strength and deformability of unweathered closely jointed New Zealand greywacke. Unpubl. PhD thesis, University of Canterbury, New Zealand, p 455

Stoops GR, Sheridan MF (1992) Giant debris avalanches from the Colima volcanic complex, Mexico: implications for long-runout landslides (> 100 km) and hazard assessment. Geology 20:299–302

Takarada S, Ui T, Yamamoto Y (1999) Depositional features and transportation mechanism of valley-filling Iwasegawa and Kaida debris avalanches, Japan. Bull Volcanol 60:508–522

Wyk V, de Vries B, Self S, Francis PW, Keszthelyi L (2001) A gravitational spreading origin for the Socompa debris avalanche. J Volcanol Geotherm Res 105:225–247

Voight B, Glicken HX, Janda RJ, Douglas PM (1981) Catastrophic rockslide-avalanche of May 18 1980. In: Lipman PW, Mullineaux DR (eds), The 1980 Eruption of Mt St Helens, Washington. US Geol Surv Prof Paper 1250, pp 347–37

Wadge G, Francis PW, Ramirez CF (1995) The Socompa collapse and avalanche event. J Volcanol Geotherm Res 66:309–336

Zeleny RA, Piret EL (1962) Dissipation of energy in single particle crushing. Ind Eng Chem Process Des Dev 1:37–41. doi:10.1021/i260001a007;PublicationDate(Web):01May2002

Bull Volcanol
DOI 10.1007/s00445-008-0201-6

RESEARCH ARTICLE

Topographic reflection of the Socompa debris avalanche, Chile

Karim Kelfoun · Tim Druitt · Benjamin van Wyk de Vries · Marie-Noëlle Guilbaud

Received: 17 June 2007 / Accepted: 1 February 2008
© Springer-Verlag 2008

Abstract One of the most remarkable features of the exceptionally well preserved 26 km^3 Socompa debris avalanche deposit is the evidence for topographically driven secondary flow. The avalanche formed by sector collapse of Socompa stratovolcano and spread 40 km across a pre-existing basin, forming a sheet of ~50 m average thickness. As the avalanche impinged on the western and northern margins of the basin, it was reflected back, forming a secondary flow that continued to travel 15 km down a gentle slope at an oblique angle to the primary flow, the front of the return wave being preserved frozen on the surface of the deposit as a prominent escarpment. Satellite images, aerial photos, digital elevation models and field observations were used to reconstruct the sequence of events during avalanche emplacement, and in particular during secondary flow. The avalanche sheet was divided into distinct terrane groups, each believed to have experienced a particular strain history during emplacement. Evidence for avalanche reflection includes clearly recognizable secondary slide masses, sub-parallel sets of curvilinear shear zones, headwall scarps separating the (primary) levée from the secondary terranes, extensional jigsaw breakup of surface lithologies during return flow, and cross cutting, or deflection, of primary flow fabrics by secondary terranes. Reflection off the basin margin took place in an essentially continuous manner, most major return motions being simultaneous with, or shortly following, primary flow. The secondary flow occurred as a wave that swept obliquely across the primary avalanche direction, remobilizing the primary material, which was first compressed, then stretched, as it passed over and rearward of the wave front. As return flow occurred, surface lithologies were rifted in a brittle manner, and the slabs were sheared pervasively as they glided and rotated back into the basin; some sank into the more fluidal interior of the avalanche, which drained out into a prominent distal lobe. Extension by factors of up to 1.8 took place during return flow. Secondary flow took place on slopes of only a few degrees, and the distal lobe flowed 8 km on a slope of ~1°. Overall the avalanche is inferred to have slid into place as a fast-moving sheet of fragmental rock debris, with a leading edge and crust with near-normal friction and an almost friction-less, fluidal interior and base. The avalanche emplacement history deduced from field evidence is consistent with the results of a previously published numerical model of the Socompa avalanche.

Keywords Socompa · Debris avalanche · Reflection · Secondary flow · High mobility

Editorial responsibility: JDL White

K. Kelfoun (✉) · T. Druitt · B. van Wyk de Vries
Laboratoire Magmas et Volcans, OPGC,
UMR Clermont Université-CNRS-IRD,
5 rue Kessler,
63038 Clermont-Ferrand, France
e-mail: k.kelfoun@opgc.univ-bpclermont.fr
URL: http://wwwobs.univ-bpclermont.fr/lmv/pperm/kelfoun_k

Present address:
K. Kelfoun
Instituto Geofísico, Escuela Politécnica Nacional,
Casilla 1701-2759,
Quito, Ecuador

Present address:
M.-N. Guilbaud
Instituto de Geofísica,
Universidad Nacional Autónoma de México,
Cuidad Universitaria,
04510 México D.F., México

Introduction

Long-runout rock (or debris) avalanches are major natural hazards on Earth. This is due to the ability of large volumes (typically >> 10^6 m^3) of comminuted rock debris to travel large distances, forming thin deposits over large areas. Many long-runout avalanches have observed, or inferred, velocities of 20–100 m s^{-1} and runouts reaching up to many tens of km. They occur both in volcanic and non-volcanic environments by the sudden mobilization of large rock masses. The ability of avalanches to travel long distances is not well understood, requiring apparent dynamic friction coefficients for granular materials much lower than normal static values (see recent articles by Davies and McSaveney 1999; Legros 2002; Collins and Melosh 2003 and references therein).

Socompa long-runout rock avalanche (Fig. 1) in Chile was emplaced by sector collapse of Socompa stratovolcano about 6300–6400 years ago (Francis et al. 1985; Wadge et al. 1995; van Wyk de Vries et al. 2001; new unpublished ^{14}C age obtained on underlying soil by S. Self, personal communication). Immediately following collapse, about 26 km^3 of rock debris spread across an area of 490 km^2, forming a sheet of average thickness 50 m. Thin vegetation cover and near-perfect deposit preservation in the arid climate of the Atacama Desert make Socompa arguably the best preserved large-volume subaerial avalanche on Earth, and an excellent target for the study of emplacement dynamics. One of the most remarkable features is the evidence for topographically driven secondary flow (Francis et al. 1985). As the primary avalanche lost momentum it was reflected back, forming a return wave that continued to travel many km down a gentle slope at an oblique angle to the primary flow. The front of the return wave is preserved as a prominent escarpment on the deposit surface. Reflection is an illustration of the extraordinarily high mobilities of long-runout avalanches.

In a previous paper we found that we were able to simulate this behaviour by numerical modelling of the avalanche motion, as well as to reproduce the resulting deposit to a surprising degree of accuracy (Kelfoun and Druitt 2005). This prompted us to study in more detail how reflection and secondary flow took place. We use satellite images, aerial photos, digital elevation models and field observations to reconstruct the sequence of events during avalanche emplacement, and in particular during secondary flow. We also discuss some implications of our results for the rheological behaviour of the avalanche.

Geological setting and previous work

The collapse origin of the Socompa deposit was first recognized by Peter Francis and colleagues, who demonstrated the existence of primary and secondary avalanches (e.g. Francis et al. 1985; Francis and Self 1987). An analysis of satellite images was presented by Wadge et al. (1995), who mapped spectrally distinct surface lithologies, compiled thickness data and calculated collapse-scar and deposit volumes. Van Wyk de Vries et al. (2001) used aerial photos and field observations to describe structural and stratigraphic relationships on and around the volcano, and they discussed the processes leading up to, and immediately following, sector collapse.

Socompa Volcano lies at the southeastern end of the Atacama Basin. It is bordered to the southeast, east and northeast by other volcanoes of the western volcanic chain. To the north and northwest lies the broad Monturaqui Basin, across which the avalanche was emplaced. The basin is bordered to the west by Palaeozoic and Mesozoic rocks, and to the east by Miocene to Pliocene sedimentary and volcanic rocks of the Quebrada Salin Formation (Ramirez 1988), which also underlie the volcano. Lavas of the Holocene El Negrillar field lie north of the volcano and northeast of the avalanche deposit (Figs. 1 and 2).

The avalanche deposit extends across the Monturaqui Basin, forming a broadly elliptical sheet 35 km long and 20 km wide, with a prominent distal lobe (Figs. 1 and 2). The curved trajectory from the volcano to the terminus of the distal lobe is 40 km. The limits of the avalanche sheet are steep and well defined, commonly with a distinct levée. The term levée as used here describes the raised outer edge of the avalanche sheet, without dynamic implications. The thickness of the deposit ranges from 90 m to a few metres (Wadge et al. 1995). The surface is divided into two morphologically distinct parts by a NE–SW-trending escarpment up to 50 m high (median escarpment). The deposit south of the median escarpment was emplaced entirely by northwestwardly directed primary flow, whereas that to the north experienced first primary flow, then secondary return flow off the western and northwestern basin margins (Francis et al. 1985; Kelfoun and Druitt 2005).

The avalanche deposit is a mixture of two main components (Francis et al. 1985; van Wyk de Vries et al. 2001): (1) brecciated lavas and volcanoclastic deposits from the Socompa edifice itself (Socompa Breccia Facies; SB),

Fig. 1 Image of Socompa avalanche deposit generated by superimposing aerial photos and a false-colour Landsat image (channels 7, 4 and 1). The colours on the image reflect surface lithologies and their different degrees of oxidation. Variably weathered and oxidized lavas appear *pink* (dacites) or *red* (andesites); non-oxidised lavas appear *dark blue* (dacites) or *black* (andesites). A fresh, black glassy dacite (including fragments with prismatic jointing), interpreted as the remains of a lava flow that was still hot at the time of avalanche emplacement (Wadge et al. 1995), appears *dark green* (co-ordinates 564000, 7324000). Mixing of oxidized and non-oxidised lavas produces a brown colour. RIF lithologies appear pale blue to white. The inset shows the location of Socompa

Easting (UTM, WGS84)
560000
565000
570000
575000
580000
Northing (UTM, WGS84)
7330000
7325000
7320000
7315000
7310000
7305000
7300000
N
Bolivia
Socompa
Chile
Argentina
20
30
40
50
80
0 1 2 5 10 km

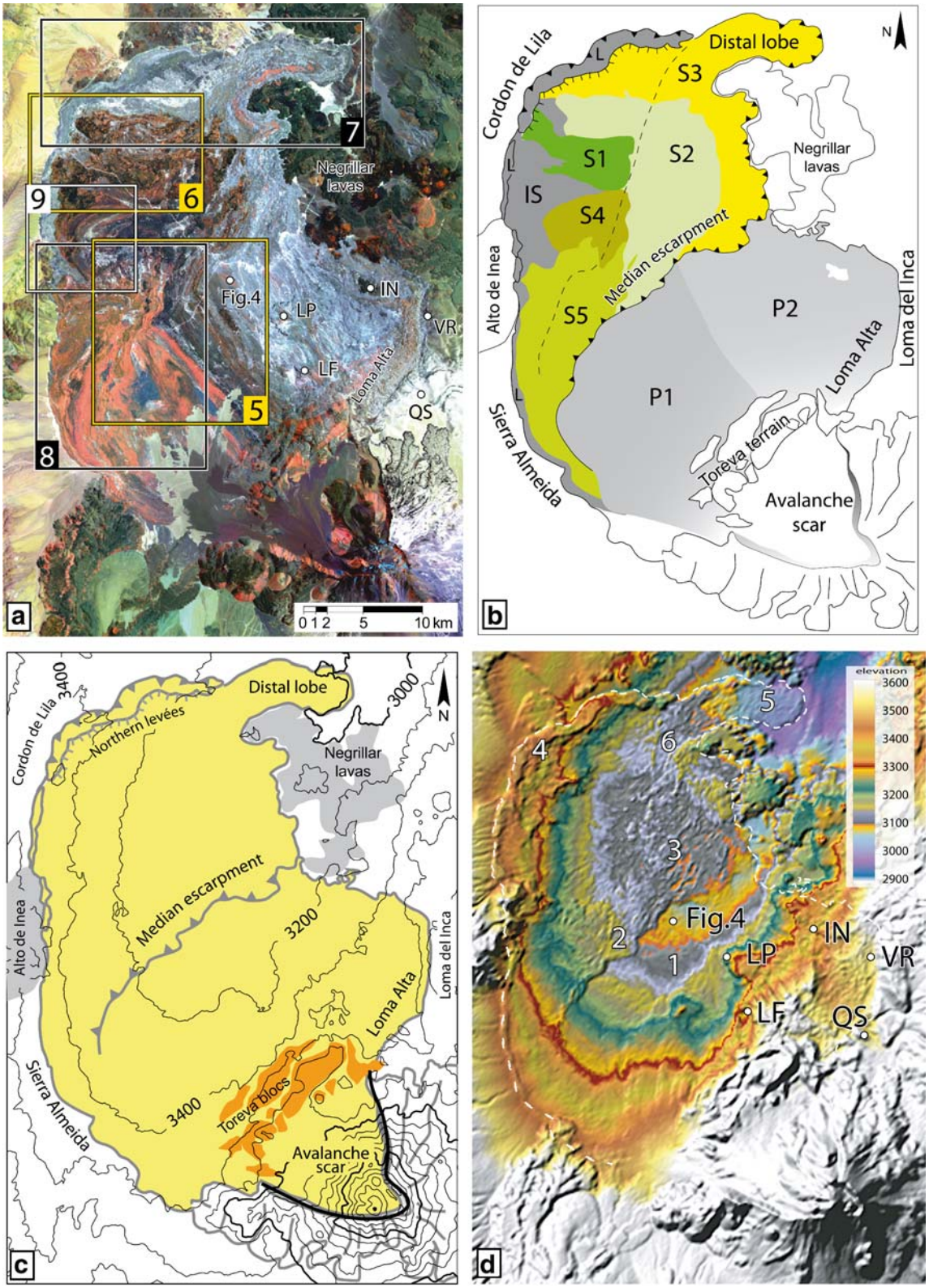

Fig. 2 **a** Locations of Figs. 5 to 9, shown by the rectangles; the location of Fig. 4 is also shown. **b** Avalanche terranes discussed in the text. **c** Socompa avalanche (in *yellow*), the Toreva blocks (in *orange*), topographic contours (at intervals of 200 m above sea level), and locations of prominent topographic features and avalanche structures. Note the form of the Monturaqui Basin, as shown by the contours. **d** Topography of the avalanche, using a colour scale for altitude in metres. Marked on the image are (*1*) the proximal primary terranes, (*2*) the median escarpment, (*3*) horsts and grabens of the secondary terranes, (*4*) the northern levée, (*5*) the distal lobe, and (*6*) the zone of drainage and subsidence upstream of the distal lobe. *LF* La Flexura anticline, *LP* Lion's Pawn, *IN* inlier of Negrillar lava, *QS* Quebrada Salín, *VR* Veneer of RIF

and (2) ignimbrites, gravels, sands and minor lacustrine evaporites from the Salin Formation that forms the basement of the volcano (Reconstituted Ignimbrite Facies; RIF). The eastern half and northern margin of the deposit consist almost entirely of RIF, partially mixed with blocks of SB at the surface, whereas the western half is composed of RIF overlain by up to 15 m of SB. RIF accounts for about 40% (Wadge et al. 1995) of the avalanche surface (pale blue and white on Fig. 1), but more than 80% volumetrically (van Wyk de Vries et al. 2001). Sector collapse of the 6000-m-high stratovolcano left a 70° amphitheatre 12 km wide at its mouth, with cliffs at least 300–400 m high (Figs. 1 and 2). The foot of the amphitheatre is choked with huge Toreva blocks that slid several km into place during avalanche emplacement. The vertical drop from the volcano summit to the lowest point of the basin is 3000 m. The volume of the avalanche deposit is estimated to be about 26 km^3, with the Torevas accounting for another 11 km^3. Huge toppled blocks within the amphitheatre, now covered by subsequent volcanic products, probably account for a further 23 km^3 (Wadge et al. 1995).

Kelfoun and Druitt (2005) explored the emplacement dynamics of the avalanche by solving the depth-averaged equations of flow. By extracting the avalanche deposit and Toreva blocks, they constructed a 3D digital model of the pre-avalanche topography, then ran model avalanches numerically across it using a range of geologically realistic initial conditions. Different rheological laws were used, but only one involving a constant basal stress (Dade and Huppert 1998) generated a realistic deposit. In this model (Fig. 3) the rock avalanche spread across the Monturaqui basin, accumulated along the western and northwestern margins of the basin, then reflected back as a secondary flow. The model succeeded in reproducing (1) realistic deposit thicknesses, particularly on the inclined basin margins, (2) the median escarpment, (3) the distal lobe, and (4) realistic surface lithology patterns. It also produced a raised outer edge analogous to the levée. Overall, the model provided a satisfactory first-order approximation of the natural system.

Description of the avalanche terranes

Methods

A composite image of the avalanche deposit was constructed by superposing 2-m-resolution ortho-rectified black and white aerial photos and a false-colour 28-m Landsat image (channels 1, 4 and 7 for presented images). This was draped over either the Shuttle Radar Topographic Mission digital elevation model, or a 16-m-resolution elevation model calculated from aerial photographs. The image was then studied from all angles in a fly-over manner using commercial software. The 3D ortho-image (Fig. 1) is a useful tool for analysing surface lithological patterns and structures ranging in scale from meters to kilometers, and for making deductions concerning emplacement dynamics. It is essential for recognizing and mapping fault systems which, since they affect a granular material, may be marked by no more than low hummocks in the field (Fig. 4). Anaglyphs generated from aerial photos facilitated visualization of fine 3D structures. The results of three field campaigns at Socompa provided ground truth for image interpretation (van Wyk de Vries et al. 2001; KK, unpublished data).

Terrane definitions

We divide the avalanche sheet into four terrane groups, each believed to have experienced a particular strain history during emplacement (Fig. 2b): (1) the Torreva terrane, (2) the proximal lineated terranes (P1 and P2), (3) the levée (L) and western in situ terrane (IS), and (4) the secondary terranes and distal lobe (S1 to S5). The median escarpment separates the proximal lineated terranes from the more distal secondary terranes (Fig. 2). The Toreva terrane is composed mainly of huge blocks up to 2×1 km wide and 400 m high that slid 5–8 km into place. This terrane was described in detail by Wadge et al. (1995) and van Wyk de Vries et al. (2001), and is not described further here.

Proximal lineated terranes (P1 and P2)

The proximal lineated terranes lie between the Torrevas and the median escarpment. They are composed of two intergradational parts: a slightly larger southwestern part with a surface composed mainly of SB debris from the volcano (terrane P1), and a northeastern part composed mainly of RIF (terrane P2).

The surface of P1 is characterized by elongated debris ridges and highly stretched lithological units that form streaks that are continuous over many kilometres (Figs. 1 and 5). The NW–SE streaks are oriented in the direction of the regional slope in the northeastern half of P1, but oblique to it in the southwestern half (Fig. 2d). Despite their visual prominence, the streaks have only subtle (<10 m) topographic expression and, overall, terrane P1 is very smooth (Fig. 2d). The surface of P1 in the southwest is scarred by a series of perfectly parallel NW–SE surface ridges and furrows with individual lengths of more than 3.5 km, lateral wavelengths of 10–30 m, and heights of a few meters (Fig. 1, 561500 W, 7312500 S, and Fig. 5). In this area, the regional (NE-dipping) slope is almost perpendicular to the direction of avalanche propagation. It is surprisingly difficult to recognize the ridges and

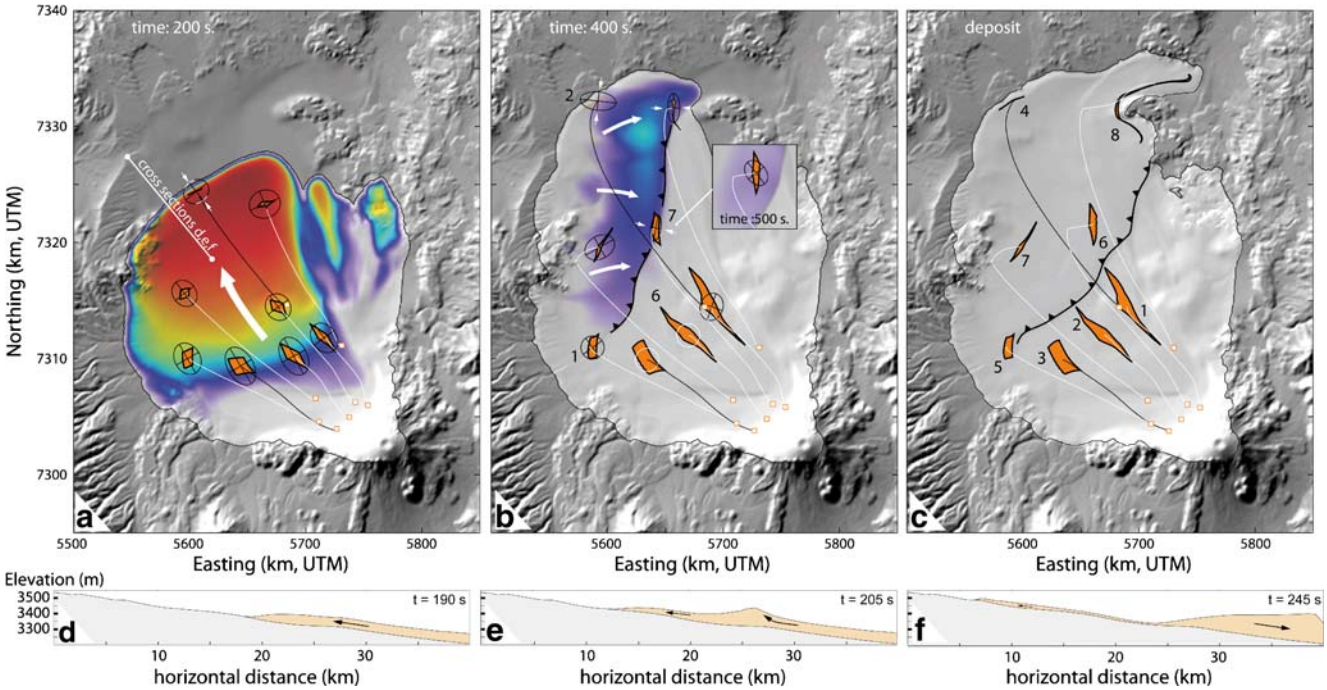

Fig. 3 Numerical model of the emplacement of Socompa avalanche (after Kelfoun and Druitt 2005): **a** 200 s, **b** 400 s, and **c** final deposit. The model assumes a constant basal stress of 52 kPa during flow. The *large white arrows* show the main movements during emplacement, and the *small white arrows* show compression directions. The ellipses depict incremental surface deformation. The *orange shapes* show the forms of initially square (400×400 m^2) surface areas, deformed by flow. *Below*: cross-sections of the avalanche at the location given by the *white line* in (**a**) at **d** 190 s, **e** 205 s and **f** 245 s after the onset of the collapse. The origin of terrane IS (see text), the only western zone not to have experienced secondary flow, is possibly explained by the cutting of the primary flow by the initial return wave off the southwest basin margin. This would have prevented local mass accumulation and reflection, allowing terrane IS to rest in its primary emplacement position

furrows in the field, the area being covered by trains of low hummocks.

The lithological streaking of P1 is interpreted as indicative of primary flow direction. The ridges and furrows are also attributed to primary avalanche flow because they are parallel to the main lithological fabric, and they disappear at the median escarpment.

While the surface of P1 is composed almost entirely of SB, field outcrops show that this is underlain at most locations by RIF. The RIF commonly comes to the

Fig. 4 Faults visible on aerial and satellite photos are commonly not visible in the field, but appear as fields of low, elongated hummocks (location on Fig. 2a and d). Such faults are found in vertical exposures, such as road cuttings (van Wyk de Vries et al. 2001). Person (*encircled*) for scale

surface between lava streaks, where it contains inmixed blocks of lava (Figs. 1 and 5). This two-layer structure of the avalanche deposit is interpreted as a source-derived stratigraphy, greatly thinned by stretching during emplacement (Francis et al. 1985; van Wyk de Vries et al. 2001). In the field we have observed a 20-cm-thick layer of oxidised rocks (pink on Figs. 1 and 5) covering non-oxidized ones (blue on Figs. 1 and 5) with a very sharp limit (e.g. 561970 W, 7314013 S). Such deep oxidation cannot be due to post-avalanche weathering, and is probably the oxidized surface of the lava, greatly thinned by stretching.

Terrane P2 is lithologically and morphologically different from P1. It is composed mainly of RIF and minor SB draped over a number of pre-existing structures, including the La Flexura frontal anticline (LF on Fig. 2a), Loma Alta ridge and Negrillar lava field (van Wyk de Vries et al. 2001). The morphologies of certain of these structures, such as the Lion's Paw lava (LP on Fig. 2), are in places visible through the avalanche sheet. Where the avalanche impinged on the Negrillar lava field, tongues of debris penetrated valleys passively without significant runup, showing that the velocity here was quite low. In the same manner, low velocity near the eastern margin allowed preservation of an inlier of Negrillar lava as the RIF flowed around it (IN on Fig. 2).

In the extreme southeast of terrane P2 the presence of a veneer of RIF (VR on Fig. 2) on the SE basin margin shows that the moving avalanche was at its maximum 100 to 200 m thicker than the present thickness of the deposit. The edge of the avalanche is here composed of a strongly faulted lava flow that appears to have been stretched out parallel to the basin margin (van Wyk de Vries et al. 2001). Streaks of this lava were pulled out to the northwest parallel to the main avalanche transport direction. As discussed in detail by van Wyk de Vries et al. (2001), it appears that initial flow of this RIF-dominated material was directed northeastwards; a high wave of material then accumulated along the SE basin margin before being deflected at lower velocity towards the northwest. The lava flow was transported and thinned on this wave before then being stranded along the SE margin as the underlying RIF drained out from beneath it towards the northwest. The site of maximum drainage corresponds to a palaeovalley.

A notable feature of terrane P2 is the presence of abundant surface erosion and a fine-scale drainage network, today normally dry. Some of the drainages appear to be fed by springs situated at the base of the avalanche deposit. The drainage network is attributed to rain and snow meltwater off the high land to the east of Socompa, fed by a complex of major streams (Quebrada Salin, QS on Fig. 2). Some of the erosion may also be due to rain and meltwater runoff on P2 itself. There is no evidence to suggest that this erosion pattern is related to decantation of water from the avalanche immediately following emplacement.

Secondary terranes and distal lobe (S1 to S5)

Each of the five secondary terranes has a characteristic assemblage of structures and/or lithologies. Terrane S1 is an area of highly deformed SB, 3 km wide and 7 km long (area 1 on Fig. 6). The northern margin is defined by a complex set of left-lateral strike-slip faults (*A* on Fig. 6). The southern margin is defined by two right-lateral strike-slip faults (*B* on Fig. 6) with significant normal components that allowed RIF with admixed SB to inject upwards from below, forming ridges several metres high. S1 is interpreted as a huge coherent slab that slid off the northwestern edge of the avalanche sheet. It detached along a headwall scarp forming the inner boundary of the western levée and slid about 5 km southeastwards, exposing an area of underlying RIF (area 2; Fig. 6). The site of detachment (and probably most of the area of S1) corresponds to a local palaeovalley, as shown by convergence of the pre-avalanche drainage pattern west of S1 (Fig. 6). The slide direction of S1 is parallel to the local slope of the basin (Fig. 2d).

Terrane S2 is situated immediately north and east of S1 (Figs. 2b and 6). It is composed of a jigsaw pattern of huge, elongated slabs of SB, separated by expanses of exposed RIF. The slabs are wrapped around a topographically high area composed of thin avalanche deposit draped over a pre-existing hill (3 on Fig. 6). The slabs have a pervasive shear fabric indicative of clockwise rotation north of the palaeo-high and anticlockwise south of it. Visual reconstruction of jigsaw fits shows that the slabs were derived by eastward sliding of an accumulated mass of SB off the northwestern edge of the avalanche. As the mass slid parallel to ground slope, the slabs deformed around the palaeo-high, then broke up into a series of elongate slabs, exposing underlying RIF (4 on Fig. 6).

Terrane S3 is defined as including all the area north and east of S2 that is composed mainly of RIF and hybrid RIF-SB lithologies (Figs. 2b and 7); it includes the distal lobe of the avalanche. The western edge of S3 is marked by a series of detachment scarps along the inside of the levée, where the impinging avalanche accumulated, then slumped back towards the east and southeast. The scarps are up to 30 m high and have angles of up to ~30°. The RIF inside the detachment headwall is scarred by large faults with throws of several tens of meters. The curved shapes of these faults trace the path taken by the back-sliding mass, which moved first southeastwards, then turned northeastwards towards the distal lobe, parallel to the local ground slope (Fig. 7b).

The southeastern part of S3 has a surface that is densely normally faulted, producing a curvilinear, flow-normal horst-and-graben fabric (Figs. 1 and 2d). Lobes forming

the eastern limit penetrate into valleys of the Negrillar lava field, and the largest tongue forms the distal lobe of the avalanche. Along the western edge of the Negrillar Hills the avalanche forms a 1.5-km-wide band 50 to 100 m higher than the adjacent avalanche surface (Fig. 2d). This, along with the shape of a prominent pink-coloured lithology wrapped around the massif (PL on Fig. 7a), shows that the avalanche was moving eastwards before impinging on the relief.

The distal lobe is about 25 m thick, with steep (~30–35°), well defined margins and no evidence for post-emplacement decantation of water. The thickness of the lobe margins decreases progressively downstream, showing that the lobe thinned as it drained eastwards. The distal lobe is covered with flow-normal extensional faults that in the field form fields of north–south elongated hummocks; large flow-parallel strike-slip faults (sinistral in the north, dextral in the south) lie just inboard of the margins. The RIF forming the distal lobe flowed eastwards about 8 km on a slope of less than 1°.

If the axis of the distal lobe is traced towards the interior of the avalanche (terrane S3), it leads to an arcuate, elongated zone, the surface of which is 15 to 30 m lower than that of the surrounding deposit (feature 6 on Fig. 2d; Fig. 7b and c). This topographic low cross-cuts surface lithology fabrics and appears to be an area of the avalanche surface that has subsided, perhaps due to late-stage drainage of underlying material towards the distal lobe. Two SB horsts at the rear end of the subsided area appear to have been stretched northeastwards by this drainage (white arrows; Fig. 7b).

Terrane S4 lies south of S1 (Fig. 2b). It is composed of a quasi-coherent slab that detached along a curved headwall to the west and slid eastwards about 1 km. The underlying RIF is exposed along the base of the headwall, intermittently within the sheet, and along the southern margin (Fig. 1). The boundary between S4 and S2 is formed by a complex set of wide (nearly 1 km across, location: 564000 W, 7323000 S) pull-apart grabens. These are the largest grabens observed on the surface of the deposit, showing that extension was particularly strong in this area.

Terrane S5 (Figs. 2b and 8) is composed of the same surface SB lithologies as the southwestern part of P1. It is separated from the western levée by normal faults, and from P1 by the median escarpment (except in the extreme southwest were S5 and P1 merge). The northern limit, where S5 abuts S4, is marked by a mixture of lithological units and by strong extension that permitted exposure and upward extrusion of underlying RIF. These structures are indicative of differential movement between S5 and S4, the former having moved eastwards several kilometers further than the latter. The displacement during secondary motion decreases towards the south in terrane S5; surface lithologies are distorted and faulted in a complex manner due to the return motions (Fig. 8). The (eastward) direction of return flow follows the local slope of the Monturaqui Basin (Fig. 2d).

The median escarpment

The median escarpment forms the limit between the secondary and primary terranes, the former being everywhere thicker than the latter (Figs. 1, 2 and 5). The escarpment is highest (up to 50 m) in the centre, and decreases in height to the southwest and northeast.

While the surface of the secondary terranes is dominated by extensional structures, the escarpment itself, and the area immediately north of it, is marked by a narrow belt of compression. This compressional belt, less than a few hundred m wide, is composed of overlapping thrust sheets, shear zones, and anastomosing, en echelon anticlines mostly composed of SB, but with rare ones composed of SB cored by RIF. Some shear zones are transtensional, as shown by the presence along them of ridges of extruded RIF (e.g., area 3 on Fig. 8); others lacking RIF appear to be transpressional or pure strike-slip.

The escarpment cross-cuts the primary flow fabric of the proximal terranes, rotating the bands sharply clockwise by 60° in the centre to 90° in the southwest (Figs. 1 and 5). The base of the escarpment is interpreted almost everywhere as a thrust overriding the primary terranes. Some short stretches near area 4 on Fig. 8 more closely resemble eastward-dipping normal faults, perhaps due to local uplift of S5 relative to P1 or to landslips off the escarpment.

The compressional belt passes abruptly northwards into the extensional structures typical of the surface of the secondary terranes. At some localities (e.g., area 4 on Fig. 8) compressional ridges are bounded to the north by sets of large normal faults, with downthrow towards the secondary terranes.

Levée (L) and western in situ terrane (IS)

The levée at Socompa (Figs. 2 and 7) is a raised margin of the avalanche sheet, delimited by normal faults on its inner edge. It is best developed along the northern, northwestern

Fig. 5 High-resolution image covering parts of terrane P1 (*centre* and *lower left*), terrane P2 (*upper right*), and the secondary terranes (*upper left*). The location of the image is shown in Fig. 2a. Surface lithologies of terrane P1 are strongly stretched in the NW–SE direction. The cross sections show the higher elevation of the secondary terranes relative to the primary terranes, due largely to their greater thickness. Horsts and grabens of the secondary terranes are also evident. The primary terranes are morphologically smoother than the secondary terranes (see also Fig. 2d)

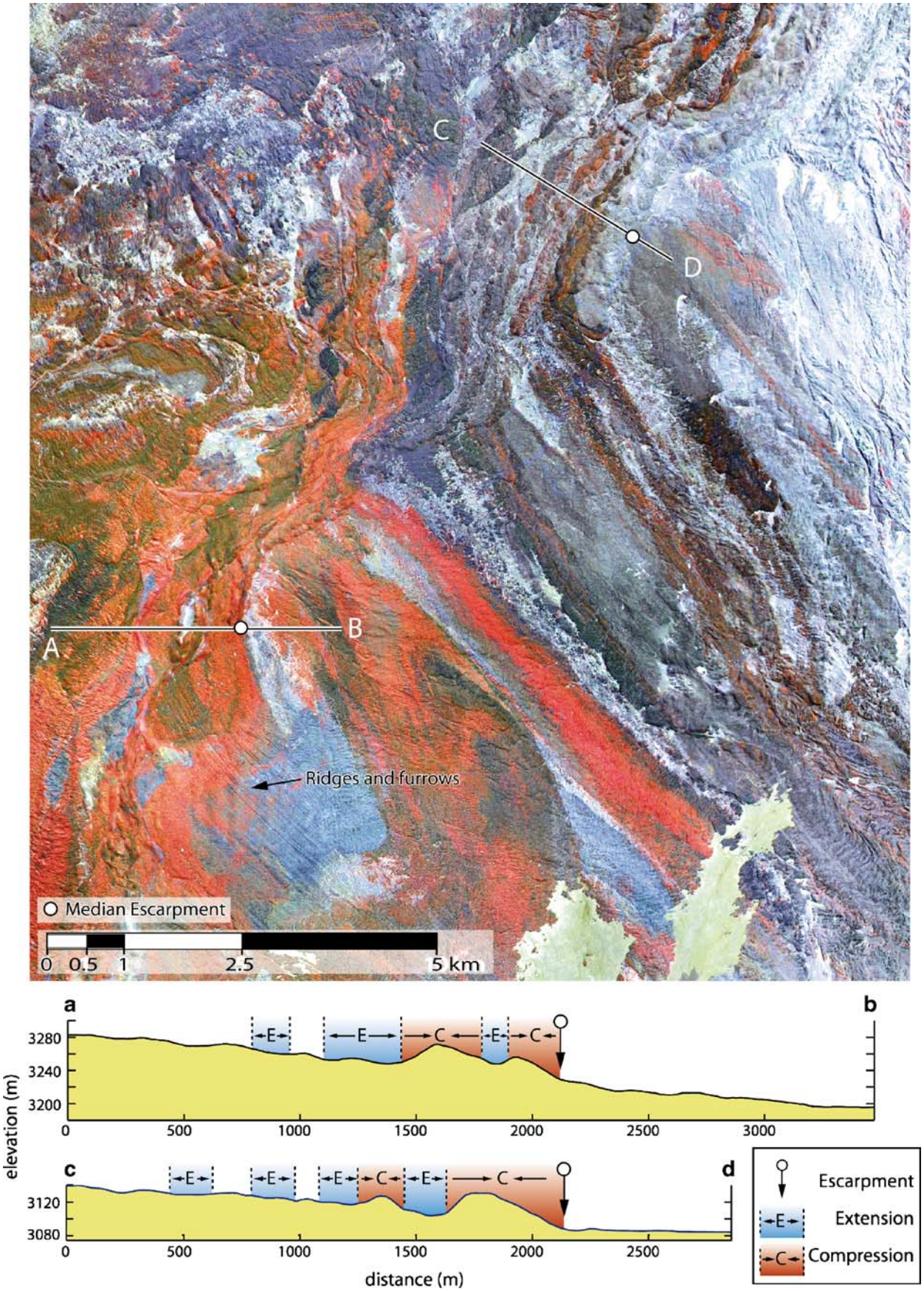
C
D
A
B
Ridges and furrows
Median Escarpment
0 0.5 1 2.5 5 km
a
b
c
d
3280
3240
3200
3120
3080
elevation (m)
0 500 1000 1500 2000 2500 3000
distance (m)
E
C
Escarpment
Extension
Compression

and western limits, and is absent to the east (Fig. 2). The strandline along the southeastern margin (VR, Fig. 2) is a thin veneer of RIF left on the basin margin, and is morphologically different from the levée.

The levée rises 40–80 m above the surrounding terrain; it is about 1 km wide, with an outer slope of ~30° and a flat surface inclined ~5° inwards towards the avalanche interior. Successions of steep (20–30°) scarps defining the inner limit form the headwall detachments of the secondary terranes. The levée is composed predominantly of sediments and ignimbrites of the Salin Formation (RIF) with a prominent circumferential banding, individual bands being continuous over many km. Superimposed on the banding are radial lineations, defined by subtle colour variations on the Landsat image, which fan around the avalanche sheet. In the northwestern corner, the lineations offset the outer edge of the levée by up to 100 m along left-lateral strike-slip faults. The radial lineations are interpreted to be primary flow features, since they cut the bands, but are themselves cut by the headwall detachment faults. Traced to the east-northeast, the levée becomes less prominent, then disappears abruptly near the source of the distal lobe. In the southwest the levée is composed mainly of SB with a thin outer rim of RIF. Normal and strike-slip faults define the inner edge of the levée in contact with terrane S5. The substratum, readily observed at the outer margin, shows no evidence of bulldozing by the avalanche.

While the distal lobe also has raised lateral margins, they differ from the levee, being thinner, less well defined, lacking lithological banding, and being delimited on their inner edges by strike-slip faults and anastamosing shear zones. The northern margin of the distal lobe passes inside of the levée when traced westwards (Fig. 7a).

The levée is interpreted as material deposited by the primary avalanche wave, then left behind by eastward movement of the secondary terranes. The evidence for this is: (1) that it has a fanning flow lineation, and (2) that it is restricted to direct line of sight from the scar, being absent in the shadow of the Negrillar lava field (Fig. 7a, b). The lithological banding is inferred to have formed by flow-parallel compression, thickening, and circumferential stretching as the avalanche spread and decelerated up the margin of the Monturaqui Basin, before then slumping back. Compression was probably essential in generating the levée, since the latter is only present where the primary flow direction ran up the slope, and is absent along the (primary-flow-parallel) eastern margin.

On the western margin just inside of the levée lies a 4×4 km triangular terrane with a surface composed of highly deformed SB with a fine-scale flow-transverse lithological banding cut by multiple low-angle (in plan view) discordances (in situ terrain, IS, on Fig. 2b; Fig. 9). Terrane IS also displays radial lineations similar to those of the levée, which fan through about 20° clockwise from SW to NE. The similarity of both (1) the flow-tranverse banding and (2) the radial lineations with corresponding structures of the levée leads us to interpret this area as also in situ primary material. The low-angle discordances that cut the banding may be thrusts or discordant contacts derived from source. The eastern part of this terrane is cut by a series of *en echelon* right-lateral strike-slip faults (Fig. 6b). The strike-slip faults and clockwise rotation of banding are attributed to differential shearing as this part of the avalanche impacted topography immediately to the north. This was then accentuated by back-sliding of the adjacent S1 terrane. Terrane IS, along with the levée, provides a relict of the primary surface texture of the avalanche prior to overprinting by deformation associated with secondary flow.

Late-stage extensional faults

Small-scale normal, strike-slip and transtensional faults, typically less than 500 m long with vertical displacements of a few metres, are observed all over surface of the avalanche on both primary and secondary terranes. They indicate movement directions that are commonly oblique to local avalanche flow direction, but parallel to the local topographic slope. For example in the southwestern half of P1, primary flow was towards the northwest, almost parallel to local topographic contours, but the small-scale surface faulting indicates motion to the northeast, downslope towards the basin interior. Similar relationships are observed widely across the avalanche sheet. There are also, near the Toreva Blocks in particular, sets of small-scale structures deformed by up to several km in broad shear-zones. Some of these faults are interpreted as the result of late-stage creep of the emplaced avalanche sheet, while others are clearly small-scale surface faulting that occurred during transport. The fault traces appear in the field as fields of low, elongated hummocks that have been confirmed as normal faults in road cuttings (van Wyk de Vries et al. 2001).

Fig. 6 **a** High-resolution image showing terrane S1 and parts of terranes S2 and IS. The location of the image is shown in Fig. 2a. **b** Interpretative structural map. The legend is the same for Figs. 6, 7, and 8. Primary terranes are shown in *grey* (levée and in situ terranes). Secondary terranes are shown as *dark green* (SB lithologies), *pale blue* (rifted areas, composed mostly RIF), and *pale green* (rifted areas composed of mixed RIF and SB). *Black arrows* depict return displacement vectors inferred from shear zones (marked *A* and *B*) defining the limits of the S1 slide mass (marked *1*), the zone of extension upstream of S1 (marked *2*), deformation of the surface lithology pattern of terrane S2 around the palaeotopographic high (marked *3*), and the formation of flow-transverse horsts and grabens in terrane S2 (marked *4*). The 3,430-m topographic contour and convergence of the pre-avalanche drainage pattern both indicate that slide S1 is located in a palaeovalley

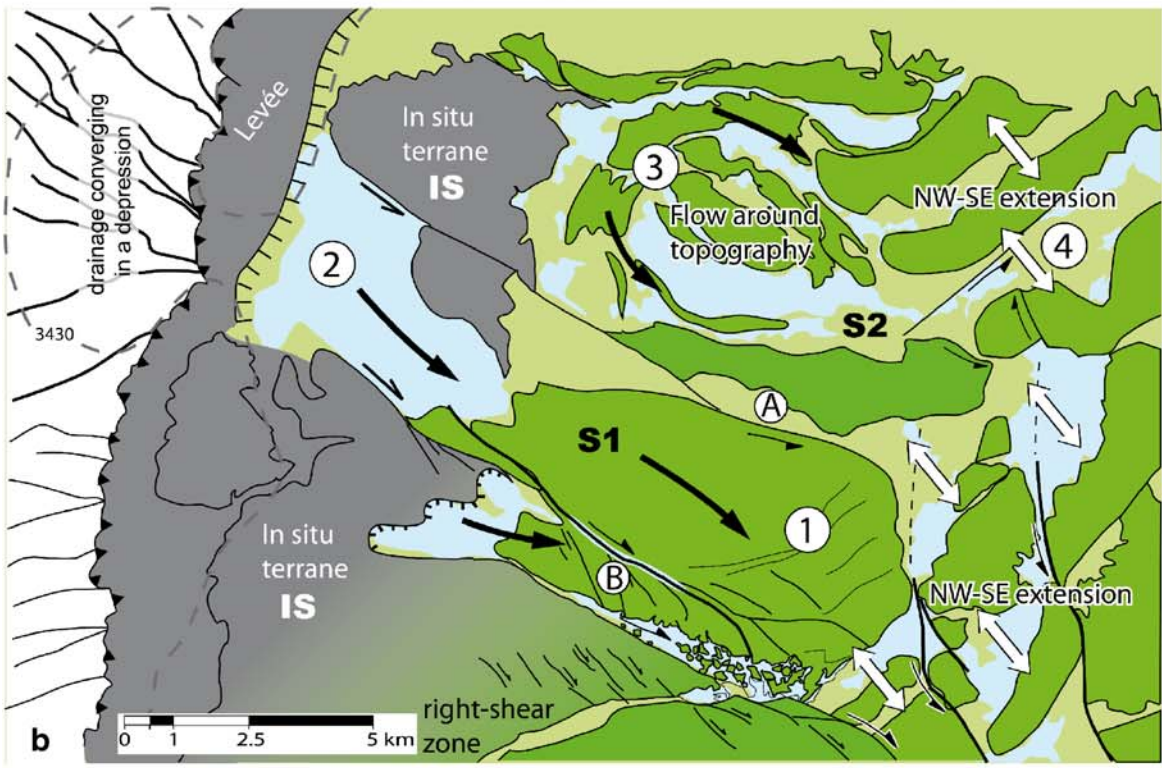

primary terrain (P) | in situ terrane (IS) and levées (L) | secondary terrane (S) | coherent units of SB in S

high extension areas | folds | normal faults | thrusts

extensions | shear zones | primary direction of emplacement | secondary displacements

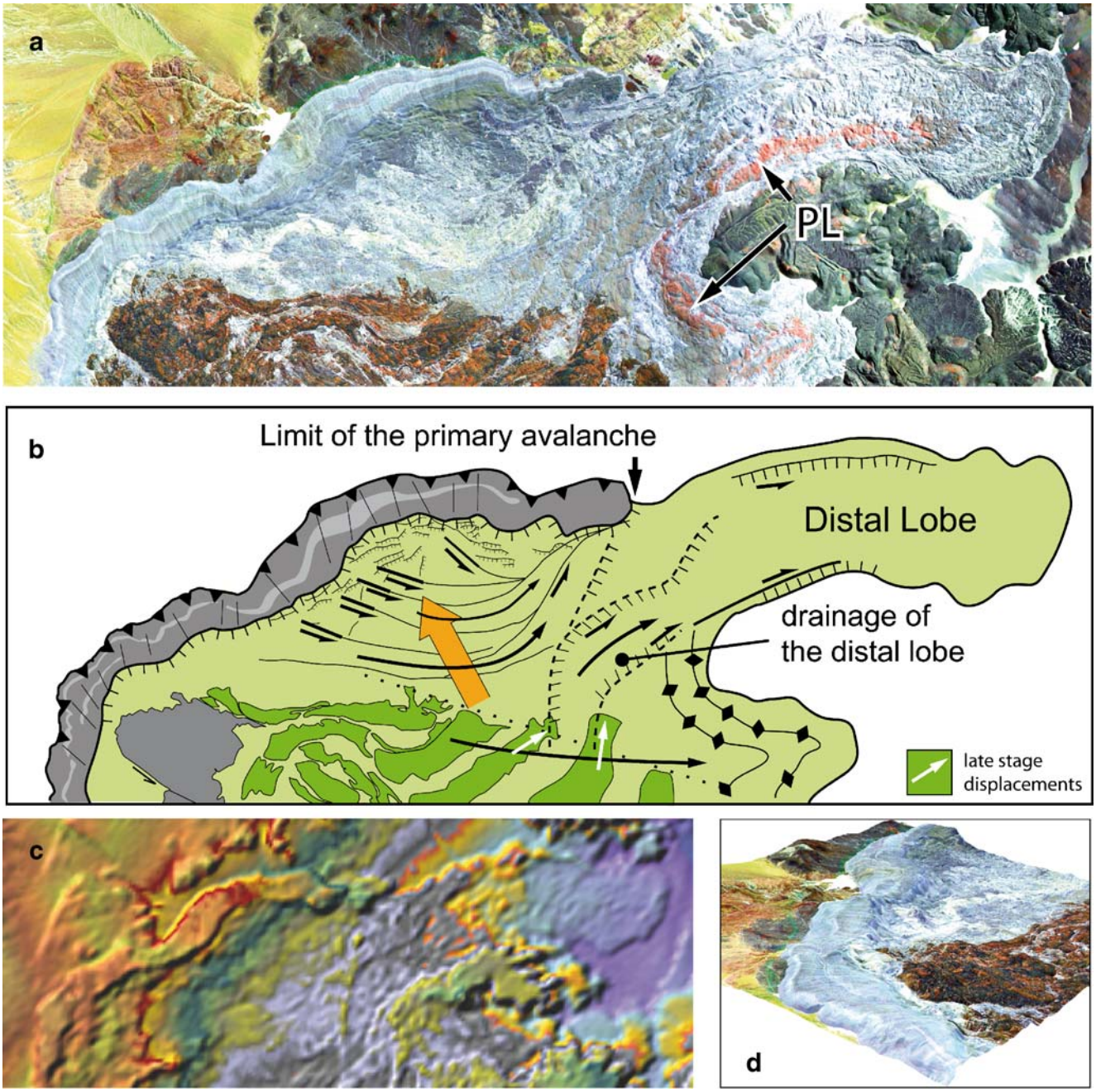

Fig. 7 Terrane S3 and the northern levée. **a** High-resolution image, the location of which is shown in Fig. 2a. **b** Sketch showing return displacements determined from strike-slip faults and lithological offsets. **c** Topography, with the same altitude scale as in Fig. 2d. **d** 3D view of the levée from SE, showing the steep outer, primary margin, and the steep inner margin formed by detachment headwall faults of the secondary terrane S3. Same legend as for Fig. 6. The orange arrows indicate primary displacement vectors. *PL* pink-coloured lithology, see text

Discussion

Summary of events

We now combine our observations with those of previous authors to reconstruct the emplacement of Socompa avalanche (Fig. 10). We restrict inferences to those made on the basis of geological observations; in a subsequent section we compare the events with those generated by the numerical model of Kelfoun and Druitt (2005).

The avalanche was initiated following a probably prolonged period of gravitational spreading that formed a belt of anticlines and thrusts at the base of the volcano to the north and northwest (La Flexura and Loma Alta anticlines, Fig. 2a;

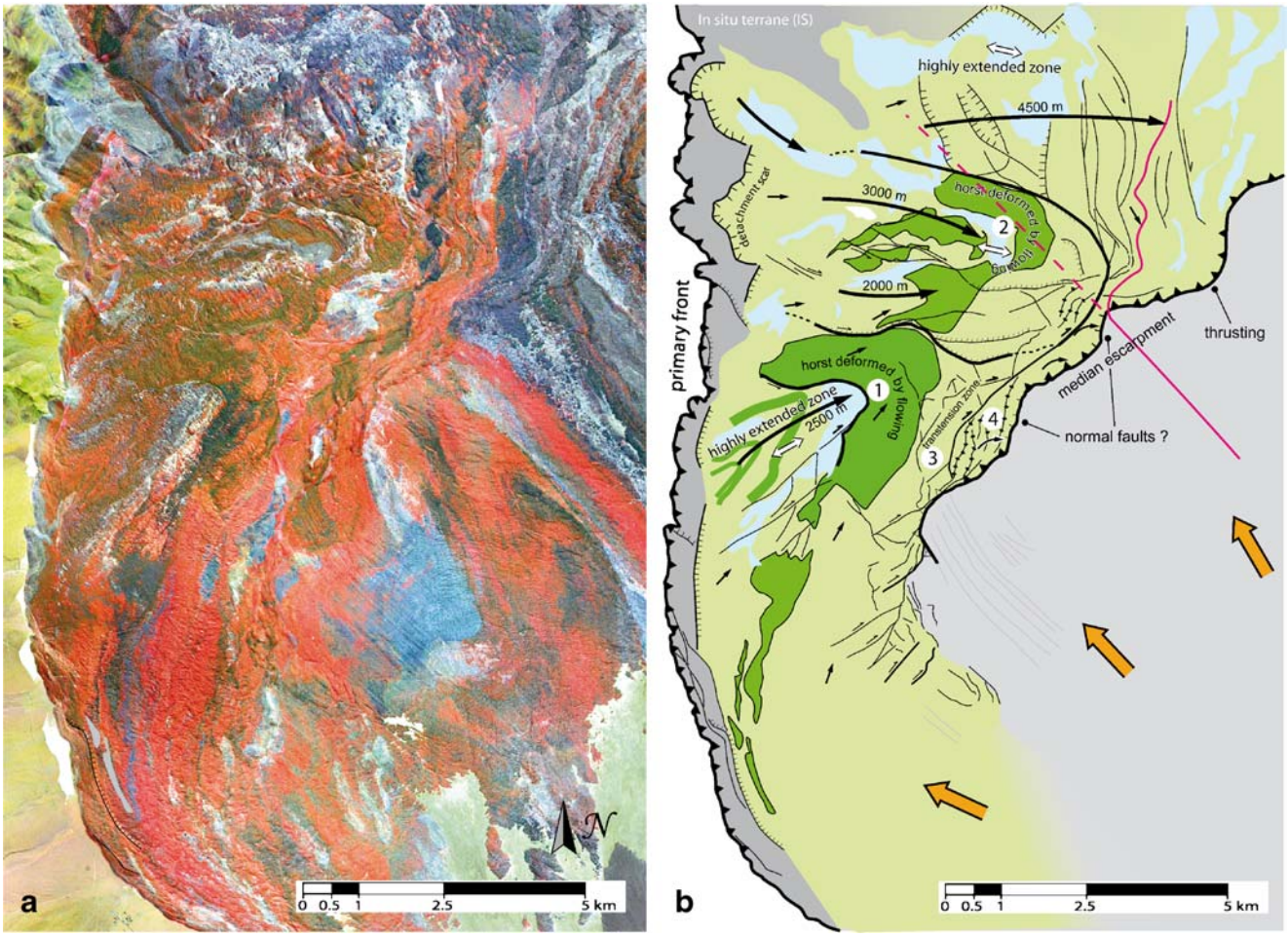

Fig. 8 Terrane S5. **a** High-resolution image, the location of which is shown in Fig. 2a. **b** Interpretative sketch. The black arrows are inferred vectors of secondary flow. Secondary flowage from the W-to-SW towards the E-to-NE is inferred from the orientations of shear zones and compression zones, and by the deformation patterns of surface lithologies. Same legend as for Fig. 6. *1* and *2*, folding of surface lithologies; *3*, transtensional zones; 4, compressional zones. The *pink line* indicates the boundary between the blue and the pink areas of the image, the *dotted line* indicating the initial inferred position. They imply flow-back of about 4,500 m

van Wyk de Vries et al. 2001). Spreading took place mainly on basement lithologies of the Salin Formation that would subsequently form the RIF component of the avalanche. Following collapse, the avalanche accelerated northwestwards across the Monturaqui basin, accompanied by strong stretching and thinning of the RIF and its overlying load of SB. High initial velocity enabled the avalanche to travel obliquely (and in the southwest and southeast, even perpendicular) to the local ground slope. That part of the avalanche extruded northeastwards from the volcano impinged on the southeast basin margin. A lava flow transported on top of this part of the avalanche was stretched and faulted, then dumped along the southeastern margin, as the RIF (following the main drainage) drained out from underneath it to the northwest at relatively low speed.

As the front of the avalanche ran obliquely up the western and northwestern basin margins, the constituent lithological units, strongly extended during the initial acceleration phase, were compressed, reassembled and thickened, forming a distinctive circumferential banding preserved as the front came to rest. Where the front impinged on obstacles, it was offset along strike-slip faults. Reflection began off the western basin margin, then propagated clockwise northwards (Fig. 10). Huge slabs of coherent surface material (SB in terranes S1, S2, S4 and S5; RIF in terrane S3) detached and slid back into the basin. Detachment everywhere took place 0.3 to 1 km inboard of the avalanche margin, leaving a well defined levée. A large area of banded terrane in the west (terrane IS) also appears to have escaped secondary flow. As sliding occurred, the slabs of SB rifted in a brittle manner, exposing the RIF below. Differential flow then sheared the slabs internally as they glided and rotated back into the basin. Owing probably to their higher densities, some SB slabs settled to different degrees into the RIF, while the lower-density RIF injected upwards along extensional faults, forming upstanding ridges and pinnacles once motion had ceased. Directed by the return wave, the RIF-dominated material constituting

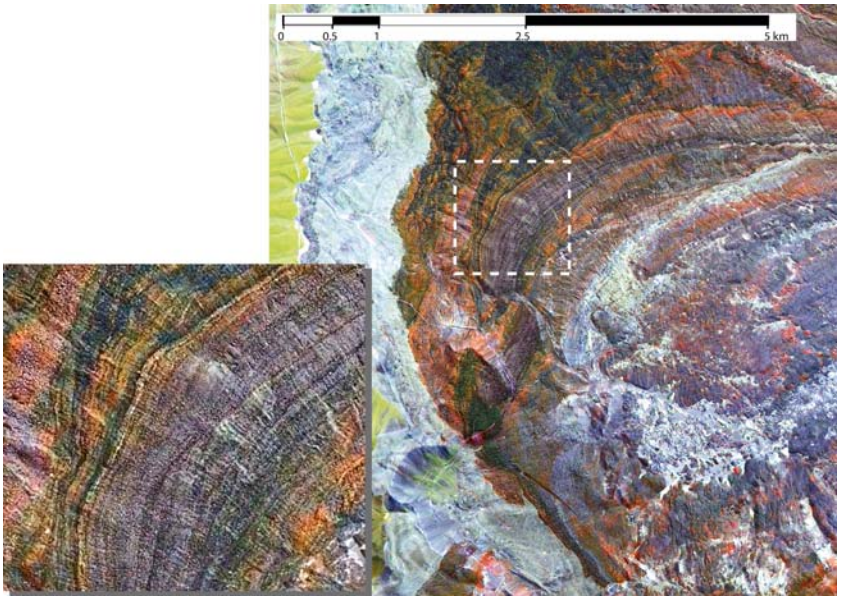

Fig. 9 Terrane IS, characterized by circumferential lithological banding similar to that in the levée (Fig. 7a). The banding is interpreted as having formed by re-assemblage and compression of previously stretched lithologies as the primary flow piled up along the western basin margin. Preservation of this banding, and the absence of other indictors of return flow, suggest that IS is an in situ, primary terrane. The banding is cross cut by very low angle discordances, interpreted either as thrusts or as strongly deformed discordance surfaces derived from source. The shape of the banding, together with the radial lineations, confirm the emplacement from SE to NW

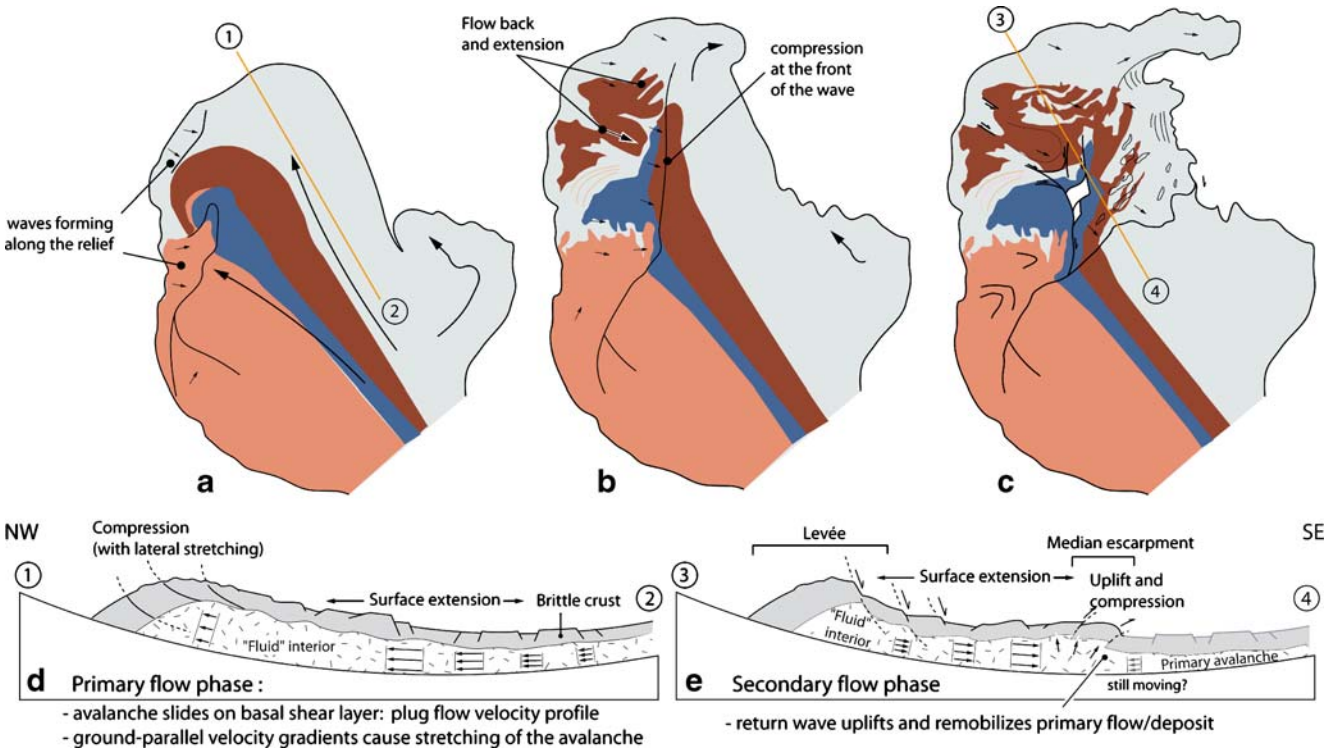

Fig. 10 Reconstruction of the emplacement of Socompa avalanche. **a** The primary avalanche accumulated along the western basin margin (the orange line locates the cross-section *1–2* in **d**), then began to reflect back towards the centre. **b** The return flow affected all the western part of the avalanche. **c** The surface of the return wave was characterized by extension, apart from along the front, where compression occurred (cross-section *3–4* in **e**). Below, **d** and **e**: summary of the rheological nature of the avalanche. A frictional front and crust enclosed a more fluid interior that remobilized the primary deposit during secondary flow. The thickness of the fluid interior is not well constrained

the eastern part of the avalanche spread southwards and eastwards, the latter merging with that pouring off the northern margin to feed the distal lobe. Where the secondary flow impinged on the Negrillar Hills, it was compressed and thickened to 50–100 m. Drainage of RIF towards the distal lobe caused subsidence of part of the avalanche surface further upstream (Fig. 7b and feature 6, Fig. 2d). Late-stage creep caused final small-scale downslope faulting of the avalanche surface.

The nature and timing of secondary flow

The hypothesis of avalanche reflection is supported by the existence of (1) clearly recognizable slide masses, such as S1 (Fig. 6), S4 and those of S5 (Fig. 8), (2) sub-parallel sets of curvilinear strike-slip faults and shear zones indicative of return flow of terrane S3 (Fig. 7), (3) headwall scarps separating the (primary) levée from the secondary terranes, in particular those bounding S1 (Fig. 6), S3 (Fig. 7) and S5 (Fig. 8), (4) extensional jigsaw breakup of surface SB lithologies during return flow of terrane S2 (Fig. 6), and (5) cross cutting of primary flow fabrics of the proximal terranes by the median escarpment (Fig. 5).

The following observations place constraints on the nature of the secondary return flow. (1) On a large scale the lithological streaking of terrane P1 is continuous across the median escarpment into the secondary terranes, being deflected clockwise by about 60° (Fig. 5). (2) On a smaller scale some cross-cutting relationships are evident (Figs. 5 and 8). For example, the prominent ridge-and-furrow lineations of P1 are cross-cut by the median escarpment. (3) Deformation of the surface of the secondary terranes is mostly extensional, the compressional front being only a few hundred m across.

We now consider some simple endmember mechanisms for the secondary flow. Perhaps the simplest hypothesis is that the return flow swept back across the top of the primary avalanche, which could have either been stationary or still moving. In this simple scenario the base of the return flow would have coincided with the top of the primary avalanche, which would not have been affected by the secondary motion. However, the continuity of lithological streaking across the median escarpment shows conclusively this cannot have been the case, as the return wave front would cross-cut the primary flow fabrics everywhere, even on a large scale. This mechanism can therefore be excluded.

Another simple mechanism would be that the front of the avalanche first accumulated on the slopes of the Monturaqui basin, then slid back downslope en masse towards the centre of the basin, bulldozing the primary terranes ahead of it as an enormous slump. While this mechanism might explain lithological continuity across the escarpment, it would be expected that surface deformation across most of the secondary terranes would be compressive. However, this is not the case, compressive structures being confined only to a narrow zone adjacent to the escarpment.

The evidence suggests rather that the return flow took place in the form of a wave, with movement taken up vertically throughout the entire avalanche, not just at the surface as in the first mechanism above. As the wave front impinged on material of the primary terranes, the latter was first (1) compressed, then (2) lifted up onto the wave, then (3) thinned and stretched as it passed rearward of the wave front. As the primary lithological streaks were lifted up onto the wave they were rotated clockwise by it. This mechanism explains both the dominance of surface extension of the secondary terranes, and deflection of primary flow fabrics. It requires that the wave, rather than overriding material of the primary terranes, incorporated it in a fluidal manner into the return motion. This is independent of whether or not the primary avalanche was still moving northwestwards, which is not constrained by our evidence.

In detail, the motions were more complex than this. Local cross cutting of primary fabrics by the median escarpment show that significant overthrusting of the primary terranes took place on a local scale at the leading edge of the wave. Moreover, some of the return motions took place as discrete slumps superimposed on the overall wave motion, for example terranes S1 and S4.

The extension of surface lithologies during secondary motions was accommodated in part by brittle rifting and in part by ductile thinning. Rifting of surface SB lithologies during the return of terrane S2 revealed the underlying RIF, which can be distinguished by its different colour on the false-colour images. Summing the RIF grabens between the levée and SE boundary of S2 yields 5.5 km. This is a minimum because it does not take into account possible extension by internal thinning. If we add 1.5 km of flow around the palaeo-high, the total minimum extension is 7 km, or approximately 55% of the total NW–SE width of S2. This implies an S2 surface extensional strain of at least 1.8 during secondary flow. Eastward displacements on the surface of terrane S5 estimated from the folding of surface lithologies (areas 1 and 2, Fig. 8), displacements on strike-slip faults, and exposure of RIF by rifting range from 2 to 4.5 km, or approximately 35 to 55% of the width of S5 parallel to return flow in each relevant part of this terrane. The implied extension factors are 1.5–1.6, and are again probably minimum estimates. We conclude that return flow was accompanied by surface extensional strains of at least 1.5–1.8.

We can draw an analogy between the return wave at Socompa and certain types of water waves. The aim is not to imply that the physical mechanism was exactly the same, the avalanche being composed of granular debris, but to help the reader envisage the type of process proposed. A normal deep-water wave causes only oscillatory surface

motion, with extension at the wave crest and compression at the wave trough, but no net translation of mass. A hydraulic bore (moving hydraulic jump), on the other hand, can involve mass transfer (e.g., Simpson 1987). In this context the return wave at Socompa probably most closely resembled a bore, with significant mass translation (recorded by the surface extensions of the secondary terranes). A crude analogy may be the bores formed by flow reversals in turbidity currents (Edwards 1993).

The continuity of the median escarpment, and the systematic deflection of primary lithological streaking across it, provide constraints on the timing of the return flow. The displacement of the reflected wave back into the Monturaqui Basin increases systematically from south to north, producing a laterally continuous NE–SW median escarpment and associated compression front. This argues convincingly that most major motions of the secondary terranes took place simultaneously and were continuous with primary flow. The curvilinear form of the escarpment, and the observed smooth clockwise displacement gradient, are both consistent with continuous reflection of the primary avalanche (Kelfoun and Druitt 2005). Back-slumping of multiple slide masses over a prolonged time period would, on the other hand, have produced an irregular front, and the smooth displacement gradient observed would have to be coincidental. Overall, the continuity and nature of the median escarpment across the entire avalanche sheet strongly imply that most of the Socompa avalanche deposit was emplaced as a single, short-lived event, as also concluded by Wadge et al. (1995). Creep and minor slumping may have continued for a long while following the main emplacement phase.

Comparison of primary and secondary flow

There are significant textural differences between the primary and secondary terranes that reflect their different emplacement dynamics.

Primary flow occurred at velocities high enough for motion oblique to the regional slopes of the Monturaqui Basin. The primary avalanche surface is characterized by longitudinal lithological streaks, the origin of which may be due to original radial lithology distributions on the volcano (e.g., radial lava-flow tongues), and/or to rotations of flow-transverse horst-and-graben fabrics into parallelism with primary flow by differential shear during high-velocity emplacement. Primary flow was accompanied by very strong transport-parallel extensional strains of surface lithologies. The primary avalanche surface is remarkably smooth, possibly due to extreme, pervasive thinning at high speeds. The ridge-and-furrow fabric at Socompa is unique to terrane P1, and may also have its origin in high-velocity granular flow.

Secondary flow, on the other hand, took place at sufficiently low speeds for flow direction to be controlled largely by regional slope. It involved a combination of wave motion and unidirectional translation, the latter rifting surface lithologies into flow-transverse horsts and grabens. However the strain imposed on surface lithologies during secondary flow was much smaller than that during primary flow. Only where the secondary flow was deflected around palaeo-relief was the surface fabric rotated parallel to flow by differential shear (location 3 on Fig. 6). Owing to this low-velocity rifting, as well as differential foundering of surface blocks, the surface of the secondary terranes is much rougher than that of the primary terranes.

Other examples of avalanche reflection

The Socompa avalanche is not unique in having been reflected off topography. Many rock avalanches show evidence of having been deflected at oblique angles off slopes or obstacles, and as such involved a component of reflection (e.g., database of Shaller 1991). For example, the 0.005 km^3 Pandemonium Creek avalanche in British Columbia was generated on the side of a steep valley and upon reaching the valley floor proceeded to run 335 m up the opposite side, before being deflected downstream (Evans et al. 1989). The 2.8 km^3 Mount St Helens avalanche in 1980 ran 250 m up Coldwater Ridge (Voight et al. 1981) and was then deflected. The 0.004 km^3 Gros Ventre avalanche swept across a valley, piled up ~100 m high against the opposing cliffs, then partly slumped back (Voight 1978). The Socompa example is, however, distinct from these other examples in involving a much larger volume of debris. It also has the return wave preserved, frozen as an escarpment, on its surface. A key feature at Socompa was that the avalanche reflected back into a closed basin, so that the return wave was amplified to as much as 50 m in height as it converged on the basin centre.

Implications for rheological behaviour

As noted by previous authors (e.g., van Wyk de Vries et al. 2001), most of the avalanche cannot have been saturated with water during flow, since there is no evidence for mudflows formed by post-emplacement decantation. Socompa is therefore an example of a ‘dry’ debris avalanche. Saturation of a thin basal layer, or of underlying sediments incorporated into the motion cannot, however, be ruled out.

Our observations have the following implications for the rheological behaviour of the avalanche.

1. Two lines of evidence show that the avalanche slid into place on a basal layer. First, lateral stratigraphy is preserved, the RIF basement lithologies of the frontal anticlines forming the distal levée, as described by van

Wyk de Vries et al. (2001) and Kelfoun and Druitt (2005). Second, although much of the avalanche surface is covered in coarse bouldery debris, there are no frontal accumulations of such material as would be expected if the leading edge had involved a rolling motion. This very convincing argument was also used by Shreve (1968) for the Blackhawk avalanche.

We infer that, to a first approximation, Socompa avalanche travelled in the manner of a plug flow, with most of the shear deformation taken up at the flow base. Many other avalanches have been inferred to have slid into place in a similar manner (e.g., Fahnestock 1978; Erismann 1979; Shaller 1991 and references therein; Clavero et al. 2007). Of course in detail significant departures from ideal plug flow would have occurred due to effects such as avalanche heterogeneity, temporal and spatial variations or pore pressure, and/or local topography, and we stress that this is certainly only a crude approximation of the real behaviour. Note that the idea that the avalanche slid into place is not inconsistent with the avalanche thickness variations inferred to have taken place during emplacement, as described above. Thinning or thickening of a moving avalanche requires ground-parallel gradients of velocity; for example, for an avalanche to thin simply requires that the front travels faster than the rear, and vice versa for thickening. The shape of the horizontal-velocity profile remains vertical overall; i.e. the top, middle and base of the avalanche are travelling at the same velocity. In detail, internal deformation of the avalanche involves additional relative motion, but this is of very small magnitude relative to that of avalanche motion overall.

2. The ability of the avalanche to travel 35 km across the floor of the Monturaqui Basin, then reflect and flow back another 15 km down a regional slope of less than 5°, attests to very low basal friction. Low friction must also have persisted to a late stage during emplacement, because the distal lobe, which appears to have been the last part of the avalanche to move, was able to travel 8 km down a slope of less than 1° before coming to rest.
3. The evidence for very low basal friction contrasts with abundant indicators that much of the moving mass actually had high friction. First, the outer margins of the avalanche levées and distal lobe have angles similar to the angle of rest of granular materials (30–35°). Second, headwall scarps forming the inner margins of the levée also have high angles, again suggesting that this part of the avalanche had normal friction, even though huge masses of immediately adjacent material were actively sliding eastwards on very low gradients. Third, much of the avalanche surface is faulted, with scarps of ~30°, suggesting normal friction. These include the km-scale horst and graben topography of the secondary terranes, as well as the much smaller late-stage normal faults and hummocks. Fourth, it is common in extensional zones of the avalanche for the underlying RIF to have been injected upwards during motion through the overlying SB lithologies. In many such cases, the RIF forms upstanding ridges or even subvertical pinnacles, showing that the internal friction was high. We infer that the avalanche was emplaced as a fast-moving sheet of fragmental rock debris with a leading edge (forming the levées) and crust with near-normal friction, and an almost frictionless, fluidal interior and base. As the mass slid and stretched, internal stresses were sufficiently high that the frictional rock debris constituting the front and upper levels of the avalanche deformed by a combination of (1) ductile granular flow, and (2) faulting on a wide range of scales, from kilometres (in the case of the jigsaw terrane of S2) to metres or less. The thickness of the frictional crust is not well constrained. The throws on late-stage surface faults are up to a few m, indicative of a 'crust' of frictional material at least this thick. Moreover, observations in a few road cuts show faults passing down into diffuse horizontal banding at depths of up to ~10 m. The crust thickness probably varied spatially and temporally in the avalanche during emplacement. However, the ability of the returning wave to remobilise and lift up the primary terranes would appear to imply that a significant fraction of the thickness of the avalanche interior had the ability to behave in a fluid manner.
4. There appears to have been a positive relationship between the thickness of the avalanche and its ability to flow. Where the avalanche was thick, flow occurred readily on gradients as low as 1°. Examples of this include the distal lobe and the front of the return wave. Moreover, the thicker the avalanche, the greater the apparent ability to flow. For example, return flow of terranes S1 and S2 was greatest down palaeovalleys, but much less on the palaeo-relief that separates these two terranes. Where thin, the avalanche was capable of ceasing motion and leaving a deposit on all slopes of the basin lower than 30°, for example, primary terrane P1, in situ terrane IS, the western levée, the palaeo-relief separating S1 and S2, and the western part of S5.

Comparison with the numerical model

We now compare our observations and deductions based on field evidence with the numerical model of Kelfoun and Druitt (2005). The most realistic simulation presented in that paper assumed that the avalanche was subject to a constant resistance stress of about 50 kPa during flow; i.e., it behaved as a yield-strength fluid. This very simple assumption succeeded in reproducing several first-order features of the

flow and its deposit, such as topographic reflection and secondary flow, the median escarpment (by freezing of the leading edge of the return wave), and raised marginal levées. It also succeeded in generating realistic surface lithology patterns on the model avalanche, in particular the continuity of lithological streaks, and the clockwise deviation of those streaks, across the median escarpment from primary to secondary terrains (Kelfoun and Druitt 2005; their Fig. 10).

Two key aspects of the model are consistent with the avalanche dynamics inferred from field evidence. First, the model was depth-averaged and assumed a plug-like velocity profile, the avalanche sliding on a thin basal layer, (point 1 of the previous section). Moreover, where the model return wave impinged on the primary flow, it remobilized and incorporated the entire depth of the primary flow, just as inferred for the natural system. Second, while unlikely to represent an accurate rheological description, the constant-stress condition is consistent with the behaviour of the avalanche. The relationship between the thickness of the avalanche and its ability to flow, described in point 4 of the previous section, is simulated crudely by a yield-strength fluid, and cannot be reproduced using a Mohr–Coulomb-type frictional law (Kelfoun and Druitt 2005). It is also consistent with the analysis of long-runout avalanche data published by Dade and Huppert (1998). This combination of features of the model adopted by Kelfoun and Druitt (2005), in part fortuitously, probably explains why the model succeeded in reproducing the first-order dynamics of the natural system.

To use the numerical model to better visualise the main movements within the avalanche, we have extended it to show 2D surface strain (Fig. 3). Two parameters are depicted as a function of time for a number of points on the avalanche surface: (1) the ellipse of instantaneous strain, and (2) the shape of a surface area that was initially square with dimensions 400×400 m on the flank of the volcano prior to collapse. The relevant equations are given in the Appendix. The surfaces of proximal terranes P1 and P2 (squares 1–3 on Fig. 3) suffer strong flow-parallel stretching during emplacement that is consistent with extreme thinning while preserving stratigraphic order (SB over RIF). Rocks deposited on the northwestern levée (square 4) are first stretched, then compressed strongly in the direction of avalanche displacement, probably explaining the circumferential banding observed on the levée. An area initially on the southwest flank of the volcano (square 5) is first stretched in the NW–SE direction, compressed on the margin, then re-stretched by the reflected wave before being deformed by the NNE-directed downslope flow. Rocks incorporated into the secondary terranes (squares 6 and 7) are first stretched as they accelerate away from the volcano, compressed by the front of the wave, then re-stretched in the NW–SE direction and sheared in an anticlockwise sense by the return wave. This direction of stretching is fully compatible with the orientation of horsts and grabens observed on terranes S2, S4 and S5. Finally, an area derived from the RIF-dominated northern flank of the volcano (square 8) finishes up as a highly stretched streak wrapped around the Negrillar lava field. The strong similarity between this simulated streak and the corresponding pink (false colour) streak on the avalanche (marked PL on Fig. 7a) is a striking demonstration of the predictive capacity of the model.

Finally, the model provides a possible explanation for the origin of in situ terrane IS. This is the only part of the western avalanche interior that did not undergo secondary flow, although return movement of adjacent terrane S4 was also small. A possible reason, deduced from the model, may have been that as the secondary wave was initiated along the west margin of the basin, it swept back across the NW-directed primary flow, cutting off the flux to area IS, which was thereafter no longer fed with material (Figs. 3, d–f and 10a). The avalanche over IS was then thinner than elsewhere which, given the relationship between mobility and thickness, prevented it from remobilization, and caused it to freeze.

Conclusions

We have generated a composite 3D ortho-image of the Socompa long-runout debris avalanche deposit from satellite images, aerial photos and digital elevation models, and have used it, along with field observations and the results of previously published work, to reconstruct the sequence of events during avalanche emplacement. Our study has focussed in particular on the evidence for large-scale topographic reflection and secondary flow, as well as some inferences concerning avalanche rheology.

As the avalanche spread across the Monturaqui sedimentary basin, it experienced strong stretching and thinning before being reflected back off the western margin oblique to the primary flow direction. Reflection commenced in the west and southwest and migrated progressively northwards. Evidence for reflection includes the existence of huge, clearly recognizable slide masses, sub-parallel sets of strike slip faults and shear zones indicative of return flow, headwall scarps separating the primary levée from the secondary terranes, and extensional jigsaw rifting of surface lithologies incompatible with primary flow directions.

As the return wave swept back across the basin it uplifted and remobilized primary avalanche materials, the leading wave edge finally freezing to form a prominent escarpment. Most major motions of the secondary terranes must have taken place simultaneously with, or shortly after, primary flow in order to explain the curvilinear form of the escarpment and the observed smooth clockwise displacement gradient related

to it. Late-stage drainage of material from the secondary terranes formed a prominent distal lobe and caused subsidence of part of the avalanche surface upstream of the lobe.

The avalanche slid into place on a thin basal layer, like many other long-runout avalanches. It is inferred to have been emplaced as a fast-moving sheet of fragmental rock debris, with a leading edge and crust with near-normal friction, and an almost frictionless, fluidal interior and base. The basal friction was low enough to allow secondary motion on regional gradients of a few degrees and emplacement of the distal lobe on a slope of only 1°. That the leading edge and crust of the avalanche had high friction is shown by the steep angles exhibited by surface faults, the outer margins of levées and the distal lobe, and headwall scarps forming the inner margins of the levée, as well as ridges and pinnacles of RIF lithologies from the avalanche interior that that locally pierce the surface.

The numerical model of Kelfoun and Druitt (2005) succeeded in capturing the essential dynamics of the Socompa avalanche because the assumptions of plug flow and yield-strength rheology were, to a first approximation, geologically realistic.

Acknowledgments This work was financed by the 'Relief' and '*Aleas et Changements Globaux*' programmes of the French CNRS. We thank S. Self for allowing us to cite his new age determination of the Socompa avalanche. Comments by Geoff Wadge, an anonymous reviewer and the editor, James White, helped us improve the manuscript.

Appendix

Axes λ_1 and λ_2 of the strain ellipse (Fig. 11) are calculated by the square roots of eigenvalues of **F** defined by:

$$\mathbf{V}^t = \begin{bmatrix} X_2^t - X_1^t & X_3^t - X_1^t \\ Y_2^t - Y_1^t & Y_2^t - Y_1^t \end{bmatrix},$$

$$\mathbf{V}^{t+dt} = \begin{bmatrix} X_2^{t+\mathrm{d}t} - X_1^{t+\mathrm{d}t} & X_3^{t+\mathrm{d}t} - X_1^{t+\mathrm{d}t} \\ Y_2^{t+\mathrm{d}t} - Y_1^{t+\mathrm{d}t} & Y_2^{t+\mathrm{d}t} - Y_1^{t+\mathrm{d}t} \end{bmatrix}$$

$$\mathbf{D} = \mathbf{V}^{t+d\,t} \times (\mathbf{V}^t)^{-1}$$

and

$$\mathbf{F} = \mathbf{D} \times \mathbf{D}^T$$

where X^t and Y^t define the positions of three points (Fig. 11) at time t, and $X^{t+\mathrm{d}t}$ and $Y^{t+\mathrm{d}t}$ define the positions of the same points at time $t+\mathrm{d}t$.

Orientation α of the ellipse is defined by the ratio of the eigenvectors of **F**:

$$\tan\alpha = {}^{\mathrm{EigVect1}}/_{\mathrm{EigVect2}}$$

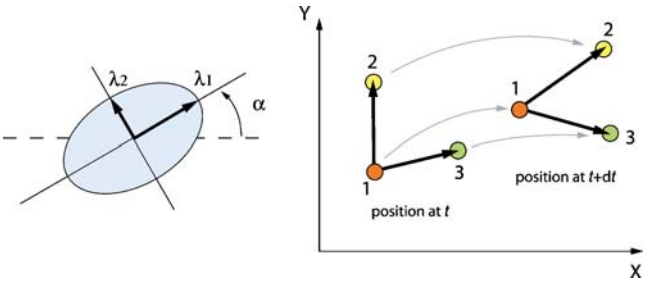

Fig. 11 Axes and orientation of the strain ellipse and representation of the three points used at times t and $t+\mathrm{d}t$ for their calculation

References

Clavero JE, Polanco E, Godoy E, Aguilar G, Sparks S, van Wyk de Vries B, Pérez de Arce C, Matthews S (2007) Substrata influence in the transport and emplacement mechanisms of the Ollagüe debris avalanche, northern Chile. Acta Vulcanol 16:59–76

Collins GS, Melosh HJ (2003) Acoustic fluidization and the extraordinary mobility of sturzstroms. J Geophys Res 108:2473–2486

Dade WB, Huppert HE (1998) Long-runout rockfalls. Geology 26:803–806

Davies TR, McSaveney MJ (1999) Runout of dry granular avalanches. Can Geotech J 36:313–320

Edwards DA (1993) Turbidity currents: dynamics, deposits and reversals. Lect Notes Earth Sci 44: 1–173

Erismann TH (1979) Mechanisms of large landslides. Rock Mech 12:5–46

Evans SG, Clague JJ, Woodsworth GJ, Hungr O (1989) The Pandemonium Creek rock avalanche, British Columbia. Can Geotech J 26:427–446

Fahnestock RK (1978) Little Tahoma Peak rockfalls and avalanches, Mount Rainier, Washington, U.S.A. In: Voight B (ed) Rockslides and avalanches. Elsevier, New York, pp 181–196

Francis PW, Self S (1987) Collapsing volcanoes. Sci Am 256:91–96

Francis PW, Gardeweg M, Ramirez CF, Rothery DA (1985) Catastrophic debris avalanche deposit of Socompa volcano, northern Chile. Geology 13:600–603

Kelfoun K, Druitt TH (2005) Numerical modeling of the emplacement of Socompa rock avalanche, Chile. J Geophys Res 110:B12202

Legros F (2002) The mobility of long-runout landslides. Eng Geol 63:301–331

Ramirez CF (1988) The geology of Socompa and its debris avalanche deposit, northern Chile. MS thesis, Open University, Milton Keynes

Shaller PJ (1991) Analysis and implications of large Martian and terrestrial landslides. PhD thesis, California Institute of Technology, Pasadena

Shreve RL (1968) The Blackhawk landslide. Geol Soc Am Spec Pap 108:1–47

Simpson JE (1987) Gravity currents in the environment and the laboratory. Ellis Horwood, Chichester

Van Wyk de Vries B, Self S, Francis PW, Keszthelyi L (2001) A gravitational spreading origin for the Socompa debris avalanche. J Volcanol Geotherm Res 105:225–247

Voight B (1978) Lower Gros Ventre slide, Wyoming, U.S.A. In: Voight B (ed) Rockslides and avalanches. Elsevier, New York, pp 113–166

Voight B, Glicken H, Janda RJ, Douglass PM (1981) Catastrophic rockslide avalanche of May 18. In: Lipman PW, Millineaux DL (eds) The 1980 eruptions of Mount St Helens, Washington. U S Geol Surv Prof Pap 1250, 347–378

Wadge G, Francis PW, Ramirez CF (1995) The Socompa collapse and avalanche event. J Volcanol Geotherm Res 66:309–336

Numerical modeling of the emplacement of Socompa rock avalanche, Chile

K. Kelfoun and T. H. Druitt

Laboratoire Magmas et Volcans, OPGC, UBP–CNRS–IRD, Clermont-Ferrand, France

Received 1 April 2005; revised 27 June 2005; accepted 14 September 2005; published 16 December 2005.

[1] The 7.5 ka Socompa sector collapse emplaced 25 km^3 of fragmented rock as a thin, but widespread (500 km^2), avalanche deposit, followed by late stage sliding of 11 km^3 as Toreva blocks. Most of the avalanche mass was emplaced dry, although saturation of a basal shear layer cannot be excluded. Modeling was carried out using the depth-averaged granular flow equations in order to provide information on the flow behavior of this well-preserved, long run-out avalanche. Results were constrained using structures preserved on the surface of the deposit, as well as by deposit outline and run-up (a proxy for velocity). Models assuming constant dynamic friction fail to produce realistic results because the low basal friction angles (1 to 3.5°) necessary to generate observed run-out permit neither adequate deposition on slopes nor preservation of significant morphology on the deposit surface. A reasonable fit is obtained, however, if the avalanche is assumed simply to experience a constant retarding stress of 50–100 kPa during flow. This permits long run-out as well as deposition on slopes and preservation of realistic depositional morphology. In particular the model explains a prominent topographic escarpment on the deposit surface as the frozen front of a huge wave of debris reflected off surrounding hills. The result that Socompa avalanche experienced a small, approximately constant retarding stress during emplacement is consistent with a previously published analysis of avalanche data.

Citation: Kelfoun, K., and T. H. Druitt (2005), Numerical modeling of the emplacement of Socompa rock avalanche, Chile, *J. Geophys. Res.*, *110*, B12202, doi:10.1029/2005JB003758.

1. Introduction

[2] Long run-out rock or debris avalanches are one of the most hazardous of geological phenomena [*Melosh*, 1990]. During emplacement, the center of mass follows a low-angle ($\ll 30°$) trajectory, forming a thin, widespread deposit. Avalanches on Earth with volumes greater than 10^6 m^3 are generally of long run-out type. Long run-out avalanches are emplaced in a catastrophic manner, with observed or inferred velocities of 20–100 m s^{-1} and run-outs reaching in some cases many tens of km. They occur both in terrestrial and marine environments by sudden mobilization of large rock masses, either in volcanic or nonvolcanic contexts. The ability of avalanches to travel large distances in a fluid-like manner is not well understood, apparently requiring greatly reduced dynamic friction, and a number of possible friction reduction mechanisms have been proposed (see recent articles by *Davies and McSaveney* [1999], *Legros* [2002], and *Collins and Melosh* [2003] and references therein).

[3] In this paper we use numerical modeling to place constraints on the flow dynamics of the long run-out avalanche that formed 7500 years ago by sector collapse of Socompa Volcano in northern Chile. The model solves the equations of motion for a granular flow and has the advantage of taking into account basal friction, internal friction and volumetric spreading behavior in a rigorous manner. The modeling is constrained by deposit outline, run-up (a proxy for velocity), and structures preserved on the surface of the deposit when the avalanche ceased motion. In particular we seek to explain the formation of high topographic escarpment that is a prominent feature of the avalanche deposit. The study provides some crude, but intriguing, constraints on the rheological behavior of the avalanche during motion.

2. Socompa Avalanche

[4] Socompa avalanche in northern Chile (Figure 1) has been described in papers by *Francis et al.* [1985], *Wadge et al.* [1995], and *Van wyk de Vries et al.* [2001], on which the following summary is based. It formed by gravitational collapse of the northwestern flank of the 6000-m-high stratovolcano, leaving an amphitheater 12 km wide at its mouth and with cliffs 300–400 m high. The avalanche flowed across a broad topographic basin northwest of the volcano (Monturaqui Basin) to a maximum distance of 40 km, and covered 500 km^2. The vertical drop from the volcano summit to the lowest point of the basin was 3000 m; at its northwestern limit the avalanche rode part way up a range of hills before being deflected to the

Copyright 2005 by the American Geophysical Union.
0148-0227/05/2005JB003758$09.00

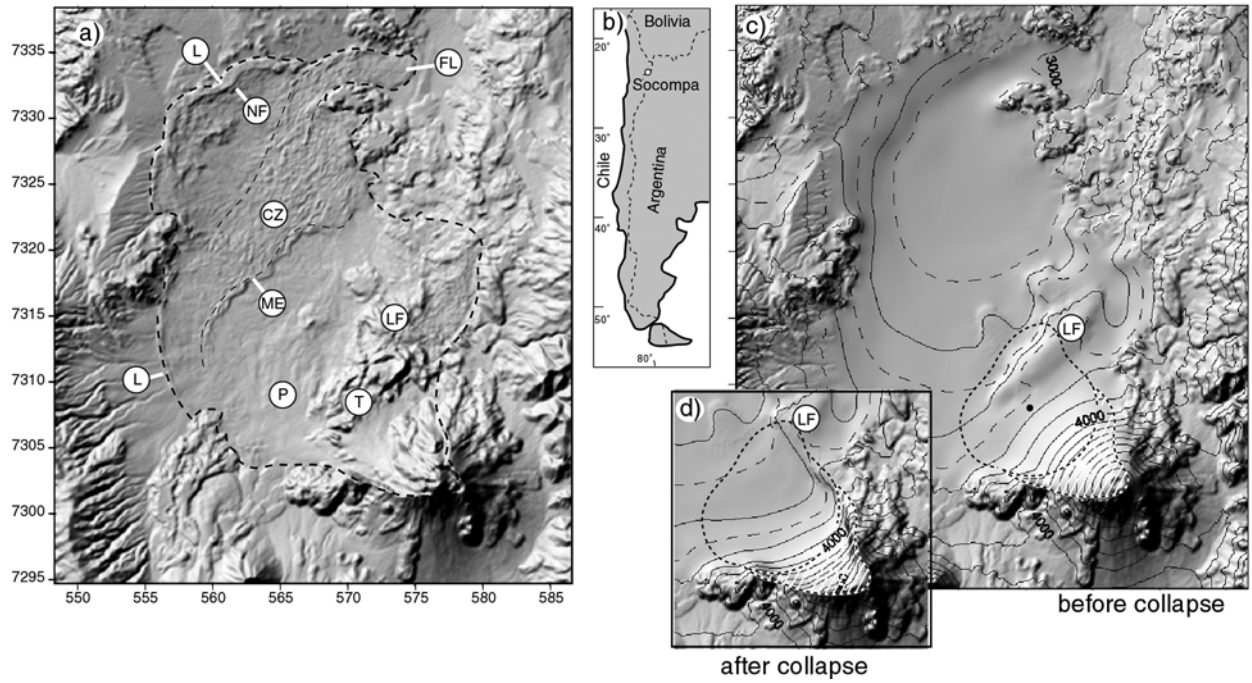

Figure 1. (a) Shaded topography of Socompa avalanche, showing the median escarpment (ME), the frontal lobe (FL), thick distal levees (L) cut by large normal faults (NF), and the central morphologically rough zone (CZ). The accumulation of Toreva blocks is marked (T). La Flexura (LF) is a basement anticline predating sector collapse. Deposits from later pyroclastic flows are marked (P). Coordinates are given in km (UTM, WGS84). (b) Location of Socompa Volcano in northern Chile. Reconstructed topography (c) of the area before collapse and (d) of the failure surface. The 25 km^3 that collapsed to form the avalanche in the ''deep'' collapse model is outlined by a black dotted line; the white ruled area is the 11 km^3 that slumped after collapse and which was left in place in our calculations. The contact between the two volumes is taken as a hemi-cylindrical headwall scarp 5 km in radius. In the ''shallow'' collapse model the 25 km^3 that collapsed is taken as a slab representing the upper 69.4% (=25/36) of the entire 36 km^3 area.

northeast, forming a frontal lobe. The volume of rock transported is estimated to be about 25 km^3, with another 11 km^3 preserved as intact (''Toreva'') blocks up to 400 m high at the foot of the collapse scarp.

[5] The morphology of the avalanche deposit is perfectly preserved in the hyperarid climate of the Atacama Desert (Figure 1a). The margins are steep and well defined, with thicknesses ranging from 10 to 60 m [*Wadge et al.*, 1995]. In some places, levees are present (labeled L on Figure 1a). A zone of convergence and SE verging thrusting called the ''median escarpment'' (ME on Figure 1a) separates the proximal part of the deposit, characterized by longitudinal surface ridges, from the distal part characterized by convoluted surface texture [*Van wyk de Vries et al.*, 2001]. A complex assemblage of surface structures including normal faults, strike-slip faults, thrusts, and longitudinal and transverse ridges records the last increments of movement of the avalanche on a local scale. The 5-km-wide central zone (CZ on Figure 1a) immediately north of the median escarpment is particularly rich in structures (Figure 1a) and lies 30–60 m higher than neighboring areas.

[6] Ignimbrites, gravels, sands, and minor lacustrine evaporites from the subvolcanic Salin Formation dominate the avalanche sheet (reconstituted ignimbrite facies; RIF $\sim$ 80%). Brecciated lavas and volcaniclastic deposits from the edifice itself (Socompa breccia facies; SB) constitute $\sim$20% and are confined mainly to the upper levels of the deposit. The eastern half and outer margins of the deposit consists almost entirely of RIF, with a thin overlying layer of SB no thicker than a couple of meters, whereas the southwestern half is composed of RIF overlain by up to 15 m of SB (see Figure 10e in section 5).

[7] Most of the avalanche probably formed by a series of retrogressive failures that merged to form a single moving mass [*Wadge et al.*, 1995]. Spreading took place as a semirigid mass on a basal layer of shearing RIF [*Van wyk de Vries et al.*, 2001]. The RIF behaved in a ductile fashion and must have been very weak mechanically to accommodate flow on slopes of 5° or less, as confirmed by the modeling presented below. The SB, on the other hand, behaved in a brittle fashion, breaking up passively as it rode on a layer of RIF lubricant. Perfect preservation of the avalanche margins, and the absence of distal mudflows, shows that any interstitial water was present in insufficient quantities to saturate the majority of the flowing debris.

3. Numerical Modeling of the Avalanche

3.1. Basic Equations

[8] The assumption is made in our model that the bulk of the avalanche slid on a thin basal layer. This is commonly

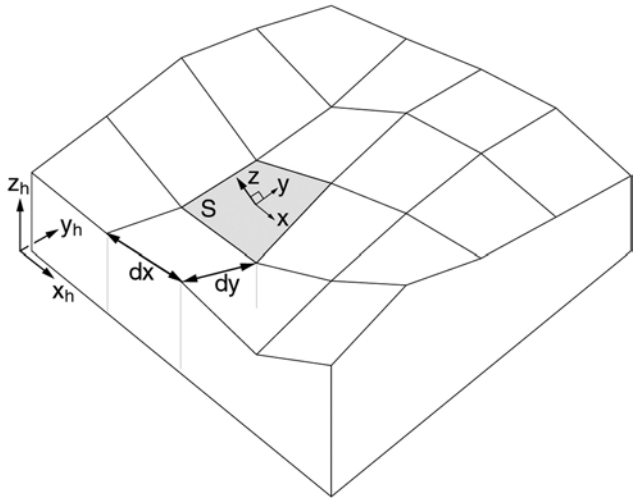

Figure 2. Geometry of the calculation domain. The ground topography is defined using horizontal axes x_h and y_h, and vertical axis z_h. The avalanche coordinates and thickness are defined using topography-linked axes x, y, and z. The cell dimensions are dx and dy.

assumed in modeling granular flows [e.g., *Savage and Hutter*, 1989, 1991; *Iverson*, 1997; *Iverson and Denlinger*, 2001; *Denlinger and Iverson*, 2001; *Heinrich et al.*, 2001; *Patra et al.*, 2005] and is consistent with field evidence at Socompa and other long run-out avalanches [*Shaller*, 1991; *Takarada et al.*, 1999; *van Wyk de Vries et al.*, 2001].

[9] Using a topography-linked coordinate system (Figure 2), with x and y parallel to the local ground surface and h perpendicular to it, the general depth-averaged equations of mass (equation (1)) and momentum (equations (2) and (3)) conservation are

$$\frac{\partial h}{dt}+\frac{\partial}{\partial x}(hu)+\frac{\partial}{\partial y}(hv)=0 \tag{1}$$

$$\frac{\partial}{\partial t}(hu)+\frac{\partial}{\partial x}\left(hu^2\right)+\frac{\partial}{\partial y}(huv)=gh\sin\alpha_x - \frac{1}{2}k_{\text{actpass}}\frac{\partial}{\partial x}\left(gh^2\cos\alpha\right)+\frac{T_x}{\rho} \tag{2}$$

$$\frac{\partial}{\partial t}(hv)+\frac{\partial}{\partial x}(hvu)+\frac{\partial}{\partial y}\left(hv^2\right)=gh\sin\alpha_y - \frac{1}{2}k_{\text{actpass}}\frac{\partial}{\partial y}\left(gh^2\cos\alpha\right)+\frac{T_y}{\rho} \tag{3}$$

where h is flow thickness, $\mathbf{u}=(u, v)$ is flow velocity, α is ground slope, $\mathbf{T}$ is retarding stress, ρ is bulk density of the avalanche, k_{actpass} is Earth pressure coefficient (ratio of ground-parallel to ground-normal stress), and subscripts denote components in the x and y directions.

[10] For a dry frictional material, the retarding stress is of the form

$$T_x=-\rho h\left(g\cos\alpha+\frac{\mathbf{u}^2}{r}\right)\tan\varphi_{\text{bed}}\frac{u}{\|\mathbf{u}\|} \tag{4}$$

where φ_{bed} is the angle of dynamic friction between the avalanche and the ground surface and any excess pore fluid pressure is assumed to be negligible. Use of this law, even in cases of rapid granular flow, is justified by *Savage and Hutter* [1989]. Shear cell tests show that the ratio of shear to normal stresses in a rapidly deforming granular material can be represented by an approximately constant dynamic friction coefficient, even if interparticle collisions are important. The second term in parentheses is the centrifugal stress, where r is the radius of curvature of the ground [*Savage and Hutter*, 1991]. The y component of $\mathbf{T}$ is obtained by replacing u by v.

[11] Following *Iverson and Denlinger* [2001], the expression for k_{actpass} used if the internal behavior is frictional is

$$k_{\text{actpass}}=2\frac{1\pm\left[1-\cos^2\varphi_{\text{int}}(1+\tan^2\varphi_{\text{bed}})\right]^{1/2}}{\cos^2\varphi_{\text{int}}}-1 \tag{5}$$

where φ_{int} is the internal angle of friction of the avalanche. This expression is valid if $\varphi_{\text{bed}} < \varphi_{\text{int}}$. The sign $\pm$ is negative (and k_{actpass} active) where the local flow is divergent and is positive (and k_{actpass} passive) where the local flow is convergent. If, on the other hand, $\varphi_{\text{bed}} \geq \varphi_{\text{int}}$, then k_{actpass} is given by

$$k_{\text{actpass}}=\frac{1+\sin^2\varphi_{\text{int}}}{1-\sin^2\varphi_{\text{int}}} \tag{6}$$

3.2. Numerical Scheme

[12] The equations were solved numerically using a shock-capturing method based on a double upwind Eulerian scheme (Appendix A). The scheme can handle shocks, rarefaction waves, and granular jumps and is stable even on complex topography and on both numerically "wet" and "dry" surfaces. Some numerical schemes require the ground ahead of the avalanche to be covered with a very thin artificial layer of avalanche material: a so-called numerically wet surface [*Toro*, 2001].

[13] In order to check the accuracy of our numerical scheme we performed tests to compare the numerical results with analytical solutions and with simulations based on other numerical schemes. Some of these are presented here. Figures 3–5 show comparisons between numerical and exact solutions of dam break problems. In the first case (Figure 3) the slope is horizontal and there is zero friction. This problem simulates the breakage of a dam separating an initial layer 1.5 m thick (left) from a layer 0.5 m thick (right). Our solution reproduces almost exactly the analytical solution, and particularly the frontal shock wave and the thickness of the central plateau.

[14] Figure 4 shows three comparisons with exact solutions obtained by *Mangeney et al.* [2000] for a dam break problem on a slope with nonzero friction and with zero thickness in front of the initial dam. The shape and velocity of the flow are accurately reproduced, even for the least favorable case of a steep slope and high friction angle. Note that vertical expansion of the y axis exaggerates the difference between numerical and analytical solutions.

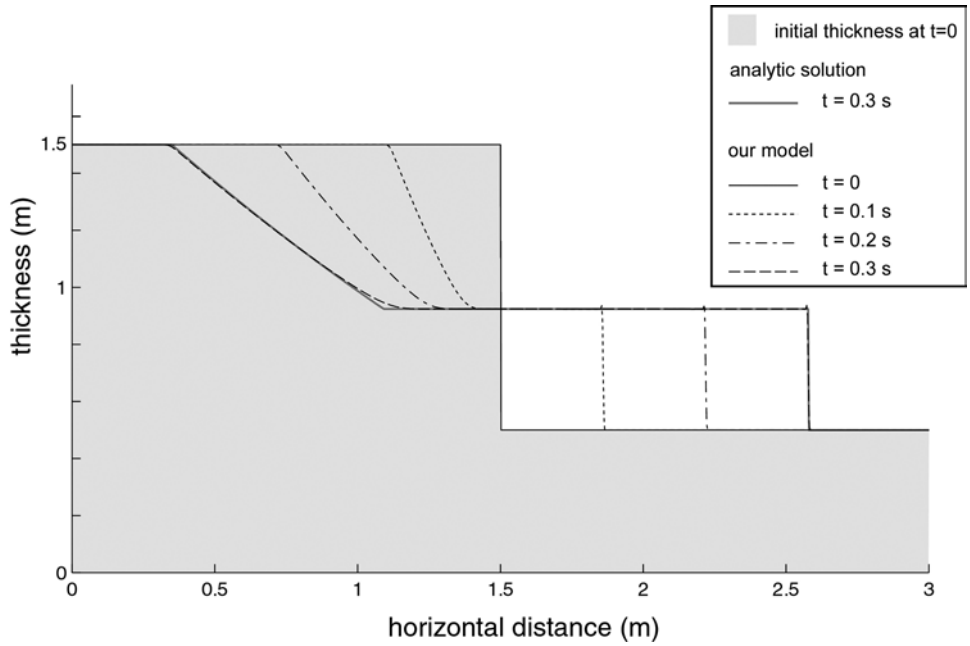

Figure 3. Comparison between numerical and analytical solutions for a dam break onto a numerically "wet" surface, in the absence of friction. An initial 1.5-m-thick layer is released onto a 0.5-m-thick layer. Points of the analytical solution for $t = 0.3$ s are ($x = 0$, $h = 1.5$) (0.3492, 1.5) (1.0915, 0.924289) (2.5781, 0.924289) (3 0.5). Note the good fit between the two solutions at $t = 0.3$ s and the accurate reproduction of the front. The thickness of the plateau obtained by our numerical solution is between 0.9240 and 0.9244, compared with 0.924289 for the analytical solution. Parameters used are $dx_h = 2.5$ mm, $dt = 1 \times 10^{-4}$ s, and $g = 9.81$ m s^{-2}.

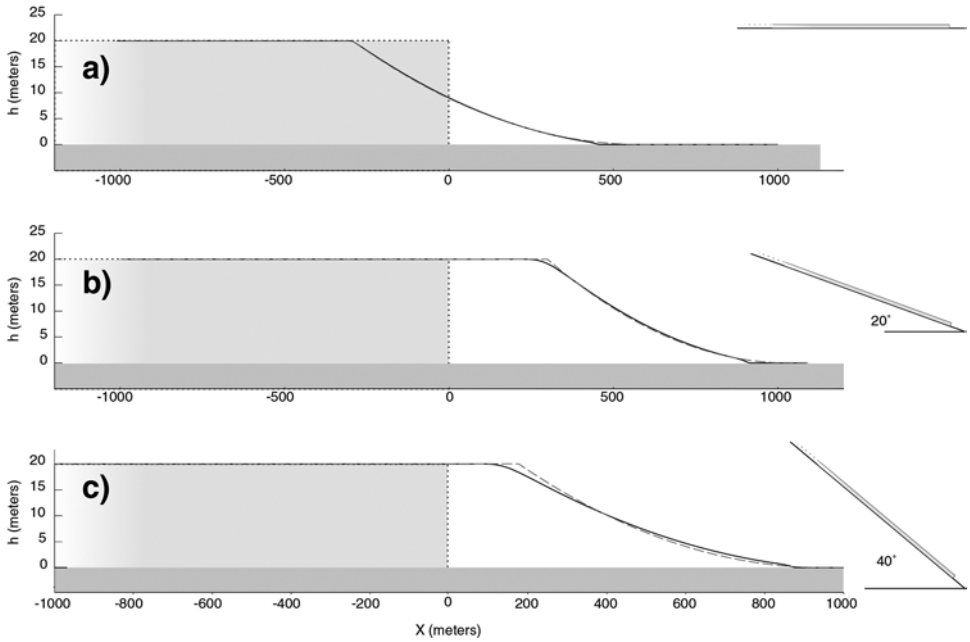

Figure 4. Comparison between the analytical solution of *Mangeney et al.* [2000] (dashed gray), and our numerical model (solid black) for a frictional dam break flow onto a numerically "dry" surface. (a) Horizontal surface ($\alpha = 0°$) with no friction ($\varphi_{bed} = 0°$) at $t = 21$ s; (b) $\alpha = 20°$, no friction ($\varphi_{bed} = 0°$) at 18 s, and (c) $\alpha = 40°$, $\varphi_{bed} = 30°$ at 21 s. Parameters used are $dx_h = 1$ m, $dt = 10^{-2}$ s, and $g = 9.81$ m s^{-2}. The figures to the right show the initial shape at $t = 0$, without vertical exaggeration.

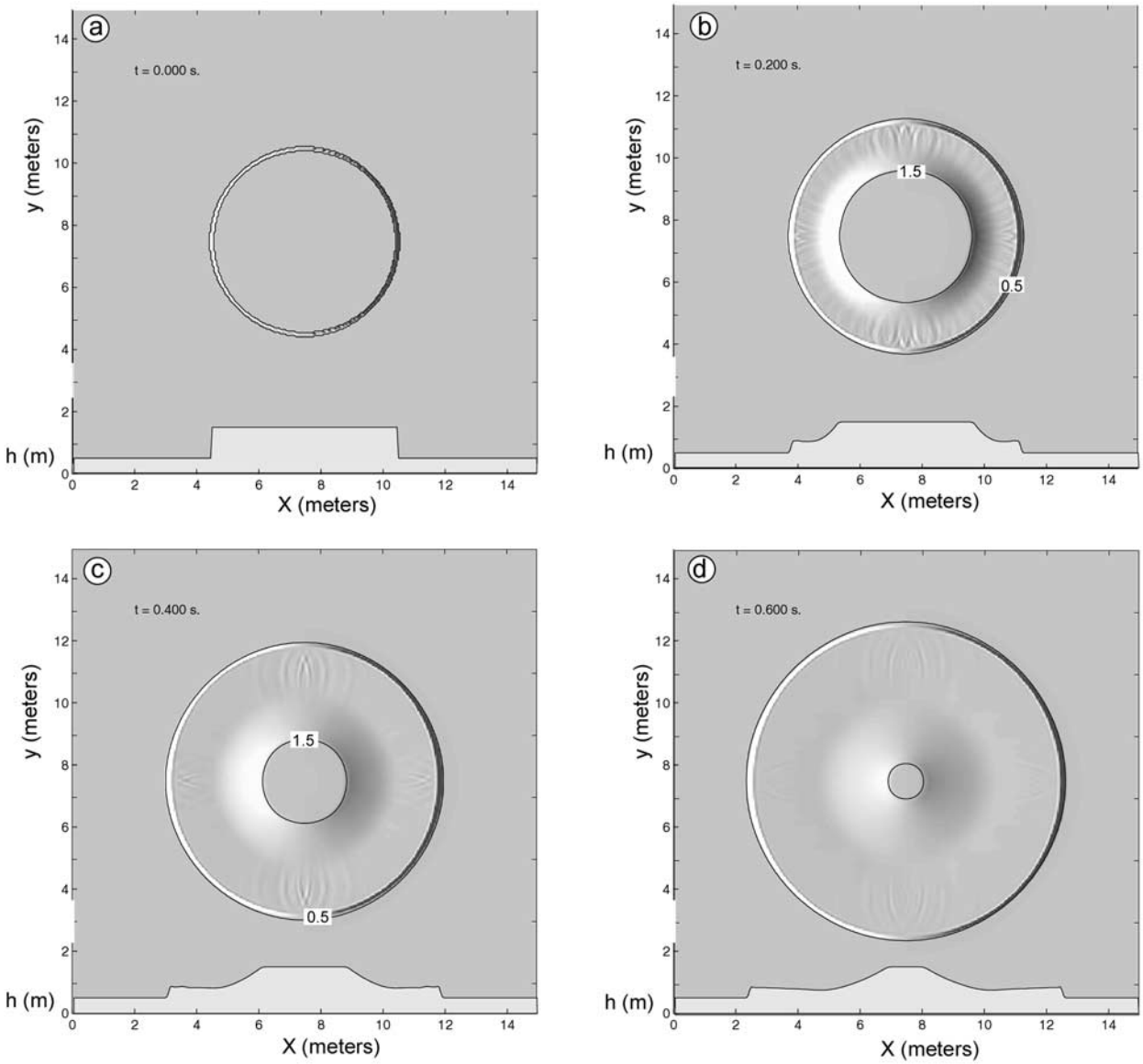

Figure 5. Circular dam break tests viewed from above (and in cross section in the lower part of each figure) show the isotropy of our numerical scheme. An initial 1.5-m-thick layer flows onto a 0.5-m-thick static layer. The surface is horizontal, and there is no friction. Parameters are $dx_h = 0.05$ m, $dt = 0.005$ s, and $g = 9.81$ m s^{-2}. Small numerical instabilities present in Figure 5b disappear as the flow propagates.

[15] Since our numerical scheme is based on a rectilinear coordinate system, we also performed circular dam break tests to ensure that the calculations are isotropic. In Figure 5, a 6-m-diameter cylinder of zero - friction fluid, 1.5 m thick, is released onto a 0.5-m-thick, horizontal layer of the same fluid. The resulting degree of isotropy and the shock resolution are both satisfactory, some small numerical oscillations disappearing progressively during the calculation.

[16] We also applied our code to published laboratory experiments of granular flows down chutes. These include the experiments of *Savage and Hutter* [1991], *Pouliquen and Forterre* [2002], and *Gray et al.* [2003]. In all cases our code is able to reproduce the experimental results as well as schemes presented by the authors and based on other numerical approaches (the frictional law of our model can be easily changed to take into account the various frictional laws used by the authors to reproduce their experimental results). In one numerically challenging experiment, in which a high-friction flow at high velocity encounters an obstacle [*Gray et al.*, 2003] (Figure 4), our scheme reproduces the shape and velocity of the flow; however, it is somewhat less stable than the numerical scheme used by the same authors to simulate their experiment (using the same time and space steps). The advantage of our scheme is that the computing time necessary for simulating flow over terrain with a large number of mesh cells is less than for many published methods. In this paper we calculate the emplacement of an avalanche on a 460 $\times$ 570 mesh topography in about 1 day with 3 GHz computer. The

computation time could be reduced, but we have chosen a time step 5 times lower than necessary to ensure stability.

3.3. Geological Starting Conditions

[17] The preavalanche topography north of Socompa Volcano was estimated as follows. The present-day topography of the volcano and avalanche (Figure 1a) was extracted from Shuttle Radar Topography Mission (SRTM) data. Field and borehole constraints on deposit thickness [*Wadge et al.*, 1995] were used to subtract the 25 km^3 of avalanche deposit and to obtain a best estimate of the preavalanche landscape (Figure 1c). The $\sim$11 km^3 accumulation of Toreva blocks at the northern foot of the volcano were removed, and the sectorial scar filled in using Figure 13 of *Van Wyk de Vries et al.* [2001] to reconstruct the precollapse morphology of the volcano (Figure 1c). We reconstruct the La Flexura anticline north of the volcano (LF, Figure 1a) from descriptions of *Van Wyk de Vries et al.* [2001], as well as the small preexisting relief north of La Flexura. The combination of these constraints resulted in little freedom in reconstructing the precollapse morphology. Since in this paper we only model emplacement of the (fluid) 25 km^3 avalanche, 11 km^3 of the scar fill was left in place during our calculations (to slump subsequently as Toreva blocks).

[18] One significant uncertainty is the exact geometry of the initial collapse volume. In the absence of precise evidence concerning the shape of the avalanche headwall scarp (partly buried by postavalanche products), we assume two end-member cases: (1) a wedge-shaped volume with hemicylindrical headwall scarp 5 km in radius (Figures 1c and 1d), referred to in what follows as the ''deep'' collapse geometry, and (2) a slab-like initial slide volume, referred to as the ''shallow'' geometry (see the legend of Figure 1 for details). The deep geometry appears to be most compatible with field evidence [*Van wyk de Vries et al.*, 2001] and has been used for most of the simulations. The shallow geometry is not really compatible with field evidence, but provides an alternative limiting case.

4. Numerical Results

[19] Different models were run with the aim of satisfying the following field constraints: (1) best fit to the northwestern margin, where the avalanche ran up a distal slope approximately perpendicular to the flow axis, (2) best fit to the overall outline of the avalanche deposit, including the frontal lobe, and (3) reproduction of major structures observed on the avalanche deposit, in particular the median escarpment. Only models satisfying reasonably all three constraints are taken as acceptable approximations of reality. All the results presented below were obtained by flow across numerically dry topography.

4.1. Frictional Rheology

[20] Models were run assuming a frictional avalanche rheology (equation (4)) considering three combinations of basal and internal angles of dynamic friction: (1) $\varphi_{bed} \ll \varphi_{int} = 30°$, the static angle of friction for dry granular debris; (2) $\varphi_{bed} \neq 0°$ but $\varphi_{int} = 0°$; and (3) $\varphi_{bed} = \varphi_{int} \neq 0°$. In each case the parameters were varied in multiple simulations. The visual best fit solutions are presented in Figure 6 using the deep collapse geometry.

[21] In the first best fit model (Figures 6a–6d), $\varphi_{int} = 30°$, and a value of $\varphi_{bed} = 1°$ is necessary to reach the northwestern margin of the Monturaqui Basin and to produce the observed runup. A high internal friction may be realistic for Socompa avalanche, which exhibits field evidence for rafting and progressive brittle breakup of SB material on top of a base of shearing, low-friction RIF [*Van wyk de Vries et al.*, 2001]. Bed friction angles higher than 1° result in reduced run-out, and lower ones cause excess spreading. The avalanche first accelerates away from the volcano, attaining a maximum velocity of $\sim$100 m s^{-1}, before reflecting progressively off the northwestern margins of the basin (Figures 6a–6c).

[22] In model 2 (Figures 6e–6h), $\varphi_{bed} \neq 0°$ but $\varphi_{int} = 0°$, so that $k_{actpass} = 1$. This is not necessarily unrealistic because recent experiments show that the ratio of ground-parallel to ground-normal stress is close to unity in laboratory granular flows [*Pouliquen and Forterre*, 2002]. In the absence of internal friction, a slightly higher basal friction angle (2.5°) is now required for best fit. The evolution is close to the previous case, but here waves can be observed reflecting off the western, northern, and northeastern sides of the basin (Figure 6f).

[23] Model 3 (not shown in Figure 6), in which the basal and internal angles are assumed to be the same (best fit for $\sim$2.5°), produces a result very similar to the second model. This is because the values of $k_{actpass}$ are very similar: 1 in model 2 and 1.0038 in model 3.

[24] All three of these frictional models reproduce only very crudely the shape of the real avalanche deposit. A major failing is that, owing to the very low basal friction, the model avalanches flow off any gradients greater than 1 to 2.5° (depending on the case). After reaching their maximum limits, the avalanches drain back into the center of the Monturaqui Basin. Consequently the model deposits each have negligible thickness along their limits of maximum extent, whereas thicknesses of up to 60 m are observed along the margins of the real avalanche [*Wadge et al.*, 1995]. The effect of topographic draining is to cause excess concentration of debris on the floor of the Monturaqui Basin. Models 2 and 3 with low internal friction generate essentially flat-topped ponds that are quite different from the real avalanche. The high angle of internal friction in model 1 permits the preservation of surface topography, but comparison with that of the real avalanche is not favorable. None of the models generate a well defined surface feature resembling the 30- to 60-m-high median escarpment. The frictional models therefore fail in reproducing some first-order morphological characteristics of the real avalanche deposit.

[25] In order to assess the effect of initial slide conditions on our results, we also ran the same models using the shallow collapse geometry (Figure 7). Using the same values of φ_{int} as in Figure 6 (30° and 0°), we find best fit values of φ_{bed} (1° and 3.5°, respectively), deposit shapes, and surface morphologies that are similar to those for the deep geometry. We conclude that the form of the resulting deposit is only weakly dependent on the geometry of the collapse volume, so that our uncertainty of the latter does

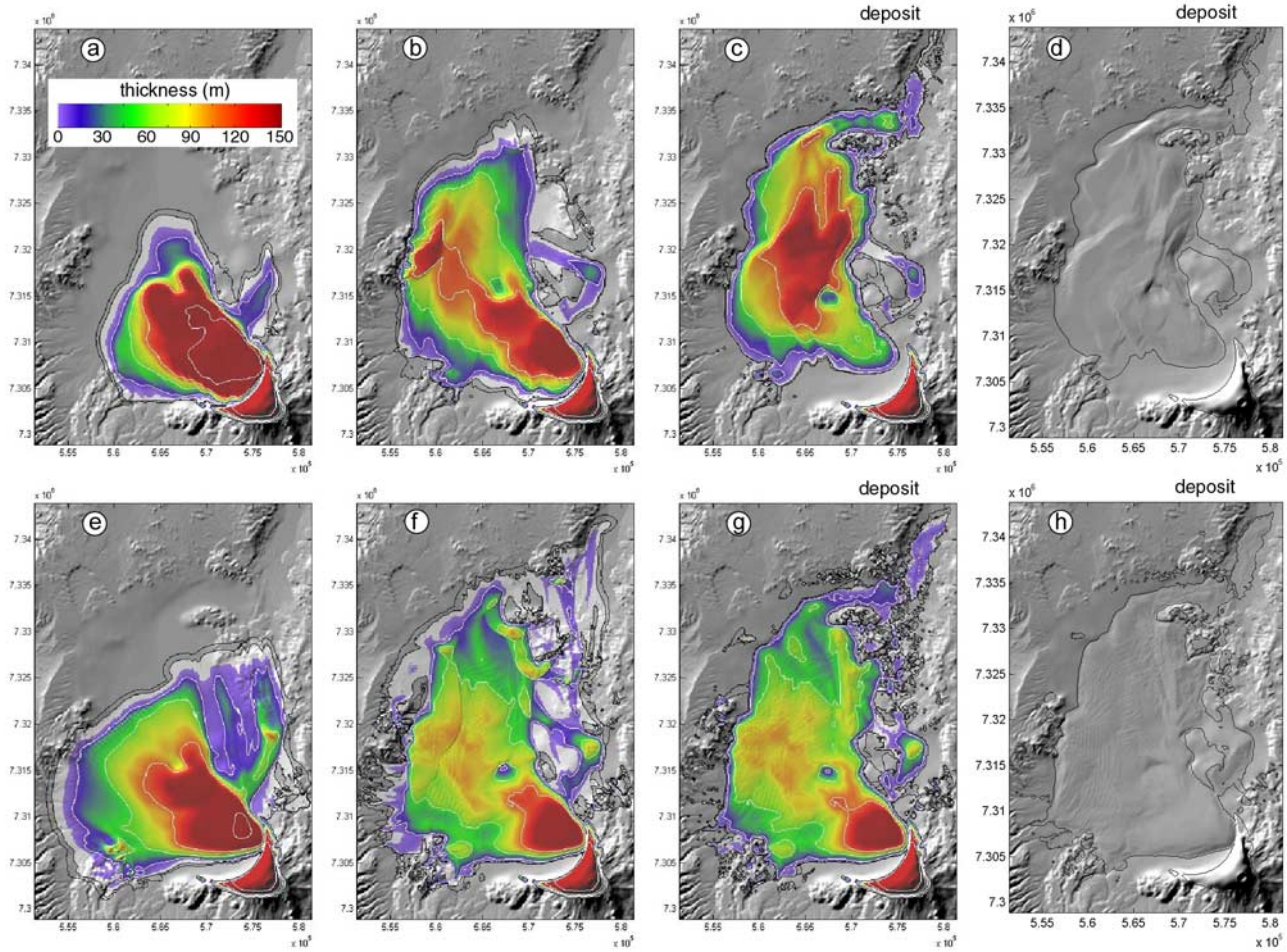

Figure 6. Snapshots of the emplacement of frictional avalanche models 1 and 2 at t = 200 s and t = 400 s, with the corresponding deposits. See text for full discussion. (a–d) Model 1, avalanche with φ_{bed} = 1° and φ_{int} = 30°. (e–h) Model 2, avalanche with φ_{bed} = 2,5° and φ_{int} = 0°. The color scale denotes the thicknesses (m) of the avalanche. Figures 6d and 6h are shaded relief maps of the final deposits. Both models assume an initial deep slide surface and vertical headwall scarp of hemicylindrical shape. Distances are given in meters (UTM).

not invalidate the apparent failure of the simple frictional models used above.

[26] We also allowed φ_{bed} to vary with the Froude number ($\| \mathbf{u} \|/\sqrt{gh}$) of the avalanche, as found for laboratory granular flows [*Pouliquen and Forterre*, 2002] and approximated [*Heinrich et al.*, 2001] by

$$\tan\varphi_{bed} = \tan\varphi_1 + (\tan\varphi_2 - \tan\varphi_1)\exp\left(-\frac{h}{D}\frac{\sqrt{gh}}{\| \mathbf{u} \|}\right) \qquad (7)$$

where φ_1 and φ_2 are limiting angles of friction (with $\varphi_2 > \varphi_1$) and D is approximately an order of magnitude larger than the mean particle size. Here, $k_{actpass}$ is considered to equal 1. Equation (6) in fact gives results comparable to model 2 ($\varphi_{bed} \neq 0°$ and $\varphi_{int} = 0°$) described above (Figures 6e–6h). The effect of velocity is to increase φ_{bed} over and above the static value (φ_1). For the mean value of φ_{bed} necessary to reproduce the observed run-out (2.5°), φ_1 needs to have an even lower value, irrespective of D and φ_2. Once a given part of the avalanche is slowing down, φ_{bed} reverts to φ_1 and, as in the constant-φ_{bed} case, formation of surface topography is prevented by the high fluidity of the material. It is worth noting that values for φ_1, φ_2 and D used by *Heinrich et al.* [2001] to simulate the ~0.005 km^3 26 December 1997 debris avalanche on Montserrat (11°, 25° and 15 m, respectively) result in a run-out for Socompa that is much smaller than that observed. Using a more complete form of equation (7) [*Pouliquen and Forterre*, 2002] gives slightly better results because the friction angle increases just as the avalanche comes to rest, allowing structures to be preserved. However, while this law gives very good results for simulated laboratory experiments, we have not found any combination of the six free parameters that give a good fit in the case of Socompa.

[27] Finally, we note that the well known Voellmy rheological law also fails to satisfy all three constraints at Socompa. The Voellmy law consists of a frictional stress plus a positive stress term proportional to velocity squared [e.g., *Evans et al.*, 2001]. Although entirely empirical, it has been widely used to model snow and rock avalanches in two dimensions. However, in the case of Socompa we find that it fails to generate realistic results for a similar reason as equation (7).

[28] In summary, simple frictional models are able to reproduce the approximate run-out of Socompa avalanche

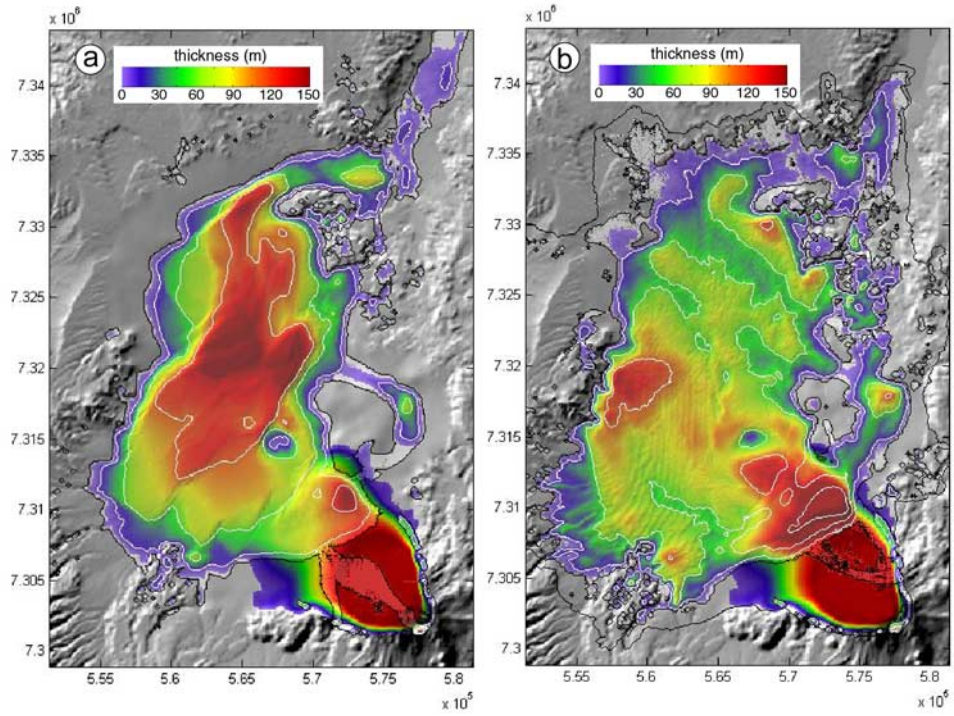

Figure 7. Best fit simulations using a shallow slab-like initial slide geometry, to be compared with the deep geometry shown in Figure 6. The color scale denotes thickness. (a) Avalanche with $\varphi_{int} = 30°$. Visual best fits require approximately the same value of $\varphi_{bed} = 1°$ for this shallow geometry as for a deep geometry. (b) Avalanche with $\varphi_{int} = 0°$. Visual best fits require $\varphi_{bed} = 3.5°$ for this shallow geometry compared with the 2.5° for the deep case in Figure 6.

only if very low values are used for the basal dynamic friction. However, they are unable to generate deposits either with realistic thicknesses on slopes greater than about three degrees, or realistic surface morphology such as the median escarpment. This is because the low basal friction angles necessary for long run-out also result in strong topographic drainback.

4.2. Constant Retarding Stress

[29] In view of the apparent inadequacy of the simple frictional models, we also ran models in which the retarding stress T in equations (2) and (3) was constant ($k_{actpass}$ was taken as unity). This very simple assumption was motivated by the study of *Dade and Huppert* [1998], who found that the field data for a large number of avalanches can be explained by an approximately constant retarding stress.

[30] The models produce surprisingly good fits to the real avalanche provided that T lies in the range 50–100 kPa, depending on the initial slide geometry chosen. Using the deep collapse geometry the overall distribution is reproduced reasonably well with a value of 52 kPa (Figure 8), but with slight excess spreading to the west and east. A 75 kPa resistance produces realistic fits to the western and eastern boundaries, but the northwestern limit is not reached. In the case of a (geologically less realistic) shallow collapse, a resistance of 100 kPa is required, but the frontal lobe is less well produced.

[31] Unlike the frictional rheologies, this law produces a deposit with a well defined edge and leaves a deposit of realistic [*Wadge et al.*, 1995] thickness on all slopes, irrespective of angle. Surface structures on the model deposit are remarkably similar to those of the real avalanche (Figures 8d and 8e). In particular, a well-defined NE-SW trending topographic discontinuity (ME, Figure 8) strongly resembles the median escarpment, both in height (20 to 50 m) and location.

[32] Snapshots of the 52 kPa simulation (Figure 9, colored for velocity, see also Animation 1) provide an explanation for the origin of the median escarpment. The avalanche accelerates down the northern flank of the volcano, attaining a maximum speed of ~100 m s^{-1}. As it runs up the western, then northwestern, slope of the basin, it reflects as three waves (one main one and two smaller ones) that then merge and wash back across the basin. The front of this composite wave then freezes to form the median escarpment. The elevated zone located north of the frozen wave front is also observed on the real avalanche deposit, and in the model represents the peak of the reflected wave (CZ, Figure 8). This area, which in the natural deposit is rich in complex fault structures, experiences a complex history during the simulation, involving (1) initial stretching as the avalanche accelerates away from the volcano (Figure 9a), (2) compression as the material decelerates and accumulates against the northwest margin (Figure 9c), and (3) stretching and shearing during reflection off the northwest margin (Figures 9d and 9e). Other similarities between the simulated and real deposits include the frontal lobe (FL, Figure 8) and the overthickened margins along the northwestern limit of the avalanche that in the model

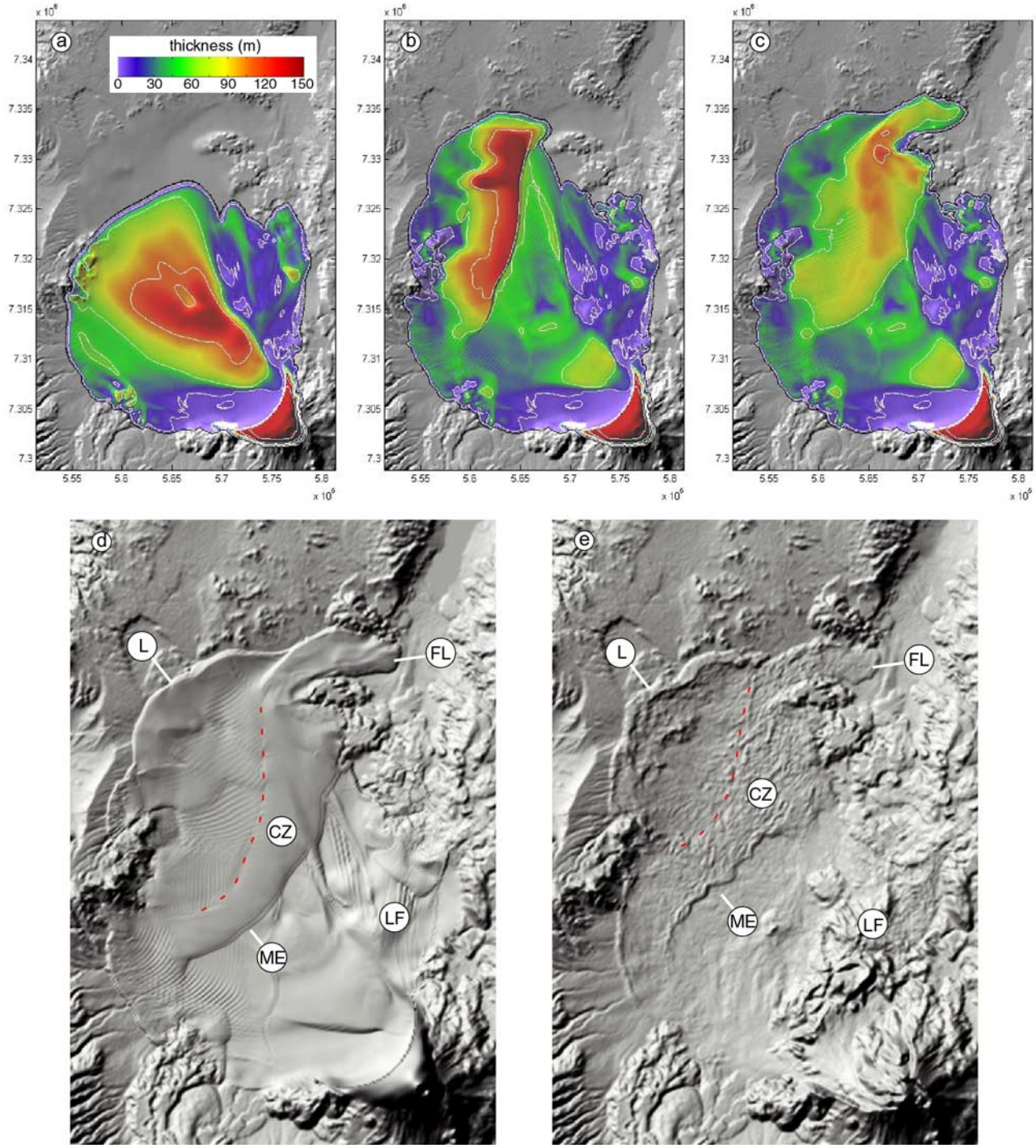

Figure 8. Avalanche evolution using a constant retarding stress T = 52 kPa. The color scale denotes thickness. The initial deep slide geometry is used in this simulation. (a–c) Snapshots at 200 s, 400 s, and 600 s. (d) Shaded relief map of the simulated deposit. (e) Shaded relief map of the real deposit.

form by accumulation, then back slumping, of material during wave reflection.

5. Discussion

[33] We have carried out numerical modeling of the emplacement of Socompa avalanche using the depth-averaged equations for granular flow and a numerical scheme capable of resolving shocks to a high degree of accuracy. The models assume transport of the avalanche on a basal slip layer, as suggested by evidence at Socompa and avalanche deposits. Starting conditions are consistent with field observations. The avalanche is assumed to have traveled as a single mass, with the exception of the Toreva blocks, which in our models are left to slump after avalanche emplacement.

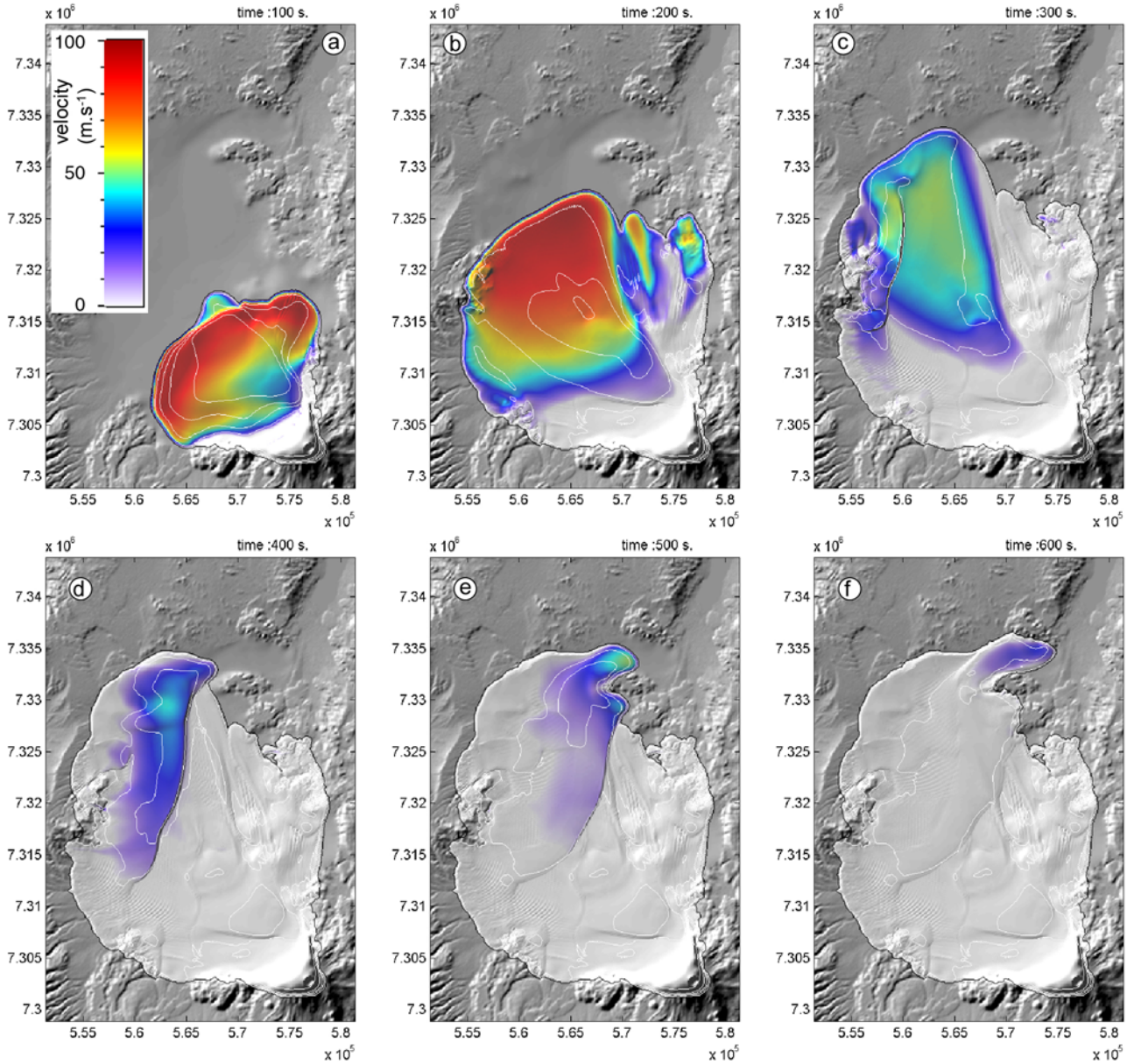

Figure 9. Snapshots every 100 s of the constant stress (52 kPa) simulation of Figure 8, colored according to velocity (m s^{-1}). The reflected wave is particularly clear in these figures, as is the late stage emplacement of the frontal lobe. See Animation 1 for video version.

[34] The high "mobility" of long run-out avalanches is normally interpreted in terms of reduced dynamic friction. The results of our modeling using frictional laws indeed confirm that very low basal friction (3° or less) is required to explain run-out at Socompa, irrespective of the internal value. This agrees approximately with the value of arctan (H/L) for the avalanche, which is 4.3° if the maximum values of H (height drop) and L (horizontal run-out) are used. Simple scaling arguments show that (H/L) $\sim$ tan ϕ, where ϕ is the mean dynamic friction angle during emplacement [e.g., *Pariseau and Voight*, 1979]. The long run-out cannot be explained by gravitational spreading of a very large volume of rock debris with normal friction. Use of values of ϕ in the range 20°–30° typical of dry granular materials results in run-outs that are grossly inferior to that observed. No variation of the geometry of the initial slide mass within geologically realistic limits changes this conclusion.

[35] Many hypothetical mechanisms of friction reduction have been proposed for rock avalanches; see *Davies and McSaveney* [1999], *Legros* [2002], and *Collins and Melosh* [2003] for recent summaries. We focus here on just a few that are relatively well constrained physically. Elevated pore fluid pressure may play an important role in friction reduction in many avalanches by decreasing the effective normal stress at the bed. Fluid pressures close to lithostatic have been measured in debris flows [*Major and Iverson*, 1999] and are likely in wet rock avalanches such as Mount St. Helens [*Voight et al.*, 1983]. Although there was insufficient water in Socompa avalanche for subsequent decantation and mudflow formation, saturation of a thin

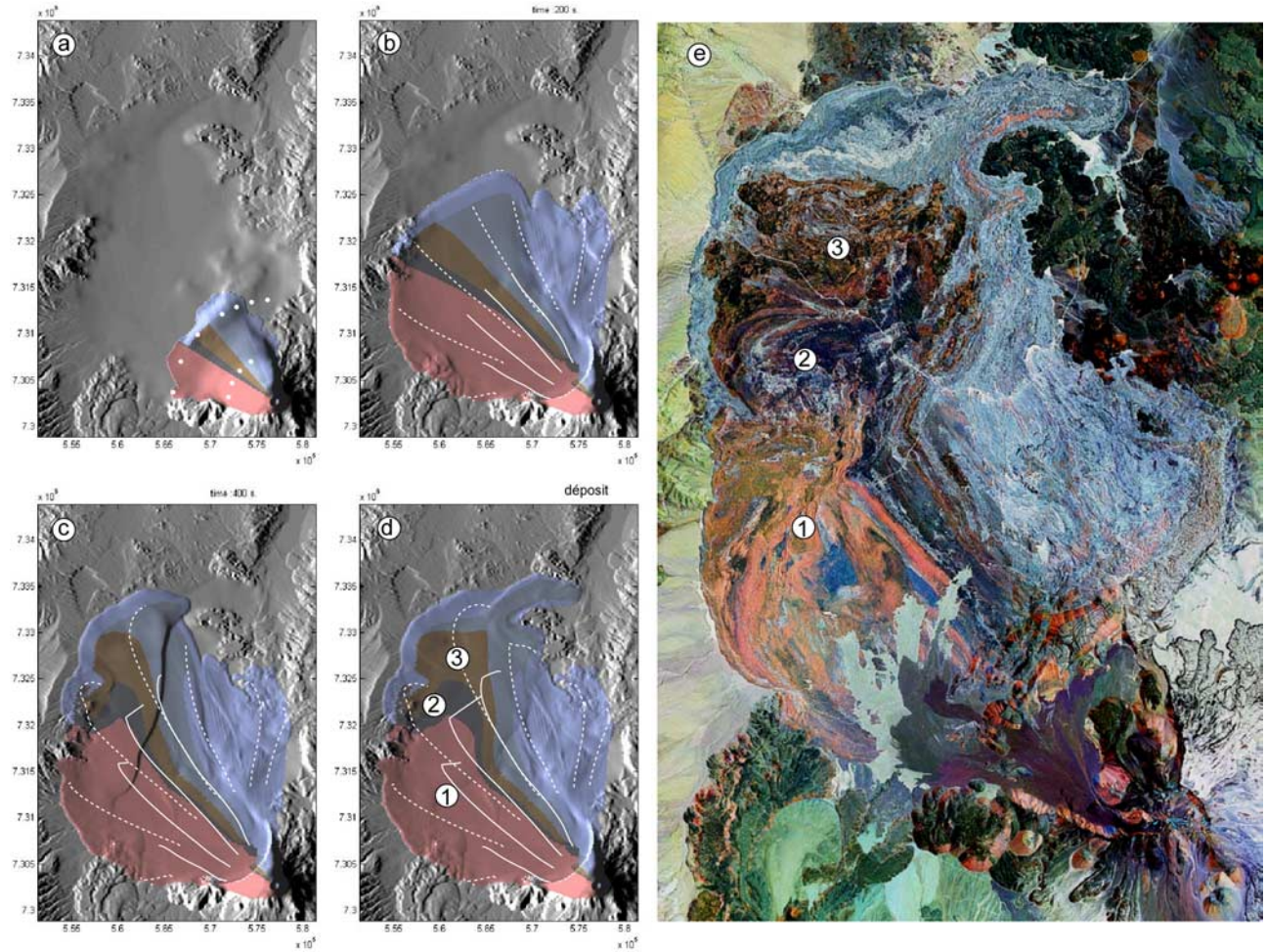

Figure 10. (a–d) Constant stress (52 kPa) simulation of Figures 8 and 9, with surface rocks colored according to lithology. Pink indicates altered Socompa lavas. Grey and brown indicate fresh lavas. Pale blue indicates ignimbrite. Ignimbrite bordering the initial avalanche front to the northeast represents the ignimbrite-cored La Flexura anticline that formed the thrust front of the initial avalanche slump. The distribution of lithology colors has been arbitrarily adjusted but is geologically realistic. White lines show the trajectories of points on the avalanche surface advected by the flow. The snapshots are at (a) $t = 200$ s, (b) 300 s, (c) 400 s and (d) the final deposit. (e) Landsat image. Numbers refer to structures visible on the simulated deposit and on the Landsat (channels 7 4 2) image.

basal layer cannot be excluded. Water could have been derived from the water table beneath the volcano or from the ground surface over which the avalanche traveled. It is possible that a shallow lake or water-saturated sediments existed in the Monturaqui Basin in late postglacial times [*Van wyk de Vries et al.*, 2001]. Pressurized hydrothermal fluids derived from the edifice and/or overridden atmospheric air could also have played a role. Other mechanisms, such as acoustic fluidization [*Melosh*, 1983; *Collins and Melosh*, 2003], mechanical fluidization [*Davies*, 1982], self-lubrication [*Campbell*, 1989; *Campbell et al.*, 1995], or dynamic fragmentation [*Davies and McSaveney*, 1999] may generate velocity dependencies of dynamic friction in the absence of pore fluids.

[36] Although frictional models can account crudely for the long run-out of Socompa avalanche, the low basal friction allows neither realistic deposition on slopes nor preservation of surface morphology like the median escarpment. A better fit is obtained if we simply assume a constant retarding stress in the range 50–100 kPa. We emphasize that we do not consider this to be necessarily an accurate rheological description of the avalanche; constraints on the starting conditions are too crude to enable any unique rheology to be inferred. Avalanches will probably exhibit very complicated time-dependent and spacially variable mechanical behavior [*Iverson and Vallance*, 2001]. Most likely, the condition represents some average value of a retarding stress that varied with time during run-out. However, it is consistent with the finding of *Dade and Huppert* [1998] that an approximately constant stress in the range 10–100 kPa can explain the spreading behavior of rock avalanches with a wide range of volumes. Indeed, it was this observation that led us to try models of this type. Other authors have also concluded that long run-out avalanches exhibit some kind of yield strength by comparing avalanche deposit thicknesses on

Earth and Mars [*McEwen*, 1989; *Shaller*, 1991]. That a constant retarding stress can also capture to a first order the emplacement dynamics of Socompa avalanche lends some support to Dade and Huppert's analysis and raises the question of the origin of this behavior.

[37] We speculate that conditions in the avalanche may have varied with time in such a way that the retarding stress could have remained approximately constant, even though the rheological behavior was fundamentally frictional (i.e., basal shear stress was a product of an apparent friction coefficient times the lithostatic normal stress, modified by a centrifugal term (equation (4)). Consider a hypothetical avalanche in which high fluid pressure is initially present in the basal shear zone, so that motion commences (when the avalanche is thick) with low basal friction. During run-out, pore fluids migrate away from the shear zone, so that friction increases progressively by pressure diffusion at the same time that the avalanche spreads and thins [e.g., *Iverson and Denlinger*, 2001]. The result could be that the basal stress remains approximately constant due to the competing effects of basal friction and flow thickness (i.e., lithostatic normal stress). In the case of a velocity-dependent process such as acoustic fluidization or mechanical fluidization, the basal friction might be reduced at initial high velocity (when the flow is thick), but would increase at lower velocities and approach the value of static friction as the avalanche comes to rest (once the flow had thinned). In both examples, acquisition of high apparent friction as avalanche motion ceased would permit preservation of surface morphology. A third possibility is that basal friction remains negligible throughout run-out (for example due to fluid pressure $\approx$ lithostatic overburden), and that the retarding stress is a cohesive component related to grinding and crushing of particles in the basal layer and/or to rock breakage within the overriding mass as it spreads across the landscape. Stresses of 50–100 kPa indeed lie in the range of cohesive strengths of volcanic materials measured in laboratory experiments [e.g., *Voight et al.*, 2002].

[38] Irrespective of the exact dynamics, our study provides two general constraints on the flow behavior of the avalanche. First, all models investigated require peak velocities of $\sim$100 m s^{-1} to achieve the observed run-out. This is due to the large height differential between the volcano summit and the basin floor (3000 m): one of the largest known for a terrestrial avalanche. Second, the results suggest that the median escarpment is the frozen front of a huge composite wave of rock debris reflected off the western, northwestern, and northern margins of the Monturaqui Basin. Reflection is observed to different extents in all the models run, but it is only in the constant-stress simulation that the wave front is preserved as a high escarpment.

[39] The reflection hypothesis is further investigated in Figures 10a–10d, in which the 52 kPa constant-stress model is rerun with the avalanche surface colored according to rock lithology. The initial distribution of lithology colors is arbitrarily adjusted, but is geologically realistic (B. Van wyk de Vries, oral communication, 2001). White tracer particles track the motion of the avalanche as they are advected along. The distribution of surface lithologies on the resulting numerical deposit closely resembles that evident on the Landsat image of the avalanche (Figure 10e). Moreover the back-reflected trails of the tracer particles mimic the stretching and folding fabrics on the avalanche surface. As the wave is reflected back in the model, material behind the wave drains northwestward to form the frontal lobe. Although certainly not a unique solution, Figure 10 demonstrates that avalanche reflection, as well as generating the median escarpment, can plausibly account for the surface textures observed on the deposit surface for a geologically realistic precollapse distribution of lithologies on and around the volcano.

[40] The topographic reflection of a huge wave of fragmented rock debris off the side of the Monturaqui Basin is a striking illustration of the high fluidity that characterizes long run-out avalanches like Socompa.

Appendix A: Numerical Scheme

[41] We use a Eulerian explicit upwind scheme where scalars (flow thickness h and ground elevation z) are defined and computed at the centers of cells, and vectors (fluxes ϕ and velocities $\mathbf{u} = (u, v)$ at the edges (Figure A1a). Mean values of flow thickness ($\overline{h}$) are computed at the edges of cells, and mean values of velocities, $\overline{\mathbf{u}} = (\overline{u}, \overline{v})$, at the centers of cells.

[42] We use cell edge $(i - 1/2, j)$ to illustrate the main steps of the algorithm (Figure A1b). For each time increment we first compute the source terms of the conservation equations, then the advection terms. The governing equations contain three source term accelerations:

$$\mathbf{a_w} = (-g \sin\theta_z \sin\alpha, -g \cos\theta_z \sin\alpha)$$
$$\mathbf{a_p} = \left(-g\ k_{\text{actpass}} \cos\alpha\ dh/dx, -g\ k_{\text{actpass}} \cos\alpha\ dh/dy\right)$$
$$\mathbf{a}_r = \left(-\frac{\tau}{\rho h}\frac{u}{\|\mathbf{u}\|}, -\frac{\tau}{\rho h}\frac{v}{\|\mathbf{u}\|}\right)$$

where α is the local slope, θ_z is the horizontal azimuth of that slope, and τ is the retarding stress dependant on the rheological law chosen. The algorithm first calculates a fictive velocity due just to terms $\mathbf{a}_w$ and $\mathbf{a}_p$. The retarding acceleration $\mathbf{a}_r$ is then computed in the direction opposed to this fictive velocity. This approach increases the stability of the algorithm and ensures isotropy of the solutions. The value of new velocity (called $\mathbf{s}$) due to the action of source terms is then

$$\mathbf{s}_{i-1/2,j} = \mathbf{u}^{t-dt}_{i-1/2,j} + \left(\mathbf{a}_w + \mathbf{a}_p + \mathbf{a}_r\right)dt$$

[43] The second stage of the algorithm computes the advection terms. The fluxes of mass and momentum are calculated using an upwind scheme. For example, if the x component of $\mathbf{s}_{i-1/2,j}$ is negative, fluxes through the side are computed by

$$\phi^{h}_{i-1/2,j} = s_{i-1/2,j}\ h^{t-dt}_{i,j}\ dy$$
$$\phi^{hu}_{i-1/2,j} = s_{i-1/2,j}\ \overline{u}^{t-dt}_{i,j} h^{t-dt}_{i,j}\ dy$$
$$\phi^{hv}_{i-1/2,j} = s_{i-1/2,j}\ \overline{v}^{t-dt}_{i,j} h^{t-dt}_{i,j}\ dy$$

Note that the superscripts of ϕ indicate the quantity advected: mass h and momentum hu and hv. From these

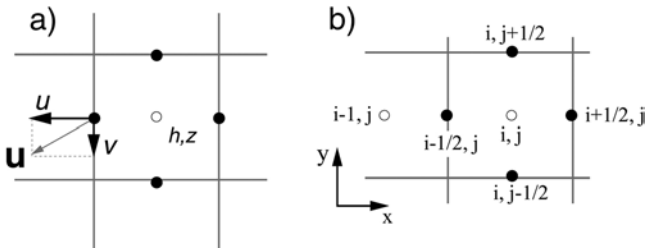

Figure A1. Definitions of (a) scalars, vectors, and (b) cell notation in the numerical scheme.

fluxes, we calculate the new thickness and the new mean velocity at the center of each cell:

$$h^t_{i,j} = h^{t-\mathrm{d}t}_{i,j} + \left(\phi^h_{i-1/2,j} - \phi^h_{i+1/2,j} + \phi^h_{i,j-1/2} - \phi^h_{i,j+1/2}\right)\mathrm{d}t/S$$

$$\overline{u}^t_{i,j} = \frac{\overline{u}^{t-\mathrm{d}t}_{i,j} h^{t-\mathrm{d}t}_{i,j} + \left(\phi^{hu}_{i-1/2,j} - \phi^{hu}_{i+1/2,j} + \phi^{hu}_{i,j-1/2} - \phi^{hu}_{i,j+1/2}\right)\mathrm{d}t/S}{h^t_{i,j}}$$

$$\overline{v}^t_{i,j} = \frac{\overline{v}^{t-\mathrm{d}t}_{i,j} h^{t-\mathrm{d}t}_{i,j} + \left(\phi^{hv}_{i-1/2,j} - \phi^{hv}_{i+1/2,j} + \phi^{hv}_{i,j-1/2} - \phi^{hv}_{i,j+1/2}\right)\mathrm{d}t/S}{h^t_{i,j}}$$

where S is the surface of the cell.

[44] Finally, the x and y components of the new velocities at the edges, modified by advection, are calculated using a second upwind scheme. For example, if $\overline{\mathbf{u}}^t_{i,j}$ and $\overline{\mathbf{u}}^t_{i-1,j}$ are both negative, $\overline{\mathbf{u}}^t_{i,j}$ will modify only the value of $\mathbf{u}^t_{i-1/2,j}$, and the new velocity at time t at edge $(i - 1/2, j)$ is given by

$$\mathbf{u}^t_{i-1/2,j} = \mathbf{s}_{i-1/2,j} + \left(\overline{\mathbf{u}}^t_{i,j} - \overline{\mathbf{u}}^{t-\mathrm{d}t}_{i,j}\right)\frac{h^t_{i,j}}{\overline{h}^{t-\mathrm{d}t}_{i-1/2,j}}$$

[45] **Acknowledgments.** Ben van Wyk de Vries shared his knowledge of Socompa with us and advised us on reconstructing the preavalanche terrain. Thierry Buffard and Stephan Clain helped us test the numerical code. Barry Voight, Geoff Wadge, Herbert Huppert, and two anonymous reviewers provided useful feedback. The work was financed by two research programs of the French CNRS: "Relief de la Terre" and "Aléas et Changements Globaux."

References

Campbell, C. S. (1989), Self-lubrication for long-runout landslides, *J. Geol.*, *97*, 653–665.

Campbell, C. S., P. W. Cleary, and M. Hopkins (1995), Large-scale landslide simulations: Global deformation, velocities, and basal friction, *J. Geophys. Res.*, *100*, 8267–8283.

Collins, G. S., and H. J. Melosh (2003), Acoustic fluidization and the extraordinary mobility of sturzstroms, *J. Geophys. Res.*, *108*(B10), 2473, doi:10.1029/2003JB002465.

Dade, W. B., and H. E. Huppert (1998), Long-runout rockfalls, *Geology*, *26*, 803–806.

Davies, T. R. (1982), Spreading of rock avalanche debris by mechanical fluidization, *Rock Mech.*, *15*, 9–24.

Davies, T. R., and M. J. McSaveney (1999), Runout of dry granular avalanches, *Can. Geotech. J.*, *3*, 313–320.

Denlinger, R. P., and R. M. Iverson (2001), Flow of variably fluidized granular masses across three-dimensional terrain: 2. Numerical predictions and experimental tests, *J. Geophys. Res.*, *106*, 553–566.

Evans, S. G., O. Hungr, and J. J. Clague (2001), Dynamics of the 1984 rock avalanche and associated distal debris flow on Mount Cayley, British Columbia, Canada: Implications for landslide hazard assessment on dissected volcanoes, *Eng. Geol.*, *61*, 29–51.

Francis, P. W., M. Gardeweg, C. F. Ramirez, and D. A. Rothery (1985), Catastrophic debris avalanche deposit of Socompa volcano, northern Chile, *Geology*, *13*, 600–603.

Gray, J. M. N. T., Y.-C. Tai, and S. Noelle (2003), Shock waves, dead zones and particle-free regions in rapid granular free-surface flows, *J. Fluid Mech.*, *91*, 161–181.

Heinrich, P., G. Boudon, J. C. Komorowski, R. S. J. Sparks, R. Herd, and B. Voight (2001), Numerical simulation of the December 1997 debris avalanche in Montserrat, Lesser Antilles, *Geophys. Res. Lett.*, *28*, 2529–2532.

Iverson, R. M. (1997), The physics of debris flows, *Rev. Geophys.*, *35*(3), 245–296.

Iverson, R. M., and R. P. Denlinger (2001), Flow of variably fluidized granular masses across three-dimensional terrain: 1. Coulomb mixture theory, *J. Geophys. Res.*, *106*, 537–552.

Iverson, R. M., and J. W. Vallance (2001), New views of granular mass flows, *Geology*, *29*, 115–118.

Legros, F. (2002), The mobility of long-runout landslides, *Eng. Geol.*, *63*(3–4), 301–331.

Major, J. J., and R. M. Iverson (1999), Debris-flow deposition: Effects of pre-fluid pressure and friction concentration at flow margins, *Geol. Soc. Am. Bull.*, *111*, 1424–1434.

Mangeney, A., P. Heinrich, and R. Roche (2000), Analytical solution for testing debris avalanche numerical models, *Pure Appl. Geophys.*, *157*, 1081–1096.

McEwen, A. S. (1989), Mobility of large rock avalanches; evidence from Valles Marineris, Mars, *Geology*, *17*, 12, 1111–1114.

Melosh, H. J. (1983), Acoustic fluidization, *Am. Sci.*, *71*, 158–165.

Melosh, H. J. (1990), Giant rock avalanches, *Nature*, *348*, 483–484.

Pariseau, W. G., and B. Voight (1979), Rockslides and avalanches: Basic principles, and perspectives in the realm of civil and mining operations, in *Rockslides and Avalanches*, vol. 2, edited by B. Voight, pp. 1–92, Elsevier, New York.

Patra, A. K., et al. (2005), Parallel adaptative numerical simulation of dry avalanches over natural terrain, *J. Volcanol. Geotherm. Res.*, *139*, 1–21.

Pouliquen, O., and Y. Forterre (2002), Friction law for dense granular flows: Application to the motion of a mass down a rough inclined plane, *J. Fluid Mech.*, *453*, 133–151.

Savage, S. B., and K. Hutter (1989), The motion of a finite mass of granular material down a rough incline, *J. Fluid Mech.*, *199*, 177–215.

Savage, S. B., and K. Hutter (1991), The dynamics of avalanches of granular materials from initiation to runout. part I: Analysis, *Acta Mech.*, *86*, 201–223.

Shaller, P. J. (1991), Analysis and implications of large Martian and terrestrial landslides, Ph.D. thesis, 586 pp., Calif. Inst. of Technol., Pasadena.

Takarada, S., T. Ui, and Y. Yamamoto (1999), Depositional features and transportation mechanism of valley-filling Iwasegawa and Kaida debris avalanches, Japan, *Bull. Volcanol.*, *60*, 508–522.

Toro, E. F. (2001), *Shock-Capturing Methods for Free-Surface Shallow Flows*, 309 pp., John Wiley, Hoboken, N.J.

Van Wyk de Vries, B., S. Self, P. W. Francis, and L. Keszthelyi (2001), A gravitational spreading origin for the Socompa debris avalanche, *J. Volcanol. Geotherm. Res.*, *105*, 225–247.

Voight, B., R. Janda, H. Glicken, and P. M. Douglas (1983), Nature and mechanics of the Mount St. Helens rockslide-avalanche of 18 May 1980, *Geotechnique*, *33*, 243–273.

Voight, B., et al. (2002), The 26 December (Boxing Day) 1997 sector collapse and debris avalanche at Soufrière Hills Volcano, Montserrat, in *The Eruption of Soufrière Hills Volcano, Montserrat, From 1995 to 1999*, edited by T. H. Druitt and B. P. Kokelar, *Mem. Geol. Soc. London*, *21*, 363–407.

Wadge, G., P. W. Francis, and C. F. Ramirez (1995), The Socompa collapse and avalanche event, *J. Volcanol. Geotherm. Res.*, *66*, 309–336.

T. H. Druitt and K. Kelfoun, Laboratoire Magmas et Volcans, OPGC, UBP-CNRS-IRD, 5 rue Kessler, F-63038 Clermont-Ferrand, France. (k.kelfoun@opgc.univ-bpclermont.fr)

Landslide-generated tsunamis at Réunion Island

Karim Kelfoun,[1,2,3] Thomas Giachetti,[1,2,3] and Philippe Labazuy[1,2,3]

Received 8 May 2009; revised 31 January 2010; accepted 1 March 2010; published 20 October 2010.

[1] Landslides that occur on oceanic volcanoes can reach the sea and trigger catastrophic tsunamis. Réunion Island has been the location of numerous huge landslides involving tens to hundreds of cubic kilometers of material. We use a new two-fluid (seawater and landslide) numerical model to estimate the wave amplitudes and the propagation of tsunamis associated with landslide events on Réunion Island. A 10 km^3 landslide from the eastern flank of Piton de la Fournaise volcano would lift the water surface by about 150 m where it entered the sea. The wave thus generated would reach Saint-Denis, the capital of Réunion Island (population of about 150,000 people), in only 12 min, with an amplitude of more than 10 m, and would reach Mauritius Island in 18 min. Although Mauritius is located about 175 km from the impact, waves reaching its coast would be greater than those for Réunion Island. This is due to the initial shape of the wave, and its propagation normal to the coast at Mauritius but generally coast-parallel at Réunion Island. A submarine landslide of the coastal shelf of 2 km^3, would trigger a ~40 m high wave that would severely affect the proximal coast in the western part of Réunion Island. For a landslide of the shelf of only 0.5 km^3, waves of about 2 m in amplitude would affect the proximal coast.

Citation: Kelfoun, K., T. Giachetti, and P. Labazuy (2010), Landslide-generated tsunamis at Réunion Island, *J. Geophys. Res.*, *115*, F04012, doi:10.1029/2009JF001381.

1. Introduction

[2] Tsunamis have been extensively studied and have experienced a renewed interest after the dramatic tsunami in Indonesia, on 26 December 2004, which revealed the vulnerability of coastal areas around the Indian Ocean and demonstrated the enormous damage that this type of cataclysm may produce [e.g., *Synolakis et al.*, 2008, and references therein]. The triggering of a tsunami originates either from large-scale earthquakes or from landslides [e.g. *Ward*, 2001; *Harbitz et al.*, 2006; *Fritz et al.*, 2008; *Waythomas et al.*, 2009]. The term "landslide" is used here to describe all types of mass movements mobilizing rocks and soil by gravity. It encompasses the term "debris avalanche" that we use to refer to the sudden and very rapid movement of an incoherent and unsorted mass [*Hoblitt et al.*, 1987] that reaches a long runout (>10 km) and is generally of large volume (>1 km^3).

[3] The hot-spot volcano of Réunion Island is one of the largest volcanic edifices in the world, comparable to the Kilauea volcano (Hawaii) in size and in vertical accumulation of volcanic products (i.e., about 7 km from the oceanic floor). The formation of the island probably began about 5 My ago by the construction of underwater volcanic edifices that have been largely dismantled by huge flank collapses, and later re-covered by the more recent activity [*Oehler et al.*, 2007]. The Alizés volcano, on the submarine southeast part of the island, is one of these proto edifices. The present morphology of the island is essentially due to the evolution of the two more recent volcanic centers, the Piton des Neiges complex and the active volcano of the Piton de la Fournaise. The Piton des Neiges complex lies in the northwest part of the island and was built from about 2 My ago to about 12,000 B.P. Three large depressions, ~10 km wide and up to 2000 m deep (Figure 1), shape its morphology. A large number of outcrops in the depressions show deposits of numerous debris avalanches [*Oehler et al.*, 2007]. The explanation of the formation of the depressions is still in debate: Tectonic activity above underlying rift zones, vertical subsidence of underlying dense rock complexes, and scar formations by debris avalanches have been invoked [*Oehler et al.*, 2004, 2007; *Michon and Saint-Ange*, 2008; and references therein]. The Piton de la Fournaise volcano lies in the southeast part of the island. The present eruptive center is very active (1 to 2 eruptions per year on average). The edifice is cut by horseshoe-shaped structures that are interpreted to have been formed by eastward sliding [*Lénat and Labazuy*, 1990; *Labazuy*, 1996; *Merle and Lénat*, 2003], perhaps coupled with a subsidence component [*Michon*, 2007]. Recent measurements by radar interferometry agree with the eastward sliding hypothesis and show that the more recent

[1]Laboratoire Magmas et Volcans, Université Blaise Pascal, Clermont Université, Clermont-Ferrand, France.
[2]Centre National de la Recherche Scientifique, Clermont-Ferrand, France.
[3]Institut de Recherche pour le Développement, Clermont-Ferrand, France.

Copyright 2010 by the American Geophysical Union.
0148-0227/10/2009JF001381

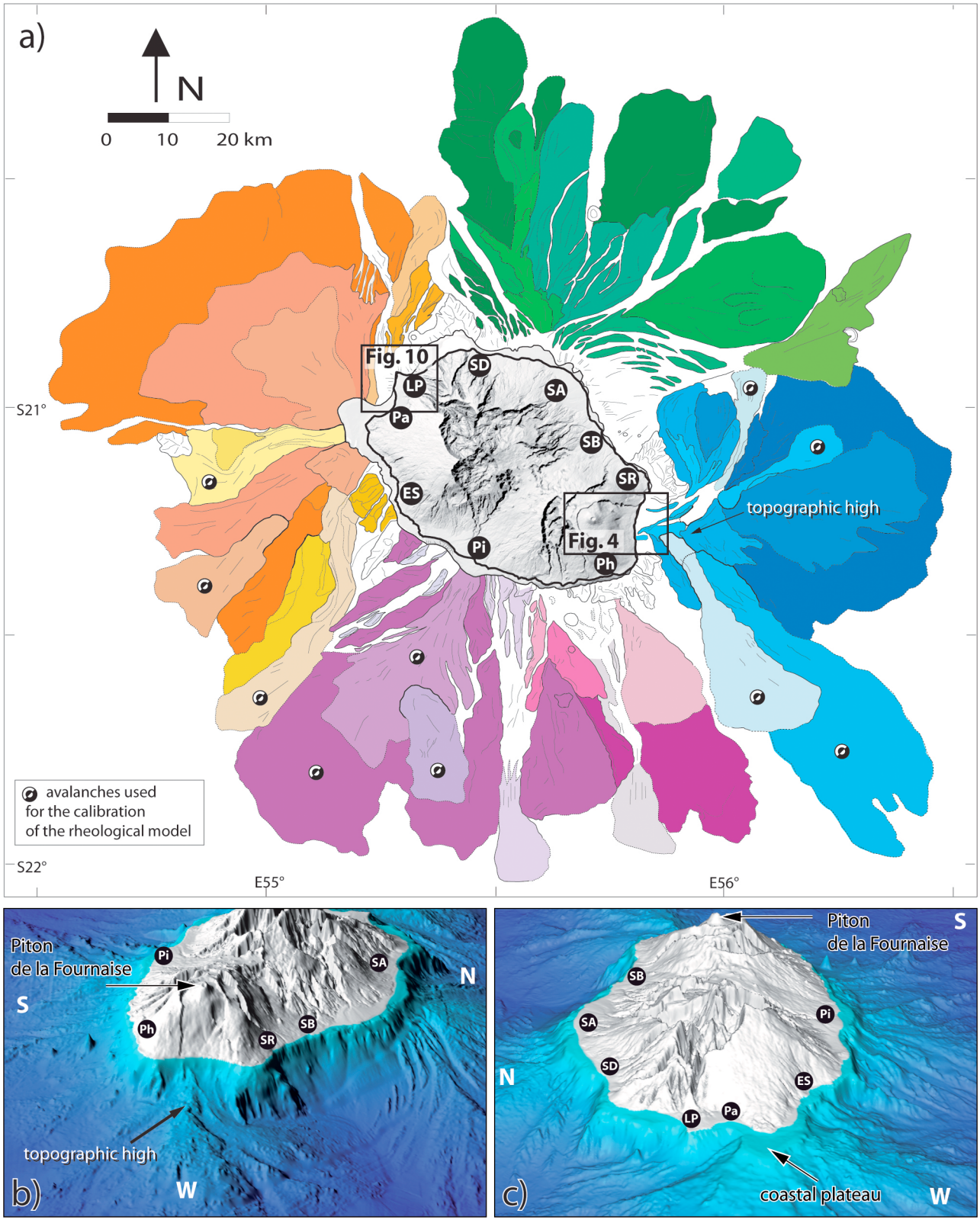

Figure 1. (a) Map of debris avalanche deposits around Réunion Island [after *Oehler et al.*, 2007]. Black circles indicate densely populated regions: SD, St Denis; LP, Le Port; Pa, St Paul; ES, Etang Salé; Pi, St Pierre; Ph, St Philippe; SR, Ste Rose; SB, St Benoît; SA, St André. Frames locate Figures 4 and 10. The coast is marked by the black line and the coastal shelf is the pale gray zone, encircled by a line, between the island and the avalanche deposits. (b and c) 3-D views focused on the frames that show the steep bathymetry of the island.

structure, called the Grand Brûlé, is sliding eastward (J.-L. Froger et al., manuscript in preparation, 2010).

[4] Detailed bathymetric studies around the island have shown the presence of huge landslide submarine deposits. About 50 large-scale debris avalanche deposits in the last 2 My (i.e., one every 40,000 years on average, a recurrence time that corresponds to the last events that affected the recent Piton de la Fournaise volcano), have been mapped (Figure 1) with volumes ranging from less than 1 to more than 1000 km^3 [*Labazuy*, 1996; *Oehler et al.*, 2004, 2007]. The last event would have occurred 4200 years ago [*Bachelery and Mairine, 1990*]. The present resolution of the bathymetry does not allow for the detection of events smaller than 1 km^3. Moreover, small events are easily covered by more recent deposits. It is thus probable that the recurrence time of smaller events is shorter than that deduced for huge events. *Keating and McGuire* [2000] identified not less than 23 processes that contribute to edifice collapse. The origin of the landslides observed at Réunion Island is still being debated, and many processes could be invoked: pressure from the magmatic system, bulging, rock weakness through alteration, basal erosion by the sea, and so on (see *Oehler et al.* [2007] for more details). Large landslides of several cubic kilometers are potentially catastrophic tsunami generators [*Okal and Synolakis*, 2003], and the introduction of the landslides mapped around Réunion Island into the ocean has certainly triggered tsunamis that reached neighboring islands like Mauritius Island (about 175 km from Réunion Island). Some of the rapid changes of sea level (up to 40 meters) observed in this area in the recent past and the presence of several tens of cubic meter reef blocks lying between 3 and 7 m above present sea level [*Camoin et al.*, 2004] might have been brought about by tsunamis originating from debris avalanches.

[5] The majority of the population of Réunion Island and Mauritius live close to the shore. The main cities, infrastructures, industries and airports are also located at low elevation and in close proximity to the sea. We stress that slow sliding of the volcano, as inferred from the horseshoe-shaped structures and from the radar interferometry (*Lénat and Labazuy* [1990]; *Labazuy* [1996]; *Merle and Lénat* [2003]; J.-L. Froger et al., manuscript in preparation, 2010) does not mean that the movement will necessarily evolve into a debris avalanche. We also stress that, to our present knowledge, huge landslides are very rare and that the risk they represent is probably negligible on a human scale. However, it is now recognized that, on a geological timescale, debris avalanches are common events for volcanoes that are on land or are oceanic [*Moore et al.*, 1989; *Normark et al.*, 1993; *Holcomb and Searle*, 1991; *McMurtry et al*., 2004], and we have no idea of the order of magnitude of the wave amplitude that would be related to a landslide at Réunion Island, whatever the volume involved. The evaluation of hazards related to these phenomena and to associated tsunamis has never been performed at Réunion Island.

[6] In the present study, we analyze the consequences of two kinds of potential landslides using a new two-fluid numerical model. We first envisage a landslide of the recent part of the island, on the eastern flank of the Piton de la Fournaise volcano, inside the Grand Brûlé structure. We also discuss the consequences of a smaller submarine landslide that could involve parts of the coastal coral reef shelf in the north western part of the island.

2. Models of Landslide-Generated Tsunamis

[7] Tsunami generation by landslides has already been studied using numerical simulations [e.g., *Heinrich et al.*, 1998; *Tinti et al.*, 1999, 2000, 2006a, 2006b; *Ward and Day*, 2001; *Waythomas and Watts*, 2003; *Waythomas et al.*, 2009; *Geist et al.*, 2009]. All the existing models applied to natural cases are 2-D and are often depth averaged. One difference between the 2-D models of water displacement is the way in which Navier-Stokes equations are approximated. For example, models based on the Boussinesq approximation allow wave dispersion to be taken into account (the velocity of the wave is dependent on its wavelength), whilst the shallow water approximation does not. The former is more accurate for the dynamics of waves whose wavelength is small compared to the water depth. For more details about the methods, the reader should refer to *de Saint-Venant* [1871], *Boussinesq* [1872], *Wei et al.* [1995], *Watts et al.* [2000], *Harbitz et al.* [2006] and *Dutykh and Dias* [2007], among others.

[8] Most of the previous models of landslide-generated tsunamis do not simulate the underwater landslide propagation. Some models implicitly take it into account by imposing the initial shape of the water surface close to the impact [e.g., *Waythomas and Watts*, 2003; *Ioualalen et al.*, 2006]. This approach is motivated by the fact that the initial stages, at the point of impact, are often the most important for the wave generation, especially in the far field. However, it cannot take into account the effects of the dynamic behavior, or the shape of the landslide on waves generated. Other models consider the landslide as blocks moving with an imposed path, shape, and velocity [e.g. *Tinti et al.*, 1999, 2000; *Ward and Day*, 2001; *Haugen et al.*, 2005]. Once again, the behavior of the landslide and its interaction with the underlying topography cannot be predicted. To improve the simulation, other authors [*Fryer et al.*, 2004; *Tinti et al.*, 2006a, 2006b; *Waythomas et al.*, 2006, 2009] simulate the landslide by calculating first the displacement of discrete sliding blocks and, subsequently, the waves generated by these blocks. Other models consider both the landslide and the water as independent fluids. *Jiang and LeBlond* [1992], for example, consider that the landslide behaves as a viscous flow. *Heinrich et al.* [1998] use a more complex numerical approach which integrates a 3-D model close to the landslide-water impact in order to calculate the initial shape of the waves more accurately. Wave propagation is subsequently calculated using a classic 2-D depth-average approach. The best approach would be a full 3-D model with two fluids exhibiting not only density differences, as for *Heinrich et al.* [1998], but also their own rheological behaviors in the whole calculation domain. However, computation times needed for such a code, as well as the lack of well-constrained and defined rheological laws for submarine landslides, are currently limiting factors.

[9] Our model simulates tsunami genesis by two fluids (landslide and water), which interact at each time step. The landslide influences the water; in return, the water influences the landslide. The novelty of our approach is also that

the scheme simulates the morphology and emplacement of the landslide using a rheological law calibrated through the comparison of the numerical results with natural deposits. The numerical model is based on the 2-D depth-average approach, modified to incorporate the 3-D interactions with greater accuracy.

3. Basic Equations and Rheologies

[10] Both the landslides and seawater are simulated using the general shallow water equations of mass conservation and momentum balance. As shown later, the ratio of wave length to water depth of about 10 justifies this approximation [e.g., *Harbitz et al.*, 2006]. The equations were solved using a modified version of the code *VolcFlow* that takes two fluids into account. The scheme is tested and presented in more detail in *Kelfoun and Druitt* [2005] for one "fluid" (debris avalanche), where it successfully reproduces and explains the formation of all the first-order features (extension, thickness, levées, distal lobe, median escarpment) of the Socompa debris avalanche [*Kelfoun and Druitt*, 2005; *Kelfoun et al.*, 2008]. The scheme used (the "double upwind scheme" described by *Kelfoun and Druitt* [2005]) limits the numerical dissipation of the velocity and allows for a good calculation of wave amplitudes even at large distances from the source.

3.1. Simulation of the Landslide

[11] The landslide is simulated by the following set of equations, where equations (1) and (2) are momentum balance and equation (3) is mass conservation:

$$\frac{\partial}{\partial t}(h_a u_x) + \frac{\partial}{\partial x}\left(h_a u_x^2\right) + \frac{\partial}{\partial y}\left(h_a u_x u_y\right) = g h_a \sin\alpha_x - \frac{1}{2} k_{\mathrm{act/pass}} \frac{\partial}{\partial x} \cdot \left(g h_a^2 \cos\alpha\right) + \frac{T_x}{\rho}, \quad (1)$$

$$\frac{\partial}{\partial t}\left(h_a u_y\right) + \frac{\partial}{\partial y}\left(h_a u_y^2\right) + \frac{\partial}{\partial x}\left(h_a u_y u_x\right) = g h_a \sin\alpha_y - \frac{1}{2} k_{\mathrm{act/pass}} \frac{\partial}{\partial y} \cdot \left(g h_a^2 \cos\alpha\right) + \frac{T_y}{\rho}, \quad (2)$$

$$\frac{\partial h_a}{dt} + \frac{\partial}{\partial x}(h_a u_x) + \frac{\partial}{\partial y}\left(h_a u_y\right) = 0. \quad (3)$$

The variable h_a is the landslide thickness, ρ is its relative density equaling the landslide density ρ_a (2000 kg m^{-3}) where the landslide is subaerial and $\rho_a - \rho_w$ where it is submarine, and ρ_w being water density (see annotation list at end of text for variables and units). The variable $\mathbf{u} = (u_x, u_y)$ is the landslide velocity, $k_{\mathrm{act/pass}}$ the earth pressure coefficient (ratio of ground-parallel to ground-normal stress used with basal and internal friction angles [*Iverson and Denlinger*, 2001]) and g is gravity. The ground slope is defined by α; α_x and α_y being the ground slope angles in the xz and yz planes, respectively (x and y are the axes defined along the slope, z is the axis normal to the slope, see *Kelfoun and Druitt* [2005] for details). Other subscripts x and y denote the components of vectors in the x and y directions. The terms on the right-hand side of the equations for momentum balance indicate, from left to right, the effect of the weight, the pressure gradient and the total retarding stress, $\mathbf{T}$.

[12] The main difficulty in modeling landslide propagation is to define the total retarding stress, $\mathbf{T}$. Landslides exhibit a complex behavior that is at present impossible to describe physically in a robust way. Moreover, in the case of submarine landslides, interactions between landslide and water add complexity and probably involve mixing, dilution, water infiltration, and density variations. Little is known about these mechanisms and how to quantify them. It is important, however, to estimate the rheology since it controls the way the landslide is emplaced, which directly influences the characteristics of the tsunami.

[13] $\mathbf{T}$ can be first expressed as being the sum of $\mathbf{T}_{aw}$, the drag between the water and the landslide, and of $\mathbf{T}_{ag}$, the stress between the landslide and the ground:

$$\mathbf{T} = \mathbf{T}_{aw} + \mathbf{T}_{ag}. \quad (4)$$

The expression of $\mathbf{T}_{aw}$ is defined in section 3.3. In order to estimate $\mathbf{T}_{ag}$, we used morphological characteristics of past event deposits (runout, width and width variations, form of the lateral edges and the front), and we tried to reproduce these same characteristics numerically using various rheological laws, and by varying the values of their parameters. Ten cases (Figure 1) have been used from submarine data of *Oehler et al.* [2007], covering more than one order of magnitude in volume. Two main conclusions can be drawn from the results of these simulations:

[14] 1. The Mohr-Coulomb frictional law (simply called frictional below) is often used in granular flow dynamics, this law representing the behavior of deposits at rest and of sand flows in the laboratory. The frictional retarding stress is defined by

$$\mathbf{T}_{ag} = -\rho h\left(g\cos\alpha + \frac{\mathbf{u}^2}{r}\right)\tan\varphi_{bed} \times \frac{\mathbf{u}}{\|\mathbf{u}\|}. \quad (5)$$

The best fit value of the basal friction angle φ_{bed}, obtained by reproducing past events, ranges from 3° to 5°, depending on the effect of the water (see section 3.4). However, if $\mathbf{T}_{ag}$ is considered as a frictional law, it gives unrealistic deposits whatever the value of the friction angles and the expression of $\mathbf{T}_{aw}$ chosen.

[15] 2. Considering $\mathbf{T}_{ag}$ as a constant retarding stress (i.e., constant whatever the thickness or velocity of the landslide) generally gives better results. It allows for an approximate reproduction of the extension, the thickness on all slopes and some morphological features (levées, front) of natural deposits. Although difficult to explain from a physical point of view, a similar conclusion has been obtained for subaerial debris avalanches [e.g., *Dade and Huppert*, 1998; *Kelfoun and Druitt*, 2005; *Kelfoun et al.*, 2008]. Values of the best fit constant retarding stress describing the interactions between the ground and the landslide depend on the stress exerted by the water. If the latter is considered as zero, $\mathbf{T}_{ag}$ ranges from 20 to 100 kPa, with a mean value of about 50 kPa. For a high retarding stress of the water (C_f = 2, C_s = 0.01, see section 3.3), $\mathbf{T}_{ag}$ ranges between 10 and 50 kPa, with a mean value of about 20 kPa. It is, however, impossible to state if these ranges reflect variations of past event rheologies or if they are related to the high uncertainties

of the reconstructions: submarine mapping, prelandslide topography, estimation of sliding volumes, and so on.

3.2. Simulation of the Water

[16] The water is simulated using a similar set of equations to those for the landslide:

$$\frac{\partial}{\partial t}(h_w v_x) + \frac{\partial}{\partial x}\left(h_w v_x^2\right) + \frac{\partial}{\partial y}(h_w v_x v_y) = g h_w \sin\beta_x - \frac{1}{2}\frac{\partial}{\partial x}\left(g h_w^2 \cos\beta\right) + \frac{R_x}{\rho_w} - 3\frac{\mu_w}{\rho_w h_w} v_x, \quad (6)$$

$$\frac{\partial}{\partial t}(h_w v_y) + \frac{\partial}{\partial y}\left(h_w v_y^2\right) + \frac{\partial}{\partial x}(h_w v_y v_x) = g h_w \sin\beta_y - \frac{1}{2}\frac{\partial}{\partial y}\left(g h_w^2 \cos\beta\right) + \frac{R_y}{\rho_w} - 3\frac{\mu_w}{\rho_w h_w} v_y, \quad (7)$$

$$\frac{\partial h_w}{dt} + \frac{\partial}{\partial x}(h_w v_x) + \frac{\partial}{\partial y}(h_w v_y) = 0, \quad (8)$$

where β is the slope of the ocean bottom formed by the initial topography plus the landslide thickness calculated by equation (3). The water viscosity, μ_w, is fixed at 1.14×10^{-3} Pa s and ρ_w is water density, fixed at 1000 kg m^{-3}. The terms on the right-hand side of the equations for momentum balance indicate, from left to right, the effect of the weight, the pressure gradient, the drag between water and landslide and the drag between water and the ocean bottom. To permit free propagation of waves, open boundaries are defined at the border of the domain by calculating the water velocity normal to the border, v_b, from the water thickness h_w:

$$v_b = 2(c_1 - c_0), \quad (9)$$

where $c_1 = \sqrt{g h_w}$ and c_0 equals the value of c_1 at $t = 0$.

[17] The water is able to interact with the bathymetry/topography and to flood onto the land. However, due to the shallow-water approach, waves breaking and other complex second-order 3D effects that occur at the shore are not taken into account. Sediment erosion and transport are also ignored. Since the main goal of this paper is to calculate an order of magnitude for the time of arrival, height and inland penetration of the waves, it is not essential to constrain these second-order effects.

3.3. Interaction Between Landslide and Water

[18] The two sets of equations (equations (1)–(3) and (6)–(8)) are calculated at the same time step, and several assumptions rule the interactions between the two "fluids." The aim of our assumptions is to simplify the problem and to avoid the use of too many unconstrained parameters.

[19] First, we assume that no mixing between the landslide and ocean occurs and that the densities of the two fluids remain constant over time. This assumption precludes mixing between the landslide and the seawater, which could result in turbidity currents and affect the wave dynamics. It is supported by the observations of *Oehler et al.* [2007], who describe the levées and front of the deposits as being more compatible with a homogenous flow emplacement, as for subaerial debris avalanches, than with turbidity deposits. Possibly the emplacement time is too short to allow water to penetrate deep into the landslide. In our model, the landslide is affected by the water in two ways. First, the reduced density of the landslide ($\rho_a - \rho_w$) is used where the landslide is underwater, with density ρ_a being used above the water. This reduces the driving forces and thus the velocity of the submarine flow. The second effect is related to $\mathbf{T}_{aw}$, the drag exerted by the water on the landslide. It is considered by some of the previous authors [e.g., *Tinti et al.*, 2006a] to depend on the surface of the landslide in contact with the water and on the square of the relative velocity of the landslide with respect to the fluid. For use in equations (1) and (2), the equations of *Tinti et al.* [2006a] have been rewritten as follows:

$$\mathbf{T}_{aw} = -\frac{1}{2}\rho\left(\tan\beta_{\mathrm{m}} C_{\mathrm{f}} + \frac{1}{\cos\beta_n} C_{\mathrm{s}}\right) \| \mathbf{u} - \mathbf{v} \| (\mathbf{u} - \mathbf{v}) \quad (10)$$

where β_n is the angle formed by the intersections of both the surface of the landslide and the surface of the bathymetry with a plane normal to the displacement. The angle β_m is the slope of the landslide surface in the direction of the relative displacement and is given by

$$\tan\beta_m = -\nabla h_a \frac{\mathbf{u} - \mathbf{v}}{\| \mathbf{u} - \mathbf{v} \|} \quad (11)$$

[20] The coefficients C_f and C_s fix the drag on the surface of the landslide, respectively, normal and parallel to the displacement. C_f and C_s both equal 0 outside the water. Underwater, C_s and C_f are greater than 0 where the scalar product of the relative velocity $\mathbf{u} - \mathbf{v}$ by the outward normal vector $\mathbf{I}$ of the landslide surface is positive (i.e., where the landslide faces the direction of propagation), and is fixed to 0 elsewhere [*Tinti et al.*, 2006a]. Following previous studies [e.g., *Ward and Day*, 2001; *Tinti et al.*, 2006a; *Jiang and LeBlond*, 1992], we assume that the water depth has no influence on the underlying landslide dynamics.

[21] The water is displaced by the landslide in two ways. It can be accelerated by the displacement of the landslide (equations (6) and (7)). $\mathbf{R}$ thus equals $-\mathbf{T}_{aw}$ (equations (1) and (2)). This allows the landslide to "push" the water which is close to the shore. The transfer of momentum has a small effect on the velocity of the water at depth, where the mass of the landslide is small relative to the mass of the surrounding ocean. The second effect is due to the elevation of the base of the water by the landslide, which is expressed by a change of the basal slope β in equations (6) and (7). A direct combination of the two sets of equations, however, overestimates the amplitude of the waves generated. At a given point, a displacement of the landslide along the ocean floor induces a variation of its thickness h_a and thus a vertical displacement of the base of the water. This would induce the same variation of the sea level z_w, $\frac{\partial z_w}{\partial t} = \frac{\partial h_a}{\partial t}$ because an elevation of the base from equation (3) does not act directly on the water thickness of equations (6)–(8) but only lifts the water column (strictly speaking, it changes the basal slope, which has an equivalent effect). This is far from what is observed in reality. If, for example, a solid is introduced into a tank of water, the overall water surface is lifted by less than the height of the solid, and over a large

Table 1. Scenarios Used for the Simulation of the Landslide From the Active Edifice

Scenario	Volume (km^3)	Type of Collapse	Model	Value	C_s	C_f	Momentum Transfer to Water
1	10	Single	Constant stress	20 kPa	0.01	2	No
2	10	Single	Constant stress	20 kPa	0.01	2	Yes
3	10	Single	Constant stress	35 kPa	0.005	1	No
4	10	Single	Constant stress	50 kPa	0	0	No
5	10	Single	Frictional	5°	0	0	No
6	10	Single	Frictional	3°	0.01	2	No
7	25	Single	Constant stress	20 kPa	0.01	2	No
8	10	Retrogressive	Constant stress	20 kPa	0.01	2	No

surrounding area rather than just above the solid. This elevation is not related to a rapid flow of water initially lifted above the solid but is an immediate consequence of the onset of the impact.

[22] This problem has already been discussed by several authors [e.g., *Sander and Hutter*, 1996; *Heinrich et al.*, 1998], and this is why *Heinrich et al.* [1998] used a full 3-D calculation for where the landslide impacts the water. Other authors used an attenuation coefficient, $0 < \chi < 1$, which depends on a characteristic length of the slide and reduces the wave amplitude [e.g., *Tinti et al.*, 2000]. The elevation of the sea surface is then calculated by

$$\frac{\partial z_w}{\partial t} = \chi \frac{\partial h_a}{\partial t} \tag{12}$$

However, if the characteristic length can be defined for a landslide when it is considered as a nondeformable block, it is much more difficult to define if this landslide spreads with time, changes in shape and presents strong velocity variations. Another problem is that equation (12) implies that the water column thickness is artificially reduced and that mass conservation is not respected. Finally, for a rigid block, the water is only lifted above it and not over a large area surrounding the impact.

[23] To address this problem, we have chosen to calculate the surface elevation induced by a sudden displacement at the ground using a 3-D model. Then we have determined the 2-D mathematical expression of this surface elevation by fitting to the 3-D results. This avoids the prohibitive computational time of a 3-D approach along the 50 km long interaction between the water and the landslide.

[24] In the 3-D model, the water is considered as being incompressible and surface elevation is calculated by mass conservation:

$$\nabla \mathbf{v} = 0 \tag{13}$$

Here only, the water velocity is defined in three dimensions: $\mathbf{v} = (v_x, v_y, v_z)$. This 3-D model reproduces a sudden elevation of the water all around a basal displacement rather than just above it (Figure 2).

[25] If the bottom is a horizontal plane, the sudden elevation of the water calculated by solving equation (13) is fitted by

$$\Delta z = c \times \frac{V}{d^2} \times e^{-\ln(\pi) \times d/h_w}, \tag{14}$$

where V is the volume displaced vertically at the bottom, c is a parameter that allows mass conservation in order that $\int_{x=-\infty}^{\infty} \int_{y=-\infty}^{\infty} \Delta z dx dy = V$, and $d = \sqrt{x^2 + y^2 + h_w^2}$ is the distance between a given point (x, y, h_w) of the water surface and the point at the bottom ($x = 0$, $y = 0$, $z = 0$) where volume change occurs. Δz is assumed to be equal zero where there is no water. Figure 2a indicates crosscut profiles of the elevation obtained by 3-D simulations and by equation (14) for a bottom located at $h_w = 25$, 50, and 100 m beneath the sea surface. The uplift is 1 m and affects a 1 m^2 surface (volume displaced is 1 m^3).

[26] Equation (14) fits exactly for a horizontal base and is thus well suited to a landslide on the ocean floor. It is less good in the vicinity of steep slopes and close to the shore, but it still fits correctly (Figure 3b). It should be noted, therefore, that without correction the uplift of the base would affect 1 m^2 of the water surface and would lift it 1 m in amplitude. Also note that the 45° slope used in the simulation is an extreme case as the underwater slopes around Réunion Island are less than 20°.

[27] For a change of volume locally, the difference between the direct coupling and correction appears to be very great (four to five orders of magnitude, Figure 2). However, this effect is much more limited for a large landslide and where the interactions are long term because stacking all the surface elevations generated by each point of the landslide may give a similar thickness at the center of the landslide to that with no correction.

3.4. Numerical Resolution of Water/Landslide Interactions

[28] Numerically, at each time step dt, the displacement of the landslide is first computed (equations (1–3)), taking into account the water velocity of the previous time step, which is chosen to be small enough to consider velocity variations during the time step as negligible (<0.1 s). The effect of each variation of the landslide thickness, dh_a, on the water surface elevation is then calculated using equation (14) to reduce wave amplitude taking more accurately into account the 3D effects. Lastly, the water dynamics are computed by equations (6–8) using, if needed, the acceleration caused by the stress of the landslide and computed by equation (10).

3.5. Tests of Sensitivity

[29] The rheology of the landslide and the stress caused by the water are not accurately constrained. To test the sensitivity of results on assumption done, we have performed simulations varying the following parameters (Table 1).

[30] Simulations were done with C_f and C_s fixed to 2 and 0.01, respectively, following *Tinti et al.* [2006a]. Other simulations were done with the endmember case, where the

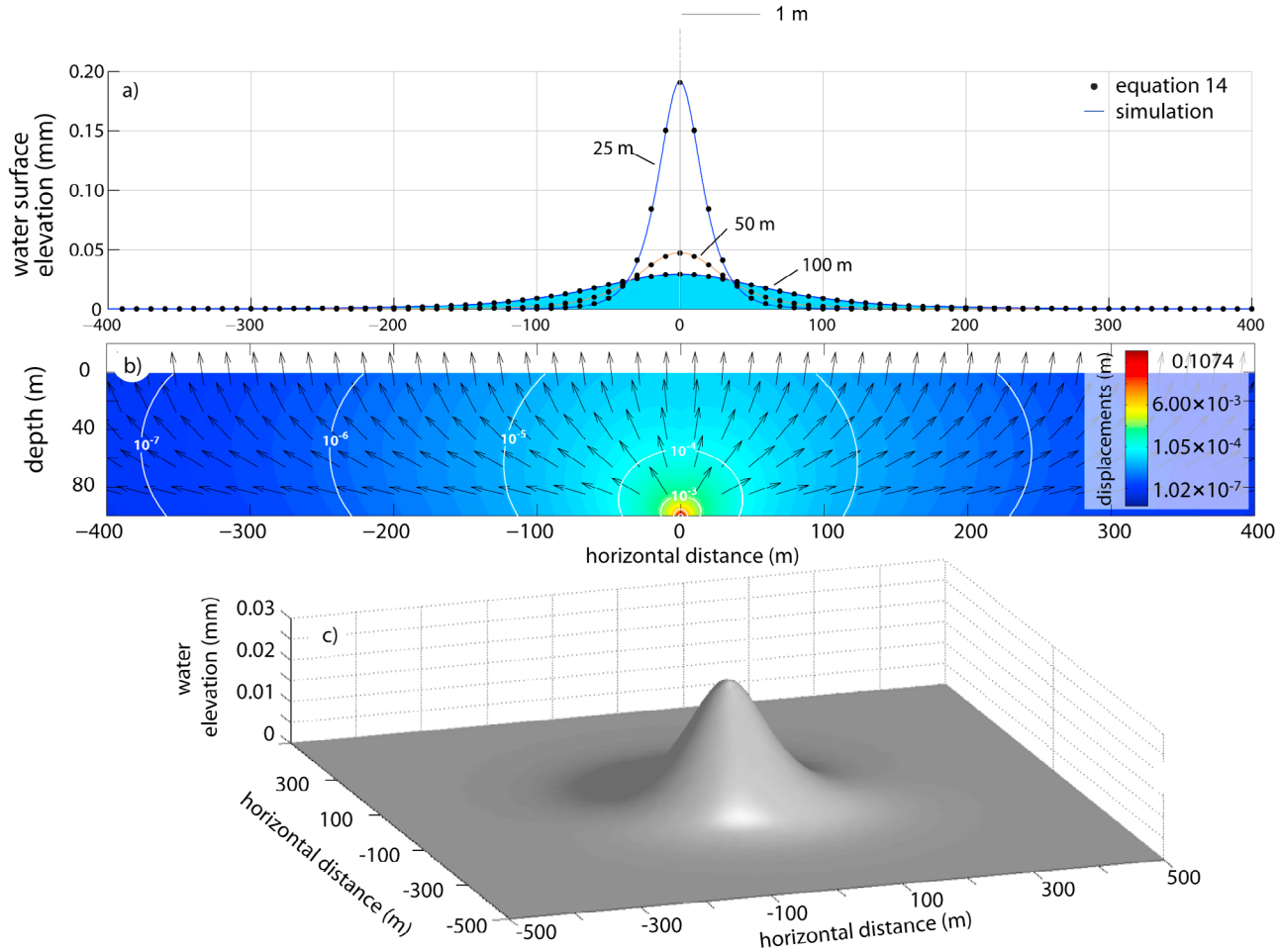

Figure 2. (a) Solid lines: 3-D calculation of the elevation of water surface induced by a sudden displacement at the bottom for a flat topography. The volume displaced is 1 m^3 and water depth is, respectively, 25, 50, and 100 m (the colored surface corresponds to the elevations obtained in Figure 2b). Points are calculated by equation (14). (b) 2-D vertical slice of the 3-D displacements. The water depth is 100 m. Arrow lengths are constant to allow visualization of small movements. Without 3-D calculation, a displaced volume of 1 m^3 with the 1 m × 1 m mesh size used would induce a very localized surface elevation of 1 m (out of the graphic, central black line). (c) 3-D view of the surface elevation.

water does not exert any stress on the landslide (C_f and C_s both fixed to 0, the reduced density only affecting the landslide velocity). We also simulated cases where coefficients C_f and C_s were fixed to 1 and 0.005, respectively. Depending on the values chosen, a mean value of $\mathbf{T}_{ag}$ = 20, 50, and 35 kPa, respectively, allowed the landslide runouts to be reproduced using a constant retarding stress rheology.

[31] We also performed simulations with the commonly used Mohr-Coulomb rheology. The best fit value of the basal friction angle, φ_{bed}, obtained by reproducing past events, is about 5° if C_f and C_s both equal 0, and 3° if they equal 2 and 0.01, respectively. Since the internal angle has a minor influence on the simulations, we only present here results obtained with internal isotropic stresses (i.e., no internal friction angle, $k_{act/pass}$ = 1, equations (1) and (2)).

[32] Finally, we performed simulations in which the energy lost by the landslide is entirely transferred, as momentum, to the water: $\mathbf{R} = -\mathbf{T}$. The stress $\mathbf{R}$ has also been artificially fixed to 0 to take into account that all the mechanical energy is transformed into heat in the water (50% to nearly 100% can be lost according to *Ruff* [2003]).

[33] Other variations related to specific scenarios are discussed below.

4. Scenarios Envisaged

4.1. Landslide From the Active Edifice

[34] We first envisage a landslide on the eastern flank of the Piton de la Fournaise volcano (Figure 4). Following previous studies [*Labazuy*, 1991; *Merle and Lénat*, 2003], the geometry of the sliding zone has been defined from morphological evidence: ramparts and headwalls of the *Grand Brûlé* caldera to the north and south, with an underwater break in slope to the east. The base of the sliding zone has been defined from a geothermal borehole that shows the existence of gliding interfaces [*Rançon*, 1990; *Labazuy*, 1991]. Two landslide volumes were tested, the western boundary of the collapse being defined respectively

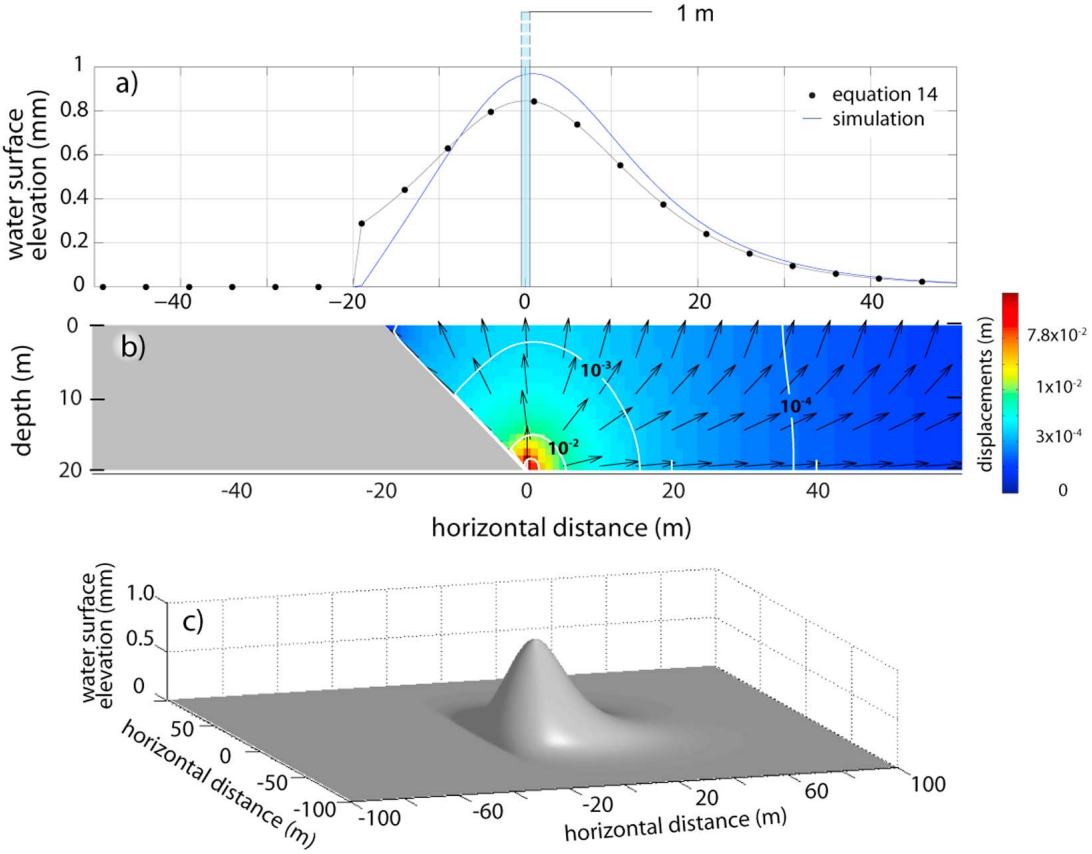

Figure 3. (a) Surface elevation obtained by 3-D modeling (line) and equation (14) (points) for a volume of 1 m^3 displaced at the foot of a 45° talus. (b) The water depth is 20 m. Fit is not exact but is clearly better than the 1 m column obtained without correction. (c) 3-D view of the surface elevation.

by (1) the break in slope of the Grandes Pentes and (2) the summit crater. The volumes of these areas are, respectively, 10 and 25 km^3, which is in the order of magnitude of the more recent debris avalanche deposits mapped by *Oehler et al.* [2007]. For each case, the landslide was simulated both as a single event and as three retrogressive landslides of the same volume (3.3 and 8.3 km^3, each landslide being separated by 1 min).

[35] Height scenarios are presented in Table 1 for the landslide of the active edifice. The varying parameters are the volume of the landslide, the type of landslide (single event, retrogressive), the rheological model of the landslide (frictional, constant), the value of the rheological parameters, the value of the drag of the water and whether or not the energy lost by the landslide through water drag is dissipated as heat or fully transferred to the water.

4.2. Submarine Landslide of the Coastal Shelf

[36] In the second scenario, we envisage what would occur in the case of a landslide of the coastal shelf, corresponding to the transition between subaerial and submarine environments. The shelf is well developed in the northwestern region, adjacent to the St Paul (Figure 1) area, where it is bounded by 250 m high cliffs. Here the coastal shelf is composed of a coral reef plateau built on old, unstable landslide deposits and river fan sediments. Its boundaries probably correspond to a paleo coastline related to eustatic sea level variations [*Oehler et al.*, 2007]. Large landslides of the shelf, several cubic kilometers in volume, were mapped by *Oehler et al.* [2007]. Smaller landslides probably occurred too, but, because of their small volumes, they are easily eroded and/or covered by other deposits, and both their detection and estimation of recurrence times are difficult since the imagery data available (sonar, seismic) are not accurate enough to observe their form in detail. It is thus difficult to check if the rheology obtained for larger landslides is suitable for the simulation of smaller events (<1 km^3), but we assume here that their rheologies are similar. However, as for landslides of the active edifice, other rheologies were tested.

[37] We tested three examples of landslides, one with a large volume of 2 km^3 to the west of the shelf, and two with smaller volumes of 0.5 and 0.1 km^3 to the north.

4.3. Bathymetry and Topography Used

[38] The digital elevation model (DEM) was obtained by combining our data of the local bathymetry, ETOPO2 data for the regional bathymetry and Shuttle Radar Topography Mission (STRM) data for the aerial topography. The resolution is 200 m × 200 m, the regional simulations being

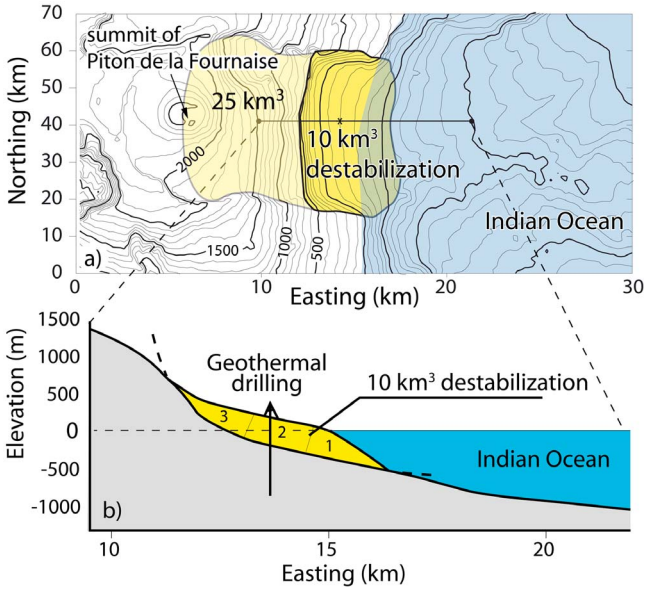

Figure 4. (a) Location of the simulated 10 and 25 km^3 landslides (the 25 km^3 landslide includes all the 10 km^3 area). The location of the figure is represented on Figure 1. (b) East/west outcrop showing the location of the geothermal drilling (* on Figure 4a). The numbers identify the three blocks used for a retrogressive scenario.

performed on a 400 m × 400 m resolution DEM in order to limit calculation time.

5. Results

5.1. Landslide from the Active Edifice—Scenario 1

[39] Numerical results presented here were calculated using a volume of 10 km^3, in a single-event landslide, values of $C_s = 0.01$ and $C_f = 2$ and a constant retarding stress rheology of 20 kPa (scenario 1, Table 1). Other results are presented in the following section.

[40] The simulated landslide of scenario 1 spreads eastwards and then splits up into two major lobes due to a topographic high facing the scar (Figure 5a). The northern lobe then divides into three lobes that follow the bathymetric depressions. The landslide reaches a maximum distance of ~45 km to the northeast at a mean velocity of ~45 m s^{-1}. Each lobe of the deposit has a mean thickness of between 10 to 20 m, the thickness increasing downstream from 10 m at the scar to 60 m close to the front.

[41] Where the landslide enters the sea, it pushes and lifts the water surface 150 m above the initial sea level. A giant wave then propagates, hugging the shoreline of Réunion Island (Figure 6). It severely affects the east coast, with wave amplitudes that could exceed 100 m. The amplitude (Figure 7) remains high (>50 m) along the northeast and southeast coasts of the island, within sight of the location of the wave formation, locally reaching 100 m where waves reflected by the bathymetry superimpose themselves.

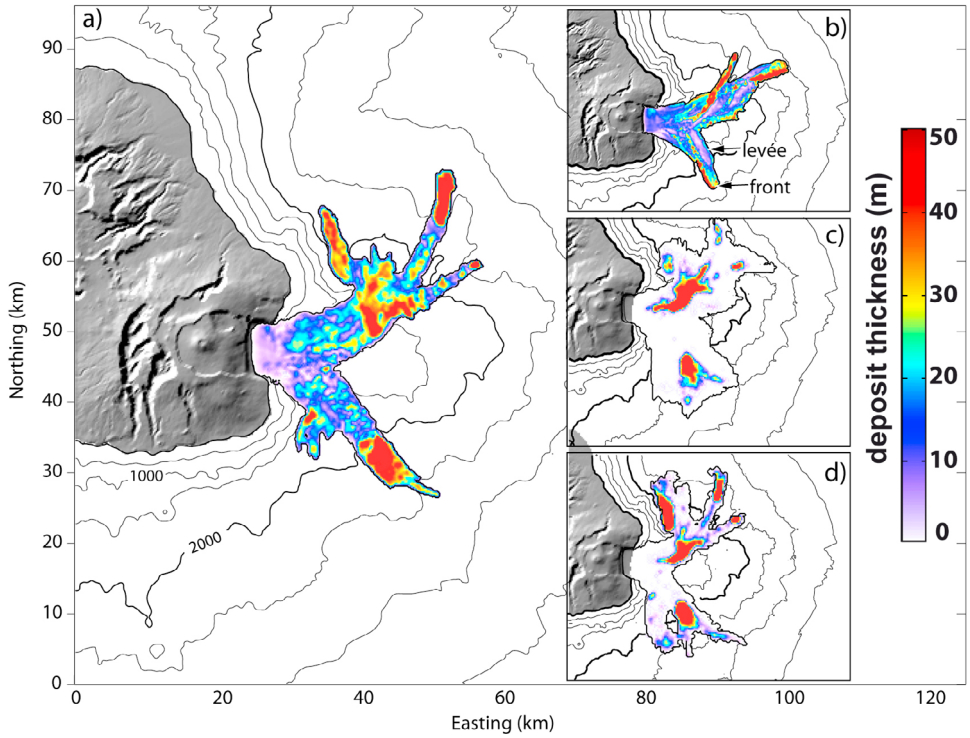

Figure 5. Thickness of computed landslide deposits obtained for scenarios (a) 1, (b) 4, (c) 5, and (d) 6. The pure constant retarding stress rheology in Figure 5b forms levées and well-defined fronts as observed on natural deposits. The frictional rheology forms very spread out deposits with material accumulated as piles. Adding a water drag and shown in Figure 5a and 5d conserves the characteristics of both rheologies even if the differences are less.

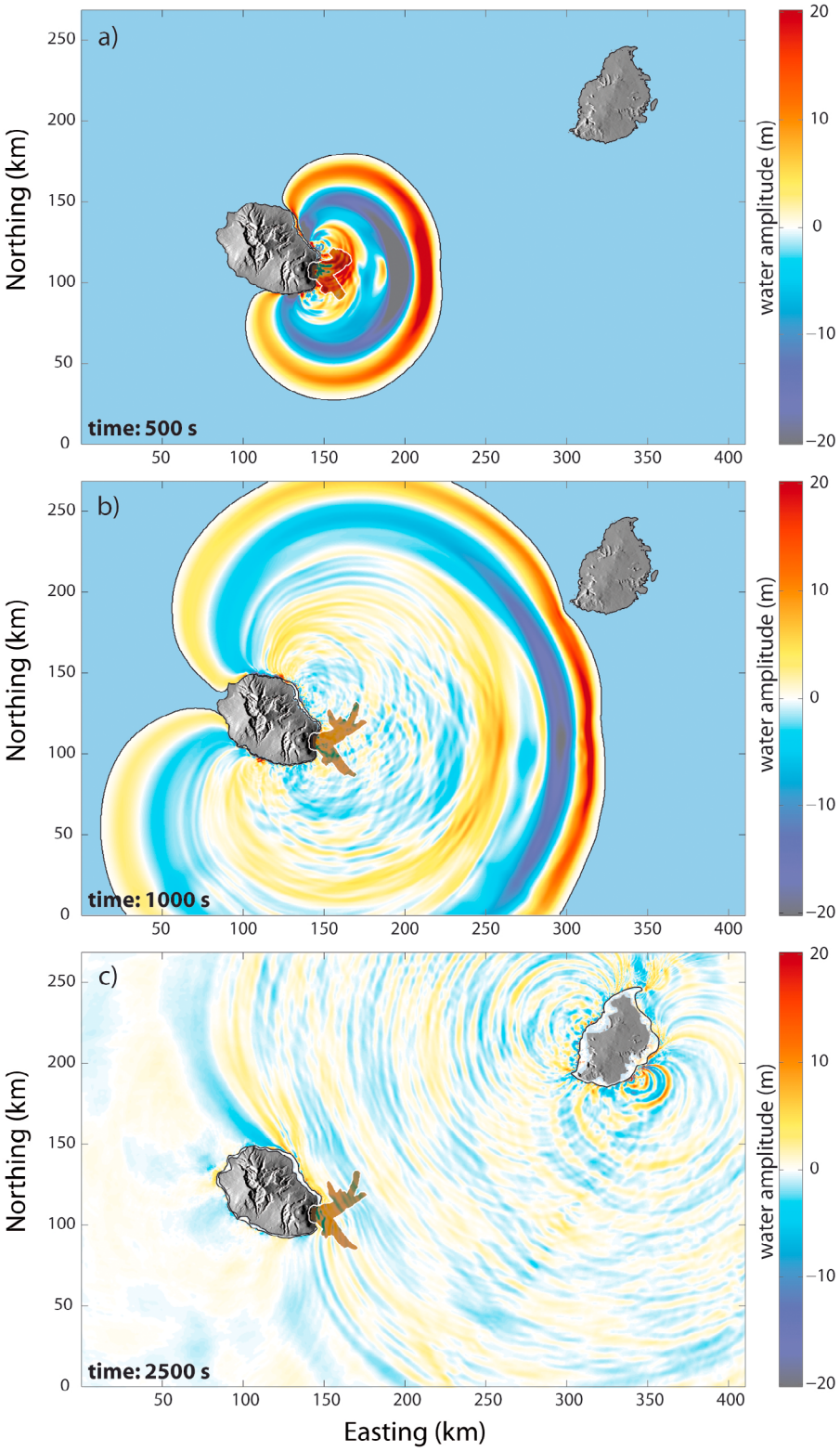

Figure 6. Water amplitude (meters) generated by a 10 km^3 landslide at (a) t = 500 s (8.33 min), (b) 1000 s (16.66 min), and (c) 2500 s (41.66 min). Landslide deposits appear in dark.

Highest water amplitudes and penetration of seawater inland occurs locally where the coast is perpendicular to the direction of propagation, allowing the wave to strike the island frontally. The low area of St André, on the north-eastern part of the island, is in this configuration, and the water runs several kilometers inland.

[42] The amplitude decreases rapidly around the southern and northern shores, the shape of the island protecting these

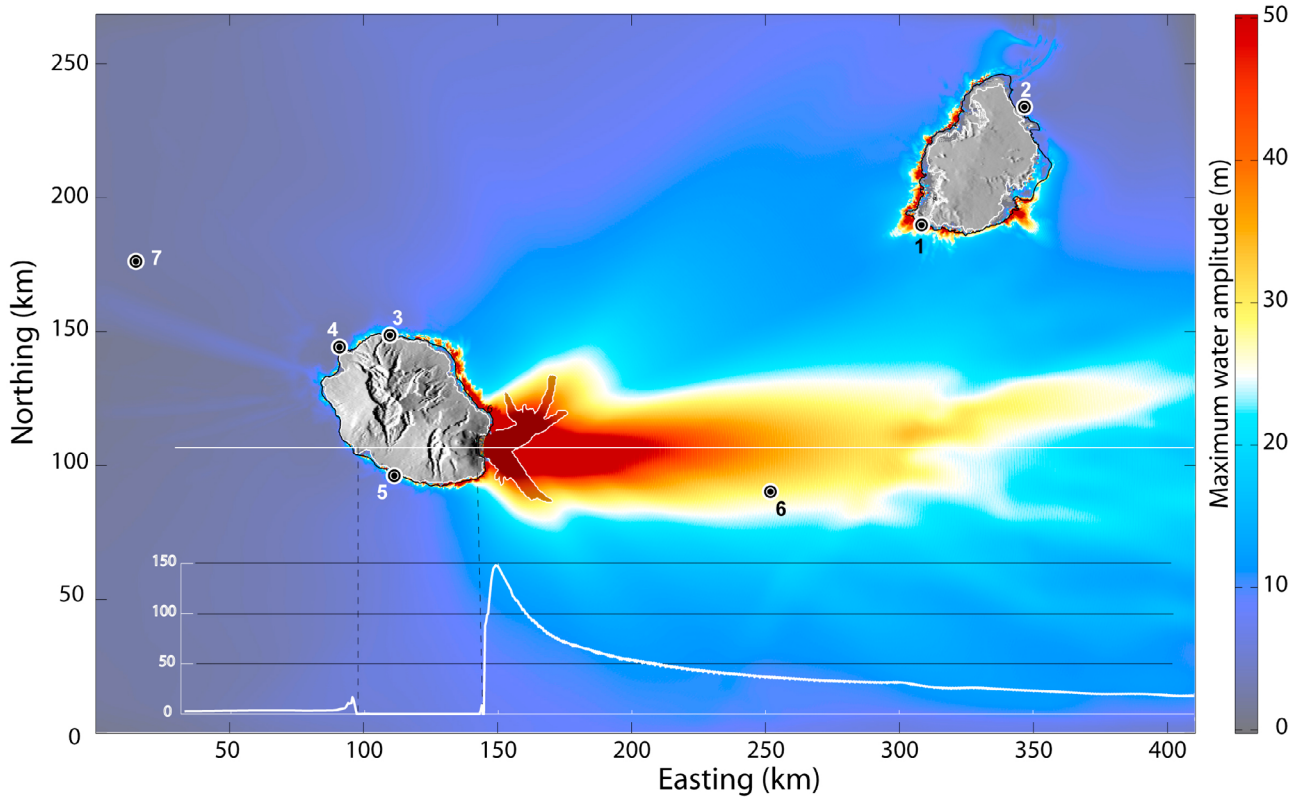

Figure 7. Maximum water amplitude (meters) generated by a 10 km^3 landslide (scenario 1). Note the amplitude increase over the ridge of the Mauritius Fracture Zone ($x = 300$, $y = 100$) and close to the shore. Axes are distances in kilometers. The black contour indicates the shoreline. The white contour along the coasts indicates the area inundated by the tsunami. The curve draws the maximum water amplitude recorded along the west/east line. The circles locate the tide gauges of Figure 8.

areas from waves arriving normal to the coast. The area of St Pierre, to the south, is affected by a >10 m wave approximately 10 min after the landslide (Figures 6a and 8a, Tables 2 and 3). A second wave of ~30 m, formed by the reflux of the sea into the landslide scar, reaches the area 5 min later. The first wave reaches the main city of the island, St Denis, 12 min after the onset of the landslide with an amplitude of nearly 10 m and the second wave, >25 m in amplitude, after 18 min (Figure 8a, Tables 2 and 3). Le Port, which is located to the northwest, on the opposite side of the island to the landslide, is one of the last places affected by the tsunami, after 15 min. This northwestern coast is protected by the shape of the island and is affected by waves less than 5 m in amplitude (Figure 8a). However, waves are amplified by the superposition of the two groups of waves encircling the island, one coming from the south, the other from the north (Figure 6b).

[43] To the east, the tsunami propagates out into the deep ocean, and its amplitude decreases due to the radial dissipation of the energy (Figure 7). But, 150 km to the northeast of the impact, the water depth decreases around Mauritius: The tsunami slows down and, consequently, increases in amplitude. Waves of more than 40 m hit the southern part of the island 18 min after the tsunami genesis (Figures 6b and 8b). Locally, due to the shape of the island, reflections produce amplitudes that can exceed 100 m. The capital, Port Louis, in the northwest, and the airport, in the southeast, are affected by waves greater than 20 m in amplitude. Waves of less than 10 m (except scenario 7, 18.5 m, 25 km^3) are recorded in the northeast of Mauritius. The inland penetration is also further (~5 km) for Mauritius than for Réunion Island because of the low-lying topography of the island. About 10%–15% of the island would be inundated by water.

[44] The waves reflected off the Mauritius coast move back to Réunion Island. According to the model, these waves hit the northeast coast of Réunion Island frontally, reaching an amplitude higher than those of the first waves. They reach St Denis about 45 min after the landslide (at 2700 s in Figure 8a).

[45] In the Indian Ocean, the amplitude of the waves decreases exponentially away from the island (Figure 7). The highest amplitudes are recorded to the east of the landslide, still reaching 40 m at 100 km (Figure 7). To the west, the amplitudes are very low, less than 5 m at some kilometers from the coast (Figures 7 and 8c).

5.2. Landslide From the Active Edifice—Other Scenarios

[46] The transmission of the momentum lost by the avalanche to the water has minor consequences on the results obtained (scenarios 1 and 2, Table 1). It only increases the velocity and the wave amplitude close to the shore, but its

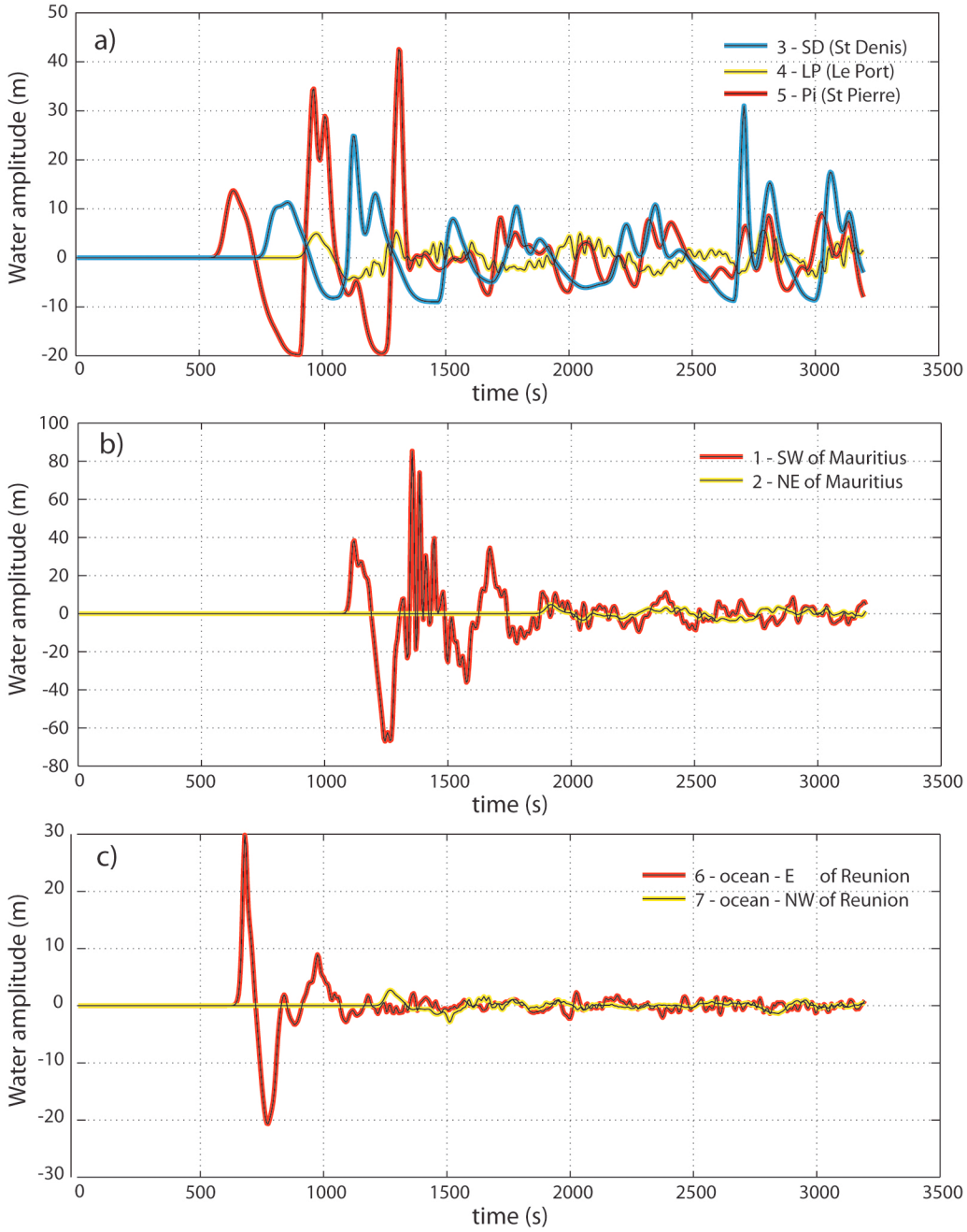

Figure 8. Tide gauges of the numerical simulation (for a 10 km^3 landslide, scenario 1): (a) at Réunion Island, (b) at Mauritius, and (c) in the ocean. The measurement for Figures 8a and 8b is made off the coast (1 km distance) to avoid complex effects that may arise at the shore and that would not be taken into account by our depth-average approach. At the shore, the waves slow down; consequently, their amplitudes are higher than presented. See location in Figure 7.

effect is small compared to the uplift of the water. The effect of momentum transmission is difficult to predict a priori. It increases the velocity of the water where the landslide enters the sea, and thus the wave amplitude in the ocean facing the landslide, but it also changes the wavelength. Along the coast, where the wave amplitudes increase together with a shortening of the wavelengths, and where wave interactions are high due to reflections, the waves are sometimes higher, sometimes lower than if no transmission of the momentum were calculated. The feedback effect on the landslide is negligible, the mass of the landslide not being sufficient to significantly accelerate the huge mass of surrounding water.

[47] The effect of C_s and C_f (scenarios 1, 3, and 4) is to reduce the velocity of the landslide when it is underwater, the front being strongly affected by C_f. The mass of the landslide then accumulates behind the front, forming a flow thick enough to overflow into depressions bordering the main channel. Lowering this value accelerates and thins the

Table 2. Maximal Wave Amplitude (m) at Different Locations for Various Scenarios

Scenario	SW of Mauritius Point 1	NE of Mauritius Point 2	St Denis Point 3	Le Port Point 4	St Pierre Point 5	Ocean, West Point 6	Ocean, East Point 7
1	85 (38)[a]	5	31 (11)	5.5 (5)	42 (14)	2.7	30
2	75 (60)	7.5 (7)	28 (15)	9 (7)	36 (18)	3.8	46
3	76	12	31	5.5	40	2.8	35
4	70 (65)	9 (6)	30 (10)	6 (5)	56 (12)	2.7	49
5	88 (30)	3.5	36 (10)	4 (3)	14	1.7	19
6	62 (37)	11 (5)	27 (13)	7 (5.5)	39 (15)	2.7	30
7	128	18 (14)	34 (23)	16	41 (29)	11	113
8	30 (18)	5 (2)	19 (4.5)	5.5 (1.6)	37 (4)	1.5 (1.0)	25 (15)

[a]Values in parentheses indicate the amplitude of the first wave if it is not the highest wave. Locations are represented in Figure 7.

landslide, resulting in the deposits being more channelized. In the extreme case, where C_s and C_f are both considered as 0, the deposits are mainly concentrated in 2 lobes (Figure 5b). They are bordered by 20 to 40 m thick levées and are thicker at the front. This morphology appears closer to natural deposits than with high values of C_s and C_f. The very high mean velocity of 80 m s^{-1}, with a maximal velocity of more than 100 m s^{-1}, forms deposits within sight of the scar, and which are less spread out.

[48] If the landslide is considered as frictional, with $C_f = 2$ and $C_s = 0.01$, a basal friction of 3° is needed to fit the runout of past events (scenario 6). The landslide deposits are spread out (Figure 5c), have very thin edges, a thick mass locally and do not show any levées or a well marked front. If C_s and C_f both equal 0, the best fit friction angle is 5° (scenario 5). Deposits formed are widely dispersed (Figure 5), covering an area of about 2000 km^2. Simulated deposits with the frictional model have less of a resemblance to the

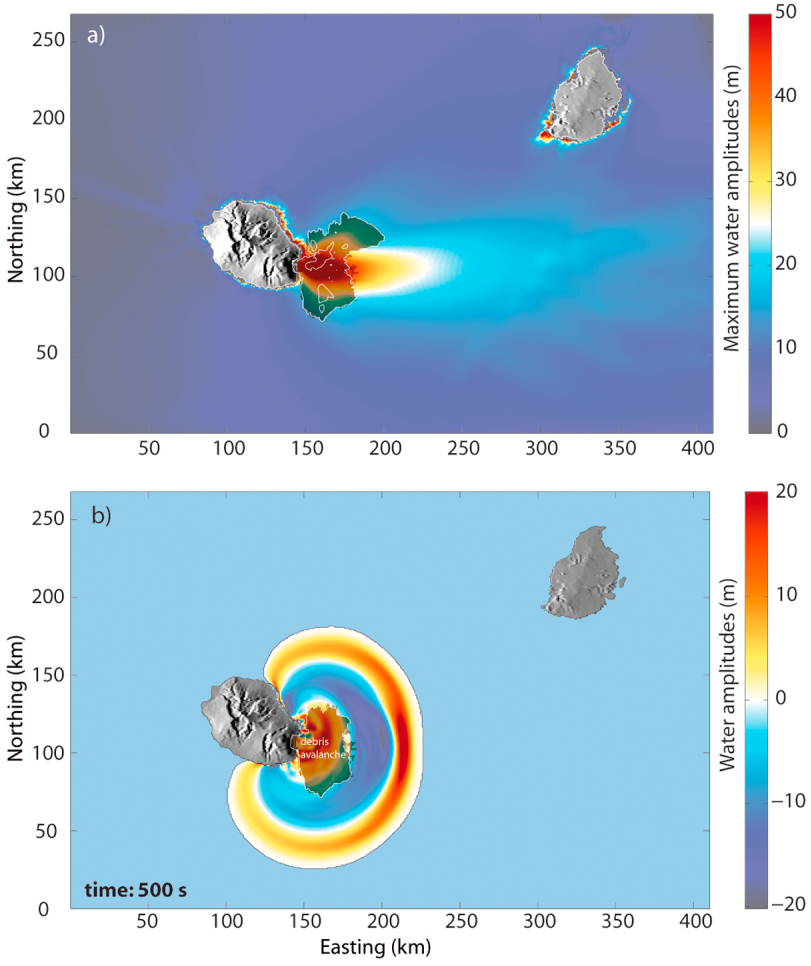

Figure 9. (a) Maximum water amplitude generated by a landslide with a frictional behavior ($\varphi_{bed} = 5°$, $V = 10$ km^3, scenario 5). The submarine internal white contours indicate deposits thicker than 10 m. (b) Wave amplitudes at $t = 500$ s. The deposit simulated is the darker area, to the east of the island.

Table 3. Time of Arrival (in seconds) of the Crest of the First Wave at Different Locations for Various Scenarios[a]

Scenario	SW of Mauritius Point 1	NE of Mauritius Point 2	St Denis Point 3	Le Port Point 4	St Pierre Point 5	Ocean-W Point 6	Ocean-E Point 7
1	1120 (30)[b]	1920 (60)	860 (120)	975 (75)	635 (75)	1270 (50)	680 (30)
2	1110 (30)	1905 (25)	845 (95)	975 (75)	635 (75)	1260 (30)	670 (25)
3	1115 (55)	1910 (60)	845 (125)	975 (70)	635 (85)	1265 (50)	675 (35)
4	1100 (25)	1890 (50)	810 (60)	965 (65)	635 (85)	1260 (50)	665 (40)
5	1125 (60)	1910 (95)	810 (95)	985 (100)	1005 (85)	1275 (60)	685 (70)
6	1120 (40)	1915 (50)	860 (110)	975 (75)	635 (70)	1275 (60)	680 (40)
7	1100 (20)	1895 (45)	790 (50)	970 (60)	620 (55)	1260 (140)	670 (30)
8	1120 (45)	1915 (50)	810 (70)	960 (60)	620 (70)	1255 (50)	685 (50)

[a]Locations are represented in Figure 7.
[b]Values in parentheses indicate the duration of the sea level elevation preceding the crest.

deposits mapped by *Oehler et al.* [2007] than those produced with the constant retarding stress model.

[49] Although different in the near field, the overall times of arrival and tsunami kinematics obtained for all scenarios with the same volume of 10 km^3 released in a single episode are close to those described in section 5.1 (Tables 2 and 3). The initial wave amplitude may change, but the same volume of water is displaced over a similar period of time. For example, with the frictional model (scenario 5), the wider spread landslide generates smaller wave amplitudes (Figure 9b) but with larger wavelength. Where the tsunami reaches the coast, wavelengths decrease, and amplitudes increase to reach amplitudes of more than 50 m (about 100 m locally), the order of magnitude of waves obtained with the constant retarding stress (Figure 9a, Table 2).

[50] Wave amplitude obviously depends on the way the mass slides and the volume that impinges on the sea. Should the same landslide volume of 10 km^3 move by retrogressive failures, or by slow sliding, waves three times smaller would be formed (however, deposits formed by scenarios 1 and 8 are very similar). In a more catastrophic scenario, which envisages that all of the Grand Brulé scar (between the summit and the sea, Figure 4) slides rapidly as a single mass (25 km^3), waves could reach two to three times the amplitude previously shown for the 10 km^3 case (scenario 7, Tables 1–3).

5.3. Submarine Landslide of the Coastal Platform

[51] The larger landslide in the west (Figure 10a) induces waves of about 20–30 m in amplitude that affect about 40 km of the neighboring shore. Waves of more than 10 m in amplitude form locally along about 50 km of the shoreline, but the amplitude decreases rapidly, reaching less than 2 m 30–40 km from the landslide. The 0.5 km^3 landslide to the northeast (Figure 10b) affects the adjacent 10 km of shoreline with waves higher than 20 m (40 m locally). However, the zone affected by smaller waves is more limited than in the previous case. For both larger landslides, the seawater penetrates more than 2 km inland, into the flat-lying area of St Paul. In the case of the ~0.1 km^3 volume landslide (Figure 10c), the resulting waves are only about 3 m high along 20 km of the proximal coast. Their effects are negligible (<0.2 m) at 30 km from the landslide, and they are unable to penetrate inland.The wave is positive in all areas facing the landslide. Behind the landslide, the first wave is negative: The water level decreases for about 2 min before the arrival of the first positive wave. Due to the proximity of the potential landslide area (less than 10 km from the shoreline), waves reach the coast in less than 2 min.

6. Discussion

[52] The occurrence of landslides of several cubic kilometers only occur at Réunion Island on a geological timescale and are very scarce on a human timescale. This sparcity of events explains why it is very difficult to validate any numerical model of these exceptional phenomena using field data due to the lack of direct observations. It is also impossible to measure the rheology and to quantify accurately interactions between the landslide and water. This problem of validation, however, also highlights the purpose of numerical simulations, which give an idea of the wave amplitude that such landslides could cause. Of course, uncertainties remain, due to the assumptions and simplifications implicit in the model and in the rheological behaviors chosen. In addition, the rheology we have chosen through the simulation of past events is not fully understood. However, this law seems to be able to capture the first-order behavior of this kind of complex flow and to form numerical deposits with levées, lobes, and thicknesses which appear to be in good accordance with the morphological features of the older deposits mapped by *Oehler et al.* [2007]. Note that the value used for the retarding stress, 20 kPa, with $C_f = 2$ and $C_s = 0.01$ (50 kPa if $C_f = 0$ and $C_s = 0$), is approximately half of the ~50 kPa mean value of *Dade and Huppert* [1998], and of the stress obtained by *Kelfoun and Druitt* [2005] for the subaerial Socompa avalanche. The main part of the emplacement being underwater, the same ratio is observed between the relative density used underwater (1000 kg m^{-3}) and subaerial density (2000 kg m^{-3}). The value of the constant retarding stress might then be implicitly related to the density of the landslide and thus to the internal stresses that are related to its weight.

[53] Overall, the greatest uncertainties are linked to the scenario chosen: How does the mass slide? What is the destabilized volume? This is why our aim is not to forecast the effect of a hypothetical landslide on Réunion Island, but to estimate the magnitude of the waves that could be produced, to determine the time before wave arrival and to characterize the dynamics of the tsunami, should a landslide occur here. It is also why we have simulated landslides which differ in volume (0.5, 1, 2, 10, 25 km^3), rheology, drag of water, landslide location and way of collapsing (in one go or by retrogressive failures).

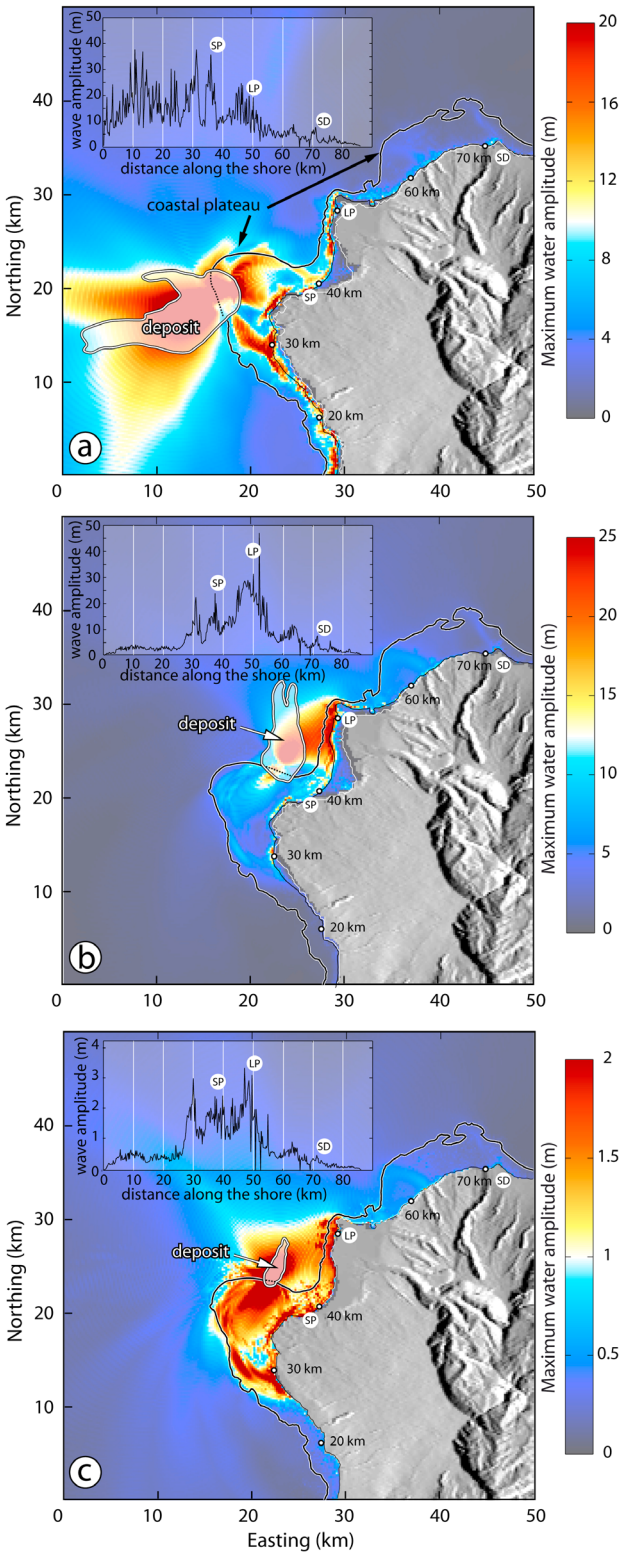

Figure 10. Waves generated by a submarine landslide of coastal platform (a) west sliding, 2 km^3, (b) northeast sliding, 0.5 km^3, and c) north sliding, 0.1 km^3. T = 20 kPa, C_f = 2, C_s = 0.01, no momentum transfer to water, resolution 200 m. The scale of amplitude in Figures 10a, 10b, and 10c is different. The graphics show the maximal wave amplitude along the shore (numbers indicate the distance in kilometers from the bottom of the simulation domain.)

[54] Simulations of the landslide from the active edifice show that waves as high as 100 m in amplitude could affect the coasts of Réunion Island and Mauritius if volumes greater than 10 km^3 are involved. It also enables the kinematics of such an event to be predicted, and the effects of the topography/bathymetry on the wave amplitude and dynamics to be quantified. For example, for all scenarios envisaged, the southwestern coast of Mauritius Island, located at 175 km from the impact, is more affected by the tsunamis than the Réunion coastline itself due to the dynamics explained in the results section.

[55] In the deep ocean, the amplitude of the waves decreases progressively eastward, reaching about 20 m at 250 km from the impact (east boundary of the calculation grid, Figure 7). Extrapolation of the wave amplitude further out into the deep ocean to the east gives <1 mm waves at 2000 km from the impact whatever the type of extrapolation chosen. Even though wave amplitude increases as the water depth decreases, the effect on the Australian coasts, the first land encountered by the tsunami, more than 5500 km from the impact, appears to be negligible.

[56] To the west, the wave amplitude becomes negligible closer to the island because the latter protects this sector from the initial wave (Figure 8c). Madagascar, 750 km to the west of Réunion Island, would thus be little affected by a landslide from the Piton de la Fournaise. Waves generated by a 2 km^3 landslide of the coastal shelf (Figures 10a and 10b) are smaller than for a landslide of the volcano itself because of the smaller volume involved, but also because of the slow velocities and small runout of the landslide. The driving forces are reduced by the effect of the water in a submarine environment, and the submarine slides do not experience subaerial acceleration. The less-steep geometry of the coastal shelf also generates lower velocities and smaller runout. Increasing the velocity and runout of the landslide, by changing the rheological model or lowering the value of the constant retarding stress, would generate slightly higher waves, but their amplitude is always <40 m and the effect is local (covering 50 km of the coastline), the bathymetry playing a fundamental role in the dynamics. The waves are also restricted to a limited portion of the shore due to the form of the bay facing the coastal shelf that protects the more distant shores from direct impact of the tsunami.

[57] The tsunami hazard associated with a landslide event on Réunion Island would thus be dramatic on a local scale (proximal shore for a landslide of the shelf, shores of Réunion Island and Mauritius for a large landslide of the active part of the volcano), but small on a regional scale. This is mainly because the wave generation is localized to a relatively small area of several tens of square kilometers and because the energy dissipates rapidly in a radial manner.

[58] If wave amplitude is the main parameter, the evacuation time should also really be taken into account for hazard assessment. This evacuation time is long enough for the case of a tsunami triggered by huge seismic shock occurring at the opposite side of the Indian Ocean (as in the 26 December 2004 case). It would, however, be very short for Réunion coasts in the case of a landslide on or around the island: less than 2 min to reach the nearest coast for a coastal landslide, 10–20 min depending on the landslide volume for the wave to encircle the island, and 10–30 min to reach Mauritius Island.

[59] The amplitudes of 100 m for the large landslide may intuitively appear huge; however, they are compatible with the enormous volumes (10 km^3) chosen to slide. Waves are ~10 times higher than that generated following the collapse of Stromboli in December 2002: A 10 m high wave was formed [*Maramaï et al.*, 2005], but the landslide was only 17.10^6 m^3, 500 times smaller than the volume tested in our simulation. The wave generated by the Lituya Bay landslide (volume of 30.10^6 m^3; 300 times smaller than our volume), in Alaska in 1958 [*Miller*, 1960; *Fritz et al.*, 2001] propagated into the bay, reaching 500 m close to the impact, 60 m laterally at 6 km from the collapse, and 30 m at 12 km. Even if we cannot make a direct comparison between the case of Lituya Bay, in which water was channeled by the bay, and our case in which waves propagate in the open sea, this example also supports the fact that our amplitudes and times are realistic. In Hawaii, waves as high as 300 m, originating from debris avalanches, are believed to have affected the islands in the past [e.g., *Moore and Moore*, 1984, 1988].

7. Conclusion

[60] Our simulations use a rheological behavior for the landslide which is compatible with real deposits and allows for the estimation of wave amplitudes, times of wave arrival, and inland penetration with the limitation of the approach used. They give a new insight into the risk assessment at Réunion Island and Mauritius. On a geological timescale, these islands may be hit by huge tsunamis which could cause disaster for superstructures and inhabited areas located on or near the destabilized areas, not to mention the possibility of the direct impact on the shorelines, where hundreds of thousands of people live, and on the main social infrastructures. For example, Réunion Island airport is close to the sea, at an elevation of 5 m, and the main road is located between 5 and 10 m above sea level.

[61] However, to our present knowledge, the frequency of large landslides at Réunion Island is approximately 1 every 40,000 years on average. The magnitude of such events would be catastrophic, but hazard (magnitude × occurrence) is very low because of the very low recurrence time.

[62] On a human timescale, the most pertinent events are the small-volume landslides. These landslides are smaller but more frequent. Their effect would only be local but could cause damage and fatalities and could be very devastating for harbor infrastructures. Due to their small size, small event deposits (<1 km^3) are difficult to detect, are easily eroded, and are rapidly covered by more recent deposits, resulting in the underestimation of their recurrence. An effort to carry out high-resolution underwater mapping should be made to estimate more accurately the frequency of such landslides. The results presented here also reinforce the necessity to set up a local alert network (wave amplitude, deformation, seismic) to forecast such events. However, the evacuation time would be very short for Réunion coasts in the case of a landslide around the island. Forecast strategies for subaerial and submarine landslides thus need to be developed on Réunion Island, but also on most other oceanic islands that show huge landslide deposits, such as the Canary Islands [*Ablay and Hürlimann*, 2000; *Krastel et al.*, 2001; *Ward and Day*, 2001; *Masson et al.*, 2002] or the Hawaiian Islands [Moore et *al.*, 1989, 1994].

Notation

C_f	Frontal drag coefficient, dimensionless
C_s	Surface drag coefficient, dimensionless
g	Gravity, m s^{-2}
h_a	Landslide thickness, m
h_w	Water depth, m
$k_{act/pass}$	Earth pressure coefficient, dimensionless
z	Fixed topography elevation, m
z_w	Water surface elevation, m
Δz	Variation of water surface elevation, m
$\mathbf{R} = (R_x, R_y)$	Stress exerted by the landslide on the water, Pa
$\mathbf{T} = (T_x, T_y)$	Retarding stress of the landslide, Pa
$\mathbf{u} = (u_x, u_y)$	Landslide velocity, m s^{-1}
$\mathbf{v} = (v_x, v_y)$	Water velocity, m s^{-1}
V	Volume, m^3
α	Slope of the fixed topography, degrees
β	Slope of the ocean bottom (fixed topography + landslide), degrees
μ_w	Water dynamic viscosity, Pa s
ρ_a	Landslide density, kg m^{-3}
ρ_w	Water density, kg m^{-3}
ρ	Relative density of the landslide, $\rho = \rho_a - \rho_w$, kg m^{-3}
χ	Attenuation coefficient, dimensionless

[63] **Acknowledgments.** Those studies have been funded by the French *Centre national de la Recherche Scientifique* (CNRS), by the *Institut de Recherche pour le Développement* (IRD), and by the *Agence Nationale de la Recherche* (ANR, project 08-JCJC-0042, Vitess). We thank Ariel Provost for his help in the formulation of the equations. The paper was improved by Fran van Wyk de Vries and by the very useful comments of three anonymous reviewers and the editors.

References

Ablay, G., and M. Hürlimann (2000), Evolution of the north flank of Tenerife by recurrent giant landslides, *J. Volcanol. Geotherm. Res.*, *103*, 135–159.

Bachelery, P., and P. Mairine (1990), Evolution volcano-structurale du Piton de la Fournaise depuis 0.53 M.a., in *Le volcanisme de la Réunion, monographie*, edited by J.-F. Lénat, pp. 213–242, Centre de Recherches Volcanologiques, Clermont-Ferrand, France.

Boussinesq, J. (1872), Théorie des ondes et des remous qui se propagent le long d'un canal rectangulaire horizontal, en communiquant au liquide contenu dans ce canal des vitesses sensiblement pareilles de la surface au fond, *J. Math. Pures Appl.*, *17*, 55–108.

Camoin, G., L. Montaggioni, and C. Braithwaite (2004), Late glacial to post glacial sea levels in the Western Indian Ocean, *Mar. Geol.*, *206*, 119–146.

Dade, W. B., and H. E. Huppert (1998), Long-runout rockfalls, *Geology*, *26*, 803–806.

de Saint-Venant, A. J. C. (1871), Théorie du mouvement non-permanent des eaux, avec application aux crues des rivières et à l'introduction des marées dans leur lit, *C. R. Acad. Sci. Paris*, *73*, 147–154.

Dutykh, D., and F. Dias (2007), Dissipative Boussinesq equations, *C. R. Mecanique*, *335*, 559–583. Special issue dedicated to J. V. Boussinesq, doi:10.1016/j.crme.2007.08.003.

Fritz, H. M., W. H. Hager, and H. E. Minor (2001), Lituya Bay case: Rockslide impact and wave run-up, *Sci. Tsunami Hazards*, *19*(1), 3–22.

Fritz, H. M., N. Kalligeris, J. C. Borrero, P. Broncano, and E. Ortega (2008), The 15 August 2007 Peru tsunami runup observations and modeling, *Geophys. Res. Lett.*, *35*, L10604, doi:10.1029/2008GL033494.

Geist, E. L., J. L. Patrick, and D. C. Jason (2009), Hydrodynamic modeling of tsunamis from the Currituck landslide, *Mar. Geol.*, *264*, 41–52, doi:10.1016/j.margeo.2008.09.005.

Harbitz, C. B., F. Løvholt, G. Pedersen, and D. G. Masson (2006), Mechanisms of tsunami generation by submarine landslides: A short review, *Norweg. J. Geol.*, *86*, 255–264.

Haugen, K. B., F. Lovholt, and C. B. Harbitz (2005), Fundamental mechanisms for tsunami generation by submarine flows in idealised geometries, *Mar. Petr. Geol.*, *22*, 209–217.

Heinrich, P., A. Mangeney, S. Guibourg, and R. Roche (1998), Simulation of water waves generated by a potential debris avalanche in Montserrat, Lesser Antilles, *Geophys. Res. Lett.*, *25*, 3697–3700.

Hoblitt, R. P., C. D. Miller, and W. E. Scott (1987), Volcanic Hazards with Regard to Siting Nuclear-Power Plants in the Pacific Northwest, *U. S. Geol. Surv. Open File Report* 87–297.

Holcomb, R. T., and R. C. Searle (1991), Large landslides from oceanic volcanoes, *Mar. Geotech.*, *10*, 19–32.

Ioualalen, M., B. Pelletier, P. Watts, and M. Regnier (2006), Numerical modeling of the 26 November 1999 Vanuatu tsunami, *J. Geophys. Res.*, *111*, C06030, doi:10.1029/2005JC003249.

Iverson, R. M., and R. P. Denlinger (2001), Flow of variably fluidized granular masses across three-dimensional terrain: 1. Coulomb mixture theory, *J. Geophys. Res.*, *106*, 537–552.

Jiang, L., and P. H. LeBlond (1992), The coupling of a submarine slide and the surface waves which it generates, *J. Geophys. Res. 97* (C8), 12,731–12,744.

Keating, B. H., and W. J. McGuire (2000), Island edifice failures and associated tsunami hazards, *Pure Appl. Geophys. 157*, 899–955.

Kelfoun, K., and T. H. Druitt (2005), Numerical modelling of the emplacement of Socompa rock avalanche, Chile, *J. Geophys. Res.*, *110*, B12202, doi:10.1029/2005JB003758.

Kelfoun, K., T. H. Druitt, B. van Wyk de Vries, and M.–N. Guilbaud (2008), Topographic reflection of Socompa debris avalanche, Chile, *Bull. Volcanol.*, *71*(9), 1057–1075, doi:10.1007/s00445-008-0201-6.

Krastel, S., H. U. Schmincke, C. L. Jacobs, R. Rihm, T. M. Le Bas, and B. Alibés (2001), Submarine landslides around the Canary Islands, *J. Geophys. Res.*, *106*, 3977–3997.

Labazuy, P. (1991), Instabilités au cours de l'évolution d'un édifice volcanique en domaine intraplaque océanique: Le Piton de la Fournaise (Ile de Réunion Island), Ph.D. dissertation, 260 pp., Univ. Blaise Pascal, Clermont-Ferrand.

Labazuy, P. (1996), Recurrent landslides events on the submarine flank of Piton de la Fournaise volcano (Réunion Island), *Geol. Soc. London*, *110*, 293–305.

Lénat, J.-F., and P. Labazuy (1990), Morphologies et structures sous-marines de la Réunion, in *Le volcanisme de la Réunion, monographie*, edited by J.-F. Lénat, pp. 43–74, Centre de Recherches Volcanologiques, Clermont-Ferrand, France.

Maramaï, A., L. Graziani, G. Alessio, P. Burrato, L. Colini, L. Cucci, R. Nappi, A. Nardi, and G. Vilardo (2005) Near- and far-field survey report of the 30 December 2002 Stromboli (Southern Italy) tsunami, *Mar. Geol.*, *215*, 93–106.

Masson, D. G., A. B. Watts, M. J. R. Gee, R. Urgeles, N. C. Mitchell, T. P. Le Bas, and M. Canals (2002), Slope failures on the flanks of the western Canary Islands, *Earth Sci. Rev.*, *57*, 1–35.

McMurtry, G. M., P. Watts, G. J. Fryer, J. R. Smith, and F. Imamura (2004), Giant landslides, mega-tsunamis, and paleo-sea level in the Hawaiian Islands, *Mar. Geol.*, *203*, 219–233, doi:10.1016/S0025-3227(03)00306-2.

Merle, O., and J.-F. Lénat (2003), Hybrid collapse mechanism at Piton de la Fournaise volcano, Réunion Island, Indian Ocean, *J. Geophys. Res.*, *108*(B3), 2166, doi:10.1029/2002JB002014.

Michon, L., and F. Saint-Ange (2008), Morphology of Piton de la Fournaise basaltic shield volcano (La Réunion Island): Characterization and implication in the volcano evolution, *J. Geophys. Res.*, *113*, B03203, doi:10.1029/2005JB004118.

Michon, L., F. Saint-Ange, P. Bachelery, N. Villeneuve, and T. Staudacher (2007), Role of the structural inheritance of the oceanic lithosphere in the magmato-tectonic evolution of Piton de la Fournaise volcano (La Réunion Island), *J. Geophys. Res.*, *112*, B04205, doi:10.1029/2006JB004598.

Miller, D. J. (1960), The Alaska earthquake of July 10, 1958: Giant wave in Lituya Bay, *Bull. Seism. Soc. Am.*, *50*(2), 253–266.

Moore, G. W., and J. G. Moore (1988), Large-scale bedforms in boulder gravel produced by giant waves in Hawaii. in *Sedimentologic Consequences of Convulsive Geologic Events*, Geol. Soc. Am. Special Pap. 229, pp. 101–110.

Moore, J. G., and G. W. Moore (1984), Deposit from a giant wave on the island of Lanai, Hawaii, *Science*, *226*, 1312–1315.

Moore, J. G., D. A. Clague, R. T. Holcomb, P. W. Lipman, W. R. Normark, and M. E. Torresan (1989), Prodigious submarine landslides on the Hawaiian Ridge, *J. Geophys. Res.*, *94*, 17465–17484.

Moore, J. G., W. B. Bryan, and K. R. Ludwig (1994), Chaotic deposition by giant wave, Molokai, Hawaii, *Geol. Soc. Am. Bull.*, *106*, 962–967.

Normark, W. R, J. G. Moore, and M. E. Torresan (1993), Giant volcano-related landslides and the development of the Hawaiian Islands, in *Submarine Landslides: Selected Studies in the U.S. Exclusive Economic Zone*, edited by W. C. Schwab, H. J. Lee, and D. C. Twichell, *U.S. Geol. Surv. Bull.* 2002, 184–196.

Oehler, J.–F., P. Labazuy, and J.–F. Lénat (2004), Recurrence of major flank landslides during the last 2-Ma-history of Réunion Island, *Bull. Volcanol.*, *66*, 585–598.

Oehler, J.–F., J. –F. Lénat, and P. Labazuy (2007), Growth and collapse of the Réunion Island volcanoes, *Bull. Volcanol.*, *70*(6), 717–742, DOI 10.1007/s00445-007-0163-0.

Okal, E. A., and C. E. Synolakis (2003), A theoretical comparison of tsunamis from dislocations and landslides (2003), *Pure Appl. Geophys.*, *160*, 2177–2188, doi:10.1007/s00024-003-2425-x.

Rançon, J. P. (1990), Lithostratigraphie du forage du Grand Brûlé. Implications volcanologiques. in *Le volcanisme de La Réunion*, edited by J. F. Lénat, pp. 187–200, CRV, Clermont-Ferrand.

Ruff, L. J. (2003), Some aspects of energy balance and tsunami generation by earthquakes and landslides, *Pure Appl. Geophys.*, *160*, 2155–2176, doi:10.1007/s00024-003-2424-y.

Sander, J., and K. Hutter (1996), Experimental and computational study of channelized water waves generated by a porous body, *Acta Mech.*, *91*, 119–155.

Synolakis, C. E., E. N. Bernard, V. V. Titov, U. Kanoglu, and F. I. Gonzalez (2008), Validation and verification of tsunami numerical models, *Pure Appl. Geophys.*, *165*, 2197–2228, doi:10.1007/s00024-004-0427-y.

Tinti, S., E. Bortolucci, and C. Romagnoli (1999), Modelling a possible holocenic landslide-induced tsunami at Stromboli volcano, Italy, *Phys. Chem. Earth*, *24*, 423–429.

Tinti, S., E. Bortolucci, and C. Romagnoli (2000), Computer simulations of tsunamis due to sector collapse at Stromboli, Italy. *J. Volcanol. Geotherm. Res.*, *96*, 103–128.

Tinti, S., G. Pagnoni, and F. Zaniboni (2006a), The landslides and tsunamis of the 30th of December 2002 in Stromboli analysed through numerical simulations. *Bull. Volcanol.*, *68*, 462–479.

Tinti, S., A. Armigliato, A. Manucci, G. Pagnoni, F. Zaniboni, A. C. Yalçiner, and Y. Altinok (2006b), The generating mechanism of the August 17, 1999 İzmit Bay (Turkey) tsunami: Regional (tectonic) and local (mass instabilities) causes, *Mar. Geol.*, *225*, 311–330.

Ward, S. N. (2001), Landslide tsunami, *J. Geophys. Res.*, *106*(6), 11,201–11,215.

Ward, S. N., and S. Day (2001), Cumbre Vieja Volcano—Potential collapse and tsunami at La Palma, Canary Islands, *Geophys. Res. Lett.*, *28*, 3397–3400.

Watts, P., F. Imamura, and S. T. Grilli (2000), Comparing model simulations of three benchmark tsunami generation cases, *J. Sci. Tsunami Hazzards*, *18*(2), 107–123.

Waythomas, C. F., and P. Watts (2003), Numerical simulation of tsunami generation by pyroclastic flow at Aniakchak Volcano, Alaska, *Geophys. Res. Lett.*, *30*(14), 1751, doi:10.1029/2003GL017220.

Waythomas, C. F., P. Watts, and J. S. Walder (2006), Numerical simulation of tsunami generation by cold volcanic mass flows at Augustine Volcano, Alaska, *Nat. Hazzards Earth Syst. Sci.*, *6*, 671–685.

Waythomas, C. F., P. Watts, F. Shi, and J. T. Kirby (2009), Pacific Basin tsunami hazards associated with mass flows in the Aleutian arc of Alaska *Quat. Sci. Rev.*, *28*(11–12), 1006–1019, doi:10.1016/j.quascirev.2009.02.019.

Wei, G., J. T. Kirby, S. T. Grilli, and R. Subramanya (1995), A fully nonlinear Boussinesq model for surface waves. Part 1. Highly nonlinear unsteady waves. *J. Fluid Mech.*, *294*, 71–92.

T. Giachetti, K. Kelfoun, and P. Labazuy, Laboratoire Magmas et Volcans, Université Blaise Pascal, Clermont Université, 5, rue Kessler, Clermont-Ferrand, 63038, France. (k.kelfoun@opgc.univ-bpclermont.fr)

Downloaded from http://sp.lyellcollection.org/ by guest on March 12, 2012

Tsunami hazard related to a flank collapse of Anak Krakatau Volcano, Sunda Strait, Indonesia

T. GIACHETTI[1,3]*, R. PARIS[2,4,6], K. KELFOUN[2,4,6] & B. ONTOWIRJO[5]

[1]*Clermont Université, Université Blaise Pascal, Geolab, BP 10448, F-63000 Clermont-Ferrand, France*

[2]*Clermont Université, Université Blaise Pascal, Laboratoire Magmas et Volcans, BP 10448, F-63000 Clermont-Ferrand, France*

[3]*CNRS, UMR 6042, Geolab, F-63057 Clermont-Ferrand, France*

[4]*CNRS, UMR 6524, LMV, F-63038 Clermont-Ferrand, France*

[5]*Coastal Dynamics Research Center, BPDP-BPPT, 11th Floor, Building 2, BPPT, Jl, M. H. Thamrin no 8, Jakarta 10340, Indonesia*

[6]*IRD, R 163, LMV, F-63038 Clermont-Ferrand, France*

**Corresponding author (e-mail: giachettithomas@club-internet.fr)*

Abstract: Numerical modelling of a rapid, partial destabilization of Anak Krakatau Volcano (Indonesia) was performed in order to investigate the tsunami triggered by this event. Anak Krakatau, which is largely built on the steep NE wall of the 1883 Krakatau eruption caldera, is active on its SW side (towards the 1883 caldera), which makes the edifice quite unstable. A hypothetical 0.280 km^3 flank collapse directed southwestwards would trigger an initial wave 43 m in height that would reach the islands of Sertung, Panjang and Rakata in less than 1 min, with amplitudes from 15 to 30 m. These waves would be potentially dangerous for the many small tourist boats circulating in, and around, the Krakatau Archipelago. The waves would then propagate in a radial manner from the impact region and across the Sunda Strait, at an average speed of 80–110 km h^{-1}. The tsunami would reach the cities located on the western coast of Java (e.g. Merak, Anyer and Carita.) 35–45 min after the onset of collapse, with a maximum amplitude from 1.5 (Merak and Panimbang) to 3.4 m (Labuhan). As many industrial and tourist infrastructures are located close to the sea and at altitudes of less than 10 m, these waves present a non-negligible risk. Owing to numerous reflections inside the Krakatau Archipelago, the waves would even affect Bandar Lampung (Sumatra, *c.* 900 000 inhabitants) after more than 1 h, with a maximum amplitude of 0.3 m. The waves produced would be far smaller than those occurring during the 1883 Krakatau eruption (*c.* 15 m) and a rapid detection of the collapse by the volcano observatory, together with an efficient alert system on the coast, would possibly prevent this hypothetical event from being deadly.

Most recorded historical tsunamis have a seismic origin, but such events may also be triggered by phenomena related to huge volcanic eruptions, such as large pyroclastic flows entering the water (e.g. de Lange *et al.* 2001; Maeno & Imamura 2007), submarine explosions (e.g. Mader & Gittings 2006), caldera collapse (e.g. Nomanbhoy & Satake 1995; Maeno *et al.* 2006) or by a large, rapidly sliding mass impacting the water (e.g. Tinti *et al.* 1999, 2000, 2006; Keating & McGuire 2000; Ward 2001; Harbitz *et al.* 2006; Fritz *et al.* 2008; Waythomas *et al.* 2009; Kelfoun *et al.* 2010). The December 2002 17×10^6 m^3 flank collapse of Stromboli triggered a 8 m-high run-up on the coast of Stromboli, but had little effect on coasts located more than 200 km from the collapse (Maramai *et al.* 2005). The tsunami generated by the 30×10^6 m^3 Lituya Bay collapse in Alaska in 1958 (Fritz *et al.* 2001) reached 60 m at 6 km laterally from the collapse and 30 m at 12 km. These tsunamis had very few fatalities as they occurred either in isolated locations (Lituya Bay, Alaska) or during a period of no tourist activity (Stromboli). The largest lateral collapse of an island volcano recorded in historical times (*c.* 5 km^3) took place during the 1888 eruption of Ritter Island (New Guinea), producing witnessed waves of up to 10–15 m at tens to hundreds of kilometres from the source (Ward & Day 2003). With 15 000 fatalities, the tsunami generated by the 1792 sector collapse of Mount

From: TERRY, J. P. & GOFF, J. (eds) 2012. *Natural Hazards in the Asia–Pacific Region: Recent Advances and Emerging Concepts*. Geological Society, London, Special Publications, **361**, 79–90, http://dx.doi.org/10.1144/SP361.7
© The Geological Society of London 2012. Publishing disclaimer: www.geolsoc.org.uk/pub_ethics

Downloaded from http://sp.lyellcollection.org/ by guest on March 12, 2012

Mayuyama in Ariake Bay (Kyushu Island, Unzen volcanic complex) was the second worst disaster in Japan, and the second deadliest volcanic tsunami (after that produced by the eruption of Krakatau in 1883). The failure was most probably triggered by a strong earthquake, and its volume was about 340×10^6 m^3 (Michiue *et al.* 1999). Tsunami run-ups ranged from 8 to 24 m on the opposite side of Ariake Bay (Tsuji & Hino 1993).

The 26–28 August 1883 Plinian eruption of Krakatau Volcano, and its subsequent tsunamis, caused more than 35 000 casualties along the coasts of the Sunda Strait in Indonesia (Self & Rampino 1981; Simkin & Fiske 1983; Sigurdsson *et al.* 1991*a*, *b*). This eruption was one of the most powerful and devastating eruptions in recorded history. Many tsunamis were produced during this approximately 2 day eruption, the largest one occurring after 10 a.m. on the 27 August (Warton & Evans 1888; Yokoyama 1981). The leading wave reached the cities of Anyer and Merak on Java after 35–40 min, and after approximately 1 h for the city of Bandar Lampung (Teluk Betung) on Sumatra. A tide gauge located near Jakarta (Batavia Harbour, Java) registered the wave arrival approximately 140 min after its inferred initiation at Krakatau Island. Using the tsunami run-ups determined along the coasts of Java and Sumatra (Verbeek 1885), the tsunami heights before run-up were estimated to be about 15 m at the coastline all around the Sunda Strait (Symons 1888). The generation mechanism of these 1883 tsunamis is still controversial and several processes may have acted successively or together (Self & Rampino 1981; Yokoyama 1981; Camus & Vincent 1983; Francis 1985). Based on low-resolution numerical simulations, Nomanbhoy & Satake (1995) concluded that a series of submarine explosions over a period of 1–5 min was the most probable source for the major tsunami. Nevertheless, pyroclastic flows formed by the gravitational collapse of the eruptive columns are also a possible source for most of the tsunamis observed before and during the paroxysm (Carey *et al.* 1996; de Lange *et al.* 2001).

Nearly 45 years after this 1883 cataclysmal eruption, Anak Krakatau ('Child of Krakatau' in Indonesian) emerged from the sea in the same location as the former Krakatau, and has since grown to its current height of more than 300 m (Hoffmann-Rothe *et al.* 2006). It exhibits frequent activity, still posing a risk to the coastal population of Java and Sumatra, and for the important shipping routes through the Sunda Strait. Following the active phase of Anak Krakatau in 1980, a permanent volcano observatory was established in Pasauran on the western coast of Java, about 50 km east of the Krakatau Archipelago. A short-period seismometer placed on the volcano flank, visual control and daily seismic event statistics are used to determine the current alert level, on the basis of which Indonesian authorities decide about preventive measures, sometimes prohibiting tourism around the archipelago (Hoffmann-Rothe *et al.* 2006).

One possible major hazard emerging from Anak Krakatau would be a tsunami triggered by a collapse of its flank, as the volcano is partly built on a steep wall of the caldera resulting from the 1883 eruption. A small tsunami (*c.* 2 m high) was experienced on Rakata Island in October 1981 during an awakening of Anak Krakatau (Camus *et al.* 1987). In the present study, we numerically simulate a sudden southwestwards destabilization of a large part of the Anak Krakatau Volcano, and the subsequent tsunami formation and propagation. We show results concerning the time of arrival and the amplitude of the waves produced, both in the Sunda Strait and on the coasts of Java and Sumatra. We then discuss the relationships between the morphology of Anak Krakatau, the locations of the surrounding islands, the bathymetry of the strait and the triggered waves.

Geography, population and infrastructures in the Sunda Strait

The Sunda Strait, in which Anak Krakatau Volcano lies, has a roughly NE–SW orientation, with a minimum width of 24 km at its NE end between Sumatra and Java (Fig. 1). Its western end is deep (< -1500 m), but it shallows significantly as it narrows to the east, with a depth of only about 20 m in parts of the eastern end, making it difficult to navigate due to sandbanks and strong tidal flows. The numerous islands in the strait and the nearby surrounding regions of Java and Sumatra were devastated by the 1883 Krakatau eruption. The eruption drastically altered the topography of the strait, with approximately 12 km^3 (DRE, dense rock equivalent) of ignimbrite being deposited around the volcano (Carey *et al.* 1996). The small to moderate volcanic explosions of Anak Krakatau, which is partly built on the site of the former Krakatau Island, attract tourist boats that circulate between the islands of the Krakatau Archipelago.

Some areas have never been resettled since the 1883 eruption (e.g. the SW of Java), but much of the coastline is now densely populated, especially in Bandar Lampung (*c.* 900 000 inhabitants) on Sumatra, and on the west coast of the Cilegon District (*c.* 400 000 inhabitants) in Java (Fig. 1). Moreover, many of the roads on western Java and southern Sumatra are located near the sea and at low altitude (< 10 m), as well as important economic infrastructures such as power stations (e.g. Labuhan, NE of Merak and SE of Banda

Downloaded from http://sp.lyellcollection.org/ by guest on March 12, 2012

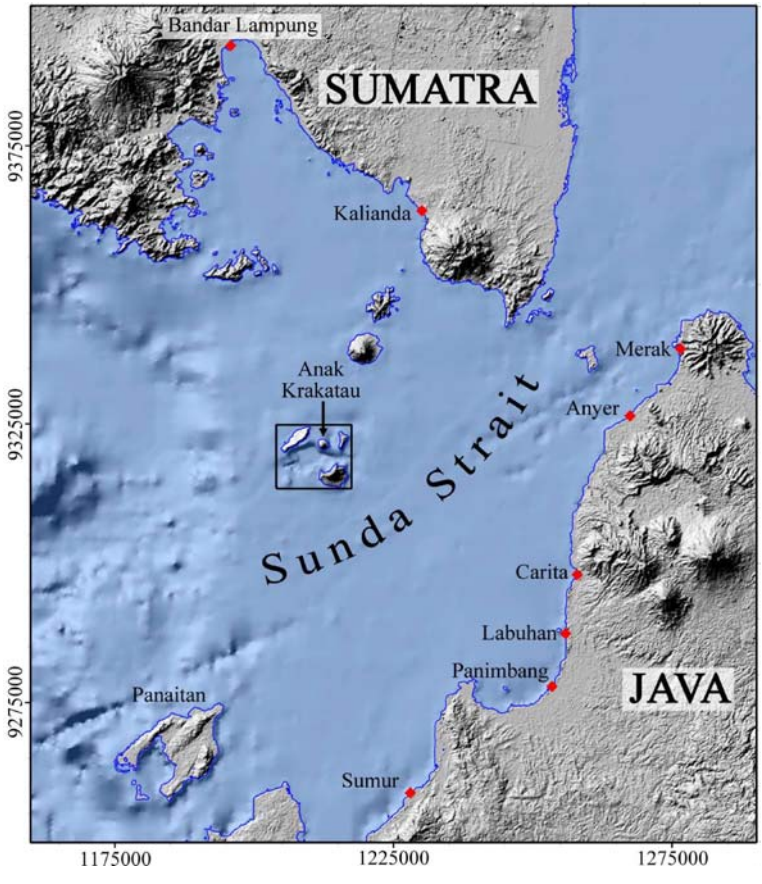

Fig. 1. Shaded relief representation of the DEM (100 m resolution) of Sunda Strait, based on ASTER topography, GEBCO bathymetry and a digitization of the bathymetric map of Krakatau from Deplus *et al.* (1995, their fig. 7). This DEM is the calculation grid used to simulate the Anak Krakatau landslide and the subsequent tsunami propagation (calculations were made at a resolution of 200 m). The main coastal cities or important infrastructures around the Sunda Strait are indicated by red diamonds. The black frame around the Krakatau Archipelago corresponds to the limits of Figure 2b, c. Geographical co-ordinates are in metres.

Lampung), industries (e.g. steel industries in Cilegon), major harbours connecting Java and Sumatra (Merak, Bakaheuni), and tourist resorts (e.g. Anyer, Kalianda). There are also several oil platforms in the strait, notably off the Java coast. Such infrastructures would potentially be badly affected by a tsunami of several metres, as was produced during the 1883 eruption.

In October 2007, the Indonesian government planned the construction of a 30 km road and railway connection between the islands of Sumatra and Java (the Selat Sunda Bridge), across the 26 km Sunda Strait, at an altitude of 70 m asl (above sea level). In 2009, the 'pre-feasibility' study for this 10 billion dollar project was completed and the construction is expected to begin in 2012. Owing to the seismic and volcanic activity in the Sunda region, this project faces many challenges. Krakatau Volcano is located only 40 km away from the future bridge. Some of the bridge's piles may suffer from tsunamis crossing the Sunda Strait, therefore such hazards need to be quantified.

Anak Krakatau Volcano: evolution and actual morphology

Anak Krakatau first rose up out of the sea in 1928, sited just off the steep NE wall of the basin formed by the collapse of the 1883 Krakatau eruption caldera. This volcano was built where the main vent for the 1883 eruption is supposed to have been located, about midway between the former craters of Danan and Perbuatan (Deplus

Downloaded from http://sp.lyellcollection.org/ by guest on March 12, 2012

et al. 1995). Between 1928 and 1930, the volcano receded and reappeared three times until it established itself permanently above sea level. In 1959, an uninterrupted 152 m-high hyaloclastic tuff-ring developed (Sudradjat 1982) and a lake formed in the crater. The eruption style was Surtseyan during the 1928–1930 period (Stehn 1929; Camus *et al.* 1987), then Vulcanian until 1960, before shifting to Strombolian explosions that created a cone reaching 200 m asl in 1981 (Oba *et al.* 1983). In 1981, a Vulcanian eruption marked a southwestwards shift of Anak Krakatau activity (Sudrajat 1982) with more differentiated volcanic products (acid andesites, dacites) than previously erupted (mainly basalts and andesites before 1981: Camus *et al.* 1987). At the time of writing, the latest eruption of Anak Krakatau, which started on 25 October 2010, is still ongoing, with dense ash clouds forming plumes 100–1000 m high.

Rapid soundings in 1928 have shown that the western slope of the volcano was considerably steeper ($>28^{\circ}$) than the eastern, as a consequence of its position on the steep wall of the basin and also of the strong current that is generally running from SW to NE (Stehn 1929). Deplus *et al.* (1995) showed that this slope was still in existence in 1995, and that the successive eruptions had not resulted in an infilling of the caldera. According to these data concerning the steep slopes on which Anak Krakatau is built and the fact that this volcano is growing towards the SW, landslides along its southwestern flank cannot be excluded (Deplus *et al.* 1995). Such a landslide would be directed southwestwards into the 1883 caldera and would trigger waves that would propagate into the Sunda Strait, possibly affecting the Indonesian coasts.

Methodology

Digital elevation model used and scenario envisaged

The collapse of the Anak Krakatau Volcano was simulated on a digital elevation model (DEM) obtained by merging the ASTER (*Advanced Spaceborne Thermal Emission and Reflection* Radiometer) topography (*c.* 30 m resolution), bathymetric maps (one from Dishidros Indonesian Navy and a Sunda Strait navigation chart) and the GEBCO (General Bathymetric Chart of the Oceans) bathymetry (*c.* 900 m resolution) of the whole Sunda Strait region (Fig. 1). In addition, the bathymetric map of the Krakatau Archipelago from Deplus *et al.* (1995, their fig. 7) was digitized and added to the DEM in order to obtain a better resolution of the zone where the collapse occurs and where the waves are initially produced (Fig. 2b). The final DEM produced, which is the calculation grid used for the numerical simulation, is a 1500×1300 pixel grid with a spatial resolution of 100 m (Fig. 1). In order to maximize on the best spatial resolution available to register the initial waves produced, some of the simulations were performed on a portion of the grid centred on the landslide event. Owing to the long calculation times we down-sampled the grid by a factor of 2 (i.e. 750×650 pixel calculation grid and a spatial resolution of 200 m) for the simulations of tsunami propagation over the entire Sunda Strait area.

Some level lines of the DEM were modified to build the sliding surface of the hypothetical landslide; that is, to define the hypothetical collapse scar. This was done so that: (1) the upper end of the scar is broadly defined by the limit between the older tuff-ring and the new cone (Fig. 2a, c); (2) the base of the scar lies at the bottom of the 1883 caldera (Fig. 2a); and (3) the scar is horseshoe-shaped (Fig. 2c). The scar is oriented southwestwards, with an average slope of 8.2° (Fig. 2a) and a width of *c.* 1.9 km, defining a collapsing volume of 0.280 km^3. This scar probably cuts the NE wall of the 1883 caldera, but this cannot be clearly traced on the DEM as no precise bathymetric data immediately following the 1883 eruption are available. In our simulation, the debris avalanche is released in a single event.

Numerical model

We used the numerical code *VolcFlow* (Kelfoun *et al.* 2010; Giachetti *et al.* 2011) to simulate both the Anak Krakatau landslide and the tsunami propagations. A full explanation of the code and equations is given in the previously cited papers. This code is based on the two-dimensional (2D) depth-average approach, modified to incorporate 3D interactions with greater accuracy; both the landslide and the sea water being simulated using the general shallow-water equations of mass conservation and momentum balance. In the model, the water interacts with the bathymetry/topography and floods onto the land, but waves breaking and other complex second-order 3D effects are not taken into account, and sediment erosion and transport are also ignored.

We simulated the water propagation using a density of 1000 kg m^{-3} and a viscosity of 0.001 Pa s. As emissions from Anak Krakatau are mainly composed of scoriaceous material with a basaltic (common) to dacitic (rarer) chemical composition (Sudradjat 1982; Camus *et al.* 1987), we used a density of 1500 kg m^{-3} to simulate the landslide. Kelfoun *et al.* (2010) and Giachetti *et al.* (2011) showed that the rheology used to simulate the landslide propagation may be important when dealing with second-order variations of the profile

Downloaded from http://sp.lyellcollection.org/ by guest on March 12, 2012

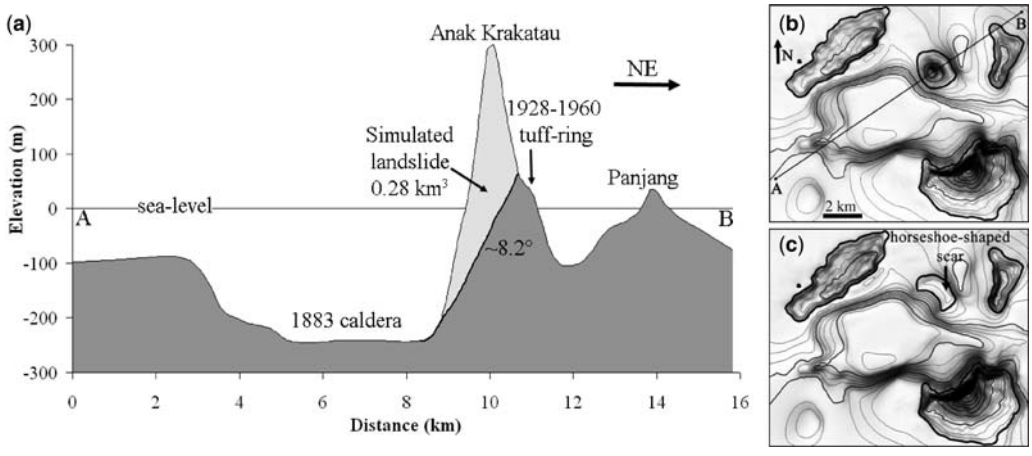

Fig. 2. (**a**) Cross-section of Anak Krakatau (inset: Fig. 1) and the 1883 eruption caldera. The landslide scar, defined by modifying some level lines on our initial DEM, is drawn in black. It is orientated southwestwards, with a slope of 8.2°, delimiting a collapsing volume of about 0.28 km^3. (**b**) Topography before the simulated landslide, with the location of the cross-section presented in (a). The caldera resulting from the 1883 Krakatau eruption is clearly visible, as well as Anak Krakatau, which is built on the NE flank of this caldera. (**c**) Topography after the simulated landslide, with the horseshoe-shaped scar clearly visible.

and amplitude of the triggered waves. Thus, we tested four sets of rheological parameters to simulate the debris avalanche propagation: a commonly used Mohr–Coulomb frictional law with a basal friction angle of 1° or 2° (hereafter referred to as rheologies 1 and 2, respectively) and a constant retarding stress of 5 or 10 kPa (rheologies 3 and 4, respectively). Although the Mohr–Coulomb frictional law is often used in granular-flow dynamics because it represents the behaviour of deposits at rest and of sand flows in the laboratory, the constant retarding stress appears to be better adapted to the reproduction of the extent, thickness on all slopes and some morphological features of natural deposits (e.g. Dade & Huppert 1998; Kelfoun & Druitt 2005). Figure 3a shows that the surface area covered by the simulated debris avalanche deposits varies depending on the rheology used (the numerical deposits obtained using rheologies 1–2 and rheologies 3–4 are quasi-identical and are thus drawn together). Figure 3b presents the water surface displacement recorded using a gauge placed approximately 15 km southwestwards from the landslide scar (black diamond in Fig. 3a), in

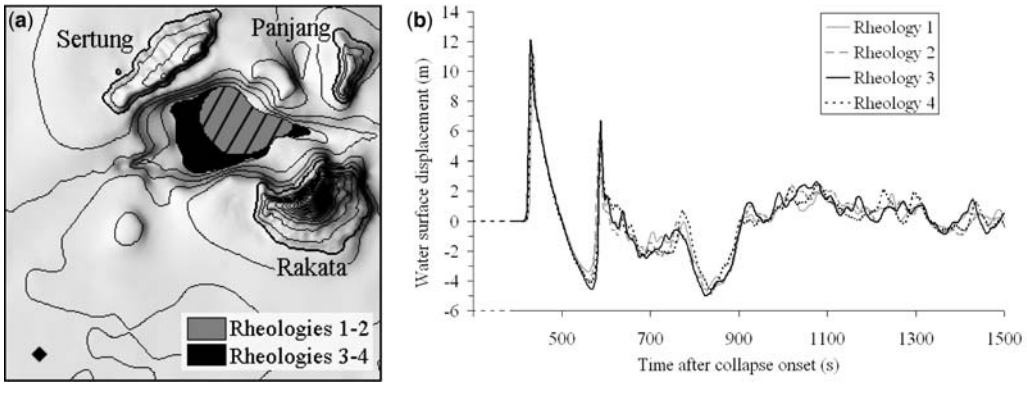

Fig. 3. (**a**) Simulated debris avalanche deposits obtained using rheologies 1–2 (grey) and 3–4 (black hatching and black) to simulate the landslide propagation. (**b**) Simulated water surface displacement recorded at the gauge located in Figure 2a (black diamond). This figure shows that the waves produced are very similar, whatever the rheology used to simulate the landslide propagation.

Downloaded from http://sp.lyellcollection.org/ by guest on March 12, 2012

the direction of propagation of the major triggered waves, where the water depth is aproximately 100 m. It shows that the wave profiles and amplitudes created are very similar, whichever of the four rheologies are used. The maximum amplitude recorded at the gauge placed approximately 15 km southwestwards varies between 11 (rheology 2) and 12 m (rheology 3).

We believe that the similarity between the wave profiles presented in Figure 3b is due to the initial geometry of the collapsing volume and the landslide scar. Indeed, as the collapsing volume is initially partly submerged and the landslide scar directs the debris avalanche southwestwards, the initial waves triggered by the landslide–water impact are poorly influenced by the rheology used to simulate landslide propagation. This rheology, however, plays a role in the final run-out of the modelled debris avalanche deposits (Fig. 3a). The morphology of the modelled deposits (not shown here) is very similar whatever the rheology used because of the dominant controlling factor of the structure of the 1883 caldera. The rheology used to simulate the landslide propagation is also responsible for the small second-order discrepancies existing between the wave profiles registered, which are amplified over time (Fig. 3b). However, since in this paper we focus on the tsunami hazards and not on the simulated morphology of the debris avalanche deposits, we arbitrarily chose the constant retarding stress of 10 kPa (rheology 4) to simulate the landslide propagation for the whole calculation grid.

Results

When interacting with the water, the debris avalanche triggers waves whose maximum initial amplitude is around 45 m, measured approximately 45 s after the collapse onset at 2.5 km southwestwards from the landslide scar. The waves produced then propagate in a radial manner away from the impact region, reaching the islands of Sertung, Panjang and Rakata (Fig. 3a) in less than 1 min, with amplitudes from 15 to 30 m. Owing to the southwestwards propagation of the landslide, the highest waves are produced in this direction. The wave profile obtained about 15 km SW from the landslide scar (Fig. 3b, rheology 4) shows a first wave with an amplitude of 11.3 m and a period of around 162 s (wavelength of c. 3.4 km). This is followed by another 5.3 m wave, with a smaller period of approximately 60 s (wavelength of c. 1.3 km). This is then followed by several smaller and shorter waves, the sea level regaining its initial position after a few tens of minutes. The travel time of the first wave is shown in Figure 4, and is given more precisely in Table 1 for the main coastal cities and infrastructures located in Figure 1. The cities situated on the western coast of Java are all touched by the first wave between 36 and 47 min after the onset of the Anak Krakatau collapse. The first wave reaches Kalianda and Bandar Lampung, located on Sumatra, 45 and 68 min after the onset of the collapse, respectively. Note that everywhere in the Sunda Strait the wavelength of the simulated waves is always more than 25 times the water depth. This demonstrates that the use of the general shallow-water equations of mass conservation and momentum balance to simulate the water propagation is appropriate in this case (e.g. Synolakis *et al.* 1997).

Figure 5 presents the maximum wave amplitude registered over 6000 s of simulation. It shows that the highest waves are mainly concentrated around

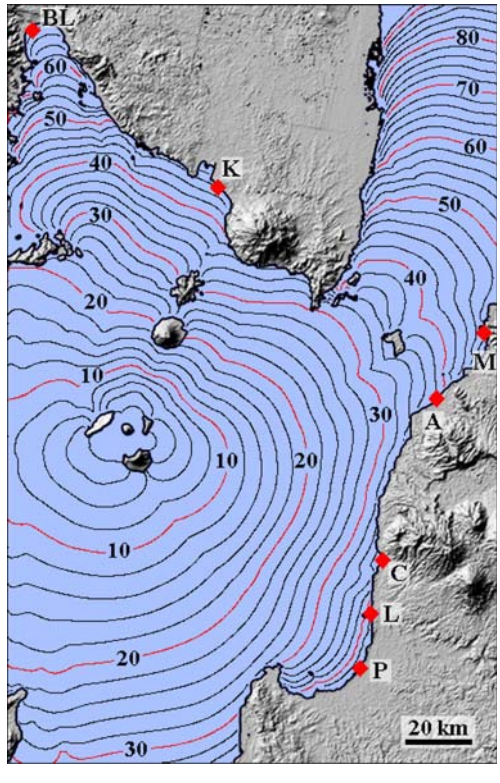

Fig. 4. First wave travel time (expressed in min) for the first 90 min of simulation. Black lines are at 2 min intervals. Main coastal cities (names in Fig. 1) are shown by red diamonds. The impact of the sudden increase in water depth westwards from the Krakatau Archipelago is clearly seen (see Fig. 1 for bathymetry), the waves being more rapid than those crossing the shallow strait. BL, Bandar Lampung; K, Kalianda; M, Merak; A, Anyer; C, Carita; L, Labuhan; P, Panimbang. The simulation of the landslide propagation was carried out using a constant retarding stress of 10 kPa.

Downloaded from http://sp.lyellcollection.org/ by guest on March 12, 2012

Table 1. *Travel time and maximum wave amplitude recorded at gauges located close (<900 m) to the main coastal cities of the Sunda Strait (see Fig. 1)*

	Bandar Lampung (−13 m)	Kalianda (−5 m)	Merak (−12 m)	Anyer (−12 m)	Carita (−12 m)	Labuhan (−4 m)	Panimbang (−2 m)	Sumur (−7 m)
Travel time (min)	68	44	47	38	37	40	43	36
Maximum wave amplitude (m)	0.3	2.7	1.5	1.4	2.9	3.4	1.5	1.2

For each city, the initial water depth at the gauge site is given in brackets.

the Krakatau Archipelago, as it is the location of the triggering event, and their amplitude logically decreases away from Anak Krakatau. Westwards, at about 20 km from the landslide, the wave amplitude is slightly reduced because of the strong increase in water depth, and waves do not exceed 1–2 m when they reach the western edge of the calculation grid. The highest waves produced are directed southwestwards and their amplitude decreases when they reach greater water depths in the SW. However, they still have an amplitude of more than 3–4 m when they arrive near Panaitan and near the southwestern coast of Java (Ujung Kulon National Park). The presence of the islands of Sertung and Rakata (Fig. 3a) – NW and SW of the landslide, respectively – also causes the wave amplitude to be reduced. The maximum amplitude of the waves recorded northwards and northeastwards is not related to the first wave produced. It appears that they come from the reflection of the initial waves off the coasts of Sertung and Rakata (the former consisting of a high cliff orientated NNW). However, owing to the numerous interactions of the waves with the four islands of the Krakatau Archipelago, it is difficult to establish exactly what happens near the impact point. Figure 5 also shows some reflections of the waves, in particular off the western coast of Java.

Figure 6 presents the evolution of the water level over 6500 s of simulation, recorded at gauges placed in the sea a few hundreds of metres (<900 m) off eight of the main coastal cities or infrastructures of the Sunda Strait (located in Fig. 1). The gauges were placed in the sea near the coasts to free the sea-level profiles recorded from the 3D interactions that the program fails to reproduce in an accurate manner. The maximum wave amplitudes measured at these gauges are indicated in Table 1 (the vertical water depth at each gauge is indicated in Table 1). The water-level profiles are different from one city to another, being complicated by numerous reflections of the waves throughout the Krakatau Archipelago, as well as around the Sumatran and Javanese coasts. All of the cities are touched by a first positive wave with amplitude ranging from 0.3 to 2.3 m, but this first wave is never the highest one. Near Bandar Lampung and Kalianda, the maximum wave amplitude measured is 0.3 and 2.7 m respectively, and the coastal cities of western Java are generally affected by waves with maximums of between 1.2 (Sumur) and 3.4 m (Labuhan).

Discussion

Influence of the initial parameters on the wave characteristics

The volume of a debris avalanche and the way it occurs (e.g. in one go, by retrogressive failures) are the parameters that most influence the characteristics of the triggered tsunami (Locat *et al.* 2004; Giachetti *et al.* 2011). In the present case, the hypothetical scar has a slope of 8.2°, for an initial Anak Krakatau average slope of 24.2° (Fig. 3a). These values are lower than those observed for other scars of debris avalanches that triggered tsunamis, like the Palos Verdes debris avalanche (California, scar slope of 10°–17°: Locat *et al.* 2004) or 29 submarine events identified at Stromboli (average scar slope of *c*. 25°, and pre-failure slope of *c*. 28° for debris avalanches between 5 and 200 m b.s.l.: Casalbore *et al.* 2011). In this study, we decided to base the structural definition of the hypothetical scar on the known structural evolution of Anak Krakatau: the upper end of the scar being defined by the limit between the older tuff-ring and the new cone, and its base by the bottom of the 1883 caldera. Therefore, our numerical model of Anak Krakatau involves a debris avalanche volume of 0.280 km^3. The definition of a steeper scar (closer to the values observed by Locat *et al.* 2004 or Casalbore *et al.* 2011) would lead to a more rapid landslide into the water, and thus possibly to higher waves. However, a steeper scar would also result in a smaller collapsing volume (considering the lower end of the scar as fixed) and thus to slightly smaller waves. Since in this study our aim is to quantify the tsunami hazard linked to a realistic partial flank collapse of Anak Krakatau, we decided to maximize the volume involved in the debris avalanche (and

Downloaded from http://sp.lyellcollection.org/ by guest on March 12, 2012

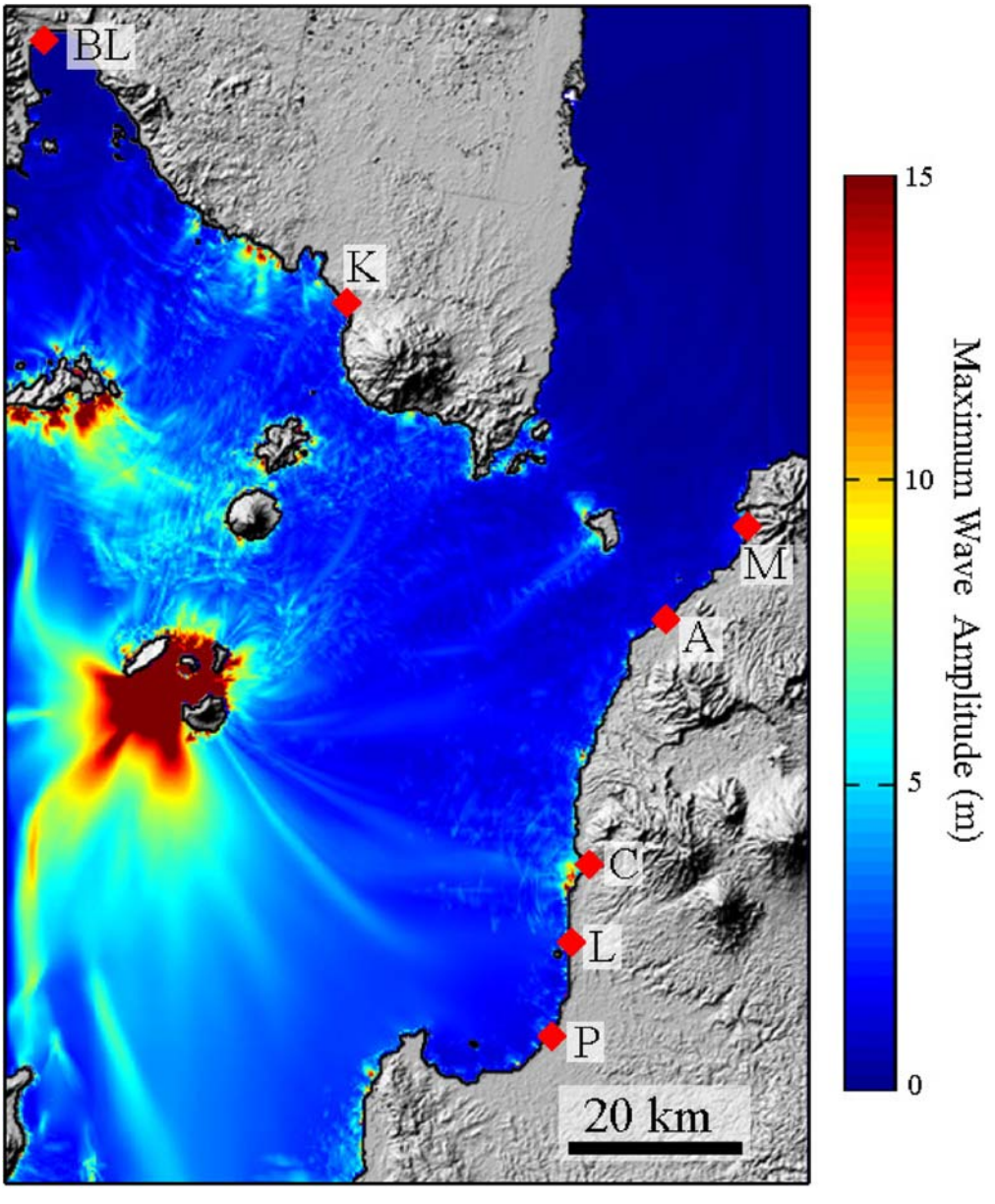

Fig. 5. Maximum wave amplitude (m) recorded over 6000 s of simulation, using a constant retarding stress of 10 kPa to simulate the landslide propagation.

thus the waves produced) while remaining consistent with the structure of the volcano.

Influence of the bathymetry/topography on the tsunami characteristics

To define the initial volume that would hypothetically collapse, we used the available topography data (ASTER data, spatial resolution of 30 m) for Anak Krakatau Island. However, there is no up-to-date high-resolution topography and bathymetry data for this volcano, whose morphology changes rapidly due to its numerous eruptions. For this reason, we think that high-resolution topographical and bathymetric surveys of the Anak Krakatau Volcano should be performed in order to

Downloaded from http://sp.lyellcollection.org/ by guest on March 12, 2012

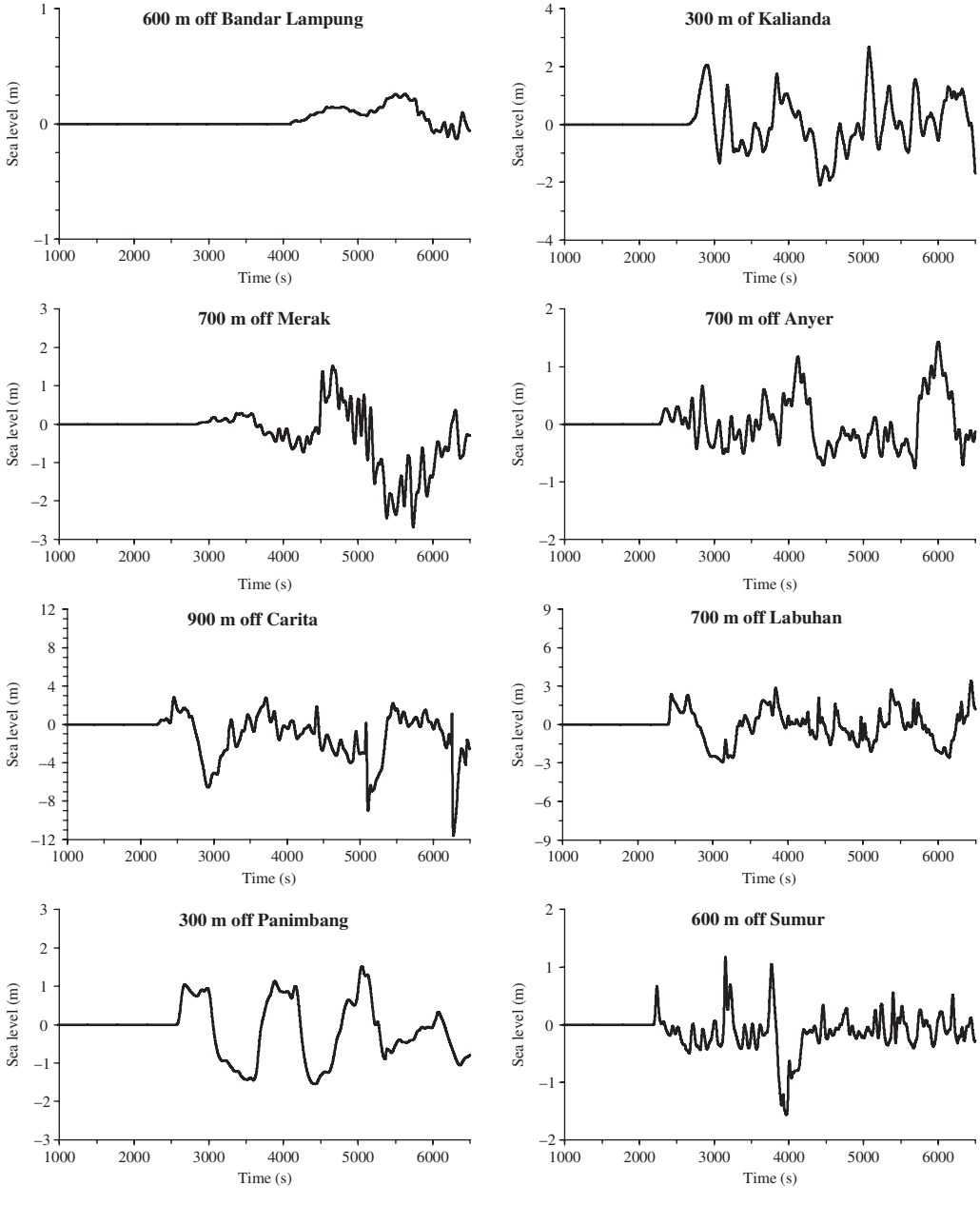

Fig. 6. Simulated sea-level profiles (m) registered several hundred metres (indicated on the plots) off eight of the main coastal cities located in Figure 1. The simulation of the landslide propagation was carried out using a constant retarding stress of 10 kPa. Time is expressed in seconds after the collapse onset. The water depth below each gauge is indicated in Table 1.

improve the accuracy when defining the initial conditions of the landslide. Side-scan sonar surveys coupled with INSAR (Interferometric Synthetic Aperture Radar) monitoring may also reveal evidence of slope instability. The travel time map of the first wave based on the simulations (Fig. 4) is consistent with the refraction diagram of the tsunami caused by the 1883 Krakatau eruption (Yokoyama 1981). However, the wave travel time estimated may suffer from artefacts in the

Downloaded from http://sp.lyellcollection.org/ by guest on March 12, 2012

bathymetry used for calculations. The inclusion of bathymetric maps of parts of Sunda Strait in the constructed DEM allowed us to minimize these artefacts, but new bathymetric maps of this region would be useful for a better tsunami hazard assessment.

Tsunami hazards

Our simulation shows that the first wave produced has a maximum amplitude of about 45 m. This height is reached at approximately 2.5 km SW of the landslide scar (i.e. Anak Krakatau Island), inside the Krakatau Archipelago. Moreover, the waves produced reach the surrounding islands of Sertung, Rakata and Panjang in less than 1 min, with heights of up to 30 m. These waves could be a serious hazard for the many tourist boats that visit these islands every day. Further from the Krakatau Archipelago, the wave amplitude decreases in Sunda Strait and waves are generally smaller than 10 m at a distance of more than 20 km from the landslide scar. However, these waves could still be dangerous for the small boats crossing the strait between the Krakatau Archipelago and the coasts of Java or Sumatra. It should be noted that the islands of the Krakatau Archipelago (Anak Krakatau, Sertung, Panjang and Rakata), as well as those of Sebesi and Sebuku in the NE, those of Legundi and Siuntjal in the NNW, and Panaitan in the SSW are uninhabited, and thus the risk is drastically reduced. Between the two islands of Java and Sumatra, where the planned bridge is to be constructed (see the explanation in the earlier section on 'Geography, population and infrastructures in the Sunda Strait'), the waves do not reach more than 3.8 m, and the construction should be able to absorb the strain developed by such a wave.

Our numerical simulation of the sudden collapse of Anak Krakatau Volcano into the 1883 caldera shows that all the coasts around the Sunda Strait could potentially be affected by waves of more than 1.0 m in less than 1 h after the event. Even the southern coasts of Sumatra, which are located more than 40 km to the north of the landslide, would be touched by the tsunami because of the numerous wave reflections off the islands of the Krakatau Archipelago. All of the main cities or infrastructures of the Sunda Strait would be affected within 1 h of the collapse. The highest waves registered off these coastal cities are those near Labuhan (3.4 m) on the western coast of Java, but most of the gauges give values of less than 3 m for the highest wave. These values are far less than those observed during the 1883 Krakatau eruption, which reached an average value of 15 m on the coasts of Sumatra and Java (Symons 1888; Yokoyama 1981), with a local wave height of up to 30 m. Moreover, Figure 5 shows that some parts of the coast are partially protected by the numerous islands in Sunda Strait (e.g. Rakata prevents the propagation of very high waves towards the large bay off Panimbang). Waves become smaller with increasing distance from the triggering event. During the 1883 tsunami, Jakarta was touched by a wave approximately 1.8 m high about 140 min after the eruption of Krakatau, whereas Merak and Anyer were touched by 15 m-high waves. Likewise, the 1883 tsunami also reached locations thousands of kilometres from the volcano (Choi *et al.* 2003, Pelinovsky *et al.* 2005). Considering that the maximum wave height recorded off Anyer and Merak is around 1.5 m in our simulation, we believe that the tsunami triggered by a flank collapse at Anak Krakatau would be negligible at Jakarta.

Conclusion

Our numerical simulation shows that a partial destabilization (0.28 km^3) of Anak Krakatau Volcano towards the SW would possibly be dangerous on a local scale (tourist and fishing activities around the volcano) or even on a regional scale (coasts of Sumatra and Java). This event would trigger an initial wave of 43 m that would reach all of the islands in the Krakatau Archipelago in less than 1 min, with amplitudes ranging from 15 to 30 m, and would be extremely dangerous for boats in the Krakatau Archipelago. Waves would then propagate in a radial manner across Sunda Strait at an average speed of 80–110 km h^{-1}, the first wave reaching cities on the western coast of Java after 35–45 min, with a maximum amplitude of between 2.9 (Carita) and 3.4 m (Labuhan). These waves would be considerably smaller than those produced during the 1883 Krakatau eruption (average wave height of *c.* 15 m around the Sunda Strait).

Owing to the high population, the concentration of road and industrial infrastructure along some parts of the exposed coasts of Java and Sumatra, and the low elevation of much of this land, the tsunami might present a significant risk. However, as the travel time of the tsunami is several tens of minutes between the Krakatau Archipelago and the main cities along these coasts, a rapid detection of the collapse by the volcano observatory, coupled with an efficient alert system on the coast, could prevent this hypothetical event from being deadly. A tsunami preparedness project was initiated in 2006 by UNESCO and the Indonesian Institute of Sciences (LIPI). However, it should be noted that the ground deformation of the volcano is not permanently monitored, and the available data (e.g. bathymetry) are not sufficient to allow for an accurate assessment of slope instability.

Downloaded from http://sp.lyellcollection.org/ by guest on March 12, 2012

The example of Krakatau Volcano illustrates the point that tsunamis generated by volcanic eruptions and flank instability are a neglected hazard. They represent 25% of all the fatalities directly attributable to volcanoes during the last 250 years (Latter 1981; Begét 2000). At least 115 volcanic tsunamis have been observed since 1600 AD (death toll >54 000), with 36 events during the nineteenth century and 54 events during the twentieth. Volcanic tsunamis can be dangerous because they can occur with little warning, and cause devastation at great distances. South Asian and South Pacific regions are particularly exposed to volcanic tsunamis because of the high density of active volcanoes located near the coasts (volcanic island arcs). Systematic monitoring of flank instability and the integration of tsunamis into volcanic hazard assessments (e.g. maps, evacuation routes) would reduce the impact of future events.

This work is part of the 'Vitesss' project (Volcano-Induced Tsunamis: numErical Simulations and Sedimentary Signature) supported by the French National Research Agency (ANR project 08-JCJC-0042) and whose leader is R. Paris (Geolab, CNRS). ASTER GDEM is a product of METI and NASA. We thank two anonymous reviewers for their constructive reviews of this manuscript. We are also grateful to Anaïs Ferot who first suggested we perform this study.

References

Begét, J. E. 2000. Volcanic tsunamis. *In*: Sigurdsson, H., Houghton, B., McNutt, S. R., Rymer, H. & Stix, J. (eds) *Encyplopedia of Volcanoes*. Academic Press, New York, 1005–1013.

Camus, G. & Vincent, P. M. 1983. Discussion of a new hypothesis for the Krakatau volcanic eruption in 1983. *Journal of Volcanology and Geothermal Research*, **19**, 167–173.

Camus, G., Gourgaud, A. & Vincent, P. M. 1987. Petrologic evolution of Krakatau (Indonesia): implications for a future activity. *Journal of Volcanology and Geothermal Research*, **33**, 299–316.

Carey, S., Sigurdsson, H., Mandeville, C. W. & Bronto, S. 1996. Pyroclastic deposits from flows and surges which travelled over the sea during the 1883 eruption of Krakatau volcano. *Bulletin of Volcanology*, **57**, 493–511.

Casalbore, D., Romagnoli, C., Bosman, A. & Chiocci, F. L. 2011. Potential tsunamigenic landslides at Stromboli Volcano (Italy): insight from marine DEM analysis. *Geomorphology*, **126**, 42–50, doi: 10.1016/j.geomorph.2010.10.026.

Choi, B. H., Pelinovsky, E., Kim, K. O. & Lee, J. S. 2003. Simulation of the trans-oceanic tsunami propagation due to the 1883 Krakatau volcanic eruption. *Natural Hazards and Earth System Sciences*, **3**, 321–332.

Dade, W. B. & Huppert, H. E. 1998. Long-runout rockfalls. *Geology*, **26**, 803–806.

de Lange, W. P., Prasetya, G. S. & Healy, T. R. 2001. Modelling of tsunamis generated by pyroclastic flows (ignimbrites). *Natural Hazards*, **24**, 251–266.

Deplus, C., Bonvalot, S., Dahrin, D., Diament, M., Harjono, H. & Dubois, J. 1995. Inner structure of the Krakatoa volcanic complex (Indonesia) from gravity and bathymetry data. *Journal of Volcanology and Geothermal Research*, **64**, 23–51.

Francis, P. W. 1985. The origin of the 1883 Krakatau tsunamis. *Journal of Volcanology and Geothermal Research*, **25**, 349–363.

Fritz, H. M., Hager, W. H. & Minor, H. E. 2001. Lituya Bay case: rockslide impact and wave run-up. *Science of Tsunami Hazards*, **19**, 3–22.

Fritz, H. M., Kalligeris, N. J., Borrero, C., Broncano, P. & Ortega, E. 2008. The 15 August 2007 Peru tsunami runup observations and modeling. *Geophysical Research Letters*, **35**, L10604-4, doi: 10.1029/2008GL033494.

Giachetti, T., Paris, R., Kelfoun, K. & Pérez-Torrado, F. J. 2011. Numerical modelling of the tsunami triggered by the Güìmar debris avalanche, Tenerife (Canary Islands): comparison with field-based data. *Marine Geology*, **284**, 189–202, doi:10.1016/j.margeo.2011.03.018.

Harbitz, C. B., Løvholt, F., Pedersen, G. & Masson, D. G. 2006. Mechanisms of tsunami generation by submarine landslides: a short review. *Norwegian Journal of Geology*, **86**, 255–264.

Hoffmann-Rothe, A., Ibs-von Seht, M. *et al.* 2006. Monitoring Anak Krakatau Volcano in Indonesia. *Eos Transactions of the American Geophysical Union*, **87**, 581, doi: 10.1029/2006EO510002.

Keating, B. H. & McGuire, W. J. 2000. Island edifice failures and associated tsunami hazards. *Pure and Applied Geophysics*, **157**, 899–955.

Kelfoun, K. & Druitt, T. H. 2005. Numerical modelling of the emplacement of Socompa rock avalanche, Chile. *Journal of Geophysical Research*, **110**, B12202.

Kelfoun, K., Giachetti, T. & Labazuy, P. 2010. Landslide-generated tsunamis at Reunion Island. *Journal of Geophysical Research*, **115**, F04012, doi: 10.1029/2009JF001381.

Latter, J. N. 1981. Tsunamis of volcanic origin: summary of causes with particular references to Krakatoa, 1883. *Bulletin of Volcanology*, **44**, 467–490.

Locat, J., Lee, H. J., Locat, P. & Irman, J. 2004. Numerical analysis of the mobility of the Palos Verdes debris avalanche, California, and its implication for the generation of tsunamis. *Marine Geology*, **203**, 269–280.

Mader, C. L. & Gittings, M. L. 2006. Numerical model for the Krakatoa hydrovolcanic explosion and tsunami. *Science of Tsunami Hazards*, **24**, 174–182.

Maeno, F. & Imamura, F. 2007. Numerical investigations of tsunamis generated by pyroclastic flows from the Kikai caldera, Japan. *Geophysical Research Letters*, **34**, L23303-1, doi: 10.1029/2007GL031222.

Maeno, F., Imamura, F. & Taniguchi, H. 2006. Numerical simulation of tsunami generated by caldera collapse during the 7.3 ka Kikai eruption, Japan. *Earth Planets and Space*, **58**, 1013–1024.

Downloaded from http://sp.lyellcollection.org/ by guest on March 12, 2012

MARAMAI, A., GRAZIANI, L. *ET AL.* 2005. Near- and far-field survey report of the 30 December 2002 Stromboli (Southern Italy) tsunami. *Marine Geology*, **215**, 93–106.

MICHIUE, M., HINOKIDANI, O. & MIYAMOTO, K. 1999. Study on the Mayuyama tsunami disaster in 1792. *In*: *Proceedings of the 28th IAHR Congress, Graz, Austria, 22–27 August 1999*. International Association of Hydro-Environment Engineering and Research, Madrid (CD-ROM).

NOMANBHOY, N. & SATAKE, K. 1995. Generation mechanism of tsunamis from the 1883 Krakatau eruption. *Geophysical Researc. Letters*, **22**, 509–512.

OBA, N., TOMITA, K. *ET AL.* 1983. Geochemical study of volcanic products, in particular to pumice flow, of the Krakatau Group, Indonesia. *Report of the Faculty of Science, Kagoshima University (Earth Science, Biology)*, **16**, 21–41.

PELINOVSKY, E., CHOI, B. H., STROMKOV, A., DIDENKULOVA, I. & KIM, H. S. 2005. Analysis of tide-gauge records of the 1883 Krakatau tsunami. *In*: *Tsunamis: Case Studies and Recent Developments. Advances in Natural and Technological Hazards Research*, **23**, 57–77.

SELF, S. & RAMPINO, M. R. 1981. The 1883 eruption of Krakatau. *Nature*, **294**, 699–704.

SIGURDSSON, H., CAREY, S. & MANDEVILLE, C. 1991*a*. Submarine pyroclastic flows of the 1883 eruption of the Krakatau Volcano. *National Geographic Research and Exploration*, **7**, 310–327.

SIGURDSSON, H., CAREY, S., MANDEVILLE, C. & BRONTO, S. 1991*b*. Pyroclastic flows of the 1883 Krakatau eruption. *Eos Transactions of the American Geophysical Union*, **72**, 377.

SIMKIN, T. & FISKE, R. S. 1983. *Krakatau 1883: The Volcanic Eruption and its Effects*. Smithsonian Institution Press, Washington, DC.

STEHN, C. E. 1929. The geology and volcanism of the Krakatau Group. *In*: *Proceedings of the Fourth Pacific Science Congress, Batavia-Bandoeng (Java), May–June, 1929*. Martinus Nijhoff, The Hague, 1–55.

SUDRADJAT, A. 1982. The morphological development of Anak Krakatau Volcano, Sunda Strait. *Geology of Indonesia*, **9**, 1–11.

SYMONS, G. J. 1888. *The Eruption of Krakatoa, and Subsequent Phenomena. Report of the Krakatoa Committee of the Royal Society*. Trübner, London.

SYNOLAKIS, C. E., LIU, P. L. F., YEH, H. & CARRIER, G. F. 1997. Tsunamigenic seafloor deformations. *Science*, **278**, 598–600.

TINTI, S., BORTOLUCCI, E. & ROMAGNOLI, C. 1999. Modelling a possible holocenic landslide-induced tsunami at Stromboli volcano, Italy. *Physics and Chemistry of the Earth*, **24**, 423–429.

TINTI, S., BORTOLUCCI, E. & ROMAGNOLI, C. 2000. Computer simulations of tsunamis due to sector collapse at Stromboli, Italy. *Journal of Volcanology and Geothermal Research*, **96**, 103–128.

TINTI, S., PAGNONI, G. & ZANIBONI, F. 2006. The landslides and tsunamis of the 30th of December 2002 in Stromboli analysed through numerical simulations. *Bulletin of Volcanology*, **68**, 462–479.

TSUJI, Y. & HINO, T. 1993. Damage and inundation height of the 1792 Shimabara landslide tsunami along the coast of Kumamoto prefecture. *Bulletin of the Earthquake Research Institute, University of Tokyo*, **68**, 91–176.

VERBEEK, R. D. M. 1885. Krakatau. *In*: SIMKIN, T & FISKE, R. S (eds) *Krakatau 1883: The Volcanic Eruption and its Effects*. Smithsonian Institution Press, Washington, DC, 169–277.

WARD, S. N. 2001. Landslide tsunami. *Journal of Geophysical Research*, **106**, 11 201–11 215.

WARD, S. N. & DAY, S. 2003. Ritter Island Volcano-lateral collapse and the tsunami of 1888. *Geophysical Journal International*, **154**, 891–902.

WAYTHOMAS, C. F., WATTS, P., SHI, F. & KIRBY, J. T. 2009. Pacific Basin tsunami hazards associated with mass flows in the Aleutian arc of Alaska. *Quaternary Science Reviews*, **28**, 1006–1019.

WARTON, W. J. L. & EVANS, F. J. 1888. On the seismic sea waves caused by the eruption at Krakatoa, August 26th and 27th, 1883. Part III. *In*: SYMONS, G. L. (ed.) *The Eruption of Krakatoa and Subsequent Phenomena*. Report of the Krakatoa Commission of the Royal Society of London, 89–151.

YOKOYAMA, I. 1981. A Geophysical interpretation of the 1883 Krakatau eruption. *Journal of Volcanology and Geothermal Research*, **9**, 359–378.

Bull Volcanol
DOI 10.1007/s00445-011-0554-0

RESEARCH ARTICLE

Sector collapse at Kick 'em Jenny submarine volcano (Lesser Antilles): numerical simulation and landslide behaviour

Frédéric Dondin · Jean-Frédéric Lebrun · Karim Kelfoun · Nicolas Fournier · Auran Randrianasolo

Received: 7 October 2010 / Accepted: 14 September 2011
© Springer-Verlag 2011

Abstract Kick 'em Jenny volcano is the only known active submarine volcano in the Lesser Antilles. It lies within a horseshoe-shaped structure open to the west northwest, toward the deep Grenada Basin. A detailed bathymetric survey of the basin slope at Kick 'em Jenny and resulting high-resolution digital elevation model allowed the identification of a major submarine landslide deposit. This deposit is thought to result from a single sector collapse event at Kick 'em Jenny and to be linked to the formation of the horseshoe-shaped structure. We estimated the volume and the leading-edge runout of the landslide to be *ca.* 4.4 km^3 and 14 km, respectively. We modelled a sector collapse event of a proto Kick 'em Jenny volcano using *VolcFlow*, a finite difference code based on depth-integrated mass and momentum equations. Our models show that the landslide can be simulated by either a Coulomb-type rheology with low basal friction angles (5.5°–6.5°) and a significant internal friction angle (above 17.5°) or, with better results, by a Bingham rheology with low Bingham kinematic viscosity ($0<\nu_B<30$ m^2/s) and high shear strength ($130<\gamma\leq180$ m^2/s^2). The models and the short runout distance suggest that the landslide travelled as a stiff cohesive flow affected by minimal granular disaggregation and slumping on a non-lubricated surface. The main submarine landslide deposit can therefore be considered as a submarine mass slide deposit that behaved like a slump.

Keywords Kick 'em Jenny · Sector collapse · Submarine landslide · Numerical modelling · Rheology · VolcFlow · Lesser Antilles

Editorial responsibility: J. McPhie

F. Dondin (✉) · J.-F. Lebrun · A. Randrianasolo
EA 4098 LaRGE–UFR Sciences Exactes et Naturelles,
Université des Antilles et de la Guyane–Campus de Fouillole,
Pointe-à-Pitre 97159 Guadeloupe, France
e-mail: fredericdondin@gmail.com

K. Kelfoun
Laboratoire Magmas et Volcans, OPGC, UBP—CNRS—IRD,
Clermont-Ferrand, France

N. Fournier
GNS Science, Wairakei Research Centre,
Taupo, New Zealand

Introduction

Since the Mount St. Helens volcano sector collapse in 1980, volcano sector collapses have been recognised as a major destructive process in the evolution of most major types of volcanoes, in all geodynamic settings. For volcanoes close to coasts (or underwater), this process can generate devastating tsunami (e.g. Siebert et al. 1987).

Many sector collapses have been recognised in the Lesser Antilles over the past 25 years (Roobol et al. 1983; Wadge and Isaac 1988; Vincent et al. 1989; Mattioli et al. 1995; Deplus et al. 2001; Le Friant et al. 2002, 2003a, 2009; Lindsay and Shepherd 2005; Boudon et al. 2007). The last sector collapse in the region occurred on 26 December 1997 at Soufrière Hills volcano and was followed by a lateral blast and a small tsunami (Heinrich et al. 2001; Sparks et al. 2002; Voight et al. 2002; Belousov et al. 2007). Most studies in the Lesser Antilles have focused on the identification and location of submarine landslide deposits related to observed horseshoe-shaped structures on land (Mattioli et al. 1995; Deplus et al. 2001; Le Friant et al. 2002, 2003a, 2009; Boudon et al. 2007). They demonstrate that the major

Published online: 21 October 2011

landslide deposits rest in the deep sea Grenada Basin, west of the volcanic arc (Deplus et al. 2001; Boudon et al. 2007). The only published modelling of a volcanic landslide in the Lesser Antilles was attempted by Le Friant et al. (2003b) for a sector collapse originating onland at Mount Pelée, in Martinique, the deposits from which are mainly submarine. They showed that a model with a Coulomb-type friction law, using a variable friction angle below 10°, could reproduce fairly well the deposit related to this collapse event. They suggested that the low friction angle value could result from marine sediments that acted as a boundary layer, decreasing the basal friction angle. However, little is known about sector collapses originating underwater.

In this study, we attempt to numerically model a major landslide deposit that originated underwater at the Kick 'em Jenny volcano, an active submarine edifice in the southern Lesser Antilles arc (Fig. 1a). This volcano lies within a horseshoe-shaped structure, as first suggested by Boudon et al. (1999) from SEACARIB survey data (Bouysse et al. 1988). The collapse scar (Fig. 1a) was more accurately defined by a March 2002, high-resolution National Oceanic and Atmospheric Administration (NOAA) survey (Lindsay et al. 2005). The associated deposits were mapped in March 2003 by a second NOAA survey (Fig. 1). This dataset is the basis for our defining of the submarine landslide deposit morphology.

We first estimate the volume of the deposit from the last major collapse event at Kick 'em Jenny and (1) propose a pre-collapse edifice model, (2) test several rheological laws to best mimic the deposit's first-order morphology using a "two-fluid" version of the numerical code *VolcFlow* (Kelfoun and Druitt 2005; Kelfoun et al. 2010), and (3) discuss the dynamic behaviour of this flowing mass, together with the implications for our understanding of the history of Kick 'em Jenny volcano.

Kick 'em Jenny volcano

Kick 'em Jenny‘s summit is located at 12° 18.024′N, 061° 38.388′W (Fig. 1a; Lindsay et al. 2005). It is the only submarine volcano of the Lesser Antilles arc known to have erupted in historical times, at least 12 times since its presence first became known in 1939. The recent eruption styles have ranged from effusive (dome-forming eruptions) to explosive (tephra-producing eruptions; Devine and Sigurdsson 1995). Samples of pyroclastic deposits and pillow lavas from the volcano consist of amphibole-rich basalt and basaltic andesite (Sigurdsson and Shepherd 1974; Devine and Sigurdsson 1995). Eleven bathymetric surveys have been carried out at Kick 'em Jenny, since 1962 (Robson and Tomblin 1966). The high-resolution survey of the edifice in March 2002 (Lindsay et al. 2005) showed that the summit of the active cone bears a ~300-m wide and 264-m deep crater, breached to the northeast; the highest point on the crater rim is at 185 m below sea level. This active edifice is seated within a larger horseshoe-shaped structure open to the west northwest (WNW). This horseshoe-shaped structure could be related to several landslide deposits covering *ca.* 67 km^2 that can be seen from the March 2003 multibeam bathymetric survey (Lindsay and Shepherd 2005; Fig. 1). Lindsay and Shepherd (2005) estimated the total volume of these deposits to be at least 10±0.5 km^3 and related to an edifice 2.1 km high from base to top. These estimates are revisited and discussed below.

Identification of the main submarine landslide deposit and volume estimates

We focus here on defining the deposits from the largest single collapse event in order to model its dynamic behaviour. We used the 2003 bathymetric data collected using a Seabeam 2112 (12 kHz) multi-beam echo sounder (up to 134 depth soundings with a swath coverage equal to about 75% of the water depth and a beam width of 2° (Shepherd 2004). The spatial density of the 2003 bathymetric data enabled us to produce a high-resolution digital elevation model (DEM) of the landslide area with a grid spacing of 15 m and calculated using a Kriging interpolation method (Fig. 1).

The main submarine landslide deposit morphology

Levees extend from the horseshoe-shaped structure around the active edifice, downslope into the Grenada Basin (Fig. 1a). The southern levee is continuous from the horseshoe-shaped structure to the deep Grenada Basin floor. The northern levee is more irregular in elevation and deeper compared to the southern one (Fig. 1c). This difference in elevation is most likely due to the slope of the basin floor towards the northwest (NW) obliquely across the trend of the levees. Between the levees, we observe an area with irregular topography limited westward (downslope) by steep slopes (10°–30°; Fig. 1a, b). We suggest that the area of irregular topography defines the main submarine landslide deposit that originated from sector collapse at Kick 'em Jenny volcano. No canyon network is visible, neither at the slightly tilted top of the main submarine landslide deposit nor along the steep slopes of its NW limit (Fig. 1a, b). Hence we infer that the main submarine landslide deposit has not been eroded. Steep relief on the scale of few tens of metres and sharp slope breaks particularly at the toe of the main submarine

landslide deposit suggest that the main submarine landslide deposit has not been covered, except a few kilometres from the active edifice toe. There, the deposit appears to be overlain by a lobe of rounded topography that abuts the cone (Fig. 1a). We interpret this lobe as a small landslide possibly associated with a very recent, small sector collapse episode at Kick 'em Jenny.

The NW limit of the main submarine landslide deposit sits in the vicinity of the basin slope break (Fig. 1b). Beyond the NW limit of the main submarine landslide deposit, a smooth lobe suggests the presence of some older landslide deposits (Fig. 1a). Furthermore, the levees on both sides of the main submarine landslide deposit extend far beyond the NW limit of the main submarine landslide deposit under study here. This morphology strongly suggests that these levees were in fact formed during a larger collapse predating the main submarine landslide deposit, and that the main submarine landslide deposit occupies a pre-existing channel. Therefore, our estimate of the extent of the main submarine landslide deposit is smaller than the area covered by landslide deposits presented in Lindsay and Shepherd (2005). We conclude that this newly defined main submarine landslide deposit represents a single collapse and rests at the bottom slope break of the Grenada Basin margin. The main submarine landslide deposit extends 14 km downslope from the active edifice (avalanche runout value) and covers *ca.* 45 km^2.

The main submarine landslide deposit volume

Calculating the main submarine landslide deposit volume requires information on the underlying surface. Unfortunately, no data such as seismic reflection profiles are available. Instead, we consider a range of simple yet realistic geometries for the pre-landslide surface in order to obtain lower and upper bounds for the main submarine landslide deposit volume. Parallel to the landslide direction, the reconstructed pre-landslide surface follows the regional slope of the Grenada Basin margin. Transverse to the main slope direction, in cross-section, one simple solution is to extrapolate the topography of the channel borders as if the channel was initially V-shaped (i.e. a channel devoid of sediment fill; Fig. 1c). A second simple solution is a channel filled up to the current base of the levees with a planar top surface (Fig. 1c) as suggested by the morphology of the channel floor outside the main landslide deposit (Fig. 1a, b). Finally, an intermediate solution is given by a polynomial function to define a U-shaped pre-landslide surface (Fig. 1c). Such a geometry has been observed in landslide channels for which the base is visible (e.g. Deplus et al. 2001; Le Friant et al. 2003a).

The main submarine landslide deposit volumes were obtained by subtracting the DEM produced with the reconstructed pre-landslide surface from the 2003 bathymetric DEM, both gridded at 100 m spacing (Fig. 2). We used a low-resolution DEM to minimise model computation time and because, at this lower resolution, first-order characteristics of the morphology remain identical. The volume was then calculated by double-integration of the residual between the two DEM in the main submarine landslide deposit area. We obtained a main submarine landslide deposit volume ranging from 4.4 to 10.4 km^3 for the filled (minimum), U- to V-shaped (maximum) channels. The systematic error in the volume estimate due to the echo sounder accuracy (±5 m) relative to the main submarine landslide deposit thickness (up to 327 m in the case of V_{MSLD}=4.4 km^3; Fig. 2) and the aliasing effect due to the grid spacing choice (about 1%) are negligible given the uncertainty on the main submarine landslide deposit volume. Despite the wide range of values due to the use of geometries described above, the subsequent reconstruction of the proto-edifice provides independent constraints on volume estimates.

Proto-edifice reconstruction

The reconstruction of the proto-Kick 'em Jenny was based on two main assumptions: (1) the external flanks of the horseshoe-shaped structure belonged to the base of former edifice (Fig. 3a) and (2) the reconstructed slopes of the upper proto-edifice did not exceed 40°, as observed on most volcanoes worldwide (Siebert and Simkin 2002). As the base of the modern volcano is seated on the steep Grenada Basin margin, the proto-edifice base (i.e. on the open side of the horseshoe-shaped structure) most likely extended downslope in a similar way. Therefore, we reconstructed the proto-edifice with a shape similar to that of the present-day volcano (Fig. 3b).

The reconstructed edifice we obtain culminates close to sea level. The volume of the missing section of the reconstructed edifice ranges from 4 to 5 km^3 depending on the exact (but realistic) slope given to the reconstructed volcano flanks. This value falls in the lower range of volumes estimated for the main submarine landslide deposit, using the "filled channel" scenario (i.e. 4.4 km^3). Lindsay and Shepherd (2005) reconstructed a 10.5 km^3 proto-edifice from their estimate of the total volume of deposits. Their reconstructed edifice had a base that extended beyond the limits of the horseshoe-shaped structure. The good match between the missing volume above the horseshoe-shaped structure and the main submarine landslide deposit volume supports our interpretation that the main submarine landslide deposit represents a single collapse event of the proto Kick 'em

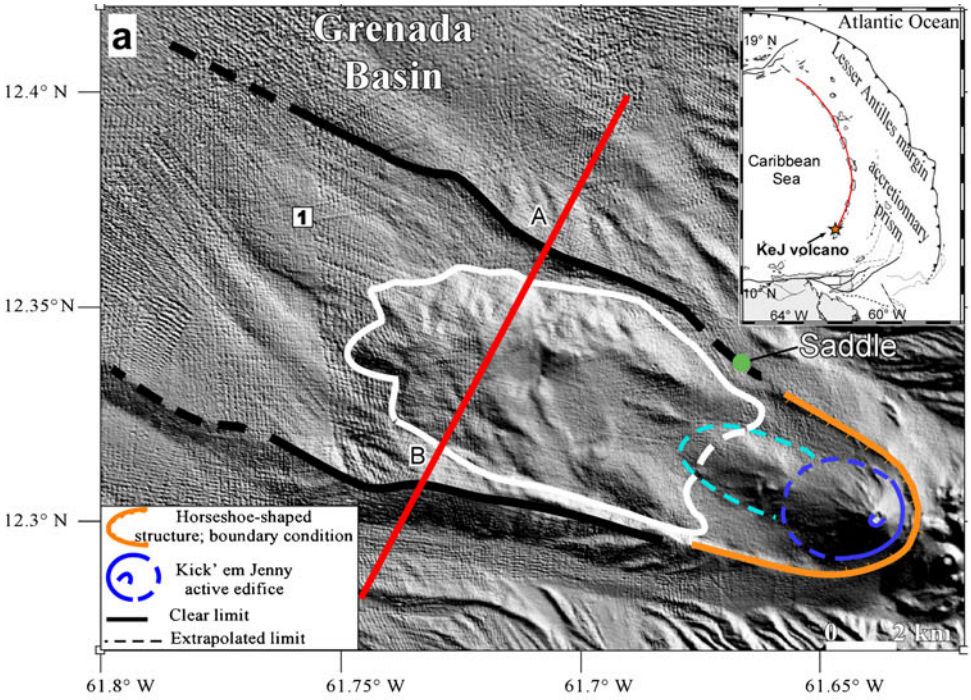
a
Grenada Basin
12.4° N
12.35° N
12.3° N
61.8° W
61.75° W
61.7° W
61.65° W
A
B
1
Saddle
0
2 km
Horseshoe-shaped structure; boundary condition
Kick' em Jenny active edifice
Clear limit
Extrapolated limit
Atlantic Ocean
19° N
10° N
64° W
60° W
Lesser Antilles margin
accretionnary prism
Caribbean Sea
KeJ volcano

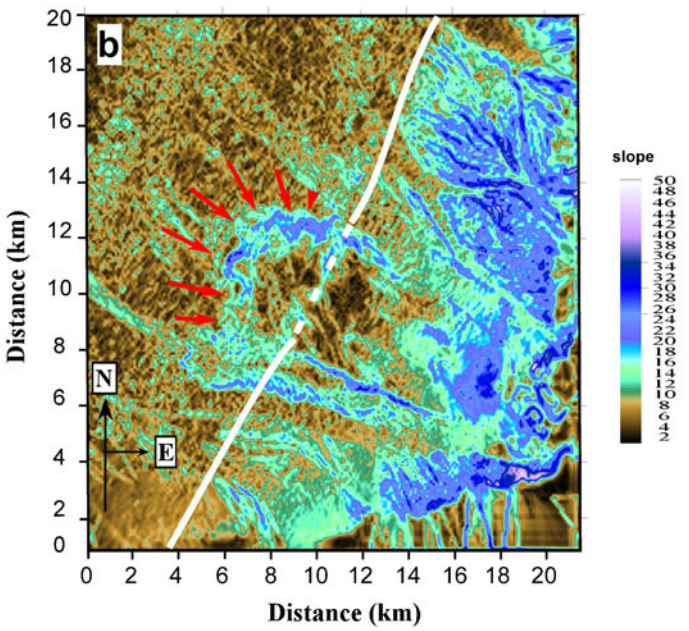
b
Distance (km)
Distance (km)
N
E
slope

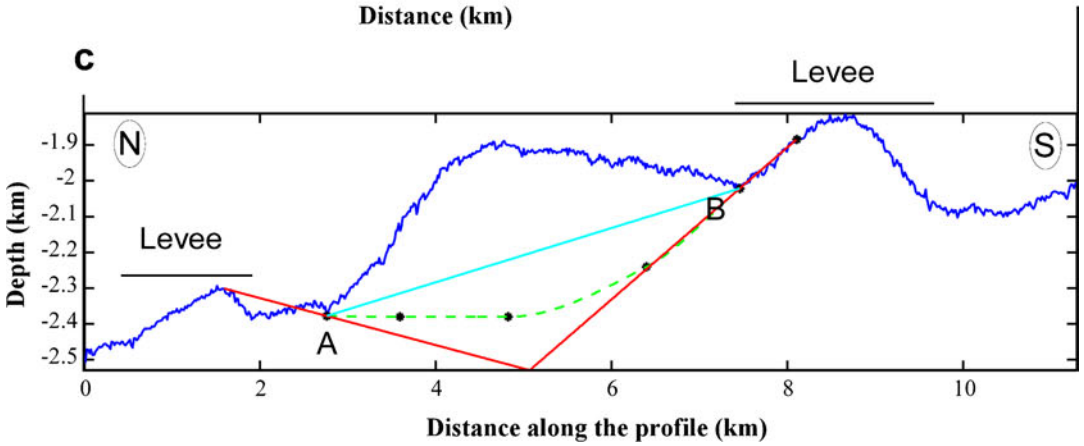
c
Levee
Levee
N
S
A
B
Depth (km)
Distance along the profile (km)

◀ **Fig. 1** Morphology of Kick 'em Jenny volcano and landslide deposits. **a** High-resolution digital elevation model of Kick 'em Jenny volcano area from the March 2003 survey (UTM projection). *Inset* Lesser Antilles arc map, *red line* shows the active volcanic arc, and star locates Kick 'em Jenny volcano (KeJ). *1* Possible old landslide deposits. *White line* bounds the main submarine landslide deposit. *Sky blue line* bounds the youngest landslide deposit. **b** Slope map of the Kick' em Jenny area (slope values in degrees). *Red arrows* point to the steep front of the main submarine landslide deposit. *White line* underlines Grenada Basin slope break. **c** North–south cross-section through the main submarine landslide deposit along *red section line* on **a**. The main submarine landslide deposit extends from *A* to *B*. *Red*, *green* and *pale blue lines* represent models of pre-landslide bottom surface considering a V-shape, a U-shape (generated by a polynomial interpolation of order 4) and a planar bottom surface, respectively

Jenny Volcano that once occupied this horseshoe-shaped structure.

Numerical model

Here, we focus on a simple model that takes into account an initial volcano, the missing part of which had a similar volume to the main submarine landslide deposit (4.4 km^3). This volume slides en masse in a channel with a planar-inclined floor and with no major loss or gain of volume during the process. We believe such a model is adequate for evaluating first-order parameters that control a landslide originating underwater. Moreover, a model with a planar inclined pre-landslide surface involves few assumptions regarding the behaviour of the landslide whereas a U-shaped surface implies and infers channelization.

Three-dimensional numerical modelling of the landslide responsible for the main submarine landslide deposit was carried out assuming that the landslide generated by the sudden collapse of a solid mass (with ρ_{ls}=2,000 kg/m^3, Table 1) gravitationally slides under seawater (ρ_w=1,000 kg/m^3, g=9.8 m/s^2, Table 1). The landslide is treated as a homogeneous and incompressible continuum because our model does not explicitly take into account sediment incorporation (i.e. no bed erosion), pore fluids or density variations due to landslide dilation or incorporation of air or water.

We used *VolcFlow* (Kelfoun et al. 2010), a code based on depth-integrated mass and momentum equations (Savage and Hutter 1989), and on the shallow water assumption that the moving mass is long and wide relative to the flow depth (e.g. Pudasaini and Hutter 2007). Using our bathymetry-linked coordinate system with *x*- and *y*-axes parallel to the local ground surface (*x* is oriented in the transport direction, *y* is horizontally perpendicular to it, *h* is normal to the topography and perpendicular to both *x*- and *y*-axes), the general depth-averaged equations of mass conservation (1) and momentum balance (2 and 3) in this Cartesian coordinates system can be respectively expressed as:

$$\frac{\partial h}{\partial t}+\frac{\partial}{\partial x}(hu)+\frac{\partial}{\partial y}(hv)=0 \tag{1}$$

$$\frac{\partial}{\partial t}(hu)+\frac{\partial}{\partial x}(hu^2)+\frac{\partial}{\partial y}(huv) = gh\sin\alpha_x-\frac{1}{2}k_{act/pass}\frac{\partial}{\partial x}(gh^2\cos\alpha)+\frac{T_x}{\rho} \tag{2}$$

$$\frac{\partial}{\partial t}(hv)+\frac{\partial}{\partial x}(hvu)+\frac{\partial}{\partial y}(hv^2) = gh\sin\alpha_y-\frac{1}{2}k_{act/pass}\frac{\partial}{\partial y}(gh^2\cos\alpha)+\frac{T_y}{\rho} \tag{3}$$

where, *h* is the flow thickness, **u**=(*u*, *v*) is the flow velocity comprising two topography-parallel depth-averaged velocity components u and v, α is the ground slope, ρ the apparent density of the landslide (i.e. its density in water) and $k_{act/pass}$ is the Earth pressure coefficient (the ratio of ground-parallel to ground-normal stress) defined as a function of the internal friction angle (φ_{int}) and of the basal friction angle (φ_{bed}; Pudasaini and Hutter 2007). *T* is the total retarding stress defined by the sum of the drag between the water and the landslide (T_{aw}) and the stress between the landslide and the ground or ground stress, (T_{ag}):

$$T=T_{ag}+T_{aw} \tag{4}$$

Subscripts denote components in the *x* and *y* directions (Kelfoun et al. 2010).

Because the landslide occurs underwater, the model has to take into account water interaction with the landslide. The water reduces the apparent density of the sliding mass (Table 1) compared to a subaerial landslide. As a result, the gravitational driving force is also reduced, leading to a slower velocity of the landslide than in subaerial cases. The water also acts on the landslide as a drag (i.e. T_{aw}). According to Tinti et al. (2000, 2006), this drag applies at the surfaces transverse and parallel to the landslide motion. Both actions are represented by the dimensionless coefficients C_s and C_f in the models (Table 1). The drag also varies as the square of relative velocity of the landslide with respect to the fluid. Tinti et al. (2000, 2006) proposed for submarine landslides to set C_f and C_s to 2 and 0.01, respectively. Kelfoun et al. (2010)

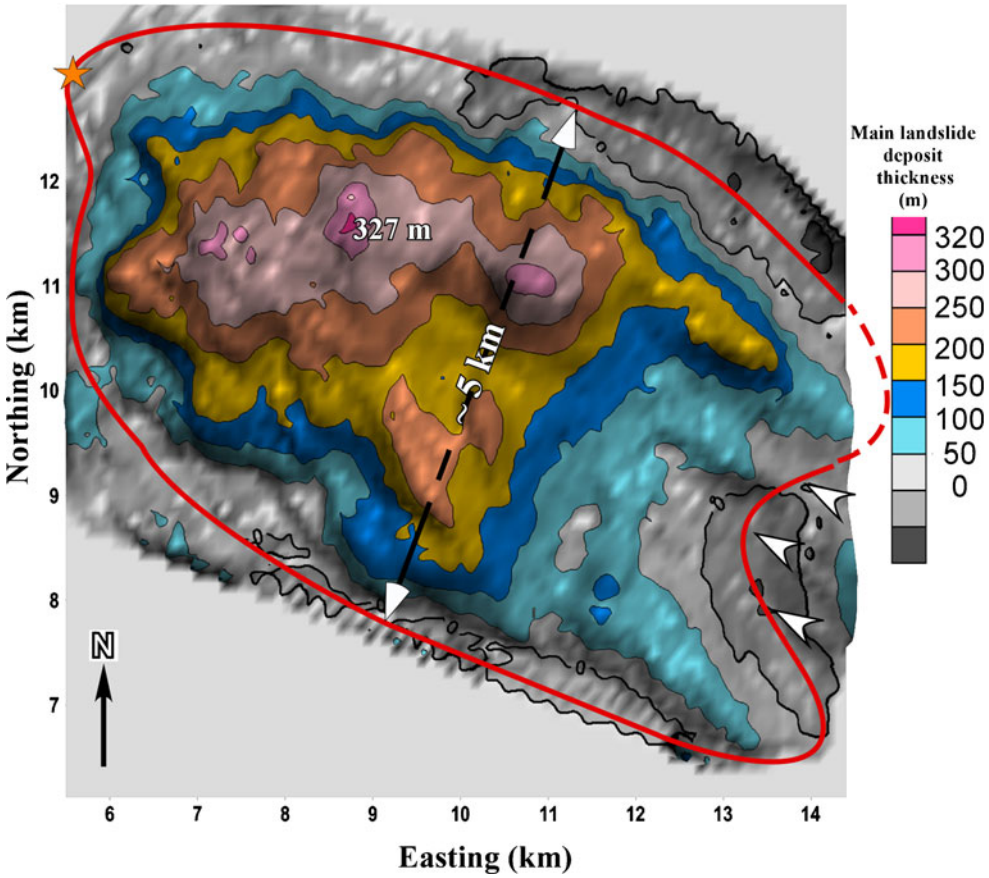

Fig. 2 Thickness map of the main landslide deposit generated considering an inclined plane as the pre-landslide bottom surface. The volume of the main submarine landslide deposit (*inside the red line*) is 4.4 km^3. The main submarine landslide deposit maximum thickness is 327 m. *Whites arrows* give the flow direction from the volcano. *Star* symbolises the position of the runout (14 km away from the volcano)

introduced the water drag in the two-fluid version of *VolcFlow* in the form:

$$\mathbf{T}_{\mathrm{aw}} = -\frac{1}{2}\rho\left(\tan\beta_m C_f + \frac{1}{\cos\beta_n}C_s\right)\|\mathbf{u}-\mathbf{v}\|(\mathbf{u}-\mathbf{v}) \quad (5)$$

in which β_n is the angle formed by the intersection of both the surface of the landslide and the surface of the seafloor with a plane normal to the displacement, and β_m is the slope of the landslide surface in the direction of the relative displacement. β_m is given by (Kelfoun et al. 2010):

$$\tan\beta_m = -\nabla h_\alpha \frac{\mathbf{u}-\mathbf{v}}{\|\mathbf{u}-\mathbf{v}\|} \quad (6)$$

Another convenient feature of *VolcFlow* is that it can account for different possible rheologies of the landslide. Two classical laws are generally used for landslide models. Firstly, the sliding mass can adopt a Coulomb-type dry frictional behaviour during motion. This law is usually used to simulate sand flows in laboratory experiments (e.g. Pudasaini and Hutter 2007). The Coulomb-resisting stress, T_{ag} is given by:

$$\mathbf{T}_{ag} = -\rho h\left(g\cos\alpha + \frac{\mathbf{u}^2}{r}\right)\tan\phi_{\mathrm{bed}}\frac{\mathbf{u}}{\|\mathbf{u}\|} \quad (7)$$

in which φ_{bed} is the bed friction angle and α is the topographic slope angle.

Secondly, the landslide mass can be modelled with a visco-plastic behaviour or Bingham rheology (i.e. a fluid-type rheology; Johnson 1970; Norem et al. 1990; Huang and Garcia 1998; Imran et al. 2001). Sliding is triggered and driven by the kinematic viscosity (ν_B) as soon as a threshold shear strength (γ=k/ρ; k is the yield strength) is exceeded by the ground stress (T_{ag}). In the case of a 2-D landslide, in the direction of the displacement the relation is of the form:

$$\frac{\partial u}{\partial z} = 0 \qquad \|\mathbf{T}_{ag}\| \le k \quad (8)$$

$$\frac{\mathbf{T}_{ag}}{\rho} = \gamma + \nu_B\left(\frac{\partial u}{\partial z}\right) \qquad \|\mathbf{T}_{ag}\| > k \quad (9)$$

in which ρ is the landslide apparent density, $\partial u/\partial z$ is the strain rate, with u being the velocity in the x-direction parallel to the bed and z being the vertical direction.

Fig. 3 Models of the reconstructed proto-Kick 'em Jenny edifice. **a** 2-D model showing a second-order polynomial extrapolation of the external flanks of the horseshoe-shaped structure used to reconstruct the *ca.* 4 km^3 missing part of a volcano with an apex at 80 m below sea level. **b** 3-D model of a volcano with a *ca.* 5 km^3 missing part. This volcano was reconstructed with a similar shape to the present-day Kick 'em Jenny volcano (*dark line*). In this case, the edifice reaches *ca.* 230 m above sea level. View from the northwest

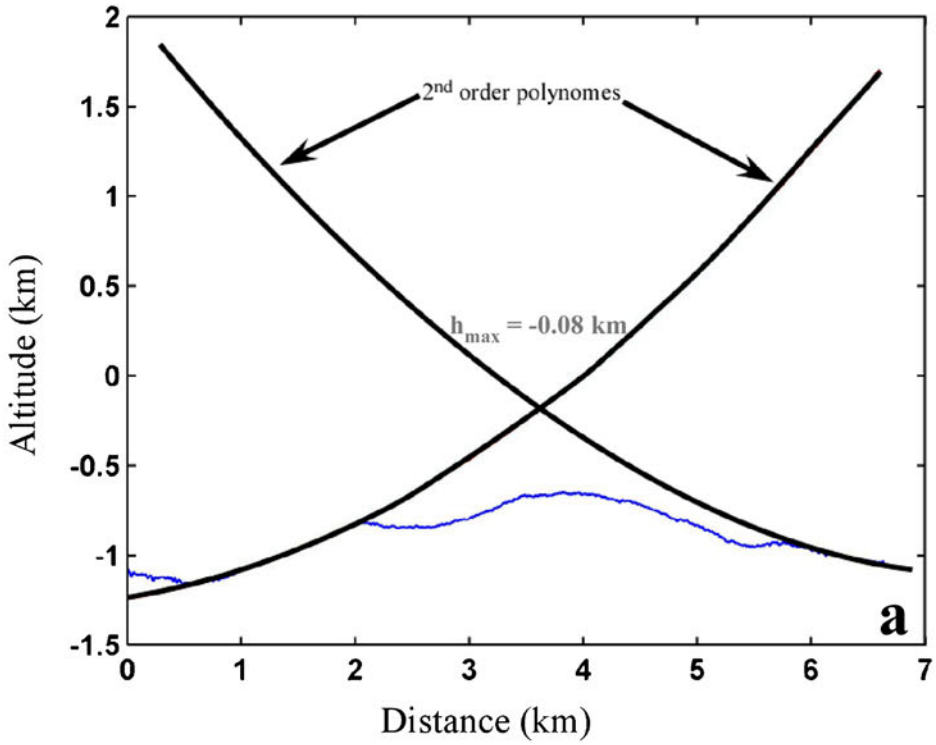
2nd order polynomes
h_{max} = -0.08 km
Altitude (km)
Distance (km)
a

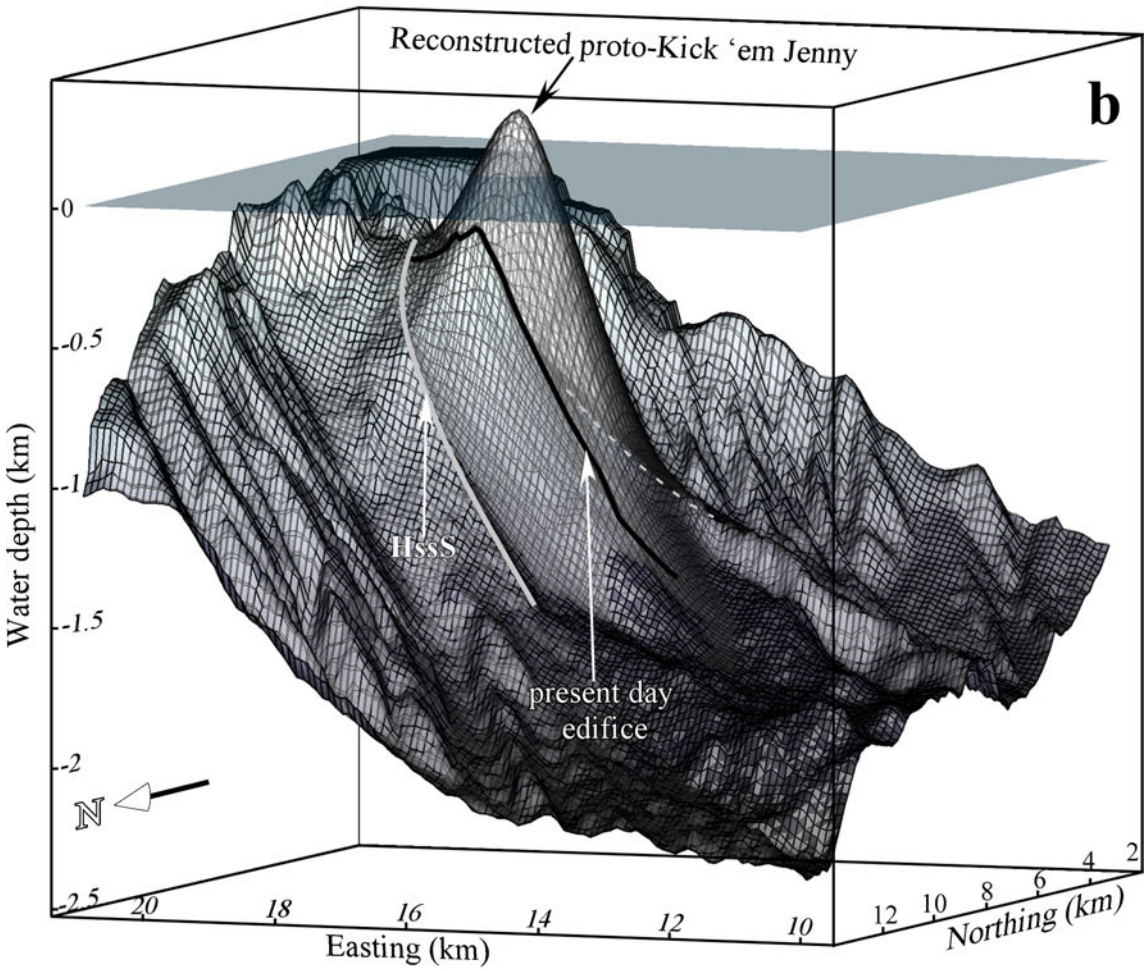
Reconstructed proto-Kick 'em Jenny
b
HssS
present day edifice
Water depth (km)
Easting (km)
Northing (km)
N

Table 1 Parameters used to simulate the Kick 'em Jenny main submarine landslide deposit

Model type	Symbol	Variable	Unit	Typical Values
	C_f	Drag coefficient of landslide front	dimensionless	2
	C_s	Drag coefficient of landslide lateral surfaces	dimensionless	0.01
	g	Gravity	m/s^2	9.8
	ρ_{ls}	Landslide density	kg/m^3	2000
	ρ_w	Water density	kg/m^3	1000
	$\rho = (\rho_{ls} - \rho_w)$	Apparent density	kg/m^3	1000
Simple Coulomb	φ_{bed}	Basal friction angle	degree	7.3 (Model Fig. 4-A) 5.8 (Model Fig. 4-B) 5.5 (Model Fig. 4-C)
Simple Coulomb	φ_{int}	Internal friction angle	degree	0 (Model Fig. 4-A) 17.5 (Model Fig. 4-B) 30 (Model Fig. 4-C)
Bingham	$\gamma = k/\rho$	Shear strength	m^2/s^2	see Figure 5 and 6
Bingham	ν_B	Bingham Kinematic viscosity	m^2/s	see Figure 5 and 6
	h	Landslide thickness	m	calculated at each time step
	$\mathbf{u} = (u_x, u_y)$	Landslide velocity	m/s^1	calculated at each time step Landslide considered at rest when u = 0/2 $m.s^1$

If ν_B is equal to zero (i.e. a model with a null Bingham kinematic viscosity), we are in the case of an extreme Bingham rheology for which the landslide behaves like a plug. The landslide behaviour is only controlled by a constant overall resisting shear stress (γ) independent of the landslide motion. This approach assumes the landslide is a granular mass flow subject to a constant retarding stress (T_{ag}=constant; Dade and Huppert 1998). The landslide behaviour is thus plastic.

We tested both rheological laws to determine which one best reproduced the first-order morphology of the main submarine landslide deposit (Fig. 2), based on four criteria: (1) runout, (2) lateral extent, (3) position of the maximum thickness area (crests), and (4) overall thickness and volume of the deposit.

Results

Coulomb-type dry friction law models

We modelled a single collapse of 4.4 km^3 assuming that a Coulomb-type dry friction law defined the resisting stress. Initial boundary conditions prevented the landslide from moving eastward from the horseshoe-shaped structure (Fig. 1a; i.e. the edifice started collapsing toward the open side of the horseshoe-shaped structure). The two parameters, φ_{bed} and φ_{int} (Table 1, Fig. 4), were chosen within a realistic range of values commonly found in the literature on natural subaerial volcanic landslides (e.g. Pouliquen 1999; Le Friant et al. 2003b; Kelfoun and Druitt 2005). We selected the two parameters from models that best reproduced the 14-km long runout of the main submarine landslide deposit (Fig. 4). The runout is reached when the calculated landslide front speed equals 0 m/s.

The model shows that part of the landslide overflows the northern levee (Fig. 4b, c). The overflow volume reaches 0.6 km^3, which corresponds to approximately 14% of the total collapsed volume. This overflow initiates upslope along a saddle in the levee (Fig. 1a) and is maintained because the northern limit of the landslide overrides the northern levee. This outflow is a consequence of the NW slope direction of the pre-landslide surface (Fig. 1c) within the WNW trending channel.

To reduce this overflow, we first tested a model with a U-shaped pre-landslide surface. We increased the initial

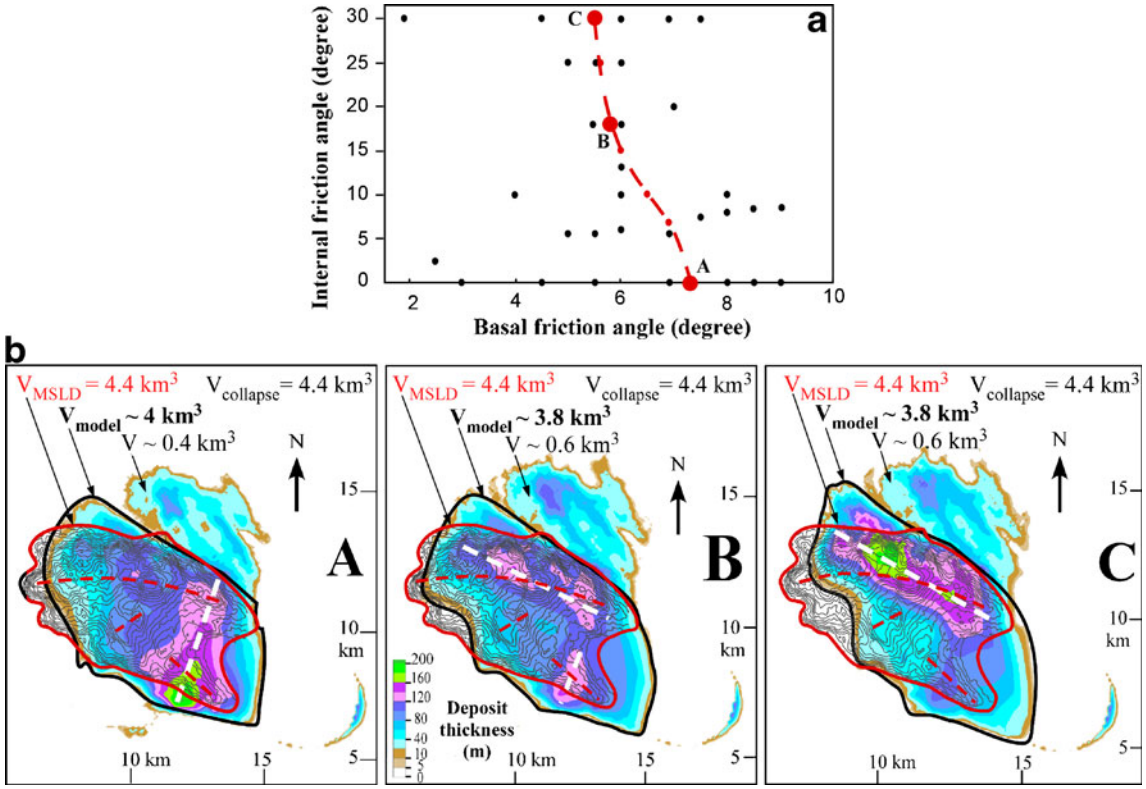

Fig. 4 Simple Coulomb friction law models. **a** Graph shows tested internal and basal friction angles used in the case of a 4.4 km^3 collapse volume (see text and Table 1 for other models parameters). *Red dots* highlight the parameters used for models that reproduce the main submarine landslide deposit 14 km runout and large dots (*A*, *B* and *C*) are those parameters for models presented on maps *A*, *B* and *C*. **b** Thickness maps (colour contoured) of modelled landslides deposits. Thin contour lines overlapping the colour map show the real main submarine landslide deposit thickness map (same as Fig. 2). *Red lines* delimit the main submarine landslide deposit boundaries and *red dashed lines* underline the main crests of the main submarine landslide deposit, whereas the *thick black line* delimits the area used to calculate the modelled landslide volume (V_{MSLD} on each map) and the *dashed white lines* highlight the main crests of the modelled landslide

volcano size by as much volume as the U-shaped pre-landslide surface increases the main submarine landslide deposit volume. However, this attempt did not significantly limit the overflow, as the height of the landslide mass remained much higher than that of the levees. Then we tried to reduce the overflow by using a higher internal friction angle value, implying the landslide was more cohesive. We also simulated multiple successive collapses (three collapses of equal volume every 15 s), inspired by the case of Mount St. Helens (e.g. Sousa and Voight 1995). However,

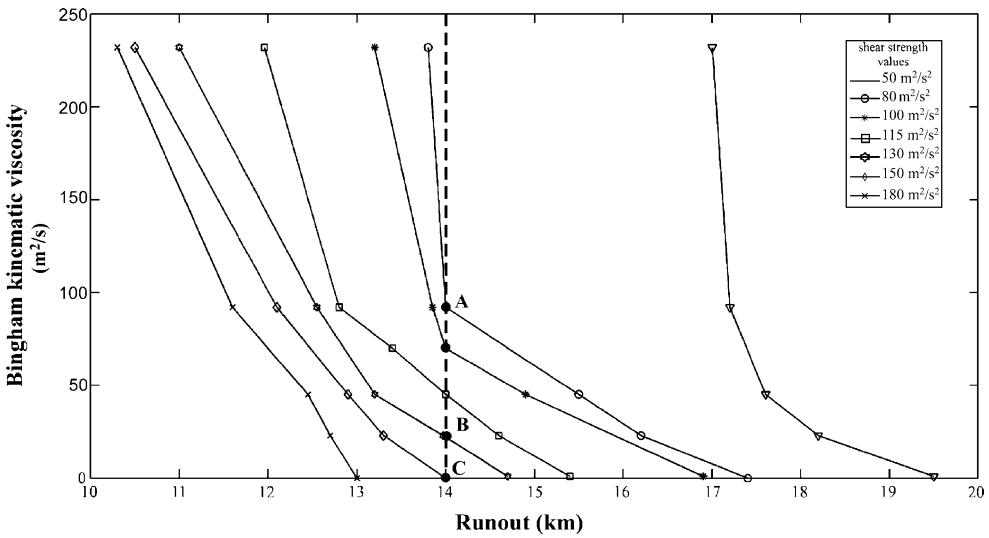

Fig. 5 Bingham rheology models. Graph shows the runout value reached for various Bingham kinematic viscosity and shear strength parameters (see text and Table 1 for other model parameters) in the case of a 4.4 km^3 collapse volume. Thick dashed line represents the main submarine landslide deposit 14 km runout. Large dots labelled *A*, *B* and *C* correspond to models presented in Fig. 6

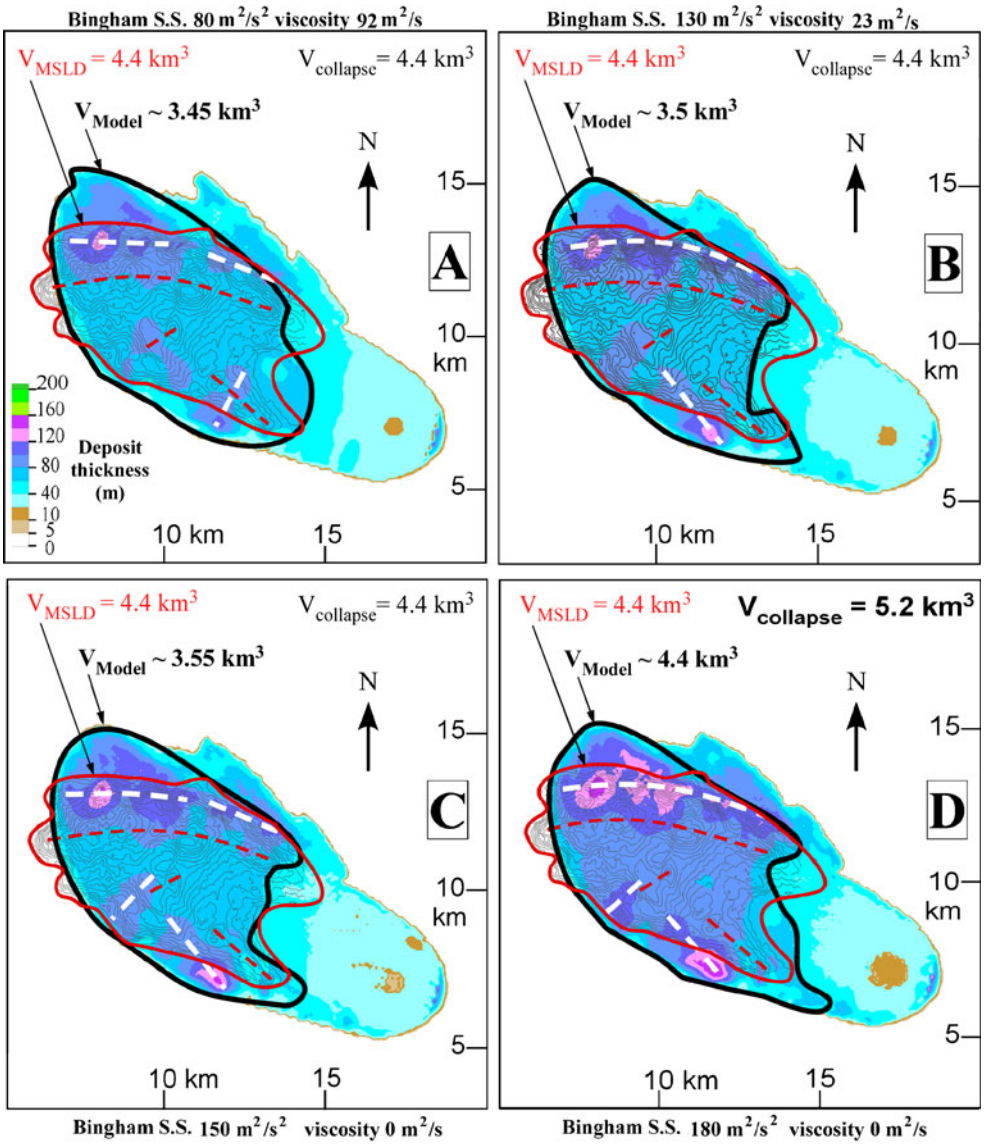

Fig. 6 Thickness maps (colour contoured) of modelled Bingham rheology landslide deposit. **a**–**c** Models identified in Fig. 5. In **d**, a 5.2 km^3 collapse volume is used in order to retrieve a 4.4 km^3 landslide deposit in the main submarine landslide deposit area. Bingham kinematic viscosity and shear strength values for the models are indicated next to the maps

the volume of overflow did not change significantly using these models (Fig. 4). Step-by-step assessment of models during the runs revealed that as soon as the landslide reached the northern levee saddle, some of the mass started to overflow. Thereafter, the levee acted as a plough at the base of the landslide, ejecting a part that evolved independently from the rest of the landslide. Further adjusting the boundary conditions to avoid an overflow not exceeding 14% of the total volume would only make the models more unrealistic.

Coulomb-type dry friction law models succeed in reproducing the runout (Fig. 4a, b). However, they present some discrepancies with the main submarine landslide deposit's first-order morphology. Modelled morphologies display the typical spread-out shape (flank slopes have a concave shape) of a granular flow deposit, whereas the overall main submarine landslide deposit is in fact a compact body with flank steep slopes and maximum thickness along its boundaries (flank slopes have a convex shape; e.g. Fig. 2). Models using a low internal friction produce a deposit with the maximum thickness area located at the upslope end of the deposit (Fig. 4a). Increasing the internal friction angle above 10° contributes to a much better distribution of the thickness compared to the main submarine landslide deposit but does not affect the overall spread-out morphology (Fig. 4b).

We conclude that models with a granular flow behaviour associated with low basal friction angles (5.5°–6.5°) and a significant internal friction angle (above 17.5°) reproduce some of the main submarine landslide deposit's features despite the discrepancies mentioned above.

Bingham rheology models

We tested models taking into account a resisting stress expressed by a Bingham rheology, with the same initial

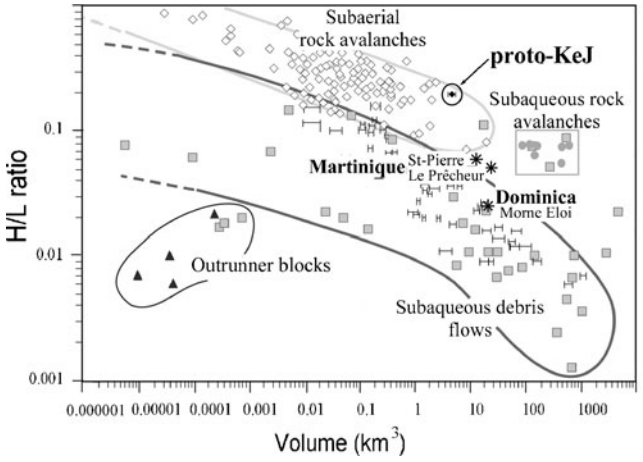

Fig. 7 Maximum vertical fall height (*H*) over runout (*L*) ratio as a function of landslide volume (*V*) modified after De Blasio et al. (2006). *Black diamond H/L* ratio related to the main landslide deposit for the proto-Kick 'em Jenny edifice (this study). *Black stars H/L* ratio related to Dominica, and Martinique debris avalanche deposits (*L* values from Boudon et al. 2007)

conditions as for the Coulomb-type models above (Table 1). We used various values for the Bingham kinematic viscosity and the shear strength commonly used in the literature (e.g. Sousa and Voight 1995; Fig. 5).

Models that best reproduced the runout involved shear strength values ranging from 80 to 150 m^2/s^2 and Bingham kinematic viscosity ranging between 92 and 0 m^2/s, respectively. For these models, the central part of the deposit was fairly well constrained between the levees, i.e. overflow above the northern levee was limited (Figs. 6a, b and 4c). They better reproduced the flank convex shape of the main submarine landslide deposit than Coulomb-type friction models. The modelled landslide deposit has a large flat top and steep slopes on the sides. The upslope part of the landslide deposits also has a shape comparable to that of the main submarine landslide deposit. The crests are also better reproduced, especially the main frontal crest that shows a similar curved shape to that in the main submarine landslide deposit except that it is located a little farther downslope. Models with low Bingham kinematic viscosities and high shear strength displayed a more pronounced frontal crest and the total volume of the deposit inside the levee increased very slightly.

The maximum volume of the landslide reached only 3.55 km^3 of the 4.4 km^3 initial collapse volume (Fig. 6c). This discrepancy is due to the Bingham rheology models leaving a 10–40 m thick layer all along the landslide path, as well as some overflow (less than 7% of the total volume) over the northern levee. We found that a model with the same null viscosity as model 6 C, which reproduced a 4.4 km^3 landslide within the main submarine landslide deposit area, would require a collapse volume of 5.2 km^3, a value close to the maximum estimated volume for the proto-Kick 'em Jenny missing part (Fig. 6d). In that case, the shear strength value had to be increased (180 m^2/s^2), but the overall morphology of the modelled landslide deposit was identical to that of models with a 4.4 km^3 collapse volume. We conclude that the main submarine landslide morphology can be best reproduced using a Bingham rheology with low Bingham kinematic viscosity ($0<\nu_B<$ 30 m^2/s) and high shear strength ($130<\gamma\leq180$ m^2/s^2).

Discussion

So far in this study, we have used the generic term *landslide deposit* to describe the main submarine landslide deposit. However, the models give insight into the rheology of the landslide that generated the main submarine landslide deposit and allow genetic classification according to the scheme of Masson et al. (2006).

The models that best describe the main submarine landslide deposit morphology, whether involving a Coulomb-type rheology or, more accurately a Bingham rheology, all consider a body with high internal cohesion, i.e. the main submarine landslide deposit was made of material that remained cohesive during the movement.

Kelfoun and Druitt (2005) used *VolcFlow* to model the Socompa subaerial debris avalanche of 25 km^3 that travelled *ca.* 40 km and dropped 3,000 m in elevation. Using a constant retarding stress (Bingham kinematic viscosity=0), their model revealed a much lower value (52 kPa) than that of the main submarine landslide deposit ($130<\times\leq180$ m^2/s^2 equivalent to 130–180 kPa). They conclude that at Socompa, as for many other long-runout debris avalanche deposits, the low values can only be explained by the presence of "Reconstituted Ignimbrite Facies" (more than 80% of the total volume) made of disaggregated ignimbrite, gravel, sand and some lacustrine evaporite units that behave in a ductile fashion and that must have been very weak. Conversely, the values of shear strength we obtained for the main submarine landslide deposit are in good agreement with those used to model the first pulse of the debris avalanche of Mount St. Helens at North Fork (Sousa and Voight 1995). That debris avalanche is considered to have undergone incomplete granular disaggregation. We conclude that the underwater Kick 'em Jenny landslide remained as a stiff flow affected by minimal granular disaggregation. Considering *H* as the height of fall and *L* the horizontal distance, *H/L* ratio expresses the mobility of landslide (Hayashi and Self 1992). Theoretically, *H* and *L* should be taken as that for the centre of mass of the moving landslide. However, for natural cases, the centre of mass is difficult to constraint. Therefore, the mobility parameter *H/L* was estimated from maximum *H* and *L*, respectively. With an *H/L* ratio *ca.* 0.21

and a volume of about 4–5 km^3, the main submarine landslide deposit falls in the upper part of the rock avalanche group, implying that it had limited mobility (Fig. 7; De Blasio et al. 2006). The main submarine landslide deposit probably did not slide on a lubricated layer. Instead, cohesion acted as a "brake" on the landslide motion and was responsible for a short runout.

A main submarine landslide deposit volume of *ca.* 4.4 km^3 is comparable to many big debris avalanche deposits from the southern volcanoes of the Lesser Antilles arc (from Dominica southward, Boudon et al. 2007). As for these southern volcanoes, Kick 'em Jenny lies on the hinge of the upper slope of the Grenada Basin. Therefore, its collapse events are primarily directed westward into the deep basin. Boudon et al. (2007) distinguished two extreme cases of debris avalanches for the southern Lesser Antilles volcanoes. The first type has a hummocky morphology made of megablocks several kilometres long and several hundreds of metres thick, and results from the collapse of a volcano composed essentially of domes and lavas. The second type has a smooth morphology that would have resulted from the collapse of a volcano composed mainly of pyroclastic deposits. The main submarine landslide deposit has an irregular surface but no hummocky morphology. Of course, blocks can be rapidly masked by erosion or further avalanche deposits. Although we cannot date the main submarine landslide deposit, we argue that its morphology is pristine. Thus, it is unlikely that mega blocks (bigger than tens of metres) would have been totally covered by sediments over the whole area of the main submarine landslide deposit.

Another important difference between the main submarine landslide deposit and the large debris avalanche deposits in the southern Lesser Antilles, is that the inferred runout of the main submarine landslide deposit is much lower. We calculated that the H/L ratios of Dominican and Martiniquan debris avalanche deposits are 0.2–0.1 times smaller (Fig. 7). Hence, the landslide that produced the main submarine landslide deposit was less mobile than the other Lesser Antilles large landslides. The main submarine landslide deposit stops close to the lower slope break of the Grenada Basin margin whereas the other debris avalanche deposits spread far over the abyssal plain. Therefore, the main submarine landslide deposit could represent a third type of landslide in the Lesser Antilles. Based on the genetic classification of Masson et al. (2006), the main submarine landslide at Kick 'em Jenny is a *mass slide* that behaved as a *slump* ($H/L>0.15$, low disaggregation, thick cohesive block) rather than a debris avalanche.

Voluminous submarine landslides represent an important tsunamigenic hazard (e.g. Moore et al. 1989; Heinrich et al. 2001; Kelfoun et al. 2010). With a *ca.* 4.4 km^3 volume, a relatively short runout and a high cohesion, the main submarine landslide at Kick 'em Jenny could have generated a tsunami comparable to the devastating 1998 Papua New Guinea tsunami (Heinrich et al. 2001; Tappin et al. 2008). The present-day Kick 'em Jenny edifice is installed within the horseshoe-shaped structure (Figs. 1 and 3b) and has now reached a volume of 1.5 km^3. If it is destabilised in a similar fashion as was the main submarine landslide deposit and slumps en masse, it could have the potential to generate a destructive tsunami.

Acknowledgements We would like to thank Professor JB Shepherd and Dr. JM Lindsay for providing bathymetric data. FD is particularly grateful to Dr. REA Robertson for welcoming him and providing facilities at the Seismic Research Centre at the University of the West Indies, St Augustine, Trinidad. We thank Dr. JF Dorville for helpful discussions, Dr. S Sherburn for improving the English text, associate editor J. McPhie, Dr. J Beget and anonymous referees for the manuscript evaluation. This work was funded by the European Union–Interreg 3B "caribbean spaces" project–group1–subproject 1.2.

References

Belousov A, Voight B, Belousova M (2007) Directed blasts and blast-generated pyroclastic density currents: a comparison of the Bezymianny 1956, Mount St. Helens 1980, and Soufrière Hills, Montserrat 1997 eruptions and deposits. Bull Volcanol 69:701–740. doi:10.1007/s00445-006-0109-y

Boudon G, Komorowski J-C, Semet MP, Le Friant A (1999) Frequent volcanic flank collapse in the Lesser Antilles Arc: origin and hazards. Eos Trans AGU 80:46

Boudon G, Le Friant A, Komorowski J-C, Deplus C, Semet MP (2007) Volcano flank instability in the Lesser Antilles Arc: diversity of scale, processes, and temporal recurrence. J Geophys Res 112:1–28

Bouysse Ph, Mascle A, Mauffret A, Mercier de Lepinay B, Jany I, Leclerc-Vanhoeve A, Montjarret MC (1988) Reconnaissance de structures tectoniques et volcaniques sous-marines de l'arc recent des Petites Antilles (Kick 'em Jenny, Qualibou, Montagne Pelée, Nord Ouest de la Guadeloupe). Mar Geol 81:261–287

Dade WB, Huppert HE (1998) Long-runout rockfalls. Geology 26 (9):803–806

De Blasio FV, Elverhøi A, Engvik LE, Issler D, Gauer P, Harbitz CB (2006) Understanding the high mobility of subaqueous debris flows. Nor J Geol 86:275–284

Deplus C, Le Friant A, Boudon G, Komorowski J-C, Villemant B, Harford C, Segoufin J, Cheminee JL (2001) Submarine evidence for large-scale debris avalanches in the Lesser Antilles Arc. Earth Planet Sci Lett 192:145–157

Devine J, Sigurdsson H (1995) Petrology and eruption styles of Kick 'em Jenny submarine volcano, Lesser Antilles island arc. J Volcanol Geotherm Res 69:35–58

Hayashi JN, Self S (1992) A comparison of pyroclastic flow and debris avalanche mobility. J Geophys Res 97(B6):9063–9071

Heinrich Ph, Piatanesi A, Hébert H (2001) Numerical modeling of tsunami generation and propagation from submarine slumps: the 1998 Papua New Guinea event. Geophys J Int 145:97–111

Huang X, Garcia MH (1998) A Herschel–Buckley model for mud flow down a slope. J Fluid Mech 374:305–333

Imran J, Harff P, Parker G (2001) A numerical model submarine debris flowswith graphical user interface. Comput Geosci 274 (6):717–729

Johnson AM (1970) Physical processes in geology. Freeman, San Francisco

Kelfoun K, Druitt T (2005) Numerical modeling of the emplacement of Socompa rock avalanche, Chile. J Geophys Res 110:B12202. doi:10.1029/2005JB003758

Kelfoun K, Giachetti T, Labazuy P (2010) Landslide-generated tsunamis at Réunion island. J Geophys Res. doi:10.1029/2009JF001381

Le Friant A, Boudon G, Komorowski J-C, Deplus C (2002) L'Île de la Dominique, à l'origine des avalanches de debris les plus volumineuses de l'arc des Petites Antilles. CR Geosci 334:235–243

Le Friant A, Boudon G, Deplus C, Villemant B (2003a) Large-scale flank collapse events during the activity of Montagne Pelée, Martinique, Lesser Antilles. J Geophys Res 108(B1):2055. doi:10.1029/2001JB001624

Le Friant A, Heinrich P, Deplus C, Boudon G (2003b) Numerical simulation of the last flank-collapse event of Montagne Pelée, Martinique, Lesser Antilles. Geophys Res Lett 30: 1034

Le Friant A, Boudon G, Arnulf A, Robertson R (2009) Debris avalanche deposits offshore St. Vincent (West Indies): impact of flank-collapse events on the morphological evolution of the island. J Volcanol Geotherm Res 179:1–10

Lindsay JM, Shepherd JB (2005) Kick 'em Jenny and Île de Caille. In: Lindsay JM, Robertson REA, Shepherd JB, Ali S (eds) Volcanic hazard atlas of the Lesser Antilles. Seismic Research Unit, The University of the West Indies, Trinidad and Tobago, W. I, pp 105–125

Lindsay JM, Shepherd JB, Wilson D (2005) Volcanic and scientific activity at Kick 'em Jenny submarine volcano 2001–2002: implications for volcanic hazards in the Southern Grenadines, Lesser Antilles. Nat Hazards 34:1–24

Masson DG, Harbitz CB, Wynn RB, Pedersen G, Løvholt F (2006) Submarine landslides: processes, triggers and hazard predictions. Philos Trans R Soc A 364:2009–2039

Mattioli GS, Jansma PE, Jaramillo L, Smith AL (1995) Sector collapse in the Island Arc Volcanoes: a digital topographic and bathymetric investigation of the Qualibou depression, St. Lucia, Lesser Antilles. Caribb J Sci 31:163–173

Moore JG, Clague DA, Holcomb RT, Lipman PW, Normark WR, Torresan ME (1989) Prodigious submarine landslides on the Hawaiian ridge. J Geophys Res 94:17465–17484

Norem H, Locat J, Schieldrop B (1990) An approach to the physics and the modeling of submarine flowslides. Mar Geotechnol 9:93–111

Pouliquen O (1999) Scaling laws in granular flows down rough inclined planes. Phys Fluids 11:542–548

Pudasaini SP, Hutter K (2007) Avalanche dynamics: dynamics of rapid flows of dense granular avalanches. Springer, Berlin

Robson GR, Tomblin JF (1966) Catalogue of the active volcanoes of the world including solfatara fields, part 20, the West Indies. Internal Association of Volcanologists, Bulletin of the Association of Engineering Geologists, pp 1–56

Roobol MJ, Wright JV, Smith AL (1983) Calderas or gravity-slide structures in the Lesser Antilles Island Arc? J Volcanol Geotherm Res 19:121–134

Savage SB, Hutter K (1989) The motion of a finite mass of granular material down a rough incline. J Fluids Mech 189:177–215

Shepherd JB (2004) Report on studies of Kick 'em Jenny submarine volcano March 2002 an March 2003 with updated estimates of marine and coastal hazards, Internal Report, Seismic Research Unit, The Univ. of the West Indies

Siebert L, Simkin T (2002) Volcanoes of the World: an Illustrated Catalog of Holocene Volcanoes and their Eruptions. Smithsonian Institution, Global Volcanism Program Digital Information Series,B. (1974) Amphibole-bearing basalts from submarine volcano Kick 'em Jenny in the Lesser Antilles island arc. Bull Volcanol 38:891–910

Siebert L, Glicken H, Ui T (1987) Volcanic hazards from Bezymianny- and Bandai-type eruptions. Bull Volcanol 49:435–459

Sigurdsson H, Shepherd JB (1974) Amphibole-bearing basalts from submarine volcano Kick 'em Jenny in the Lesser Antilles island arc. Bull Volcanol 38:891–910

Sousa J, Voight B (1995) Multiple-pulsed debris avalanche emplacement at Mount St. Helens in 1980: evidence from numerical continuum flow simulations. J Volcanol Geotherm Res 66:227–250

Sparks RSJ, Barclay J, Calder ES, Herd RA, Komorowski J-C, Luckett R, Norton GE, Ritchie L, Voight B, Woods AD (2002) Generation of a debris avalanche and violent pyroclastic density current: the 26 December 1997 (Boxing Day) at Soufrière Hills volcano, Montserrat. In: Druitt TH, Kokelaar BP (eds). The eruption of Soufrière Hills volcano, Montserrat, from 1995 to 1999. Mem Geol Soc London 21, pp 409–434

Tappin DR, Watts P, Grilli ST (2008) The Papua New Guinea tsunami of 17 July 1998: anatomy of a catastrophic event. Nat Hazards Earth Sci Syst 8:243–266

Tinti S, Bortolucci, Romagnoli C (2000) Computer simulations of tsunamis due to sector collapse at Stromboly, Italy. J Volcanol Geotherm Res 96:103–128

Tinti S, Armigliato A, Manucci A, Pagnoni G, Zaniboni F, Yalçiner AC, Altinok Y (2006) The generating mechanisms of the August 17, 1999 Izmit bay (Turkey) tsunami: regional (tectonic) and local (mass instabilities) causes. Mar Geol 225:311–330

Vincent PM, Bourdier JL, Boudon G (1989) The primitive volcano of mount Pelée: its construction and partial destruction by flank collapse. J Volcanol Geotherm Res 38:1–15

Voight B, Komorowski JC, Norton GE, Belousov AB, Belousova M, Boudon G, Francis PW, Franz W, Heinrich P, Sparks RSJ, Young RS (2002) The 26 December (Boxing Day) 1997 sector collapse and debris avalanche at Soufrière Hills Volcano, Montserrat. In: Druitt TH, Kokelaar BP (eds) The eruption of Soufrière Hills Volcano, Montserrat, from 1995 to 1999. Mem Geol Soc London 21, pp 363–407

Wadge G, Isaac MC (1988) Mapping of the volcanic hazards from Soufrière Hill Volcano, Montserrat, West Indies usin an image processor. J Geol Soc 145:541–551

Marine Geology 284 (2011) 189–202

Contents lists available at ScienceDirect

Marine Geology

journal homepage: www.elsevier.com/locate/margeo

Numerical modelling of the tsunami triggered by the Güìmar debris avalanche, Tenerife (Canary Islands): Comparison with field-based data

Thomas Giachetti [a,d,*], Raphaël Paris [a,d], Karim Kelfoun [b,e,f], Francisco José Pérez-Torrado [c]

[a] Clermont Université, Université Blaise Pascal, GEOLAB, BP 10448, F-63000 Clermont-Ferrand, France
[b] Clermont Université, Université Blaise Pascal, Laboratoire Magmas et Volcans, BP 10448, F-63000 Clermont-Ferrand, France
[c] Departamento de Física (Geología), Universidad de Las Palmas de Gran Canaria, 35017-Las Palmas de Gran Canaria, Spain
[d] CNRS, UMR 6042, GEOLAB, F-63057 Clermont-Ferrand, France
[e] CNRS, UMR 6524, LMV, F-63038 Clermont-Ferrand, France
[f] IRD, R 163, LMV, F-63038 Clermont-Ferrand, France

ARTICLE INFO

Article history:
Received 21 September 2010
Received in revised form 14 March 2011
Accepted 31 March 2011
Available online 15 April 2011

Communicated by J.T. Wells

Keywords:
tsunami
numerical modelling
debris avalanche
Güìmar flank collapse
Canary Islands
Tenerife
Gran Canaria
Agaete Valley
tsunami deposits
field-based data

ABSTRACT

Some tsunami deposits have been previously identified 41–188 m asl in the Agaete Valley on the northwest coast of the island of Gran Canaria, in the Canary Islands. In this paper, the Güìmar sector collapse (Tenerife, ~0.83 Ma), and its expected associated tsunami that is thought to be at the origin of these tsunami deposits, are tentatively reproduced using a two-fluid numerical code. Two failure processes are considered: 1) the whole 44 km^3 volume is released in one go, or 2) the 44 km^3 are released in five retrogressive failures of equal volume, occurring each 120 s. In both cases, two rheologies are used to simulate the landslide propagation: the Mohr–Coulomb frictional law and a constant retarding stress. Two hypotheses concerning the origin of the offshore mapped deposits are also considered: 1) the mapped deposits are the direct result of a single collapse event occurring either in one go or by near retrogressive failures, or 2) the mapped deposits result from a collapse followed by later partial remobilization of its deposits. In all scenarios, the subaerial destabilisation spreads out eastwards into the sea, triggering waves 390–500 m high when considering a collapse in one go, and 225–380 m when considering successive retrogressive failures. The first wave reaches the coast of Gran Canaria, located at 70 km from the scar, 495–560 s after the collapse onset, whatever the scenario considered. Water enters the Agaete Valley on Gran Canaria 555–690 s after the onset of collapse, reaching up to 9.1 km inland for a collapse in one go, and 5.0 km when considering five retrogressive failures. In this valley, the simulated waves inundate all the locations where tsunami deposits were identified, with the flow depth measured reaching a maximum of 50 m (collapse by retrogressive failures) to 150 m (collapse in one go) at these particular places. The directions of maximum kinetic energy as a function of time for the simulated waves are consistent with the current directions recorded by the cobble fabrics present in the run-up and backwash layers of the tsunami deposits at one outcrop. This study shows that the major source of uncertainty when reproducing landslide-triggered tsunamis is linked to the way the landslide happens (failure mechanisms), that should be thus more precisely taken into account for landslide-triggered-tsunamis hazard assessment. The rheology chosen to simulate the landslide propagation has only a second-order impact on the produced waves.

© 2011 Elsevier B.V. All rights reserved.

1. Introduction

Historical tsunamis were triggered either by large-scale earthquakes, as highlighted by the dramatic tsunami in Indonesia on December 26th 2004, or by a large, rapidly-moving sliding mass entering water (e.g. Keating and McGuire, 2000; Ward, 2001; Harbitz et al., 2006). Landslide-tsunami are usually characterised by a more local occurrence but high run-up compared to earthquake tsunamis. The sliding masses that can enter water include large flank collapses, which are now recognised as a common phenomenon affecting oceanic volcanoes. Large debris avalanche deposits have notably been identified in Hawaii (68 events, Moore and Moore, 1984; Moore et al., 1989, 1994a, 1994b; Normark et al., 1993; Robinson and Eakins, 2006), at Reunion Island (47 events, Oehler et al., 2004; 2007) and in the Canary Islands (~25 events, Krastel et al., 2001; Masson et al., 2002; Paris et al., 2005). Some of these debris avalanches are inferred to have involved volumes of up to 1000 km^3 or more.

In Hawaii, marine conglomerates found at unusually high elevations were interpreted as being the result of giant tsunami waves generated by massive flank failures (Moore and Moore, 1984, 1988; Moore et al., 1994a; Moore, 2000), even if the majority of the units or

* Corresponding author at: Clermont Université, Université Blaise Pascal, GEOLAB, BP 10448, F-63000 Clermont-Ferrand, France. Tel.: +33 4 73 34 68 43.
E-mail address: thomas.giachetti@univ-bpclermont.fr (T. Giachetti).

0025-3227/$ – see front matter © 2011 Elsevier B.V. All rights reserved.
doi:10.1016/j.margeo.2011.03.018

facies of the enigmatic conglomerates on the islands of Lanai and Molokai (Hawaii) were also interpreted as uplifted coastal and shallow marine deposits (Grigg and Jones, 1997; Felton 2002; Felton et al., 2006; Crook and Felton, 2008). The coral-bearing deposits studied by McMurtry et al. (2004) at Kohala (Hawaii), are less controversial, since the subsidence of this island is well established (e.g. Moore, 1971). Considering the subsidence rate and the present-day maximum elevation of the deposits (61 m asl), the run-up of the tsunami is estimated to be >400 m.

Although numerous debris avalanche deposits have been mapped around the world and tsunami deposits have been found at high altitude inland, there are very few eye-witness accounts of tsunamis triggered by landslides or rock slides. This lack of observation deprives us of information about amplitude, run-up or arrival time of such landslide-triggered waves. The tsunami generated by the 30×10^6 m^3 Lituya Bay collapse in Alaska in 1958 (Fritz et al., 2001) was the result of a rock avalanche falling directly into deep water, more or less vertically, creating an initial 500 m wave (Weiss et al. 2009) that was then channelled by the bay, reaching laterally 60 m at 6 km from the collapse and 30 m at 12 km. The December 2002 rock slide of Stromboli involved a volume of 17×10^6 m^3 and generated a 8 m-high wave on the coasts of Stromboli, with only a limited effect on the coasts far (>200 km) from the collapse (Maramai et al., 2005). The largest lateral collapse of an island volcano recorded in historical times took place in 1888 at Ritter Island (New Guinea) when ~5 km^3 of rock fell en masse into the sea northeast of New Guinea, producing witnessed waves up to 10–15 m at tens to hundreds of km from the source (Ward and Day, 2003).

Numerical modelling of landslides emplacement and associated tsunamis is therefore the only way to define the characteristics of such potential waves (Tinti et al., 1999, 2000, 2006; Geist et al., 2009; Waythomas et al., 2009). Recently, Kelfoun et al. (2010) showed that a hypothetic 10 km^3 flank collapse at Reunion Island could trigger waves as high as 100 m on Reunion Island coasts, and also on Mauritius, located 175 km from the impact. The leading wave would reach Mauritius about 18 min after the collapse onset. These wave characteristics are realistic compared to those observed at Stromboli in December 2002 (Maramai et al., 2005) if we take into account that the volume involved in the simulations of Kelfoun et al. (2010) is 500 times larger than this event. However, cited studies, like many of the other numerical models of tsunami triggered by landslides, lack a direct comparison with natural cases.

The Canary Islands are located in the Atlantic Ocean, close to the continental margin of Northwest Africa (Fig. 1). They developed over oceanic lithosphere as the result of the west-to-east movement of the African plate over a mantle hotspot (e.g. Carracedo et al., 1998, 2002). The island of Gran Canaria, located in the centre of the archipelago, is nearly circular, with a diameter of about 40 km and a maximum altitude of 1949 m asl (Fig. 1). It has a broadly conical morphology dissected by a dense radial network of deep gullies, many of them preserving the same pattern since Miocene (Schmincke, 1990; Carracedo et al., 2002). Paris et al. (2004) and Pérez-Torrado et al. (2006) interpret marine conglomerates found at seven outcrops 41–188 m asl on the walls of the Agaete Valley on Gran Canaria (Fig. 1) as having been generated by tsunami waves. They proposed that the Güìmar flank failure on the eastern coast of Tenerife (~0.83 Ma;

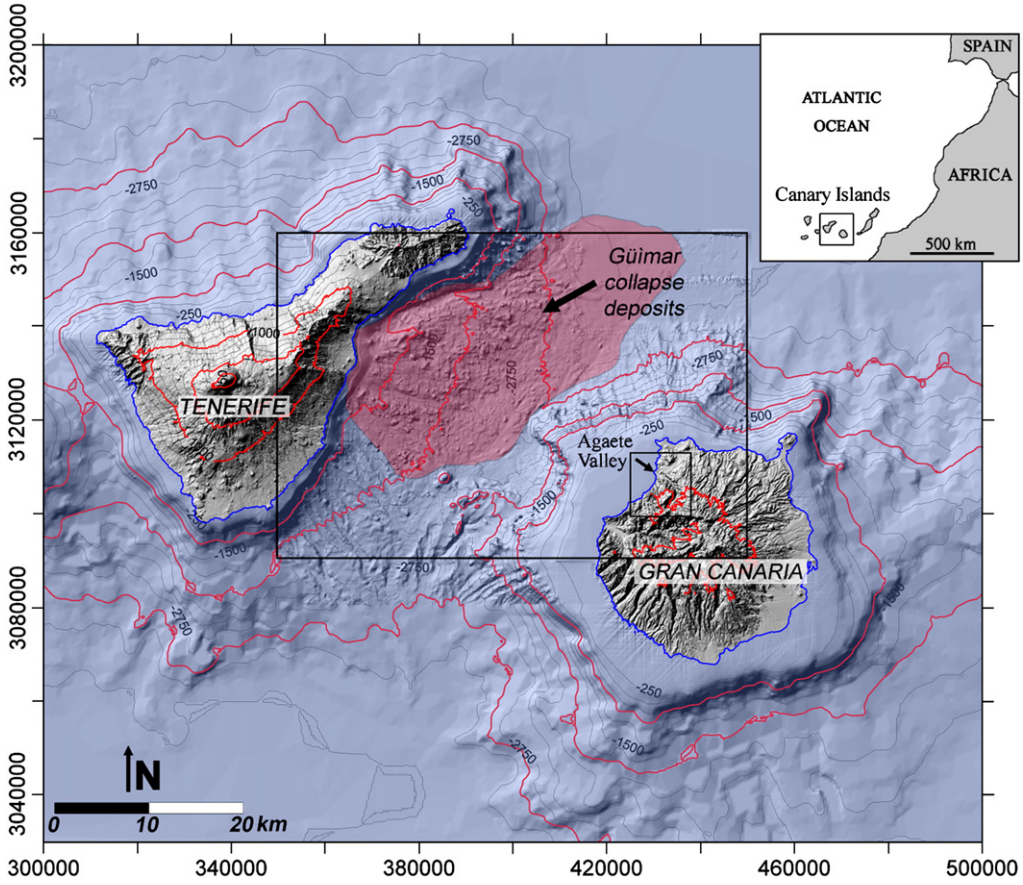

Fig. 1. Topography and bathymetry of Tenerife and Gran Canaria islands corresponding to our 2000×1700 pixels^2 DEM with a resolution of 100 m (see text for details about the compilation of this DEM). The localisation of this area is shown by the black frame on the top-right inset map. The 1000×700 pixels^2 100 m-resolution computation grid used to perform some simulations is delimited by the larger frame. The 1300×1280 pixels^2 10 m-resolution computation grid centred on the Agaete Valley is delimited by the smaller frame, and the entrance of the Agaete Valley is figured by the arrow. The maximum extension of the Güìmar collapse deposits mapped by Krastel et al. (2001) and Krastel and Schmincke (2002) is highlighted. Contours are in metres; thick lines are at 1000 m intervals. Coordinates are in metres UTM.

Ancochea et al., 1990; Carracedo et al., 2010) is the most probable source of this tsunami. Of at least nine major flank failures documented in the Canary Islands during the Pleistocene, the Güímar failure is the only one that is not directed towards the open ocean, and the closest tsunamigenic source for the Agaete tsunami deposits. The Güimar collapse, with its well-constrained tsunami deposits, provides a unique chance to test the reliability of numerical codes simulating landslide-triggered tsunamis.

In this paper, we reproduce numerically the Güimar sector collapse and the subsequent triggered tsunami together, according to two different failure scenarios and using several rheologies to simulate the landslide propagation. We then directly compare the waves obtained by our numerical simulations with the spatial distribution and sedimentological characteristics of the tsunami deposits described by Paris et al. (2004) and Pérez-Torrado et al. (2006) in the Agaete Valley. We also discuss the influences on the triggered tsunami of the failure mechanisms, the rheology used to simulate the landslide propagation, and the sea level used which may have been different to the actual one in this particular case.

2. The Güimar debris avalanche

The Güimar debris avalanche scar is located on the eastern coast of Tenerife (Fig. 1). A large majority of the scar is subaerial, covering a surface of about 127 km^2 (Paris et al., 2005), and the collapse volume estimates range from 37 km^3 (Teide Group, 1997) to 47 km^3 (Carracedo et al., 2010). The corresponding submarine deposits have been identified and cover a ~1600 km^2 surface area if we include the very distal blocks which spread mainly eastwards, the central area of the avalanche covering only ~1200 km^2 (Fig. 1; Krastel et al., 2001). Single blocks have been identified up to 70 km off the Güimar Valley, but most of the blocks are within 50 km of the coast (Krastel et al., 2001; Masson et al., 2002) and the biggest ones (>1 km^3) within 10 km. Debris flow deposits interpreted to be the distal equivalent of the Güimar debris avalanche are thought to have been detected in Ocean Drilling Program (ODP Lag 157) drill holes 954 and 953, the later being located at 136 km from the landslide scar (see Fig. 1 of Krastel et al., 2001). Since there is a lack of clear net seismic profiles in this local area because of the presence of a large number of hummocks that hamper deeper reflections (Funck et al., 1996), we do not know the deposit thickness, and their contours are not all well defined. However, comparison with well described debris avalanches of the same volume from Réunion Island or the Hawaiian Islands suggests that the central part of the Güimar debris avalanche will have an average thickness of 100 m (Krastel et al., 2001).

To our knowledge, there is no evidence telling whether the landslide occurred in one go (one large single collapse of 37–47 km^3) or by several retrogressive failures of smaller volumes. Indeed, Wynn and Masson (2003) showed that single bodies of debris avalanche deposits around the Canary Islands could be correlated with several turbidity current pulses further offshore. However, Le Bas et al. (2007) also showed for another large submarine debris avalanche deposits (the Monte Amarelo ones on Fogo Island, Cape Verde, 130–160 km³) that their characteristics suggest a single failure event. Therefore, both types of failure scenario should be taken into account when modelling such large oceanic debris avalanches, since the volume involved in the collapse will have a direct influence on the tsunami produced.

After the emplacement of the Güimar debris avalanche, volcanism took place both in the subaerial scar and on the submarine flanks of the Güimar Valley, seamounts being numerous between Tenerife and Gran Canaria islands (Teide Group, 1997; Ruiz et al., 2000; Krastel and Schmincke, 2002). Sedimentation also largely took place since the collapse event, covering the debris avalanche deposits with a thick layer of marine sediments. The volume calculated offshore that is supposed to be linked to the Güimar debris avalanche and estimated to be at least 120 km^3 (Krastel et al., 2001) corresponds to the volume associated with the failure of Güimar plus the post-collapse volcanic/detritus. The large discrepancy with the onshore volume loss estimate (<50 km^3) is possibly explained by the sediment contribution from submarine slopes (syn-collapse bulking and post-collapse hemipelagic sedimentation), the superposition of several collapse events, and the poor accuracy of offshore volumes estimates (Masson et al., 2002; Paris et al., 2005). The real Güimar debris avalanche deposits may spread either (1) over the whole surface mapped by Krastel et al. (2001, cf. Fig. 1) or (2) only over the internal part (within a few tens of km from the scar) of the mapped deposit. If (2) is right, the distal parts of the mapped deposits (thought to have been detected in ODP Lag 157 drill holes 954 and 953) may represent post-collapse remobilization of the Güimar debris avalanche deposits. In both cases, the collapse deposits have been affected by post-collapse volcanism and sedimentation.

3. Methodology

3.1. Numerical model

Numerical simulations of the Güimar collapse and its associated tsunami were performed using the *VolcFlow* code which is fully described in Kelfoun and Druitt (2005) for its "one fluid" version. The model was revised by Kelfoun et al. (2010) to simulate water propagation at the same time as landslide propagation. These two papers should be referred to for full equations since only the general features of the code are provided here.

The code is based on the 2D depth-averaged approach, modified to incorporate 3D interactions between the sea and the landslide to give greater accuracy. Both landslide motion and sea surface displacement are simulated using the general shallow water equations of mass conservation and momentum balance. The water is able to interact with the bathymetry/topography and to flood onto the land, but waves breaking and other complex second-order 3D effects not being taken into account due to the shallow-water approach. Erosion and transportation of sediments are also ignored. No mixing between the debris avalanche and the water is taken into account and the densities of the two fluids remain constant over time. A reduced density of the avalanche (=density of the avalanche − density of the water) is used where the avalanche is under water, the real density being used out of water. This assumption precludes mixing with the sea water, which could result in turbidity currents and affect the wave dynamics. The model also assumes that the water depth has no

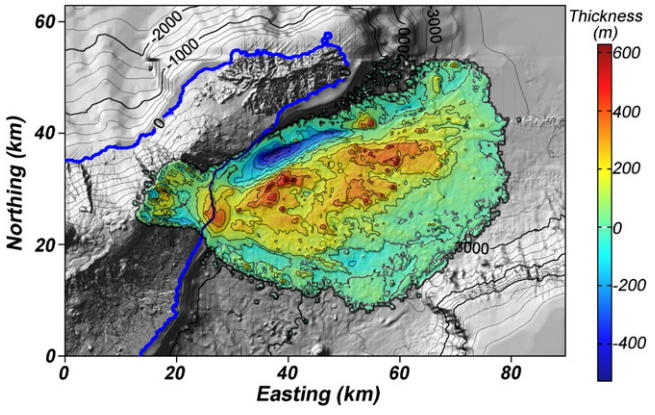

Fig. 2. Shaded DEM of the Guimar debris avalanche deposit onto which is superposed the artificially removed collapse deposits and refilled post-collapse-formed valleys, represented by different shades. Post-collapse seamounts and subaerial volcanism are clearly identifiable on this image as well as submarine valleys that were eroded after the collapse along the extension of subaerial rivers or gullies. The removed thickness exceeds 600 m at very local places, but the average thickness removed is 106 m. Contours are in metres and the coast is drawn by a thicker line. Contour lines for deposits thickness are at 100 m intervals.

influence on the underlying avalanche dynamics. The avalanche thickness and morphology influence the water by changing the bottom of the ocean and thus the slope. In our simulations, the coefficients C_f and C_s that fix the drag on the surface of the avalanche normal and parallel to the displacement are fixed at 2 and 0.01 respectively (Tinti et al., 2006; Kelfoun et al., 2010).

3.2. Bathymetry, topography and calculation grids

To simulate the Güìmar debris avalanche, we first built a Digital Elevation Model (DEM) of the region comprising the islands of Tenerife and Gran Canaria, using four separate DEMs. For the two onshore DEMs of Tenerife and Gran Canaria islands, the original databases are the Geographical Information Systems provided by GRAFCAN (1/5000[e]). For these two onshore DEMs, we first merged all the vector maps and selected the altitude layers, thus obtaining a single vector file for each island. Triangulated Irregular Networks were then created using the polylines and converted to raster DEMs with a pixel resolution of 10 m for Gran Canaria and 20 m for Tenerife. The bathymetry of the channel between Gran Canaria and Tenerife (~83 m using the pixel size resolution) was provided by Tim Le Bas and Doug Masson (National Oceanography Centre, Southampton). Finally, a fourth DEM of the submarine flanks, obtained after scanning and digitising the contours of the bathymetric map (Instituto Español de Oceanografia, 1/100,000[e]) was used to complete the offshore part. The final DEM produced is a 2000 × 1700 px grid with a spatial resolution of 100 m (Fig. 1). We first down-sampled the resolution of this grid by a factor of 2 (thus working with a spatial resolution of 200 m) and ran several simulations to find the best rheologies for the landslide propagation (see Section 3.4 for explanation concerning this point). This down-sampling was done in order to minimise calculation times. Then, we performed new simulations using the best landslide rheologies at a resolution of 100 m, but using a resized grid centred on the landslide region (Fig. 1).

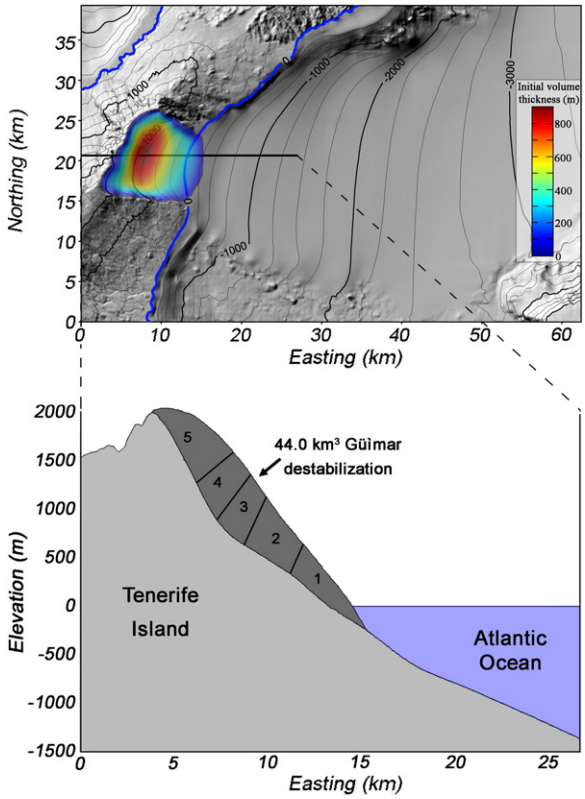

Fig. 3. (upper) Shaded DEM of the sliding surface used in the simulations, the thick line indicating the coast of Tenerife. Products from the post-collapse subaerial and submarine volcanism have been removed as well as the collapse deposits. The thickness of the initial collapse volume obtained by subtracting the sliding surface from the pre-collapse topography is also shown. (lower) West–East cross section of the initial landslide features (thick black line in the upper figure). The numbers 1–5 indicate the five equal volumes (8.8 km^3 each) used in the scenario involving retrogressive failures. In this scenario, the volume 1 is released at t = 0 s, and the following ones are released each 120 s. In the scenario involving a collapse in one go, the whole volume (44 km^3, 1–5 on the figure) is released at t = 0 s.

In order to investigate properly the similarities and differences between the modelled waves and the real mapped deposits in the Agaete Valley (Paris et al., 2004; Pérez-Torrado et al., 2006), we ran some simulations on a 10 m-resolution calculation grid centred on the Agaete Valley (Fig. 1). Since it is impossible to run the model on a 10 m-resolution grid covering the whole region of Tenerife and Gran Canaria due to insufficient computing capacities, we recreated the arriving waves on the borders of the 10 m-resolution grid. For this purpose, the simulation was first run on the 100 m-resolution grid covering the channel between the two islands, all the data referring to the displacement of both the landslide and the water (e.g., amplitudes, velocity vectors, and water fluxes) being registered at each time step. These data were then interpolated to a resolution of 10 m to determine the input conditions necessary to recreate the waves at the borders of the 10 m-resolution DEM. It has been verified that the waves recreated on the 10 m-resolution grid have the same amplitude and velocity as the initial ones obtained on the 100 m-resolution grid.

3.3. Initial conditions of the simulations

In the numerical model, the characteristics of the initial collapse volume are determined by subtracting (A) a DEM with the post-collapse scar and without the final debris avalanche deposits and post-collapse events (sedimentation and volcanism) from (B), a DEM of the pre-collapse topography. We have therefore redrawn some contour lines on our initial DEM in order to: (1) remove the post-collapse volcanism (both aerial and seamounts) and take away the debris avalanche submarine deposits (Fig. 2), and (2) refill the scar with the collapse volume to obtain the pre-collapse topography. We assumed, for the purpose of these operations, that the pre-avalanche topography and bathymetry were smooth, with a slope decreasing eastwards from the top of Tenerife down to the ocean bottom, as it is the case off to the north of the island of Tenerife (Fig. 1). We also removed, on both the pre- and post-avalanche DEMs, a sea wall that is present at the entrance of the Agaete Valley and that is a human construction. However, we did not remove the lava flow, present in the Agaete Valley and that is considered to be of Holocene age (Pérez-Torrado et al., 2006), and so, posterior to the Güìmar debris avalanche. Nevertheless, as the lava is located only in the bottom of the valley and since its thickness is small compared to the waves produced, it does not affect the results of the model.

These operations lead to the removal of 7.9 km^3 of aerial deposits including mainly post-collapse volcanism and erosion deposits, and 129 km^3 of submarine deposits (covering 1700 km^2) and that include the landslide deposits and the post-collapse volcanism and sediments. These values are consistent with the 120 km^3 and 1600 km^2 proposed by Krastel et al. (2001) for the submarine volume and surface covered by the deposits. The collapse volume calculated is 44.0 km^3, in agreement with data from the literature (37 km^3, Teide Group, 1997; 47 km^3, Carracedo et al., 2010), more than 99.2% of the collapse volume being subaerial in the simulations (Fig. 3). The surface of the collapsing volume is 124 km^2, again consistent with the 127 km^2 calculated by Paris et al. (2005), and its maximum thickness is 900 m. The subaerial sliding surface has a slope varying between 7 and 20° and the submarine slope ranges from 5° above −2300 m down to 2° below −2300 m. The collapsing material being composed of basaltic lava units with some layers of basaltic pyroclasts and breccias (Carracedo et al., 2010), we used a density of 2600 kg·m^{-3} for the avalanche. Note that, in our simulations, there is no change in the volume of the debris avalanche during its emplacement.

In this paper, we use the term "failure scenario" to describe how the total volume involved in the landslide is released (e.g., in one go, by retrogressive failures) and the term "rheology" to describe the sets of equations used to simulate the landslide propagation once released (e.g., Mohr–Coulomb rheology, and plastic rheology). As previously explained, there is no evidence suggesting how the collapsing 44 km^3 failed into the sea. Therefore, we tested two failure scenarios in our simulations: (1) a single sudden collapse of 44 km^3 and (2) five sudden discrete failures of 8.8 km^3 each, that occur every 120 s (Fig. 3). In the second scenario, the number of collapses and the duration between two successive collapses were chosen arbitrarily. We did not test more failure scenarios due to time-consuming simulations, lack of constrains concerning the failure mechanism of such large submarine landslides, and infinite failure possibilities that may be investigated.

3.4. Rheologies of the landslide and the water

As discussed in Kelfoun et al. (2010), a difficulty in the numerical modelling of debris avalanches is to define, at each time step, the value of the total retarding stress that slows and ultimately stops the propagation of the landslide. This total retarding stress includes the interactions of the debris avalanche with the ground and those between the avalanche and the water. Actually, there is no physically-based equation that allows all these complex behaviours to be described in a robust way. However, tsunami characteristics in the proximal field may be dependent on the way the avalanche is emplaced, thus the complex rheology of the landslide must be estimated. As in Kelfoun et al. (2010), we tested two different laws for the stress between the landslide and the ground: (1) the classically used Mohr–Coulomb frictional law, and (2) a constant retarding stress (i.e., constant whatever the thickness or the velocity of the avalanche). The Mohr–Coulomb frictional law is often used in granular flow dynamics since this law represents the behaviour of deposits at rest and of sand flows in the laboratory. However, a constant retarding stress better reproduces the extension, the thickness on all slopes, and some morphological features (levees and front) of natural deposits (Dade and Huppert, 1998; Kelfoun and Druitt, 2005; Kelfoun et al., 2010). We simulated the water using a density of 1000 kg·m^{-3} and a viscosity of 0.001 Pa·s.

Since we simulate a past event, the best rheology for the landslide propagation would be that which produces numerical deposits that are the most similar to the real extent and thickness of the Guimar debris–avalanche deposit. However, as explained above, few details about the thickness and the morphological features of these deposits are available in the literature. We therefore tested two hypotheses: (1) the real Güìmar debris avalanche deposits spread over the whole surface mapped by Krastel et al. (2001, cf. Fig. 1), or (2) the real Güìmar debris avalanche deposits spread only over the internal part of the mapped deposit, within a few tens of km from the scar. For this second case, the best rheology would be that which produces numerical deposits that form a cone-shaped within a few tens of km of the scar, that is estimated by eyeballing. For each of these two hypotheses, we determined the values of both the basal friction angle φ_{bed} and the constant retarding stress that allow the most accurate reproduction of the deposits.

To sum up, eight simulations were run (Table 1), taking into account:

- 2 failures scenarios (one go/retrogressive failures),
- 2 rheologies to simulate the landslide propagation (Mohr–Coulomb frictional law/constant retarding stress), and
- 2 ways to interpret the surface covered by the real debris avalanche deposits (whole surface of mapped deposits/only the internal part of mapped deposits).

4. Results

4.1. Debris avalanche

The main physical characteristics of the emplacement and the deposits simulated according to the scenario envisaged are listed in Table 1. The extent and thickness of the obtained deposits are shown in Fig. 4.

4.1.1. Case of a collapse in one go

For the hypothesis in which the real Güìmar debris avalanche deposits spread over the whole surface mapped by Krastel et al. (2001), the best results are obtained using a frictional law with $\varphi_{bed} = 1.3°$ (Fig. 4a) or a constant retarding stress of 17 kPa (Fig. 4c). With

Table 1
Modelled debris avalanche and triggered tsunami characteristics, and maximum water depth recorded at seven outcrops in the Agaete Valley, according to the way the failure occurs and the rheology used to simulate the landslide propagation.

Type of failure process		In one go (1×44 km^3)				Retrogressive failure (5×8.8 km^3)			
Type of rheology		Frictional $\varphi_{bed}=1.3°$	Frictional $\varphi_{bed}=3.9°$	Constant l7kPa	Constant l50 kPa	Frictional $\varphi_{bed}=1.30$	Frictional $\varphi_{bed}=3.9°$	Constant 16.5 kPa	Constant 145 kPa
Landslide run-out (km)		66	38	75	36	67	39	77	38
Duration of landslide emplacement (s)		2160	990	2200	660	2250	1390	2460	1220
Landslide maximum front velocity (m·s^{-1})[a]		79	41	82	60	60	50	64	58
Landslide average front velocity (m·s^{-1})		31	38	34	54	30	28	31	31
Landslide deposits maximum thickness (m)		181	166	223	109	197	179	236	124
Surface area covered by landslide deposits (km^2)		1371	965	1866	744	1358	703	1646	689
Average thickness of landslide deposits (m)		33	47	24	59	33	64	28	66
Initial maximum wave amplitude (m)[b]		466	387	500	503	343 (5)[c]	223 (5)[c]	312 (5)[c]	378 (5)[c]
Time before entering into the Agaete Valley (s)		571	603	555	566	657	689	646	667
Amplitude when entering the Agate Valley (m)		167 (230)[d]	147 (180)[d]	173 (249)[d]	168 (234)[d]	94 (101)[d]	76	97	91 (130)[d]
Maximum inland penetration in the Agaete Valley (km)		–	7.1	–	9.1	–	5.0	–	3.8
Max water depth recorded (m)	Gasolinera	–	67	–	117	–	41	–	24
	Juncal	–	103	–	142	–	46	–	31
	LL Turman	–	32	–	124	–	50	–	35
	Aerogeneradores	–	36	–	66	–	7	–	0
	Berrazales	–	106	–	137	–	48	–	24
	La Aldea	–	110	–	151	–	35	–	19
	Azotavientos	–	32	–	52	–	6	–	0

[a] Maximum value of the “instantaneous” velocity of the avalanche front, calculated using the distance covered by the front from the bottom of the scar over a period of 10 s.
[b] Measured at 5 km eastwards from the coast line.
[c] The number in brackets indicates which of the five waves observed is the highest one.
[d] The number in brackets indicates the amplitude of the highest wave if it is not the first one.

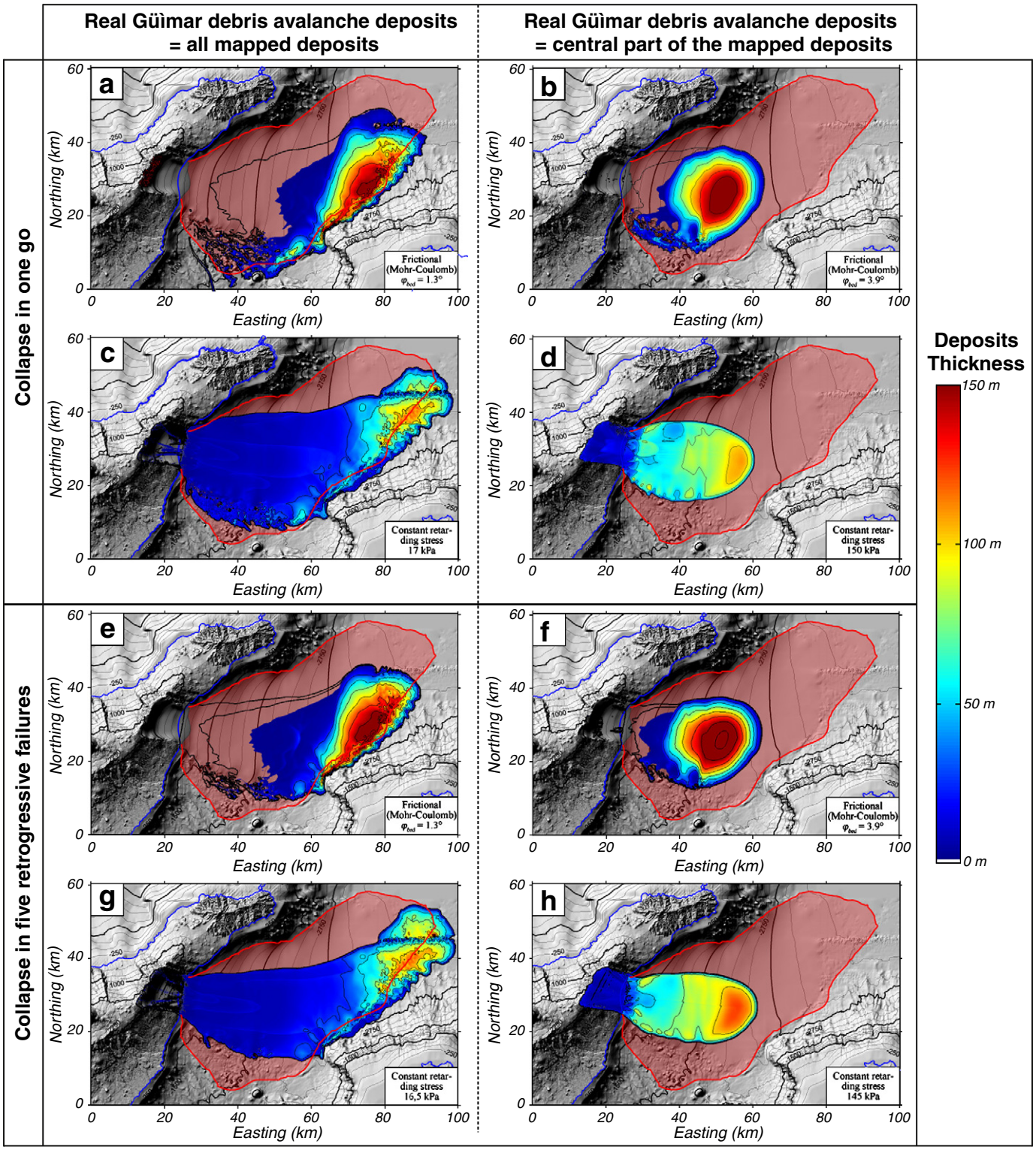

Fig. 4. Simulated landslide deposits for a collapse in one go (a–d) or a collapse by five retrogressive failures (e–h). a) frictional behaviour with $\varphi_{bed} = 1.3°$, b) frictional behaviour with $\varphi_{bed} = 3.9°$, c) constant retarding stress of 17 kPa, d) constant retarding stress of 150 kPa, e) frictional behaviour with $\varphi_{bed} = 1.3°$, f) frictional behaviour with $\varphi_{bed} = 3.9°$, g) constant retarding stress of 16.5 kPa, h) constant retarding stress of 145 kPa. The scale is the same for all cases. Contour lines for deposits thickness are at 25 m intervals.

$\varphi_{bed} = 1.3°$, the landslide reaches 66 km eastwards from the scar in 2160 s, with an average front velocity of 31 $m \cdot s^{-1}$, and a maximum front velocity of 79 $m \cdot s^{-1}$. There is no deposition until the submarine flanks reach a depth of 1000 m, when the deposits then concentrate to form a bulge with a maximum thickness of 180 m at 40–70 km from the coast, that is not consistent with the observations that most of the largest blocks are within 10–50 km of the coast of Tenerife (Krastel et al., 2001; Krastel and Schmincke, 2002). The model reproduces the contours of the southern part of the deposits well, but it is unable to reach the maximal northwards extension. With a constant retarding stress of 17 kPa, the maximal extension of the deposits is 75 km, for a duration of emplacement of 2300 s, an average front velocity of 34 $m \cdot s^{-1}$,

and a maximum front velocity of 82 $m \cdot s^{-1}$. The modelled deposits also match the southern limit well, but fail to reach the northern limit. The deposits have a thickness of 5 to 25 m from the base of the scar down to a depth of 3000 m, and form, at greater depth, a bulge 100–150 m high with a maximum thickness of 225 m. Although more realistic than the frictional law, the use of a constant retarding stress of 17 kPa still fails to reproduce the entire surface area of the mapped deposits.

For the hypothesis in which the real Güìmar debris avalanche deposits spread only over the internal part (within a few tens of km from the scar) of the mapped deposit, the best results are obtained using a frictional law with $\varphi_{bed} = 3.9°$ (Fig. 4b) or a constant retarding stress of 150 kPa (Fig. 4d). With $\varphi_{bed} = 3.9°$, the landslide reaches 38 km eastwards from the scar in 990 s (average and maximum front velocities of 38 and 41 $m \cdot s^{-1}$ respectively). With this Mohr–Coulomb rheology, the model produces deposits that form a "pile" between −1200 and −2900 m, with a maximum thickness of 165 m. Most of the deposits are thus concentrated at 10–40 km from the landslide scar. With a constant retarding stress of 150 kPa, the maximal extension of the modelled deposits is 36 km and the duration of emplacement is 660 s (average and maximum front velocities of 54 and 60 $m \cdot s^{-1}$ respectively). The deposits form a single elongated lobe whose thickness increases eastwards, from 20 m close to the scar up to 110 m at the furthest eastern point, leading to an average thickness of 60 m.

4.1.2. Case of a collapse by retrogressive failures

For the hypothesis in which the real Güìmar debris avalanche deposits spread over the whole surface mapped by Krastel et al. (2001), the best results are obtained using a frictional law with $\varphi_{bed} = 1.3°$ (Fig. 4e) or a constant retarding stress of 16.5 kPa (Fig. 4f). With $\varphi_{bed} = 1.3°$, the landslide reaches 67 km with an average front velocity of 30 $m \cdot s^{-1}$ (60 $m \cdot s^{-1}$ at a maximum). The deposits are similar to those obtained considering a single collapse in one go, forming a bulge with a maximum thickness of 197 m at a depth comprised between 1000 and 3500 m, but are narrower (compare Fig. 4e with Fig. 4a). With a constant retarding stress of 16.5 kPa, the debris avalanche stops after 2460 s (average and maximum front velocities of 31 and 64 $m \cdot s^{-1}$ respectively), the run-out is 77 km, and the deposits form a bulge 90–120 m high with, locally, a maximum thickness of 236 m. Again, the deposits are similar to those produced when considering a collapse in one go, but they are narrower (compare Fig. 4g with Fig. 4c). Using a retrogressive failures scenario, the model also fails to reproduce the maximal extension of the contours of the northern part of the deposits.

For the hypothesis in which the real Güìmar debris avalanche deposits spread only over the internal part of the mapped deposit, a frictional law with $\varphi_{bed} = 3.9°$ (Fig. 4f) or a constant retarding stress of 145 kPa (Fig. 4h) give the best results. With $\varphi_{bed} = 3.9°$, the landslide reaches 39 km eastwards from the scar in 1380 s, the deposits forming of a cone-shaped between −750 and −2850 m, with a maximum thickness of 179 m. With a constant retarding stress of 145 kPa, the maximal extension of the modelled deposits is 38 km and the duration of emplacement is 1200 s. The deposits form a single elongated lobe (narrower than that obtained when considering a collapse in one go), whose thickness reaches a maximum of 124 m at the furthest eastern point.

4.2. Tsunamis formed

We simulated the tsunamis formed by the landslide for all the eight cases described above on the 100 m-resolution DEM, the physical characteristics of the wave trains and their propagation varying depending on the case considered. Some of these parameters are provided in Table 1, and the general features of the tsunamis produced are detailed below. For each of the two failure scenarios,

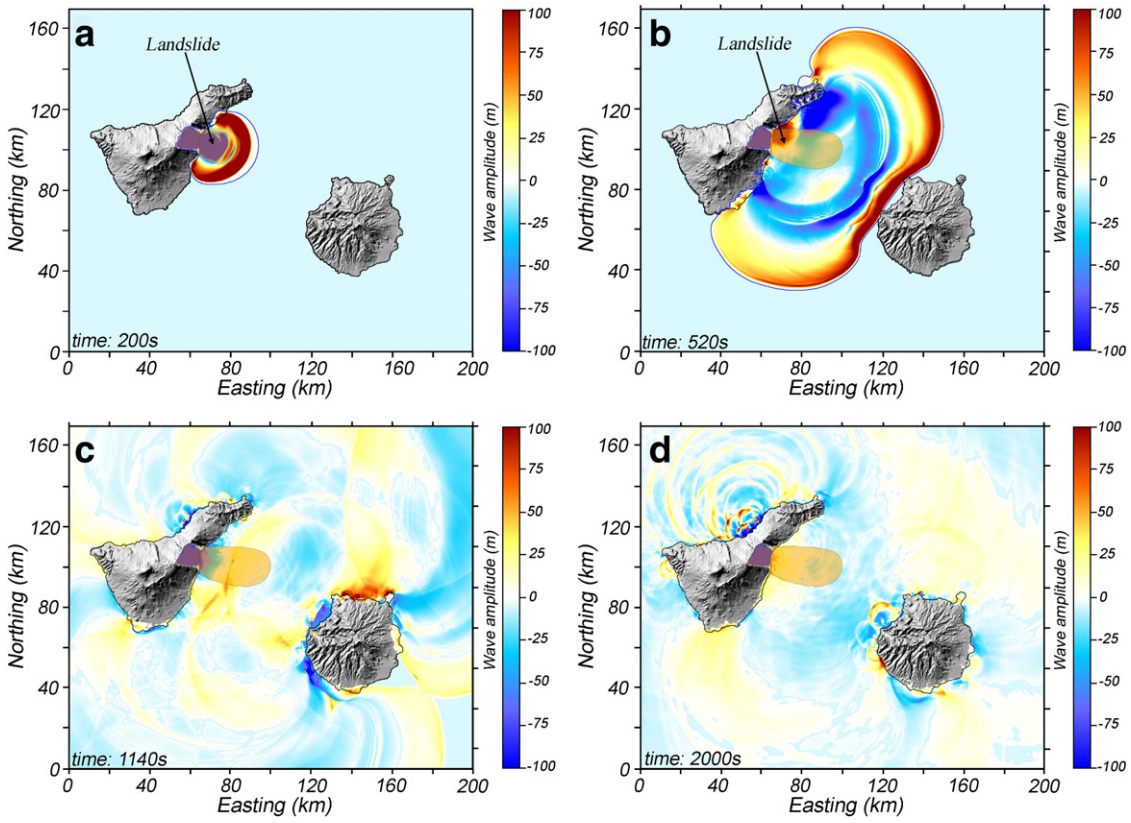

Fig. 5. Amplitude of waves at times of: a) 200 s, b) 520 s, c) 1140 s and d) 2000 s after the onset of collapse. The landslide deposits are also shown. The rheology used to simulate the landslide propagation here is a constant retarding stress of 150 kPa.

only the two rheologies giving the smallest and highest initial waves were used in the simulations run on the 10 m DEM. Fig. 5 shows four steps of the propagation of the produced waves using a collapse in one go and a constant retarding stress of 150 kPa to simulate the landslide propagation. Fig. 6 shows the water surface vertical displacement registered at a) 5 km east of the landslide scar where the initial wave is the highest, and b) at the entrance of the Agaete Valley on Gran Canaria (where the initial water depth is 21 m). On this figure, the distinction is made between the two failure scenarios envisaged. However, for reasons of clarity and because of their similarities, for a given failure scenario, the waves profiles corresponding to the different rheologies used to simulate the landslide propagation are gathered together, the two coloured zone being delimited by the minimum and maximum wave profiles.

4.2.1. Case of a collapse in one go

When released in one go, the whole volume pushes and lifts the water surface 390–500 m above the initial sea level, the maximum wave amplitude being observed at ~5 km east of the landslide scar (Figs. 5a and 6a, Table 1). This first wave is followed by a hollow 430–580 m deep and by another wave which amplitude varies between 110 and 135 m. The water level then fluctuates during several hundreds of seconds before regaining its initial level. The wave profiles registered at this gauge are very similar whatever the rheology used to simulate the landslide propagation. The waves then propagate, affecting the coast of Tenerife (Fig. 5b), with an amplitude reaching 250 m on the south-eastern coast and penetrating up to 5 km inland in some valleys of the north-eastern coast.

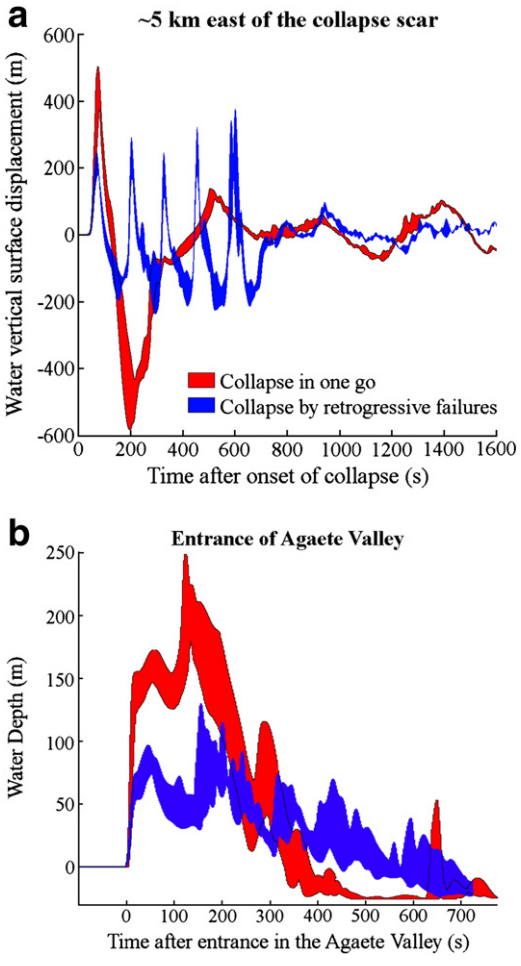

Fig. 6. Profiles of water surface vertical displacements at gauges placed at a) 5 km offshore, east of the landslide scar (location of the maximum wave amplitude registered) and b) at 1 km offshore from the entrance of the Agaete Valley on Gran Canaria. For a given failure scenario (one go or retrogressive failures) and for clarity reasons, the four rheologies tested to simulate the landslide propagation are grouped together, the two coloured zone being delimited by the minimum and maximum wave profiles.

Nearly 400 s after the onset of the collapse, the first wave reaches the insular shelf of Gran Canaria (−250 m) to the southeast of the collapse scar, slows down and increases in amplitude. The first wave reaches the north-western coast of Gran Canaria, entering some of the valleys on Gran Canaria and propagating around the island both northwards and southwards, the two waves meeting in the southeast of Gran Canaria at ~1140 s (Fig. 5c). The first wave reaches the entrance of the Agaete Valley 555–605 s after the onset of the collapse with an average velocity of 35–45 $m \cdot s^{-1}$ and an amplitude of 150–175 m (Table 1). The wave has a complex profile, with the maximum amplitude (180–250 m) being registered ~80 s after the entrance in the Agaete Valley (Table 1, Fig. 6b). However, we can recognise one main wave that reaches 7.1–9.1 km inland due to its large wavelength, depending on the rheology chosen to simulate the landslide. On the simulations run on the 10 m DEM, we see that water tends to follow the bed of the valley, but the waves sometimes reach altitudes of up to >500 m at some points (Fig. 7). The water reaches its maximal inland penetration in the Agaete Valley ~700 s after the onset of collapse, and starts to leave the valley (backwash) nearly 30 s later. After 1000 s, the Agaete Valley is again nearly empty of water. Fig. 7 shows that the maximum water depth measured in the Agaete Valley is 170 m when using the frictional rheology with $\varphi_{bed} = 3.9°$ and 200 m with the 150 kPa-constant retarding stress. After 2000 s, only small waves persist in the whole calculation grid, with some reflections into the valleys still creating higher wave peaks locally (Fig. 5d).

4.2.2. Case of collapse by retrogressive failures

With this failure scenario, the five retrogressive collapses trigger five distinct initial waves, that are, once again, very similar whatever the rheology used to simulate the landslide propagation (Fig. 6a). Moreover, for a given rheology, the five initial waves are very similar among themselves, the highest being always the fifth one with an amplitude of 223–378 m (Table 1). There is 510–530 s between the first and the fifth (and last) wave crests (Fig. 6a), whereas the first and the last collapses are separated by only 480 s (one collapse every 120 s). The difference (30–50 s) between these two related parameters corresponds to the duration for the last released volume to cover the distance between the top of the subaerial scar where it initially lies down, to the water level where it pushes and lifts the water creating the last of the five initial registered waves.

The waves then propagate in the same manner as for a collapse in one go. With this failure scenario, the water starts to enter into the Agaete Valley 650–670 s after the collapse onset, with an amplitude of 75–100 m, depending on the rheology used to simulate the landslide (Table 1, Fig. 6b). Again, the water depth profile is complex and for two of the four rheologies, the highest wave is not the first but the second one, which has an amplitude of 100–130 m. The water inundates the Agaete Valley 3.8–5.0 km inland, far less than in the case of a single collapse (Fig. 7c–d). The wave sometimes reaches altitudes up to 275 m at some points, and starts to withdraw 760 s after the collapse onset.

5. Discussion

5.1. Importance of the failure scenario on the triggered tsunami

For a given rheology used to simulate the landslide propagation, the two failure scenarios tested in this study (a collapse in one go and five retrogressive collapses) give debris avalanche deposits that are very similar (compare Fig. 4a/e, b/f, c/g and d/h). However, the velocity of the debris avalanche (and especially the maximum front velocity) differs from a failure scenario to another since the collapsing

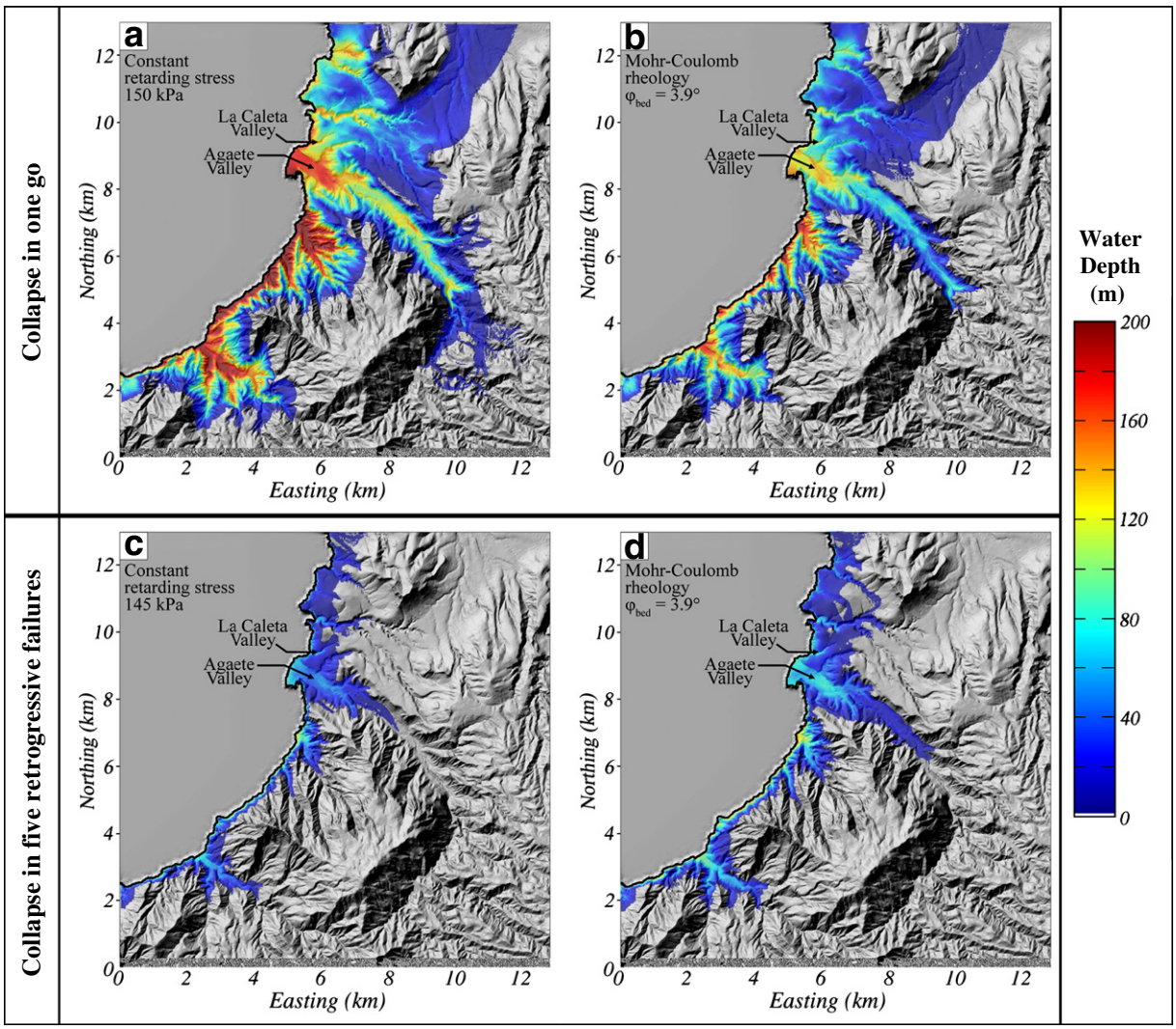

Fig. 7. Maximum water depth registered inland according to the failure scenario envisaged (a–b in one go; c–d by retrogressive failures) and the rheology used to simulate the landslide propagation (a and c, constant retarding stress; b and d Mohr–Coulomb rheology). The coast is marked by the thick black line. The scale is the same for all pictures.

volume (that controls the driven force and thus the velocity) is not released in the same way. The failure scenario seems to be the main parameter that controls the characteristics of the triggered tsunami, after the whole collapsing volume itself, since it gives wave profiles that are very different. Indeed, when released in one go, the debris avalanche produces one initial wave with an amplitude of 390–500 m whereas the five retrogressive failures produce five distinct initial waves 225–380 m high (Table 1, Fig. 6a). Due to their smaller amplitude, the waves produced by retrogressive collapses propagate more slowly and reach the entrance of the Agaete Valley 85–100 s later than those produced when considering a collapse in one go. It is difficult to exactly recognise the initial waves produced on the wave profiles registered at the entrance of the Agaete Valley (Fig. 6), due to the evolution of the wave train while propagating in deep ocean and on the insular shelf of Gran Canaria. However, these profiles show that, although smaller, incoming waves produced by retrogressive collapses are more numerous compare to those produced by the collapse in one go.

In the scenario implying five retrogressive failures, each of the five volumes represents 20% of the whole 44 km^3 volume involved in the collapse in one go. However, the amplitude of the highest initial wave produced by retrogressive failures is 58–75% of that produced when the whole volume is released in one go (Fig. 6a), and it is 39–66% at the entrance of the Agaete Valley (Fig. 6b). These comparisons show that, for a given total volume, there is no simple and direct relationship between the volume of the individual collapse(s) and the amplitude of the triggered tsunamis. Since the aim of the paper is not to deal with hazard assessment, we did not test more failure scenarios and rheologies (e.g., less/more retrogressive failures, shorter/longer duration between two successive collapses, creeping, “en masse” sliding) to investigate the possible relationship between the failure mechanism and the amplitude of the tsunami produced. Moreover, the failure mechanisms of such very large volumes (>several km^3) remain largely unknown, and an infinity of scenarios could be tested. However, the two simple failure scenarios tested in this study show that the way by which the volume collapsing volume is released should be carefully investigated when dealing with landslide-triggered tsunami hazard assessment.

5.2. Importance of the landslide rheology on the triggered tsunami

Whatever the rheology used to simulate the landslide emplacement, the debris avalanche deposits simulated are more or less comparable with real ones, depending on the interpretation we make of the mapped deposits (whether the real Güìmar debris avalanche deposits spread over the whole surface mapped by Krastel et al. 2001,

or only over the internal part of the mapped deposits). For a given failure scenario, the four rheologies tested lead to wide ranges of duration of emplacement (variation of 233% for a collapse in one go, 102% for retrogressive collapses), maximum velocity (variation of 100% for a collapse in one go, 28% for retrogressive collapse) and run-out (variation of 108% for a collapse in one go, 103% for retrogressive collapse) of the debris avalanche. Despite these major variations of the landslide emplacement characteristics, the produced tsunamis have the same main pattern (Fig. 6). Moreover, the maximum amplitude of the initial wave produced does not vary as much as the landslide deposits characteristics (variation of 30% for a collapse in one go, 70% for retrogressive failures), and when the first wave reaches the entrance of the Agaete Valley (our main place of interest), its amplitude varies of 18% for a collapse in one go, and 28% for retrogressive failures (Table 1).

This shows that, when considering a landslide resulting from a sudden and rapid destabilisation, a knowledge of the volume, the failure scenario (in one go, by retrogressive failures, etc.) and the main physical characteristics of the landslide (e.g. initial morphology, density, and direction of propagation) is sufficient to provide a rough estimate of the amplitude of a tsunami triggered by a debris avalanche, without requiring an accurate knowledge of the landslide rheology. Our simulations confirm that the more information available concerning the real debris avalanche deposits (run-out, thickness, covered surface area, morphological features, etc.), the better the estimate of the rheology of the landslide. It should be noted that we have not tested processes like creeping or "en masse" sliding, but these failure and emplacement scenarios should be investigated for hazard purpose, that was not the aim of this paper.

5.3. Comparison with field data: tsunami deposits

Paris et al. (2004) and Pérez-Torrado et al. (2006) identified and detailed seven outcrops of tsunami deposits in the Agaete Valley on the northwest coast of Gran Canaria, which they hypothesised to be the results of the Güìmar debris avalanche collapse that occurred 0.83 Ma ago (Ancochea et al. 1990; Carracedo et al., 2010). Fig. 8 shows the seven locations of outcrops where tsunami deposits were found (explanations concerning the absence of such tsunami deposits in other Gran Canaria valleys are given in Section 5.4). These deposits are located 41–188 m asl, and are only preserved on the valley walls, at a distance of up to 2.65 km from the coast (Azovientos outcrop, Fig. 8). The distribution of the different outcrops in patches indicates that they may be the remains of a more extensive deposit that partially filled the mouth of the Agaete Valley and surrounding ravines as La Caleta Valley (LL. Turman outcrop, Figs. 7 and 8).

The deposits are 1–5 m thick, decrease in thickness with altitude, and consist of heterogeneous, angular to rounded heterometric volcanic clasts and marine fossils that are covered by soil and colluviums or by deposits of an anthropic origin (Pérez-Torrado et al., 2006). The tsunami deposits in the Agaete Valley appear, in general, to be internally stratified into two main layers. Each layer can be subdivided into various sub-layers, but they show very poor lateral continuity. The lower layer is clast-supported, heterometric, very poorly sorted and is reversely graded (sometimes there is more than one sequence). The upper layer is clast-supported, less coarse, poorly sorted, richer in fossils and shows a weak reverse grading. The contact between the two layers is clear, but not discordant. Scour and fill features of the upper layer penetrate the lower layer. The basal contact with the substratum shows clear erosive features such as cut dykes and rip-up clasts (mud pebbles). The tsunami deposits were fed both by platform-beach marine deposits (contributing the fossils, the rounded clasts and the beachrock clasts) and by alluvial deposits along the Agaete ravine and tributaries (providing the angular clasts and the increased felsic clast content), the latter being more dominant towards the outcrops located at higher altitudes and farthest from the coast. Molluscan fauna is typical of the Pleistocene (20% of the molluscan taxa are extinct) and of an interglacial stage with a sea temperature similar to the present, or slightly warmer (Pérez-Torrado et al., 2006).

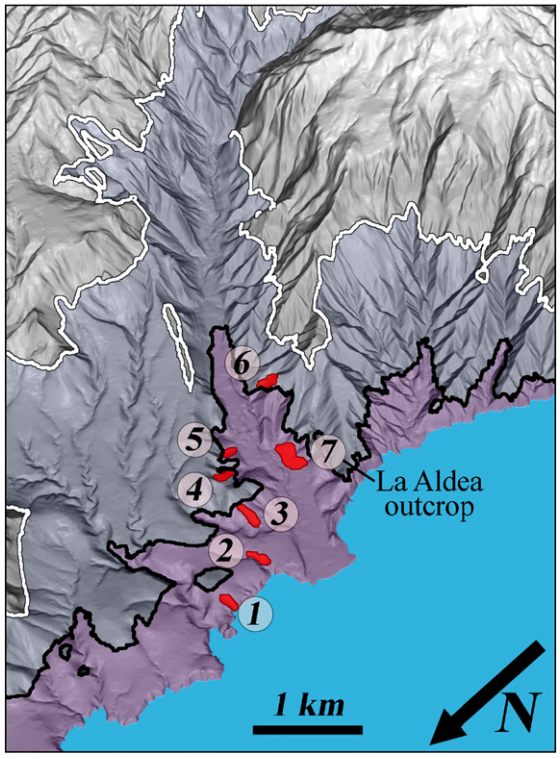

Fig. 8. Locations of the seven outcrops where tsunami deposits have been identified (Pérez-Torrado et al. 2006), placed on the 10 m-resolution DEM. These are (with their altitudes): 1) Juncal (50–65 m), 2) Llanos de Turman (41–58 m), 3) Gasolinera (73–78 m), 4) Aerogeneradores (138–162 m), 5) Berrazales (89–91 m), 6) Azotavientos (120–188 m), 7) La Aldea road outcrop (50–170 m). The thick lines represent the maximum run-ups reached by waves in our simulations, considering either a collapse in one go and a 150 kPa constant-retarding stress to simulate the landslide propagation (white line), and a collapse by retrogressive failures and a 145 kPa constant-retarding stress to simulate the landslide propagation (black line).

Neither the altitudes nor the geomorphological–sedimentolological characteristics of the Agaete deposits have any equivalent in the remaining Pleistocene or even Miocene marine deposits exposed in Gran Canaria or on the other Canary Islands, thus a genesis related to changes in sea level has been proposed. Based on the stratigraphic relationships described above, the age of these conglomerates is estimated to range between 1.75 Ma and 32 ka (Pérez-Torrado et al., 2006). Radiometric methods cannot be applied, the K–Ar method because of the lack of host volcanic material inside the marine conglomerates, and the deposits are beyond the range of C-14 dating.

Fig. 9 shows the evolution of water depth recorded by a water gauge placed at these seven described outcrops after the arrival of the first numerical wave, and according to the failure scenario and the rheology used to simulate the landslide. Table 1 indicates the maximum water depth measured at these points. For both failure scenarios, the water depths profiles registered at the seven gauges are difficult to interpret since they are rapidly perturbed by the numerous reflections of the waves occurring in the valley. For each scenario, the water reaches all the locations where tsunami deposits were identified, except for a collapse by retrogressive failures and when a constant retarding stress of 145 kPa is used to simulate the landslide propagation. In this case, the water does not reach the locations of Aerogeneradores and Azotavientos (outcrops 4 and 6 respectively on Figs. 8 and 9) but stops very close to these locations. Figs. 8 and 9 reinforce the hypothesis that the Güìmar debris avalanche certainly

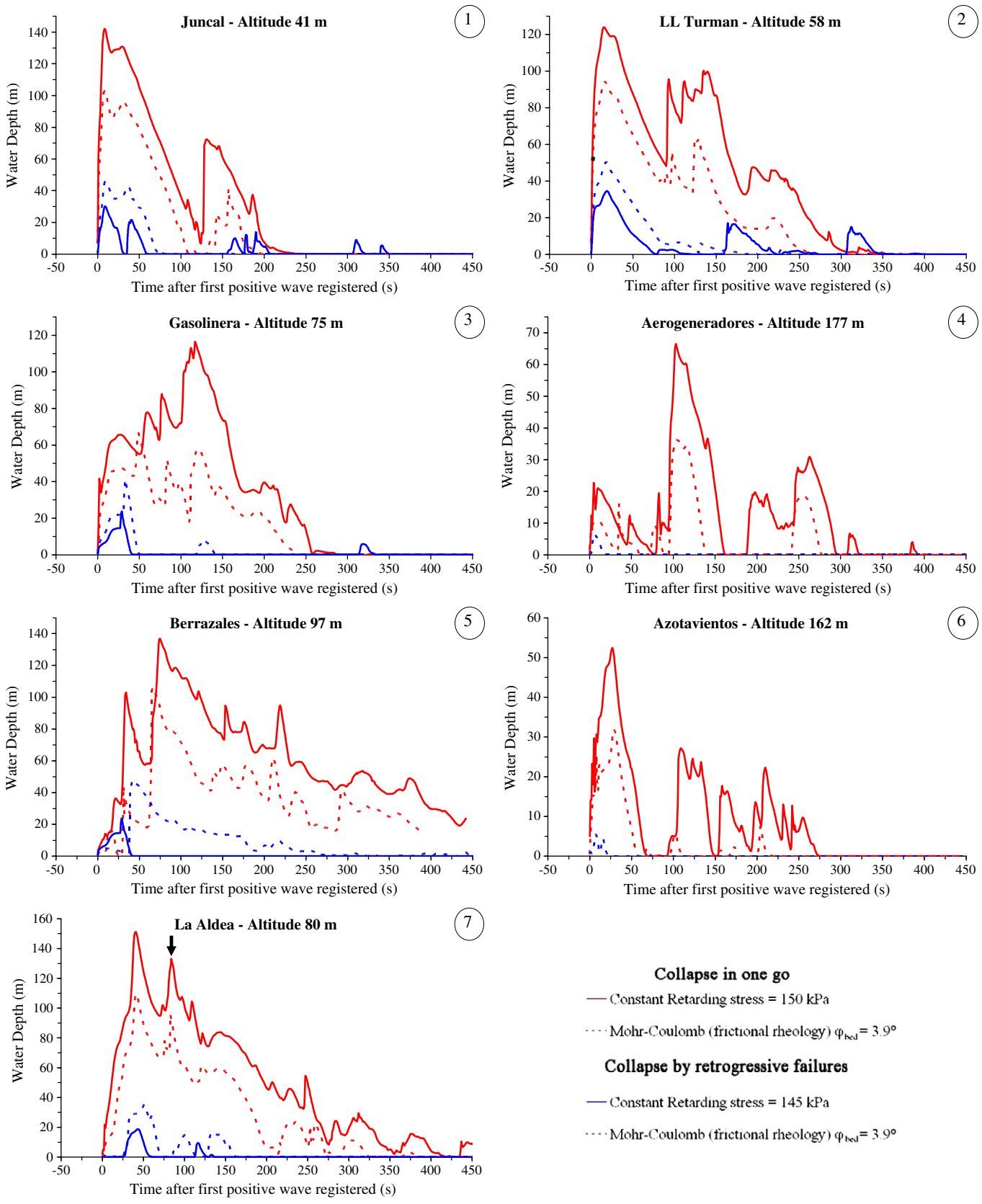

Fig. 9. Water depth profiles as a function of time after the first positive wave recorded, and according to the failure scenario and the rheology used to simulate the landslide propagation, at the seven outcrops described by Pérez-Torrado et al. (2006). We chose to use the first increase in water depth as the origin point for the abscissa to allow a better comparison between the four profiles (see Fig. 8 for reference numbers). Note that the altitudes at the emplacement of the seven numerical wave gauges (given on each graph) are within the different ranges given by Pérez-Torrado et al. (2006) for the corresponding outcrops. On the La Aldea flow depth profile (outcrop 7) the black arrow represents the limit between the run-up (before the arrow) and backwash (after) phases for both rheologies (seeSection 5.3 for explanation).

triggered the tsunami that left deposits in the Agaete Valley on Gran Canaria.

The thickness of the tsunami deposits indicates that the waves should have been at least 1–5 m in amplitude at the seven locations, and probably more, since sediments would constitute mostly the bed load of the wave (Pérez-Torrado et al. 2006). Our profiles show that the water depth attains >140 m at some locations (Juncal, Berrazales, and Aldea, Figs. 8 and 9) when considering a collapse in one go, probably much higher than the expected wave. Moreover, with this failure scenario, the waves reach altitudes of >500 m and up to 9.1 km inland, much higher and further in the Agaete Valley than the tsunami deposits, which were found at a maximum altitude of 188 m and only up to 2.65 km inland (Azotavientos outcrop, Fig. 8). Flow depth of >200 m (collapse in one go) seems unlikely considering the decrease of the thickness and mean size of the tsunami deposits, not far from the inundation limit (e.g., Azotavientos at 188 m asl). It is thus possible that the tsunami deposits were present further upstream and higher on the flanks of the Agaete Valley, but have been more eroded (because they were thinner and higher in altitude) than the deposits closer to the coast. Chances for preserving deposits higher than 200 m are very low because of the high slope angle. Indeed, slopes range from 5 to 10° where tsunami deposits are preserved, and are commonly >25° at altitudes higher than 100 m.

Considering a collapse by retrogressive failures, the maximum water depth registered at one of the seven outcrops is 'only' 50 m (LL Turman outcrop) and the waves reach a maximum altitude of 275 m and a maximal inland distance of 5.0 km. These values are closer to the minimum values constrained by the tsunami deposits found in the Valley, thus suggesting that the Güìmar debris avalanche have been initiated by several retrogressive failures rather than one single collapse. More numerous smaller individual failures (e.g., 10 failures of 4.4 km^3 each) would likely produce smaller waves than those registered in our present simulations, that would possibly not reach the altitudes where tsunami deposits were found in the Agaete Valley. Therefore, it is unlikely that the Güìmar debris avalanche occurred in very numerous small individual failures.

Pérez-Torrado et al. (2006) provide some stereograms of the cobble fabrics along the outcrop of La Aldea road (see Fig. 8 for location, outcrop number 7) that show different directions of the paleocurrents: landward in the lower layer and seaward in the upper layer. In the lower layer of tsunami deposits at La Aldea road, the flow coming from the sea is oriented N50–N120, whereas in the upper layer the deposits record a direction of the flow oriented towards N210–N280. In our simulations we recorded the velocity vector of the waves at this La Aldea road outcrop, as a function of time, and for a collapse in one go. We can thus directly compare the velocity of the wave with the main direction of the cobble fabrics described by Pérez-Torrado et al. (2006). For this purpose, in our simulations, we differentiated the run-up and backwash phases that occur respectively before and after the arrow placed on the water depth profile recorded at the La Aldea road outcrop (outcrop 7 of Fig. 9). Fig. 10 shows that the rose diagrams illustrating the velocity direction during the run-up and backwash phases in our simulations are consistent with those corresponding to the cobble fabrics recorded in the field (Pérez-Torrado et al., 2006). Indeed, the wave velocity has a direction of N100–N140 during the run-up phase, which is included in the N50–N120 direction recorded by the cobble fabrics, and the backwash phase (main direction of N260–N310 and N280–N290) is also compatible with that recorded by the cobble fabrics (main direction comprised between N210 and N280).

5.4. Far-field waves and tsunami deposits

While propagating in the deep ocean, the amplitude of the first wave decreases progressively. At 140 km eastwards from the landslide scar (at the eastward extremity of our largest calculation grid, Fig. 1), the amplitude of the first wave is 50–78 m for a collapse in one go and 10–19 m for the scenario involving retrogressive failures. Extrapolation of the wave amplitude further to the east in the deep ocean gives waves of 4–10 m (collapse in one go) and 1–3 m (retrogressive failures) at 250 km, where the island of Fuerteventura is located. This basic calculation shows that tsunami deposits from the Güìmar flank collapse could have been (and possibly still are) present around the western coastline of Fuerteventura. Along the western rocky coast of Gran Canaria, the Agaete and La Aldea valleys are the only places where tsunami waves could penetrate inland. Extensive agriculture in the La Aldea Valley probably destroyed evidence of the tsunami. Elsewhere (on Tenerife and the north of Gran Canaria), post-tsunami volcanism

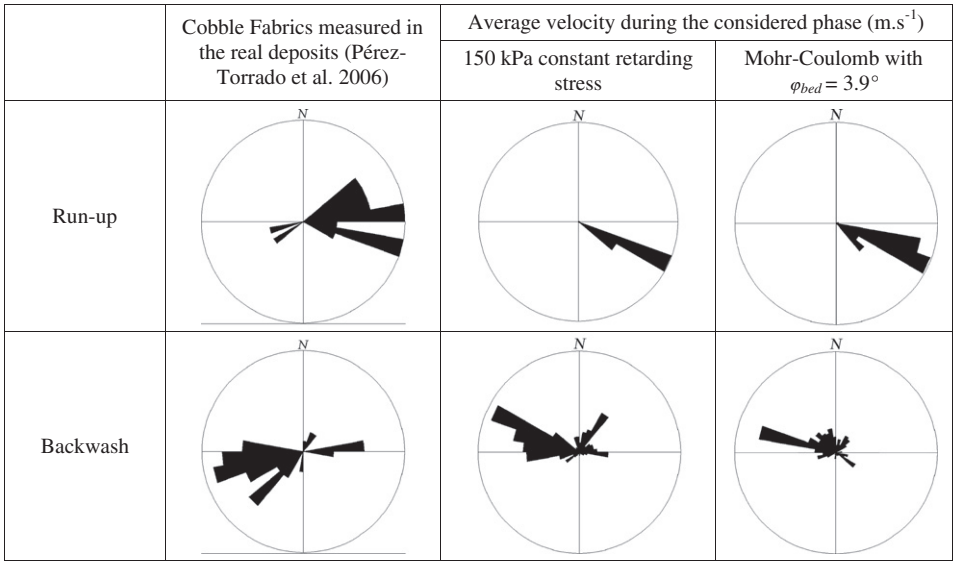

Fig. 10. Stereograms of the cobble fabrics along the outcrop of La Aldea (see. Fig. 8 for location) corresponding to the run-up and backwash phases (from Pérez-Torrado et al. 2006), and stereograms of the wave velocity recorded during these two phases in our simulations, depending on the rheology used to simulate the debris avalanche and considering a collapse in one go. We differentiated the run-up and backwash phases that occur respectively before, and after, the arrow placed on the water depth profile recorded at the La Aldea road outcrop (outcrop 7 of Fig. 9).

has completely reshaped the coasts and filled palaeo-valleys (Carracedo et al. 2010), thus limiting the possibility of observing tsunami deposits there. It is unlikely that tsunami deposits due to this event occurred further afield (e.g., on African western coasts), because of wave amplitude attenuation but also due to the numerous reflections on the other Canary Islands which dissipates the energy of the tsunami.

5.5. Influence of sea-level change

The overall distribution of Pliocene and Quaternary paleo-shorelines in Gran Canaria demonstrates that both differential uplift and apparent westwards tilting of the island occurred (Menéndez Gonzáles et al., 2008). As described by Pérez-Torrado et al. (2006), the sea-level 0.83 Ma ago may have been 40–50 m higher than the present level. We therefore simulated the Güìmar flank collapse considering a sea-level at +50 m, a collapse in one go, and a 150 kPa-constant retarding stress to simulate the landslide propagation (not shown in the results section). The characteristics of the debris avalanche deposits produced when using a sea level of +50 m are nearly identical to those obtained when the sea level is at 0 (actual sea level). The profile and behaviour of the waves produced are very similar to those obtained when using the present sea-level. The first wave produced in the case of a sea-level at +50 m has a maximum initial amplitude of 510 m at 5 km eastwards of the scar (compared to 500 m using the present sea-level, Table 1). At the outcrops described by Pérez-Torrado et al. (2006, see Fig. 8) in the Agaete Valley, water depths measured for a sea-level at +50 m are 13–42 m higher than those obtained using a sea-level at 0 (i.e., variation of 7–42%). From the Agaete coast up to ~10 km offshore, the actual water depth on the insular shelf of Gran Canaria is <100 m. Given a sea level of +50 m, this increases the water depth by a third, and thus limits the increase of the wave amplitude when it reaches these shallow waters. This also explains why the increase of the water depth recorded inland (+13 to +42 m) is less than the initial increase of sea-level (+50 m).

6. Conclusions

Using numerical modelling we showed that tsunami deposits found at 40–188 m asl in the Agaete Valley of Grand Canaria (Canary Islands) have certainly been formed by a tsunami caused by the 44 km^3 Güìmar flank collapse that occurred ~0.83 Ma, on the neighbouring island of Tenerife. Due to the lack of information concerning the failure mechanism, we envisaged two scenarios: a single collapse of 44 km^3 and five discrete failures of 8.8 km^3 each, occurring every 120 s. The landslide should have produced one initial 390–500 m wave if it occurred in one go, and five similar but distinct 225–280 m waves if it occurred in five retrogressive failures. In all cases, the first wave reached the entrance of the Agaete Valley 550–690 s after the collapse onset, and had an amplitude of 75–100 m (collapse by retrogressive failures) to 180–250 m (collapse in one go). These waves entered the Agaete Valley, reached more than 7 km inland and altitudes of >500 m in places when considering a single collapse. However, if we consider a collapse by five retrogressive failures, the waves are smaller but more numerous and reach 'only' 275 m in altitudes and do not entered in the Agaete Valley further than 5.0 km, that is more concordant with the maximum altitude (188 m asl) of the tsunami deposits. The directions of highest velocity of the simulated waves at La Aldea road outcrop are in a good agreement with the directions of currents recorded by the cobble fabrics in the tsunami deposits (Pérez-Torrado et al. 2006).

This study shows that the failure mechanism is as essential to constrain as the whole volume of a landslide, because it will control the number of waves, their amplitude, and thus their time of arrival. Our simulations also show that the rheology that controls the landslide propagation can be estimated only roughly in a first approach, since it has only a minor effect on the wave train produced and has only a second-order impact on the amplitude of the waves. However, in order to accurately predict the characteristics of the waves at certain inland locations, the rheology of the landslide must be looked at in detail, as well as the height of the sea-level at the time of the collapse event. This study, like all those dealing with numerical modelling of tsunamis triggered by large landslides, would be greatly improved if better knowledge concerning the large volcano-flank collapse events and especially their failure was available.

Acknowledgements

This work is part of the "Vitesss" project (Volcano-Induced Tsunamis: numErical Simulations and Sedimentary Signature) supported by the French National Research Agency (ANR project 08-JCJC-0042, Geolab, CNRS; leader: Raphaël Paris). The paper benefited from useful discussions with Budianto Ontowirjo and from useful comments from John Wells and two anonymous reviewers. We also thank Tim Le Bas and Doug Masson from the National Oceanography Centre (Southampton) for kindly providing the offshore data of the channel between Gran Canaria and Tenerife. We thank Fran van Wyk de Vries for her English checking. ASTER GDEM is a product of METI and NASA.

References

Ancochea, E., Fuster, J.M., Ibarolla, E., Cendrero, A., Coello, J., Hernan, F., Cantagrel, J.M., Jamond, C., 1990. Volcanic evolution of the island of Tenerife (Canary Islands) in light of new K–Ar data. Journal of Volcanology and Geothermal Research 44, 231–249.

Carracedo, J.C., Day, S., Guillou, H., Rodrìguez Badiola, E., Canas, J.A., Pérez-Torrado, F.J., 1998. Hotspot volcanism close to a passive continental margin: the Canary Islands. Geological Magazine 135 (5), 591–604.

Carracedo, J.C., Pérez-Torrado, F.J., Ancochea, E., Meco, J., Hernan, F., Cubas, C.R., Casillas, R., Rodríguez Badiola, E., 2002. Cenozoic volcanism: II. The Canary Islands. In: Gibbons, F. A.W., Moreno, T. (Eds.), The Geology of Spain. Geological Society of London, London, pp. 438–472.

Carracedo, J.C., Guillou, H., Nomade, S., Rodriguez-Badiola, E., Pérez-Torrado, F.J., Rodriguez-Gonzalez, A., Paris, R., Troll, V.R., Wiesmaier, S., Delcamp, A., Fernandez-Turiel, J.L., 2010. Evolution of ocean island rifts: the Northeast rift zone of Tenerife, Canary Islands. Geological Society of America Bulletin 30119, 30142. doi:10.1130/B30119.1.

Crook, K.A.W., Felton, E.A., 2008. Sedimentology of rocky shorelines: 5. The marine samples at +326 m from 'Stearns swale' (Lanai, Hawaii) and their paleo-environmental and sedimentary process implications. Sedimentary Geology 206, 33–41.

Dade, W.B., Huppert, H.E., 1998. Long-runout rockfalls. Geology 26, 803–806.

Felton, E.A., 2002. Sedimentology of rocky shorelines: 1. A review of the problem, with analytical methods, and insights gained from the Hulopoe Gravel and the modern rocky shoreline of Lanai, Hawaii. Sedimentary Geology 152, 221–245.

Felton, E.A., Crook, K.A.W., Keating, B.H., Kay, E.A., 2006. Sedimentology of rocky shorelines: 4. Coarse gravel lithofacies, molluscan biofacies, and the stratigraphic and eustatic records in the type area of the Pleistocene Hulopoe Gravel, Lanai, Hawaii. Sedimentary Geology 184, 1–76.

Fritz, H.M., Hager, W.H., Minor, H.E., 2001. Lituya Bay case: rockslide impact and wave run-up. Science of Tsunami Hazards 19 (1), 3–22.

Funck, T., Dickmann, T., Rihm, R., Krastel, S., Lykke-Andersen, H., Schmincke, H.-U., 1996. Reflection seismic investigations in the volcaniclastic apron of Gran Canaria and implications for its volcanic evolution. Geophysical Journal International 125, 519–536.

Geist, E.L., Parsons, T., ten Brink, U.S., Lee, H.J., 2009. Tsunami probability. In: Bernard, E.N., Robinson, A.R. (Eds.), The Sea. v. 15. Harvard University Press, Cambridge, Massachusetts, pp. 93–135.

Grigg, R.W., Jones, A.T., 1997. Uplift caused by lithospheric flexure in the Hawaiian archipelago, as revealed by elevated coral deposits. Marine Geology 141, 11–25.

Harbitz, C.B., Løvholt, F., Pedersen, G., Masson, D.G., 2006. Mechanisms of tsunami generation by submarine landslides: a short review. Norwegian Journal of Geology 86, 255–264.

Keating, B.H., McGuire, W.J., 2000. Island edifice failures and associated tsunami hazards. In: Keating, B.H., Waythomas, C.F., Dawson, A.G. (Eds.), Landslides and Tsunamis. Birkhäuser Verlag, Basel, pp. 899–955.

Kelfoun, K., Druitt, T.H., 2005. Numerical modelling of the emplacement of Socompa rock avalanche, Chile. Journal of Geophysical Research 110, B12202.

Kelfoun, K., Giachetti, T., Labazuy, P., 2010. Landslide-generated tsunamis at Reunion Island. Journal of Geophysical Research. doi:10.1029/2009JF001381.

Krastel, S., Schmincke, H.-U., 2002. The channel between Gran Canaria and Tenerife: constructive processes and destructive events during the evolution of volcanic islands. International Journal of Earth Sciences (Geol Rundsch) 91, 629–641. doi:10.1007/s00531-002-0285-8.

Krastel, S., Schmincke, H.U., Jacobs, C.L., Richm, R., Le Bas, T.P., Alibés, B., 2001. Submarine landslides around the Canary Islands. Journal of Geophysical Research 106 (B3), 3977–3997.

Le Bas, T.P., Masson, D.G., Holtom, R.T., Grevemeyer, I., 2007. Slope failures on the flanks of the southern Cape Verde Islands. In: Lykousis, V., Sakellariou, D., Locat, J. (Eds.),

Submarine Mass Movements and Their Consequences. Springer, Dordrecht, Netherlands, pp. 337–345.
Maramai, A., Graziani, L., Alessio, G., Burrato, P., Colini, L., Cucci, L., Nappi, R., Nardi, A., Vilardo, G., 2005. Near- and far-field survey report of the 30 December 2002 Stromboli (Southern Italy) tsunami. Marine Geology 215, 93–106.
Masson, D.G., Watts, A.B., Gee, M.R.J., Urgeles, R., Mitchell, N.C., Le Bas, T.P., Canals, M., 2002. Slope failures on the flanks of the western Canary Islands. Earth Science Reviews 57, 1–35. doi:10.1016/S0012-8252(01)00069-1.
McMurtry, G.M., Fryer, G.J., Tappin, D.R., Wilkinson, I.P., Williams, M., Fietzke, J., Garbe-Schoenberg, D., Watts, P., 2004. Megatsunami deposits on Kohala Volcano, Hawaii, from flank, collapse of Mauna Loa. Geology 32 (9), 741–744.
Menéndez Gonzáles, I., Silva, P.G., Martín Betancur, M., Pérez Torrado, F.J., Guillou, H., Scaillet, S., 2008. Fluvial dissection, isostatic uplift, and geomorphological evolution of volcanic islands (Gran Canaria, Canary Islands, Spain). Geomorphology 102, 189–203.
Moore, J.G., 1971. Relationship between subsidence and volcanic load, Hawaii. Bulletin Volcanologique 34, 562–576.
Moore, A.L., 2000. Landward fining in onshore gravel as evidence for a late Pleistocene tsunami on Molokai, Hawaii. Geology 28 (3), 247–250.
Moore, J.G., Moore, G.W., 1984. Deposit from a giant wave on the island of Lanai, Hawaii. Science 226, 1312–1315.
Moore, G.W., Moore, J.G., 1988. Large-scale bedforms in boulder gravel produced by giant waves in Hawaii. Geological Society of America Special Paper 229, 101–110.
Moore, J.G., Clague, D.A., Holcomb, R.T., Lipman, P.W., Normark, W.R., Torresan, M.E., 1989. Prodigious submarine landslides on the Hawaiian Ridge. Journal of Geophysical Research 94, 17465–17484.
Moore, J.G., Bryan, W.B., Ludwig, K.R., 1994a. Chaotic deposition by a giant wave, Molokai, Hawaii. Geological Society of America Bulletin 106, 962–967.
Moore, J.G., Normark, W.R., Holcomb, R.T., 1994b. Giant Hawaiian landslides. Annual Review of Earth and Planetary Science 22, 119–144.
Normark, W.R., Moore, J.G., Torresan, M.E., 1993. Giant volcano-related landslides and the development of the Hawaiian Islands. In: Schwab, W.C., Lee, H.J., Twichell, D.C. (Eds.), US Geological Survey Bulletin, 2002, pp. 184–196.
Oehler, J.-F., Labazuy, P., Lénat, J.F., 2004. Recurrence of major flank landslides during the last 2 Ma — history of Réunion Island. Bulletin of Volcanology 66, 585–598.
Oehler, J.-F., Lénat, J.-F., Labazuy, P., 2007. Growth and collapse of the Reunion Island volcanoes. Bulletin of Volcanology 70, 717–742. doi:10.1007/s00445-007-0163-0.
Paris, R., Pérez-Torrado, F.J., Cabrera, M.C., Wassmer, P., Schneider, J.L., Carracedo, J.C., 2004. Tsunami-induced conglomerates and debris-flow deposits on the western coast of Gran Canaria (Canary Islands). Acta Vulcanologica 16 (1–2), 133–136.
Paris, R., Carracedo, J.C., Pérez-Torrado, F.J., 2005. Massive flank failures and tsunamis in the Canary Islands: past, present, future. Zeitschrift für Geomorphologie, Supplement 140, 37–54.
Pérez-Torrado, F.J., Paris, R., Cabrera, M.C., Schneider, J.-L., Wassmer, P., Carracedo, J.-C., Rodrìguez-Santana, A., Santana, F., 2006. Tsunami deposits related to flank collapse in oceanic volcanoes: the Agaete Valley evidence, Gran Canaria, Canary Islands. Marine Geology 227, 135–149.
Robinson, J.E., Eakins, B.W., 2006. Calculated volumes of individual shield volcanoes at the young end of the Hawaiian Ridge, in: Coombs, M.L., Eakins, B.W., Cervelli, P.F. (Eds.), Growth and Collapse of Hawaiian Volcanoes. Journal of Volcanology and Geothermal Research 151, 309–317.
Ruiz, C.R., Garca-Cacho, L., Araña, V. Yanes, Luque, A., Felpeto, A., 2000. Submarine volcanism surrounding Tenerife, Canary Islands: implications for tectonic controls, and oceanic shield forming processes. Journal of Volcanology and Geothermal Research 103, 105–119.
Schmincke, H.U., 1990. Geological Field Guide, Gran Canaria. IAVCEI, International Volcanological Congress, Mainz, Germany. 212 pp.
Teide Group, 1997. Morphometric interpretation of the north-west and south-east slopes of Tenerife, Canary Islands. Journal of Geophysical Research 102 (B9), 20325–20342.
Tinti, S., Bortolucci, E., Romagnoli, C., 1999. Modelling a possible Holocenic landslide-induced tsunami at Stromboli Volcano, Italy. Physics and Chemistry of the Earth 24, 423–429.
Tinti, S., Bortolucci, E., Romagnoli, C., 2000. Computer simulations of tsunamis due to sector collapse at Stromboli, Italy. Journal of Volcanology and Geothermal Research 96, 103–128.
Tinti, S., Pagnoni, G., Zaniboni, F., 2006. The landslides and tsunamis of the 30th of December 2002 in Stromboli analysed through numerical simulations. Bulletin of Volcanology 68, 462–479.
Ward, S.N., 2001. Landslide tsunami. Journal of Geophysical Research 106, 11,201–11,215.
Ward, S.N., Day, S., 2003. Ritter Island Volcano—lateral collapse and the tsunami of 1888. Geophysical Journal International 154, 891–902.
Waythomas, C.F., Watts, P., Shi, F., Kirby, J.T., 2009. Pacific Basin tsunami hazards associated with mass flows in the Aleutian arc of Alaska. Quaternary Science Reviews 28 (11–12), 1006–1019.
Weiss, R., Fritz, H.M., Wünnemann, K., 2009. Hybrid modeling of the mega-tsunami runup in Lituya Bay after half a century. Geophysical Research Letters 36 (6), L09602. doi:10.1029/2009GL037814.
Wynn, R.B., Masson, D.G., 2003. In: Locat, J., Mienert, J. (Eds.), Canary Islands landslides and tsunami generation, submarine mass movements and their consequences. Advances in Natural and Technological Hazards Research, 19. Kluwer, pp. 325–332.

CONSULTORIA PARA LA MODELIZACION DE LOS FLUJOS PIROCLASTICOS DEL VOLCAN TUNGURAHUA

Proyecto Sistema de Alerta Temprana y Gestión del Riesgo Natural
Instituto Geofísico / Secretaría Nacional de Gestión de Riesgos

Dr. **Karim Kelfoun**
Laboratoire Magmas et Volcans, Université Blaise Pascal – CNRS – IRD
5 rue Kessler, 63038 Clermont-Ferrand, Francia

Objetivo General

Realizar la modelización numérica de los flujos piroclásticos del volcán Tungurahua, empleando un DEM de alta resolución y secciones de control de campo, previamente llevadas a cabo.

Objetivos específicos

- Diseñar un modelo numérico de simulación de flujos piroclásticos
- Calibrar dicho modelo en base a los datos de campo de un evento tipo
- Aplicar el modelo numérico previamente calibrado a los diferentes escenarios eruptivos
- Presentar los resultados en formato compatible con ArcGis 9.X
- Capacitar al personal del Área de Vulcanología del IG, en el uso del modelo numérico.

Índice

1. Dinámica de flujos piroclásticos y las aleas asociadas 1
2. Utilización de mapas estadísticos 4
3. Presentación de VolcFlow 4
4. Condiciones fuentes 5
5. Resultados 6
5.1. Simulación 1: Calibración del modelo 6
5.2. Simulación 2: flujo 5 veces más elevado que el de agosto del 2006 9
5.3. Simulación 3: flujo 5 veces más elevado que el del 2006 11
5.4. Simulaciones 4 – método probabilista, 1-10 millones de m^3 (38 simulaciones) 12
5.5. Simulaciones 5 – método probabilista, 10-50 millones de m^3 (89 simulaciones) 14
5.6. Simulaciones 6 – método probabilista, 50-500 millones de m^3 (43 simulaciones) 16
5.7. Simulación 7 – simulaciones de alta resolución, zona de Baños 19
5.7.1. Escenario tipo 2006 pero con tasa más elevada 19
5.7.2. Escenario de tipo 2006, tasa más fuerte, surges más poderosas 20
5.7.3. Escenario de tipo 2006, erupción más larga y acumulación de depósitos 22
5.8. Simulaciones 8 – simulaciones de alta resolución, zona de Cusua 21
5.9. Simulaciones 9 – simulaciones de alta resolución, zona de Mapayacu 23
5.10. Inclinación del eje de la columna 25
5.11. Colapso de una parte del cráter del Tungurahua 27
6. Conclusiones 29

1. Dinámica de flujos piroclásticos y las aleas asociadas

Los flujos piroclásticos que son asociados a la actividad del volcán Tungurahua pueden ser divididos en dos tipos: los flujos densos y los flujos diluidos.

Los flujos densos están constituidos de bloques que van del tamaño de cenizas (<< 1 mm) a bloques de tamaño de decímetros cuadrados. Las partículas se mantienen en contacto durante el flujo: los flujos tienen por consecuencia una densidad cercana al de las partículas que los constituyen y su espesor es cercano al de los depósitos. Los flujos densos son poco espesos (generalmente < 1m) y son canalizados en el fondo de los valles. Cubren zonas relativamente limitadas, pero destruyen casi todo lo que recubren.

Los flujos diluidos (o surges) están constituidos de partículas finas (< 1 mm) que se mantienen en suspensión mediante gases turbulentos. Su dinámica se parece a la de los vientos de arena. Las partículas están alejadas unas de otras. La densidad de los flujos es por consecuencia baja (<10 kg/m^3) y los depósitos bastante finos (algunas decenas de centímetros) respecto al espesor del flujo (varias decenas de metros). Estas surges se producen seguido a partir de flujos densos y la puesta en suspensión de las partículas más finas de su superficie. Las surges pueden no destruir las construcciones. Sin embargo, son particularmente móviles y se salen fácilmente de los valles, lo que las hace particularmente amenazantes para las poblaciones.

Figura 1: Erupción del volcán Merapi (Indonesia) en 1994. El flujo denso, canalizado por los ríos, está recubierto por la surge que el flujo denso creó, y no se ve en la imagen. El flujo diluido está indicado como *surge >>.* La parte convectiva se sitúa sobre la surge y sube hacia la atmósfera.

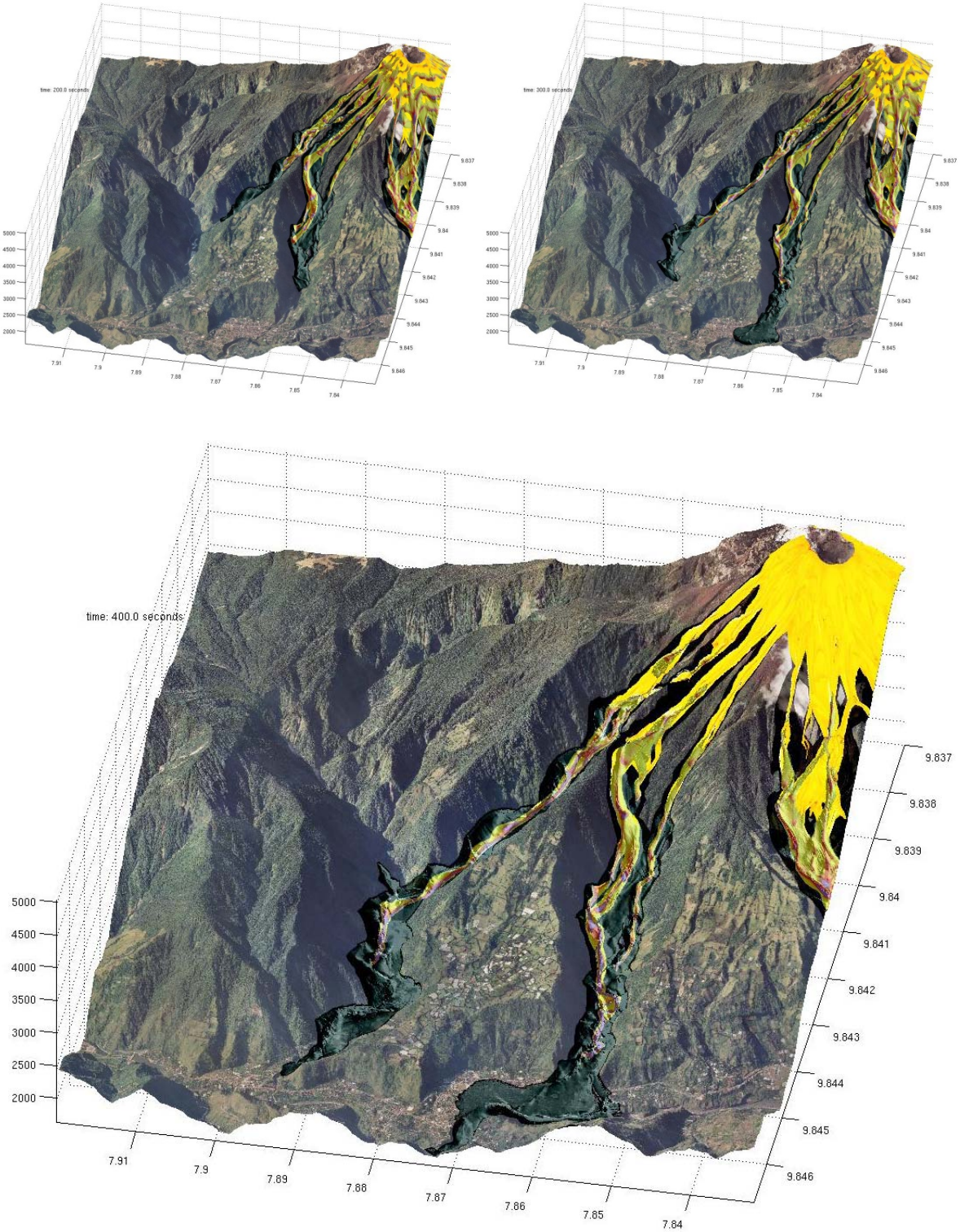

Figura 2: Flujos densos y surges asociadas en los valles de Ulba y Vazcúm, zona de Baños. Durante su desplazo, los flujos densos producen surges que una vez creadas, adquieren su dinámica propia. Más móviles, estas se salen de los valles (ver figura 12 para el mapa de las zonas afectadas).

2. Utilización de mapas estadísticos

Es imposible prever exactamente las características de futuras erupciones. Por esta razón, seguido es necesario el uso de técnicas estadísticas para evaluar las aleas volcánicas. Tres escenarios fueron definidos correspondiendo a las erupciones pasadas del Tungurahua (ver capítulos 5.4-5.6). Para cada escenario, hemos estimado las características de las erupciones y las posibles variaciones. La técnica estadística escoge de manera aleatoria parámetros eruptivos dentro de rango de valores que han sido impuestos, y después simula los flujos asociados a estos parámetros eruptivos. Varias simulaciones se crean y los resultados se suman. Esta técnica permite determinar la vulnerabilidad de cada zona: algunas zonas son afectadas por cada simulación, otras rara vez, y otras nunca.

3. Presentación de VolcFlow

Todas las simulaciones que se presentan en este reporte fueron realizadas con el programa *VolcFlow* : http://wwwobs.univ-bpclermont.fr/lmv/pperm/kelfoun_k/VolcFlow/VolcFlow.html

VolcFlow es un modelo de flujo, que se basa sobre el promediamiento vertical de ecuaciones de conservación de la masa y la cantidad de movimiento. Este principio es la base de la mayoría de los modelos de flujos granulares (por ejemplo: Savage and Hutter, 1991; Iverson, 1997; Heinrich et al., 2001; Patra et al., 2005) y es compatible con las evidencias de terreno relativas a la mayoría de las avalanchas de escombros y de los flujos piroclásticos densos (Shaller, 1991; Takarada et al., 1999; van Wyk de Vries et al., 2001). Utilizando un sistema de coordenadas relacionado con la topografía, con *x* e *y* paralelos a la superficie topográfica local y *h* perpendicular a esta, las ecuaciones de la conservación de la masa (ecuación 1) y la cantidad de movimiento (ecuaciones 2,3) promediadas verticalmente son:

$$\frac{\partial h}{dt}+\frac{\partial}{\partial x}(hu)+\frac{\partial}{\partial y}(hv)=0 \qquad [1]$$

$$\frac{\partial}{\partial t}(hu)+\frac{\partial}{\partial x}(hu^2)+\frac{\partial}{\partial y}(huv)=gh\sin\alpha_x-\frac{1}{2}k_{actpass}\frac{\partial}{\partial x}\left(gh^2\cos\alpha\right)+\frac{T_x}{\rho} \qquad [2]$$

$$\frac{\partial}{\partial t}(hv)+\frac{\partial}{\partial x}(hvu)+\frac{\partial}{\partial y}\left(hv^2\right)=gh\sin\alpha_y-\frac{1}{2}k_{actpass}\frac{\partial}{\partial y}\left(gh^2\cos\alpha\right)+\frac{T_y}{\rho} \qquad [3]$$

Donde *h* representa el espesor del flujo, $\mathbf{u}=(u,v)$ su velocidad, α la pendiente, ρ la masa volúmica, **T** estrés de resistencia y k_{actpass} el factor de las fuerzas paralelas a la topografía sobre las fuerzas perpendiculares.

Las ecuaciones son resueltas utilizando un método numérico capaz de capturar los choques y las relajaciones (Toro, 2001). Este esquema numérico es estable hasta para las topografías complejas. El esquema fue probado a partir de soluciones analíticas exactas (Mangeney et al.

2000) y de experiencias de laboratorio (Savage and Hutter, 1991; Pouliquen and Forterre, 2002; et Gray et *al.*, 2003).

La ventaja de *VolcFlow* es que su esquema numérico fue escrito de manera a integrar toda ley reológica basada sobre el espesor y la velocidad: comportamiento de fricción, viscoso, turbulento, etc. *VolcFlow* puede de esta manera simular la erosión y la sedimentación.

La nueva versión de VolcFlow permite simular la formación de flujos diluidos a partir de los flujos densos y por lo tanto la sedimentación de los flujos diluidos. Esta nueva versión fue utilizada para la mayoría de las simulaciones que presentamos aquí. La dinámica de los flujos diluidos fue determinada a partir de las mismas ecuaciones que para los flujos densos. Para las simulaciones que se presentan, la densidad fue considerada como fija y la sedimentación influye únicamente el espesor del flujo.

4. Condiciones fuentes

Los flujos piroclásticos nacen alrededor del cráter en una zona más o menos amplia, que depende de la magnitud de la erupción. Las erupciones pequeñas generan flujos que salen de los puntos más bajos del cráter, mientras que las erupciones más poderosas pueden generar flujos alrededor de la cima.

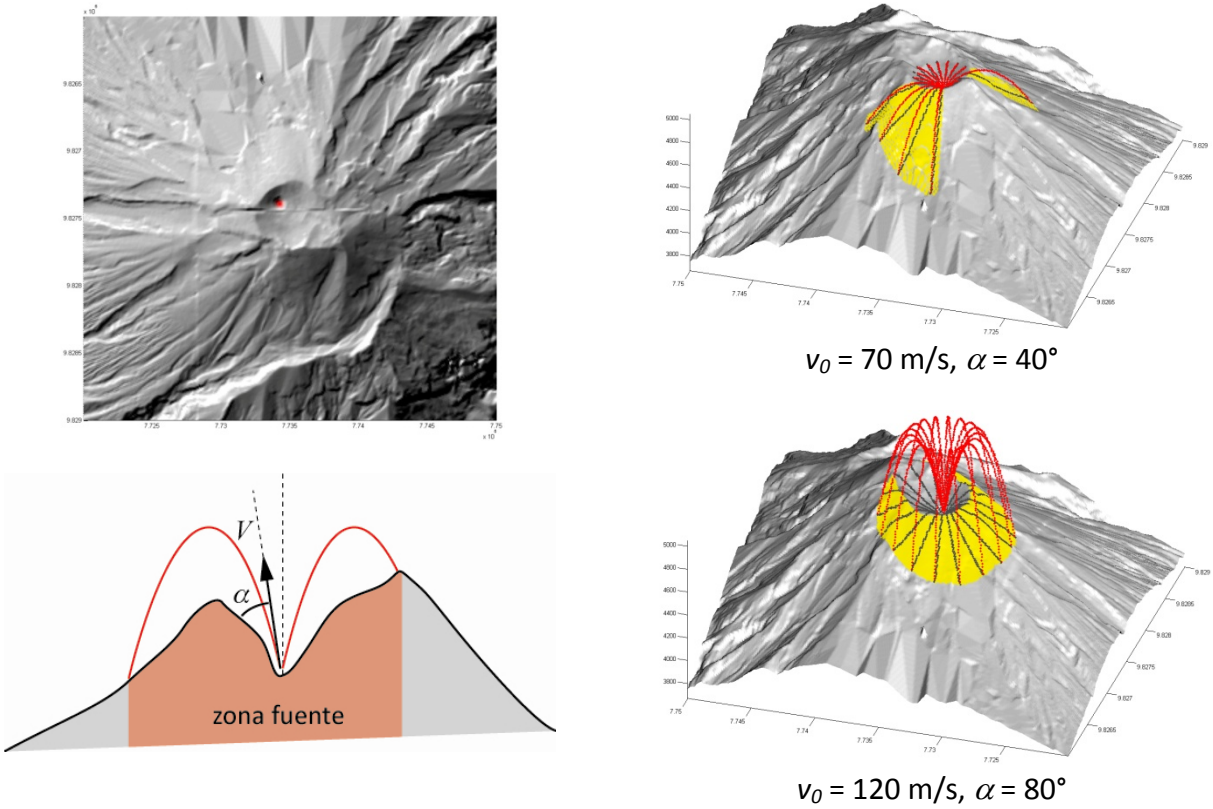

Figura 3: definición de “zona fuente” de flujos piroclásticos a partir de trayectorias balísticas y ejemplos de zonas fuentes para diferentes valores de v_0 y α.

Es difícil actualmente conocer exactamente la manera en la que se generan los flujos piroclásticos del volcán de Tungurahua: a partir de explosiones, por la acumulación de productos volcánicos asociados a una actividad estromboliana, caída de una columna eruptiva o un mecanismo intermediario.

Con el fin de simular los diferentes medios potenciales de generación, la zona fuente fue definida a partir de trayectorias balísticas (Figure 3). Las trayectorias balísticas se caracterizan por un punto de lanzamiento localizado en el nivel del conducto, una velocidad y un ángulo de lanzamiento. Una explosión se define por un ángulo de lanzamiento leve, una actividad estromboliana por un ángulo de lanzamiento intermedio, el colapso de una columna por un ángulo elevado y una velocidad de lanzamiento alta.

La zona fuente (en amarillo en la figura 3) está localizada entre el cráter y la zona de impacto de trayectorias balísticas (Figura 3). El volumen total de la erupción está repartido igualmente entre cada célula que define la zona fuente a lo largo de la duración de la erupción escogida.

La velocidad v_0 y el ángulo de lanzamiento α forman parte de los parámetros fijados aleatoriamente para la técnica probabilista.

5. Resultados

5.1. Simulación 1: Calibración del modelo

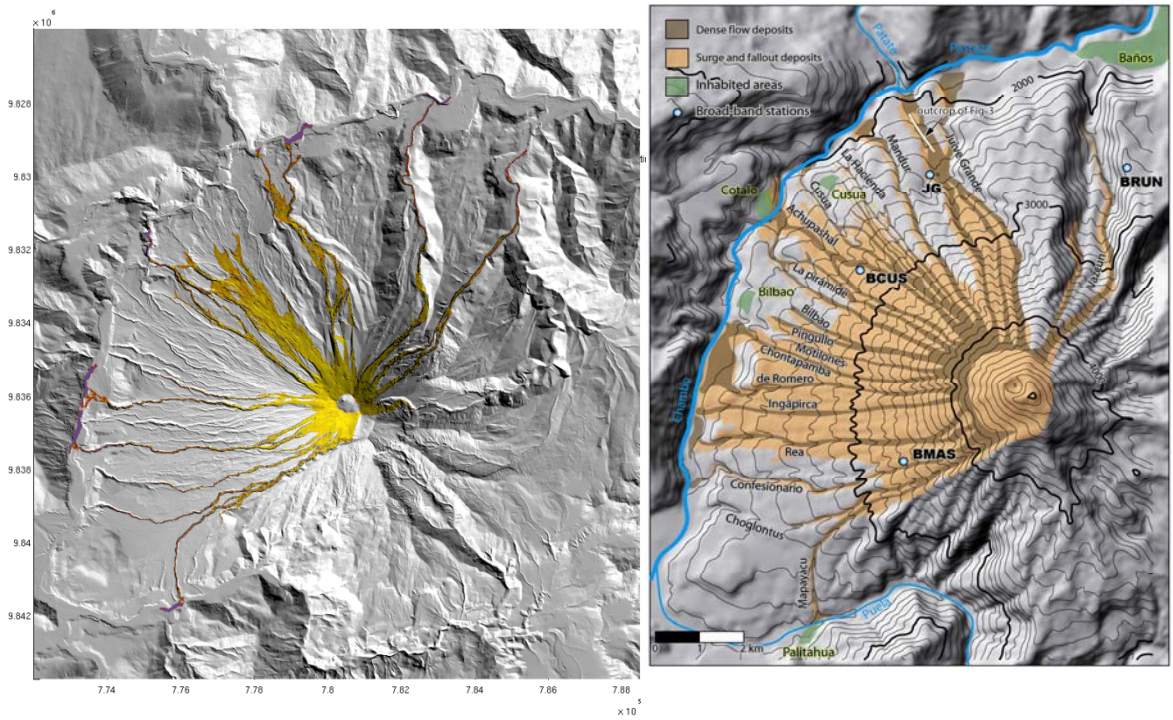

Figura 4: Comparación entre resultados numéricos y los depósitos de la erupción del 2006.

La primera simulación tenía por objetivo verificar la calidad de la topografía y del modelo numérico, comparando los resultados numéricos a los datos naturales. La erupción de agosto del 2006 fue escogida pues fue observada de cerca por el Instituto Geofísico, que dispone de informaciones precisas. El volumen de la fase paroxismal fue estimado a 10 millones de metros cúbicos y la duración de 40 minutos (2400 s). La resolución de la topografía utilizada para estas simulaciones es de 10 metros.

Parámetros del cálculo

Resolución	10 m	v_0 =	300 m/s	***V*** **=**	**$10x10^6$ m^3**
ρ_d =	1400 kg / m^3	α =	88		
T_0 =	3000 Pa	t_s =	2400 s		

Folder de datos:	simulacion_1.dat
Folder input:	simulacion_1.m
Folder .mat:	simulacion_1.mat

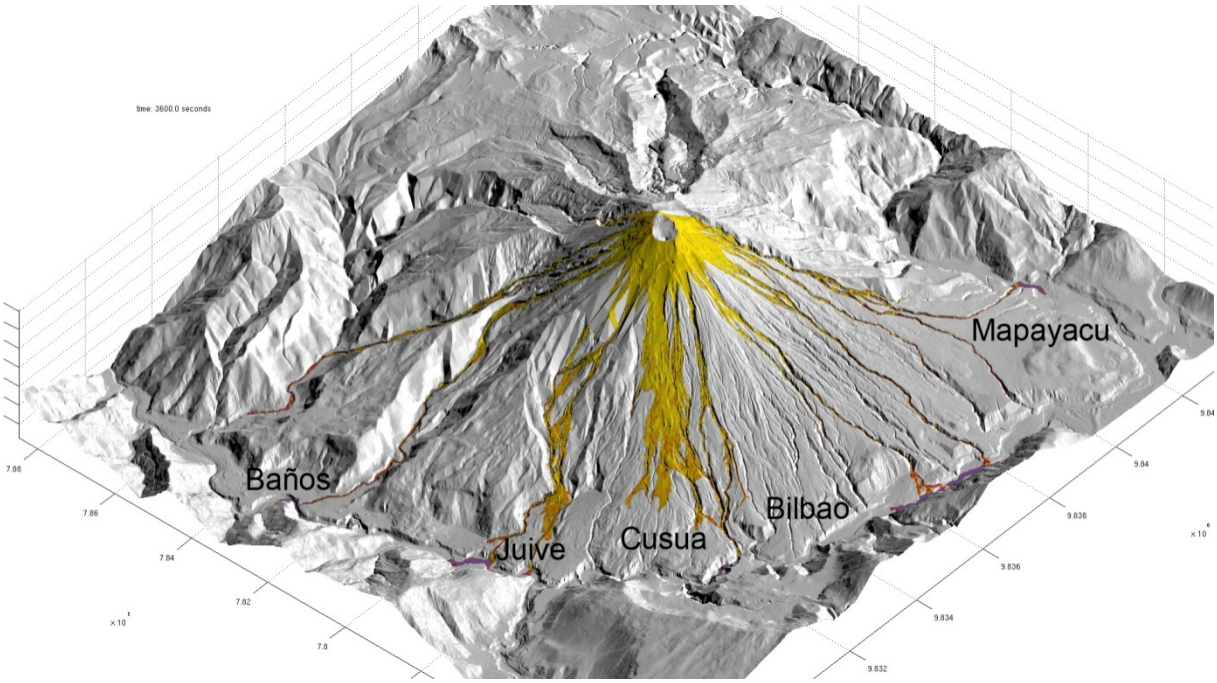

Figure 5: Vista 3D de la simulación numérica de los depósitos de la erupción del 2006. Los colores representan los espesores de los depósitos (ver animación adjunta: simulacion_1_foto.avi).

Globalmente, hay una muy buena correspondencia entre los flujos densos naturales y los simulados. Hay que notar, sin embargo, que las simulaciones no son perfectas: los flujos numéricos son largos en la zona de Ulba, se salen de los ríos en la zona de Cusua y no forman depósitos en abanico al nivel de los ríos Chontapamba y Rea. Estas diferencias muestran el poder del cálculo numérico, pero al mismo tiempo sus límites. Las diferencias se explican por las condiciones de alimentación demasiado simples (flujo constante, zona afectada fija…), por la topografía localmente inexacta (fuertes interpolaciones arriba de zonas de Cusua-Juive-Vazcúm) y por la simplificación de la

física de flujos (depósitos en abanico). Un modelo un poco más complejo, permitiendo simular las transiciones flujos/depósitos, será utilizado en el capitulo 5.7.3.

5.2. Simulación 2: flujo 5 veces más elevado que el de agosto del 2006

El objetivo de esta simulación es el de analizar los daños ocasionados por los flujos densos de una erupción, con una tasa cinco veces más grande que en agosto del 2006 (misma duración, volumen cinco veces más grande).

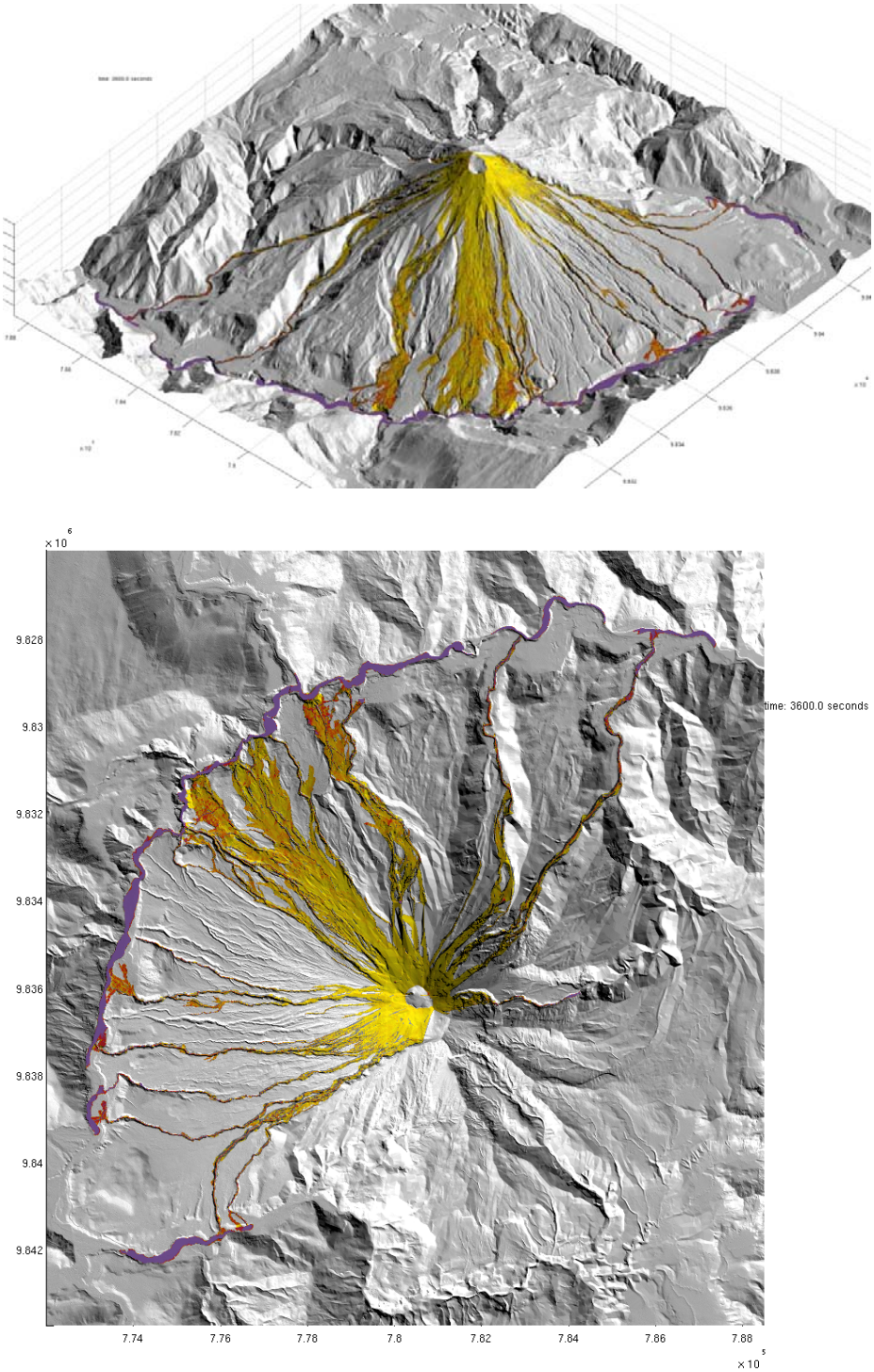

Figura 6: erupción de tipo 2006 con un volumen 5 veces más grande (ver animación adjunta: simulacion_2_foto.avi).

Parámetros del cálculo

Resolución	10 m	v_0 =	300 m/s	***V* =**	**50×10^6 m^3**
ρ_d =	1400 kg / m^3	α =	88		
T_0 =	3000 Pa	t_s =	2400 s		
Folder de datos:	simulacion_2.dat				
Folder input:	simulacion_2.m				
Folder .mat:	simulacion_2.mat				

Presentamos los resultados en la figura 6. Dichos resultados muestran globalmente que las zonas amenazadas son aproximadamente las mismas que en el 2006. Los flujos son más largos, pero sus extensiones son bloqueadas por el río Chambo/Pastaza. Se espera entonces fuertes acumulaciones de sedimentos al nivel del río, al mismo tiempo que consecuencias importantes para la presa de Agoyan.

Al contrario del 2006, los flujos de Ulba y de Vazcúm, llegarían hasta las zonas habitadas de la zona de Baños, al mismo tiempo que al río Chambo/Pastaza y formarían de esta manera grandes depósitos en abanico.

Un flujo más elevado llevaría al desbordamiento de los ríos menos profundos. La zona más afectada respecto al 2006 seria por consecuencia la de Cusua.

5.3. Simulación 3: flujo 5 veces más elevado que el del 2006 y zona de formación más amplia

Con el fin de probar la influencia de la extensión inicial de la zona fuente sobre los depósitos, la simulación 3 utiliza una zona fuente más ancha que por la simulación 2. Los demás parámetros son idénticos.

Los resultados indican que la extensión de la zona inicialmente afectada por la erupción tiene poca influencia sobre la distribución final de los depósitos. Las variaciones más importantes son observadas al este pues la zona inicial de la simulación 2 no permitía a los flujos pasar la barrera topográfica de la caldera somital. Se constata también que los flujos de la simulación 3 afectan todos los ríos del flanco oeste del volcán, mientras que por la simulación 2, únicamente los valles más importantes son afectados, aquellos que nacen a proximidad del cono somital.

Parámetros del cálculo

Resolución	10 m	**v_0 =**	**500 m/s**	*V* =	10×10^6 m^3
ρ_d =	1400 kg / m^3	α =	88		
T_0 =	3000 Pa	t_s =	2400 s		
Folder de datos:	simulacion_3.dat				
Folder input:	simulacion_3.m				
Folder mat:	simulacion_3.mat				

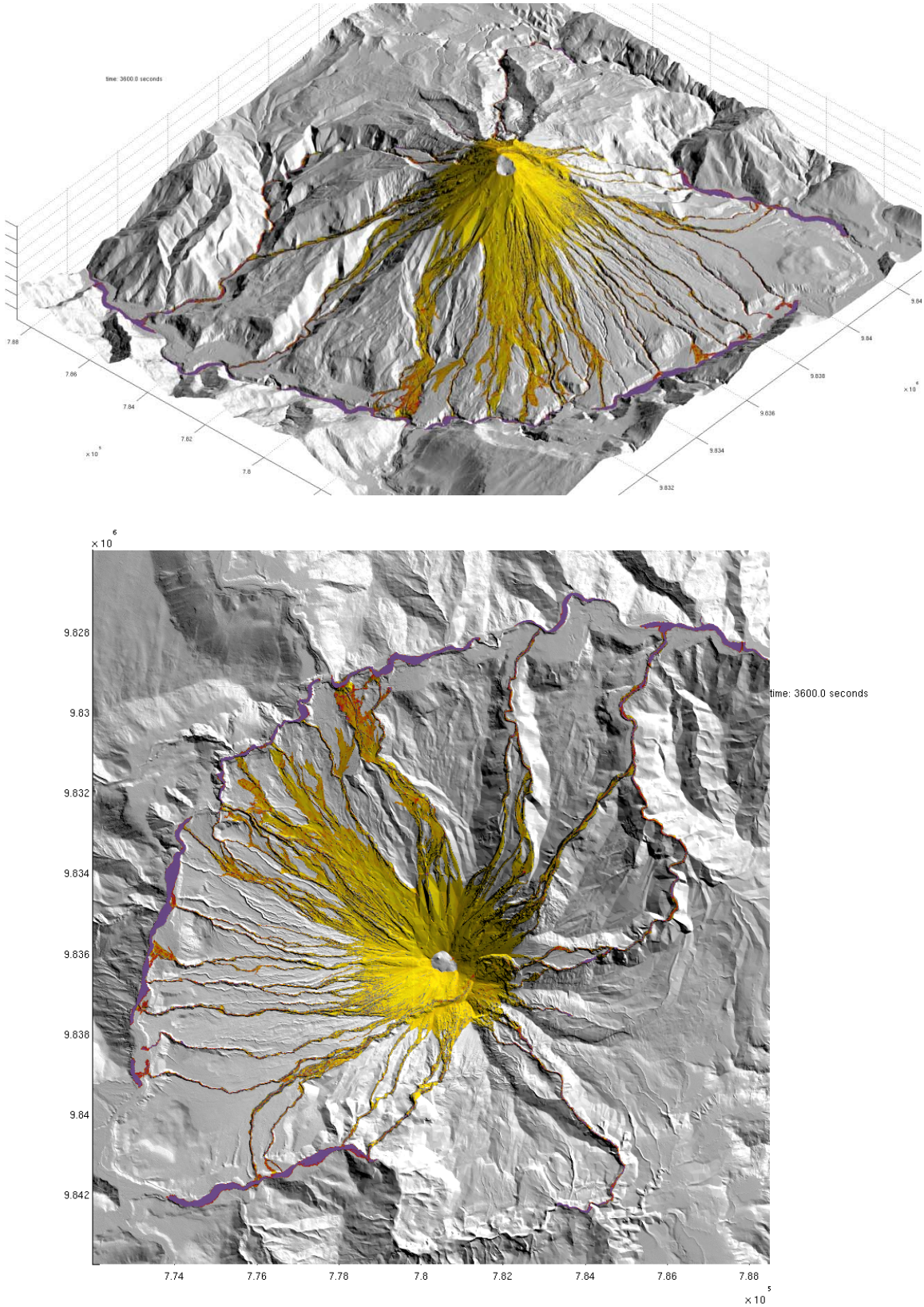

Figura 7: simulación realizada por un flujo 5 veces más elevado que el de 2006 y la zona de formación más amplia que la de la figura 6.

5.4. Simulaciones 4 – método probabilista, 1-10 millones de m^3 (38 simulaciones)

Con este método, ciertos parámetros son determinados aleatoriamente en un rango dado (ver capitulo 2). El primer escenario corresponde a erupciones un poco más débiles o idénticas que las del 2006. El volumen varía entre 1 y 10 millones de metros cúbicos.

Los demás parámetros fijados aleatoriamente son descritos en la tabla siguiente:

Variable	Valor min	Valor max	Unidad
Volumen emitido	1	10	millones de m^3
Tiempo de formación de fp	100	2000	s
Velocidad de lanzamiento	10	100	m/s
Angulo de lanzamiento	70	85	grados
Creación de surges	0	0.75	kg/m²/s
Sedimentación de surges	0	1.5	kg/m²/s
Folder de datos:	escenario1.mat		
Folder input:	script_scenario1.m / topo_Tungu_script_scenario1.m		
Folder .mat:	script_scenario1_***.mat		

Los resultados probabilistas se constituyen de varias decenas de simulaciones y necesitan por consecuencia un tiempo largo de cálculo. Con el fin de obtener los resultados en un lapso de tiempo compatible con la duración de la consultoría, la resolución de los cálculos ha sido disminuida a 25 m. Los valles mas angostos son por lo tanto bastante mal definidos, lo que puede localmente tener una influencia (flujos demasiado cortos en Mapayacu por ejemplo).

Las simulaciones toman en cuenta la simulación de los flujos densos y las de las surges asociadas.

Al contrario de las figuras anteriores, los colores de la figura 8 representan el número de veces que las zonas han sido afectadas. La escala de color en la izquierda es la de los flujos densos, y la escala a la derecha la de los flujos diluidos. Por ejemplo, la zona que se sitúa al Noroeste del cráter (color rojo obscuro, figura 8) es sistemáticamente afectada independientemente de la magnitud de la erupción. Las zonas en verde, son raramente afectadas por una erupción de este tipo.

Globalmente, los datos indican que independientemente de los parámetros que se escoja, las zonas amenazadas son cercanas a las zonas destruidas en el 2006.

La zona más amenazada se sitúa sobre el flanco Noroeste, en el sector de los ríos Achupashal, Cusua, Mandur. La zona de Rea y de Juive son afectadas por alrededor de 20% de las simulaciones. La planicie ubicada entre Juive y Ulba nunca fue afectada.

La zona de Baños se muestra relativamente a salvo de los flujos densos y de las pequeñas erupciones.

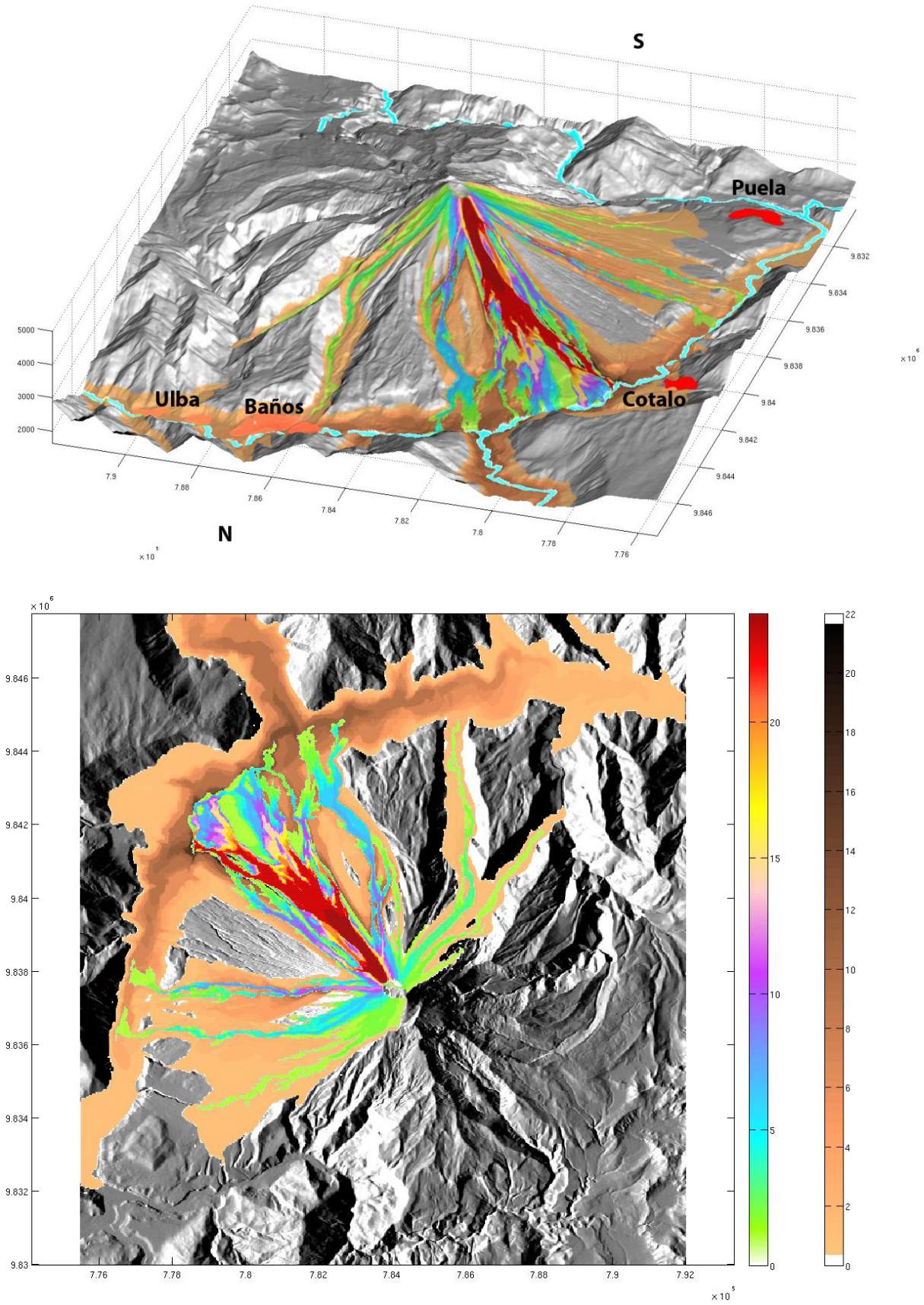

Figura 8: Simulación de flujos densos y diluidos utilizando volúmenes eruptivos entre 1 y 10 millones de m^3

Sin embargo, las zonas parecen particularmente amenazadas por las surges. Se tiene que ser prudente respecto a la dinámica de las surges puesto que su conocimiento en vulcanología es aún limitado. El rango de formación y depósitos fue escogido probando el modelo sobre las erupciones de Tungurahua y de Merapi (en Indonesia). Queda sin embargo difícil de saber si el Tungurahua puede engendrar surges tan poderosas como las del Merapi.

En los peores casos, las surges formadas sobre las pendientes superiores del volcán, se deslizan para afectar todas las zonas alrededor de los ríos Patate, Chambo y Pastaza. Los pueblos de Cotalo, Palitahua y de la ciudad de Baños son destruidos por estos fenómenos. Las surges podrían aproximarse al observatorio de Guadalupe.

5.5. Simulaciones 5 – método probabilista, 10-50 millones de m^3 (89 simulaciones)

Los resultados indican que para erupciones de estos volumenes, todas las quebradas de los flancos SW, W, N y NE son recubiertas por los flujos. Las erupciones más grandes son capaces de formar flujos al SE. Las zonas de Cusua y de Bilbao son destruidas por los flujos densos. Los flujos más grandes desbordan sobre Vazcúm y son capaces de destruir una parte de la Ciudad de Baños.

Los flujos diluidos son muy destructores y son capaces de destruir todas las zonas situadas a lo largo de los ríos Chambo, Patate y Pastaza. Los eventos más grandes pueden destruir la zona de Penipe. Ningún flujo puede subir el río Patate. Al contrario, 20% de los flujos diluidos llegan al observatorio.

Variable	valor min	valor max	unidad
Volumen emitido	10	50	millones de m^3
Tiempo de formación de fp	300	3000	s
Velocidad de emisión	30	300	m/s
Angulo de lanzamiento	80	87.5	grados
Creación de surges	0	0.75	kg/m²/s
Sedimentación de surges	0	1.5	kg/m²/s
Folder de datos:	escenario2.mat		
Folders input:	script_scenario2.m / topo_Tungu_script_scenario2.m		
Folders .mat:	script_scenario2_***.mat		

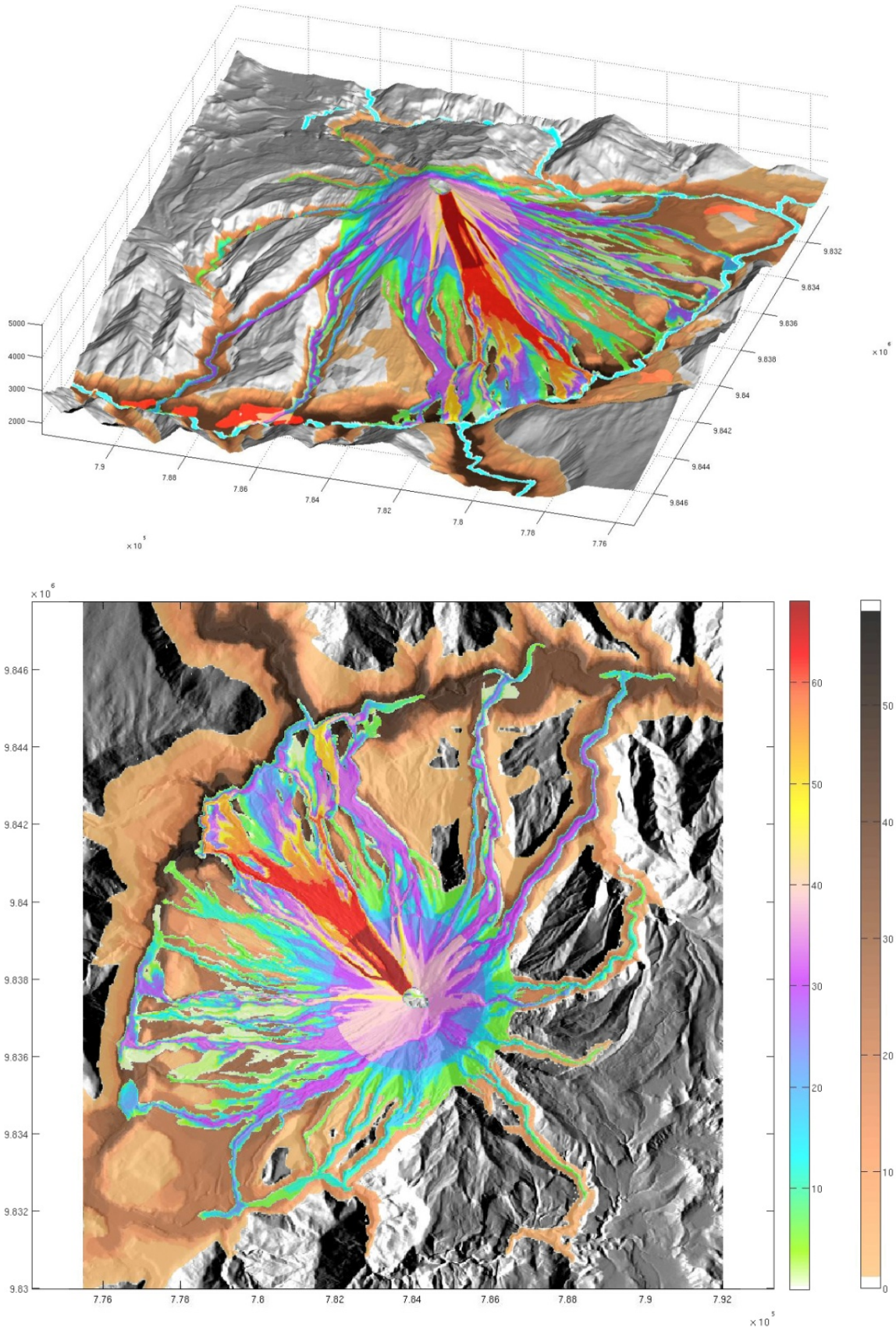

Figura 9: simulaciones de flujos densos y diluidos para volúmenes eruptivos entre 10 y 50 millones de m^3

5.6. Simulaciones 6 – método probabilista, 50-500 millones de m^3 (43 simulaciones)

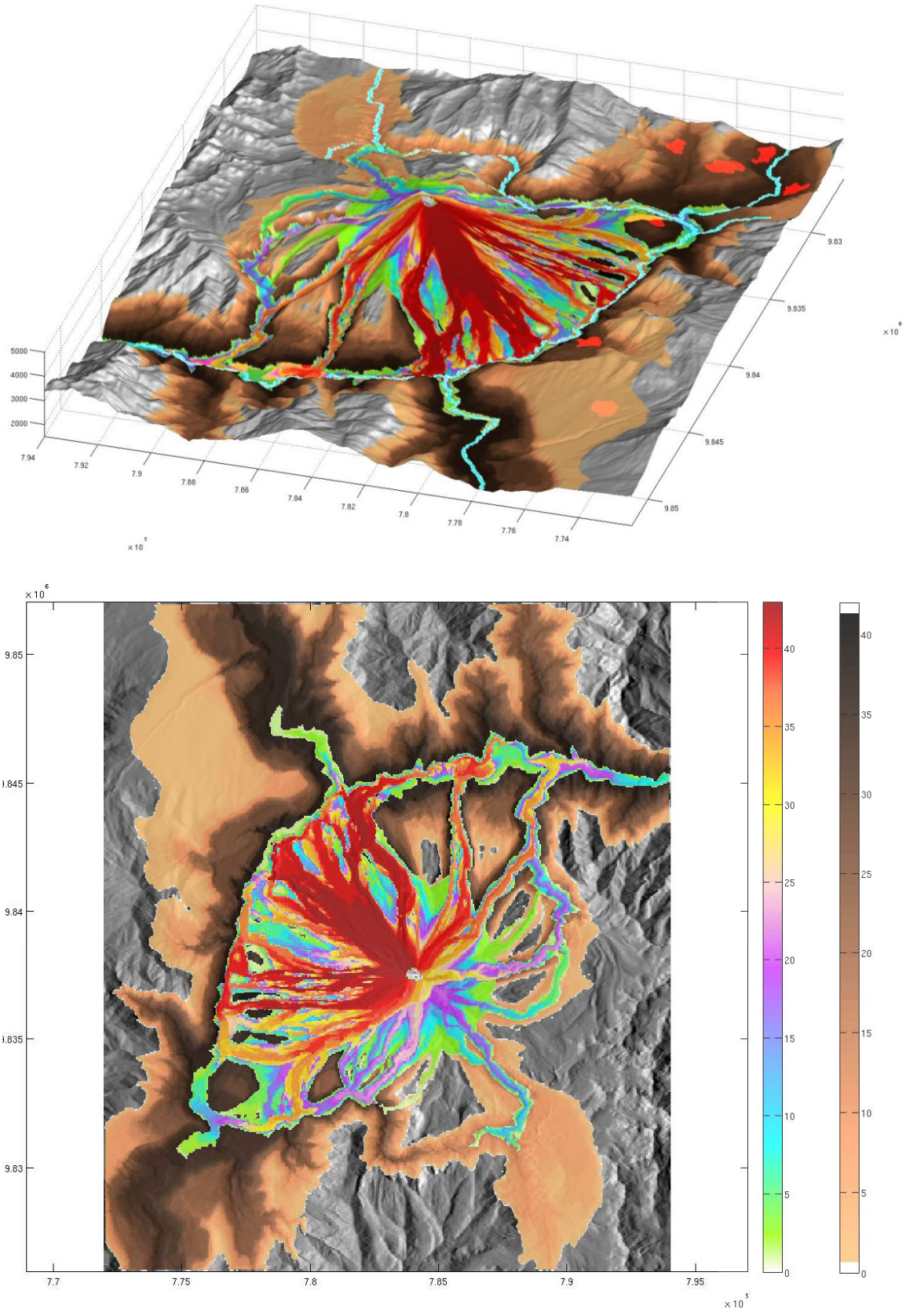

Figura 10: simulaciones de flujos densos y diluidos de volúmenes eruptivos entre 50 y 500 millones de m^3

Variable	valor min	valor max	unidad
Volumen emitido	50	500	millones de m^3
Tiempo de formación de fp	300	3000	s
Velocidad de lanzamiento	30	300	m/s
Angulo de lanzamiento	80	87.5	grados
Creación de surges	0	0.75	kg/m²/s
Sedimentación de surges	0	1.5	kg/m²/s
Folder de datos:	escenario3.mat		
Folders input:	script_scenario3.m / topo_Tungu_script_scenario3.m		
Folders .mat:	script_scenario3_***.mat		

Los flujos densos de una erupción de esta magnitud destruirían todas las zonas de los flancos del Tungurahua, a excepción de las partes más elevadas: planicies entre Juive y Ulba, planicies al sureste. Aunque hay que ser prudente con los resultados obtenidos por las surges, parece ser que las más grandes pueden ser capaces de destruir zonas muy alejadas del cráter: Pinguli, la planicie de Huambalo, el observatorio Tungurahua al norte, las zonas habitadas de Penipe al sureste y todas las zonas habitadas alrededor de Baños.

5.7. Simulación 7 – simulaciones de alta resolución, zona de Baños

5.7.1. Escenario tipo 2006 pero con tasa más elevada

Las simulaciones de alta resolución (5m) necesitan cálculos que duran varios días. Con el propósito de acelerar los cálculos, las simulaciones siguientes no toman en cuenta la fase de acumulación sin flujo que se produce al inicio de cada simulación. Un espesor constante de 20 cm se deposita al inicio de cada simulación. Esto explica una duración de erupción de 300 s, mucho más corta que anteriormente (2400 s).

Parámetros del cálculo

Resolución	5 m	ξ =	0.05	V =	$25x10^6$ m^3 *
ρ_d =	1400 kg / m^3	v_0 =	90 m/s	Φ_{ds} =	0.05 kg/m²/s
ρ_s =	3 kg / m^3	α =	50	Φ_{sg} =	0.5 kg/m²/s
T_0 =	2500 Pa	t_s =	300 s		

Folder de datos: Banos3.dat
Folder input: Banos3.m
Folder .mat: Banos3. mat

***** el volumen indicado corresponde al volumen total. El volumen que fluye sobre la zona elegida es más pequeño

Este escenario de alta resolución estudia los riesgos asociados a una tasa 2.5 veces más fuerte que en 2006. Si solamente un flujo se produce, este atravesará Baños hasta el río Pastaza. Sin embargo, parece ser que los daños se mantienen limitados en las zonas colindantes del río Vazcúm. Las surges parecen poder afectar la ciudad de Baños de algunos cientos de metros únicamente alrededor del río. Un riesgo suplementario – mal simulado aquí – es la acumulación de depósitos llegando al río Pastaza con desbordamiento posible sobre Baños y la creación de posibles flujos de lodo (lahares).

El río Ulba parece muy amenazado por los flujos. Se escapó relativamente en el 2006. Sin embargo, una actividad ligeramente más fuerte parece poder generar flujos muy destructivos en esta zona.

Es importante remarcar que en caso de una erupción más fuerte que la del 2006 (alrededor de una tasa 2.5 veces más fuerte), los flujos piroclásticos cortaran las vías de comunicación lo que hará particularmente difícil la evacuación de la ciudad de Baños.

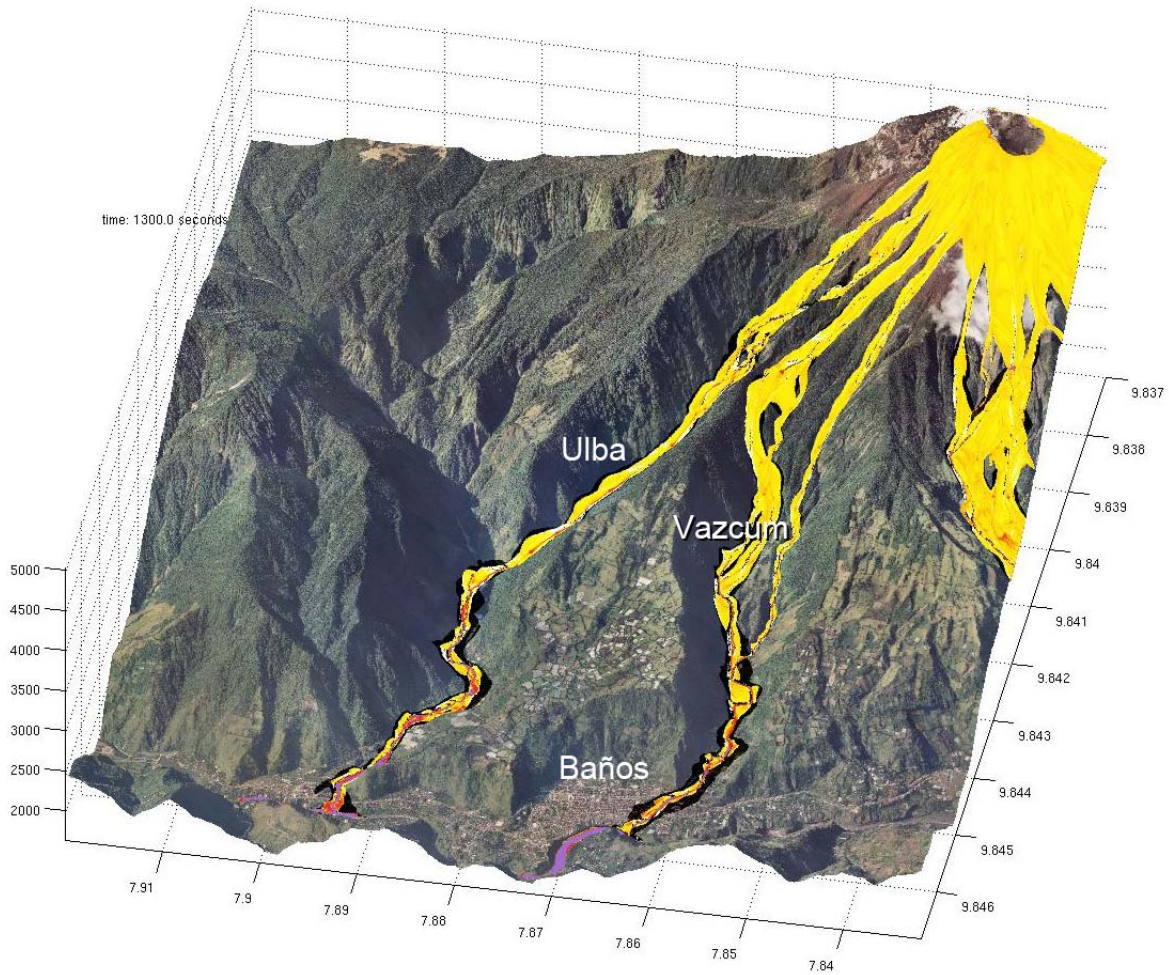

Figure 11: flujos densos y surges en el sector de Baños para una tasa 5 veces más fuerte que en el 2006 (ver animación adjunta: Banos_3.avi).

5.7.2. escenario de tipo 2006, tasa más fuerte, surges más poderosas

Las surges piroclásticas fueron débiles en el 2006. El escenario siguiente estudia las destrucciones asociadas a la producción de surges cuatro veces más poderosas que en el 2006. Las surges más poderosas se podrían explicar con la emisión de un magma más viscoso o más rico en gases, por lo tanto más explosivo.

En este escenario, las surges aparecen sobre las pendientes elevadas del edificio a causa del cizallamiento entre el flujo denso y el aire y el envío de las partículas más finas en

suspensión. Las surges, una vez creadas, adquieren su propia dinámica y son capaces de sobrepasar el flujo denso que las ha formado.

Parámetros del cálculo

Resolución	5 m	ξ =	0.05	V =	$25x10^6$ m^3 *
ρ_d =	1400 kg / m^3	v_0 =	90 m/s	Φ_{ds} =	0.2 kg/m²/s
ρ_s =	3 kg / m^3	α =	50	Φ_{sg} =	0.5 kg/m²/s
T_0 =	2500 Pa	t_s =	300 s		

Folder de datos: Banos5.dat
Folder input: Banos5.m
Folder .mat: Banos.mat

***** el volumen indicado corresponde al volumen total. El volumen que fluye sobre la zona elegida es más pequeño

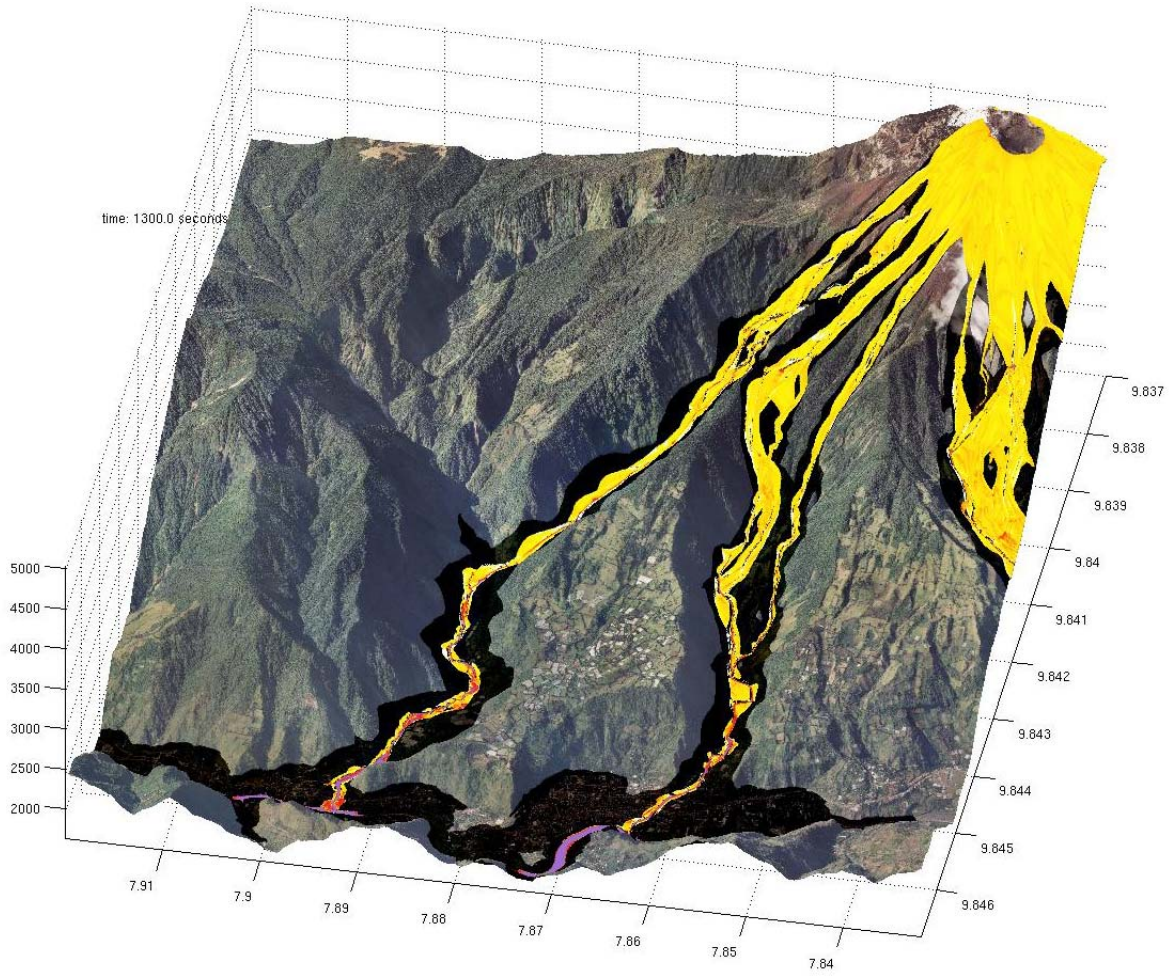

Figure 12: flujos densos y surges en el sector de Baños para una tasa 5 veces más fuerte que en el 2006 y una tasa de producción de surges 4 veces más fuerte (ver animación adjunta: Banos_5.avi).

Las surges se quedan retenidas en las barrancas mientras las paredes laterales de estas tengan una fuerte pendiente. Sin embargo, son suficientemente espesas para desbordar los

valles al llegar sobre las planicies habitadas de Baños y de Ulba. Su gran movilidad les permite destruir la mayor parte de las zonas habitadas.

Es importante remarcar que las surges van a perder su masa con la sedimentación, volverse menos densas que el aire y van a elevarse de las zonas afectadas. Este « lift-off » amenaza las paredes y eventualmente las planicies alrededor de los valles atravesados por las surges.

5.7.3. Escenario de tipo 2006, erupción más larga y acumulación de depósitos

El escenario 5.7.1 muestra que la zona de Baños esta poco amenazada por un flujo denso único a menos de que la tasa no sea suficiente para desbordar directamente la barranca de Vazcúm. Se tiene sin embargo que relativizar estas conclusiones. Durante una erupción, varios flujos se suceden y se acumulan los unos sobre los otros. El caso es más crítico para Baños puesto que la ciudad se sitúa cerca del río Pastaza. Los flujos llegando al río deben cambiar brutalmente de dirección e interactuar con el agua. Los flujos de Juive, Mapayacu, Achupashal, etc, que estaban en una configuración similar en el 2006 formaron grandes depósitos en abanico en la desembocadura de estos rios.

En las simulaciones presentadas aquí, los flujos se depositan como anteriormente (comportamiento plástico) pero una función suplementaria permite formar un depósito con un comportamiento mecánico Mohr-Coulomb. Este cambio de reología permite formar depósitos muy realistas.

Una serie de 15 simulaciones fue realizada. Una vez que cada simulación fue terminada, el depósito es adicionado a la topografía para formar la topografía de la simulación siguiente. La topografía se modifica de esta manera a través del tiempo con la acumulación de depósitos piroclásticos sucesivos.

Esta simulación ilustra claramente los riesgos que corre Baños en caso de erupción prolongada. Los depositos acumulados en el río Pastaza al nivel de la desembocadura de Vazcúm, acaban por obturar el nivel actual del río. Los flujos piroclásticos siguientes se ven obligados a pasar lateralmente afectando progresivamente las zonas habitadas. Recordamos que se trata de flujos densos, mucho más destructivos que las surges y capaces de destruir todas las viviendas que encuentren.

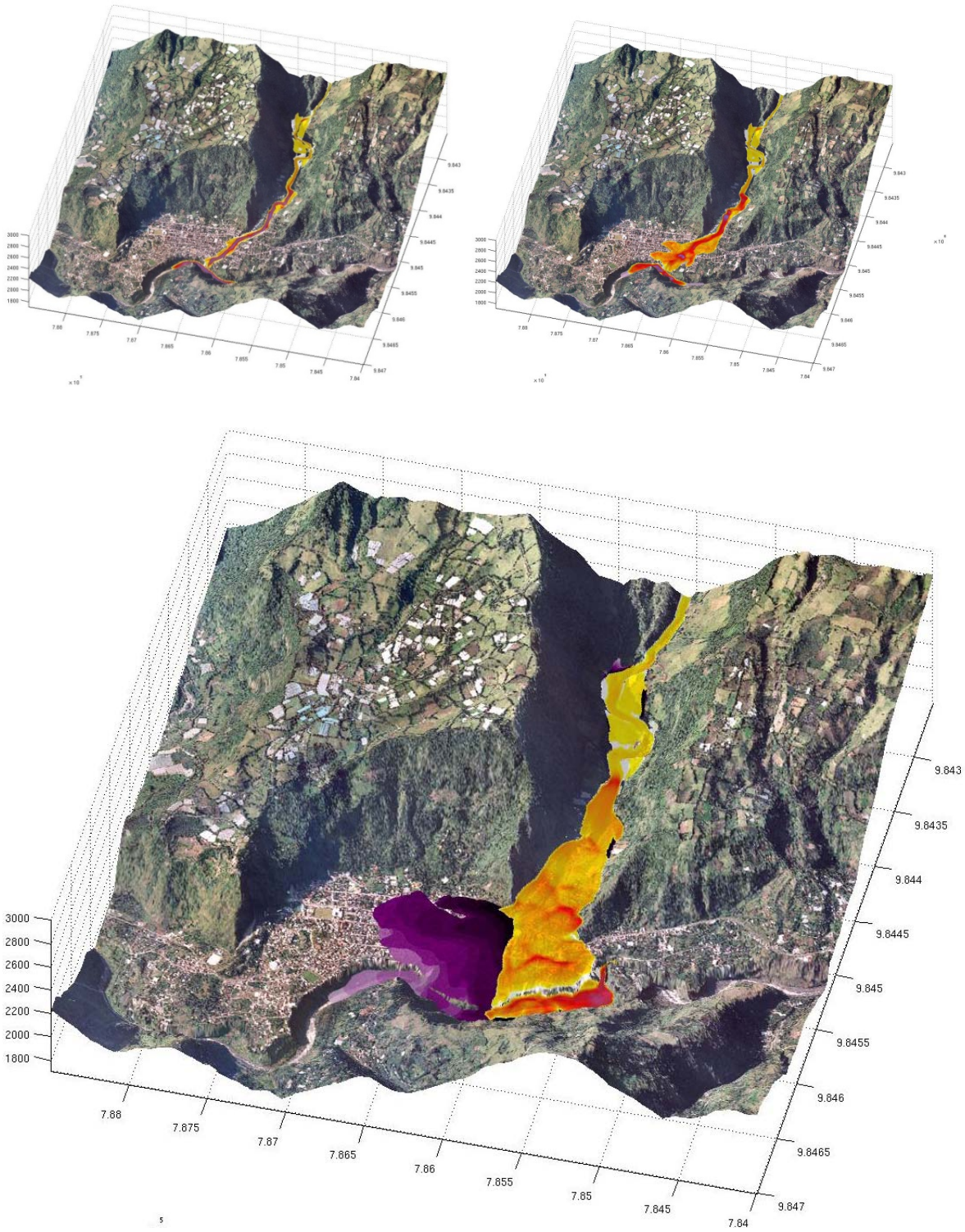

Figure 13: evolución de las zonas de depósitos a través del tiempo por sedimentación de flujos anteriores. El primer flujo afecta poco la zona de Baños. Con el tiempo, los depósitos desbordan cada vez más sobre las zonas habitadas. Las figuras muestran de manera sucesiva los depósitos del primero, del tercero y del decimoquinto flujo (ver animación adjunta: Banos_15flujos.avi).

Parámetros del cálculo

Resolución	5 m	ξ =	0.05	V =	1.8×10^6 m^3
ρ_d =	1400 kg / m^3	v_0 =	90 m/s	Φ_{ds} =	0.2 kg/m²/s
ρ_s =	3 kg / m^3	α =	50	Φ_{sg} =	0.5 kg/m²/s
T_0 =	2500 Pa	t_s =	300 s		

Folder de datos: Banos_zoom_***.dat
Folder input: topo_Banos_zoom.m, script_zoom_Banos.m
Folder .mat: Banos_zoom_***.mat

5.8. Simulaciones 8 – simulaciones de alta resolución, zona de Cusua

Los resultados de alta resolución de la zona de Cusua tienen que interpretarse con cuidado. Efectivamente, la topografía arriba de estas zonas (*x*=783600, *y*=9812000 o *x*=781000, *y*=9814000) parece haber sido interpolada a partir de poca información (cálculo de la topografía probablemente perturbado por la presencia de nubes). Si la morfología de los ríos no es fiable, los resultados no lo son tampoco. Aparte, la comparación con el 2006 es difícil pues las lavas del 2006 y la erosión que hubo después modificaron fuertemente la topografía.

Por lo que concierna el volumen y la tasa de la erupción del 2006, el modelo reproduce correctamente los depósitos en la barranca de Achupashal. Sin embargo, no reproduce los flujos en las pequeñas barrancas arriba de los pueblos de Cusua y en las quebradas de Cusua, La Hacienda y Mandur (localizaciones en la Figura 4).

Con una tasa 5 veces más grande (y un volumen cinco veces más grande también, la duración de la erupción siendo la misma), los flujos desbordan barrancas estrechas que afectan los alrededores de las barrancas de Achupashal, Cusua y la Hacienda. Sin embargo, hasta con una tasa de ese tamaño, la topografía utilizada no permite afectar la barranca de Mandur mientras que fue afectada en el 2006.

A excepción de estos problemas de topografía, las simulaciones indican que el obstáculo topográfico arriba del pueblo de Cusua lo protege muy bien. Sin cambios importantes en la topografía, es poco probable que el pueblo sea afectado por los primeros episodios de flujos densos.

Sin embargo, la evacuación sería difícil una vez que los flujos lleguen a la desembocadura de los ríos de Cusua y de Achupashal. El pueblo podría de esta manera fácilmente ser afectado tanto por los surges (Figura 15) como por los flujos densos, los cuales tendrían su trayectoria modificada por la acumulación de depósitos de flujos precedentes (ver capítulo 5.7.3).

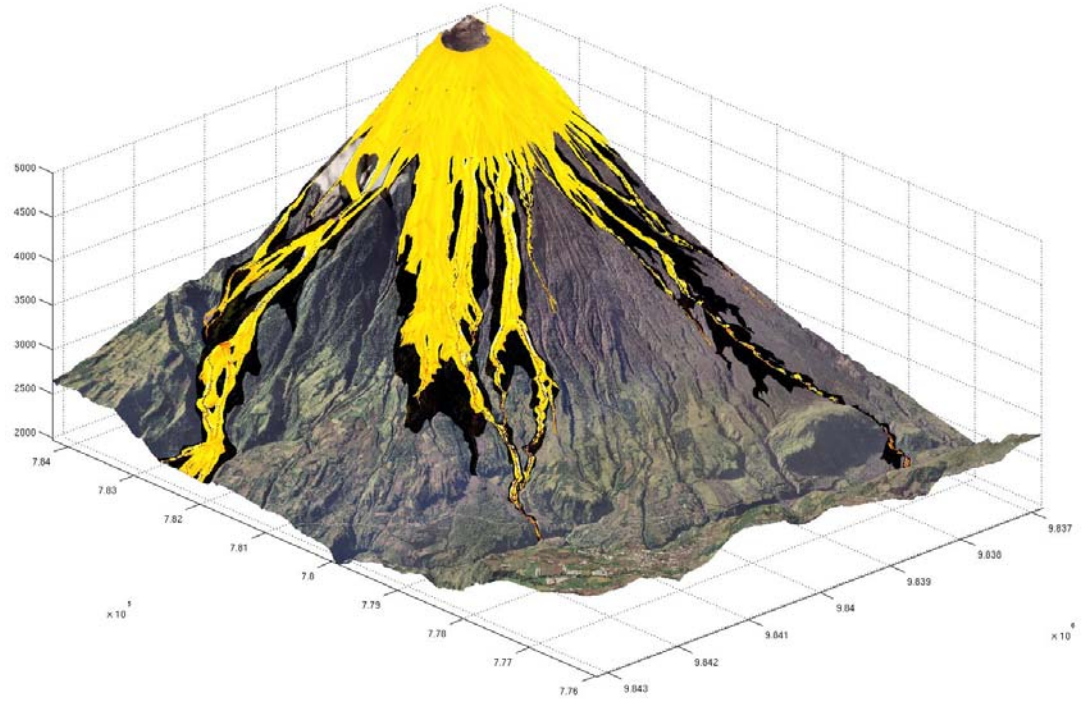

Figura 14: simulación de alta resolución al nivel de Cusua – volumen: 5x10^6 m^3.

Parámetros del cálculo

Resolución	5 m	ξ =	0.05	V =	5x10^6 m^3 *
ρ_d =	1400 kg / m^3	v_0 =	90 m/s	Φ_{ds} =	0.2 kg/m²/s
ρ_s =	3 kg / m^3	α =	50	Φ_{sg} =	0.5 kg/m²/s
T_0 =	2500 Pa	t_s =	300 s		

Folder de datos: Cusua4.dat
Folder input: Cusua4.m
Folder .mat: Cusua4.mat

***** el volumen indicado corresponde al volumen total. El volumen que fluye sobre la zona elegida es más pequeño

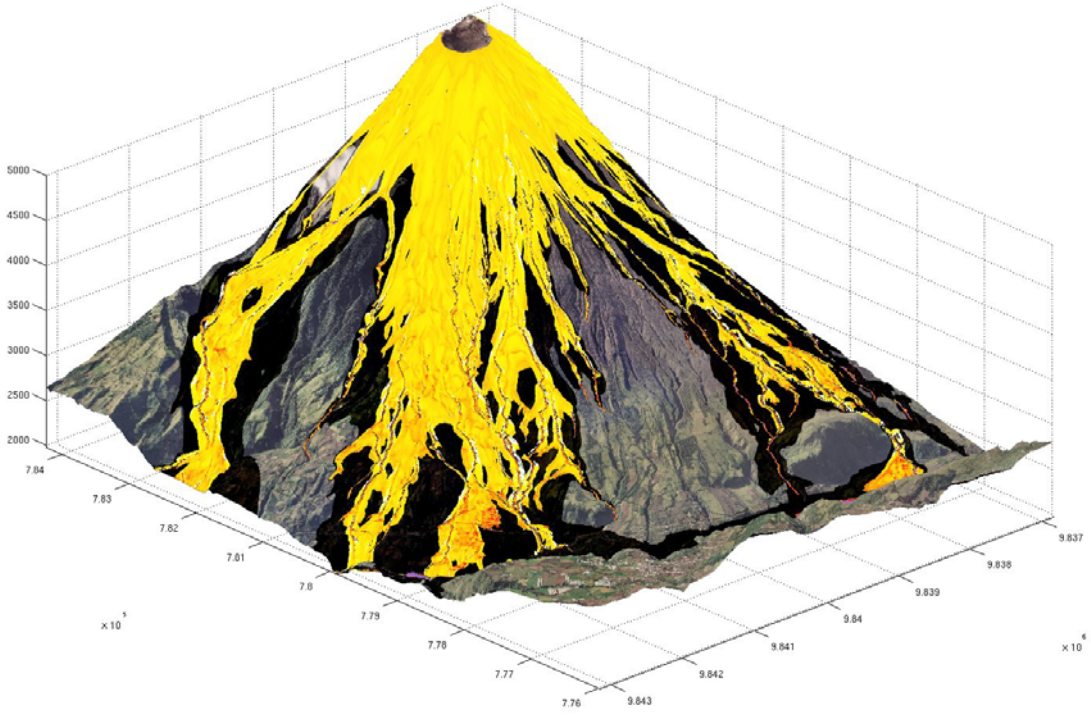

Figura 15: simulación de alta resolución al nivel de Cusua – volumen: 25x10^6 m^3.

Parámetros del cálculo

Resolución	5 m	ξ =	0.05	V =	$25x10^6$ m^3 *
ρ_d =	1400 kg / m^3	v_0 =	90 m/s	Φ_{ds} =	0.2 kg/m²/s
ρ_s =	3 kg / m^3	α =	50	Φ_{sg} =	0.5 kg/m²/s
T_0 =	2500 Pa	t_s =	300 s		

Folder de datos: Cusua3.dat
Folder input: Cusua3.m
Folder .mat: Cusua3.mat

***** el volumen indicado corresponde al volumen total. El volumen que fluye sobre la zona elegida es más pequeño

5.9. Simulaciones 9 – simulaciones de alta resolución, zona de Mapayacu

Los resultados alta-resolución de la zona de Mapayacu reproducen la erupción de agosto del 2006 (Figura 16). Con una taza 5 veces más grande que en el 2006, la zona destruida cambia poco. Todas la barrancas son afectadas por los flujos hasta los ríos Puela/Chambo. Los flujos no tienen ni la velocidad, ni el espesor necesarios para pasar el borde de la caldera al sur del río Mapayacu. Sin embargo, al contrario del 2006, los flujos podrían fácilmente salir de Mapayacu para entrar y fluir dentro del río Shaguil (al oriente de Mapayacu). Las surges podrían penetrar el río El Batán y formar eventualmente flujos densos secundarios por la sedimentación de volúmenes grandes de partículas de surges. La acumulación de sedimentos podría ser fuerte cerca de Palitahua y el pueblo podría ser destruido, tanto por los flujos densos como por los surges y los lahares.

Parámetros del cálculo

Resolución	5 m	ξ =	0.05	T_0 =	2500 Pa
ρ_d =	1400 kg / m^3	v_0 =	100 m/s	Φ_{ds} =	0.05 kg/m²/s
ρ_s =	3 kg / m^3	α =	60	Φ_{sg} =	0.5 kg/m²/s
***V* = 5x10⁶ m³ (Mapayacu_1)**		***V* = 25x10⁶ m³ (Mapayacu_2)**		t_s =	300 s

Folder de datos:	Mapayacu_1.dat	Mapayacu_2.dat
Folder input:	topo_Mapayacu_1.m	topo_Mapayacu_2.m
Folder .mat:	Mapayacu_1.mat	Mapayacu_2.mat

***** los volumenes indicados corresponden al volumen total. El volumen que fluye sobre la zona elegida es más pequeño

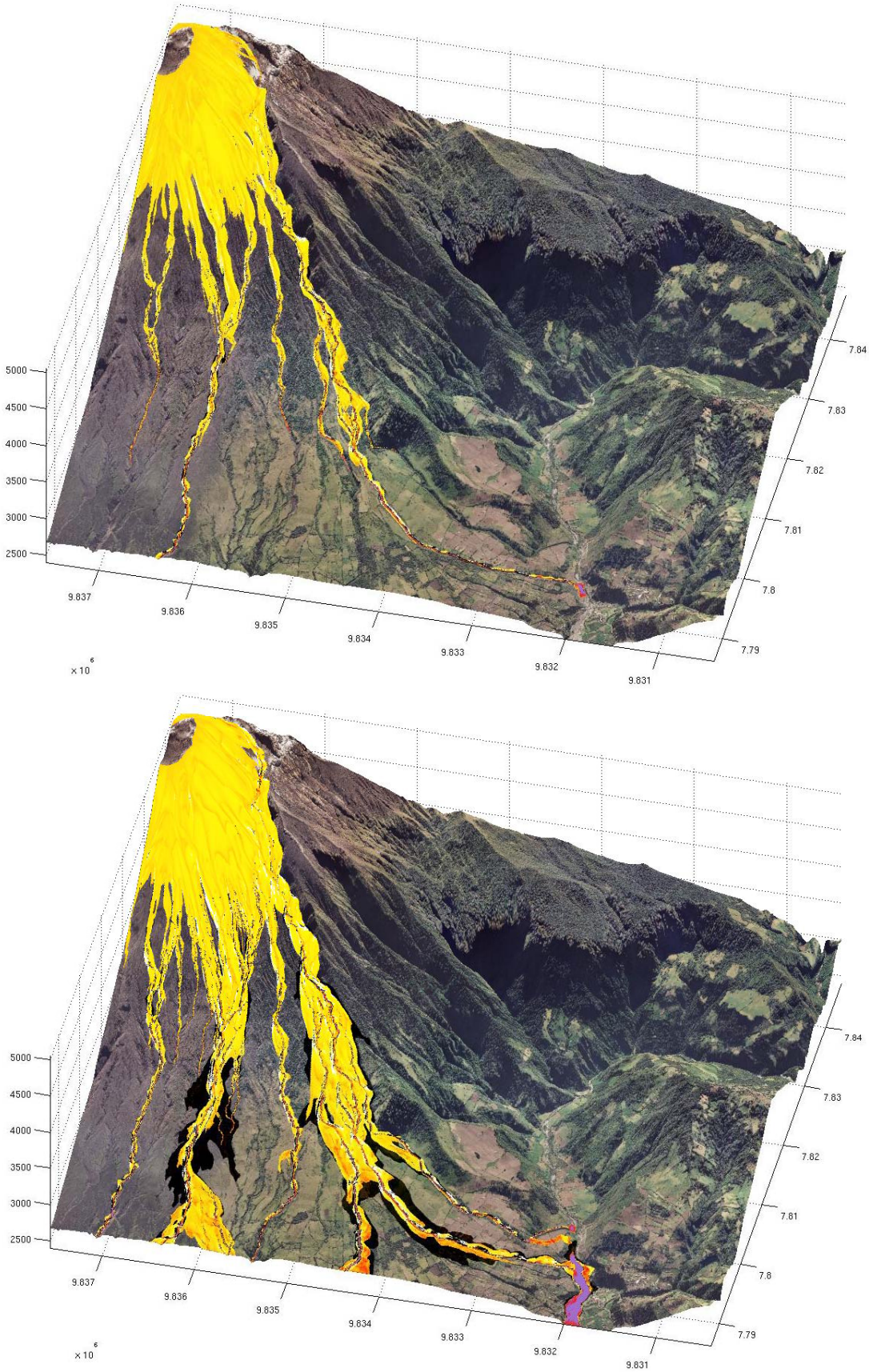

Figura 16: Simulaciones de alta resolución de los flujos de la zona de Mapayacu / Puela para volúmenes de 5 y 25 m^3 (los parámetros utilizados son los de la tabla precedente).

5.10. Inclinación del eje de la columna

La inclinación de la columna influye de manera importante la distribución de los depósitos. Las figuras siguientes simulan los flujos piroclásticos emitidos en 2400 s y con un volumen de 10 millones de metros cúbicos para un eje con inclinación hacia el oeste de 0°, 2° y 4° respecto a la vertical.

Si el eje es vertical, todas las barrancas de oeste a norte (de Mapayacu a Ulba) serán afectadas por los flujos (Figura 17a). Con una inclinación del eje de 4° hacia el oeste, los flujos ya no se forman en los ríos de Vascún, Juive al noroeste, Confesionario, Chonglotus y Mapayu al suroeste (Figura 17c). La masa de la erupción se concentra en los ríos del oeste creando flujos más largos y capaces de desbordar más fácilmente los ríos.

Ligeras variaciones de la morfología del conducto o del cráter pueden entonces explicar que las barrancas al borde de la zona más amenazada (Vazcúm y Ulba al norte, Mapayacu al sur) sean a veces afectadas y a veces a salvo de las erupciones. Una erupción de tipo 2006 podría entonces fácilmente afectar Baños y Ulba con ligeras mordicaciones al nivel del cráter.

El efecto del viento sobre la inclinación de la columna no puede ser determinado a partir del modelo numérico utilizado. Se tendría que utilizar modelos más complejos (multifacéticos 3D).

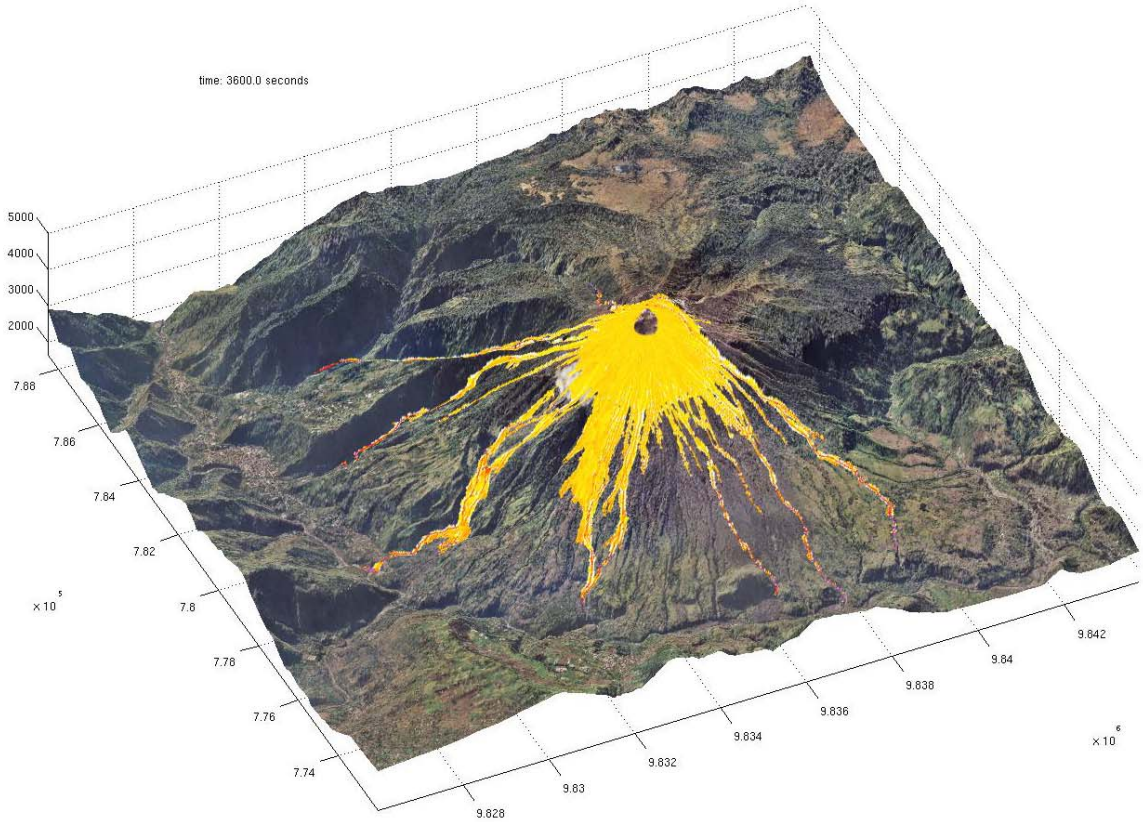

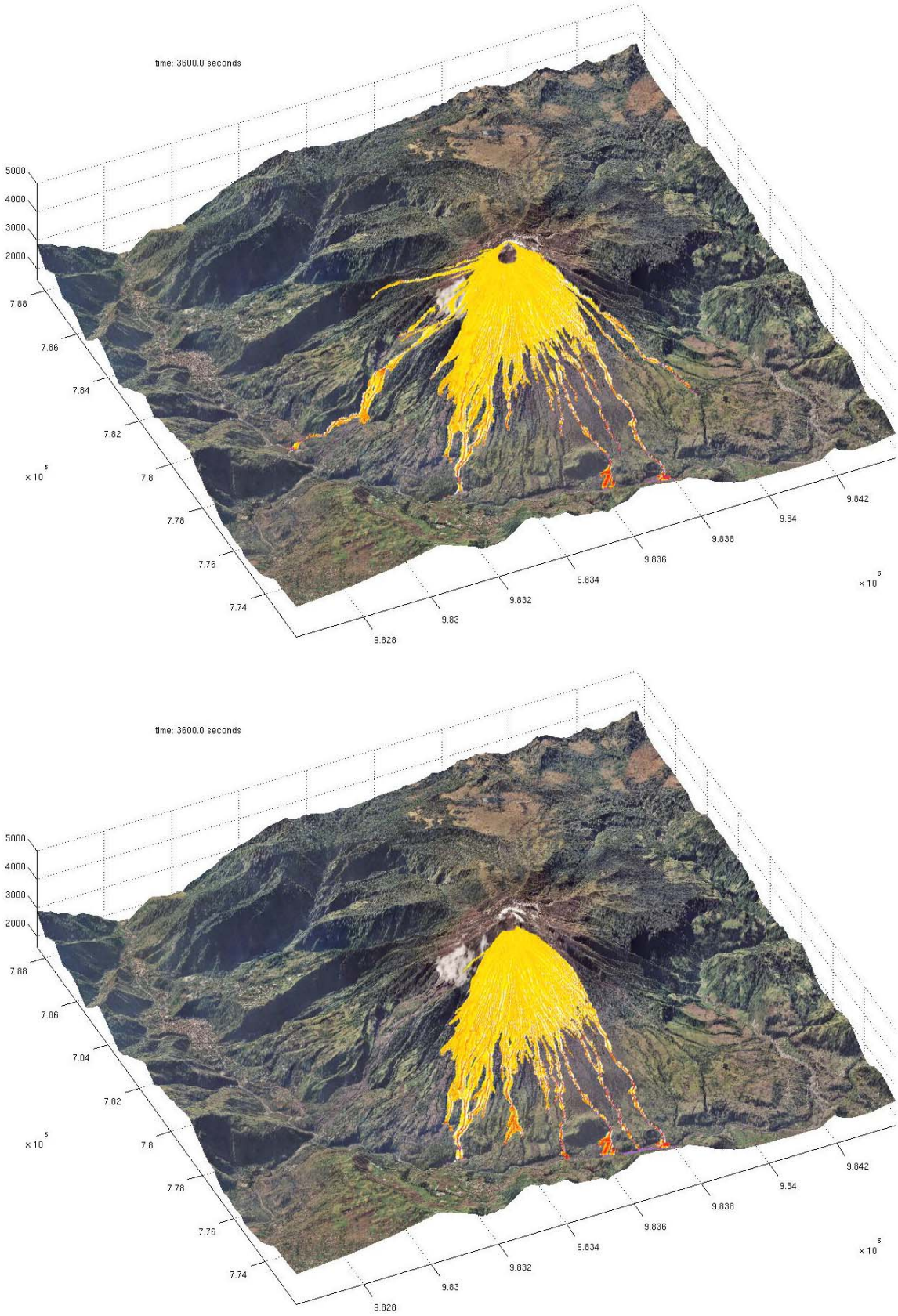

Figura 17 : Distribución de depósitos piroclásticos para ejes de columna inclinados de 0° (vertical), 2° y 4° hacia el oeste. Los parámetros de las simulaciones son los datos de la tabla siguiente.

Parámetros del cálculo

Resolución =	10 m	ρ_d =	1400 kg / m^3	ξ =	0.05	t_s =	2400 s
V =	10^7 m^3	v_0 =	300 m/s	α =	86°	T_0 =	3000 Pa

	axe_variable_0°.dat	*axe_variable_2°.dat*	*axe_variable_3°.dat*
$\Delta\alpha$	0°	2° hacia el oeste	4° hacia el oeste

Folders de datos: axe_variable_0°.dat, axe_variable_2°.dat, axe_variable_4.dat°
Folder input: topo_axe_variable.m
Folder .mat: axe_variable_0°.mat, axe_variable_2°.mat, axe_variable_4.mat°

5.11. Colapso de una parte del cráter del Tungurahua

Las paredes de los cráteres volcánicos se forman a menudo por depósitos cerca del ángulo de estabilidad. Estas son seguido estrechas y debilitadas mecánicamente por gases volcánicos. Una parte puede despegarse y derrumbar.

Esta parte estudia el efecto de un derrumbe de dicho tipo. La zona escogida se sitúa sobre la parte oeste del cráter donde los depósitos inestables parecen ser recientemente acumulados. El volumen se fijó entre 0.5 y 1.5 millones de m^3. La figura 18 presenta la zona supuesta a desestabilizarse.

El comportamiento plástico se escogió para simular un derrumbe de ese tipo. Este reproduce bien tanto el comportamiento de los flujos piroclásticos como las avalanchas de escombros (Kelfoun and Druitt, 2005 ; Kelfoun et al., 2009). Es difícil sin embargo fijar el valor del límite de plasticidad (**T** = (T_x, T_y) en las ecuaciones 2 y 3) de un derrumbe de éste tipo, pues éste último depende mucho de la cohesión inicial del material que se derrumba. Es por esto que se utilizaron 3 valores: 2 500 Pa, 10 000 Pa y 25 000 Pa. 2 500 Pa correspondería a la mezcla de partículas finas no cohesivas (escorias y cenizas secas recientemente acumuladas), 25 000 Pa a un material consolidado.

Las simulaciones indican que las zonas amenazadas se sitúan alrededor de los ríos La Hacienda, Cusua y Achupashal (Figura 19). Un derrumbe inmediato de 1.5x10^6 m^3 de material consolidado formaría depósitos espesos y limitados a las zonas inhabitadas (zona roja, Figura 19). El mismo derrumbe compuesto de material fino no cohesivo llegaría hasta el río Chambo entre 3 y 4 minutos, destruyendo los alrededores de los ríos (el gran espesor del flujo provocaría un desbordamiento en las quebradas). El pueblo de Cusua parece ser a salvo del derrumbe de un tal volumen de material gracias a la topografía local.

Un volumen menor, de 0.5×10^6 m^3 con un valor de T_0=2500 Pa, da flujos más cortos: ~ 5 km en el río Cusua, por ejemplo, mientras que estos son de 7 km con un volumen de 1.5×10^6 m^3.

Sin embargo, un derrumbe más voluminoso y por lo tanto más espeso podría desbordar las quebradas y sobrepasar los relieves hasta destruir el pueblo. La extensión estando fuertemente liada al volumen desestabilizado, es por lo tanto esencial determinar el volumen de la parte que se puede desestabilizar si una amenaza de este tipo se considera como seria.

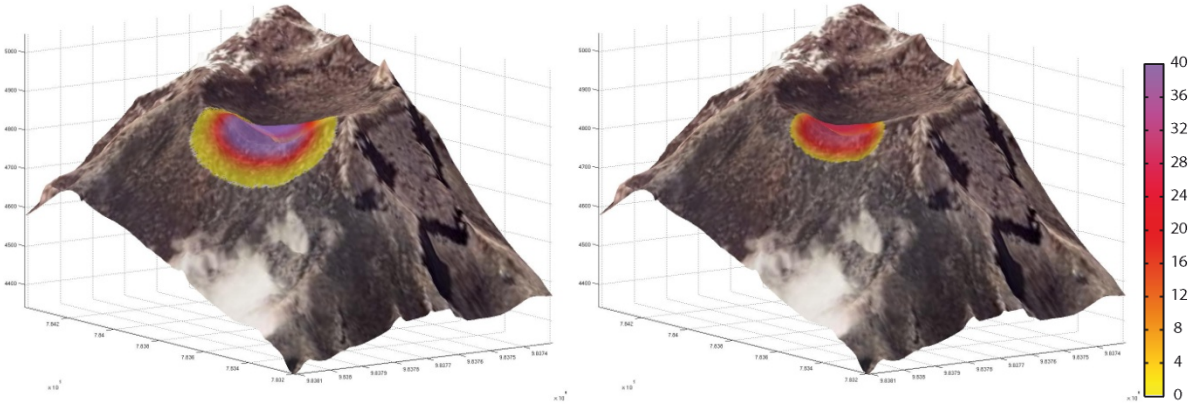

Figure 18 : formas y espesores de las zonas desestabilizadas en las simulaciones 1 a 3 (izquierda) y 4 (derecha).

La detonación de este tipo de derrumbes es generalmente muy rápida (no se sabe generalmente detectar las señales precursoras) y la activación de los flujos es muy rápida (de 3 a 4 minutos para llegar a las zonas habitadas) volviendo difícil la previsión del derrumbe y la evacuación de las zonas amenazadas.

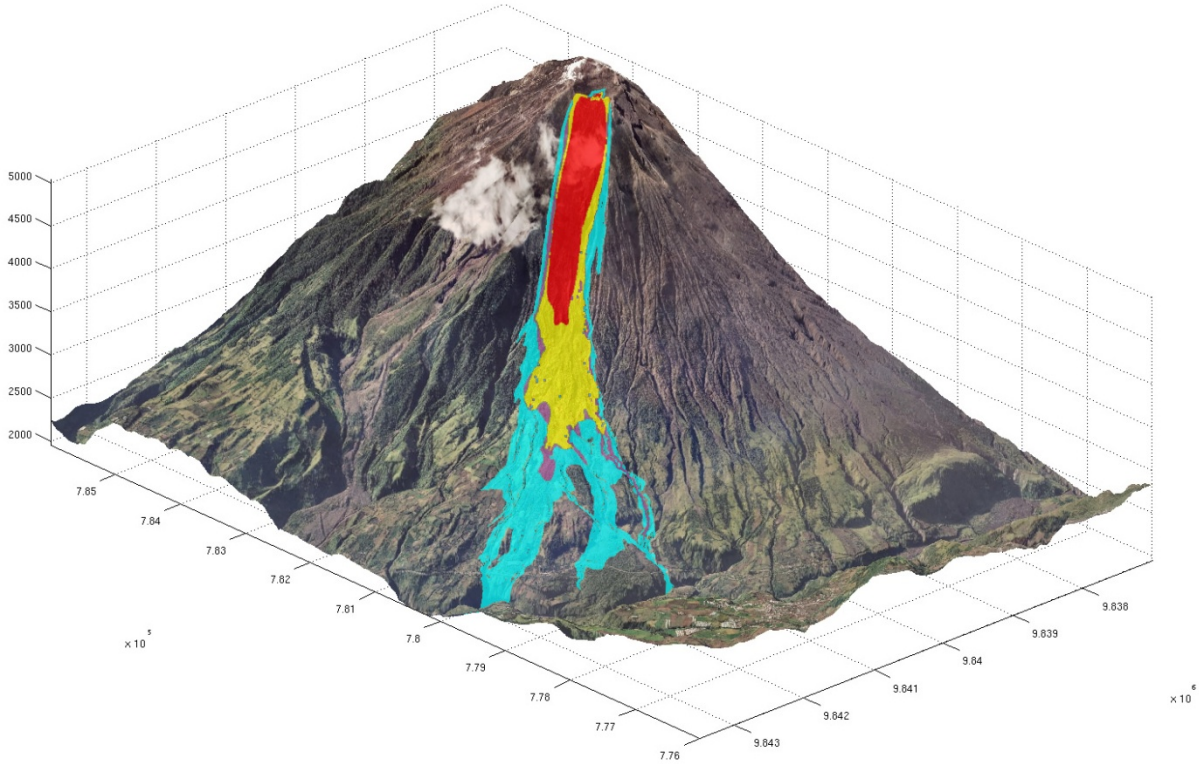

Figure 19 : zonas afectadas por el derrumbe de una parte del cráter del Tungurahua. Los parámetros de las simulaciones se pueden consultar en la tabla siguiente. Los cuadros de color de la tabla corresponden a los colores de la figura (ver animación adjunta: collapse_1.avi).

Resolución 10 m ρ_d = 1600 kg / m^3 ξ = 0.05

	collapse1.dat	*collapse2.dat*	*collapse3.dat*	*collapse4.dat*
T_0	2500	10000	25000	2500
V	1.5×10^6 m^3	1.5×10^6 m^3	1.5×10^6 m^3	0.5×10^6 m^3

Folders de datos: collapse_1.dat, collapse_2.dat, collapse_3.dat, collapse_4.dat
Folder input: topo_collapse_1.m, topo_collapse_2.m, topo_collapse_3.m, topo_collapse_4.m
Folder .mat: collapse_1.mat, collapse_2.mat, collapse_3.mat, collapse_4.mat

6. Conclusiones

Las simulaciones nos permiten sacar las conclusiones siguientes sobre los riesgos eruptivos del volcán Tungurahua.

1) Las tasas más elevadas (~10 veces más que en el 2006) crean flujos rápidos y espesos. Estos pueden desbordar localmente algunas barrancas, pero globalmente el efecto de la tasa sobre la extensión de las zonas destruidas por los flujos densos es relativamente débil. Sin embargo, una tasa más elevada provoca una velocidad más elevada del flujo y por lo tanto un tiempo para la evacuación reducido.

2) Tasas importantes provocan una velocidad de flujos densos elevada que producirá surges piroclásticas poderosas. Esta amenaza es muy importante para las poblaciones. Actualmente, no es posible simular exactamente su producción.

3) Si varios flujos piroclásticos se suceden, los depósitos pueden acumularse en el desembocadero de las barrancas y destruir las zonas vecinas. Esta amenaza debe tomarse seriamente en cuenta para la ciudad de Baños.

4) Las distancias a las que llegan los flujos densos son muy sensibles a las condiciones de la fuente para tasas inferiores a las del 2006.

5) Los flujos pueden sin problema llegar hasta Baños y afectar los alrededores de los ríos Vazcúm y Ulba. Muy pequeñas variaciones de los parámetros eruptivos del 2006 son suficientes para que los flujos puedan llegar a zonas habitadas.

6) Si las tasas fueran únicamente 2 veces más fuertes que en el 2006, los ríos Ulba y Vazcúm podrían ser afectados hasta el río Pastaza. La evacuación de Baños seria entonces particularmente delicada sobre todo puesto que los flujos podrían destruir los puentes del Pastaza.

7) La inclinación de la columna eruptiva de 1 o de 2° tiene una influencia importante sobre la distribución de los depósitos.

8) El derrumbe de alrededor de 1 millón de metros cúbicos de la parte noroeste del cráter podría destruir las zonas habitadas localizadas alrededor del pueblo de Cusua.

9) Una vez los flujos activados, el tiempo de evacuación puede ser muy corto: < 7 minutos para flujos densos y < 4 minutos para un derrumbe proveniente de la zona somital. La rapidez de los flujos depende esencialmente de la tasa en la fuente. Una tasa más baja o un derrumbe progresivo permitirían disponer de tiempos de evacuación más largos.

10) Es importante remarcar finalmente, que sí estas conclusiones son correctas, los resultados no pueden utilizarse para delimitar con exactitud las zonas a evacuar de las zonas sin evacuación necesaria. La física de los flujos piroclásticos no se conoce muy bien aún. Los flujos son muy sensibles a las condiciones de la fuente y estas condiciones no pueden actualmente ser determinadas. Finalmente, las simulaciones concertando los volúmenes más pequeños son muy sensibles a la calidad de la topografía numérica. Puesto que esta muestra en varios lugares, la falta/interpolación de datos. Finalmente, es imposible tomar en cuenta los cambios perpetuos de la topografía que se producen sobre este tipo de volcanes activos.

Références bibliographiques

Gray, J. M. N. T., Y.-C. Tai, and S. Noelle (2003), Shock waves, dead zones and particle-free regions in rapid granular free-surface flows, J. Fluid Mech., 91, 161– 181.

Heinrich, P., G. Boudon, J. C. Komorowski, R. S. J. Sparks, R. Herd, and B. Voight (2001), Numerical simulation of the December 1997 debris avalanche in Montserrat, Lesser Antilles, Geophys. Res. Lett., 28, 2529– 2532.

Iverson, R. M. (1997), The physics of debris flows, Rev. Geophys., 35(3), 245– 296.

Kelfoun, K., and T. H. Druitt (2005), Numerical modeling of the emplacement of Socompa rock avalanche, Chile: *J. Geophys. Res.*, 110, B12202.1−12202.13, doi: DOI 10.1029/2005JB 003758.

Kelfoun, K., P. Samaniego, P. Palacios, and D. Barba (2009), Is frictional behaviour suitable for pyroclastic flow simulation: comparison with a well constrained eruption at Tungurahua volcano (Ecuador), *Bull. Volcanol.,* 71(9), 1057−1075, doi: 10.1007/s00445−009−0286−6.

Mangeney, A., P. Heinrich, and R. Roche (2000), Analytical solution for testing debris avalanche numerical models, Pure Appl. Geophys., 157, 1081– 1096.

Patra, A. K., et al. (2005), Parallel adaptative numerical simulation of dry avalanches over natural terrain, J. Volcanol. Geotherm. Res., 139, 1– 21.

Pouliquen, O., and Y. Forterre (2002), Friction law for dense granular flows: Application to the motion of a mass down a rough inclined plane, J. Fluid Mech., 453, 133– 151.

Savage, S. B., and K. Hutter (1991), The dynamics of avalanches of granular materials from initiation to runout. part I: Analysis, Acta Mech., 86, 201– 223.

Shaller, P. J. (1991), Analysis and implications of large Martian and terrestrial landslides, Ph.D. thesis, 586 pp., Calif. Inst. of Technol., Pasadena.

Takarada, S., T. Ui, and Y. Yamamoto (1999), Depositional features and transportation mechanism of valley-filling Iwasegawa and Kaida debris avalanches, Japan, Bull. Volcanol., 60, 508– 522.

Toro, E. F. (2001), Shock-Capturing Methods for Free-Surface Shallow Flows, 309 pp., John Wiley, Hoboken, N.J.

Van Wyk de Vries, B., S. Self, P. W. Francis, and L. Keszthelyi (2001), A gravitational spreading origin for the Socompa debris avalanche, J. Volcanol. Geotherm. Res., 105, 225–247.